UNIVERSITY OF CALIFORNIA

Los Angeles

# Mechanical Antenna Simulations via Finite Difference Time Domain Methods

A dissertation submitted in partial satisfaction of the requirements for the degree Doctor of Philosophy in Aerospace Engineering

by

Jesse Rivera

2024

ABSTRACT OF THE DISSERTATION

Mechanical Antenna Simulations

via Finite Difference Time Domain Methods

by

Jesse Rivera

Doctor of Philosophy in Aerospace Engineering

University of California, Los Angeles, 2024

Professor Yuanxun Wang, Co-Chair

Professor Gregory P. Carman, Co-Chair

Barriers that have separated different domains of physics and isolated engineers within the silos of their own expertise have been continually eroding in recent decades. Potential exotic devices of the future continue to be actualized through designs which are optimized by evoking multiple engineering disciplines. One such family of novel devices are electrically small multiferroic mechanical resonance-based antennas, which couple acoustic and electromagnetic phenomenon, allowing for sizes which are roughly five orders of magnitude smaller than conventional antennas. As such, the ability to understand these tiny and more efficient antennas through the development of a numerical algorithm benefits a wide array of industries by allowing engineers to optimize designs without undue prototyping. For example, such a numerical algorithm would allow smaller conformal antennas on the outer skin of aircraft to be designed faster, as well as small minimally invasive implantable biomedical antennas which may serve a myriad of functions to improve patient quality of life.

The first chapter of this work provides a history of antennas, highlighting limitations to motivate interest in pursuing mechanical resonance-based radiators. Background information on the operating principle of these antennas and a literature survey follows. The second and third chapters then formulate the numerical model by presenting the continuum form of all requisite equations in the former chapter and then discretizing these expressions in the latter chapter. The finite difference time domain method is leveraged for discretization and all relevant numerical artifacts such as boundary conditions, interface conditions, and excitations are derived. The algorithm is then validated versus analytical solutions in the fourth chapter of this work to champion the reliability of the proposed numerical framework. The dissertation capstone is the fifth chapter which utilizes the code to conduct simulations on novel devices, demonstrating a large boost in performance with respect to the state of the art.

This dissertation also features guidelines for prospective modelers based on lessons learned from the author during the model formulation process. Device simulations from chapter 5 also provide engineers with useful counsel on future piezoelectric antenna array designs. This work presents a comprehensive procedural guide for the full-wave simulation of mechanical resonance-based antennas, effectively bridging a gap in the existing literature which deals almost exclusively in lower fidelity equivalent circuit models.

The dissertation of Jesse Rivera is approved.

Robert N. Candler

Ajit K. Mal

Yuanxun Wang, Committee Co-Chair

Gregory P. Carman, Committee Co-Chair

University of California, Los Angeles

2024

## DEDICATION

This work is dedicated to the most Holy Trinity, my wife, my family, and all who sacrificed much so that I can complete this manuscript.

# TABLE OF CONTENTS

## LIST OF FIGURES

# LIST OF TABLES

## ACKNOWLEDGEMENTS

The work discussed in this dissertation was funded by the NSF Nanosystems Engineering Research Center for Translational Applications of Nanoscale Multiferroic Systems (TANMS), supported by the National Science Foundation under Cooperative Agreement Award EEC-1160504.

Technical support and mentoring for the research discussed in this dissertation was provided by the following individuals: Yuanxun Ethan Wang, Zhi Jackie Yao, Gregory Carman, Robert Candler, Rashaunda Henderson.

Moral support was provided by: Dayhana Preciado, Fr. Jamie Baca, the University Catholic Center, Matthew McIntosh, Emily Burnside, Pilar O'Cadiz, my parents, my band mates, all the folks over at Antelope Valley Jiu Jitsu, and John Blaske.

# VITA

## EDUCATION

**University of Southern California**, Los Angeles

- Master of Science Degree in Aerospace Engineering May 2018

**California State University**, Northridge

- Bachelor of Science Degree in Mechanical Engineering May 2015

## SELECTED PRESENTATIONS

- August 2021: Oral presentation at International Applied Computational Electromagnetics Society (ACES) Symposium, “Verification Testing of Multi Dynamical Solver for Multiferroic Antennas”
- September 2022: Oral presentation at NSF ERC Biennial Meeting Perfect Pitch Competition, “Healing Broken through Multiferroic Antennas”
- September 2022: Poster session at Gordon Research Conference on Multifunctional Materials and Structures, “Multi-Scale Unconditionally Stable Solver for Multiferroic Antennas”

## JOURNAL PUBLICATIONS

- Rivera, J., Blaske, J., Yao, Z., Zheng, R., Carman, G., Wang, Y. (2024). *Mechanical Antenna Simulations via FDTD to Characterize Mutual Depolarization*. [Manuscript submitted for publication].
- Rivera, J., Blaske, J., Yao, Z., Zheng, R., Carman, G., Wang, Y. (In work) *Mechanical Antenna Bandwidth Bending via Alternate Poling Multimode Resonance*. [Manuscript in preparation].
- Yao, Z., Tiwari, S., Lu, T., Rivera, J., Luong, K., Candler, R., Carman, G., Wang, Y. (In press). Modeling Multiple Dynamics in the Radiation of Bulk Acoustic Wave Antennas. *IEEE Journal on Multiscale and Multiphysics Computational Techniques, Vol. 5, 2020.*

# CHAPTER 1: BACKGROUND AND HISTORY

In this chapter, a brief history of the multiple dynamic equations which mechanical resonance based (MRB) antennas utilize will be presented. Both multiferroic (MF) antennas and piezoelectric antennas (PEAs) fall under this umbrella. Then, the history of antennas will be discussed, with special emphasis on current issues affecting new designs within the aerospace and biomedical industries, amongst others. A statement on what ferroic materials are, and how they can be combined in composite structures to achieve coupling between electric and magnetic energy (for multiferroic antennas) will follow. Since piezoelectric antennas operate under similar principles, a brief discussion on these devices follows. Penultimately, a word on what multiferroic (MF) and piezoelectric antennas are, and the physical principals that undergird these novel devices will be provided. Lastly, an overview of the dissertation will conclude the chapter.

## 1.1 Introduction

Antennas are devices which are designed to radiate and receive electromagnetic signals and are the bedrock for successful performance within wireless communications systems. In recent decades the demand for a paradigm shift in antenna design has echoed through academia and industry alike as new applications in electrically lossy environments continue to emerge and data rate increases continue to be desirable. This is additionally spurred on by the benefit of integrating system components to reduce the noise floor, and the need to miniaturize antennas operating at low frequencies. The antennas of the future, therefore, need to be smaller, more efficient in lossy environments, conformal to ground planes while avoiding the platform effect, amongst other requirements. All which hint at a mechanical resonance based (MRB) antenna solution, the simulation of which requires the numerical integration of multiple dynamic systems including Newton's laws, Maxwell's equations, and potentially the Landau-Lifshitz-Gilbert (LLG) equation in the case of multiferroic antennas.

In this chapter, these three dynamic equations will be introduced first. Then a history on antennas will be presented in order to paint the picture of the current challenges in antenna design, and to argue why multiferroic and piezoelectric antennas rise to these challenges. Ferroic orders, stress, strain, and linear elasticity will then be introduced. Ferromagnetism and ferroelectricity will then be discussed in order to understand what a multiferroic system is. Finally, mechanical resonance based (MRB) antennas will be discussed in detail.

### 1.1.1 Multiple Dynamic Systems w/ History

In 1687, Sir Isaac Newton's pivotal work "Mathematical Principles of Natural Philosophy" is first published, revolutionizing mathematics and physics alike [1][2]. Among the key insights provided by the Principia, as it is often truncated, are the law of universal gravitation and a derived form of Johannes Kepler's laws of planetary motion. So important is this work that Newton's own annotated copy is kept in the Wren Library at Trinity College, Cambridge (see Figure 1-1) and a 1st edition copy recently sold for $3.7 million [3].

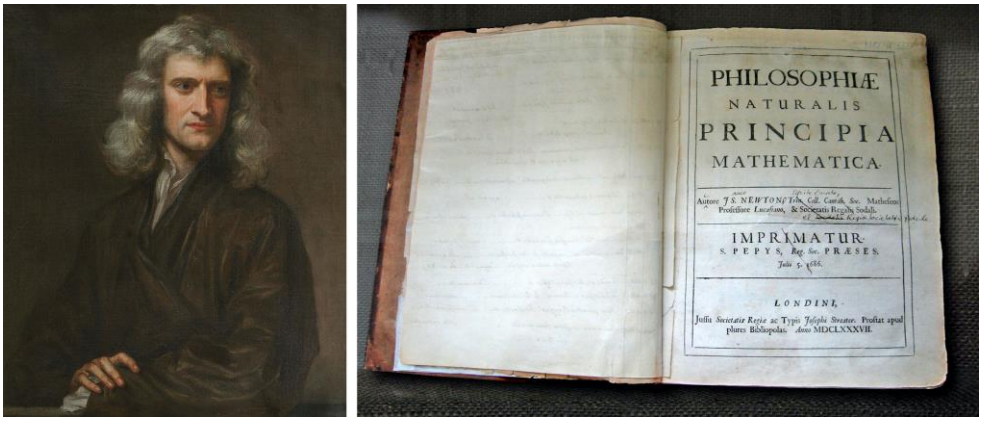


Figure 1-1: Sir Isaac Newton along with a picture of his own personal copy of his Principia

The most important part of the Principia for this work are Newton's laws of motion. More specifically, the primary concern is in the conservation of linear momentum which states that, in order to have any accelerations, there must be a net force on a body. As stated, this implies the

mass is constant which is a consistent assumption herein. This is the fundamental equation when considering mechanical wave fluctuations. For example, consider a wave propagating horizontally through a medium while generating vertical displacements as shown in Figure 1-2.

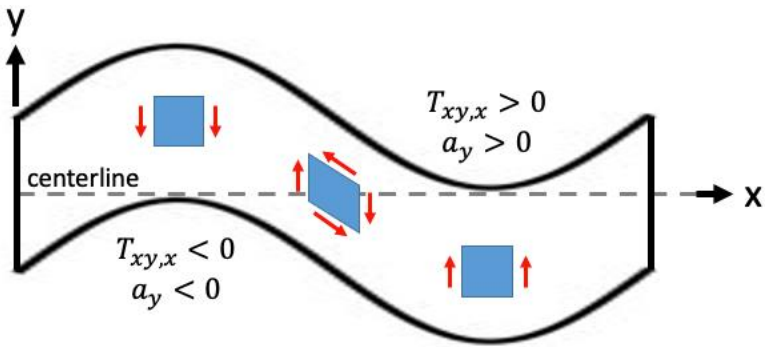


Figure 1-2: Bulk shear wave propagation and the effects on an element originally on the centerline.

Note that it has been assumed that vertical planes remain plane and do not change orientation during the motion (bulk shear wave [4]). The forces acting on the edges of a square element are drawn at different stages of the wave. Note that when the element is above the centerline, the net forces cause downward acceleration back toward the centerline. A similar behavior is observed when the element is below the centerline. In mechanics of materials terms, the acceleration is said to be caused by a “stress divergence”, where the stress (denoted $T$ in Figure 1-2) is a second order tensor describing the force over area acting on a body [4-6]. This will be explored more in section 1.1.3 and in chapter 2.

In addition to linear momentum, angular momentum is similarly related to the net torques acting on a body. This leads to the symmetry of the stress tensor in mechanics, but interestingly also has impact in the realm of magnetics. This is due to an intrinsic property of electrons to act like tiny magnets [7-11], hinted at by the Stern-Gerlach experiment [7] and others, known as spin. This was first proposed in 1924 by Uhlenbeck and Goudsmit [8][9] in response to failure of

contemporary models of the electron which only considered angular momentum generated as the electron orbits the nucleus (orbital angular momentum). The angular momentum aspect is important because moving charges create magnetic fields, as first demonstrated by Hans Christian Oersted in 1819 when he discovered magnetic fields around a current carrying conductor [12][13], beginning the field of electromagnetism. Therefore, electron magnetic properties cannot be divorced from the angular momentum that creates them, the two are synonymous and the study of their interaction is known as micromagnetics. To facilitate understanding, consider the simplest case of a magnetic field being generated by charge motion, namely the current loop shown in Figure 1-3:

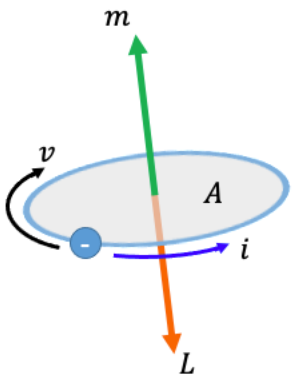


Figure 1-3: Magnetic dipole moment generated by current loop.

As the electron revolves with velocity $v$ a current $i$ is generated in the opposite direction. This generates an angular momentum $L$ and magnetic dipole moment $m$ simultaneously, which are anti-parallel to one another since the electron has a positive mass but a negative charge. Within a material, the spin angular momentum of the outer valence electrons couple to the orbital angular momentum. The orbital and spin motion then couple to the lattice, generating macroscopic magnetic moments within the material in what are known as magnetic domains [8][9]. On the macroscale, the parameter of interest is typically the dipole moment per unit

volume, which is known as the magnetization [14] and is on the same level of importance in mircromagnetics as displacement is in mechanics. A conservation of angular momentum equation exists for the electron as first proposed by Landau and Lifshitz in 1935 [15]. This was later modified by Gilbert in 1955 [16] to what is now known as the Landau-Lifshitz-Gilbert (LLG) equation which governs micromagnetics. Both forms are widely in use today and demonstrate that the motion of the magnetization is precessional in nature, like a spinning top, about an effective magnetic field excitation. For the sake of brevity, the details are left for Chapter 2.

In 1861-1862, James Clerk Maxwell introduced an early form of his famous equations within a four-part series “On Physical Lines Force” [17-20] and later he compiled his work into “A Treatise of Electricity in Magnetism” in the form of twelve equations [21]. It was not until 1893 that Oliver Heaviside condensed Maxwell’s equations down to the four that are widely used today [22-24]. Maxwell’s equations are the governing equations behind electromagnetic radiation [25], and are summarized in Figure 1-4:

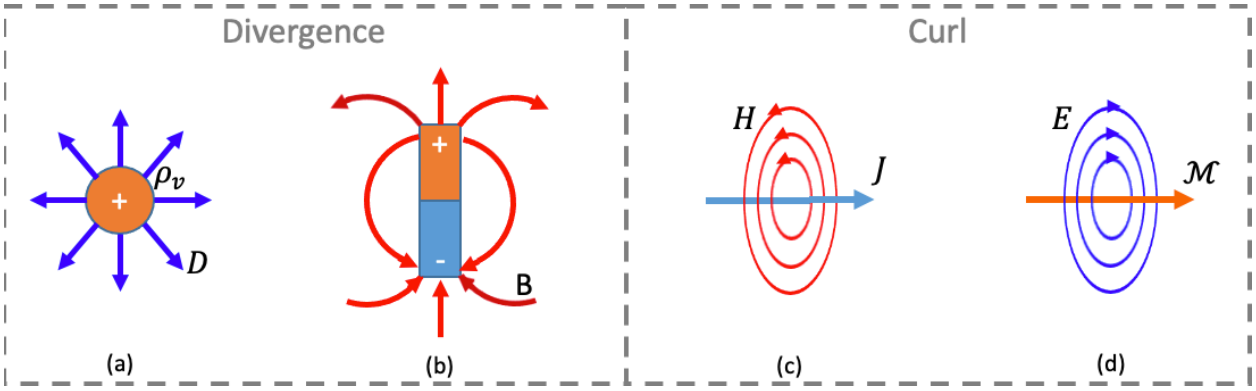


Figure 1-4: Maxwell’s Equations, (a) Gauss’s Law, (b) Gauss’s Law for Magnetism, (c) Ampere’s Law, (d) Faraday’s Law

Maxwell’s equations are split into two sets, known as the divergence equations and the curl equations. Gauss’s Law (Figure 1-4a) states that the number of electric flux lines $D$ diverging

from a point in space is proportional to the charge density $\rho_v$ in that space. Therefore, If the net charge within a surface is zero the amount of flux lines going out equals the amount coming back in. Gauss's law for magnetism (Figure 1-4b) states that the divergence of the magnetic flux lines $B$ from a point must be zero always. In other words, there is no such thing as a magnetic monopole. Wherever a north pole exists, there must be a south pole and vice versa. More interesting in terms of electromagnetic radiation are the curl equations. Ampere's law (Figure 1-4c) states that any form of electric current $J$ will induce swirling magnetic field lines $H$ whose direction may be determined by the right-hand rule, namely placing one's right thumb in the direction of the current and wrapping the fingers in the direction of magnetic field. Conversely, Faraday's law (Figure 1-4d) states that any form of magnetic current $\mathcal{M}$ will induce swirling electric field lines $E$ whose direction may be determined by the left-hand rule, namely placing one's left thumb in the direction of the current and wrapping the fingers in the direction of electric field. This back-and-forth induction of EM fields is what produces electromagnetic waves, and Maxwell was the first to postulate that light itself was this type of wave [21]. This set the stage for the explosion of antenna technology that started with Rudolph Hertz and continues to this day.

### 1.1.2 Antenna History and Motivation

Antennas fundamentally act as the components that propagate EM energy out into free space (transmitter) or accept EM energy from free space (receiver). By Ampere's law of induction, a current through a wire will be surrounded by swirling field lines, but these will not detach from the current source and propagate. To accomplish such radiation, the current itself must change with time, in other words charges must be accelerated not simply moved at constant velocity. Accelerations, however, need not be generated by changing velocity magnitude, directional changes also produce this effect. Therefore, the current carrying wire may be curved, bent, terminated, etc. in order to produce an antenna [26].

In 1886, Professor Heinrich Rudolph Hertz was the first to demonstrate wireless electromagnetic communication [26-28] when he was able to produce a spark within the gap of a metallic square loop antenna by first producing a spark in a nearby transmitting dipole antenna, as shown in Figure 1-5:

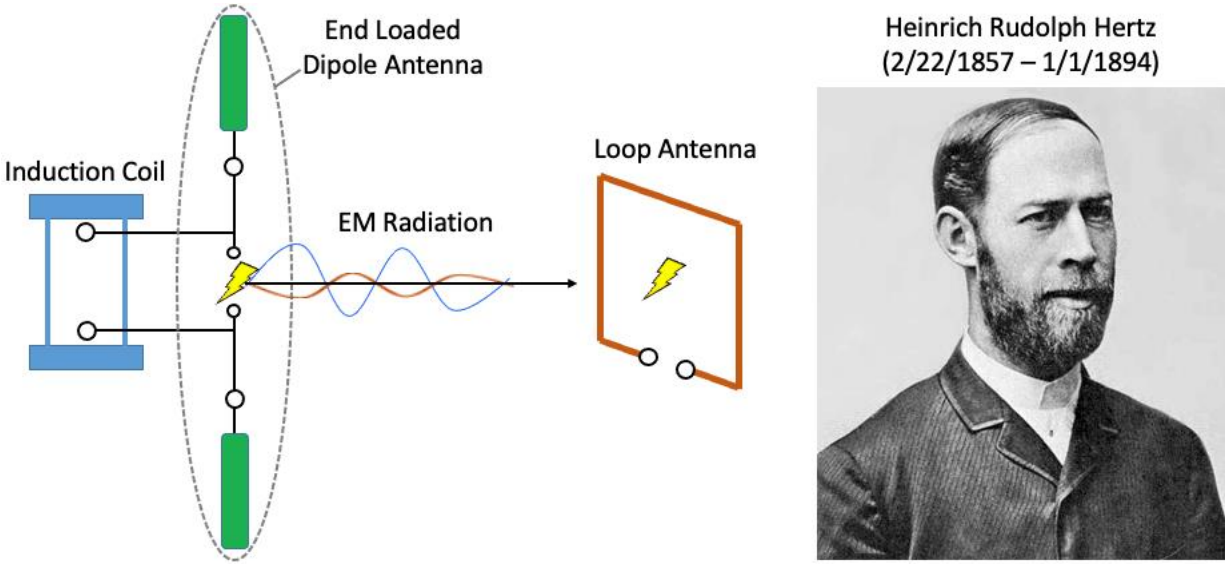


Figure 1-5: Heinrich Hertz along with his 1886 complete radio system.

This was performed within Professor Hertz's laboratory; it was not until 15 years later that Guglielmo Marconi successfully transmitted long distance. In 1901, Marconi sent the first transatlantic signals from Poldhu in Cornwall, England, to St. John's, Newfoundland [26-28]. His transmitting antenna was an array, rather than a single element, composed of 50 vertical wires arranged in a fan-like configuration, while his receiving antenna was a 200m wire pulled and supported by a kite. This great success may have been the dawn of the antenna era, but it was met with some skepticism at first from those that did not believe that radio waves could bend to match the curvature of the Earth [28]. Even amongst believers there was controversy, as the Cable Company served Marconi with a writ to cease and desist as transatlantic communications

was within their exclusive domain. In the end, however, the truth and positive impact of what happened that day in 1901 could not be denied and wire related antennas would go on to dominate the state of the art for decades to come.

World War II saw the rise of novel antenna designs which took advantage of aperture fields (waveguide apertures, horns) as well as bouncing signals off reflective surfaces (reflectors) and other methods. This was not only driven by the war itself, but also from the fact that reliable microwave sources became readily available in the 1940s [27][29]. Shortly thereafter, the microstrip patch antenna was proposed in the 1950s [30-32] but not fully investigated until the 1970s. This type of antenna is comprised of a metallic patch printed onto an electrically thin grounded dielectric material which when excited produces radiating aperture fields along two slots [26][29][30] as shown in Figure 1-6. This occurs because the device size between the two radiating slots is roughly a half wavelength. Therefore, the surface normals ($\hat{n}$) and electric fields ($E$) on the slots are both opposite in direction with respect to one another, yielding two effective magnetic currents ($\mathcal{M}$) with the same sense ($\mathcal{M} = E \times \hat{n}$) [25][30].

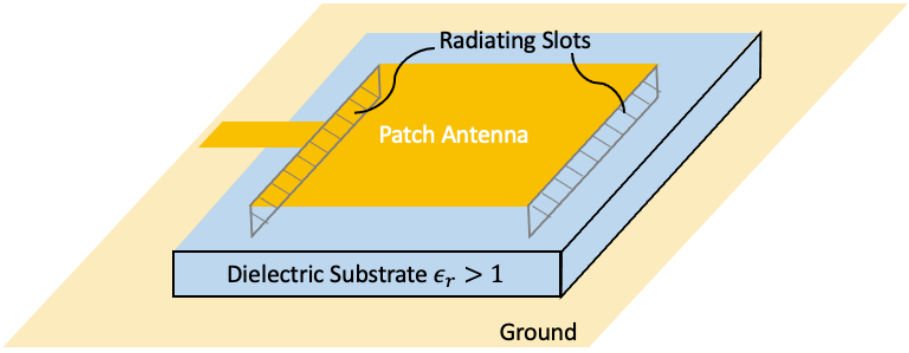


Figure 1-6: Microstrip Patch Antenna

The patch antenna is given special attention here due to its wide use in both military and civil applications including cellphones, biomedical systems, and radar. This is because patch antennas may be readily integrated into arrays conformal to surfaces, at low-weight and low-

cost [30]. As such, the fundamental question for any novel antenna designs is this: “how is this antenna any better than just printing a piece of copper onto a board?”. This question has proven surprisingly difficult to overcome for many exotic devices currently under investigation. In order formulate an answer it is important to remember that patch antennas struggle with the prevalent miniaturization issues when made sufficiently electrical small ($< \lambda_0/50$) with respect to $\lambda_0$, the free space EM wavelength. These issues are reduced radiation resistance, large stored vs. radiated energy ratios (Q-factors), and reduced radiation efficiency as ohmic losses become more pronounced [33-37]. This is further exacerbated if the electrically small antenna is radiating near a conductive surface due to the platform effect [38], or if the antenna is operating within lossy electrically conductive environments such as through the water [39], ground [40], or the human body [41]. Platform effect reduction augments the performance of conformal antennas [30] which are widely used in the aerospace industry [42-45], while improvements in water communications would benefit submarine applications [46] and through body communication aids the implantable device industry [47-50], just to name a few beneficiaries. In the remainder of this introductory section, the ohmic losses, platform effect, and lossy environment issues will be discussed in-depth along with potential solutions. It is then shown that all these potential solutions point to multiferroic antennas, which will be examined in section 1.2 along with piezoelectric antennas which partially solve these issues.

In 1827, Georg Ohm publishes his work on electrical resistance [51] which gave rise to Ohm’s law, a now seemingly obvious equation which states that electrical energy is lost as current passes through a wire [52]. This energy loss increases drastically as wire diameter is decreased, the same way that car speeds inevitably drop when there are less lanes on the highway [53], or the way fluid velocity drops just upstream of an orifice [54]. As such, drastic miniaturization in wired devices, by five orders of magnitude for example, would be akin to shutting all but one lane down in a multi-highway network, or trying to suck a milkshake out of a

coffee straw. Clearly, for such shrinkage of device dimensions to occur, wire-based methods, which dominated the antenna space for over 40 years, had to be replaced by some other methodology for many applications. To this end, Mechanical resonance based (MRB) antennas are electrically driven by a voltage across electrodes, rather than current through wires [55], eliminating this issue as will be discussed further in section 1.2. Although this is substantially beneficial, ohmic losses are mentioned first since this advantage is one that mechanical antennas share with other antennas (e.g., patch antennas). These antennas suffer from other miniaturization issues that MRB antennas (multiferroic and piezoelectric) can utterly avoid however, which will be discussed in section 1.2.2.

The platform effect is caused when the antenna element operates using electrical currents which are tangent to a nearby conducting surface. This is caused by the near cancellation of the radiation due to the anti-parallel image currents that are generated by the presence of the conductive surface when in close proximity [25][26][29]. Additionally, a large amount of energy is stored between the current and the conducting surface which increases the Q-factor [38]. If the antenna were magnetic current driven, however, the image current would be parallel instead, and the near cancellation effect/energy storing issue would be eliminated [25][26][29]. Fortunately, multiferroic antennas produce EM radiation through magnetization fluctuations and are therefore magnetic current antennas capable of operating conformal to a ground plane. This coupled with the relaxed miniaturization issues discussed in the previous paragraph make them particularly effective in the Aerospace industry as the conformal antennas currently utilized require a cavity just below the aircraft outer mold line (surface) [56]. The issues created by these cavities are reduced internal real estate, increased weight, and lightning strike complications just to name a few. A multiferroic antenna acting in a receive mode can respond to incident tangential magnetic fields which are maximal at the ground plane, and thus not require subsurface cavities. Although piezoelectric antennas are not magnetic current driven

devices and therefore will still experience the platform effect, aerospace applications exist for these devices as well. Trailing wire technology, currently utilized for low frequency transmission, can be optimized using a mechanically resonating piezoelectric as an impedance matching network for example.

Since lossy environments are characterized by free electric charges within the media, magnetic current driven multiferroic antennas also benefit since their reactive near field region is dominated by magnetic fields rather than electric fields. As such, more efficiency is realized in the reactive region of the antenna since the magnetic fields do not lose energy moving charges around the same way that electric fields do. It is not surprising then that magnetic current antennas outperform their electric equivalents within lossy media [57]. The importance of developing such magnetic current antennas cannot be underemphasized in the biomedical implantable device industry. For example, the current state of the art in the implantable pacemaker (PM) space is the leadless PM. Unfortunately, these devices are limited to single chamber pacing support and therefore only suitable for a minority of patients [48]. However, leadless pacemaker networks can alleviate these issues by allowing multi-chamber support, and magnetic current multiferroic antennas can act as the voice between these devices. In this biomedical area, piezoelectric antennas cannot provide value unfortunately.

Mechanical resonance based (MRB) antennas clearly fill a need in today's antenna design space. To fully understand their function, ferroic orders are introduced along with linear elasticity in the next section. Ferromagnetism and ferroelectricity are discussed next in order to subsequently discuss multiferroic composite devices. A discussion on MRB antennas will follow in section 1.2.

### 1.1.3 Ferroic Orders and Linear Elasticity

Ferroic materials spontaneously exhibit an order parameter under certain conditions (typically certain temperature ranges). Thus far the magnetic order parameter, magnetization,

has been introduced and the mechanical order parameter, strain, has been hinted at. In section 1.1.4, the electric order parameter of polarization will be discussed. Ferromagnetic materials will therefore spontaneously contain a magnetization within the crystal structure below a certain temperature and ferroelectric materials will similarly contain a spontaneous polarization below a certain temperature. This temperature is known as the Curie temperature (or point), named after Pierre Curie [58] whose contributions will be discussed further in the sections that follow. What happens at the Curie point is that the material goes through a phase transition which alters the crystal structure by an amount large enough to break a certain type of symmetry. For example, a cubic structure may become elongated in one direction (tetragonal) below the Curie point, breaking cubic symmetry as it becomes ferroelectric. The way in which the different ferroic orders break symmetry will be discussed in subsequent sections, but first stress, strain, ferroelasticity, and linear elasticity will be discussed.

The concept of stress is introduced in order to relate the forces acting on surfaces to the elastic reactions within the material volume (from springy atomic bonds), which is performed using Cauchy's stress theorem [4-6]. This is as opposed to body forces, which already act everywhere within the volume and therefore need no such description in terms of stress. Gravitational forces are the most notable example, which is convenient, since if gravity only acted on the surfaces of our body, we would have strange droopy skin. The stress is the force acting over an area and is typically depicted by examining a differential cube as shown in Figure 1-7. Proper description of stress therefore requires knowledge of the direction of the force, and the surface normal on which the force acts. When the force and surface normal are orthogonal, shear stresses are produced.

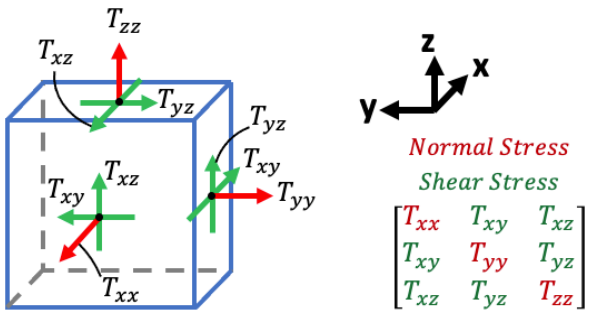


Figure 1-7: Stresses on an element with the normal and shear components marked.

Note that the stress tensor is symmetric and has six unique components, three normal and three shear. Strain is a measure of how much a differential element changes geometrically as stresses act on it. This language is intentionally vague as strain neither necessitates changes in shape, nor changes in volume. It is therefore convenient to classify strain in terms of normal strain (elongations/contractions Figure 1-8a) and shear strain (changes in angles between two edges of the element Figure 1-8b). It is also helpful to talk about strain in terms of its hydrostatic components (those that retain the shape but change the volume Figure 1-8c), and its deviatoric components (those that change the shape of the element but retain the volume Figure 1-8d). Note in Figure 1-8 that whenever a change in shape occurs, there will inevitably be an angle change (shear) somewhere within the element (even if only at a rotated axis). In fact, there will be some degree of shear in all but the “principal axes” which are the eigenvectors of the stress tensor. Herein, the normal and shear stress/strain description is utilized.

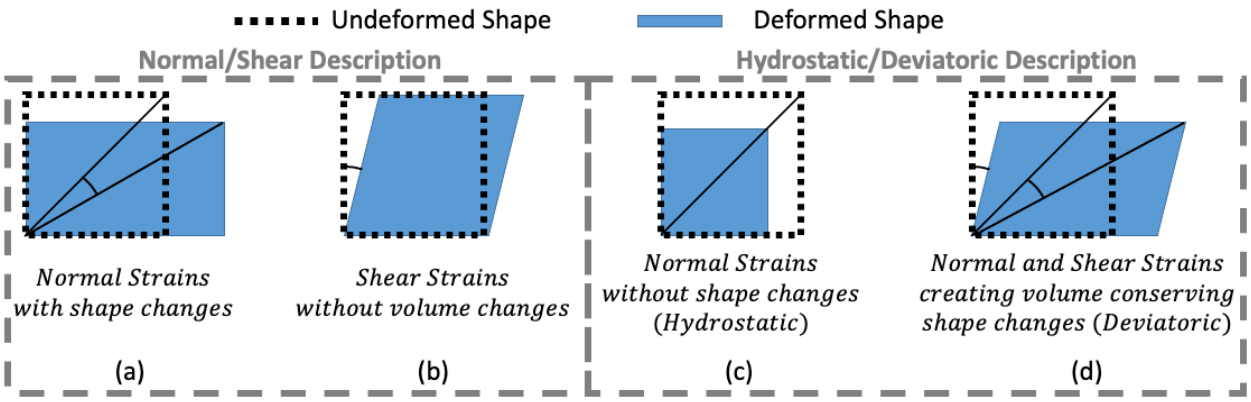


Figure 1-8: Strain and its descriptions, (a) Normal strain, (b) Shear strain, (c) Hydrostatic strain, (d) Deviatoric strain.

Ferroelastic materials are inherently non-linear, having a hysteretic stress/strain curve, and exhibit a spontaneous strain due to the presence of at least two asymmetric and stable "orientation states" [59-62]. A crystal in one orientation state can then be switched to another orientation state through mechanical stress. An example of a pure ferroelastic is lead phosphate whose ferroelasticity comes from an interesting interplay that occurs between a lead atom, and six oxygen atoms within its unit cell as shown in Figure 1-9:

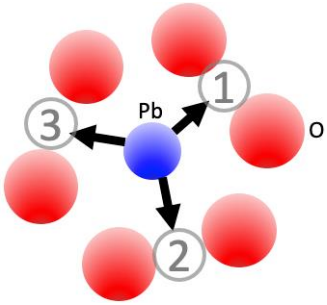


Figure 1-9: Ferroelastic mechanism within lead phosphate.

The lead atom bonds more closely with two of the oxygen atoms at the expense of the other four yielding three possible and stable configurations. A specimen will then be comprised of a

heterogenous set of these three orientation states. During mechanical loading, the Pb atom can be forced toward another orientation in a process called “ferroelastic switching”, and this new state may be retained even after the loading is removed, yielding a “plastic strain” and hysteretic behavior. This ferroelastic process is surprisingly similar to what is seen in ferroelectric and ferromagnetic materials. In fact, the magnetic equivalent to plastic strain is “remnant magnetization” which forms the basis for the memory devices widely in use today.

Although a vibrant field of research, pure ferroelasticity is not of interest in the analysis of mechanical resonance based (MRB) antennas, and ferroelasticity is only useful where it intrinsically couples to another ferroic order. What concerns multiferroics researchers is linear elasticity, in which the stress and strain are related linearly through the use of the “stiffness/compliance tensor”. This will be discussed in more detail in Chapter 2.

### 1.1.4 Ferroelectricity

An electric dipole moment is created whenever two opposite charges are separated by a distance $l$ and is equal to the charge multiplied by the separation length [63][64], directed from the negative charge to the positive charge as shown in Figure 1-10a.

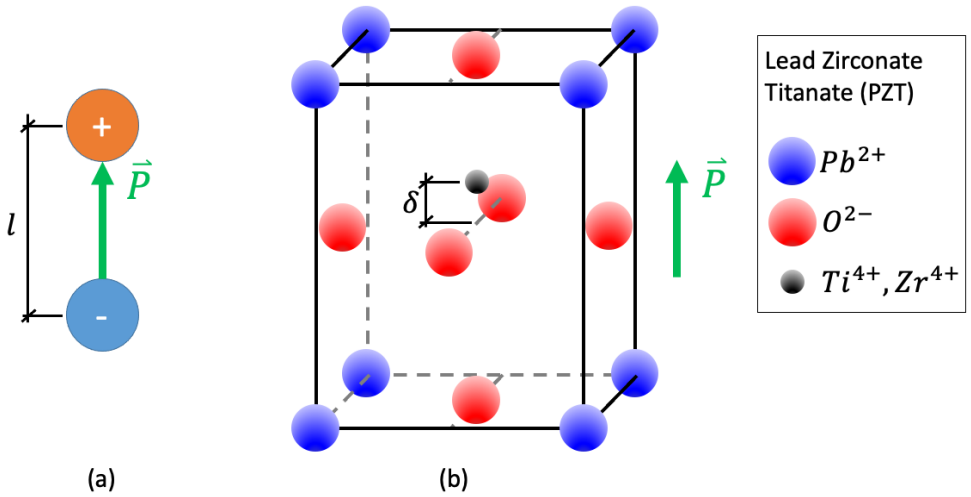


Figure 1-10: Electric dipole moment per volume (polarization $\boldsymbol{P}$), (a) Simplest dipole, (b) Lead Zirconate Titanate (PZT) with asymmetry $\boldsymbol{\delta}$ and polarization $\boldsymbol{P}$ marked.

When asymmetries exist within the unit cell, these dipole moments can be macroscopically present within a material, where it is more convenient to reference the dipole moment per unit volume known as the “polarization”. Lead Zirconate Titanate (PZT) is a famous case as shown in Figure 1-10b where the asymmetry $\delta$ and polarization $P$ are clearly marked [65]. Additionally, in the direction of asymmetry/ polarization, the lattice is distorted (tetragonal), destroying the 3-fold cubic symmetry, and opening the door for mechanically driven electric field fluctuations within the material. For example, note in Figure 1-10b that if compression was applied to the long axis the asymmetry would naturally decrease along with the polarization [63]. Alternatively, if an elongation occurred along the long axis the asymmetry/polarization would increase. This is known as the direct piezoelectric effect, which is linear, and was first discovered by Pierre and Paul-Jacques Curie in 1880 [66], though it was first thermodynamically postulated by Lord Kelvin in the early 19$^{th}$ century [63]. The converse effect where electric fields drive mechanical distortions was deduced mathematically by Gabriel Lippman in 1881, and experimentally demonstrated by the Curie brothers later that same year [63].

All nonlinear ferroelectric materials exhibit linear piezoelectricity when subjected to small excitations, but not all piezoelectric materials are ferroelectric. To see a fundamentally ferroelectric phenomenon, start by noting from Figure 1-10b that the direction of asymmetry is not arbitrary but rather pointed normal to the faces of the unit cell, known as the easy directions, and as such there are six for PZT. Applying an external electric field toward an easy axis that is not parallel to the polarization can therefore lead to the polarization becoming unstable thus switching to the new easy axis, and this state will remain even after the excitation has been removed. This “ferroelectric switching” is a nonlinear behavior akin to pushing a ball in a valley (energy well) over a hill into another valley [67][68]. Figure 1-11 demonstrates switching from an electric field applied orthogonal to the original polarization direction (90° switching), though

antiparallel ferroelectric switching can also occur (180° switching), as well as mechanically induced “ferroelastic switching”.

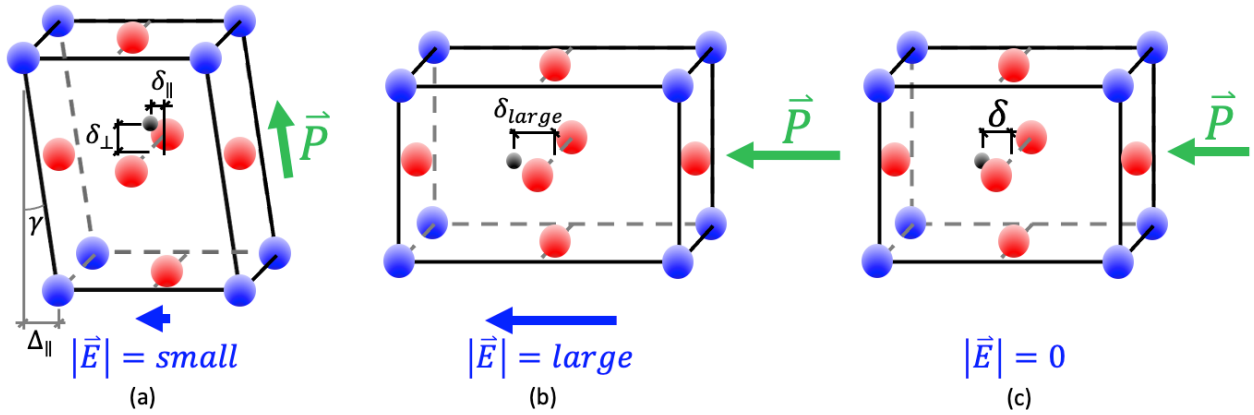


Figure 1-11: Switching of polarization direction, see also [Lynch] for accurate picture of asymmetries within PZT, (a) small electric fields producing a distortion of the unit cell. Removal of the excitation at this point will return the cell to the original state, (b) large electric field has now caused the polarization to switch to a new easy axis, (c) Removal of the large excitation does not change the polarization direction but does decrease the polarization magnitude.

If an electric field is applied to a bulk material with randomly oriented polarizations, a macroscopic order can be achieved through ferroelectric switching and the material is subsequently said to be “poled” in the direction of the DC field. From Figure 1-11a it is clear that electric fields can also produce shear strain ($\gamma$) in the material in addition to the normal strain (elongation/compression) previously discussed. Herein the focus will be on the linear converse piezoelectric effect induced by high frequency excitations.

### 1.1.5 Ferromagnetism

In a ferromagnetic material, exchange interactions occur between adjacent dipole moments which favor parallel alignment [9], thus creating macroscopic magnetizations as shown in Figure 1-12 for iron.

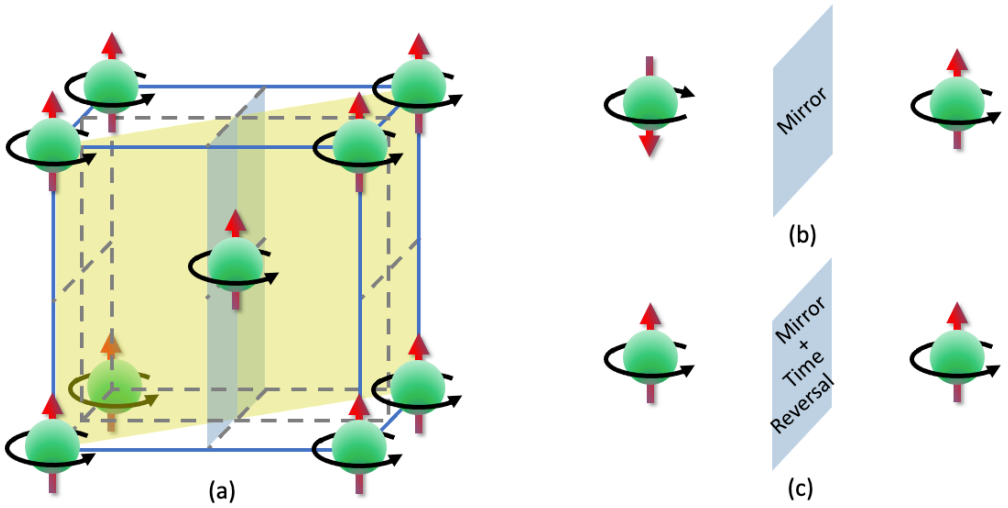


Figure 1-12: Ferromagnetism, (a) alignment of magnetic dipoles within Iron below the Curie temperature, (b) Mirror symmetry failing to represent the reality of ferromagnetism within Iron, (c) Mirror plane with time-reversal symmetry properly representing ferromagnetism of Iron.

Above the Curie temperature, the iron atoms still exhibit a dipole moment, but the thermal energy is too high for any order to be seen as the dipoles oscillate about without aligning. Based on the discussion on ferroelectricity in section 1.1.4, it may be expected that the cubic cell of iron is distorted by the presence of the spontaneous magnetization, but the three edges of the unit cell (lattice parameters) of iron at room temperature agree to five significant figures, though it is expected that some distortion does indeed take place. This applies to more than just iron, the d-orbital valence electrons within transition metals generally resist distortions typical of ferroelectrics, making it difficult for any single-phase material to exhibit both ferroic orders simultaneously [69]. It may therefore be hard to understand exactly how ferromagnetic iron breaks symmetry, but this may be understood by observing the two mirror planes shown in Figure 1-12. Examining one of the mirror planes in Figure 1-12b reveals that the dipole moment of the adjacent iron atoms is invertedly reversed during the mirror operation. If this is not clear,

one may stand in front of a mirror, put their right thumb up and note that the fingers on their mirror image are wrapping around as if left-handed. Ferromagnetic iron, therefore, breaks mirror symmetry, even if otherwise perfectly cubic in shape, when cooled below the Curie temperature. To account for this, after the mirror operation is performed, a “time-reversal” is also performed, as shown in Figure 1-14c, and thus ferromagnetic iron is said to have “time-reversal symmetry”.

Additionally, a ferromagnetic specimen will generally not be composed of a homogenous magnetization vector but rather be split up into a heterogenous set of “magnetic domains”. This occurs because magnetizations oriented normal to material boundaries increase the number of magnetic flux lines leaving the material which will then do work on any nearby charges. As such having a single magnetic domain is a high energy state, which is counteracted by a “demagnetization field” (demag for short), also known as shape anisotropy (since material surface normals determine the directionality of this effect). Demag is therefore what drives magnetic domain formation as shown in Figure 1-13 [8][9]:

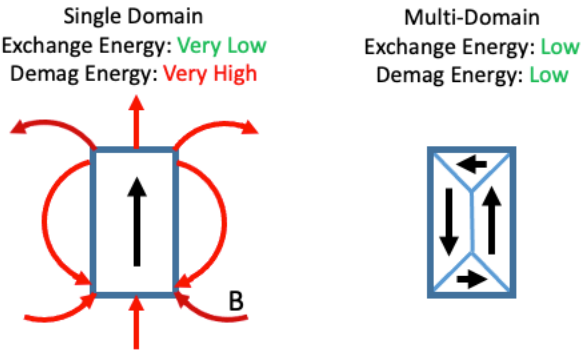


Figure 1-13: Single vs. Multi-Domain energy within a ferromagnetic material.

Still, there are such materials which extend large magnetic flux into free space known as permanent magnets. To understand why note that the magnetizations within a material will not be arbitrarily oriented but rather favor certain lattice directions known as “easy-axes” due to what is known as “magnetocrystalline anisotropy” or MCA for short. “Hard” magnetic materials

contain large MCA which counteracts demag, and as a result are capable of maintaining large "surface poles" (surface magnetizations normal to the surface). MCA arises since the valence electron spin couples to the orbital momentum and both couple to the lattice of a material resulting in easy and hard directions. The lattice itself is slightly distorted from this, opening the possibility of magnetic field driven elongations to occur known as magnetostriction. This is represented in Figure 1-14.

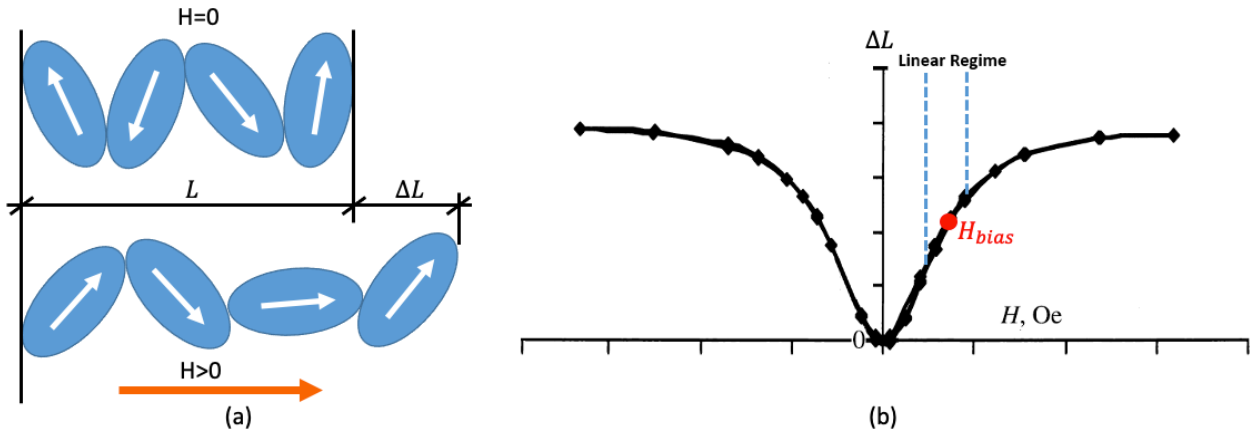


Figure 1-14: Magnetostriction, (a) pictorial representation, (b) typical strain ($\Delta \boldsymbol{L}$) vs. magnetic field (H) plot with demonstration of linear piezomagnetism.

Note in Figure 1-14a that the elongation effect will occur in the same manner if the magnetic field excitation $H$ were reversed yielding a quadratic-like response as shown in Figure 1-14b. Also, if a bias field is maintained and small perturbations are applied to the system, a linear response will result. This is known as linear "piezomagnetism" and is of particular importance in this work. James Prescott Joule first discovered magnetostriction in 1847 when he found that an iron bar would change length when magnetized [70][71]. The inverse also holds as shown by Villari in 1864 [72], when he discovered that stress induced dimensional changes produced magnetization changes in ferromagnetic materials. Magnetostriction is not limited to normal

stresses and strains, as Gustav Wiedmann discovered in 1858 that torsion was produced in a rod when electric current flowed through it [63]. Recall that, by Ampere's law, this means that were circumferential magnetic fields, namely along the curvilinear plane of shear stress. The inverse was discovered the same year by Carlo Matteucci and is known as the Matteucci effect [73].

### 1.1.6 Multiferroics

A multiferroic material is one that exhibits more than one ferroic order simultaneously [74] and is a field of research growing in popularity since the turn of the century [75-84]. The term is somewhat interchangeable with "magnetoelectric" material since the goal of researchers investigating multiferroics is to combine the ferromagnetic and ferroelectric orders together such that magnetic fields drive polarization changes (direct magnetoelectric effect DME), or, more importantly, electric fields drive magnetization changes (converse magnetoelectric effect CME). This cross-coupling of the ferroelectric and ferromagnetic orders has proven difficult within single phase materials since the d-shell electrons necessary for ferromagnetism reduce the tendency for the symmetry breaking lattice distortion necessary for ferroelectricity [69]. Additionally, the CME necessary for magnetic current antennas is more difficult to achieve than the DME due to realigning magnetic domains which inhibit large changes in observable magnetic fields. However, as shown in the previous two sections, combining ferromagnetics with ferroelastics (magnetostriction) and ferroelectrics with ferroelastics (piezoelectricity) is relatively simple. This opens the door for the ferroelastic order to be used as a telephone to communicate between electric and magnetic order parameters in a novel way using "multiferroic composites". In this section, the "multiferroic tetrahedron" (Heckmann diagram) will be presented first to facilitate understanding. Then, the history of multiferroics will be discussed. Finally, multiferroic composites will be presented.

A summary of the last three sections is represented in Figure 1-15:

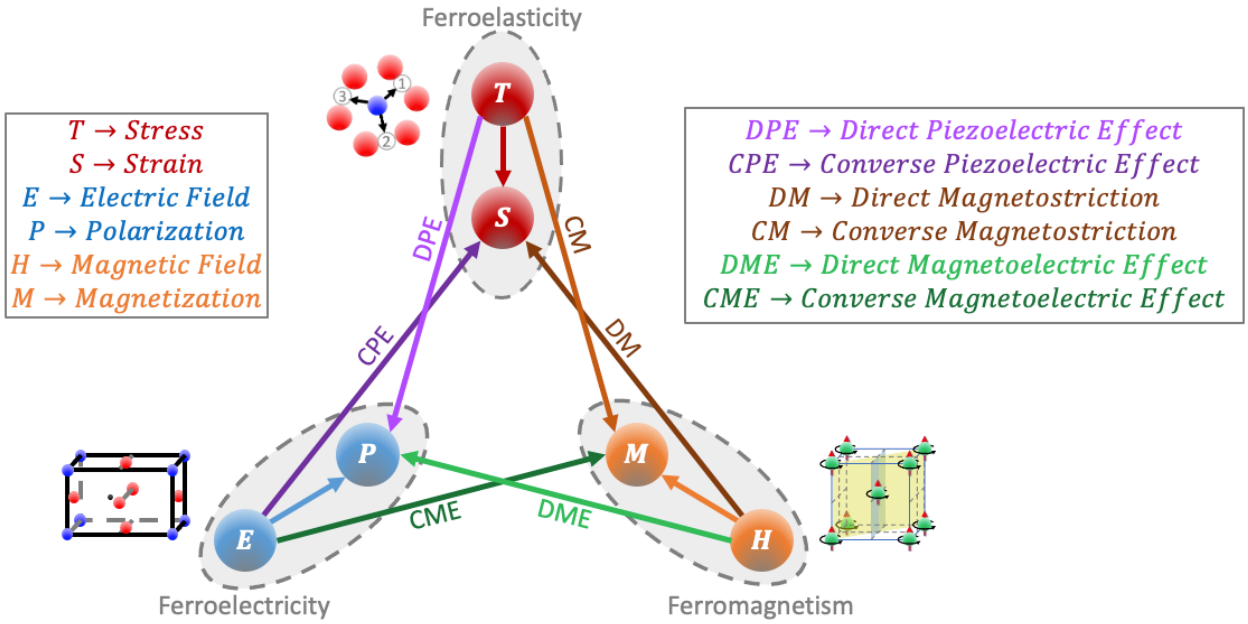


Figure 1-15: Multiferroic triangle containing ferroelasticity, ferroelectricity, and ferromagnetism along with the name of each multiferroic effect.

All processes that cross from one ferroic order to another have been labeled in Figure 1-15. Note that, strictly speaking, magnetostriction and piezoelectricity are multiferroic in nature but usually the term multiferroic is used to describe the direct and converse magnetoelectric effects. For this reason, technically piezoelectric antennas are also multiferroic antennas and a more accurate name for the magnetic current antennas discussed thus far is magnetoelectric antenna. Herein, multiferroic will be used interchangeably with magnetoelectric and piezoelectric driven devices will be referred to as such without evoking the term “multiferroic”. This is the popular nomenclature within the multiferroic research community. Diagrams like the one shown in Figure 1-15 have been named "Heckmann diagrams" [85-87], which were modified by Nye in 1957 [88], and are sometimes depicted with an additional axis for temperature ($T$) with entropy ($S$) as the order parameter [86]. Therein lies some unfortunate confusion, as Figure 1-15 depicts the stress and strain using the same letters respectively, as

opposed to the much more widely used sigma ($\sigma$) for stress, and epsilon ($\varepsilon$) for strain that mechanical engineers use. This is because electrical engineers use those Greek letters for conductivity and permittivity respectively, highlighting an interesting human element of multi-domain physics, namely that there will be some overlap in symbols. Since mechanical resonance based (MRB) antenna analysis utilizes the isothermal assumption, the use of $T$ for stress and $S$ for strain, for which there is some precedent [4], will only be a minor inconvenience in Chapter 2 when the laws of thermodynamics are evoked.

The first three milestones of multiferroics have already been discussed herein. These are 1) Oersted's discovery that electric currents induce magnetic fields in 1820 [12][13], 2) Joule's discovery of magnetostriction in 1842 [70][71], and 3) The discovery of the piezoelectric effect by the Curie brothers in 1880 [63][66]. In 1894, the Curie brothers are the first to investigate the magnetoelectric effect [89], though they were completely unsuccessful due to some incorrect crystal symmetry assumptions. In 1926, Debye coins the term "magnetoelectric" [90], predating the term "multiferroic", coined by Schmidt in 1994 [91], by almost 70 years. In 1958, Landau and Lifshitz, the same men who first proposed the governing equation of micromagnetics [15], provide a theoretical basis for the magnetoelectric effect [92]. The search for a commercially viable magnetoelectric then took decades before bearing fruit in 2002, when Ryu et al experimentally advertised giant multiferroic coupling [93] of magnetic to electrical energy (DME). In order to accomplish this, a single-phase material was not used, but rather a heterogenous laminated composite as first proposed by Van Suchtelen in 1972 [94]. This has led to an influx of interest in generating the magnetoelectric effect through the use of composite structures.

Multiferroic composites tackle the problem of the lack of commercially viable magnetoelectric materials by mechanically bonding ferroelectric and ferromagnetic material within a laminate [95-98] as shown in Figure 1-16:

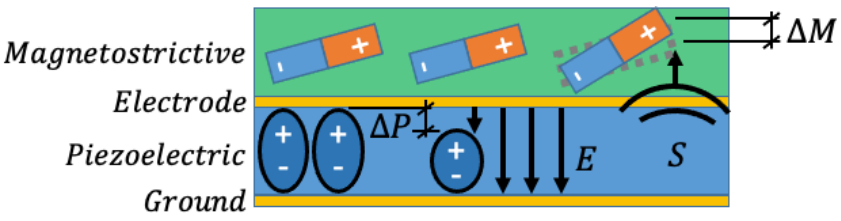


Figure 1-16: Simplest multiferroic composite.

This is the simplest design there is, but all multiferroic composites include a piezoelectric material sandwiched between two electrodes, one of which is grounded, somewhere within the layout. A voltage is applied to these electrodes, causing an electric field to pass through the piezoelectric and generating a mechanical deformation through the converse piezoelectric effect. This deformation is not apparent to the entire system simultaneously, therefore mechanical waves must communicate this distortion to the rest of the device. Eventually these mechanical waves impinge upon the ferromagnetic material causing deformation. This deformation induces magnetization changes, through magnetostriction, that have their origin in the voltage applied at the electrodes (electric field in the piezoelectric), thus achieving the CME. In the next section, the use of multiferroic composites in the design of antennas will be discussed.

## 1.2 Mechanical Resonance Based (MRB) Antennas

Thus far, Mechanical Resonance Based (MRB) antennas have been discussed indirectly and this section will focus on these devices. First, it is prudent to review all the terms so far. Herein, an MRB antenna includes both multiferroic antennas and piezoelectric antennas. Multiferroic antennas are those where the converse magnetoelectric effect is utilized to produce magnetic current. Piezoelectric antennas produce polarization current utilizing mechanical stresses and are therefore technically also multiferroic but will not be referred to as such herein. There is a more general class of devices known as mechanical antennas which encompass both MRB antennas and rotating dipole devices. These latter antennas will be discussed in

Section 1.2.4. Herein, whenever the term “mechanical antenna” is used, MRB antennas are being referred to unless otherwise stated.

### 1.2.1 History

The first instance of mechanically driven EM waves is quite alien to the discussion so far as the outgoing wave was a single pulse generated not by a multiferroic composite, but rather by a rapid change in EM boundary conditions generated by an implosion [99][100]. The setup was to generate magnetic flux within a conducting cylinder with an explosive charge fashioned to the outer circumference. Upon explosion the radius of the shell would rapidly decrease, producing an increase in magnetic flux, and generating a pulse. This dates to Joseph Fowler in 1944 [100], though the first work to be openly published on the subject was not until 1952.

The next advancement towards mechanical antennas was performed by Rowen in 1961 [101] where he investigated the potential for EM radiation from a spherical specimen of Yttrium Iron Garnet (YIG), which is a magnetostrictive. The spherical geometry was utilized to avoid the complex nature of shape anisotropy (demag), as the research focused on the anisotropy introduced by static strains (magnetoelastic anisotropy [14]). As such, the potential for microwave generation was merely proposed but not demonstrated. Also, since the strains were applied directly without the use of a piezoelectric, this is not a magnetoelectric antenna but represents a significant step in the right direction.

Analysis on EM radiation from standalone piezoelectric antennas (PEAs) in the absence of a magnetostrictive were subsequently performed by multiple authors spanning three decades. Mindlin studied the problem in 1973 [102] but claims that Tiersten was the first to conduct the study in 1970 [103], though the original paper appears to be lost. This early analysis was on an infinite quartz plate, having a shear stress excitation applied to the top and bottom, with the goal of attaining an equation for the radiated power. The full Maxwell’s equations were used everywhere, including inside of the piezoelectric quartz plate. In 1989, Lee continued this study

except with the electrostatic assumption applied within the piezo and full Maxwell's in the surrounding vacuum [104]. Interestingly, the analytical radiated power predicted with and without this assumption only exhibited a percent difference of $10^{-10}$. This allows for fully coupled numerical models of piezoelectric antennas (PEAs) to be compared with much simpler models utilizing the electrostatic assumption for the purposes of verification testing. Lee also considered the case of electric excitations applied tangential to the quartz plate, which Mindlin had previously ignored. Lee went on to generalize his work in a 1990 paper [105].

The first instance of a multiferroic composite being proposed for antenna applications was in 2008 when Petrov et al [106] argued that the simultaneous high permittivity and permeability of these laminates would allow for miniaturization. Later that same year, a group out of Northeastern University led by Nian Sun experimented with augmenting patch antenna performance through the addition of thin ferrite films thus constituting a multiferroic composite [107]. Electric field was used to alter the magnetic properties resulting in a frequency reconfigurable antenna.

In 2009, a group out of the Boeing corporation with Robert J. Miller at the helm filed a patent for a multiferroic antenna [56]. The patent widely documents many of the complications that state of the art antennas exhibit in aerospace applications, some of which have been discussed in section 1.1.2. The work was mainly concerned with the operation of the multiferroic antenna acting as a receiver immune to the platform effect. The goal was that incident magnetic fields would excite strains in a magnetostrictive which would then excite voltages across nearby bonded piezoelectric materials.

In 2011, the Translational Applications of Nanoscale Multiferroic Systems (TANMS) Engineering Research Center (ERC) begins work on multiferroic antennas. This ERC is led by Dr. Greg Carman and comprised of researchers from multiple universities, including Nian Sun who has already been mentioned in this section. Some early work was performed by Scott

Keller [108]. In 2014, Zhi (Jackie) Yao continues this research as part of the Digital Microwave Laboratory (DML) under Ethan Wang [109]. She presents a 1D finite difference time-domain (FDTD) model for a Bulk Acoustic Wave (BAW) multiferroic antenna [110] as shown in Figure 1-17.

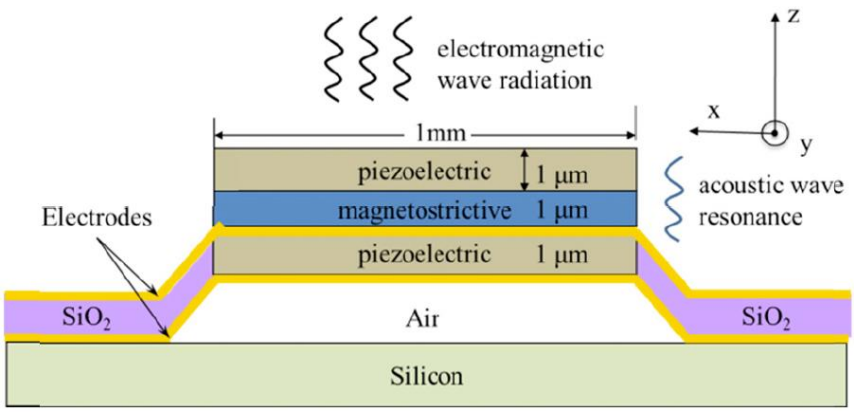


Figure 1-17: BAW resonance-based antenna, from [110].

The operation of such BAW MF antennas will be explored in the next section and this concept has been adopted by subsequent researchers [111-113]. Yao et al. then expanded on this topic in a journal publication in 2015 [114] in which she calculated the theoretical lower limit of the Q-factor for an infinite plate MF antenna much like Chu [33] for general electrically small antennas. A major assumption used within this model is that only one displacement is relevant (uniaxial strain approximation). Another assumption is that the magnetostrictive material is acted on by a sufficiently large bias field such that only a single magnetic domain exists. In addition, it is assumed that this domain is only acted on by small perturbations, which allows for a linearization of the LLG equation. The strategy is then to integrate this linearized equation into the magnetic constitutive relation to write magnetic field update equations. The magnetization in not updated directly. The code implicitly updates the electric field using a tridiagonal system of equations.

That same year of 2015, Scott Keller et al. along with the Northrop Grumman Corporation submit a patent for a Surface Acoustic Wave (SAW) Multiferroic antenna [115] as shown in Figure 1-18:

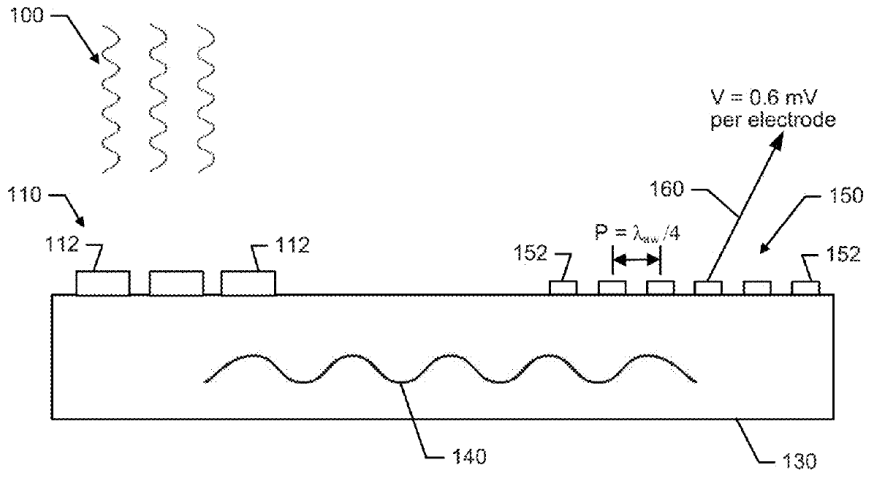


Figure 1-18: SAW multiferroic antenna from US patent [115]

This configuration is not 1D like the proposed BAW device of Figure 1-17 since the strain is relevant in more than one direction. This SAW MF antenna device utilizes intertwined “fingers” of piezoelectric material to convert EM energy into surface waves which then induce measurable voltage changes in downstream electrodes spaced a quarter acoustic wavelength apart.

In January 2017, the Defense Advanced Research Projects Agency (DARPA) holds a “Proposer’s Day” for the A MEchanically Based Antenna (AMEBA) project [116]. The goal is to develop antennas that operate at very low frequency (VLF 3-30kHz) to communicate across the globe by utilizing the Earth and the ionosphere as a waveguide at <6dB/1000km attenuation, as well as antennas that operate at ultra-low frequency (ULF 0.3-3kHz) in order to penetrate water, soil, and rock, allowing underwater and underground communication [117]. Currently, the US Navy utilizes the Naval Radio Station Cutler in Cutler, Maine in order to transmit at 24kHz

(12.5km wavelength) to good effect, but the station antenna array is about 1.2 miles in diameter and uses 1.8 megawatts of power [118-121]. DARPA therefore desires VLF and ULF transmitters with reduced size and power consumption for future high penetrating portable communications. This highlights a key benefit of multiferroic transmitters, the devices can either operate at microwave frequencies with dimensions at the micrometer level (e.g., for use in implantable devices), or be made at the tens of centimeters level to operate at VLF (e.g., AMEBA Earth-ionosphere communications).

The same year of 2017, Domann performs on eigenmode analysis to compare multiferroic and conventional antennas [122]. Using a Green's function approach, an equivalent piezoelectric and piezomagnetic current is utilized based on a prescribed strain rate. These are used to determine the electric and magnetic fields surrounding the device and the radiated power. Due to the small device size relative to the EM wavelength ($< \lambda_0/50$), a comparison to the infinitesimal dipole is appropriate and conducted. It was concluded that multiferroic antennas outperform conventional antennas at this small size.

Later in 2017, Nan et al [111], under Nian Sun, experimentally test both a nanoplate resonator (NPR) and thin-film bulk acoustic wave resonator (FBAR) multiferroic antenna in response to the lack of measurements of magnetoelectric coupling at very high frequency (VHF 30-300MHz) and ultra-high frequency (UHF 0.3-3GHz). This task had yet been performed due to low-signal levels from the MF antenna and difficulties in isolating that signal from contributing elements other than the magnetostrictive. The desired strong coupling was observed which impressed Zaeimbashi et al [123], as in 2019 these researchers, working in the biomedical implant field, proposed to use a planar array of these antennas, implanted at the cerebrospinal fluid-gray matter interface (CSF-GM) in order to establish communications with a transceiver located just outside the scalp.

Also in 2017, Kim et al investigated a multiferroic receiver that is similar to a strain rosette [112]. Within the device, five BAW resonators, like those shown in Figure 1-17, were setup at angles of 0°, 30°, 45°, 60°, and 90°. The goal was to measure the change in resonant frequency caused by incident magnetic fields due to the delta E effect, where E denotes the elastic modulus (stiffness) of the magnetostrictive (not an electric field). Since this effect depends on the re-orientation of magnetic domains within the magnetostrictive, the change in resonant frequency for a BAW device biased parallel to the incident magnetic field will be smaller than that of a BAW device biased orthogonal to the same field. As such, not only is the magnetic field detected, but the orientation is also detected, as advertised by the authors.

In 2018, Yao et al expand the 1D code developed in 2015 [124][125], to 3D while ignoring Newton's laws. As such this is not work on multiferroic antennas specifically but represents a significant steppingstone toward the first fully coupled solver, which will be discussed shortly. The most significant innovation in this code is the use of a "field-splitting strategy" to deal with magnetic field discontinuities at the magnetostrictive/air interfaces. These arise due to the use of the linearized LLG equation. This rigorous treatment of material interface conditions allows for the demagnetization field to be fully accounted for, which is typically the most time-consuming part of any simulation involving micromagnetics.

In 2019, Kubena along with colleagues at HRL laboratories and Rutgers University perform work on a multiferroic RF receiver [126]. The device is made up of two piezoelectric quartz resonators, one serving as a frequency reference and the other experiencing frequency shifts induced by incident magnetic fields due to a bonded FeGaB magnetostrictive. The frequencies are then compared using integrated electronics allowing the incident magnetic fields to be measured.

Additionally in 2019, Schneider tests 1D multiferroic antenna in the shape of a rod under uniaxial stresses [127]. The setup includes a PZT piezoelectric stack of circular cross section

experiencing a variable applied voltage. This induces compressional waves to propagate into a magnetic field biased FeGa magnetostrictive material bonded in series with the PZT. As the FeGa was stressed, a search coil would measure the changes in magnetic flux from within the material and a near field probe from without. It was found that the magnetic flux oscillations within the FeGa increased with the magnitude of the electric field applied to the PZT. The most interesting result from this study is that there was a peak in magnetization oscillations as a sweep of the magnetic bias field was performed. At no bias field, the oscillation magnitude is zero and the stress/strain hysteresis is maximal because the stress wastes energy moving magnetic domain wails around that have no macroscopic order. At large bias fields, the magnetic domains are too stiff to want to change direction and the mechanical hysteresis is virtually zero since no domain wall motion takes place. At just the right bias field, the magnetic domain walls move in an orderly fashion, producing optimal oscillations of magnetization. This trend was seen both within the FeGa, and in the surrounding air. This presents a modeling challenge, as multi-domain magnetostrictives experiencing domain wall motion are not properly characterized by the linearized LLG equation.

Also in 2019, Yao proposes a method to relax linear LLG assumption within her code by introducing the magnetization as a field to be updated, as well as swapping the implicitly updated field from electric field to magnetic field [128]. To focus on this effort, the 1D form of Newton's equation leveraged in previous iterations of the code were dropped, like in her 2018 work [124][125], meaning that a fully coupled 3D Maxwell's, Newton's, and non-linear LLG solver remains elusory. The coupling of non-linear magnetic behavior at RF frequencies dates to Suhl in 1956 [129].

In 2019, Xu et al experimentally demonstrate a multiferroic antenna operating in the transmitter mode [121]. The device was made up of a piezoelectric PZT core with magnetostrictive Metglas bonded on the top and bottom. Interesting from the study, the

radiation pattern of the antenna was measured and seen to take the “donut” shape typical of magnetic dipole antennas. Typically, however, in conventional antennas, the magnetic dipole is not in fact driven by a magnetic current but rather by an electric current loop. However, the multiferroic antenna radiation under study is driven by magnetization fluctuations, and therefore represents a true magnetic current. As such, the multiferroic transmitter was found to have anywhere from $10^3$ to $10^4$ times higher efficiency over a loop antenna with the same area. A similar study was performed in 2020 by Dong et al [130] where it was additionally proposed that an array of multiferroic antennas would increase the range of effective communication.

In 2020, Yao et al publish a paper on the first fully coupled solver to simulate a BAW multiferroic antenna [131]. The solver employed the alternating direction implicit (ADI) finite difference time-domain (FDTD) scheme in order to utilize an intermediate time step between the EM and acoustic physics. Otherwise, 100,000-time steps would need to pass on the electrodynamic side, before any useful information is transmitted on the acoustic side. The paper leveraged the field-splitting strategy described in [124][125] to model demagnetization effects. The major assumptions of the solver were uniaxial strains (1D Newton’s), and a single domain magnetostrictive under small RF perturbations (linearized LLG). The numerical results demonstrate that the optimal radiated power and efficiency are achieved when the acoustic resonance and the FMR occur at the same frequency. More details on this solver are given in Chapter 3.

Also in 2020, Rangriz et al simulated a magnetoelectric antenna for the purposes of establishing communications in implantable biomedical devices [132]. The approach was to model magnetostrictive FeGaB using a non-linear constitutive relation [133] rather than the full LLG. The EM fields in the near field around the device were then calculated using a low frequency approximation to Maxwell’s equations, though the exact equation utilized was not presented. Then the surface equivalency theorem was used to perform a near to far-field

(NTFF) transformation of the results in order to determine scattering parameters. Altogether the approach was a nice compromise between accuracy and complexity.

Finally in 2022, Kevin Luong and Ethan Wang comprehensively attack the modeling of magnetoelastic coupling within magnetostrictives in the absence of electrodynamic wave propagation [134]. This was performed to highlight the limitations of contemporary approaches of modeling magnetoelastic coupling within MF antennas solely through constitutive relations, like in [135], without evoking the full LLG equations governing the magnetization dynamics in a highly frequency dependent manner. The analysis focused on the linearized form of the LLG equation however, though this version is highly appropriate for many multiferroic antenna designs, e.g., those that utilize thin film magnetostrictives biased such that only a single magnetic domain is present. Since devices under these conditions have their magnetizations saturated in the direction of biasing, the only magnetoelastic coupling coefficients that can induce magnetization oscillations are those related to shear stresses. The results of this analytical study show that this is indeed the case as, for example, the optimal coupling in an iron material biased in the z-direction is achieved when a normal stress is applied 45° off axis, i.e., such that the magnetization experiences the maximum amount of shear. The study also demonstrates other interesting properties of magnetoelastics, namely that the resonance frequency for the coupling becomes higher with stronger magnetic bias fields due to shifts in the FMR frequency. Note that since this study focused on single domain magnetoelastics, this does not discredit experimental work that claims normal stress driven magnetizations oscillations, as the magnetostrictives in these works presumably had not been fully saturated.

One of the largest issues facing MF antennas is the small bandwidths (BWs) associated with the large total Q values since the bandwidth is inversely proportional to the Q. For example, an antenna resonating at 10kHz with a Q of 100,000 will have a bandwidth of 0.1Hz which is unpalatable and real MF antennas have had BWs on this order. Direct antenna modulation

(DAM) is one way to approach this problem but in 2022 the authors of [136] attempted to tackle the issue buy fabricating a MF antenna with 3 resonant regions based on the composite stackup. Resonant region 1 (R1) was fixed on the bottom and composed of an electrode-AlN-FeGa-electrode stack up. Resonant region 2 (R2) was the same but included a $Al_2O_3$ layer on top and R3 was the same as R2 save the bottom was a traction free boundary. Due to the three different resonance frequencies, the BW was increased. Altering the resonant frequency by changing the device capacitance via semiconductor relay switches and discrete capacitors is likely a better alternative, however.

Also in 2022, Rostami et al. [137] proposed modelling of a MF antenna via finite element software Comsol. A comparison with a micro-loop antenna of equivalent size was also performed demonstrating that the micro-loop was too small to produce resonance, radiation, and matching with a 50Ohm transmission line. This is not surprising as traditional EM driven antennas with dimensions on the order of the mechanical wavelength are too small to exhibit the spatial fluctuations necessary to radiate and essentially become lumped elements. Since a full-wave fully coupled simulation was not performed, near-field and far-field parameters were derived in a roundabout way utilizing equivalent circuits on the software CST. Interestingly, the mechanical viscous damping parameter was chosen as 1e-4 which is significantly lower than the 0.02-0.025 value that agrees well with experimental values of AlN [131]. As such, the efficiencies within the paper are likely overpredicted.

In June 2022, Will-Cole et al., as part of Professor Sun's lab, released a NEMS antenna "tutorial" [138] which gives an overview of the relevant equations, material properties, and experimental results performed on MF antennas at Northeastern University.

In April of 2023, Zheng et al. [139] from the TANMS organization published a work in which a MF antenna similar to that of Figure **1**-**18** was simulated and experimented. The difference being that the antenna did not include alternating plus and minus electrodes (IDTs) on top of a

substrate, but rather positive electrodes laced between magnetostrictive material with a large ground electrode below the piezoelectric substrate. Etching vias were also used so that an air cavity could be generated beneath the antenna, maximizing piezoelectric strain. The antenna was characterized in both the receiving and transmitting modes. For transmission, an electrostatic elastodynamic simulation was performed utilizing finite element software Comsol so that the device geometry could be properly tuned to induce a mechanical standing wave in-plane orthogonal to the driving electrodes. The stresses within the magnetostrictive material were then subsequently input into a micromagnetic solver which utilizes the LLG equation to calculate magnetization fluctuations. These fluctuations are then fed into a magnetic dipole simulation to calculate far-field parameters. As such, the analysis consisted of three uncoupled simulations performed in series.

### 1.2.2 Operating Principles

Magnetoelectric coupling in MF composites at RF frequencies has been investigated by multiple authors as seen in the previous section as well as in [140-146]. Using MF heterostructures allows the designer to bypass the two main issues with scaling down antennas to the micrometer level, namely, ohmic losses, as discussed in section 1.1.2, and wavelength constraints. Traditional antennas, like dipoles, have physical dimensions on the order of the wavelength of the EM radiation being propagated at the frequency of operation [26][27]. This concept of size being proportional to wavelength is true of all resonating devices. A notable example is the size of a trumpet operating at high frequency/pitch (short wavelength), which is relatively small compared to a tuba operating at low frequency/pitch (long wavelength). This also applies to MRB antennas of course, except that the resonance driving EM radiation is acoustic rather than electromagnetic. In the GHz range the EM wavelengths are 5 orders of magnitude longer than that of acoustic waves [114][131]. This is fundamentally because the speed of light is much faster than the speed of sound as shown in Figure 1-19:

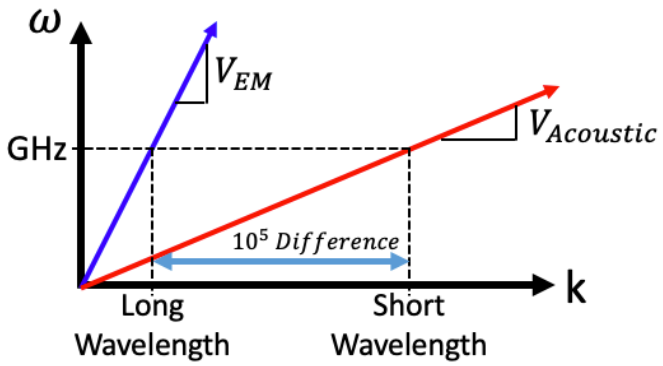


Figure 1-19: Linear dispersion relation (frequency $\boldsymbol{\omega}$ vs. wavenumber $\boldsymbol{k}$) demonstrating 5 orders of magnitude difference in acoustic to EM wavelength at the same frequency. The slope of the dispersion relation is the wave speed (group velocity). Note that the EM wave speed ($\boldsymbol{V_{EM}}$) is much larger than the acoustic wave speed ($\boldsymbol{V_{Acoustic}}$).

Therefore, mechanical antennas, which utilize acoustic waves to generate magnetic field fluctuations, can be made significantly smaller than traditional antennas and are multiscale in nature. In other words, these novel devices turn waves that generate sound, into waves that can be received by a wireless communication system. This is the fundamental mechanism motivating multiferroic antenna research which also applies to piezoelectric radiators discussed in section 1.2.3. The operation of a multiferroic antenna is shown in Figure 1-20, for the initial single time period.

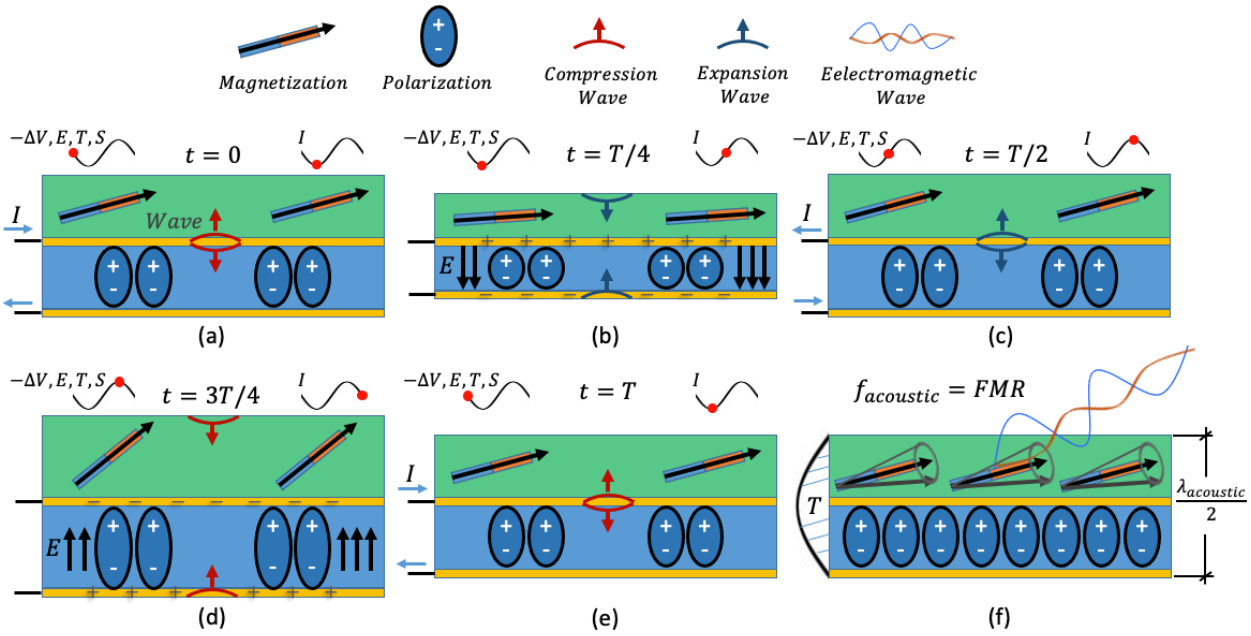


Figure 1-20: Initial period (T) of operation for a simple multiferroic antenna. $\Delta \boldsymbol{V}$ is the voltage differential across the two electrodes. The upper and lower mechanical boundary conditions are both traction free. The ordering was chosen such that the reader can follow along with the acoustic wave during propagation. The t=0 time designation was given to (a) to emphasize that the voltage cannot change instantaneously across electrodes, and therefore only (a) and (c) could possibly be the initial state. The magnetostrictive has a single magnetic domain, which is achieved using a magnetic bias field. The device is thin-film, meaning that the in-plane dimensions are significantly larger than the thickness (1D uniaxial strain case). The piezoelectric is poled out-of-plane (z-direction)

The thickness of the multiferroic antenna is half of the acoustic wavelength ($\lambda_{acoustic}/2$ [114][131]), and the quarter period (T/4) steps shown in Figure 1-20a-e will now be described in detail: (a) At t=0 a voltage input generates a compressional wave which begins to propagate to the upper and lower traction free boundaries of the device at the acoustic wave speed. Note however that there are still no electric potential (voltage) gradients as the voltage differential

between the electrodes cannot change instantaneously. Since the acoustic wave has not had time to propagate there is no stress/strain anywhere in the material nor are there electric fields in the piezoelectric or magnetization changes in the magnetostrictive. (b) At t=T/4 the compression wave has hit the upper and lower boundary of the antenna, generating a negative stress/strain throughout the device and producing a change in magnetization within the magnetostrictive. There are also electric fields and polarization changes in the piezoelectric due to the voltage differential. The compression wave reflects off the boundary as an expansion wave since the boundary is traction free and therefore cannot hold any strain. (c) At t=T/2 the reflected expansion wave has reached the center of the device, undoing the effects of the initial compressional wave. Simultaneously, the voltage input is now generating an additional expansion wave which interferes constructively with the reflected expansion wave. This constructive interference is the mechanism behind acoustic resonance. (d) At t=3T/4, the expansion has now propagated through the entire device, producing a positive stress/strain and inducing a change in magnetization in the magnetostrictive with the opposite sense as that produced at time t=T/4. The expansion wave reflects off the upper and lower boundaries as a compressional wave. (e) At time t=T the system is back to its original configuration with an additional voltage induced compressional wave constructively interfering with the reflected compressional wave. (f) Since the voltage excitation frequency is the same as the first acoustic harmonic frequency, mechanical resonance is achieved with a half sine wave eigenfunction (mode). This is accomplished since the device has a thickness equal to half of the acoustic wavelength ($\lambda_{acoustic}/2$). If additionally, the acoustic resonance and the ferromagnetic resonance (FMR) occur at the same frequency, the magnetizations within the magnetostrictive precess, optimally producing alternating magnetic currents which propagate into free space as EM waves. As it concerns resonance, there are three possibilities as shown in Figure 1-21:

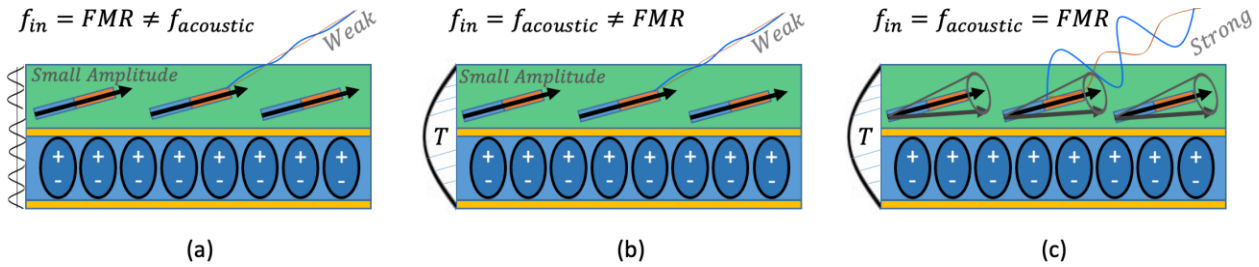


Figure 1-21: Three potential cases of resonance, (a) the frequency input $f_{in}$ is equal to the FMR frequency, (b) $f_{in}$ is equal to the first acoustic resonant frequency $f_{acoustic}$, (c) $f_{in}$ is equal to both the FMR frequency and $f_{acoustic}$

In Figure 1-21a the FMR frequency is input at the electrodes, but this does not coincide with the first acoustic resonant frequency. The acoustic wave will therefore be some amalgamation of acoustic harmonics which excite the magnetostrictive layer in a disorganized fashion. The result is small amplitude magnetization fluctuations and a weak signal. In Figure 1-21b the input frequency equals the first acoustic harmonic, generating a half sine wave stress profile through the thickness of the device. These stresses induce magnetization changes that sometimes aid the precessional motion and sometimes hinder it. Again, the result is a weak signal. In Figure 1-21c the first acoustic harmonic induces precessional motion in the magnetic material such that every time the magnetization is back to its initial position the wave excites it again in the same way, reinforcing its motion. In other words, the acoustic resonance frequency and the FMR frequency are the same. The result is large macroscopically detectable magnetization precessional motion which generates a strong signal. There has been much research performed on acoustically driven ferromagnetic resonance (ADFMR) in recent years for SAW devices [147-151], though the phenomenon has been predicted for BAW device as well [131].

Now that the operation of the multiferroic antenna design in Figure 1-20 has been explained, some additional observations will now be explored. First, since the EM wavelength is around 5 orders of magnitude larger than the device, the difference in electric field within the electrode-

piezo-electrode driving sandwich is small. Therefore, unlike patch antennas, the effective magnetic currents on the lateral walls (radiating slots in Figure **1**-**6**) of the sandwich are opposite in direction, cancelling out. This stackup therefore acts as a lumped circuit capacitor with current $I$ 90 degrees out-of-phase with voltage $V$. Thus, the electric field fluctuations within the piezo are reactive in nature, storing energy rather than radiating it, alleviating concerns that the piezoelectric is affecting the far-field radiation pattern of the antenna. Also, small fringing electric fields near the capacitor will die off too quickly to be of importance from a performance standpoint. For modeling purposes, this suggests full Maxwell's equations are not required within the domain of the driving sandwich and therefore this region could be simulated separately. However, the full elastodynamic set of equations still applies within this volume.

Second, note that the polarization vector only changes in magnitude, while the magnetization only changes in direction. As such, normal stresses applied to the magnetization can only induce significant changes if sufficiently strong enough to induce ferroelastic switching. To counteract this, note that when the device is unstrained, the magnetization is slightly canted vertically. This is so that the magnetization vector experiences shear strains rather than only normal strains (recall from Figure 1-8 that shape changes always imply shear at non-principal directions). This canting of the magnetization is accomplished by the application of an out-of-plane bias magnetic field. Unfortunately, due to the high degree of shape anisotropy favoring in-plane magnetizations, this bias field will need to be exceedingly large. Shape anisotropy has another implication. Note from Figure 1-20f that the precessional motion of the magnetization at FMR is depicted as a right circular cone. In reality, shape anisotropy will force this cone to flatten into a more ellipsoidal shape such that the magnetic current is mostly in-plane. This is not a hinderance since any out-of-plane magnetic currents would suffer from the same platform effect that in-plane electric currents do because of image currents.

Another way of getting the magnetization to experience shear strains that avoids the need for an out-of-plane bias field would be to excite a thickness shear mode, not unlike those investigated analytically by Mindlin [102] and Lee [104][105]. Since it is not reasonable to place electrodes on the lateral walls of the device, due to the small thickness, horizontal electrical excitations are not possible for thin-film devices. Therefore, a more reasonable way to excite thickness shear modes is to have an in-plane poled piezoelectric material as shown in Figure 1-22:

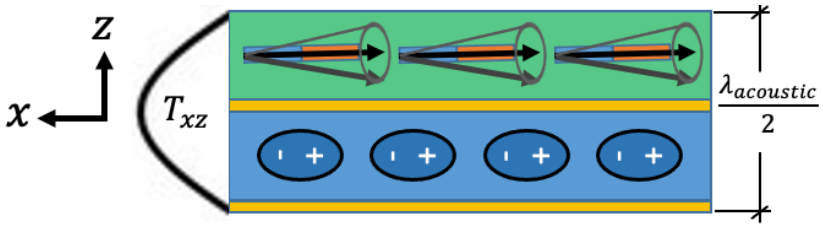


Figure 1-22: Thickness Shear Mode Multiferroic Antenna

Thin-film piezoelectrics poled in-plane are currently challenging but this could open up the possibility for future fabrication and material science research on the topic. Still, these difficulties are why emerging technologies have begun to shift focus towards piezoelectric antennas which will be discussed in the following Section 1.2.3 and are simulated in Chapter 5.

Another way of improving the performance of the antenna in Figure 1-20 is to note that the half sine wave first eigenmode, due to the traction free boundaries, will be retained if an additional layer is added to the stackup as shown in Figure 1-23:

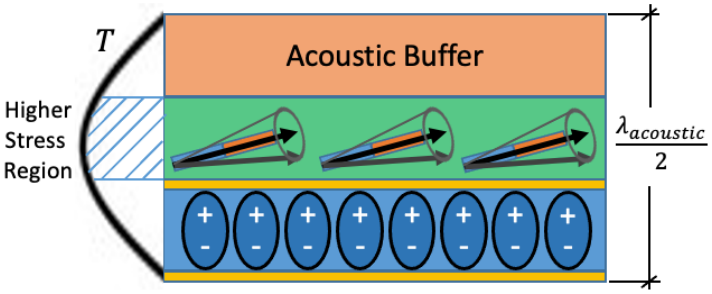


Figure 1-23: Multiferroic antenna with acoustic buffer.

The acoustic buffer has the effect of ensuring a higher stress region within the magnetostrictive layer [131], thus boosting the performance by generating a higher magnetic current. Any added layers will need to be impedance matched (same wave speed) to the rest of the stackup to ensure that the mechanical waves only reflect at the traction free boundaries rather than at the interfaces as well. This is a concern whenever interfaces between two materials exist however, and therefore even the original configuration of Figure 1-20 must take impedance matching into account. If the planar nature of the device may be sacrificed, another approach is to allow the thickness of the magnetostrictive layer to increase until an axial bar like configuration is reached. This however would introduce difficulties of retaining a single magnetic domain since shape anisotropy would no longer heavily favor in-plane magnetizations. This again highlights why research focus has shifted towards piezoelectric antennas, at least within the aerospace industry.

The discussion so far has focused on 1D bulk acoustic wave (BAW) devices, but more complex surface acoustic wave (SAW) devices are also possible and will require the use of the full 3D Newton's laws.

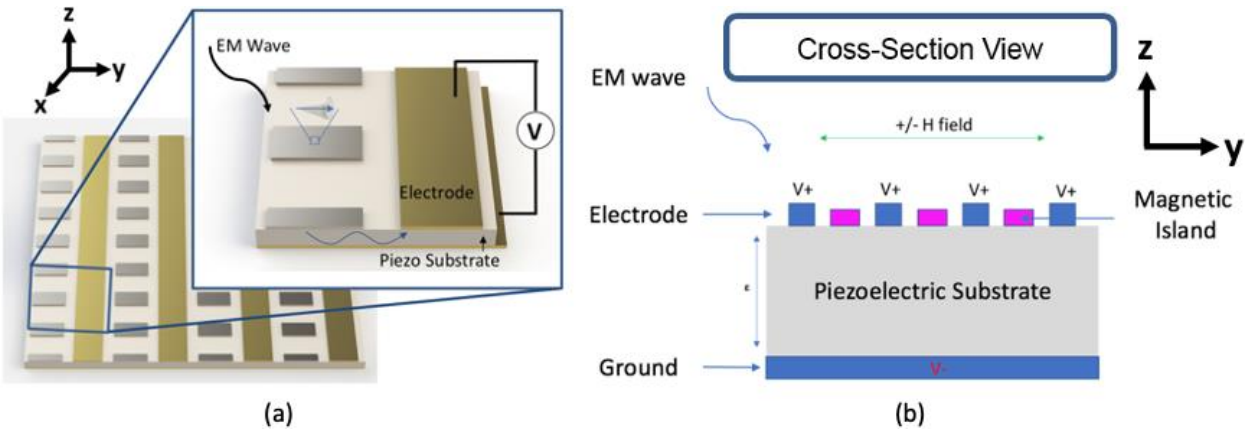


Figure 1-24: SAW multiferroic antenna, a) Structure and physical coupling mechanism, b) Cross section of the antenna.

Within the SAW device a voltage excitation is applied to the electrodes inducing surface shear waves to propagate within the piezoelectric substrate triggering magnetization changes within the intertwined magnetic islands. Such devices have proven exceedingly difficult to fabricate and model, providing motivation for further research. Although a piezoelectric material could conceivably be used instead in Figure 1-24, generating a 3D piezoelectric antenna, it is much simpler and optimally effective to utilize 1D piezoelectric devices loaded with metal wire to boost dipole moment and fill a 3D volume. This concept will be discussed in the subsequent Section 1.2.3.

While simulation of multiferroic devices is needed, the analysis performed herein is exclusively on piezoelectric antennas due to shifting interest into these radiators by organizations such as DARPA. Multiferroic devices, being the most general case, will continue to be discussed in this text but future work is needed to modify the numerical framework provided in Chapter 3 to tackle the multiferroic antenna problem.

### 1.2.3 Piezoelectric Antennas (PEAs)

The conversation so far has revolved around magnetic current multiferroic antennas, but these are not the only type of antennas that leverage mechanical resonance as the radiation

mechanism. Indeed, polarization oscillations can also be utilized to propagate EM radiation by effectively swapping the magnetostrictive material with piezoelectric material within designs similar to those discussed in section 1.2.2, in what are known as piezoelectric antennas (PEAs). These will no longer be magnetic current antennas and will therefore suffer from drawbacks largely trivial to MF antennas such as the platform effect (for currents tangential to the ground plane), and near field degradation within lossy environments. These issues do not come without counteracting benefits, however. For example, the magnitude of polarizations can be changed in contrast to magnetizations, and therefore, normal stresses may always be used to induce polarization changes unlike MF antennas utilizing single domain magnetostrictives. Also, the need for a bias field is eliminated. Impedance matching issues can additionally be eliminated if the same piezoelectric material is used within the driving sandwich and the radiating volume. Lastly, piezoelectric resonator antennas are much easier to model and verify with commercial software as the EM fields within the piezoelectric are the same whether electrostatics or full Maxwell's are utilized [104]. Therefore, if a very low frequency (VLF) transmitter is desired that is not placed within a dielectric lossy environment, a PEA solution should be chosen from a simplicity standpoint. Since readily available magnetic sensors can already receive in lossy environments [121] this would work wonderfully for portable transmitters located above water sending signals to underwater equipment like submarines. However, for scuba diver to scuba diver communications, or signals sent within implantable device networks, these radiators would work poorly. As such, there is a need that can be filled by piezoelectric radiators though multiferroic antennas have broader applicability at the cost of increased complexity.

There are two main configurations of PEAs, axial bar radiators, and planar radiators as shown in Figure 1-25a and b respectively. Note that planar radiators have two main configurations. In the first (top of Figure 1-25b), Poisson's effect is utilized to generate resonance in-plane orthogonal to the electrodes. The PEA must have a surface that is not

completely covered by an electrode, otherwise the device would act as a capacitor. In the second (bottom of Figure 1-25b) the PEA is configured much like the MF antennas of section 1.2.2, producing a thickness resonance mode. Due to large depolarization (polarization current orthogonal to large surface area), it is not recommended that planar devices be utilized, and only axial dumbbell designs are simulated in Chapter 5. Recall from Section 1.2.2 that multiferroic antennas like those at the bottom of Figure 1-25b also suffer, though from separate issues. The rest of this section focuses on the history of these PEA devices.

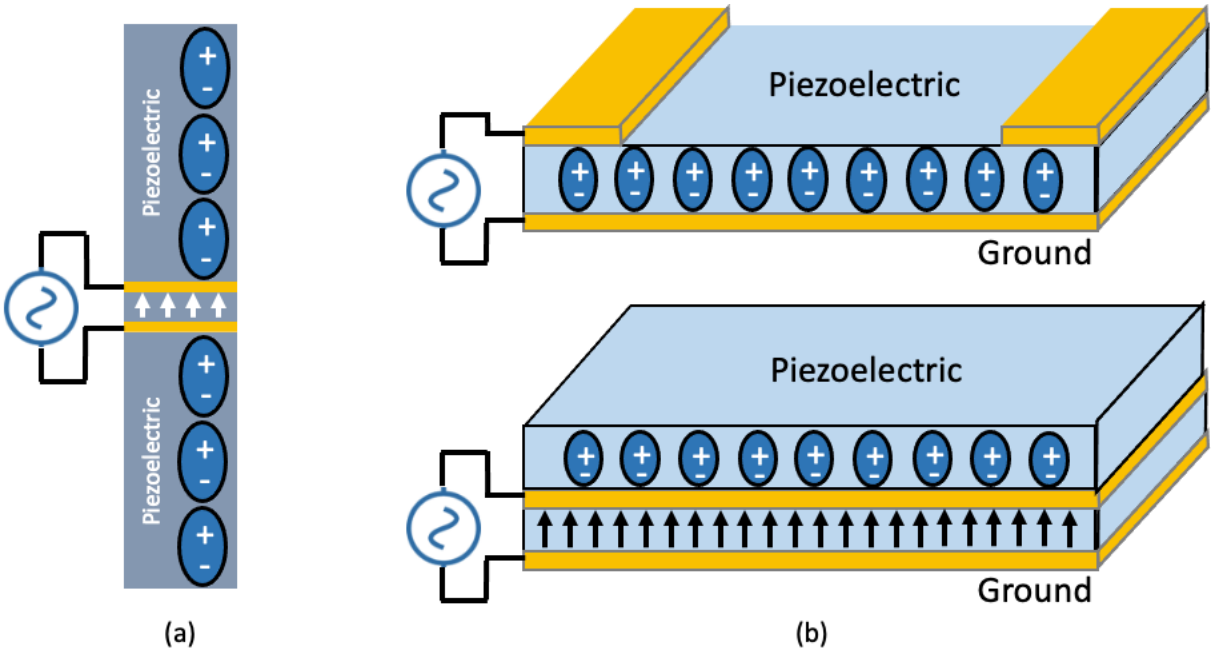


Figure 1-25: Piezoelectric Radiator Configurations, (a) Axial bar (dumbbell) design, (b) Planar designs.

As indicated previously the earliest work on piezoelectric radiators was performed by Mindlin [102], and decades later the research was continued by Lee [104][105]. Since this work has already been discussed in section 1.2.1, the conversation herein will fast-forward to 2019, where Kemp et al [152], out of Stanford, perform experiments and simulations on a low

frequency piezoelectric radiator. The device was a homogenous rod of Lithium Niobate (LN), 9.4cm long, with mechanical resonance around 35kHz. The antenna was fixed in the center and traction free on both ends with voltage excitation at the bottom. This produced a half sine wave stress profile which in turn caused the transmitter to behave like a dipole, due to piezoelectric coupling, but with an efficiency greater than 300x that of traditional antennas. The authors also compared experimental measurements of the input impedance with a multiphysics finite element model, as well as an equivalent circuit model. Within the equivalent circuit model, an RLC resonating circuit was used to model the mechanical resonance with the electromechanical coupling modeled by a transformer.

Piezoelectric radiators need not be in the shape of rods, however, as planar designs also exist as investigated by Hassanien et al in 2019 [153]. This work focused on a disk-shaped device where the bottom planar face was covered with a ground electrode, and the top electrode was confined to an area hugging the outer circumference. When excited, mechanical waves propagate towards the center of the device, producing the desired resonance. Since the piezoelectric is poled out-of-plane, this produces polarization currents normal to the ground plane which are not hindered by image currents, reducing platform effect. Hassanien continues his work through two publications in 2020 [154][155], in which he proposes adding unipolar electrets to the maximally displacing portion of a MEMS resonator to increase radiation, similar to Weldon [156] who proposed placing charge on the tip of vibrating carbon nanotubes to radiate EM waves. This crosses into the space of bulk mechanical motion driven antennas which is discussed in section 1.2.4.

Also in 2020, Dong et al [157] modeled a stress source within a piezoelectric radiator using the finite difference time-domain (FDTD) method. As a simplification, these researchers did not use the elastodynamics equation at all, but rather modeled the stress input as a lumped voltage-resistance source. Also, an unconditionally stable solver was not utilized, and results were not

presented, only derivations. Still, this represents a novel idea within the space. Interest in piezoelectric radiators has continued into 2021 as well [158][159], with Yong et al. [160] provided a summary of some prominent designs in 2022.

In 2023, Xu et al. [161] attempted to tackle the problem of small bandwidth in piezoelectric resonator antennas by utilizing PMN-PT as the radiating material. Unfortunately, there appears to be some confusion in the paper as the authors argue that the inverse piezoelectric effect inherently involves ferroelectric switching and is therefore a cause of significant friction. While poling of a piezoelectric does indeed involve ferroelectric switching, the linear piezoelectric effect only involves a displacement of the asymmetrical ion within each crystal, not a full switching, hence why piezoelectricity is a linear effect. Coincidently, the authors argued that the electrostrictive effect would be better for radiation, which would indeed suffer from temperature increases. Also, the disk-shaped resonator that was tested included electrodes on the top and bottom of the PMN-PT that covered the entire surface in contrast to Hassanien's previous work [153]. Due to the electrically tiny size, this disk was therefore an energy storing capacitor rather than an energy radiating antenna and any received power measured from their receiving loop antenna was from reactive near fields that do not contribute to radiation. The authors attempted to show that the received power during their measurements was indeed from the PMN-PT by measuring a device that only includes the electrodes and wires, but their measurements were made only within 10s of meters away, easily within the near field. Therefore, the increased received power was from the non-radiating near fields produced from the PMN-PT. Any claims about increased bandwidth are therefore also suspect. This problem of resonant capacitors being advertised as mechanical antennas is a wider issue as Cao et al. [162] appear to have fallen into the same trap. Still, Xu et al. [160] are quite accurate that materials with low mechanical to electrical energy conversion (like LN) are not well suited for mechanical antenna applications.

In 2023, Gao et al. [163] experimented with adding conducting material to the piezoelectric antennas to increase the effective length. Essentially, metal wire was added along the axial direction of the cylindrical antenna such that the resonating piezoelectric material would act as an impedance matching element. While innovative, Gao et al. did record smaller efficiencies than that of Kemp [152] when the antenna was of the same size or slightly larger. Interestingly, in the device, the piezoelectric bar has electrodes on the top and bottom, so it does not seem that the mechanical portion of the device is radiating anything. Therefore, it appears that the authors were able to hit the upper radiation efficiency bound (from [164]) for metallic electrically small antennas (MESAs) with a device that has only metallic radiating elements by utilizing a piezoelectric resonator for impedance matching. This could mean that further improvements in efficiency may be possible if the electrodes are moved around such that the piezoelectric material also radiates. This marriage between novel piezoelectric antennas and the classic current carrying wire is the optimal method of generating large dipole moments within a 3D space. Thus, 1D axial bar PEAs are the preferred configuration and 2D/3D devices are not considered herein.

Finally, in 2023, DARPA sent out a Broad Agency Announcement (BAA) seeking proposals for electrically small receivers (TA1) and transmitters (TA2) under the name “Macaroni”. The name was originally meant to be Marconi (in honor of the first transatlantic communication [26-28]) but due to a clerical error was changed to Macaroni. The exact performance metrics are classified, and the bidding process ended on October 10, 2023, when final proposals were due. Notable amongst the TA2 bidders is the Northrop Grumman Corporation, in partnership with Greg Carman and Ethan Wang of the University of California, Los Angeles. Although this proposal was ultimately not funded, the technical approach described in the proposal was well received and simulations in Chapter 5 of this work cover much of the proposed innovations.

### 1.2.4 Alternative Mechanical Antennas (Mechtennas)

In section 1.1.2, the radiation mechanism in antennas was described as fundamentally originating from charge acceleration, and in section 1.2.2, it was shown that magnetization oscillations are a magnetic equivalent to this phenomenon. So far, piezoelectric radiators have been presented as devices that produce the former, and multiferroic antennas have been presented as devices that produce the latter, both of which are strain driven methods. However, even if the mechanical antenna is thought of as rigid (not deformable), radiation will still occur if bulk mechanical motion is applied. This may be in the form of spinning an electric dipole (Bipolar Electret [154]) or permanent magnet, or linear acceleration of an electric monopole (Unipolar Electret [154]) as shown in Figure 1-26. The usefulness of unipolar electrets is mainly in the augmentation of multiferroic radiators [154][156]. As such, the remainder of this section will focus first on oscillating electric dipoles and then on spinning magnets.

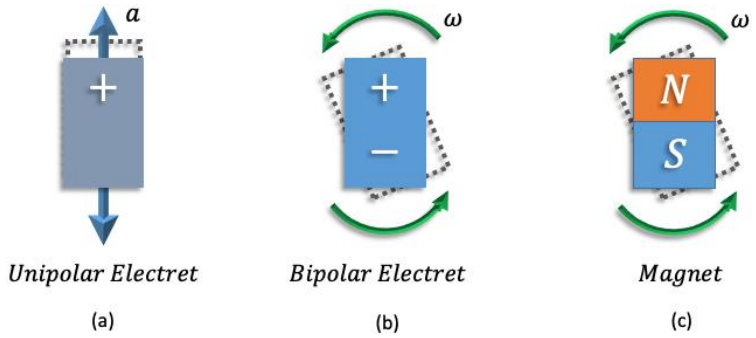


Figure 1-26: Bulk mechanical motion driven antenna concept, (a) Electric monopole under linear acceleration, (b) Oscillating electric dipole, (c) Oscillating magnet.

The earliest study of oscillating electric dipoles appears to have been made by a curious astrophysicist in 1976 [165] who noted the following: 1) gravity and acceleration are often indistinguishable, 2) charge acceleration fundamentally drives EM radiation, and 3) small positive charges appear near the surface of rotating objects. Therefore, rapidly rotating dense

celestial bodies should produce at least small amounts of radiation. While curious, this appeared to be a novelty until Bickford picked up the idea in 2017 for the purpose of super low frequency (SLF 30-300Hz) communications by spinning an electric dipole at 167Hz [166]. The idea was put forward again by Barani in 2018 [167] and expanded on by Bickford in 2019 [168] where he proposed a linear mechtenna composed of layers of electrets where adjacent layers were displaced anti-parallel with respect to one another.

The study of spinning magnets started in the 1950s [169][170], and later in 1978 [171], again with researchers based in astrophysics. Research then increased in frequency in 2014/2015 when Garraud et al began studying oscillating dipoles for the purpose of low frequency wireless power transfer with a potential application aimed toward wireless battery charging of biomedical implants [172][173]. Selvin, working under Ethan Wang, then presented on the topic of oscillating dipoles in a conference in 2017 [174], highlighting some of the main issues with the oscillating dipole method in general, namely that a 1kHz signal will require an angular speed of 60,000rpm, leading to frictional issues with additional complications introduced by frequency modulation for information transfer.

Prasad then takes up the mantle of researching spinning magnets, presenting at conferences in 2017 [175] and 2018 [176], and publishing in 2019 [177] on “magnetic pendulum arrays”. These configurations use diametrically polarized permanent magnetics in a linear array as shown in Figure 1-27.

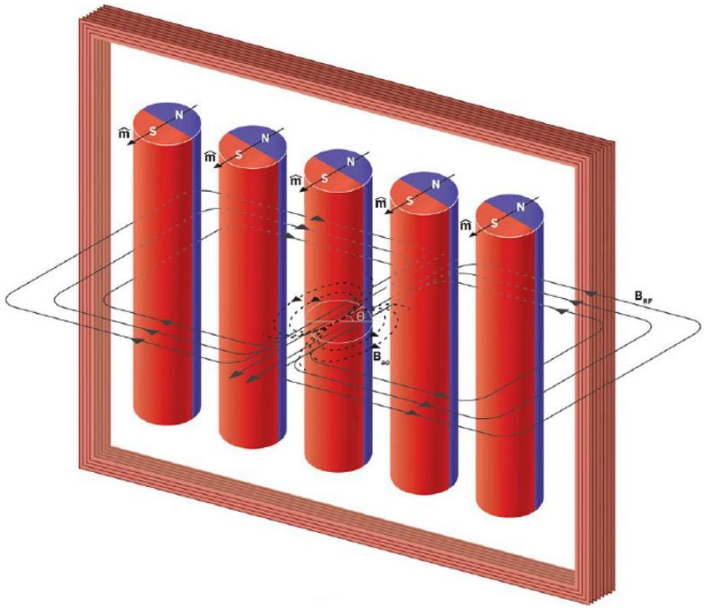

Figure 1-27: Magnetic pendulum array, from [Prasad 2019]

The adjacent elements within the array will align to one another, producing a self-biased system, and the coils surrounding the bars induce an RF magnetic field that excites oscillations. This innovative design was proposed in order to significantly reduce the mechanical loss associated with mechtennas. It was shown that the pendulum array efficiency was about 7dB higher than that of the coils operating alone.

Active research in mechtennas has continued [178-182], but the drawback of these antennas is the large inertial forces induced, producing structural integrity concerns [127], and the general power inefficiency of the proposed designs with limited magnetic field strength for long-range communications [130]. The applicability to the biomedical industry also appears to be limited, if not nonexistent, edging multiferroic antennas ahead within the mechanically driven EM radiator design space. However, for up to 1kHz, rotating magnet antennas still truly shine and appear to have a healthy future.

## 1.3 Dissertation Overview

Thus far in chapter 1, important preliminary concepts have been presented to discuss the operation and history of traditional antennas, microstrip antennas, and mechanical antennas. Three dynamic systems (elastodynamic, electrodynamic, micromagnetic) were also introduced along with the ferroic orders. Piezoelectric and piezomagnetic materials were described, along with how these materials can be combined into magnetoelectric (multiferroic) composites which can be made to radiate EM energy. The method by which these multiferroic antennas overcome the current issues facing antenna miniaturization was presented. A summary of the remainder of this dissertation follows.

In chapter 2, all relevant equations describing the electro-magneto-mechanical system, necessary for modeling multiferroic antennas, are presented. First the balance laws are discussed. Then, the 1$^{st}$ law of thermodynamics will be evoked to demonstrate the conditions under which the input power equals the output power. Then, the 2$^{nd}$ law of thermodynamics will be utilized, yielding an inequality that imposes restrictions on the constitutive relations. The laws of thermodynamics provide insight into how coupling between EM and mechanical fields can take place through constitutive relations. Then, the uncoupled and coupled constitutive relations are described. Finally, a brief discussion on dissipation is presented in the context of quality factors and other terms that may be more familiar to engineers. A summary of all the equations is then provided at the end of the chapter. All equations are presented in continuum (non-discretized) form.

In chapter 3, the discretized finite difference equations are presented along with the relevant derivations. These equations are used to update the EM fields, stress, velocity, and convolutional history variables. The order in which the updates occur is described with reasoning for why the parameters are best updated in that manner. Discussions about interface conditions, excitations, boundary conditions, and PML expressions are also provided.

In chapter 4, validation cases are discussed that test the mechanical, electrodynamic, and micromagnetic portions of the code. Comparison to analytical solutions and commercial software are both performed and numerical experiments are conducted to develop best practices for modelers. Validation cases include but are not limited to aperture antennas, electric dipoles, 1D mechanical bars, and infinite line sources.

Lastly in chapter 5, simulations on mechanical antenna devices are performed and discussions on antenna performance are conducted. The devices are compared to the theoretical limits for electrically small antennas and far field parameters are presented. Radiation efficiencies are presented and compared to the state of the art with tips on how to improve performance for future designs. Conclusions are drawn as to the efficacy of mechanical antennas to meet the challenges of future antenna platforms.

# CHAPTER 2: MULTI-PHYSICS MODEL DEVELOPMENT

Multiferroic antennas function by mechanically bonding piezoelectric material to thin film magnetostrictive material. The piezoelectric may then be excited by attached electrodes which then propagates acoustic waves to the bonded magnetostrictive generating magnetization fluctuations. Some of the mechanical energy is then dissipated due to magnetic loss within the material and some is propagated out into free space as an EM wave [131]. Therefore, any numerical algorithm wishing to properly characterize a small multiferroic antenna must be capable of not only dealing with the multi scale nature of the physics involved but also solve three sets of coupled partial differential equations: Landau-Lifshitz-Gilbert (LLG) equation governing micromagnetics within the magnetostrictive, Newton's Laws governing the acoustic waves, and Maxwell's laws governing EM waves. Currently existing finite element software like COMSOL Multiphysics have been shown to be able to solve these equations in the absence of EM waves [74][183]. Previous Work done by the TANMS ERC solved these equations including EM waves by utilizing an unconditionally stable multi-scale solver under a uniaxial strain state and in the absence of piezoelectric radiating elements [110][114][131]. This is sufficient to model a bulk acoustic wave (BAW) multiferroic antenna but is incapable of modeling 2D and 3D devices like those that utilize surface acoustic waves. The solver tackled the multi-scale problem by using a special finite difference time domain (FDTD) algorithm which will be adopted herein, where the exercise of including piezoelectricity is performed. The result is an algorithm capable of modeling mechanical resonance-based antennas which may be used to design exotic new devices.

This chapter deals with the derivation of all required equations in continuum form. These are split into two categories; balance laws, which remain unchanged when cross-coupling is introduced, and constitutive relations, where the coupling terms in a system involving multiple physical domains arise. Convolutional methods will be discussed when appropriate for

describing lossy media. The equations herein are written in indicial notation unless otherwise specified.

## 2.1 Balance Laws

### 2.1.1 Conservation of Electron Angular Momentum

Since magnetism originates from the intrinsic property of spin within the electron and the orbit of the electron about the nucleus of the atom, conservation of the associated angular momentum is particularly significant within magnetic materials. Following the approach by Landis [184] two micro-force systems are introduced that are power conjugate with the magnetization order parameter: one representing the surface interactions between magnetic domains, and the other representing magnetic forces within the volume of each magnetic domain. The power from these micro-force systems may be written as follows:

$$\iiint \pi_i \dot{M}_i dV\,, \qquad \iint \zeta_{ji} n_j \dot{M}_i dA \tag{2.1}$$

Where $n_j$ is the surface normal of differential area $dA$, $dV$ is a differential volume element, $M_i$ is the magnetization, $\zeta_{ji}$ is the surface micro-force tensor, and $\pi_i$ is the volumetric micro-force vector. Utilizing these micro-force systems, the angular momentum balance may be written as:

$$\iint \epsilon_{kji} M_j \zeta_{pi} n_p dA + \iiint \epsilon_{kji} M_j \pi_i dV = \iiint \frac{\mu_0}{\gamma_0} \dot{M}_k dV \tag{2.2}$$

Where $\frac{\gamma_0}{\mu_0} = \gamma$ is the gyromagnetic ratio of the electron magnetic moment to angular momentum, and as such is used to express the time derivative of angular momentum with respect to the time derivative of magnetization. Applying the divergence theorem and recognizing that the balance must apply to any arbitrary volume yields:

$$\epsilon_{kji} M_j \left(\zeta_{pi,p} + \pi_i\right) + \epsilon_{kji} M_{j,p} \zeta_{pi} = \frac{\mu_0}{\gamma_0} \dot{M}_k \tag{2.3}$$

Equation (2.3) relates the micro-force systems to the time derivative of magnetization, which incorporates changes in the direction and magnitude of the magnetization vector with time. The micromagnetics literature often makes assumptions about the magnitude of the magnetization and the forces acting along the direction of magnetization. To take advantage of these assumptions the cross product of equation (2.3) with respect to magnetization is taken yielding:

$$\epsilon_{mkn}\epsilon_{kji}M_nM_j\left(\zeta_{pi,p}+\pi_i\right)+\epsilon_{mkn}\epsilon_{kji}M_nM_{j,p}\zeta_{pi}=\frac{\mu_0}{\gamma_0}\epsilon_{mkn}M_n\dot{M}_k \tag{2.4}$$

Equation (2.4) no longer provides information on how the micro-forces effect the magnetization magnitude since the components of the micro-forces in the direction of the magnetization have been eliminated by the nature of the cross product. For example, had the micro-forces been completely in line with the magnetization vector then the left-hand side of equation (2.4) would be zero since the rate of change of magnetization would be parallel to its direction and be eliminated by the cross product. Recall the following identity:

$$\epsilon_{mkn}\epsilon_{kji}=\left(\delta_{nj}\delta_{mi}-\delta_{ni}\delta_{mj}\right) \tag{2.5}$$

Using (2.5), equation (2.4) may be written as:

$$\begin{aligned}&\left(\delta_{nj}\delta_{mi}-\delta_{ni}\delta_{mj}\right)M_nM_j\left(\zeta_{pi,p}+\pi_i\right)+\epsilon_{mkn}\epsilon_{kji}M_nM_{j,p}\zeta_{pi}=\frac{\mu_0}{\gamma_0}\epsilon_{mkn}M_n\dot{M}_k\\&\rightarrow|M|^2\left(\zeta_{pm,p}+\pi_m\right)-M_mM_n\left(\zeta_{pn,p}+\pi_n\right)+\epsilon_{mnk}\epsilon_{ijk}M_nM_{j,p}\zeta_{pi}\\&\qquad=\frac{\mu_0}{\gamma_0}\epsilon_{mnk}\dot{M}_nM_k\end{aligned} \tag{2.6}$$

Where $M_iM_i=|M|^2$ has been used. Also note that some manipulation of the indices has been performed. The last term on the left-hand side of the equality in equation (2.6) has been altered using the following property of permutations,

$$\epsilon_{mkn}\epsilon_{kji}=-\epsilon_{mkn}\epsilon_{ijk}=\epsilon_{mnk}\epsilon_{ijk}$$

The term on the right-hand side in equation (2.6) was altered using the anti-commutative property of the cross product ($a\times b=-b\times a$),

$$\epsilon_{mkn} M_n \dot{M}_k = -\epsilon_{mkn} \dot{M}_n M_k = \epsilon_{mnk} \dot{M}_n M_k$$

Following the assumptions made by Landis [184] the micro-forces parallel to the magnetization are assumed to be quasi-static. This means that changes in magnetization occur such that the micro-forces are in equilibrium at every instant in time. Changes in magnetization amplitude are also assumed to occur at much shorter time scales than those associated with directional changes in magnetization. Therefore, the work being done by micro-forces in the direction of the magnetizations is assumed zero:

$$M_n\left(\zeta_{pn,p} + \pi_n\right) = 0 \tag{2.7}$$

Therefore, equation (2.6) is simplified by equation (2.7) to:

$$\zeta_{pm,p} + \pi_m = \frac{\mu_0}{M^2 \gamma_0} \epsilon_{mnk} \dot{M}_n M_k - \frac{1}{|M|^2} \epsilon_{mnk} \epsilon_{ijk} M_n M_{j,p} \zeta_{pi} \tag{2.8}$$

By tinkering with the indices, this may also be written as:

$$\zeta_{ji,j} = \frac{\mu_0}{M^2 \gamma_0} \epsilon_{ijk} \dot{M}_j M_k - \frac{1}{M^2} \epsilon_{ijk} \epsilon_{krs} M_j M_{s,p} \zeta_{pr} - \pi_i \tag{2.9}$$

Equation (2.9) is the balance of electron angular momentum and will be leveraged in section 2.2.1 when the power balance is performed consistent with the continuum thermodynamics approach contained herein.

### 2.1.2 Conservation of Linear Momentum in Viscoelastic Media

If surface tractions $t_i$ (forces) are applied to the outer boundary of a body, the conservation of linear momentum equation is written as [185]:

$$\frac{d}{dt} \iiint \rho \, v_i dV = \iint t_i \, dA + \iiint b_i dV \tag{2.10}$$

Where $b_i$ is the body force, $\rho$ is the volumetric mass density, and $v_i$ is the velocity which is the time derivative of the displacement. The density is assumed to be time invariable, and the differential volume ($dV$) is assumed to not change appreciably (small deformation). Therefore, the time derivative may be moved into the volume integral and applied to the velocity directly. In

order to combine the traction term, which acts on the surface, to the inertial and body force terms, which act on the volume, Cauchy's stress theorem is applied:

$$t_i = T_{ij} n_j \tag{2.11}$$

Now the divergence theorem is used, and it is recognized that the balance must apply to any arbitrary volume yielding:

$$\rho \dot{v}_i = T_{ij,j} + b_i \tag{2.12a}$$

Equation (2.12a) is known as the elastodynamic equation, or Newton's law, or the mechanical balance equation. All three are appropriate. Often when considering elastic waves, the body force term is ignored (though not by necessity), and the divergence of stress is seen as the sole driving mechanism for mechanical accelerations as was alluded to in section 1.1.1.

$$\rho \dot{v}_i = T_{ij,j} \tag{2.13b}$$

When excitations are slow (low frequency) the mechanical wavelength may be large compared to the dimensions of the structure and the body may be considered rigid for dynamic analysis as is the case for engineers working on mechanisms like steering systems and landing gear. Alternatively, if the excitations are exceedingly slow (quasistatic) then the system may be modelled as a deformable body with stresses/strains not evolving with time. These approximations are not appropriate herein and equation (2.12) will be used to write update equations for the velocity.

### 2.1.3 Maxwell's Equations w/ Modification

Maxwell's equations governing the electrodynamics, pictorially represented in Figure 1-4, are presented below in equations (2.13a-d) [25]:

$$\text{Guass's Law} \qquad D_{i,i} = \rho_v \tag{2.13a}$$

$$\text{Guass's Law for Magnetism} \qquad B_{i,i} = 0 \tag{2.13b}$$

$$\text{Faraday's Law of Induction} \qquad \dot{B}_i + \mathcal{M}_i^S = \epsilon_{ijk} E_{j,k} \tag{2.13c}$$

$$\text{Ampere's Law with Maxwell's Addition} \qquad \dot{D}_i + \sigma_{ij}E_j + J_i^S = \epsilon_{ijk}H_{k,j} \tag{2.13d}$$

Where $D$ is the electric flux, $\rho_v$ is the volume charge density, $B$ is the magnetic flux, $\mathcal{M}^S$ is the magnetic source current, $\sigma$ is the electric conductivity, and $J^S$ is the electric source current. For the purposes of this work, Maxwell's divergence equations (2.13ab) are not particularly interesting as the proper choice of finite difference lattice automatically satisfies both expressions [186-188].

When dealing with lossy material, Maxwell's equations may be written with the spatial derivatives in terms of complex frequency shifted (CFS) stretched coordinates [187]. To see how this is the case, ignore sources and substitute $E = E_0 e^{j\omega t}$ into Ampere's law to get the following in free space:

$$j\omega\varepsilon_{ij}E_j^0 + \sigma_{ij}E_j^0 = \epsilon_{ijk}H_{k,j} \tag{2.14}$$

Where $\varepsilon_{ij}$ is the electric permittivity which relates the electric flux $D_i$ to the electric field $E_i$. Equation (2.14) may be rewritten as:

$$j\omega\varepsilon_{ij}s_{jk}E_k^0 = \epsilon_{ijk}H_{k,j} \tag{2.15}$$

Where,

$$s_{jk} = \delta_{jk} + \beta_{jl}^{\epsilon}\frac{\sigma_{lk}}{j\omega} \tag{2.16}$$

Where $\beta_{jl}^{\epsilon}$ is the inverse permittivity, and the complex $s_{ij}$ terms are called the stretching coefficients [189] and may be used to model lossy conductive material. Faraday's law may be similarly written:

$$j\omega\mu_{ij}s_{jk}^*H_k = \epsilon_{ijk}E_{j,k} \tag{2.17}$$

Where $\mu_{ij}$ is the magnetic permeability and:

$$s_{jk}^* = \delta_{jk} + \beta_{jl}^{\mu}\frac{\sigma_{lk}^*}{j\omega} \tag{2.18}$$

Where $\beta_{jl}^{\mu}$ is the inverse permeability and $\sigma_{lk}^{*}$ is the purely theoretical magnetic conduction tensor. Both $s_{ij}$ and $s_{ij}^{*}$ will be equal if the following matching condition holds:

$$\beta_{jl}^{\epsilon}\sigma_{lk} = \beta_{jl}^{\mu}\sigma_{lk}^{*}, \qquad \therefore \quad s_{jk} = s_{jk}^{*} \tag{2.19}$$

In the literature, the stretching coordinates are always written in free space and, since the conductivity tensors are diagonal, using a single index yields:

$$s_i = 1 + \frac{\sigma_i}{j\omega\varepsilon_0} \tag{2.20}$$

Ampere's and Faraday's law are then written divorced from indicial notation for now, as shown below for the x-projection of Ampere's law [189]:

$$j\omega\varepsilon_0 E_x = \frac{1}{s_y}\frac{\partial H_z}{\partial y} - \frac{1}{s_z}\frac{\partial H_y}{\partial z} \tag{2.21}$$

Equation (2.21) reveals that the $s$ values may be modified to introduce a real stretch of the x, y, and z coordinates by replacing unity in (2.20) with some value $\kappa_i > 1$ as shown below:

$$s_i = \kappa_i + \frac{\sigma_i}{j\omega\varepsilon_0} \tag{2.22}$$

Note above that if the material is lossless ($s_i = \kappa_i$) then the stretching of the coordinates is apparent from the $s_y\partial y$ and $s_z\partial z$ terms in (2.21). The stretched coordinate metrics $s_i$ can therefore be thought of as a generalized way of including both stretching and loss into the system. Of course, if the $s$ values were set to unity, there would be no stretching and the original lossless Ampere's law would be recovered. A further generalization was proposed by Kuzouglu and Mittra [190] to shift the pole away from $\omega = 0$ as follows:

$$s_i = \kappa_i + \frac{\sigma_i}{\alpha_i + j\omega\epsilon_0} \tag{2.23}$$

Where $\alpha_i$ is a positive real number which accomplishes the pole frequency shifting effect. The full benefit of this choice of stretched coordinate metrics will be explored more fully in chapter 3. Following the nomenclature of [191], define $\bar{s}_i = s_i^{-1}$, which may be written as:

$$\bar{s}_i = \frac{1}{\kappa_i + \frac{\sigma_i}{\alpha_i + j\omega\epsilon_0}} = \frac{\alpha_i + j\omega\epsilon_0}{\kappa_i\alpha_i + \sigma_i + j\kappa_i\omega\epsilon_0} = \frac{1}{\kappa_i} - \frac{\frac{\sigma_i}{\kappa_i^2\epsilon_0}}{\frac{\alpha_i}{\epsilon_0} + \frac{\sigma_i}{\kappa_i\epsilon_0} + j\omega} \tag{2.24}$$

Performing inverse Laplace transformation produces:

$$\bar{s}_i(t) = \frac{1}{\kappa_i}\delta(t) - \frac{\sigma_i}{\kappa_i^2\epsilon_0} e^{-\left(\frac{\alpha_i}{\epsilon_0} + \frac{\sigma_i}{\kappa_i\epsilon_0}\right)t} H(t) = \frac{1}{\kappa_i}\delta(t) + \zeta_i(t) \tag{2.25}$$

Where $\delta(t)$ is the dirac delta function and,

$$\zeta_i(t) = -\frac{\sigma_i}{\kappa_i^2\epsilon_0} e^{-\left(\frac{\alpha_i}{\epsilon_0} + \frac{\sigma_i}{\kappa_i\epsilon_0}\right)t} H(t) \tag{2.26}$$

Which is the impulse response of the stretched coordinate metric with $H(t)$ being the Heaviside step function. Since multiplication in the frequency domain is equivalent to convolution in the time domain, transforming the modified Maxwell's equations into time domain will require the use of convolution integrals. Ampere's equations may therefore be written as follows:

$$\dot{D}_x + \sigma_{xx}E_x + J_x^s = \frac{1}{\kappa_y}\frac{\partial H_z}{\partial y} - \frac{1}{\kappa_z}\frac{\partial H_y}{\partial z} + \int_{0^-}^{t} \zeta_y(t-\tau)\frac{\partial H_z(\tau)}{\partial y}d\tau - \int_{0^-}^{t} \zeta_z(t-\tau)\frac{\partial H_y(\tau)}{\partial z}d\tau \tag{2.27a}$$

$$\dot{D}_y + \sigma_{yy}E_y + J_y^s = \frac{1}{\kappa_z}\frac{\partial H_x}{\partial z} - \frac{1}{\kappa_x}\frac{\partial H_z}{\partial x} + \int_{0^-}^{t} \zeta_z(t-\tau)\frac{\partial H_x(\tau)}{\partial z}d\tau - \int_{0^-}^{t} \zeta_x(t-\tau)\frac{\partial H_z(\tau)}{\partial x}d\tau \tag{2.27b}$$

$$\dot{D}_z + \sigma_{zz}E_z + J_z^s = \frac{1}{\kappa_x}\frac{\partial H_y}{\partial x} - \frac{1}{\kappa_y}\frac{\partial H_x}{\partial y} + \int_{0^-}^{t} \zeta_x(t-\tau)\frac{\partial H_y(\tau)}{\partial x}d\tau - \int_{0^-}^{t} \zeta_y(t-\tau)\frac{\partial H_x(\tau)}{\partial y}d\tau \tag{2.27c}$$

Which may be shortened by using the following "history variables":

$$\Phi_{Hmq} = \int_{0^-}^{t} \zeta_q(t-\tau)\frac{\partial H_m(\tau)}{\partial q}d\tau = -\frac{\sigma_q}{\kappa_q^2\epsilon_0}\int_{0^-}^{t} e^{-\frac{1}{\epsilon_0}\left(\alpha_q + \frac{\sigma_q}{\kappa_q}\right)(t-\tau)}\frac{\partial H_m}{\partial q}d\tau, \quad \begin{matrix} m = x,y,z \\ q = x,y,z \\ m \neq q \end{matrix} \tag{2.28}$$

Therefore,

$$\dot{D}_x + \sigma_{xx}E_x + J_x^s = \frac{1}{\kappa_y}\frac{\partial H_z}{\partial y} - \frac{1}{\kappa_z}\frac{\partial H_y}{\partial z} + \Phi_{Hzy} - \Phi_{Hyz} \tag{2.29a}$$

$$\dot{D}_y + \sigma_{yy}E_y + J_y^s = \frac{1}{\kappa_z}\frac{\partial H_x}{\partial z} - \frac{1}{\kappa_x}\frac{\partial H_z}{\partial x} + \Phi_{Hxz} - \Phi_{Hzx} \tag{2.29b}$$

$$\dot{D}_z + \sigma_{zz}E_z + J_z^s = \frac{1}{\kappa_x}\frac{\partial H_y}{\partial x} - \frac{1}{\kappa_y}\frac{\partial H_x}{\partial y} + \Phi_{Hyx} - \Phi_{Hxy} \tag{2.29c}$$

An important point will now be made, note that the electric flux $D$ and the conduction current $\sigma E$ have been reintroduced. This is to allow more general constitutive relations to be utilized later, along with lossy conduction currents that do not require convolution. A constitutive relation and conduction current have already been assumed when deriving the impulse response of the stretched coordinate metrics, however, so there appears to be a contradiction. Herein, heterogeneous structures with surrounding air are modeled, and it is desirable to use one and the same equation everywhere in the simulation space. As such, it is assumed that wherever the stretched coordinate metrics are utilized the medium is vacuum, and wherever more general constitutive relations or non-convolutional lossy environments are located, the $\sigma_i$ components of the metric are zero. As such, equations (2.29a-c) will degenerate into the non-contradictory equations necessary to model the physics at each discretized point in space. These modified Ampere's equations will later be used in the finite difference chapter to derive the finite difference equations. The modified Faraday's equations may be written by utilizing the matched stretched coordinate metric of equation (2.19) as follows:

$$\dot{B}_x + \mathcal{M}_x^s = \frac{1}{\kappa_z}\frac{\partial E_y}{\partial z} - \frac{1}{\kappa_y}\frac{\partial E_z}{\partial y} + \int_{0^-}^{t} \zeta_z(t-\tau)\frac{\partial E_y(\tau)}{\partial z}d\tau - \int_{0^-}^{t} \zeta_y(t-\tau)\frac{\partial E_z(\tau)}{\partial y}d\tau \tag{2.30a}$$

$$\dot{B}_y + \mathcal{M}_y^s = \frac{1}{\kappa_x}\frac{\partial E_z}{\partial x} - \frac{1}{\kappa_z}\frac{\partial E_x}{\partial z} + \int_{0^-}^{t} \zeta_x(t-\tau)\frac{\partial E_z(\tau)}{\partial x}d\tau - \int_{0^-}^{t} \zeta_z(t-\tau)\frac{\partial E_x(\tau)}{\partial z}d\tau \tag{2.30b}$$

$$\dot{B}_z + \mathcal{M}_z^s = \frac{1}{\kappa_y}\frac{\partial E_x}{\partial y} - \frac{1}{\kappa_x}\frac{\partial E_y}{\partial x} + \int_{0^-}^{t} \zeta_y(t-\tau)\frac{\partial E_x(\tau)}{\partial y}d\tau - \int_{0^-}^{t} \zeta_x(t-\tau)\frac{\partial E_y(\tau)}{\partial x}d\tau \tag{2.30c}$$

This may be similarly shortened by introducing the following "history variables":

$$\Phi_{Emq} = \int_{0^-}^{t} \zeta_q(t-\tau)\frac{\partial E_m(\tau)}{\partial q}d\tau = -\frac{\sigma_q}{\kappa_q^2\epsilon_0}\int_{0^-}^{t} e^{-\frac{1}{\epsilon_0}\left(\alpha_q+\frac{\sigma_q}{\kappa_q}\right)(t-\tau)}\frac{\partial E_m}{\partial q}d\tau\,, \qquad \begin{matrix} m = x,y,z \\ q = x,y,z \\ m \neq q \end{matrix} \tag{2.31}$$

Therefore,

$$\dot{B}_x + \mathcal{M}_x^s = \frac{1}{\kappa_z}\frac{\partial E_y}{\partial z} - \frac{1}{\kappa_y}\frac{\partial E_z}{\partial y} + \Phi_{Eyz} - \Phi_{Ezy} \tag{2.32a}$$

$$\dot{B}_y + \mathcal{M}_y^s = \frac{1}{\kappa_x}\frac{\partial E_z}{\partial x} - \frac{1}{\kappa_z}\frac{\partial E_x}{\partial z} + \Phi_{Ezx} - \Phi_{Exz} \tag{2.32b}$$

$$\dot{B}_z + \mathcal{M}_z^s = \frac{1}{\kappa_y}\frac{\partial E_x}{\partial y} - \frac{1}{\kappa_x}\frac{\partial E_y}{\partial x} + \Phi_{Exy} - \Phi_{Eyx} \tag{2.32c}$$

This use of history variables is leveraged in recursive convolution algorithms which will be discussed throughout this text. The basic idea is that the system output right now depends on the entire history of the system inputs and the history variable records the progressive effect of all previous inputs. The curl equations expressed in this section may be further truncated into indicial notation by considering the following primed coordinates:

$$dx' = \kappa_x(x)dx, \qquad dy' = \kappa_y(y)dy, \qquad dz' = s_z(z)dz$$

This yields:

$$\dot{D}_i + \sigma_{ij}E_j + J_i^s = \epsilon_{ij'k}H_{k,j'} - \epsilon_{ijk}\Phi_{H_{jk}} \tag{2.33}$$

$$\dot{B}_i + \mathcal{M}_i^s = \epsilon_{ijk'}E_{j,k'} + \epsilon_{ijk}\Phi_{E_{jk}} \tag{2.34}$$

Where,

$$\Phi_{H_{jk}} = \begin{bmatrix} 0 & \Phi_{H_{xy}} & \Phi_{H_{xz}} \\ \Phi_{H_{yx}} & 0 & \Phi_{H_{yz}} \\ \Phi_{H_{zx}} & \Phi_{H_{zy}} & 0 \end{bmatrix}, \qquad \Phi_{E_{jk}} = \begin{bmatrix} 0 & \Phi_{E_{xy}} & \Phi_{E_{xz}} \\ \Phi_{E_{yx}} & 0 & \Phi_{E_{yz}} \\ \Phi_{E_{zx}} & \Phi_{E_{zy}} & 0 \end{bmatrix} \tag{2.35a/b}$$

## 2.2 Thermodynamics

The process flow chart for deriving the constitutive relations through thermodynamics is shown in Figure 2-1 [184][192]:

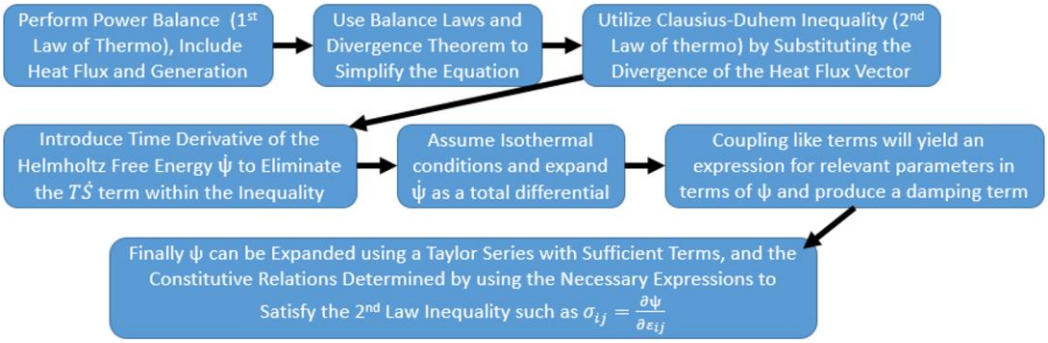


Figure 2-1: Flow chart for determination of constitutive relations.

These steps are followed in this section with the coupled constitutive relations presented in section 2.3. For simplicity, the uncoupled constitutive relations are presented first in section 2.2.2.

### 2.2.1 First Law Power Balance

The principle of total conservation of energy for the thermo-electro-magneto-elastic system is expressed as:

$$\iiint \dot{U} dV + \frac{d}{dt} \iiint \frac{1}{2} \rho \dot{u}_i \dot{u}_i dV = \iint \left( t_i \dot{u}_i + \zeta_{ji} n_j \dot{M}_i - \epsilon_{ijk} E_j H_k n_i - q_i n_i \right) dS + \iiint (b_i \dot{u}_i + h) dV \tag{2.36}$$

Where the first two terms on the left-hand side are the time rates of change of the internal and kinetic energies respectively. Now focusing on the surface integral on the right-hand side; The first and second terms are the mechanical and magnetic powers transferred at the surface of the system. The third surface integral term is the energy carried by EM waves out of the surface of the system and as such contains a minus sign. The final term in the surface integral is the rate of heat flux ($q_i$) out of the system and therefore also contains a minus sign. The volume integral on the right-hand side includes the body forces acting on the system and the heat generation within the system respectively. Applying Cauchy's stress theorem ($t_i = T_{ij} n_j$) to equation (2.36) yields:

$$\iiint \dot{U} dV + \frac{d}{dt} \iiint \frac{1}{2} \rho \dot{u}_i \dot{u}_i dV$$
$$= \iint \left( T_{ij} n_j \dot{u}_i + \zeta_{ji} n_j \dot{M}_i - \epsilon_{ijk} E_j H_k n_i - q_i n_i \right) dS + \iiint (b_i \dot{u}_i + h) dV \tag{2.37}$$

Now that all surface integral terms include the surface normal, the divergence theorem may be applied. Also, the differential volume does not change substantially during system operation, therefore the time derivative acting on the kinetic energy may be moved inside the integrand, yielding the following results:

$$\iiint \dot{U} dV + \iiint \rho \dot{u}_i \ddot{u}_i dV$$
$$= \iiint \left( T_{ij,j} \dot{u}_i + T_{ij} \dot{u}_{i,j} - \epsilon_{ijk} \left( E_{j,i} H_k + E_j H_{k,i} \right) + \zeta_{ji,j} \dot{M}_i + \zeta_{ji} \dot{M}_{i,j} \right. \tag{2.38}$$
$$\left. + b_i \dot{u}_i - q_{i,i} + h \right) dV$$

Utilize Maxwell's equations ($-\epsilon_{ijk} E_{j,i} = -\nabla \times E = \dot{B}_k$, and $-\epsilon_{ijk} H_{k,i} = \nabla \times H = \dot{D}_j$) to get:

$$\iiint \dot{U} dV + \iiint \rho \dot{u}_i \ddot{u}_i dV \, d$$
$$= \iiint \left( T_{ij,j} \dot{u}_i + T_{ij} \dot{u}_{i,j} + H_i \dot{B}_i + E_i \dot{D}_i + \zeta_{ji,j} \dot{M}_i + \zeta_{ji} \dot{M}_{i,j} + b_i \dot{u}_i \right. \tag{2.39}$$
$$\left. + H_i \dot{B}_i - q_{i,i} + h \right) dV$$

Equation (2.39) may be simplified further by noting the following geometric relation between displacements and strains:

$$\dot{u}_{i,j} = \frac{1}{2} \left( \dot{u}_{i,j} + \dot{u}_{j,i} \right) + \frac{1}{2} \left( \dot{u}_{i,j} - \dot{u}_{j,i} \right) = \dot{S}_{ij} + \dot{\omega}_{ij} \tag{2.40}$$

Where $\dot{S}_{ij}$ is the time rate of change of the green strain tensor (linear), and $\dot{\omega}_{ij}$ is the time rate of change of the rotation tensor, which is clearly anti-symmetric. Since the Cauchy stress tensor is symmetric, then:

$$T_{ij} \dot{\omega}_{ij} = 0 \tag{2.41}$$

Substituting (2.40) and (2.41) into (2.39) yields,

$$\iiint \dot{U} dV + \iiint \rho \dot{u}_i \ddot{u}_i dV$$
$$= \iiint \left( T_{ij,j} \dot{u}_i + T_{ij} \dot{S}_{ij} + H_i \dot{B}_i + E_i \dot{D}_i + \zeta_{ji,j} \dot{M}_i + \zeta_{ji} \dot{M}_{i,j} + b_i \dot{u}_i \right. \tag{2.42}$$
$$\left. - q_{i,i} + h \right) dV$$

Assuming the continuity of the integrands gives:

$$\dot{U} = \left( T_{ij,j} + b_i - \rho \ddot{u}_i \right) \dot{u}_i + T_{ij} \dot{S}_{ij} + H_i \dot{B}_i + E_i \dot{D}_i + \zeta_{ji,j} \dot{M}_i + \zeta_{ji} \dot{M}_{i,j} - q_{i,i} + h \tag{2.43}$$

Noting that the terms in the parenthesis zero out by the elastodynamic equation and substituting in equation (2.9) for the divergence of the magnetic surface micro-force $\zeta_{ji}$, yields [184]:

$$\dot{U} = T_{ij} \dot{S}_{ij} + \left( \frac{\mu_0}{|M|^2 \gamma_0} \epsilon_{ijk} \dot{M}_j M_k - \frac{1}{|M|^2} \epsilon_{ijk} \epsilon_{krs} M_j M_{s,p} \zeta_{pr} - \pi_i \right) \dot{M}_i + \zeta_{ji} \dot{M}_{i,j}$$
$$+ H_i \dot{B}_i + E_i \dot{D}_i - q_{i,i} + h \tag{2.44}$$

Note that equation (2.44) has re-introduced the volumetric micro-force term ($\pi_i$). Simplify further by noting that,

$$\frac{\mu_0}{|M|^2 \gamma_0} \epsilon_{ijk} \dot{M}_j M_k \dot{M}_i = 0$$

Since this is the dot product of two perpendicular vectors, therefore:

$$\dot{U} = T_{ij} \dot{S}_{ij} + \left( -\frac{1}{|M|^2} \epsilon_{ijk} \epsilon_{krs} M_j M_{s,p} \zeta_{pr} - \pi_i \right) \dot{M}_i$$
$$+ \zeta_{ji} \dot{M}_{i,j} + H_i \dot{B}_i + E_i \dot{D}_i - q_{i,i} + h \tag{2.45}$$

Which defines the time derivative of the volume specific internal energy. Further treatment requires the use of the second law of thermodynamics in its continuum form.

### 2.2.2 Second Law of Thermodynamics

The second law of thermodynamics on a continuum may be stated in the following form [185]:

$$\delta S \geq \frac{\delta Q}{T} \tag{2.46}$$

Where $\delta S$ is the change in volume specific entropy as the system goes from one equilibrium state to another, $\delta Q$ is the amount of heat added to the system per unit volume during the same process, and $T$ is the temperature of the system on an absolute scale. Note here that $T$ and $S$ are now being used to represent temperature and entropy respectively in addition to stress and strain. Since the latter two are second order tensors, any confusion should be eliminated by observing the indices. The equality holds for processes that are reversible (non-dissipative). Following the methodology of Mal [185], to apply this to systems that are not spatially homogenous or in thermodynamic equilibrium $S$, $T$, and internal energy $U$ are assigned the values they would have as state functions if the system were to be in equilibrium at every instant in time. Therefore, the heat added to the system may be written as:

$$\iiint \delta Q dV = \left[ - \iint q_i n_i dS + \iiint h \, dV \right] \delta t \tag{2.47}$$

Substituting equation (2.47) into equation (2.46) to get:

$$\iiint \delta S dV \geq \left[ - \iint \frac{q_i n_i}{T} dS + \iiint \frac{h}{T} dV \right] \delta t \tag{2.48}$$

Apply the divergence theorem to the surface integral in equation (2.48) and use the quotient rule of differentiation to get:

$$\iiint \delta S dV \geq \left[ \iiint \left( \frac{q_i T_{,i} - q_{i,i} T}{T^2} + \frac{h}{T} \right) dV \right] \delta t \tag{2.49}$$

Since this may be applied to any arbitrary volume, the integrands may be directly related:

$$\delta S \geq \left[ \frac{q_i T_{,i} - q_{i,i} T}{T^2} + \frac{h}{T} \right] \delta t \tag{2.50}$$

Taking the limit of equation (2.50) as $\delta t$ approaches zero, then multiplying by $T$ yields:

$$T\dot{S} \geq \frac{q_i T_{,i}}{T} - q_{i,i} + h \tag{2.51}$$

Equation (2.51) is the Clausius-Duhem dissipation inequality which is the continuum form of the second law of thermodynamics. Introduce the Helmholtz free energy ($\psi$) which is defined as the ability of a system to do work in a constant temperature environment:

$$T\psi = U - TS \tag{2.52}$$

Where the product $TS$ is the work that the system gets "for free" from the isothermal environment (hence the negative sign). The time derivative of the Helmholtz free energy is thus:

$$\dot{\psi} = \dot{U} - T\dot{S} - \dot{T}S \tag{2.53}$$

Combining equations (2.51) and (2.53) yields:

$$-\dot{\psi} \geq \frac{q_i T_{,i}}{T} - q_{i,i} + h + \dot{T}S - \dot{U} \tag{2.54}$$

But the divergence of the rate of heat flux vector and the rate of heat generation has already arisen in equation (2.45), therefore equation (2.54) above is rewritten after substitution:

$$\begin{aligned} -\dot{\psi} \geq \left[-T_{ij}\dot{S}_{ij} + \left(\frac{1}{M^2}\epsilon_{ijk}\epsilon_{krs}M_j M_{s,p}\zeta_{pr} + \pi_i\right)\dot{M}_i - \zeta_{ji}\dot{M}_{i,j} - H_i\dot{B}_i - E_i\dot{D}_i + \dot{U}\right] \\ + \frac{q_i T_{,i}}{T} + \dot{T}S - \dot{U} \end{aligned} \tag{2.55}$$

Or, by rearranging terms in equation (2.55):

$$\begin{aligned} \dot{\psi} + \frac{q_i T_{,i}}{T} - T_{ij}\dot{S}_{ij} + \left(\frac{1}{M^2}\epsilon_{ijk}\epsilon_{krs}M_j M_{s,p}\zeta_{pr} + \pi_i\right)\dot{M}_i \\ -\zeta_{ji}\dot{M}_{i,j} - H_i\dot{B}_i - E_i\dot{D}_i + \dot{T}S \leq 0 \end{aligned} \tag{2.56}$$

The inequality of equation (2.56) will lead to conditions on the constitutive equations which will be explored by considering the electrical, mechanical, and magnetic portions separately in the following sections 2.2.2.1-3. As a preliminary, to demonstrate the methodology used, say that a purely thermal system is considered, then eq (2.56) may be reduced to the following:

$$\dot{\psi} + \dot{T}S + \frac{q_i T_{,i}}{T} \leq 0 \tag{2.57}$$

It now becomes necessary to explicitly state the order parameters on which the material free energy depends, which in this case is the temperature:

$$\psi = \psi(T)$$

The variable chosen has work conjugate counterpart (entropy $S$) which may have been chosen instead. For linear systems the variable chosen is immaterial and therefore the variables most convenient for the derivation should be used. By the chain rule the time rate of change of the free energy is expanded as:

$$\dot{\psi} = \frac{\partial \psi}{\partial T}\dot{T} \tag{2.58}$$

Substituting equation (2.58) into equation (2.57) and combining like terms yields:

$$\left(\frac{\partial \psi}{\partial T} + S\right)\dot{T} + \frac{q_i T_{,i}}{T} \leq 0 \tag{2.59}$$

The first term can be made to always satisfy the equality condition by the following relation which is well known in the thermodynamics literature [193]:

$$S = -\frac{\partial \psi}{\partial T} \tag{2.60}$$

For the second term, note that, since $q_i$ and $T_{,i}$ are always anti-parallel and $T$ is measured in an absolute scale, equation (2.59) suggests that the rate of heat flux should take the following form:

$$q_i = \kappa_{ij} T_{,j} \tag{2.61}$$

Since the system herein is considered to be isothermal, these relations are only meant to highlight the methodology used in the subsequent three sections and will not be utilized to update any fields within the numerical formulation proposed herein.

#### 2.2.2.1 Purely Electrical Constitutive Relation

From eq (2.56), a purely electrical system has the following relation to the free energy [194]:

$$\dot{\psi} - E_i \dot{D}_i \leq 0 \tag{2.62}$$

The order parameter on which the material free energy depends is electric flux:

$$\psi = \psi(D_i)$$

By the chain rule the time rate of change of the free energy is expanded as:

$$\dot{\psi} = \frac{\partial \psi}{\partial D_i} \dot{D}_i \tag{2.63}$$

Substituting equation (2.63) into equation (2.56) and combining like terms yields:

$$\left(\frac{\partial \psi}{\partial D_i} - E_i\right) \dot{D}_i \leq 0 \tag{2.64}$$

Which can be made to always satisfy the equality condition by the following relation which is well known in the literature [194]:

$$E_i = \frac{\partial \psi}{\partial D_i} \tag{2.65}$$

This term leads to the inverse permittivity tensor $\beta_{ij}^{\epsilon}$ (slope of the $E$ vs. $D$ curve) if the relation above is differentiated with respect to the electric flux:

$$\frac{\partial E_i}{\partial D_j} = \frac{\partial^2 \psi}{\partial D_i \partial D_j} = \beta_{ij}^{\epsilon} = \epsilon_{ij}^{-1} \tag{2.66}$$

No additional terms related to dissipation appear in equation (2.62) as electrical losses are captured within Maxwell's equations (balance laws) rather than the electrical constitutive relation. This represents a subtle difference with the mechanical domain, which does include losses in the constitutive relation rather than the balance law (elastodynamic equation) as shown in the next section 2.2.2.2.

#### 2.2.2.2 Purely Mechanical Constitutive Relation

From eq (2.56), a purely mechanical system has the following relation to the free energy:

$$\dot{\psi} - T_{ij} \dot{S}_{ij} \leq 0 \tag{2.67}$$

Where the second term is referred to as the "stress power" [185]. A simple method of determining the relationship between free energy and stress can be made if a purely elastic

system is considered. This means that no losses, or plastic (permanent) strains are present. Therefore, there is no distinction between the total linear strain ($S_{ij}$) and the elastic strain ($S_{ij}^{el}$), namely:

$$S_{ij}^{el} = S_{ij} \equiv \frac{1}{2}\left(u_{i,j} + u_{j,i}\right)$$

The free energy is thus a function of the strain only, and, by the chain rule:

$$\dot{\psi}\left(S_{ij}\right) = \frac{\partial \psi}{\partial S_{ij}} \frac{\partial S_{ij}}{\partial t} \tag{2.68}$$

Substitution into the 2nd law inequality yields:

$$\left(\frac{\partial \psi}{\partial S_{ij}} - T_{ij}\right)\dot{S}_{ij} \leq 0 \tag{2.69}$$

Which may be satisfied always if the following holds:

$$T_{ij} = \frac{\partial \psi}{\partial S_{ij}} \tag{2.70}$$

Relation (2.70) is quite familiar to structural engineers and leads to the stiffness tensor $c_{ijkl}$ (slope of $T_{ij}$ vs. $S_{ij}$ curve) if differentiated with respect to the strain:

$$\frac{\partial T_{ij}}{\partial S_{kl}} = \frac{\partial^2 \psi}{\partial S_{ij} \partial S_{kl}} = c_{ijkl} \tag{2.71}$$

If, however, inelastic losses are considered, there are many methods that may be used to modify the relations above. One popular method, consistent with the literature on viscoelasticity [195], is to consider the Maxwell representation of the so-called “Standard Linear Solid (SLS)” shown in Figure 2-2:

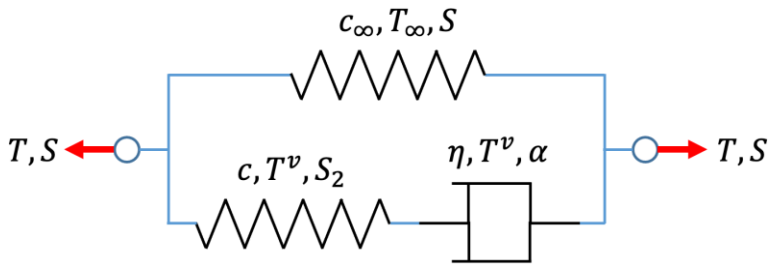


Figure 2-2: Standard Linear Solid (SLS) 1D Mechanical Model Maxwell Representation

As shown, the standard linear solid consists of a spring, with stiffness $c_\infty$, in parallel with a "Maxwell Fluid" which is a spring ($c$) in series with a dashpot with damping parameter $\eta$. A stress $T$ and stain $S$ are applied to the system at the ends, and the corresponding stresses and strains in the springs and dashpot are shown. If a Heaviside step function were applied, the stiffness $c$ would eventually relax away and the system would exhibit the stiffness $c_\infty$, hence the subscript, and therefore $c_\infty$ is a time independent stiffness term. In this case, the stiffness exhibited by the system an infinitesimally small amount of time after loading is $c_0 = c + c_\infty$, and therefore $c_0$ is the instantaneous stiffness. In mechanical systems, series elements share the same force with differing displacement, and parallel elements share the same displacement with differing force. Assume, for simplicity, that the system has unit area and length so that there is no distinction between stress and force, as well as strain and displacement. Note that the strain across the dashpot ($\alpha$) is inelastic and that the corresponding viscous stress, which is shared by the series spring, is as follows:

$$T^v = \eta\dot{\alpha} = cS_2 = c(S - \alpha) \tag{2.72}$$

Also, since the force is split between the parallel branches, the following relation holds for the total stress $T$.

$$T = T_\infty + T^v = c_\infty S + \eta\dot{\alpha}$$

Or alternatively,

$$T = T_\infty + T^v = c_\infty S + c(S - \alpha) = c_0 S - c\alpha$$

It can be shown, by using the series and parallel relations, that this constitutive relation for the standard linear solid may be re-written as follows:

$$T + \Xi\dot{T} = c_\infty S + q\dot{S} \tag{2.73a}$$

$$\Xi = \frac{\eta}{c}, \qquad q = \eta\frac{c_0}{c} = \Xi c_0 \tag{2.73b, c}$$

Where $\Xi$ is a time constant that depends on the damping parameter and stiffness $c$, which generally vary in each direction yielding a time constant tensor. Equation (2.73a) may be written as follows:

$$T = c_\infty S + \Xi\left[c_0\dot{S} - \dot{T}\right]$$

Which may be generalized to three dimensions as follows:

$$T_{ij} = c^\infty_{ijkl}S_{kl} + \Xi_{ijkl}\left[c^0_{klmn}\dot{S}_{mn} - \dot{T}_{kl}\right] \tag{2.74}$$

This form of the relation is important as it will be assumed that the magnetic damping may take the same form in section 2.2.2.3 in order to acquire a dissipative term in the magnetic constitutive relation. Note that the elastic free energy (inside the springs) for the system is as follows for the 3D case:

$$\psi(S_{ij}, \alpha_{ij}) = \frac{1}{2}T^\infty_{ij}S_{ij} + \frac{1}{2}T^v_{ij}\left(S_{ij} - \alpha_{ij}\right) \tag{2.75}$$

This may be expanded using the chain rule as follows:

$$\dot{\psi}\left(S_{ij}, \alpha_{ij}\right) = \frac{\partial\psi}{\partial S_{ij}}\frac{\partial S_{ij}}{\partial t} + \frac{\partial\psi}{\partial\alpha_{ij}}\frac{\partial\alpha_{ij}}{\partial t} = \frac{\partial\psi}{\partial S_{ij}}\dot{S}_{ij} - \frac{1}{2}T^v_{ij}\dot{\alpha}_{ij} \tag{2.76}$$

Substituting equation (2.76) into the 2nd law inequality (2.67) yields:

$$\left(\frac{\partial\psi}{\partial S_{ij}} - T_{ij}\right)\dot{S}_{ij} - \frac{1}{2}T^v_{ij}\dot{\alpha}_{ij} \leq 0 \tag{2.77}$$

The inequality (2.77) may therefore be satisfied always under the following conditions:

$$T_{ij} = \frac{\partial\psi}{\partial S_{ij}}, \qquad T^v_{ij} = \eta_{ijkl}\dot{\alpha}_{kl} \tag{2.78a, b}$$

This definition of the viscous stress ensures that the system dissipation is non-negative, which may be seen by considering the 2nd law inequality in terms of a dissipation function $\mathcal{D}_{mech}$:

$$\left(\frac{\partial \psi}{\partial S_{ij}} - T_{ij}\right)\dot{S}_{ij} - \mathcal{D}_{mech}\left(S_{ij}, \alpha_{ij}, \dot{\alpha}_{ij}\right) \leq 0 \tag{2.79}$$

Which yields the following definition of the mechanical dissipation function:

$$\mathcal{D}_{mech}\left(S_{ij}, \alpha_{ij}, \dot{\alpha}_{ij}\right) = \frac{1}{2} T_{ij}^{v} \dot{\alpha}_{kl} \equiv \frac{1}{2} \eta_{ijkl} \dot{\alpha}_{ij} \dot{\alpha}_{kl} \geq 0 \tag{2.80}$$

The purely mechanical losses of (2.80) are those where bulk mechanical motion is lost to unorganized nanoscale lattice vibrations (friction/thermal losses), which is called mechanical "damping" herein. In contrast, the mechanical energy loss from transfer to electrical energy (piezoelectric effect) or to magnetic energy (magnetostriction) is referred to as energy "conversion". Both damping and conversion are combined under the umbrella of "dissipation". Converted energy may then go on to be dissipated due to loss mechanisms within other domains of physics, such as Gilbert (magnetic) damping, or propagated out as EM radiation. The goal of introducing mechanical losses was then to apply the viscoelastic methodology to the magnetics equations to model magnetic damping. As such, the level of complexity introduced by using the SLS is not necessary. Therefore, a further simplification will now be made in that the spring with stiffness $c$ in Figure 2-2 is removed (Kelvin solid model) which yields the following relation:

$$T = T^{spring} + T^{dashpot} = cS + \eta \dot{S}$$

Which may be generalized into three dimensions as follows:

$$T_{ij} = c_{ijkl}^{\infty} S_{kl} + \eta_{ijkl} \dot{S}_{kl} \tag{2.81}$$

Where the last term on the right-hand side is a mechanical damping term, as utilized by Auld [4], that acts to resist deformation and attenuate acoustic waves. The $\eta_{ijkl}$ damping tensor always has the same form as the stiffness tensor and is populated using acoustic quality factors

which are frequency dependent. Further discussion on quality factors is presented in section 2.4. Equation (2.81) will be used to write update equations for the stress within the numerical formulation presented herein.

#### 2.2.2.3 Purely Magnetic Constitutive Relation

From eq (2.56), a purely magnetic system has the following relation to the free energy [194]:

$$\dot{\psi} + \left(\frac{1}{M^2}\epsilon_{ijk}\epsilon_{krs}M_j M_{s,p}\zeta_{pr} + \pi_i\right)\dot{M}_i - \zeta_{ji}\dot{M}_{i,j} - H_i\dot{B}_i \leq 0 \tag{2.82}$$

The order parameters on which the material free energy depends are three-fold:

$$\psi = \psi\left(B_i, M_i, M_{i,j}\right)$$

By the chain rule the time rate of change of the free energy is expanded as:

$$\dot{\psi} = \frac{\partial\psi}{\partial B_i}\dot{B}_i + \frac{\partial\psi}{\partial M_i}\dot{M}_i + \frac{\partial\psi}{\partial M_{i,j}}\dot{M}_{i,j} \tag{2.83}$$

Substituting equation (2.83) into equation (2.82) and combining like terms yields:

$$\left(\frac{\partial\psi}{\partial B_i} - H_i\right)\dot{B}_i + \left(\frac{\partial\psi}{\partial M_i} + \frac{1}{M^2}\epsilon_{ijk}\epsilon_{krs}M_j M_{s,p}\zeta_{pr} + \pi_i\right)\dot{M}_i + \left(\frac{\partial\psi}{\partial M_{i,j}} - \zeta_{ji}\right)\dot{M}_{i,j} \leq 0 \tag{2.84}$$

Ignoring the $\dot{M}_i$ term for now, eq (2.84) above can be made to always satisfy the equality condition by the following relations:

$$H_i = \frac{\partial\psi}{\partial B_i}, \qquad \zeta_{ji} = \frac{\partial\psi}{\partial M_{i,j}} \tag{2.85a, b}$$

These are the terms not related to dissipation. The first term (a) leads to the inverse permeability tensor $\beta_{ij}^{\mu}$ (slope of the $H$ vs. $B$ curve) which may be seen by differentiating (2.85a) with respect to the magnetic flux:

$$\frac{\partial H_i}{\partial B_j} = \frac{\partial^2\psi}{\partial B_i \partial B_j} = \beta_{ij}^{\mu} = \mu_{ij}^{-1} \tag{2.86}$$

The second (b) is a statement that the surface micro-force tensor is related to the magnetization gradients and therefore associated with the exchange energy within the thickness

of magnetic domain walls where such gradients are non-zero. In the absence of domain walls (single domain) this term may be ignored completely.

Now focusing on the volumetric micro-force in (2.84), this satisfies the inequality if written as follows [184]:

$$\pi_i = -\left(\frac{\partial \psi}{\partial M_i} + \frac{1}{|M|^2}\epsilon_{ijk}\epsilon_{krs}M_j M_{s,p}\zeta_{pr}\right) - \beta \dot{M}_i \tag{2.87}$$

The governing equation of micromagnetics may now be determined by substituting this expression for $\pi_i$ back into the balance of angular momentum equation (2.9):

$$\begin{aligned}\zeta_{ji,j} = \frac{\mu_0}{|M|^2\gamma_0}\epsilon_{ijk}\dot{M}_j M_k - \frac{1}{|M|^2}\epsilon_{ijk}\epsilon_{krs}M_j M_{s,p}\zeta_{pr} \\ + \left(\frac{\partial \psi}{\partial M_i} + \frac{1}{|M|^2}\epsilon_{ijk}\epsilon_{krs}M_j M_{s,p}\zeta_{pr} + \beta \dot{M}_i\right)\end{aligned} \tag{2.88}$$

Canceling and Rearranging terms yields:

$$\frac{1}{\mu_0}\left(\zeta_{ji,j} - \frac{\partial \psi}{\partial M_i}\right) = \frac{1}{|M|^2\gamma_0}\epsilon_{ijk}\dot{M}_j M_k + \frac{\beta}{\mu_0}\dot{M}_i \tag{2.89}$$

Define the effective magnetic field as follows:

$$H_i^{eff} = \frac{1}{\mu_0}\left(\zeta_{ji,j} - \frac{\partial \psi}{\partial M_i}\right) \tag{2.90}$$

This effective magnetic field will be explored more in section 2.2.3, for now substitute (2.90) into (2.89):

$$H_i^{eff} - \frac{\beta}{\mu_0}\dot{M}_i = \frac{1}{|M|^2\gamma_0}\epsilon_{ijk}\dot{M}_j M_k \tag{2.91}$$

Taking the cross product of equation (2.91) with respect to magnetization yields:

$$\epsilon_{ijk}M_j\left(H_k^{eff} - \frac{\beta}{\mu_0}\dot{M}_k\right) = \frac{1}{|M|^2\gamma_0}\epsilon_{ijk}\epsilon_{krs}M_j M_r \dot{M}_s \tag{2.92}$$

Since the isothermal assumption has been utilized, the fact that the magnetization magnitude is nearly constant at any given temperature will be leveraged. It is often assumed in

the micromagnetics literature that the magnitude of magnetization is equal to the saturation magnetization. Applying this assumption to equation (2.92) yields:

$$\epsilon_{ijk} M_j \left( H_k^{eff} - \frac{\beta}{\mu_0} \dot{M}_k \right) = \frac{1}{\gamma_0} \dot{M}_i \tag{2.93}$$

The relationship between the damping factor $\beta$ and the more familiar gilbert damping factor $\alpha$ is $\beta = \frac{\mu_0 \alpha}{\gamma_0 M_s} = \frac{\alpha}{\gamma M_s}$ therefore:

$$\frac{1}{\mu_0 \gamma} \dot{M}_i = \epsilon_{ijk} M_j \left( H_k^{eff} - \frac{\alpha}{\mu_0 \gamma M_s} \dot{M}_k \right) \tag{2.94}$$

Where equation (2.94) is the Landau-Lifshitz-Gilbert (LLG) equation describing the precessional motion of the magnetization vector about the effective field. Note that the equation involves the torque that causes the precession in the form of $\epsilon_{ijk} M_j H_k^{eff}$ in addition to a damping term of the form $\epsilon_{ijk} M_j \dot{M}_k$. Since the magnitude of the magnetization is assumed constant, this term acts to damp out directional (transverse) changes in the magnetization. The LLG equation is written such that each term has the units of magnetic torque ($M \times H$). Note that this leads to a term with units of time in front of the Gilbert damping torque:

$$\Xi = \frac{\alpha}{\mu_0 \gamma M_s} \tag{2.95}$$

The significance of this time constant will now be explored. Consider the 2nd law inequality if the magnetic microforce tensors were not considered, namely:

$$\dot{\psi} - H_i \dot{B}_i \leq 0 \tag{2.96}$$

This applies for a purely magnetic system in the absence of micromagnetic considerations. Now assume that the magnetic system behaves like the standard linear solid (SLS), presented in section 2.2.2.2, where magnetic flux is analogous to strain, and magnetic field is analogous to stress. The magnetic free energy would then be:

$$\psi\left(B_i, B_i^d\right) = \frac{1}{2} H_i^{\infty} B_i + \frac{1}{2} H_i^d \left(B_i - B_i^d\right) \tag{2.97}$$

Where $B_i^d$ and $H_i^d$ are dissipation fields and $H_i^\infty$ is the magnetic field after a large amount of time has passed since a step excitation was applied. Equation (2.97) may be expanded using the chain rule as follows:

$$\psi(B_i, B_i^d) = \frac{\partial \psi}{\partial B_i}\frac{\partial B_i}{\partial t} + \frac{\partial \psi}{\partial B_i^d}\frac{\partial B_i^d}{\partial t} = \frac{\partial \psi}{\partial B_i}\dot{B}_i - \frac{1}{2}H_i^d B_i^d \tag{2.98}$$

Substituting this into the 2nd law inequality of (2.96) yields:

$$\left(\frac{\partial \psi}{\partial B_i} - H_i\right)\dot{B}_i - \frac{1}{2}H_i^d B_i^d \leq 0 \tag{2.99}$$

The inequality may therefore be satisfied always under the following conditions:

$$H_i = \frac{\partial \psi}{\partial B_i}, \qquad H_i^d = \eta_{ij}\dot{B}_j^d \tag{2.100a, b}$$

This definition of the viscous stress ensures that the system dissipation is non-negative, which may be seen by considering the 2nd law inequality in terms of a dissipation function $\mathcal{D}_{mag}$:

$$\left(\frac{\partial \psi}{\partial B_i} - H_i\right)\dot{B}_i - \mathcal{D}_{mag}\left(B_i, B_i^d, \dot{B}_i^d\right) \leq 0 \tag{2.101}$$

Which yields the following definition of the mechanical dissipation function:

$$\mathcal{D}_{mag}\left(B_i, B_i^d, \dot{B}_i^d\right) = \frac{1}{2}H_i^d B_i^d \equiv \frac{1}{2}\eta_{ij}\dot{B}_i^d \dot{B}_j^d \geq 0 \tag{2.102}$$

These damping fields have yet to be related to the Gilbert damping seen within the LLG equation (2.94), however. To begin to write a relation, note that the magnetic constitutive relation will take the same form as eq. (2.74) for mechanics (repeated below), namely:

$$T_{ij} = c_{ijkl}^\infty S_{kl} + \Xi_{ijkl}\left[c_{klmn}^0 \dot{S}_{mn} - \dot{T}_{kl}\right] \tag{2.74}$$

$$H_i = \beta_{ij}^\infty B_j + \Xi_{ij}\left[\beta_{jk}^0 \dot{B}_k - \dot{H}_j\right] \tag{2.103}$$

$$\Xi_{ij} = \eta_{ik}\mu_{kj} \tag{2.104}$$

Note that the inverse permeability is analogous to the stiffness in this comparison. Lossy magnetic materials under a constant bias field [14] exhibit an instantaneous permeability $\beta_{jk}^0$

(shortly after a step excitation is applied) that is equal to the free space value with no directionality, therefore:

$$\beta_{jk}^{0} = \frac{1}{\mu_0} \tag{2.105}$$

Additionally, recognize that the time independent inverse permeability $\beta_{ij}^{\infty}$ is the $\beta_{ij}^{\mu}$ term that was used previously. This yields:

$$H_i = \beta_{ij}^{\mu} B_j + \Xi_{ij}\left[\frac{1}{\mu_0}\dot{B}_j - \dot{H}_j\right] \tag{2.106}$$

Interestingly, the bracketed term is the exact definition of the magnetization:

$$M_j = \frac{1}{\mu_0} B_j - H_j \tag{2.107}$$

Therefore, by substituting eq. (2.107) into (2.106) the magnetic constitutive relation may be written as follows:

$$H_i = \beta_{ij}^{\mu} B_j + \Xi_{ij}\dot{M}_j \tag{2.108}$$

Where the following relations hold:

$$\beta_{ij}^{\mu}\mu_{jk} = \delta_{jk}, \qquad \mu_{ij} = \mu_0\left(\delta_{ij} + \chi_{ij}\right) \tag{2.109a, b}$$

Here, $\mu_{jk}$ and $\chi_{ij}$ are the magnetic permeability and susceptibility respectively. The goal now is to populate the time constant tensor $\Xi_{ij}$ using additional physical arguments. Firstly, note that the form of eq. (2.108) suggests that the magnetic damping field $H_i^d$, discussed in eq. (2.100b), may also be written as follows:

$$H_i^d = \eta_{ij}\dot{B}_j^d = -\Xi_{ij}\dot{M}_j = -\eta_{ik}\mu_{kj}\dot{M}_j \tag{2.110}$$

Note that $H_i^d$ is the damping field which resists the precessional motion of the magnetization. Also, from (2.5.4), the relation of the damping magnetic flux field to the magnetization is:

$$B_j^d = -\mu_{kj}M_j \tag{2.111}$$

Which states that the damping magnetic field is anti-parallel to the magnetization in an isotropic material. The second order damping tensor $\Xi_{ij}^{T}$ will now be defined by arguing that $H_i^d$, defined in eq. (2.110), is antiparallel to the time rate of change of magnetization ($\dot{M}_i$) as shown in Figure 2-3. This is argued to be the case because the damping field resists magnetization precessional motion, therefore the $\Xi_{ij}^{T}$ damping tensor is a positive scalar since any change in directionality of the damping magnetic field would cause it to no longer be anti-parallel to the time rate of change of magnetization.

$$H_j^d = -\Xi_{jk}^{T}\dot{M}_k = -\Xi^{T}\dot{M}_j \tag{2.112}$$

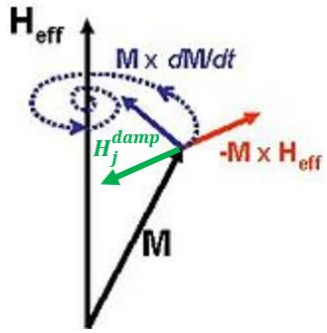


**Figure 2-3: Magnetic Damping Field**

Note that eq. (2.112) yields the desired result, namely a damping field which is antiparallel to $\dot{M}_i$. In order to determine the value of the damping constant $\Xi^{T}$, it is now postulated that the damping field must produce the same torque as the Gilbert damping torque within the LLG equation, therefore:

$$\epsilon_{ijk}M_j H_k^d = -\Xi^{T}\epsilon_{ijk}M_j\dot{M}_k = \frac{\alpha}{\gamma_0 M_s}\epsilon_{ijk}M_j\dot{M}_k \tag{2.113}$$

This yields:

$$\Xi^{T} = -\frac{\alpha}{\gamma_0 M_s} = \tau \tag{2.114}$$

Therefore, the magnetic damping tensor that was introduced degenerates into time constant $\tau$, the importance of which is further elaborated on in the next section. The time constant is

positive since the gyromagnetic ratio of the electron is a negative value (due to the negative charge of the electron). Note that the time constant is proportional to the damping constant $\alpha$ which was introduced in section **Error! Reference source not found.** to satisfy the 2nd law of thermodynamics by utilizing the dissipation micro-force $\pi_i$ and therefore eq. (2.114) is an indirect relation between these terms. The magnetic constitutive relation may now be written as:

$$B_i = \mu_{ij}^T H_j + \frac{\alpha}{\gamma_0 M_s} \mu_{ij}^T \left( \frac{1}{\mu_0} \dot{B}_j - \dot{H}_j \right) \tag{2.115}$$

The permeability terms above are time independent and represent the slope of the magnetic flux (B) versus magnetic field (H) curve at an area of interest (bias magnetic field with small excitations). The viscoelastic approximation to the micromagnetic damping presented herein is a good first approximation for linear piezomagnetic systems but must be modified in order to match the LLG solution [196]. Some of the shortcomings of the viscoelastic analog are summarized in section 1.5 of [197].

### 2.2.3 Taylor Series Expansion of Free Energy

Thus far in the formulation purely electrical, mechanical, and magnetic forms of the free energy have been presented, yielding constitutive relations in the absence of cross-coupling between physical domains. An expression for the fully coupled free energy has not been provided, however a well-behaved function can be approximated by a Taylor series expansion [192], taken with respect to a reference state. In multiferroic antennas a DC bias magnetic field ($H_i^{DC}$) is applied in order to saturate the ferromagnetic material. For this reason, it is useful to think of the reference state for the magnetic field and the magnetization as $H_i^{DC}$ and $M_s$ respectively. This means that the $H_i$ and $M_i$ terms that appear in the 2nd law of thermodynamics are fluctuations of these fields with respect to $H_i^{DC}$ and $M_s$. Therefore $H_i$ represents the dynamic magnetic field driven by electromagnetic fluctuations governed by Maxwell's equations. This has a corresponding magnetization which is as follows:

$$M_i^{maxwell} = \chi_{ij}^T H_j \tag{2.116}$$

In the reference state it is also assumed that the material is unstrained. Performing the expansion on the free energy yields:

$$\begin{aligned}
\Delta\psi = \psi \approx{}& \frac{\partial\psi}{\partial S_{ij}} S_{ij} + \frac{\partial\psi}{\partial\alpha_{ij}}\alpha_{ij} + \frac{\partial\psi}{\partial B_i} B_i + \frac{\partial\psi}{\partial D_i} D_i + \frac{\partial\psi}{\partial M_i} M_i + \frac{\partial\psi}{\partial M_{i,j}} M_{i,j} \\
&+ \frac{\partial\psi}{\partial B_i^d} B_i^d \\
&+ \frac{1}{2!}\left( \frac{\partial^2\psi}{\partial S_{ij}\partial S_{kl}} S_{ij}S_{kl} + \frac{\partial^2\psi}{\partial B_i\partial B_j} B_iB_j + \frac{\partial^2\psi}{\partial D_i\partial D_j} D_iD_j \right. \\
&+ \frac{\partial^2\psi}{\partial M_i\partial M_j} M_iM_j + \frac{\partial^2\psi}{\partial M_{i,j}\partial M_{k,l}} M_{i,j}M_{k,l} + 2\frac{\partial^2\psi}{\partial S_{ij}\partial B_k} S_{ij}B_k \\
&\left. + 2\frac{\partial^2\psi}{\partial S_{ij}\partial D_k} S_{ij}D_k + 2\frac{\partial^2\psi}{\partial S_{ij}\partial\alpha_{kl}} S_{ij}\alpha_{kl} + 2\frac{\partial^2\psi}{\partial B_i\partial B_j^d} B_iB_j^d \cdots \right) \\
&+ \frac{1}{3!}\left( \frac{\partial^3\psi}{\partial S_{ij}\partial S_{kl}\partial S_{mn}} S_{ij}S_{kl}S_{mn} + \frac{\partial^3\psi}{\partial B_i\partial B_j\partial B_k} B_iB_jB_k \right. \\
&\left. + \frac{\partial^3\psi}{\partial M_i\partial M_j\partial M_k} M_iM_jM_k + \cdots \right) + O^4
\end{aligned} \tag{2.117}$$

Where $O^4$ represents all terms of order 4 and above. Recall that when performing an expansion, all independent fields are held constant, save the fields that appear in the derivatives. For example, zone in on the following terms:

$$\left(\frac{\partial^2\psi}{\partial S_{ij}\partial S_{kl}}\right)_{\alpha_{ij},B_i,D_i,M_i,M_{i,j},B_i^d,T}, \qquad \left(\frac{\partial^2\psi}{\partial B_i\partial B_j^d}\right)_{S_{ij},\alpha_{ij},D_i,M_i,M_{i,j},T}$$

Where all of the fields that are held constant are now explicitly stated through the use of subscripts. For brevity these superscripts are almost always omitted in this work. Many of the terms in (2.117) may be eliminated by making some physical observations [192]. If the reference configuration is in a cubic state, all linear terms are removed since the energy should change by the same amount regardless of whether any order parameter changes positively or

negatively. For example, a tensile strain on a bar loaded axially increases the strain energy by the same amount as a compressive strain of the same magnitude. Similarly, a clockwise rotation of the magnetization vector changes the energy by the same amount as a counterclockwise rotation. Also, the energy related to magnetization gradients is assumed to be an uncoupled quadratic term, therefore:

$$\begin{aligned}\Delta\psi = \psi \approx \frac{1}{2!}\Bigg(&\frac{\partial^2\psi}{\partial S_{ij}\partial S_{kl}}S_{ij}S_{kl} + \frac{\partial^2\psi}{\partial B_i\partial B_j}B_iB_j + \frac{\partial^2\psi}{\partial D_i\partial D_j}D_iD_j + \frac{\partial^2\psi}{\partial M_i\partial M_j}M_iM_j \\ &+ \frac{\partial^2\psi}{\partial M_{i,j}\partial M_{k,l}}M_{i,j}M_{k,l} + 2\frac{\partial^2\psi}{\partial S_{ij}\partial B_k}S_{ij}B_k + 2\frac{\partial^2\psi}{\partial S_{ij}\partial D_k}S_{ij}D_k \\ &+ 2\frac{\partial^2\psi}{\partial S_{ij}\partial \alpha_{kl}}S_{ij}\alpha_{kl} + 2\frac{\partial^2\psi}{\partial B_i\partial B_j^a}B_iB_j^a\cdots\Bigg) \\ &+ \frac{1}{3!}\Bigg(\frac{\partial^3\psi}{\partial S_{ij}\partial S_{kl}\partial S_{mn}}S_{ij}S_{kl}S_{mn} + \frac{\partial^3\psi}{\partial B_i\partial B_j\partial B_k}B_iB_jB_k \\ &+ \frac{\partial^3\psi}{\partial M_i\partial M_j\partial M_k}M_iM_jM_k + \cdots\Bigg) + O^4\end{aligned} \tag{2.118}$$

This process of eliminating terms can be continued until a general form of the Helmholtz free energy is found. In section 2.3, the electric, magnetic, and mechanical constitutive relations are considered in their coupled states, and further terms are eliminated. First, a cubic ferromagnet will be considered in order to further elaborate on the effective magnetic field ($H_i^{eff}$) within the LLG equation (2.94). In this case, the free energy may be written as:

$$\begin{aligned}\psi\left(S_{ij}, M_i, M_{i,j}, B_j\right) = &-\mu_0 M_i H_i^{ext} + \frac{1}{2}A_{ijkl}M_{i,j}M_{k,l} + K_{ijkl}M_iM_jM_kM_l + \\ &\bar{K}_{ijklmn}M_iM_jM_kM_lM_mM_n + \frac{1}{2}c_{ijkl}\left(S_{ij} - S_{ij}^m\right)\left(S_{kl} - S_{kl}^m\right) - \frac{1}{2}\mu_0 M_i H_i^d\end{aligned} \tag{2.119}$$

The first term on the right-hand side is the energy associated with an externally applied magnetic field. The second term is the exchange energy which models the effects of the magnetization gradients on the material free energy. This term gives the magnetic domain walls energy and thickness since a domain wall is defined as a finite region in which magnetization

gradients are non-zero. The third and fourth terms model magnetocrystalline anisotropy energy. These higher order magnetization terms are necessary to model the “easy” directions within a magnetic material. The fifth term models the strain energy and includes the magnetoelastic terms. The last term is the energy associated with the demagnetizing field $H_i^{demag}$. The free energy can therefore be written as follows:

$$\psi(\varepsilon_{ij}, M_i, M_{i,j}, B_j) = E_{ext} + E_{ex} + E_{anis} + E_{demag} + E_{el} \quad (2.120)$$

Where $E_{ext}$ is the external energy density, $E_{ex}$ is the exchange energy density, $E_{anis}$ is the magnetocrystalline anisotropy energy density, $E_{demag}$ is the demagnetization energy density, and $E_{el}$ is the elastic energy density.

#### 2.2.3.1 Energy Terms

The energy terms in the previous section are now written out explicitly in terms of the direction of magnetization $m_i$ where,

$$M_i = M_s m_i \quad (2.121)$$

This is done because certain energy terms are only a function of the direction of the magnetization and not on its magnitude. The external energy density $E_{ext}$ is the energy associated with an applied external magnetic field and is written as:

$$E_{ext} = -\mu_0 M_s m_i H_i^{ext} \quad (2.122)$$

Note that this energy is minimized when the magnetization is parallel with the external field and maximized when antiparallel.

The exchange energy density $E_{ex}$ is the energy associated with magnetization gradients and as such is necessarily associated with the magnetic domain walls. This term is expressed in terms of the exchange stiffness constant $A_{ex}$ as:

$$E_{ex} = A_{ex} m_{i,j} m_{i,j} \quad (2.123)$$

The anisotropic energy density $E_{anis}$ is the energy associated with the intrinsic material preferred directions of magnetization and is expressed as:

$$E_{anis} = K_1(m_1^2 m_2^2 + m_2^2 m_3^2 + m_3^2 m_1^2) + K_2(m_1^2 m_2^2 m_3^2) \quad (2.124)$$

Which draws an energy surface in real space with energy wells in the magnetic easy directions within the material.

The demagnetization energy density $E_{demag}$ is the energy associated with surface free poles and may be written in terms of the demagnetizing field as follows:

$$E_{demag} = -\frac{1}{2}\mu_0 M_i H_i^{demag} \quad (2.125)$$

This energy is minimized when the magnetization is in the same direction as the demagnetizing field. Since the system creates this field itself, the ½ term is included which is typical in self energizing systems since the material should not be counted once as the exciter and once as the potential being excited. This energy is particularly important since magnetic domains form in order to minimize magnetostatic energy. When full Maxwell's equations are utilized within a simulation and the material interface conditions are enforced, the demagnetization field is determined automatically by the solver [131].

The elastic energy density $E_{el}$ is the strain energy associated elastic strains which in the case of isothermal ferromagnetic materials may be defined from the total strain ($S_{ij}$) as follows:

$$S_{ij} = S_{ij}^{el} + S_{ij}^{m} \;\rightarrow\; S_{ij}^{el} = S_{ij} - S_{ij}^{m} \quad (2.126a, b)$$

Therefore:

$$E_{el} = \frac{1}{2} c_{ijkl} S_{ij}^{el} S_{kl}^{el} = \frac{1}{2} c_{ijkl}\left(S_{ij} - S_{ij}^{m}\right)\left(S_{kl} - S_{kl}^{m}\right) \quad (2.127)$$

Where $S_{ij}^{m}$ is the magnetostriction, the strain caused by magnetization, which for a cubic crystal may be written as:

$$S_{ij}^{m} = \begin{cases} \frac{3}{2}\lambda_{100}\left(m_i m_j - \frac{1}{3}\right) & i = j \\ \frac{3}{2}\lambda_{111} m_i m_j & i \neq j \end{cases} \quad (2.128)$$

Where $\lambda_{100}$ and $\lambda_{111}$ are the saturation magnetostriction constants in the <100> and <111> crystallographic directions respectively. In other words, these constants represent the strain in the material in the <100> or <111> direction when all the magnetization vectors in the material are pointed in the <100> or <111> direction respectively. Note that if the material is saturated in the <100> direction ($m_1 = 1, m_2 = m_3 = 0$) the magnetostriction will be:

$$S_{ij}^{m} = \begin{bmatrix} \lambda_{100} & 0 & 0 \\ 0 & -\lambda_{100}/2 & 0 \\ 0 & 0 & -\lambda_{100}/2 \end{bmatrix} \tag{2.129}$$

#### 2.2.3.2 Effective Magnetic Field

The effective magnetic field was defined previously in equation (2.90) which is repeated here for convenience:

$$H_i^{eff} = \frac{1}{\mu_0}\left(\zeta_{ji,j} - \frac{\partial \psi}{\partial M_i}\right) \tag{2.130}$$

Recall also that the surface micro-force tensor is equal to the derivative of the free energy with respect to the magnetization gradients, therefore:

$$\zeta_{ji,j} = \left(\frac{\partial \psi}{\partial M_{i,j}}\right)_{,j} = \left(2\frac{A_{ex}}{M_s^2}M_{i,j}\right)_{,j} = 2\frac{A_{ex}}{M_s^2}M_{i,jj} \tag{2.131}$$

Therefore $\zeta_{ji,j}$ is proportional to the divergence of the magnetization gradients and accounts for the exchange energy, therefore:

$$H_i^{eff} = H_i^{ex} - \frac{1}{\mu_0 M_s}\frac{\partial \psi}{\partial m_i} = H_i^{ext} + H_i^{ex} + H_i^{anis} + H_i^{demag} + H_i^{me} \tag{2.132}$$

Where the exchange magnetic field is separated since this field is a function of magnetization gradients, whereas all other magnetic fields are a function of magnetization. Recall $H_i^{ext}$ is an externally applied magnetic field, and:

$$H_i^{ex} = \frac{2A_{ex}}{\mu_0 M_s}m_{i,jj} \tag{2.133}$$

$$H_i^{anis} = -\frac{2m_i}{\mu_0 M_s}\left[K_1\left(m_j^2 + m_k^2\right) + K_2\left(m_j^2 m_k^2\right)\right] \tag{2.134}$$

$$H_i^{me} = -\frac{1}{\mu_0 M_s} c_{ijkl}(S_{kl} - S_{kl}^m)\frac{\partial S_{ij}^m}{\partial m_j} \tag{2.135}$$

For single magnetic domain simulations, the exchange field is zero.

## 2.3 Coupled Constitutive Relations

In section 2.2.2 the uncoupled constitutive relations for a purely electrical, mechanical, and magnetic system were introduced. It was then shown in section 2.2.3 that the free energy may be expressed in terms of a Taylor series expansion that includes cross-coupled terms. In this section the fully coupled constitutive relations will be presented that include the multiferroic effects of piezoelectricity and piezomagnetism. The mechanical constitutive relation will be presented first, which is used to write update equations for the stresses. The magnetic constitutive relation will be presented next, which is used to update the magnetic fields and to derive the implicit electric field update equations known as the ADI-FDTD equations. Lastly, the electric constitutive relation is presented which is also used to derive the ADI-FDTD equations.

### 2.3.1 Mechanical Constitutive Relation

The mechanical constitutive relation may be written utilizing the proposed Taylor series expansion and the Clausius-Duhem inequality as follows:

$$\begin{aligned} T_{ij} = \frac{\partial \psi}{\partial S_{ij}} = \frac{1}{2}\frac{\partial}{\partial S_{ij}}\Bigg[ & \left(\frac{\partial^2 \psi}{\partial S_{ij}\partial S_{kl}}\right)_{B,\alpha\cdots} S_{ij}S_{kl} + 2\left(\frac{\partial^2 \psi}{\partial S_{ij}\partial B_k}\right)_{\alpha,E\cdots} S_{ij}B_k \\ & + 2\left(\frac{\partial^2 \psi}{\partial S_{ij}\partial E_k}\right)_{B,\alpha\cdots} S_{ij}D_k + 2\left(\frac{\partial^2 \psi}{\partial S_{ij}\partial \alpha_{kl}}\right)_{B,E\cdots} S_{ij}\alpha_{kl} + \cdots \Bigg] \\ & + \cdots \end{aligned} \tag{2.136}$$

Where the electric dependent variable has been switched to $E$ rather than $D$, which will simplify the ADI algorithm derived in chapter 3 since the ADI equations update the electric fields

not the electric fluxes. The higher order (non-linear) terms in (2.136) will be ignored, and the subscripts denote, for brevity, only some of the fields that are to be held constant, therefore:

$$T_{ij} = \left(\frac{\partial^2 \psi}{\partial S_{ij} \partial S_{kl}}\right)_{B,E,\alpha\cdots} S_{kl} + \left(\frac{\partial^2 \psi}{\partial S_{ij} \partial B_k}\right)_{\alpha,E\cdots} B_k + \left(\frac{\partial^2 \psi}{\partial S_{ij} \partial E_k}\right)_{B,\alpha\cdots} E_k + \left(\frac{\partial^2 \psi}{\partial S_{ij} \partial \alpha_{kl}}\right)_{B,E\cdots} \alpha_{kl} \tag{2.137}$$

The first term in parenthesis is the instantaneous stiffness tensor $c^0_{ijkl}$ discussed in section 2.1.2 (stiffness when no viscous effects exist $c^0 = c^\infty + c$), which is measured at constant magnetic flux, inelastic strain, etc. To recover the SLS constitutive relation of section 2.2.2.2, the final term is the negative of the stiffness which relaxes away over time ($c_{ijkl}$). The second and third terms are piezomagnetic and piezoelectric coupling tensors which are well documented in the IEEE literature [198][199] and elsewhere [194], therefore:

$$T_{ij} = c^0_{ijkl} S_{kl} - h^{PM}_{kij} B_k - h^{PE}_{kij} D_k - c_{ijkl} \alpha_{kl} \tag{2.138}$$

Which may be re-written into the equivalent expression:

$$T_{ij} = c^\infty_{ijkl} S_{kl} - h^{PM}_{kij} B_k - h^{PE}_{kij} D_k + \eta_{ijkl} \dot{\alpha}_{kl} \tag{2.139}$$

Where the fields to be held constant at measurement have now been omitted, and the superscripts on the third order coupling tensors denote piezomagnetism (PM) and piezoelectricity (PE) respectively. The third order $h_{ijk}$ coupling tensors relate the EM induced stress terms ($T^{PM}_{ij}$ and $T^{PE}_{ij}$) to the EM fields that induce them, namely:

$$h^{PM}_{kij} = \frac{\partial T^{PM}_{ij}}{\partial B_k}, \qquad h^{PE}_{kij} = \frac{\partial T^{PE}_{ij}}{\partial D_k} \tag{2.140a, b}$$

Also, $d^{PM}_{kij}$ and $d^{PE}_{kij}$ are the piezomagnetic and piezoelectric strain coupling tensors which relate the magnetostriction to the magnetic field ($H_i$) and the electrically driven strain to the electric field ($E_i$) respectively, namely:

$$d_{kij}^{PM} = \frac{\partial S_{ij}^{PM}}{\partial H_k}, \qquad d_{kij}^{PE} = \frac{\partial S_{ij}^{PE}}{\partial E_k} \tag{2.141a/b}$$

There are also $e_{ijk}$ and $g_{ijk}$ coupling systems and the relation between the different coupling tensors is provided in [194]. The "h-form" utilized herein has proven to be the most convenient and stable. The mechanical portion of (2.139) may be solved via a convolution integral approach. Instead, the Kelvin solid approximation ($\alpha_{kl} = S_{kl}$) will be used [200] yielding:

$$T_{ij} = c_{ijkl}^{\infty} S_{kl} - h_{kij}^{PM} B_k - h_{kij}^{PE} D_k + \eta_{ijkl} \dot{S}_{kl} \tag{2.142}$$

Since Kelvin solids include only one stiffness term, the super-script will be dropped. The system of equations (2.142) is linear, and therefore may be readily inverted yielding the following:

$$S_{ij} = s_{ijkl} T_{kl} + g_{kij}^{PM} B_k + g_{kij}^{PE} D_k - s_{ijkl} \eta_{klmn} \dot{S}_{klmn} \tag{2.143}$$

Where $s_{ijkl}$ is the compliance tensor, which is the inverse of the stiffness tensor, and:

$$g_{kij}^{PM} = \beta_{km}^{\mu} d_{mij}^{PM} = h_{kmn}^{PM} s_{mnij}, \qquad g_{kij}^{PE} = \beta_{km}^{\epsilon} d_{mij}^{PE} = h_{kmn}^{PE} s_{mnij} \tag{2.144a, b}$$

Where $\beta_{km}^{\mu}$ and $\beta_{km}^{\epsilon}$ are the inverse permeability and inverse permittivity respectively. Alternatively, these strains may be related to the magnetic and electric flux through the use of the $g_{ijk}$ coupling tensors as shown in equations 2.144a/b below:

$$g_{kij}^{PM} = \frac{\partial S_{ij}^{PM}}{\partial B_k}, \qquad g_{kij}^{PE} = \frac{\partial S_{ij}^{PE}}{\partial D_k} \tag{2.145a/b}$$

These strains are in contrast to the total strain ($S_{ij}$) in eq. (2.143) which may now be seen to be the summation of the elastic strain ($S_{ij}^{el} = s_{ijkl} T_{kl}$), driven by fluctuating stresses, the magnetostriction ($S_{ij}^{PM} = g_{kij}^{PM} B_k$), driven by fluctuating magnetic fields, the piezoelectric strain ($S_{ij}^{PE} = g_{kij}^{PE} D_k$), and the subtraction of a damping strain term ($S_{ij}^{d} = s_{ijkl} \eta_{klmn} \dot{S}_{klmn}$). This relation, written below in (2.146), therefore states that the total strain, plus the strain lost to viscoelastic damping, is equal to the sum of all strains induced in an undamped system:

$$S_{ij} = S_{ij}^{el} + S_{ij}^{PM} + S_{ij}^{PE} - S_{ij}^{damp} = \left(u_{i,j} + u_{j,i}\right)/2 \tag{2.146}$$

From eq. (2.145) and (2.140), the stress may therefore be rewritten as shown below:

$$T_{ij} = c_{ijkl} S_{kl}^{el} \tag{2.147}$$

Note that equation (2.147) regresses back to the expected mechanical relation when the electromagnetic and damping terms are zeroed out ($S_{ij} = s_{ijkl} T_{kl}$). The acoustic damping term, as utilized by Auld [4], acts to resist deformation and attenuate acoustic waves. The $\eta_{ijkl}$ damping tensor always has the same form as the stiffness tensor and is populated using acoustic quality factors which are frequency dependent. The equation for the stress is now re-written in rate form, with strain rates replaced by velocity terms using the strain-displacement relation (2.146):

$$\dot{T}_{ij} = c_{ijkl} v_{k,l} - h_{kij}^{PM} B_k - h_{kij}^{PE} D_k + \eta_{ijkl} \dot{v}_{k,l} \tag{2.148}$$

This is the so-called velocity-stress formulation [4], since the displacement is not utilized. Note that this allows for the use of a 1st order time derivative in the damping term which enables the modeler to bypass the use of a convolution integral. In fact, the relaxation function for the Kelvin solid representation utilized herein is as follows:

$$G_{xxxx}(t - \tau) = c_{xxxx} H(t - \tau) + \eta_{xxxx} \delta(t - \tau) \tag{2.149}$$

Where $H(t)$ is the Heaviside step function and $\delta(t)$ is the Dirac delta function. Therefore, the Kelvin solid model produces sudden step changes in the stress due to changes in strain which is readily input into a finite difference scheme without the use of a convolution integral. The velocity is determined by utilizing the elastodynamic equation in the following form:

$$T_{ij,j} = \rho_V \dot{v}_i \tag{2.150}$$

The piezomagnetic strain coupling tensor, truncated to include only the terms related to shear stress, may be written as follows for a system biased in the xy-plane:

$$d_{kij}^{PM} = \begin{bmatrix} cs^2 d_{15}^{PM} & -cs^2 d_{15}^{PM} & 0 & -s^2 d_{14}^{PM} & -csd_{14}^{PM} & s(s^2-c^2)d_{15}^{PM} \\ -c^2 s d_{15}^{PM} & c^2 s d_{15}^{PM} & 0 & csd_{14}^{PM} & c^2 d_{14}^{PM} & c(c^2-s^2)d_{15}^{PM} \\ csd_{14}^{PM} & -csd_{14}^{PM} & 0 & sd_{15}^{PM} & cd_{15}^{PM} & (s^2-c^2)d_{14}^{PM} \end{bmatrix} \tag{2.151}$$

$$c = cos\phi, \qquad s = sin\phi$$

Where $\phi$ is the biasing angle measured from the x to the y axis. Generally, however, due to shape effects, the tensor will differ slightly from this but still retain the same form for the in-plane biasing case. Additionally, Hexagonal 6mm symmetry is assumed for the piezoelectric [4]. Therefore, the coupling tensors and inverse permeability/permittivity tensors are as follows:

$$d_{ijk}^{PM} = \begin{bmatrix} d_{xxx}^{PM} & d_{xyy}^{PM} & 0 & d_{xyz}^{PM} & d_{xxz}^{PM} & d_{xxy}^{PM} & d_{xyz}^{PM} & d_{xxz}^{PM} & d_{xxy}^{PM} \\ d_{yxx}^{PM} & d_{yyy}^{PM} & 0 & d_{yyz}^{PM} & d_{yxz}^{PM} & d_{yxy}^{PM} & d_{yyz}^{PM} & d_{yxz}^{PM} & d_{yxy}^{PM} \\ d_{zxx}^{PM} & d_{zyy}^{PM} & 0 & d_{zyz}^{PM} & d_{zxz}^{PM} & d_{zxy}^{PM} & d_{zyz}^{PM} & d_{zxz}^{PM} & d_{zxy}^{PM} \end{bmatrix} \tag{2.152a/b}$$

$$d_{ijk}^{PE} = \begin{bmatrix} 0 & 0 & 0 & 0 & d_{15}^{PE} & 0 \\ 0 & 0 & 0 & d_{15}^{PE} & 0 & 0 \\ d_{31}^{PE} & d_{31}^{PE} & d_{33}^{PE} & 0 & 0 & 0 \end{bmatrix}$$

$$\beta_{ij}^{\mu} = \begin{bmatrix} \beta_{xx}^{\mu} & \beta_{xy}^{\mu} & 0 \\ \beta_{yx}^{\mu} & \beta_{yy}^{\mu} & 0 \\ 0 & 0 & \dfrac{1}{\mu_{zz}} \end{bmatrix}, \qquad \beta_{ij}^{\epsilon} = \begin{bmatrix} \dfrac{1}{\epsilon_{xx}} & 0 & 0 \\ 0 & \dfrac{1}{\epsilon_{yy}} & 0 \\ 0 & 0 & \dfrac{1}{\epsilon_{zz}} \end{bmatrix} \tag{2.153a/b}$$

Tensor multiplication should now be clearer. The magnetoelastic coupling term ($g_{rkl}^{PM}$) is not as intuitive in the current state so it is beneficial to simplify as follows:

$$g_{rkl}^{PM} = \beta_{rq}^{T} d_{qkl}^{PM} =$$

$$\begin{bmatrix} \beta_{xx}^T d_{xxx} + \beta_{xy}^T d_{yxx} + \beta_{xz}^T d_{zxx} & \beta_{yx}^T d_{xxx} + \beta_{yy}^T d_{yxx} + \beta_{yz}^T d_{zxx} & \beta_{zx}^T d_{xxx} + \beta_{zy}^T d_{yxx} + \beta_{zz}^T d_{zxx} \\ \beta_{xx}^T d_{xyy} + \beta_{xy}^T d_{yyy} + \beta_{xz}^T d_{zyy} & \beta_{yx}^T d_{xyy} + \beta_{yy}^T d_{yyy} + \beta_{yz}^T d_{zyy} & \beta_{zx}^T d_{xyy} + \beta_{zy}^T d_{yyy} + \beta_{zz}^T d_{zyy} \\ \beta_{xx}^T d_{xzz} + \beta_{xy}^T d_{yzz} + \beta_{xz}^T d_{zzz} & \beta_{yx}^T d_{xzz} + \beta_{yy}^T d_{yzz} + \beta_{yz}^T d_{zzz} & \beta_{zx}^T d_{xzz} + \beta_{zy}^T d_{yzz} + \beta_{zz}^T d_{zzz} \\ 2\left(\beta_{xx}^T d_{xyz} + \beta_{xy}^T d_{yyz} + \beta_{xz}^T d_{zyz}\right) & 2\left(\beta_{yx}^T d_{xyz} + \beta_{yy}^T d_{yyz} + \beta_{yz}^T d_{zyz}\right) & 2\left(\beta_{zx}^T d_{xyz} + \beta_{zy}^T d_{yyz} + \beta_{zz}^T d_{zyz}\right) \\ 2\left(\beta_{xx}^T d_{xxz} + \beta_{xy}^T d_{yxz} + \beta_{xz}^T d_{zxz}\right) & 2\left(\beta_{yx}^T d_{xxz} + \beta_{yy}^T d_{yxz} + \beta_{yz}^T d_{zxz}\right) & 2\left(\beta_{zx}^T d_{xxz} + \beta_{zy}^T d_{yxz} + \beta_{zz}^T d_{zxz}\right) \\ 2\left(\beta_{xx}^T d_{xxy} + \beta_{xy}^T d_{yxy} + \beta_{xz}^T d_{zxy}\right) & 2\left(\beta_{yx}^T d_{xxy} + \beta_{yy}^T d_{yxy} + \beta_{yz}^T d_{zxy}\right) & 2\left(\beta_{zx}^T d_{xxy} + \beta_{zy}^T d_{yxy} + \beta_{zz}^T d_{zxy}\right) \end{bmatrix} \tag{2.154}$$

Where all terms were assumed non-zero for generality. Zeroing out the appropriate terms in (2.154) using (2.152) and (2.153) yields:

$$\begin{bmatrix} \beta_{xx}^T d_{xxx} + \beta_{xy}^T d_{yxx} & \beta_{xx}^T d_{xyy} + \beta_{xy}^T d_{yyy} & 0 & 2\left(\beta_{xx}^T d_{xyz} + \beta_{xy}^T d_{yyz}\right) & 2\left(\beta_{xx}^T d_{xxz} + \beta_{xy}^T d_{yxz}\right) & 2\left(\beta_{xx}^T d_{xxy} + \beta_{xy}^T d_{yxy}\right) \\ \beta_{yx}^T d_{xxx} + \beta_{yy}^T d_{yxx} & \beta_{yx}^T d_{xyy} + \beta_{yy}^T d_{yyy} & 0 & 2\left(\beta_{yx}^T d_{xyz} + \beta_{yy}^T d_{yyz}\right) & 2\left(\beta_{yx}^T d_{xxz} + \beta_{yy}^T d_{yxz}\right) & 2\left(\beta_{yx}^T d_{xxy} + \beta_{yy}^T d_{yxy}\right) \\ \frac{d_{zxx}}{\mu_{zz}^T} & \frac{d_{zyy}}{\mu_{zz}^T} & 0 & 2\frac{d_{zyz}}{\mu_{zz}^T} & 2\frac{d_{zxz}}{\mu_{zz}^T} & 2\frac{d_{zxy}}{\mu_{zz}^T} \end{bmatrix}$$

Multiplying this by the magnetic induction current, and multiplying the piezoelectric coupling tensor by the electric field rate yields:

$$g_{rkl}^{PM}\dot{B}_r = \begin{pmatrix} \left(\beta_{xx}^T d_{xxx} + \beta_{xy}^T d_{yxx}\right)\dot{B}_x + \left(\beta_{yx}^T d_{xxx} + \beta_{yy}^T d_{yxx}\right)\dot{B}_y + \frac{d_{zxx}}{\mu_{zz}^T}\dot{B}_z \\ \left(\beta_{xx}^T d_{xyy} + \beta_{xy}^T d_{yyy}\right)\dot{B}_x + \left(\beta_{yx}^T d_{xyy} + \beta_{yy}^T d_{yyy}\right)\dot{B}_y + \frac{d_{zyy}}{\mu_{zz}^T}\dot{B}_z \\ 0 \\ 2\left[\left(\beta_{xx}^T d_{xyz} + \beta_{xy}^T d_{yyz}\right)\dot{B}_x + \left(\beta_{yx}^T d_{xyz} + \beta_{yy}^T d_{yyz}\right)\dot{B}_y + \frac{d_{zyz}}{\mu_{zz}^T}\dot{B}_z\right] \\ 2\left[\left(\beta_{xx}^T d_{xxz} + \beta_{xy}^T d_{yxz}\right)\dot{B}_x + \left(\beta_{yx}^T d_{xxz} + \beta_{yy}^T d_{yxz}\right)\dot{B}_y + \frac{d_{zxz}}{\mu_{zz}^T}\dot{B}_z\right] \\ 2\left[\left(\beta_{xx}^T d_{xxy} + \beta_{xy}^T d_{yxy}\right)\dot{B}_x + \left(\beta_{yx}^T d_{xxy} + \beta_{yy}^T d_{yxy}\right)\dot{B}_y + \frac{d_{zxy}}{\mu_{zz}^T}\dot{B}_z\right] \end{pmatrix} \quad (2.155a)$$

$$h_{rkl}^{PE}\dot{D}_r = \begin{pmatrix} h_{31}^{PE}\dot{D}_z & h_{31}^{PE}\dot{D}_z & h_{33}^{PE}\dot{D}_z & h_{15}^{PE}\dot{D}_y & h_{15}^{PE}\dot{D}_x & 0 \end{pmatrix}$$

Therefore, each of the stress components, for a piezomagnetic/piezoelectric heterostructure may be written as:

$$\begin{aligned} \dot{T}_{xx} = {} & c_{xxxx}^B v_{x,x} + c_{xxyy}^B v_{y,y} + c_{xxzz}^B v_{z,z} \\ & - \left[c_{xxxx}^B\left(\beta_{xx}^T d_{xxx} + \beta_{xy}^T d_{yxx}\right) + c_{xxyy}^B\left(\beta_{xx}^T d_{xyy} + \beta_{xy}^T d_{yyy}\right)\right]\dot{B}_x \\ & - \left[c_{xxxx}^B\left(\beta_{yx}^T d_{xxx} + \beta_{yy}^T d_{yxx}\right) + c_{xxyy}^B\left(\beta_{yx}^T d_{xyy} + \beta_{yy}^T d_{yyy}\right)\right]\dot{B}_y \\ & - \left[\frac{c_{xxxx}^B d_{zxx} + c_{xxyy}^B d_{zyy}}{\mu_{zz}^T}\right]\dot{B}_z - h_{31}^{PE}\dot{D}_z + \eta_{xxxx}^B \dot{v}_{x,x} + \eta_{xxyy}^B \dot{v}_{y,y} \\ & + \eta_{xxzz}^B \dot{v}_{z,z} \end{aligned} \quad (2.156a)$$

$$\dot{T}_{yy} = c^B_{xxyy} v_{x,x} + c^B_{yyyy} v_{y,y} + c^B_{yyzz} v_{z,z}$$
$$- \left[c^B_{xxyy}\left(\beta^T_{xx} d_{xxx} + \beta^T_{xy} d_{yxx}\right) + c^B_{yyyy}\left(\beta^T_{xx} d_{xyy} + \beta^T_{xy} d_{yyy}\right)\right]\dot{B}_x$$
$$- \left[c^B_{xxyy}\left(\beta^T_{yx} d_{xxx} + \beta^T_{yy} d_{yxx}\right) + c^B_{yyyy}\left(\beta^T_{yx} d_{xyy} + \beta^T_{yy} d_{yyy}\right)\right]\dot{B}_y \quad (2.156b)$$
$$- \left[\frac{c^B_{xxyy} d_{zxx} + c^B_{yyyy} d_{zyy}}{\mu^T_{zz}}\right]\dot{B}_z - h^{PE}_{31}\dot{D}_z + \eta^B_{xxyy}\dot{v}_{x,x} + \eta^B_{yyyy}\dot{v}_{y,y}$$
$$+ \eta^B_{yyzz}\dot{v}_{z,z}$$

$$\dot{T}_{zz} = c^B_{xxzz} v_{x,x} + c^B_{yyzz} v_{y,y} + c^B_{zzzz} v_{z,z}$$
$$- \left[c^B_{xxzz}\left(\beta^T_{xx} d_{xxx} + \beta^T_{xy} d_{yxx}\right) + c^B_{yyzz}\left(\beta^T_{xx} d_{xyy} + \beta^T_{xy} d_{yyy}\right)\right]\dot{B}_x$$
$$- \left[c^B_{xxzz}\left(\beta^T_{yx} d_{xxx} + \beta^T_{yy} d_{yxx}\right) + c^B_{yyzz}\left(\beta^T_{yx} d_{xyy} + \beta^T_{yy} d_{yyy}\right)\right]\dot{B}_y \quad (2.156c)$$
$$- \left[\frac{c^B_{xxzz} d_{zxx} + c^B_{yyzz} d_{zyy}}{\mu^T_{zz}}\right]\dot{B}_z - h^{PE}_{33}\dot{D}_z + \eta^B_{xxzz}\dot{v}_{x,x} + \eta^B_{yyzz}\dot{v}_{y,y}$$
$$+ \eta^B_{zzzz}\dot{v}_{z,z}$$

$$\dot{T}_{yz} = c^B_{yzyz}\left(v_{y,z} + v_{z,y}\right)$$
$$- 2c^B_{yzyz}\left\{\left(\beta^T_{xx} d_{xyz} + \beta^T_{xy} d_{yyz}\right)\dot{B}_x + \left(\beta^T_{yx} d_{xyz} + \beta^T_{yy} d_{yyz}\right)\dot{B}_y \quad (2.156d)$$
$$+ \frac{d_{zyz}}{\mu^T_{zz}}\dot{B}_z\right\} - h^{PE}_{15}\dot{D}_y + \eta^B_{yzyz}\left(\dot{v}_{y,z} + \dot{v}_{z,y}\right)$$

$$\dot{T}_{xz} = c^B_{xzxz}\left(v_{x,z} + v_{z,x}\right)$$
$$- 2c^B_{xzxz}\left\{\left(\beta^T_{xx} d_{xxz} + \beta^T_{xy} d_{yxz}\right)\dot{B}_x + \left(\beta^T_{yx} d_{xxz} + \beta^T_{yy} d_{yxz}\right)\dot{B}_y \quad (2.156e)$$
$$+ \frac{d_{zxz}}{\mu^T_{zz}}\dot{B}_z\right\} - h^{PE}_{15}\dot{D}_x + \eta^B_{xzxz}\left(\dot{v}_{x,z} + \dot{v}_{z,x}\right)$$

$$\dot{T}_{xy} = c^B_{xyxy}\left(v_{x,y} + v_{y,x}\right)$$
$$- 2c^B_{xyxy}\left\{\left(\beta^T_{xx} d_{xxy} + \beta^T_{xy} d_{yxy}\right)\dot{B}_x + \left(\beta^T_{yx} d_{xxy} + \beta^T_{yy} d_{yxy}\right)\dot{B}_y \quad (2.156f)$$
$$+ \frac{d_{zxy}}{\mu^T_{zz}}\dot{B}_z\right\} + \eta^B_{xyxy}\left(\dot{v}_{x,y} + \dot{v}_{y,x}\right)$$

Note that the $T_{xy}$ constitutive relation (2.156f) is left unchanged by piezoelectricity which occurs because the piezoelectric is poled normal to the xy-plane. Equations (2.156a-f) are

appropriate for writing a time marching scheme which will be explored in chapter 3 which focuses on finite differencing. The piezomagnetic terms will be omitted in that section however as industry interest and research have shifted toward piezoelectric devices.

### 2.3.2 Magnetic Constitutive Relation

In the magnetic constitutive relation, it is simpler to consider the form when the stress ($T_{ij}$) is the independent variable, rather than the strain ($S_{ij}$), and then invert the relation, both of which are acceptable for linear systems. The magnetic constitutive relation in this case is:

$$H_i = \frac{\partial \psi}{\partial B_i} = \frac{1}{2}\frac{\partial}{\partial B_i}\left[\left(\frac{\partial^2 \psi}{\partial B_i \partial B_j}\right)_{T,M^d\ldots} B_i B_j + 2\left(\frac{\partial^2 \psi}{\partial B_i \partial T_{jk}}\right)_{M^d\ldots} B_i T_{jk} + 2\left(\frac{\partial^2 \psi}{\partial B_i \partial B_j^d}\right)_{T\ldots} B_i B_j^d + \cdots\right] + \cdots \tag{2.157}$$

Or,

$$H_i = \left(\frac{\partial^2 \psi}{\partial B_i \partial B_j}\right)_{T,M^d\ldots} B_j + \left(\frac{\partial^2 \psi}{\partial B_i \partial T_{jk}}\right)_{M^d\ldots} T_{ij} + \left(\frac{\partial^2 \psi}{\partial B_i \partial B_j^d}\right)_{T\ldots} \dot{B}_j^d \tag{2.158}$$

The IEEE literature defines the first two terms in parentheses as the inverse permeability $\beta_{ij}^{\mu}$ and the piezomagnetic tensor $g_{ijk}^{PM}$ respectively [198][199], and the novel third term is a magnetic damping tensor discussed at length in section 2.2.2.3, yielding:

$$H_i = \beta_{ij}^{\mu} B_j - g_{ijk}^{PM} T_{jk} - \frac{\alpha}{\gamma_0 M_s}\left(\frac{1}{\mu_0}\dot{B}_i - \dot{H}_i\right) \tag{2.159}$$

Here, a magnetoelastic field $H_j^{me}$ may be identified as follows:

$$H_j^{me} = g_{jkl}^{PM} T_{kl} \tag{2.160}$$

Where $H_j^{me}$ is the magnetic field driven by fluctuations in stress. Relation (2.159) may also be inverted yielding:

$$B_i = \mu_{ij} H_j + d_{ijk}^{PM} T_{jk} + \frac{\alpha}{\gamma_0 M_s}\mu_{ij}\left(\frac{1}{\mu_0}\dot{B}_j - \dot{H}_j\right) \tag{2.161}$$

When this relation is put in rate form, higher order time derivatives appear which are handled using a convolutional approach as presented next:

#### 2.3.2.1 Convolution Approach

When incorporating the magnetic constitutive relation into an ADI-FDTD algorithm, the rate form of (2.161) must be utilized as follows:

$$\dot{B}_i = \mu_{ij}\dot{H}_j + d_{ijk}\dot{T}_{jk} - \frac{\alpha}{\gamma_0 M_s}\mu_{ij}\left(\frac{1}{\mu_0}\ddot{B}_j - \ddot{H}_j\right) \tag{2.162}$$

This introduces 2nd order time derivatives which are inconsistent with the 1st order derivatives in the rest of the algorithm. To avoid this, a convolution integral may be utilized [195]. Expand the constitutive relation of (2.159) as follows in (2.163a-c), which applies for a material with coupling in the x and y-directions:

$$H_x = \beta_{xx}^{\mu}B_x + \beta_{xy}^{\mu}B_y + \frac{\alpha}{\gamma_0 M_s}\left(\frac{1}{\mu_0}\dot{B}_x - \dot{H}_x\right) \tag{2.163a}$$

$$H_y = \beta_{yx}^{\mu}B_x + \beta_{yy}^{\mu}B_y + \frac{\alpha}{\gamma_0 M_s}\left(\frac{1}{\mu_0}\dot{B}_y - \dot{H}_y\right) \tag{2.163b}$$

$$H_z = \beta_{zz}^{\mu}B_z + \frac{\alpha}{\gamma_0 M_s}\left(\frac{1}{\mu_0}\dot{B}_z - \dot{H}_z\right) \tag{2.163c}$$

$$\beta_{ij}^{\mu} = \begin{bmatrix} \beta_{xx}^{\mu} & \beta_{xy}^{\mu} & 0 \\ \beta_{yx}^{\mu} & \beta_{yy}^{\mu} & 0 \\ 0 & 0 & \beta_{zz}^{\mu} \end{bmatrix} \tag{2.163d}$$

Where, in order to focus on magnetic dissipation, the piezomagnetic terms have been removed, and will be added again later as superposition applies for this linear system. Transforming into Laplace space yields:

$$\bar{H}_x = \beta_{xx}^{\mu}\bar{B}_x + \beta_{xy}^{\mu}\bar{B}_y + \frac{\alpha s}{\gamma_0 M_s}\left(\frac{1}{\mu_0}\bar{B}_x - \bar{H}_x\right) \tag{2.164a}$$

$$\bar{H}_y = \beta_{yx}^{\mu}\bar{B}_x + \beta_{yy}^{\mu}\bar{B}_y + \frac{\alpha s}{\gamma_0 M_s}\left(\frac{1}{\mu_0}\bar{B}_y - \bar{H}_y\right) \tag{2.164b}$$

$$\bar{H}_z = \beta_{zz}^{\mu}\bar{B}_z + \frac{\alpha s}{\gamma_0 M_s}\left(\frac{1}{\mu_0}\bar{B}_z - \bar{H}_z\right) \tag{2.164c}$$

Simplification yields:

$$\bar{H}_x = \left\{\frac{\gamma_0 M_s \beta_{xx}^{\mu}}{\alpha}\left[\frac{1}{s+\mathrm{a}}\right] + \frac{1}{\mu_0}\left[\frac{s}{s+\mathrm{a}}\right]\right\}\bar{B}_x + \frac{\gamma_0 M_s \beta_{xy}^{\mu}}{\alpha}\left[\frac{1}{s+\mathrm{a}}\right]\bar{B}_y \tag{2.165a}$$

$$\bar{H}_y = \frac{\gamma_0 M_s \beta_{yx}^{\mu}}{\alpha}\left[\frac{1}{s+\mathrm{a}}\right]\bar{B}_x + \left\{\frac{\gamma_0 M_s \beta_{yy}^{\mu}}{\alpha}\left[\frac{1}{s+\mathrm{a}}\right] + \frac{1}{\mu_0}\left[\frac{s}{s+\mathrm{a}}\right]\right\}\bar{B}_y \tag{2.165b}$$

$$\bar{H}_z = \left\{\frac{\gamma_0 M_s \beta_{zz}^{\mu}}{\alpha}\left[\frac{1}{s+\mathrm{a}}\right] + \frac{1}{\mu_0}\left[\frac{s}{s+\mathrm{a}}\right]\right\}\bar{B}_z \tag{2.165c}$$

Where $\mathrm{a} = \tau^{-1} = \gamma_0 M_s/\alpha$ is the inverse relaxation time. Input the following magnetic flux impulses:

$$B_i(t) = B_i^0\delta(t), \qquad \rightarrow \qquad \bar{B}_i(s) = \frac{1}{s}B_i^0, \qquad i = x, y, z \tag{2.166a/b}$$

Therefore:

$$\bar{H}_x = \left\{\frac{\gamma_0 M_s \beta_{xx}^{\mu}}{\alpha}\left[\frac{1}{s(s+\mathrm{a})}\right] + \frac{1}{\mu_0}\left[\frac{1}{s+\mathrm{a}}\right]\right\}B_x^0 + \frac{\gamma_0 M_s \beta_{xy}^{\mu}}{\alpha}\left[\frac{1}{s(s+\mathrm{a})}\right]B_y^0 \tag{2.167a}$$

$$\bar{H}_y = \frac{\gamma_0 M_s \beta_{yx}^{\mu}}{\alpha}\left[\frac{1}{s(s+\mathrm{a})}\right]B_x^0 + \left\{\frac{\gamma_0 M_s \beta_{yy}^{\mu}}{\alpha}\left[\frac{1}{s(s+\mathrm{a})}\right] + \frac{1}{\mu_0}\left[\frac{1}{s+\mathrm{a}}\right]\right\}B_y^0 \tag{2.167b}$$

$$\bar{H}_z = \left\{\frac{\gamma_0 M_s \beta_{zz}^{\mu}}{\alpha}\left[\frac{1}{s(s+\mathrm{a})}\right] + \frac{1}{\mu_0}\left[\frac{1}{s+\mathrm{a}}\right]\right\}B_z^0 \tag{2.167c}$$

Performing inverse Laplace transformation and simplifying yields:

$$H_x(t) = \left\{\beta_{xx}^{\mu} + \left(\frac{1}{\mu_0} - \beta_{xx}^{\mu}\right)e^{-\mathrm{a}t}\right\}B_x^0 + \beta_{xy}^{\mu}(1 - e^{-\mathrm{a}t})B_y^0 \tag{2.168a}$$

$$H_y(t) = \beta_{yx}^{\mu}(1 - e^{-\mathrm{a}t})B_x^0 + \left\{\beta_{yy}^{\mu} + \left(\frac{1}{\mu_0} - \beta_{yy}^{\mu}\right)e^{-\mathrm{a}t}\right\}B_y^0 \tag{2.168b}$$

$$H_z(t) = \left\{\beta_{zz}^{\mu} + \left(\frac{1}{\mu_0} - \beta_{zz}^{\mu}\right)e^{-\mathrm{a}t}\right\}B_z^0 \tag{2.168c}$$

Which may be re-written as:

$$H_i(t) = G_{ij}(t)B_j^0 \tag{2.169}$$

Where the $G$ tensor components are the time dependent inverse permeability terms and the unit impulse response functions for the magnetic field. Note that if the free space permeability tensor is input above all time dependent terms zero out and the expected free space constitutive relation is recovered, namely $H_i = B_i^0/\mu_0$. For modelling general loading conditions, the impulse response function may be written for an impulse applied at time $\tau$ with response recorded at time $t$ and summed for all time as follows:

$$H_i = \int_{0^-}^{t} G_{ij}(t-\tau)\frac{\partial B_j}{\partial \tau}d\tau \tag{2.170}$$

To be clear, the constitutive relation is expanded out as follows:

$$H_x(t) = \int_{0^-}^{t}\left[\beta_{xx}^{\mu} + \left(\frac{1}{\mu_0} - \beta_{xx}^{\mu}\right)e^{-\mathrm{a}(t-\tau)}\right]\frac{\partial B_x}{\partial \tau}d\tau + \int_{0^-}^{t}\beta_{xy}^{\mu}\left(1 - e^{-\mathrm{a}(t-\tau)}\right)\frac{\partial B_y}{\partial \tau}d\tau \tag{2.171a}$$

$$H_y(t) = \int_{0^-}^{t}\beta_{yx}^{\mu}\left(1 - e^{-\mathrm{a}(t-\tau)}\right)\frac{\partial B_x}{\partial \tau}d\tau + \int_{0^-}^{t}\left[\beta_{yy}^{\mu} + \left(\frac{1}{\mu_0} - \beta_{yy}^{\mu}\right)e^{-\mathrm{a}(t-\tau)}\right]\frac{\partial B_y}{\partial \tau}d\tau \tag{2.171b}$$

$$H_z(t) = \int_{0^-}^{t}\left[\beta_{zz}^{\mu} + \left(\frac{1}{\mu_0} - \beta_{zz}^{\mu}\right)e^{-\mathrm{a}(t-\tau)}\right]\frac{\partial B_z}{\partial \tau}d\tau \tag{2.171c}$$

Similar to section 2.1.3, history variables may be introduced to simplify equations (2.171a-c), and these are defined as follows:

$$\Phi_{mq} = \left(\frac{1}{\mu_0} - \beta_{mq}^{\mu}\right)\int_{0^-}^{t} e^{-\mathrm{a}(t-\tau)}\frac{\partial B_q}{\partial \tau}d\tau\,, \qquad \begin{matrix} m = x,y,z \\ q = x,y,z \\ m = q \end{matrix} \tag{2.172a}$$

$$\Phi_{mq} = -\beta_{mq}^{\mu}\int_{0^-}^{t} e^{-\mathrm{a}(t-\tau)}\frac{\partial B_q}{\partial \tau}d\tau\,, \qquad \begin{matrix} m = x,y \\ q = x,y \\ m \neq q \end{matrix} \tag{2.172b}$$

In other words:

$$\Phi_{mq} = \begin{bmatrix} \Phi_{xx} & \Phi_{xy} & 0 \\ \Phi_{yx} & \Phi_{yy} & 0 \\ 0 & 0 & \Phi_{zz} \end{bmatrix} \tag{2.173}$$

Therefore, after reintroducing piezomagnetism, the magnetic constitutive relation may be written as follows:

$$H_i = \beta_{ij}^{\mu} B_j - g_{ijk}^{PM} T_{jk} + \Phi_{ij} 1_j \tag{2.174}$$

Where $1_j$ is a vector populated by ones. Inputting the magnetic constitutive relation (2.174) into an unconditionally stable and 2nd order accurate finite difference scheme is covered in Chapter 3. Although this methodology may be utilized to model magnetic damping in multiferroic antennas, the device simulations of Chapter 5 will not utilize magnetic damping as only piezoelectric antennas are considered. Still, a validation case for this proposed methodology is provided in Section 4.3.

### 2.3.3 Electrical Constitutive Relation

Utilizing the stress and electric field as independent variables, any piezoelectric materials within the simulation space are governed by the following electric constitutive relation [198]:

$$\dot{D}_i = \epsilon_{ij}^{T} \dot{E}_j + e_{ijk}^{PE} \dot{S}_{jk} \tag{2.175}$$

This is written in rate form to facilitate incorporation into Ampere's law which involves the displacement current $\dot{D}_i$. Assuming that the piezoelectric material is poled out-of-plane in the global z-direction, and is transversely isotropic, yields the following strain coupling and permittivity tensors:

$$e_{ijk}^{PE} = \begin{bmatrix} 0 & 0 & 0 & 0 & e_{15}^{PE} & 0 \\ 0 & 0 & 0 & e_{15}^{PE} & 0 & 0 \\ e_{31}^{PE} & e_{31}^{PE} & e_{33}^{PE} & 0 & 0 & 0 \end{bmatrix}, \quad \epsilon_{ij}^{T} = \begin{bmatrix} \epsilon_{xx}^{T} & 0 & 0 \\ 0 & \epsilon_{xx}^{T} & 0 \\ 0 & 0 & \epsilon_{zz}^{T} \end{bmatrix} \tag{2.176a, b}$$

This constitutive relation will be substituted into Ampere's law in the finite differencing chapter in order to derive the finite difference equations.

## 2.4 Quality Factors and Dissipation

The dissipation discussed thus far in the context of the 2nd law of thermodynamics may seem foreign to some readers more familiar with concepts such as loss tangent ($\tan(\delta)$), quality factors ($Q$), and complex material properties. For example, often authors will express the mechanical stiffness as:

$$T_{ij} = c_{ijkl}S_{kl} = \left(c'_{ijkl} + jc''_{ijkl}\right)S_{kl} \tag{2.176}$$

Where $c'_{ijkl}$ and $c''_{ijkl}$ are the real and imaginary parts of stiffness $c_{ijkl}$ respectively and a loss factor can then be defined as:

$$\tan(\delta) = \frac{c''}{c'} = \frac{1}{Q} \tag{2.177}$$

This is referred to as a "tan delta" since, on the complex plane, $\delta$ is the angle from the real axis to the imaginary axis ($E''$ is opposite, and $E'$ is adjacent). In (2.177), $Q$ is the quality factor (q-factor) which is typically assumed to be frequency dependent in the following fashion [201][202]:

$$\mathrm{Qf} = constant \tag{2.178}$$

By observing (2.176) and (2.177), the conversion of the q-factor to a viscoelastic damping parameter ($\eta$) is [4]:

$$\eta = \frac{c'}{\omega Q} \tag{2.179}$$

From (2.178) and (2.179) it is seen that the viscoelastic damping parameter is assumed frequency independent and therefore the viscoelastic damping is more fundamental than $Q$. Different q-factors need to be measured for different resonant modes. $Q$ is a measure of how high the output is at resonance while $\tan(\delta)$ is a measure of how much the output is attenuated at resonance. Every dissipation mechanism will have a $Q$ associated with it, and the total $Q$ ($Q_t$) may be computed as follows [138]:

$$\frac{1}{Q_t} = \sum_{i=1}^{N} \frac{1}{Q_i} \tag{2.179}$$

Where $N$ is the number of dissipation mechanisms (both from energy loss and energy conversion). The Q for a mechanical antenna may be most simply written as:

$$\frac{1}{Q_t} = \frac{1}{Q_{rad}} + \frac{1}{Q_{mech}} \tag{2.180}$$

Where $Q_{rad}$ is the q-factor associated with radiation and $Q_{mech}$ is the q-factor associated with mechanical losses. Each individual $Q_i$ may be defined as:

$$Q_i = \frac{2\omega W_{Total}}{P_i} \tag{2.181}$$

Where $W_{Total}$ is the total energy stored within the system and $P_i$ is the power dissipated by the specific dissipation mechanism. Based on (2.179) and (2.180) the $Q_{mech}$ is ideally maximized and the $Q_{rad}$ is ideally minimized, hence why sometimes authors will describe a high $Q$ as a favorable result and sometimes as an unfavorable result. The total $Q$ may be determined by taking the resonant frequency ($f_r$) and dividing by the half-power bandwidth ($\Delta f_{HP}$), which is the range of frequencies where the dissipated power is half of the maximum or higher:

$$Q_t = \frac{f_r}{\Delta f_{HP}} \tag{2.182}$$

This expression will be used to determine the total q-factors for the devices simulated herein. The radiation efficiency ($e_{rad}$) of an antenna may be defined [152] by taking the ratio of the $Q_t$ with a theoretical bound ($Q_a$) [33-35][164]:

$$e_{rad} = \frac{Q_t}{Q_a} * 100\% \tag{2.183}$$

Equation (2.183) does not need to be used to determine the efficiency in the proposed numerical framework however since the input and radiated power are directly computed. Other authors use this approach however to approximate radiation efficiency from a measured Q value [152].

## 2.5 Summary of Equations

As a capstone to this chapter, all the equations presented will be summarized in table format to prepare for their discretization into finite difference form in the next chapter. The balance laws are shown below in Table 2-1:

| | | |
|---|---|---|
| Newton's Laws | $\rho\dot{v}_i = T_{ij,j}$ | Mechanics |
| Maxwell's Equations | $\dot{D}_i + \sigma_{ij}E_j + J_i^S = \epsilon_{ij'k}H_{k,j'} - \epsilon_{ijk}\Phi_{H_{jk}}$<br>$\dot{B}_i + \mathcal{M}_i^S = \epsilon_{ijk'}E_{j,k'} + \epsilon_{ijk}\Phi_{E_{jk}}$ | Electrodynamics |
| LLG Equation | $\frac{1}{\mu_0\gamma}\dot{M}_i = \epsilon_{ijk}M_jH_k^{eff} - \frac{\alpha}{\mu_0\gamma M_s}\epsilon_{ijk}M_j\dot{M}_k$ | Micromagnetics |

Table 2-1: Balance Laws

The constitutive relations are as shown in Table 2-2:

| | |
|---|---|
| Mechanical | $\dot{T}_{ij} = c_{ijkl}^{B,D}v_{k,l} - h_{kij}^{PM}B_k - h_{kij}^{PE}\dot{D}_k + \eta_{ijkl}^{B,D}\dot{v}_{k,l}$ |
| Electrical | $\dot{D}_i = \epsilon_{ij}^S\dot{E}_j + e_{ijk}^{PE}v_{j,k}$ |
| Magnetic | $H_i = \beta_{ij}^{\mu}B_j - g_{ijk}^{PM}T_{jk} + \Phi_{ij}1_j$ |

Table 2-2: Constitutive Relations

Within the constitutive relations of Table 2-2, three different coupling tensors are referred to which can be confusing. Fortunately, Table 2-3 documents all the expressions for piezoelectric materials [194]. For piezomagnetic materials, the expressions are identical [199], simply substitute $H$ for $E$, and $B$ for $D$.

| Independent Variable | Form | Piezoelectric Relation |
|---|---|---|
| $S, D$ | $h$-form | $T = c^D S - hD$<br>$E = -hS + \beta^S D$ |

| | | |
|---|---|---|
| $T, E$ | $d$-form | $S = s^E T + dE$<br>$D = dT + \epsilon^T E$ |
| $T, D$ | $g$-form | $S = s^D T + gD$<br>$E = -gT + \beta^T D$ |
| $S, E$ | $e$-form | $T = c^E S - eE$<br>$D = eS + \epsilon^S E$ |
| Relationships Between Constants | | |
| $d_{nij} = \epsilon^T_{nm} g_{mij} = e_{nkl} s^E_{klij}$ | | $e_{nij} = \epsilon^S_{nm} h_{mij} = d_{nkl} c^E_{klij}$ |
| $g_{nij} = \beta^T_{nm} d_{mij} = h_{nkl} s^D_{klij}$ | | $h_{nij} = \beta^S_{nm} e_{mij} = g_{nkl} c^D_{klij}$ |
| $\epsilon^T_{nm} - \epsilon^S_{nm} = d_{nkl} e_{mkl}$ | | $c^D_{ijkl} - c^E_{ijkl} = e_{mij} h_{mkl}$ |

Table 2-3: Types of Fundamental Piezoelectric Relations

These equations may be used to acquire update equations directly for all fields save the electric fields. These will require the use of Maxwell's equations as well as the electric and magnetic constitutive relations. The result is a tri-diagonal system known as the ADI-FDTD equations. This will be discussed in the subsequent chapter on the finite difference discretization of the equations contained herein.

# CHAPTER 3: FINITE DIFFERENCE ALGORITHM

Herein, the numerical formulation for modelling a mechanical resonance-based antenna is described. The continuum equations in Chapter 2, summarized in Section 2.5, are necessary to model a piezoelectric resonator antenna as shown in Figure 3-1, where a z-poled piezoelectric material is assumed.

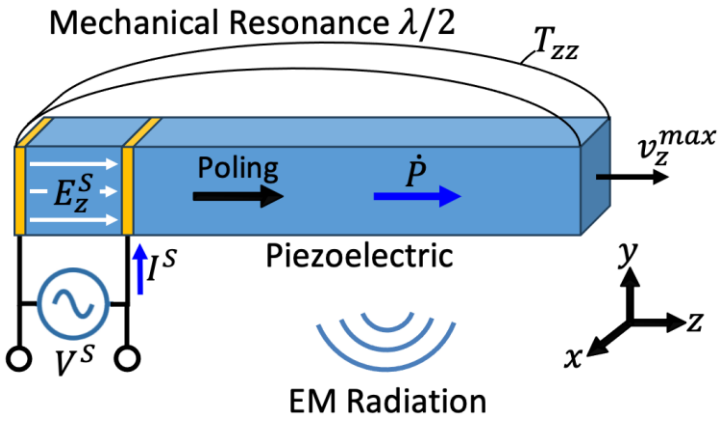


Figure 3-1: Typical mechanical axial resonance based piezoelectric antenna.

In the figure, an electrical source sends current $I^S$ into electrodes sandwiching piezoelectric material producing potential difference $V^S$ across the electrodes. This generates field $E_z^S$ within the piezoelectric. Due to the device size being electrically small, the *x* and *y* components of the electric field, along with the fringing fields, are assumed to be zero between the electrodes. The electrically small size also means that Maxwell's equations do not need to be evoked in this region as the feedline current $I^S$ is equal and opposite to the polarization current. The electrode + piezo + electrode stack therefore acts as an energy storing capacitor rather than an energy propagating antenna. Also, since field $E_z^S$ is within a piezoelectric material, mechanical stress and strain/velocity will be produced. This stress and strain will propagate in the axial direction of the mechanical bar via elastodynamics and resonate mechanical modes based on the

mechanical boundary conditions (half-sine wave mode for traction free boundaries shown in Figure 3-1). In this case, only the axial stress $T_{zz}$ will be excited and, although in-plane velocities $v_x$ and $v_y$ are non-zero via Poisson's effect, only $T_{zz}$ and $v_z$ are required to find a unique solution via (3). These resonant mechanical fields $T_{zz}$ and $v_z$ generate electrical polarization current $\dot{P}$ within the mechanical bar which lie outside of the electrodes via the direct piezoelectric effect. As such, this polarization current will induce EM radiation per Maxwell's equations. After simulating these effects, the fields immediately surrounding the antenna are input into a post-processer to determine far-field performance. A general overview is seen in Figure 3-2. Any numerical framework claiming to model piezoelectric antennas must somehow perform each task in the figure and this chapter highlights one such methodology.

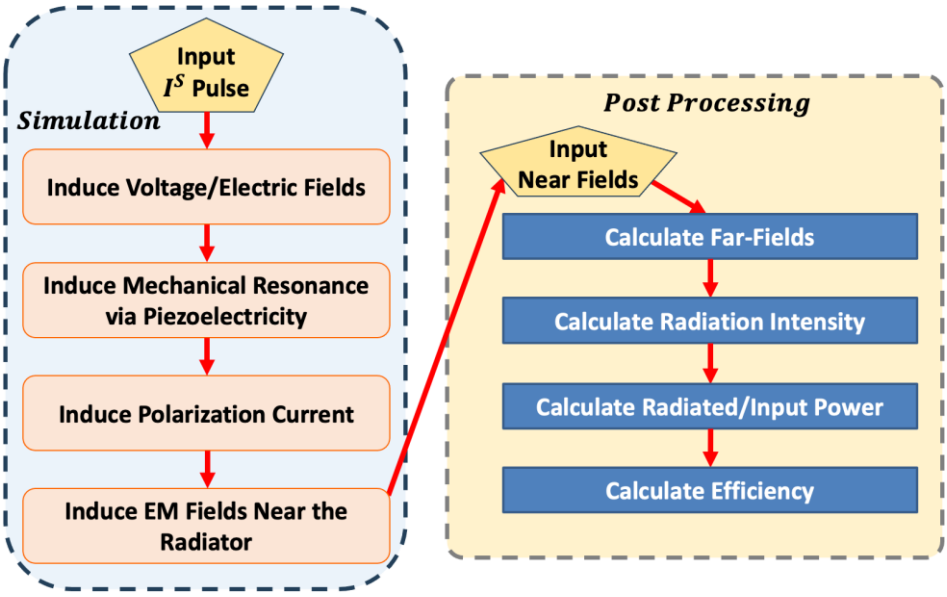


Figure 3-2: General flow of the goals for a mechanical antenna simulation.

In numerical analysis it is common to take the differential equations that govern the physical system everywhere and instead formulate new versions that are only approximations at discrete points. One popular approach is the finite difference time domain (FDTD) method in which the

spatial and temporal derivatives are analyzed across finite intervals. To demonstrate this, recall the definition of a derivative in equation (3.1):

$$\frac{\partial f}{\partial u} = \lim_{\Delta u \to 0} \frac{f(u + \Delta u, \cdots) - f(u, \cdots)}{\Delta u} \tag{3.14}$$

Where any number of dependent variables exist. The finite difference approach relaxes this definition by removing the limit and allowing the interval ($\Delta u$) to be finite as in equation (3.2a):

$$\frac{\partial f}{\partial u} \approx \frac{f(u + \Delta u, \cdots) - f(u, \cdots)}{\Delta u} \tag{3.2a}$$

The interval may be the difference in any dependent variable, and the expression above is known as a forward difference since the fields is being analyzed just ahead of the current location. Backward and central differences also exist and are, respectively:

$$\frac{\partial f}{\partial u} \approx \frac{f(u, \cdots) - f(u - \Delta u, \cdots)}{\Delta u} \tag{3.2b}$$

$$\frac{\partial f}{\partial u} \approx \frac{f(u + \Delta u/2, \cdots) - f(u - \Delta u/2, \cdots)}{\Delta u} \tag{3.2c}$$

In terms of the nomenclature utilized herein, the n index defines the time with the i, j, and k indices defining the x, y, and z directions respectively:

$$t = n\Delta t \tag{3.3a}$$

$$x = i\Delta x \tag{3.3b}$$

$$y = j\Delta y \tag{3.3c}$$

$$z = k\Delta z \tag{3.3d}$$

Herein, the spatial location of each field is written in parenthesis, the time step is written using superscripts, and the tensorial information (e.g., the direction of the field) is written using subscripts as shown in equation (3.4a) for a 1st order tensor:

$$f^n_{x,y,z}(i,j,k) = f_{x,y,z}(i\Delta x, j\Delta y, k\Delta z, n\Delta t) = f_{x,y,z}(x,y,z,t) \tag{3.4a}$$

The values of n, i, j, and k need not be integers, in fact most fields contained herein are not rectified at an integer time step or spatial location. Whenever a field varies spatially but not temporally, the spatial indices are expressed using superscripts as shown in equation (3.4b):

$$f_{x,y,z}^{i,j,k} = f_{x,y,z}(i\Delta x, j\Delta y, k\Delta z) = f_{x,y,z}(x, y, z) \tag{3.4b}$$

This is performed to shorten the notation, as some of the equations herein become lengthy. When the equations become quite long herein, all terms will have their temporal (if applicable) and spatial designations within the superscript, namely:

$$f_{x,y,z}^{n,i,j,k} = f_{x,y,z}^{n}(i\Delta x, j\Delta y, k\Delta z) = f_{x,y,z}(x, y, z, t) \tag{3.4c}$$

Herein, an unconditionally stable method known as the alternating direction implicit finite difference time-domain (ADI-FDTD) method is utilized in which the evolution of fields from time $n\Delta t$ to time $(n+1)\Delta t$ is split into two subiterations. The 1st sub-iteration updates the fields from $n\Delta t$ to $(n+1/2)\Delta t$, and the 2nd from $(n+1/2)\Delta t$ to $(n+1)\Delta t$. This method will be described in more detail in sections 3.6, 3.7, and 3.8.

## 3.1 Methodology

When leveraging the finite difference method, the left- and right-hand sides of the equation must be rectified at the same time and spatial location. This rule is known as spatial and temporal homogeneity. As an example, consider the elastodynamic equation in the absence of body forces described in section 2.1.2:

$$\rho \dot{v}_i = T_{ij,j} \tag{2.12b}$$

In finite difference form, the z-component is as follows:

$$\frac{1}{\Delta t}\left[v_z^{n+\frac{1}{4}}\left(i+\frac{1}{2},j+\frac{1}{2},k\right)-v_z^{n-\frac{1}{4}}\left(i+\frac{1}{2},j+\frac{1}{2},k\right)\right]$$
$$=\frac{1}{\Delta x}\left[T_{xz}^n\left(i+1,j+\frac{1}{2},k\right)-T_{xz}^n\left(i,j+\frac{1}{2},k\right)\right]$$
$$+\frac{1}{\Delta y}\left[T_{yz}^n\left(i+\frac{1}{2},j+1,k\right)-T_{yz}^n\left(i+\frac{1}{2},j,k\right)\right] \quad (3.5)$$
$$+\frac{1}{\Delta z}\left[T_{zz}^n\left(i+\frac{1}{2},j+\frac{1}{2},k+\frac{1}{2}\right)-T_{zz}^n\left(i+\frac{1}{2},j+\frac{1}{2},k-\frac{1}{2}\right)\right]$$

Examining each individual term in (3.5), all differences are defined at time $t=n\Delta t$, and point $x=(i+1/2)\Delta x$, $y=(j+1/2)\Delta y$, and $z=(k+1/2)\Delta z$. This homogeneity rule is typical of finite difference equations but may be broken in special cases. Note in the equation above, only one term is defined at a future time step $(n+1/4)$ with all other fields being known, either from the previous time step or from the initial conditions. This is therefore an explicit update equation for the velocity in the z-direction. Both explicit and implicit methods are utilized herein.

## 3.2 Grids

The spatial definition of the tensors updated using the FDTD method conform to grids with many useful properties. These spatial grids are discussed next.

### 3.2.1 Electromagnetic Yee Grid

Within electrodynamic simulations it is necessary to map out the discrete points in which the 3-components of the electric and magnetic fields will be determined. As a first pass it may seem prudent to collocate all fields at a single point similarly to how displacements are all collocated within the finite element method in structural analysis. However, within the finite difference method, so-called “staggered” grids produce 2nd order accurate central differences for spatial derivatives if the fields are mapped out properly. The most famous is the Yee grid first introduced by K.S. Yee in 1966 [177] as shown in Figure 3-3:

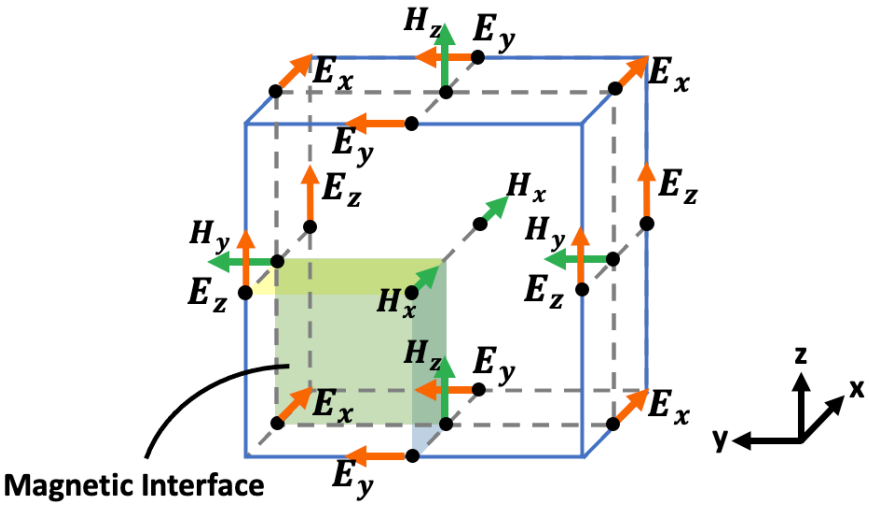


Figure 3-3: The Yee grid utilized for FDTD simulations.

In the space lattice, the magnetic field nodes lie on the face centers pointed in the normal direction and the electric fields are along the center of the cell edges and tangential to the edges. The locations of the electric and magnetic fields can be swapped so that the electric fields instead lie on the face centers, but all equations derived herein use the grid above. Also shown in Figure 3-3 is the magnetic interface which is half a cell staggered from the electric interfaces that are collocated with the cell faces. These interfaces will be discussed in section 3.3.1. Note in Figure 3-3 that the H fields are surrounded by swirling E fields (Faraday contour) and that the E fields are surrounded by swirling H fields (Ampere contour). This essentially puts each field at the center of a Faraday or Ampere loop and allows for central difference equations to be readily written which are 2$^{nd}$ order accurate. Additionally, it can be shown that the space lattice is divergence free in the absence of free charges [177-179] essentially satisfying two of Maxwell's equations upfront, namely Gauss's law for electricity and magnetism.

### 3.2.2 The Staggered Mechanical Grid

Mechanical spatial lattices are defined based on which system of dependent variables are utilized to approximate the PDEs. For example, a single PDE in terms of displacement may be written as follows:

$$\rho \ddot{u}_i = c_{ijkl} u_{k,lj} \tag{3.6}$$

Where the material stiffness is assumed to be spatially independent. Modelers that utilize this PDE make use of the so-called “conventional” grid [192] in which the three displacement components are collocated and defined at the corners of the unit cell and the stress terms do not appear as shown in Figure 3-4:

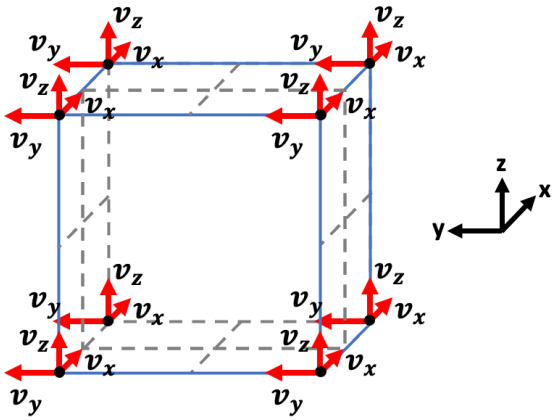


Figure 3-4: Conventional mechanical finite difference grid.

When the so-called Velocity-Stress formulation [4][192][193] is used, the velocity and stress are treated as the dependent variables, as in equation (2.12b), and two sets of PDEs are used to update the mechanical fields. This allows the PDEs to be written in terms of the first time and spatial derivatives similar to Maxwell’s equations. 2$^{nd}$ order accurate central differences for the spatial divergence of the stress in the elastodynamic equation (2.12b) and the spatial gradients of the velocity in the mechanical constitutive relation (2.148) in rate form may be achieved by

utilizing a staggered finite difference grid [192-194]. Figure 3-5 shows the spatial lattice utilized herein:

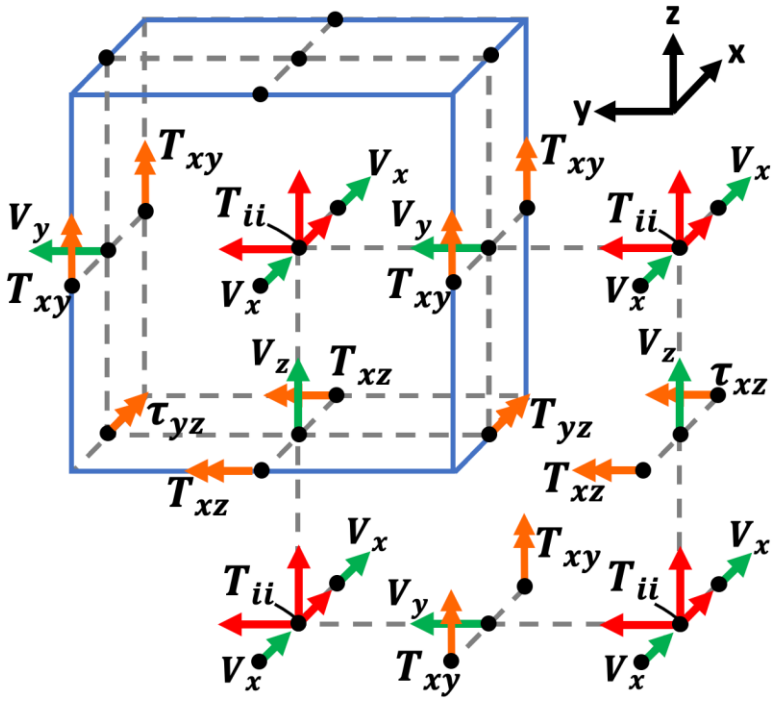


Figure 3-5: 3D Staggered mechanical finite difference grid.

This cell looks similar to the Yee grid utilized in electrodynamics in that the shear stresses are along the cell edges and tangent to the edges, like the electric field, and the velocities are at the face centers and normal to the surface, like the magnetic fields. Curiously however, the normal stresses are all collocated at the center of the cell which is a consequence of the fact that the mechanical grid is not divergence free like the Yee grid. If it were divergence free, dynamic motions would be absent since the stress divergence is proportional to the acceleration. This also leads to additional complications as it relates to boundary conditions as will be discussed in section 3.4.2. For now, it is prudent to note that the velocity fields in Figure 3-5 are surrounded by diverging stress fields, as is expected from the elastodynamic equation, and that the stress fields are surrounded by the velocity gradients, as is expected from the

mechanical constitutive relation. To help visualize the former, consider the x-component of the elastodynamic equation:

$$\rho \dot{v}_x = T_{xx,x} + T_{xy,y} + T_{xz,z} \tag{3.7}$$

Examining these terms, the three spatial derivatives diverge from a single point, namely the location of the $v_x$ field as shown in Figure 3-6.

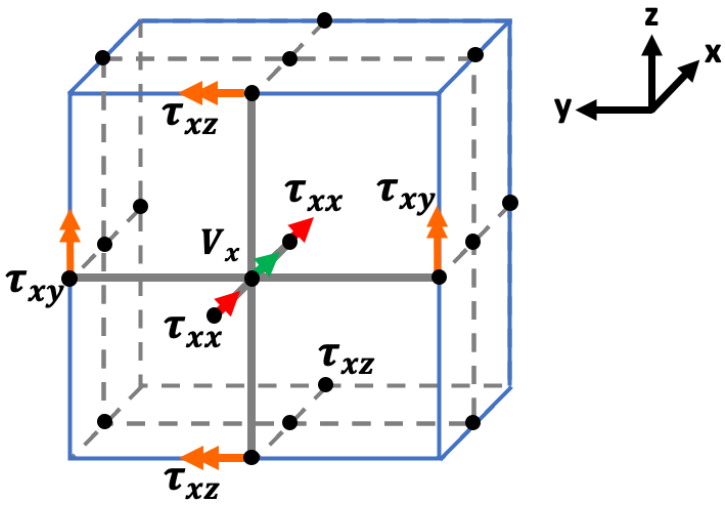


Figure 3-6: Stress divergence centered at the velocity terms.

It can similarly be shown that the grid is such that the velocity gradients are collocated with the appropriate stress terms. Although the 3D grid has been presented in this section, only 1D uniaxial stress simulations are performed herein. For these simulations, only stress $T_{zz}$ and velocity $v_z$ need be considered.

### 3.2.3 Field Values at Off-Grid Locations

If it is desired to know the value of a field at a spatial location offset from where it is defined by Figure 3-3 and Figure 3-5 then averaging between nearest grid points is necessary. Recall from Figure 3-5 that the stresses are defined at the unit cell center, namely at $x = (i + 1/2)\Delta x$,

$y = (j + 1/2)\Delta y$, and $z = (k + 1/2)\Delta z$. Say it is desired to know the normal stress $T_{zz}$ at $z = k\Delta z$ instead; Spatial averaging would yield the following value:

$$T_{zz}\left(i+\frac{1}{2},j+\frac{1}{2},k\right)=\frac{1}{2}\left(T_{zz}\left(i+\frac{1}{2},j+\frac{1}{2},k+\frac{1}{2}\right)+T_{zz}\left(i+\frac{1}{2},j+\frac{1}{2},k-\frac{1}{2}\right)\right) \quad (3.8)$$

For spatial locations that do not bisect grid points, averaging would be more complex than what is seen in (3.8), but herein bisection points are considered.

## 3.3 Interface Conditions

An interface is defined herein as the nodes where two or more materials meet with differing material properties. This is distinct from boundaries, which are the nodes where the simulation space is terminated. In this section, electrodynamic and mechanical interface conditions are explored.

### 3.3.1 EM Interfaces

The following relations (3.9a/b) must hold at all material interfaces [25][26]:

$$J_{surface} = \hat{n} \times H, \qquad \mathcal{M}_{surface} = E \times \hat{n} \quad (3.9a/b)$$

Where $\hat{n}$, is a unit vector normal to the interface and $J_{surface}$ and $\mathcal{M}_{surface}$ are the electric and magnetic surface currents, acting at the interface, respectively. In the absence of surface currents these relations state that the tangential electric and magnetic fields must be continuous across a material interface. Looking again at Figure 3-3, the E fields are tangential to the unit cell faces and the H fields are tangential to a cube that is half a cell staggered from the unit cell. Say two different materials are stacked on top of one another in a heterogenous structure and label the bottom and top layers as material 1 and 2 respectively as shown in Figure 3-7.

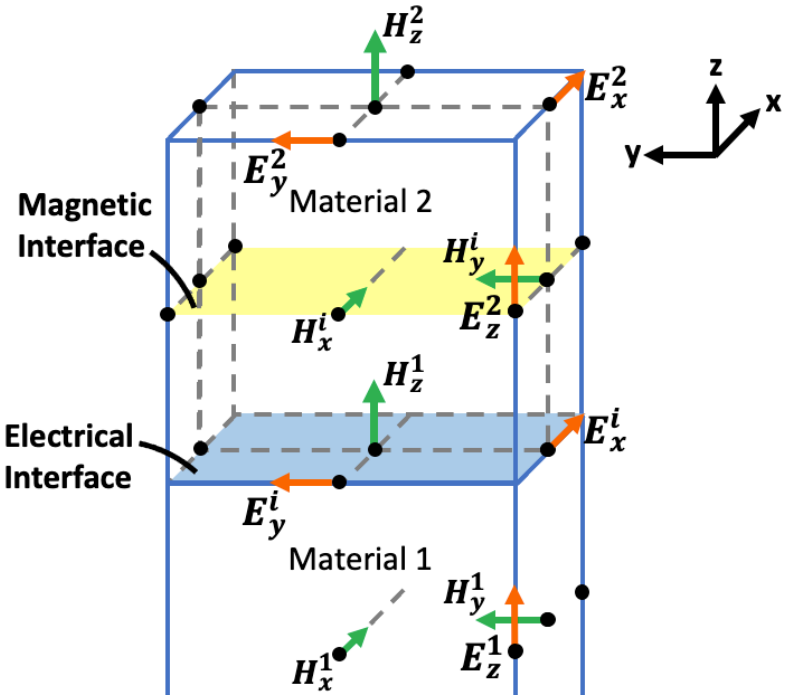


Figure 3-7: Electric and magnetic interfaces.

The plane where the electrical interface conditions are satisfied will coincide with the cube face, as highlighted in blue, but the magnetic interface conditions are satisfied on a plane half a cell above as highlighted in yellow. Within the figure all fields at an interface are labeled with an "i" superscript and those fields which uniquely belong to materials 1 and 2 are similarly labeled with corresponding superscripts. It is informative to note that the magnetic field located at the electrical interface corresponds to material 1 alone. This raises a question; what material properties should be utilized at the interface between multiple materials? This question is answered in the subsequent section.

#### 3.3.1.1 Electric and Magnetic Property Definition

It is important to note that not only must the EM fields be defined spatially but also the permittivity and permeability which are necessary for update equations. Consider that the electrical quantities are defined at the center of each cell, and the magnetic quantities are located at the corners as illustrated in Figure 3-8:

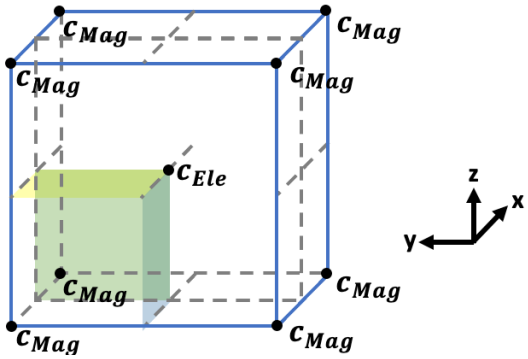


Figure 3-8: Spatial definition of electric and magnetic material properties.

These are not defined arbitrarily but such that spatial interpolation always returns an average permittivity and permeability at all interfaces between different materials. For further clarification consider a corner interface between four materials with different properties as shown in Figure 3-9. Additionally, assume that the permittivity and permeability of the materials are diagonal matrices.

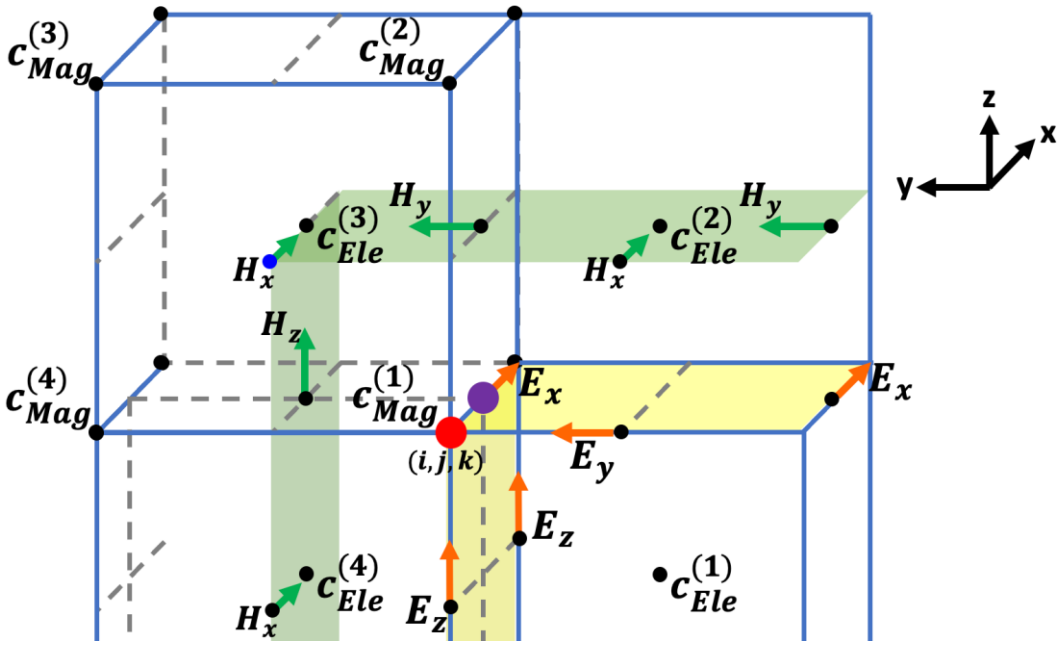


Figure 3-9: Corner Interface Between Four Different Materials

In the figure, only interface fields are shown for clarity. Note that these EM fields are not collocated with the corresponding material properties necessary for the update equations thus necessitating spatial interpolation of the permittivity and permeability terms. Say the interface occurs at the spatial location (*i,j,k*) shown as a red dot in the figure. An update equation will now be written for the interface electric field at point (*i+1/2,j,k*) shown as a purple dot. From this, the x-component of Ampere's law may be written as follows:

$$\begin{aligned}\frac{\epsilon_{xx}^{i+\frac{1}{2},j,k}}{\Delta t}&\left[E_x^{n+\frac{1}{2}}\left(i+\frac{1}{2},j,k\right)-E_x^{n-\frac{1}{2}}\left(i+\frac{1}{2},j,k\right)\right]\\&=\frac{1}{\Delta y}\left[H_z^n\left(i+\frac{1}{2},j+\frac{1}{2},k\right)-H_z^n\left(i+\frac{1}{2},j-\frac{1}{2},k\right)\right]\\&-\frac{1}{\Delta z}\left[H_y^n\left(i+\frac{1}{2},j,k+\frac{1}{2}\right)-H_y^n\left(i+\frac{1}{2},j,k-\frac{1}{2}\right)\right]\end{aligned} \tag{3.10}$$

Note that both sides of the equation are determined at the same spatial location if the permittivity term is defined at $\left(i+\frac{1}{2},j,k\right)$. Since this is not the case, spatial interpolation needs to be performed. By rearranging terms, an update equation for $E_x$ may be written as follows:

$$\begin{aligned}E_x^{n+\frac{1}{2}}\left(i+\frac{1}{2},j,k\right)&=E_x^{n-\frac{1}{2}}\left(i+\frac{1}{2},j,k\right)\\&+\frac{1}{\frac{1}{4}\left[\epsilon_{xx}^{i+\frac{1}{2},j+\frac{1}{2},k+\frac{1}{2}}+\epsilon_{xx}^{i+\frac{1}{2},j-\frac{1}{2},k+\frac{1}{2}}+\epsilon_{xx}^{i+\frac{1}{2},j+\frac{1}{2},k-\frac{1}{2}}+\epsilon_{xx}^{i+\frac{1}{2},j-\frac{1}{2},k-\frac{1}{2}}\right]}\left\{\frac{\Delta t}{\Delta y}\left[H_z^n\left(i+\frac{1}{2},j+\frac{1}{2},k\right)\right.\right.\\&\left.\left.-H_z^n\left(i+\frac{1}{2},j-\frac{1}{2},k\right)\right]-\frac{\Delta t}{\Delta z}\left[H_y^n\left(i+\frac{1}{2},j,k+\frac{1}{2}\right)-H_y^n\left(i+\frac{1}{2},j,k-\frac{1}{2}\right)\right]\right\}\end{aligned} \tag{3.11}$$

The permittivity term shown is the average permittivity between the four materials. It can similarly be shown, by examining $H_x$ at $\left(i,j+\frac{1}{2},k+\frac{1}{2}\right)$, that the magnetic permeability will also require spatial interpolation, yielding an average, or effective, permeability.

### 3.3.2 Mechanical Interfaces

The traction and the displacement at all mechanical interfaces must be continuous. Also, when considering interfaces between two or more materials with different stiffness and density it is important to make a distinction. Previously it was observed that on the EM side, when using

the Yee grid, two interfaces must be considered; electrical interface planes that line up with the faces of the unit cell and magnetic interface planes that bisect the unit cell (half a cell staggered). When dealing with mechanical fields however, only one interface exists. This highlights an interesting distinction between electrodynamics and elastodynamics, namely that the former deals with two sets of fields with two sets of constitutive relations while the latter only deals with one set of fields. It should not be surprising then that there is only one interface condition when dealing with mechanical fields. This leaves a question to be answered; should the mechanical interface planes line up with the unit cell like electrical interfaces or should the planes be half a cell staggered like the magnetic interfaces? Consider the latter approach, resulting in the interface planes shown in Figure 3-10a:

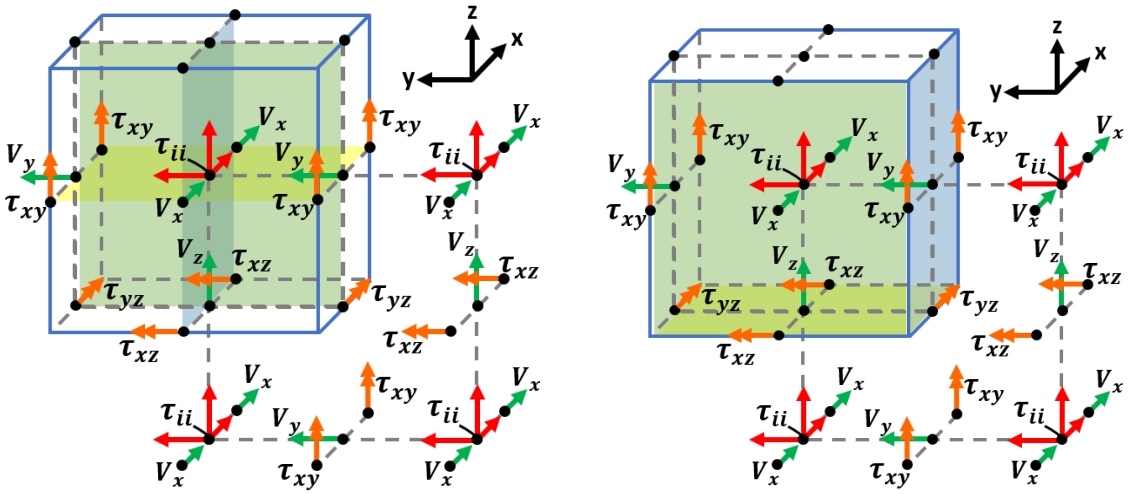


Figure 3-10: Potential mechanical interfaces.

The glaring problem with this is that all normal stresses are continuous across any interface plane, but this is not the case. Only one normal stress is continuous across an interface, and it is the one that is normal to the interface. It is then clear that the mechanical interfaces must be along the unit cell planes as shown in Figure 3-10b. Again, there are questions left to be

answered, namely that the interface planes only guarantee continuity of the shear stresses and one velocity component so what about the normal stress and the other two velocity components? These questions may be answered by considering mechanical properties which are discussed in the next section.

#### 3.3.2.1 Mechanical Property Definition

At this time, it is important to note that not only must the mechanical fields be defined spatially but also the density, stiffness, and the discretization (for graded meshes) which are necessary for update equations. Consider that the mechanical material properties are defined at the center of each cell as shown in Figure 3-11:

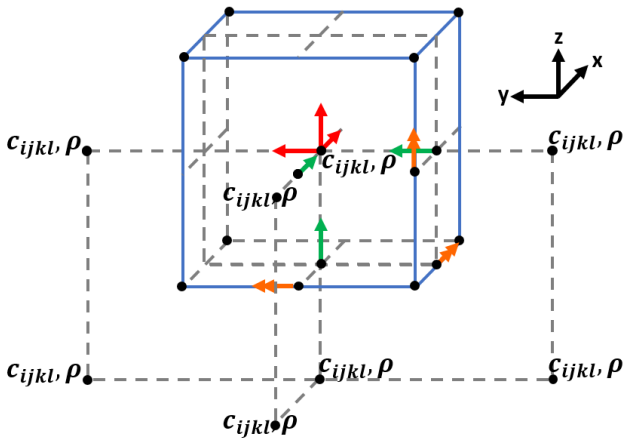


Figure 3-11: Spatial definition of mechanical material properties.

These are not defined arbitrarily but rather such that spatial interpolation always returns an average shear stiffness and density at all interfaces between structural elements. For further clarification consider a planar interface between two materials with different stiffness and density normal to the z-direction as shown in Figure 3-12. Label the bottom layer as material (1) and the top layer as material (2) with properties having corresponding subscripts.

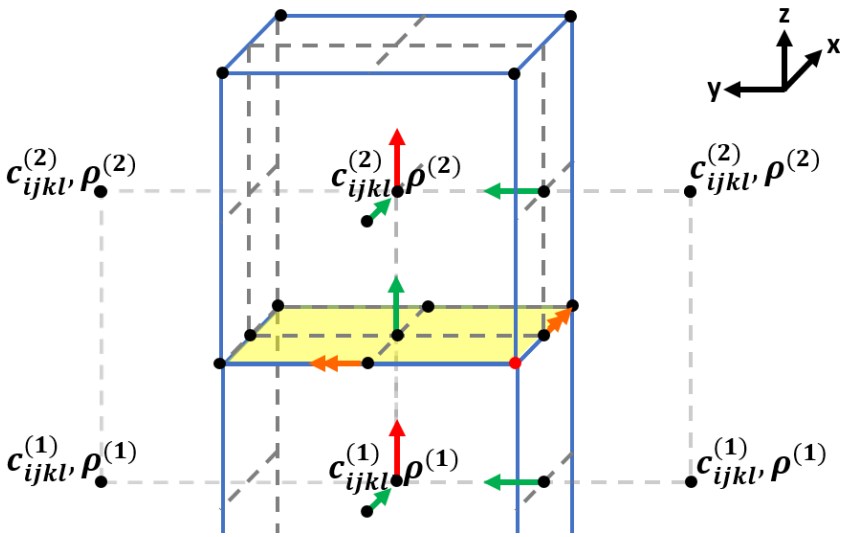


Figure 3-12: Vertical mechanical interface.

As shown, two shear stresses ($T_{yz}$, $T_{xz}$) and one velocity term ($v_z$) are defined at the interface which is highlighted yellow. Note that these mechanical fields are not collocated with the material properties necessary to define them thus necessitating spatial interpolation of the stiffness and density terms. Say the interface occurs at the spatial location (*i,j,k*), then the spatial definition of the velocity $v_z$ may be written as:

$$v_z\left(i+\frac{1}{2},j+\frac{1}{2},k\right)=\frac{1}{\frac{1}{2}\left(\rho_{(1)}^{i+\frac{1}{2}j+\frac{1}{2}k-\frac{1}{2}}+\rho_{(2)}^{i+\frac{1}{2}j+\frac{1}{2}k+\frac{1}{2}}\right)}\left\{\frac{1}{\Delta x}\left[T_{xz}\left(i+1,j+\frac{1}{2},k\right)-T_{xz}\left(i,j+\frac{1}{2},k\right)\right]\right.$$
$$+\frac{1}{\Delta y}\left[T_{yz}\left(i+\frac{1}{2},j+1,k\right)-T_{yz}\left(i+\frac{1}{2},j,k\right)\right] \quad (3.12)$$
$$\left.+\frac{1}{\Delta z}\left[T_{zz}\left(i+\frac{1}{2},j+\frac{1}{2},k+\frac{1}{2}\right)-T_{zz}\left(i+\frac{1}{2},j+\frac{1}{2},k-\frac{1}{2}\right)\right]\right\}$$

Note that both sides of the equation are determined at the same spatial location and that the density term shown is the average density between the two materials. The normal stresses require no spatial interpolation since these are collocated with the stiffness terms and are never evaluated at the interface of different materials. Based on this, the normal stress in the z-direction can be written as follows:

$$
\begin{aligned}
&T_{zz}\left(i+\frac{1}{2},j+\frac{1}{2},k+\frac{1}{2}\right) \\
&\quad=\frac{1}{\Delta x}c_{xxzz}^{i+\frac{1}{2},j+\frac{1}{2},k+\frac{1}{2}}\left[v_x\left(i+1,j+\frac{1}{2},k+\frac{1}{2}\right)-v_x\left(i,j+\frac{1}{2},k+\frac{1}{2}\right)\right] \\
&\quad+\frac{1}{\Delta y}c_{yyzz}^{i+\frac{1}{2},j+\frac{1}{2},k+\frac{1}{2}}\left[v_y\left(i+\frac{1}{2},j+1,k+\frac{1}{2}\right)-v_y\left(i+\frac{1}{2},j,k+\frac{1}{2}\right)\right] \\
&\quad+\frac{1}{\Delta z}c_{zzzz}^{i+\frac{1}{2},j+\frac{1}{2},k+\frac{1}{2}}\left[v_z\left(i+\frac{1}{2},j+\frac{1}{2},k+1\right)-v_z\left(i+\frac{1}{2},j+\frac{1}{2},k\right)\right]
\end{aligned}
\tag{3.13}
$$

So, the $T_{zz}$ is dependent on the velocity term at the interface, namely $v_z\left(i+\frac{1}{2},j+\frac{1}{2},k\right)$. Since the velocity at the interface considers both materials, the normal stress near the interface is also affected by the interface even though it is not evaluated there. In fact, complete traction continuity and velocity continuity at interfaces may be guaranteed by proper inclusion of the material properties [192]. Next, take for example the $T_{yz}$ field represented by the double headed orange arrow pointed in the x-direction. This field is surrounded by an equal number of $c_{yzyz}$ shear stiffness terms from each material.

$$
\begin{aligned}
T_{yz}\left(i+\frac{1}{2},j,k\right)=\frac{1}{4}\Big[&c_{yzyz}^{(1)}\left(i+\frac{1}{2},j-\frac{1}{2},k-\frac{1}{2}\right)+c_{yzyz}^{(1)}\left(i+\frac{1}{2},j+\frac{1}{2},k-\frac{1}{2}\right) \\
&+c_{yzyz}^{(2)}\left(i+\frac{1}{2},j-\frac{1}{2},k+\frac{1}{2}\right)+c_{yzyz}^{(2)}\left(i+\frac{1}{2},j+\frac{1}{2},k+\frac{1}{2}\right)\Big]S_{yz}\left(i+\frac{1}{2},j,k\right)
\end{aligned}
\tag{3.14}
$$

Note that both sides of the equation are determined at the same spatial location and that the stiffness term shown is the average stiffness between the two materials. It is additionally important to note that the 4 terms are necessary in case of a line interface between 4 different materials. This case is shown in Figure 3-13 for a line interface in the x-direction (corner) at the (*i,j,k*) spatial point which is colored red.

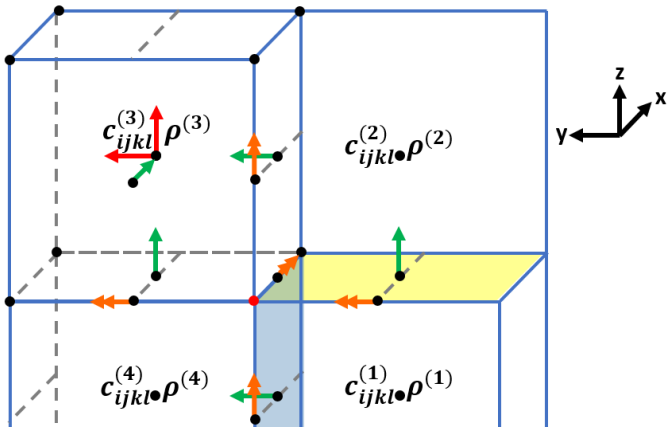


Figure 3-13: Mechanical corner interface.

Note that all line interfaces are simply two plane interfaces converging together, and in this case only the $T_{yz}$ shear stress is evaluated at the interface which may be written as:

$$T_{yz}\left(i+\frac{1}{2},j,k\right)=\frac{1}{4}\left[c^{(1)}_{yzyz}\left(i+\frac{1}{2},j-\frac{1}{2},k-\frac{1}{2}\right)+c^{(2)}_{yzyz}\left(i+\frac{1}{2},j-\frac{1}{2},k+\frac{1}{2}\right)\right.$$
$$\left.+c^{(3)}_{yzyz}\left(i+\frac{1}{2},j+\frac{1}{2},k+\frac{1}{2}\right)+c^{(4)}_{yzyz}\left(i+\frac{1}{2},j+\frac{1}{2},k-\frac{1}{2}\right)\right]S_{yz}\left(i+\frac{1}{2},j,k\right) \tag{3.15}$$

Therefore, the shear stiffness requires four terms since generally the shear stresses may be at the interface of four different materials.

### 3.3.3 Piezoelectric

As seen in this section, interface conditions are met via spatial averaging of the material properties. As such, there exist piezoelectric interface conditions which are satisfied via proper placement of the piezoelectric coupling coefficients. These will differ slightly based on which coupling coefficients are used as shown in the following sub-sections.

The interface condition between a piezoelectric and a dielectric is derived herein. The air interface is a special case of this derivation. Recall that the tangential D is not continuous at an interface, and tangential E is continuous. Refer to region (1) as the space containing the piezoelectric material and region (2) as the space containing the dielectric. The z-component of Ampere's law is:

$$\frac{2}{\Delta t}\left[D_z^{n+\frac{1}{2}}\left(i,j,k+\frac{1}{2}\right)-D_z^{n}\left(i,j,k+\frac{1}{2}\right)\right]$$

$$=\frac{1}{\Delta x}\left[H_y^{n+\frac{1}{2}}\left(i+\frac{1}{2},j,k+\frac{1}{2}\right)-H_y^{n+\frac{1}{2}}\left(i-\frac{1}{2},j,k+\frac{1}{2}\right)\right] \tag{3.16}$$

$$-\frac{1}{\Delta y}\left[H_x^{n}\left(i,j+\frac{1}{2},k+\frac{1}{2}\right)-H_x^{n}\left(i,j-\frac{1}{2},k+\frac{1}{2}\right)\right]$$

Say that spatial location $\left(i,j,k+\frac{1}{2}\right)$ is at an xz-planar interface. Split the $D_z$ terms into $D_{z1}$ and $D_{z2}$, which are located just to the interior and exterior of the piezoelectric at the interface respectively, therefore:

$$D_z^{n+\frac{1}{2}}\left(i,j,k+\frac{1}{2}\right)=\frac{D_{z(1)}^{n+\frac{1}{2}}\left(i,j,k+\frac{1}{2}\right)+D_{z(2)}^{n+\frac{1}{2}}\left(i,j,k+\frac{1}{2}\right)}{2} \tag{3.17}$$

Substituting (3.17) into Ampere's law (3.16) yields:

$$\frac{2}{\Delta t}\left[\frac{D_{z(1)}^{n+\frac{1}{2}}\left(i,j,k+\frac{1}{2}\right)+D_{z(2)}^{n+\frac{1}{2}}\left(i,j,k+\frac{1}{2}\right)}{2}-\frac{D_{z(1)}^{n}\left(i,j,k+\frac{1}{2}\right)+D_{z(2)}^{n}\left(i,j,k+\frac{1}{2}\right)}{2}\right]$$

$$=\frac{1}{\Delta x}\left[H_y^{n+\frac{1}{2}}\left(i+\frac{1}{2},j,k+\frac{1}{2}\right)-H_y^{n+\frac{1}{2}}\left(i-\frac{1}{2},j,k+\frac{1}{2}\right)\right] \tag{3.18}$$

$$-\frac{1}{\Delta y}\left[H_x^{n}\left(i,j+\frac{1}{2},k+\frac{1}{2}\right)-H_x^{n}\left(i,j-\frac{1}{2},k+\frac{1}{2}\right)\right]$$

The constitutive relation for the dielectric, assuming diagonal permittivity, is the following:

$$D_{z(2)}^{n+\frac{1}{2}}\left(i,j,k+\frac{1}{2}\right)=\epsilon_{zz}^{(2)}E_{z(2)}^{n+\frac{1}{2}}\left(i,j,k+\frac{1}{2}\right) \tag{3.19a}$$

Where $\epsilon_{zz}^{(2)}$ is the permittivity of the adjacent dielectric (for air $\epsilon_{zz}^{(2)}=\epsilon_0$). Since distinct (but equivalent) piezoelectric constitutive relations may be used, the following subsections discuss using the d-form and the e-form [194] separately, both assuming a z-poled class 6mm tetragonal crystal. Note that, since discontinuity leads to $D_z$ being split, the d and e-form are the only constitutive relations that should be used for determining interface conditions as these contain the flux on the left-hand side of the equation (i.e., using h and g-forms would not be appropriate).

#### 3.3.3.1 d-form Piezoelectric Interface Condition

From the d-form of the piezoelectric constitutive relations, the interface adjacent electric flux within the piezoelectric is:

$$D_{z(1)}^{n+\frac{1}{2}}\left(i,j,k+\frac{1}{2}\right)=d_{31}^{(1)}\left[T_{xx(1)}^{n+\frac{1}{2}}\left(i,j,k+\frac{1}{2}\right)+T_{yy(1)}^{n+\frac{1}{2}}\left(i,j,k+\frac{1}{2}\right)\right]+d_{33}^{(1)}T_{zz(1)}^{n+\frac{1}{2}}\left(i,j,k+\frac{1}{2}\right)+\epsilon_{zz}^{T(1)}E_{z(1)}^{n+\frac{1}{2}}\left(i,j,k+\frac{1}{2}\right) \tag{3.19b}$$

Here, $d_{33}^{(1)}$ and $d_{31}^{(1)}$ are the piezoelectric coupling coefficients, and $\epsilon_{zz}^{T(1)}$ is the constant stress permittivity of the piezoelectric material. Use $E_{z(1)}$=$E_{z(2)}$=$E_z$, from tangential E continuity, and substitute the constitutive relations (3.19a-b) into Ampere's law (3.18):

$$\begin{aligned}&\frac{2}{\Delta t}\left[\frac{d_{31}^{(1)}}{2}\left[T_{xx(1)}^{n+\frac{1}{2}}\left(i,j,k+\frac{1}{2}\right)+T_{yy(1)}^{n+\frac{1}{2}}\left(i,j,k+\frac{1}{2}\right)\right]+\frac{d_{33}^{(1)}}{2}T_{zz(1)}^{n+\frac{1}{2}}\left(i,j,k+\frac{1}{2}\right)\right.\\&\quad+\frac{\left(\epsilon_{zz}^{T(1)}+\epsilon_{zz}^{(2)}\right)}{2}E_z^{n+\frac{1}{2}}\left(i,j,k+\frac{1}{2}\right)\\&\quad-\frac{d_{31}^{(1)}}{2}\left[T_{xx(1)}^{n}\left(i,j,k+\frac{1}{2}\right)+T_{yy(1)}^{n}\left(i,j,k+\frac{1}{2}\right)\right]-\frac{d_{33}^{(1)}}{2}T_{zz(1)}^{n}\left(i,j,k+\frac{1}{2}\right)\\&\quad\left.-\frac{\left(\epsilon_{zz}^{T(1)}+\epsilon_{zz}^{(2)}\right)}{2}E_z^{n}\left(i,j,k+\frac{1}{2}\right)\right]\\&=\frac{1}{\Delta x}\left[H_y^{n+\frac{1}{2}}\left(i+\frac{1}{2},j,k+\frac{1}{2}\right)-H_y^{n+\frac{1}{2}}\left(i-\frac{1}{2},j,k+\frac{1}{2}\right)\right]\\&-\frac{1}{\Delta y}\left[H_x^{n}\left(i,j+\frac{1}{2},k+\frac{1}{2}\right)-H_x^{n}\left(i,j-\frac{1}{2},k+\frac{1}{2}\right)\right]\end{aligned} \tag{3.20}$$

Rearrange:

$$
\begin{aligned}
&\frac{\left(\epsilon_{zz}^{T(1)}+\epsilon_{zz}^{(2)}\right)}{2}E_z^{n+\frac{1}{2}}\left(i,j,k+\frac{1}{2}\right)\\
&\quad=\frac{\left(\epsilon_{zz}^{T(1)}+\epsilon_{zz}^{(2)}\right)}{2}E_z^{n}\left(i,j,k+\frac{1}{2}\right)\\
&\quad+\frac{\Delta t}{2\Delta x}\left[H_y^{n+\frac{1}{2}}\left(i+\frac{1}{2},j,k+\frac{1}{2}\right)-H_y^{n+\frac{1}{2}}\left(i-\frac{1}{2},j,k+\frac{1}{2}\right)\right]\\
&\quad-\frac{\Delta t}{2\Delta y}\left[H_x^{n}\left(i,j+\frac{1}{2},k+\frac{1}{2}\right)-H_x^{n}\left(i,j-\frac{1}{2},k+\frac{1}{2}\right)\right]\\
&\quad-\frac{d_{33}^{(1)}}{2}\left(T_{zz(1)}^{n+\frac{1}{2}}\left(i,j,k+\frac{1}{2}\right)-T_{zz(1)}^{n}\left(i,j,k+\frac{1}{2}\right)\right)\\
&\quad-\frac{d_{31}^{(1)}}{2}\left(T_{xx(1)}^{n+\frac{1}{2}}\left(i,j,k+\frac{1}{2}\right)-T_{xx(1)}^{n}\left(i,j,k+\frac{1}{2}\right)+T_{yy(1)}^{n+\frac{1}{2}}\left(i,j,k+\frac{1}{2}\right)\right.\\
&\quad\left.-T_{yy(1)}^{n}\left(i,j,k+\frac{1}{2}\right)\right)
\end{aligned}
\tag{3.21}
$$

As expected, the permittivity is averaged while the piezoelectric $dT$ products are multiplied by a factor of ½ with respect to the interior value. The ½ factor may be achieved by averaging the $d$ terms, just as the permittivity, while utilizing the interior normal stresses at the interface.

Mechanically, for the shear free case, no piezoelectric interface conditions need be considered as only the velocity terms exists on interfaces/boundaries and the velocities are updated using the elastodynamic equation, which makes no mention of coupling coefficients.

More generally, at a corner interface, a factor of ¼ will appear on the piezoelectric terms as the $D_z$ term is split into $D_{z(1)}$, $D_{z(2)}$, $D_{z(3)}$, and $D_{z(4)}$ (where material (1) is the piezoelectric), yielding:

$$\frac{\left(\epsilon_{zz}^{T(1)}+\epsilon_{zz}^{(2)}+\epsilon_{zz}^{(3)}+\epsilon_{zz}^{(4)}\right)}{4}E_z^{n+\frac{1}{2}}\left(i,j,k+\frac{1}{2}\right)$$

$$=\frac{\left(\epsilon_{zz}^{T(1)}+\epsilon_{zz}^{(2)}+\epsilon_{zz}^{(3)}+\epsilon_{zz}^{(4)}\right)}{4}E_z^{n}\left(i,j,k+\frac{1}{2}\right)$$

$$+\frac{\Delta t}{2\Delta x}\left[H_y^{n+\frac{1}{2}}\left(i+\frac{1}{2},j,k+\frac{1}{2}\right)-H_y^{n+\frac{1}{2}}\left(i-\frac{1}{2},j,k+\frac{1}{2}\right)\right]$$

$$-\frac{\Delta t}{2\Delta y}\left[H_x^{n}\left(i,j+\frac{1}{2},k+\frac{1}{2}\right)-H_x^{n}\left(i,j-\frac{1}{2},k+\frac{1}{2}\right)\right] \tag{3.22}$$

$$-\frac{d_{33}^{(1)}}{4}\left(T_{zz(1)}^{n+\frac{1}{2}}\left(i,j,k+\frac{1}{2}\right)-T_{zz(1)}^{n}\left(i,j,k+\frac{1}{2}\right)\right)$$

$$-\frac{d_{31}^{(1)}}{4}\left(T_{xx(1)}^{n+\frac{1}{2}}\left(i,j,k+\frac{1}{2}\right)-T_{xx(1)}^{n}\left(i,j,k+\frac{1}{2}\right)+T_{yy(1)}^{n+\frac{1}{2}}\left(i,j,k+\frac{1}{2}\right)\right.$$

$$\left.-T_{yy(1)}^{n}\left(i,j,k+\frac{1}{2}\right)\right)$$

Therefore, define the permittivity and piezoelectric coupling coefficients as follows:

$$\epsilon_{zz}\left(i,j,k+\frac{1}{2}\right)=\frac{\left(\epsilon_{zz}^{T(1)}+\epsilon_{zz}^{(2)}+\epsilon_{zz}^{(3)}+\epsilon_{zz}^{(4)}\right)}{4}$$

$$=\frac{\left(\epsilon_{zz}^{i+\frac{1}{2},j+\frac{1}{2},k+\frac{1}{2}}+\epsilon_{zz}^{i-\frac{1}{2},j+\frac{1}{2},k+\frac{1}{2}}+\epsilon_{zz}^{i+\frac{1}{2},j-\frac{1}{2},k+\frac{1}{2}}+\epsilon_{zz}^{i-\frac{1}{2},j-\frac{1}{2},k+\frac{1}{2}}\right)}{4} \tag{3.23a}$$

$$d_{33}\left(i,j,k+\frac{1}{2}\right)=\frac{d_{33}^{(1)}}{4}=\frac{\left(d_{33}^{i+\frac{1}{2},j+\frac{1}{2},k+\frac{1}{2}}+d_{33}^{i-\frac{1}{2},j+\frac{1}{2},k+\frac{1}{2}}+d_{33}^{i+\frac{1}{2},j-\frac{1}{2},k+\frac{1}{2}}+d_{33}^{i-\frac{1}{2},j-\frac{1}{2},k+\frac{1}{2}}\right)}{4} \tag{3.23b}$$

$$d_{31}\left(i,j,k+\frac{1}{2}\right)=\frac{d_{31}^{(1)}}{4}=\frac{\left(d_{31}^{i+\frac{1}{2},j+\frac{1}{2},k+\frac{1}{2}}+d_{31}^{i-\frac{1}{2},j+\frac{1}{2},k+\frac{1}{2}}+d_{31}^{i+\frac{1}{2},j-\frac{1}{2},k+\frac{1}{2}}+d_{31}^{i-\frac{1}{2},j-\frac{1}{2},k+\frac{1}{2}}\right)}{4} \tag{3.23c}$$

These definitions can be applied generally, with interface conditions handled via use of the internal stress only.

#### 3.3.3.2 e-form Piezoelectric Interface Condition

From the e-form of the piezoelectric constitutive relations, the interface adjacent electric flux within the piezoelectric is:

$$D_{z(1)}^{n+\frac{1}{2}}\left(i,j,k+\frac{1}{2}\right)=e_{31}^{(1)}\left[S_{xx(1)}^{n+\frac{1}{2}}\left(i,j,k+\frac{1}{2}\right)+S_{yy(1)}^{n+\frac{1}{2}}\left(i,j,k+\frac{1}{2}\right)\right]+e_{33}^{(1)}S_{zz(1)}^{n+\frac{1}{2}}\left(i,j,k+\frac{1}{2}\right)+\epsilon_{zz}^{S(1)}E_{z(1)}^{n+\frac{1}{2}}\left(i,j,k+\frac{1}{2}\right) \tag{3.19c}$$

Here, $e_{33}^{(1)}$ and $e_{31}^{(1)}$ are the piezoelectric coupling coefficients, and $\epsilon_{zz}^{S(1)}$ is the constant strain permittivity of the piezoelectric material. The rest of the derivation follows the same vein as that of the d-form in the previous section, yielding the following expression for the electric field in the case of a corner interface:

$$\begin{aligned}&\frac{\left(\epsilon_{zz}^{S(1)}+\epsilon_{zz}^{(2)}+\epsilon_{zz}^{(3)}+\epsilon_{zz}^{(4)}\right)}{4}E_z^{n+\frac{1}{2}}\left(i,j,k+\frac{1}{2}\right)\\&=\frac{\left(\epsilon_{zz}^{S(1)}+\epsilon_{zz}^{(2)}+\epsilon_{zz}^{(3)}+\epsilon_{zz}^{(4)}\right)}{4}E_z^{n}\left(i,j,k+\frac{1}{2}\right)\\&+\frac{\Delta t}{2\Delta x}\left[H_y^{n+\frac{1}{2}}\left(i+\frac{1}{2},j,k+\frac{1}{2}\right)-H_y^{n+\frac{1}{2}}\left(i-\frac{1}{2},j,k+\frac{1}{2}\right)\right]\\&-\frac{\Delta t}{2\Delta y}\left[H_x^{n}\left(i,j+\frac{1}{2},k+\frac{1}{2}\right)-H_x^{n}\left(i,j-\frac{1}{2},k+\frac{1}{2}\right)\right]\\&-\frac{e_{33}^{(1)}}{4}\left(S_{zz(1)}^{n+\frac{1}{2}}\left(i,j,k+\frac{1}{2}\right)-S_{zz(1)}^{n}\left(i,j,k+\frac{1}{2}\right)\right)\\&-\frac{e_{31}^{(1)}}{4}\left(S_{xx(1)}^{n+\frac{1}{2}}\left(i,j,k+\frac{1}{2}\right)-S_{xx(1)}^{n}\left(i,j,k+\frac{1}{2}\right)+S_{yy(1)}^{n+\frac{1}{2}}\left(i,j,k+\frac{1}{2}\right)\right.\\&\left.-S_{yy(1)}^{n}\left(i,j,k+\frac{1}{2}\right)\right)\end{aligned} \tag{3.24}$$

Therefore, define the permittivity and piezoelectric coupling coefficients as follows:

$$\begin{aligned}\epsilon_{zz}\left(i,j,k+\frac{1}{2}\right)&=\frac{\left(\epsilon_{zz}^{S(1)}+\epsilon_{zz}^{(2)}+\epsilon_{zz}^{(3)}+\epsilon_{zz}^{(4)}\right)}{4}\\&=\frac{\left(\epsilon_{zz}^{i+\frac{1}{2},j+\frac{1}{2},k+\frac{1}{2}}+\epsilon_{zz}^{i-\frac{1}{2},j+\frac{1}{2},k+\frac{1}{2}}+\epsilon_{zz}^{i+\frac{1}{2},j-\frac{1}{2},k+\frac{1}{2}}+\epsilon_{zz}^{i-\frac{1}{2},j-\frac{1}{2},k+\frac{1}{2}}\right)}{4}\end{aligned} \tag{3.25a}$$

$$e_{33}\left(i,j,k+\frac{1}{2}\right)=\frac{e_{33}^{(1)}}{4}=\frac{\left(e_{33}^{i+\frac{1}{2},j+\frac{1}{2},k+\frac{1}{2}}+e_{33}^{i-\frac{1}{2},j+\frac{1}{2},k+\frac{1}{2}}+e_{33}^{i+\frac{1}{2},j-\frac{1}{2},k+\frac{1}{2}}+e_{33}^{i-\frac{1}{2},j-\frac{1}{2},k+\frac{1}{2}}\right)}{4} \tag{3.25b}$$

$$e_{31}\left(i,j,k+\frac{1}{2}\right)=\frac{e_{31}^{(1)}}{4}=\frac{\left(e_{31}^{i+\frac{1}{2},j+\frac{1}{2},k+\frac{1}{2}}+e_{31}^{i-\frac{1}{2},j+\frac{1}{2},k+\frac{1}{2}}+e_{31}^{i+\frac{1}{2},j-\frac{1}{2},k+\frac{1}{2}}+e_{31}^{i-\frac{1}{2},j-\frac{1}{2},k+\frac{1}{2}}\right)}{4} \tag{3.25c}$$

These definitions can be applied generally, with interface conditions handled via use of the internal stress only.

Note from this and the previous section that the electric flux is tangential at the electric interface and therefore not continuous. This leads to averaging of the $d$ and $e$ piezoelectric coupling tensors along with the permittivity tensor. The $g$ and $h$ piezoelectric coupling tensors [194][198] must not be averaged then during FDTD simulations as it is accurate to utilize average $d$, $e$, $\epsilon^T$, and $\epsilon^S$. If the g or h-form are used, then these should be averaged as follows:

$$g_{33}\left(i,j,k+\frac{1}{2}\right)=\frac{\left(d_{33}^{i+\frac{1}{2},j+\frac{1}{2},k+\frac{1}{2}}+d_{33}^{i-\frac{1}{2},j+\frac{1}{2},k+\frac{1}{2}}+d_{33}^{i+\frac{1}{2},j-\frac{1}{2},k+\frac{1}{2}}+d_{33}^{i-\frac{1}{2},j-\frac{1}{2},k+\frac{1}{2}}\right)}{\left(\epsilon_{zz}^{i+\frac{1}{2},j+\frac{1}{2},k+\frac{1}{2}}+\epsilon_{zz}^{i-\frac{1}{2},j+\frac{1}{2},k+\frac{1}{2}}+\epsilon_{zz}^{i+\frac{1}{2},j-\frac{1}{2},k+\frac{1}{2}}+\epsilon_{zz}^{i-\frac{1}{2},j-\frac{1}{2},k+\frac{1}{2}}\right)} \tag{3.26a}$$

$$h_{33}\left(i,j,k+\frac{1}{2}\right)=\frac{\left(e_{31}^{i+\frac{1}{2},j+\frac{1}{2},k+\frac{1}{2}}+e_{31}^{i-\frac{1}{2},j+\frac{1}{2},k+\frac{1}{2}}+e_{31}^{i+\frac{1}{2},j-\frac{1}{2},k+\frac{1}{2}}+e_{31}^{i-\frac{1}{2},j-\frac{1}{2},k+\frac{1}{2}}\right)}{\left(\epsilon_{zz}^{i+\frac{1}{2},j+\frac{1}{2},k+\frac{1}{2}}+\epsilon_{zz}^{i-\frac{1}{2},j+\frac{1}{2},k+\frac{1}{2}}+\epsilon_{zz}^{i+\frac{1}{2},j-\frac{1}{2},k+\frac{1}{2}}+\epsilon_{zz}^{i-\frac{1}{2},j-\frac{1}{2},k+\frac{1}{2}}\right)} \tag{3.26b}$$

All the piezoelectric interface conditions herein have been determined for collocation with $D_z$ or $E_z$. Other similar expressions may be written for the x and y-directions also yielding spatially averaged material properties.

### 3.4 Boundary Conditions

Boundaries are defined as nodes outside of which fields are no longer updated. This means that the mechanical boundaries will generally not coincide with the EM boundaries, as the outer surface of any solid structure acts as the mechanical boundary, whereas the EM portion of the code may encompass surrounding air beyond the structure. It is therefore fruitful to treat mechanical and EM boundaries as separate entities.

### 3.4.1 Electromagnetic Boundary Conditions

In the context of the EM physics, boundaries are planes where the simulation space is truncated, therefore requiring special treatment unlike interfaces. This special treatment is known as the boundary condition and the subsequent sections cover some such relations as they pertain to electrodynamics.

#### 3.4.1.1 Perfect Electric Conductor (PEC)

A perfect electric conducting surface is a theoretical boundary that has infinite free charges to dissipate electric fields. As such any incident tangential electric fields are immediately used to move these free charges and therefore no such fields may exist on these surfaces [178][179]. Since magnetic fields are created by swirling Faraday contours, this implies that the normal magnetic field is also zero at the PEC boundary:

$$E_{tangential} = 0, \qquad E_{normal} = max/min, \qquad H_{normal} = 0, \qquad @\ PEC\ boundary \tag{3.27}$$

Of course, no such surfaces exist but many highly conductive materials may be accurately modeled using this approximation and, within this study, the ground electrode is modeled as a PEC. Since EM waves are transverse in nature, the zeroing out of the tangential electric fields has the effect of perfectly reflecting all incident waves. As such, PECs are often used to model infinite arrays of radiators using image theory. Consider for example an infinite electric line source as shown in Figure 3-14:

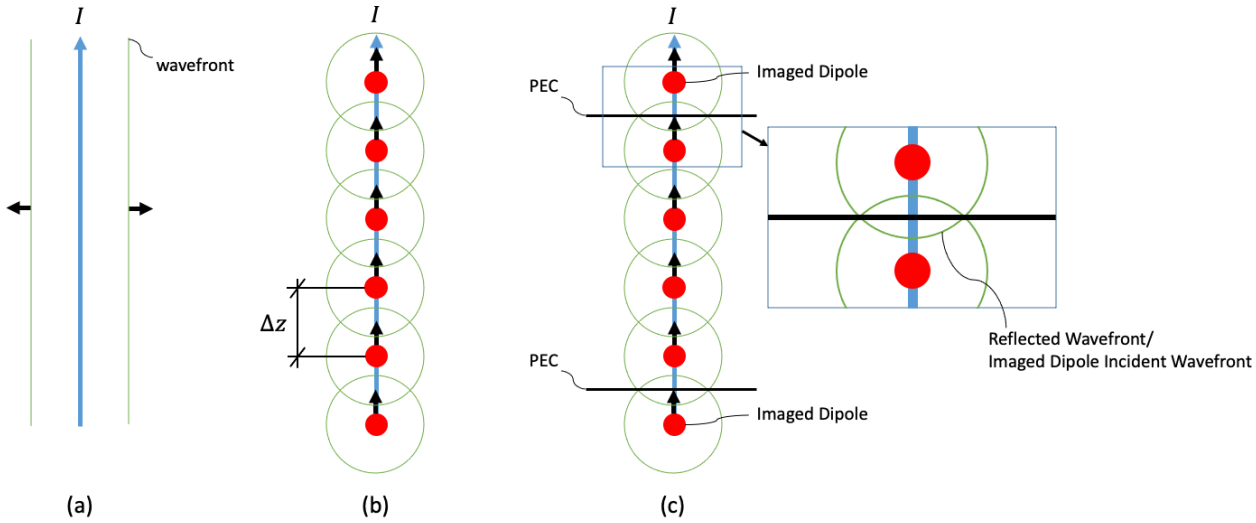


Figure 3-14: Infinite electric line source.

This continuous line source produces a cylindrical wavefront that propagates in the radial direction as shown in Figure 3-14a. When modeled in a discretized simulation space however, the continuous line source must be split up into dipole point current sources that produce a spherical wavefront as shown in Figure 3-14b. This does not perfectly recreate the cylindrical wavefront, especially near the source, but as the discretization size $\Delta z$ is made smaller and smaller the accuracy increases at the cost of an increased number of nodes and therefore simulation time. This is a constant trade-off in numerical analysis that must be made and requires some engineering intuition. Of course, the simulation space cannot contain infinitely many nodes in the vertical direction to recreate the infinitely long line source. At some location the simulation space needs to be truncated to keep the number of nodes finite. In this case a PEC is appropriate due to its ability to perfectly reflect incident EM waves by zeroing out the tangential electric fields. This becomes clear when looking at Figure 3-14c where it is shown that the PEC has the effect of creating an imaged dipole just outside the simulation space. The reflection of the dipole just within the simulation space can therefore be thought of as the

incident wavefront from this imaged dipole as shown in the zoomed in image in Figure 3-14c. The infinite electric line source is simulated in section 4.2.2.

#### 3.4.1.2 Perfect Magnetic Conductor

A perfect magnetic conducting surface is a theoretical boundary that has infinite free magnetic charges to dissipate magnetic fields. As such any incident tangential magnetic fields are immediately used to move these free magnetic charges and therefore no such fields may exist on these surfaces [178][179]. Since electric fields are created by swirling Ampere contours, this implies that the normal electric field is also zero at the PMC boundary:

$$H_{tangential} = 0, \qquad H_{normal} = max/min, \qquad E_{normal} = 0, \qquad @\ PMC\ boundary \tag{3.28}$$

Of course, no such surfaces exist as free magnetic charge is a theoretical construct but often systems may be modeled by theoretical equivalents which may include fictional magnetic currents. Aperture antennas for example may be modeled using electric and magnetic current sources which act over the aperture [25][26]. As such, PMCs may be used to model periodic structures just like PECs when appropriate.

#### 3.4.1.3 Absorbing Boundary Conditions

When performing simulations, it is often necessary to model an infinite region where a wave propagates away from the device of interest never to return. Cleary in terms of computer memory, this infinite simulation space is not realizable and as such truncation of the simulation space is necessary. The boundaries of this practical simulation space will ideally exhibit perfect transmission and no reflection of any incident waves will occur and these are known as absorbing boundary conditions. These date back to 1975 where Taflove referred to them as “soft lattice truncation conditions” [196] and later as “radiating boundary conditions” by Holland in 1977 [197]. There are many ways of attempting to realize zero reflection at a boundary, and herein so called “one-way wave equations” are utilized which only allow the wave to propagate

in one-way, namely away from the simulation space. To derive these one-way expressions, the 3D wave equation is written as [178]:

$$\frac{\partial^2 U}{\partial x^2}+\frac{\partial^2 U}{\partial y^2}+\frac{\partial^2 U}{\partial z^2}-\frac{1}{c^2}\frac{\partial^2 U}{\partial t^2}\equiv GU=G^{+}G^{-}U \tag{3.29a}$$

Where, $G^{+}$ and $G^{-}$ denote the one-way wave operators yielding the following analytical boundary conditions at x=0,h, which apply for any angle of incidence:

$$G^{-1}U(0,y,z)=0, \qquad G^{+}U(h,y,z)=0 \tag{3.29b/c}$$

The theory for equations (3.17a-c) was first derived by Engquist and Majda in 1977 for Cartesian FDTD grids [198], and was later applied to the electromagnetic field equations by Mur in 1981 [199]. The largest setback of this one-way wave approach is that equations (3.29b/c) are pseudodifferential operators which disallows direct numerical implementation. (3.29b/c) Therefore these must be approximated by Taylor series first and these approximate terms only exhibit perfect absorption at broadside (normal wave incidence). Mur derived both 1st (Mur1) and 2nd (Mur2) order finite difference versions of these boundary conditions [199] and Trefethen modified the expressions such that perfect absorption can be achieved at oblique incidences rather than broadside [200]. The Mur1 ABCs are often utilized in ADI-FDTD due to the light computational load w.r.t the 2nd order version. Yang applied the Mur1 conditions to the ADI-FDTD formulation in 2005 [201]. The 1st order accurate absorbing boundary condition for an EM wave traveling in free space is shown below and applies to the 1D, 2D, and 3D cases [178]:

$$G^{\mp}U\cong\frac{\partial U}{\partial x}\mp\frac{1}{c}\frac{\partial U}{\partial t}=0 \tag{3.30}$$

This approximation holds when the spatial variation tangential to the boundary is small, in other words, when the wave impinges upon the boundary at or near normal incidence. The minus corresponds to the start of the simulation space (left/back/bottom) and the plus for the end of the simulation space (right/front/top). $U$ is a scalar field that may be any electric or magnetic field that is evaluated at the boundary and is tangential to the boundary. If the

simulation space is aligned with the electrical interface, then the $U$ field will be the tangential electrical fields, as is the case herein. Since the normal H-field component at the boundary does not require external electric fields to update, Faraday's law may still be used. E-field update, however, will require H-field components outside of the simulation space, and will therefore instead use the following one-way wave boundary conditions:

$$\begin{aligned}
x=0:&\quad \frac{\partial E_y}{\partial x}-\frac{1}{c}\frac{\partial E_y}{\partial t}=0,\quad \frac{\partial E_z}{\partial x}-\frac{1}{c}\frac{\partial E_z}{\partial t}=0 \qquad x=L_x:\quad \frac{\partial E_y}{\partial x}+\frac{1}{c}\frac{\partial E_y}{\partial t}=0,\quad \frac{\partial E_z}{\partial x}+\frac{1}{c}\frac{\partial E_z}{\partial t}=0\\
y=0:&\quad \frac{\partial E_x}{\partial y}-\frac{1}{c}\frac{\partial E_x}{\partial t}=0,\quad \frac{\partial E_z}{\partial y}-\frac{1}{c}\frac{\partial E_z}{\partial t}=0 \qquad y=L_y:\quad \frac{\partial E_x}{\partial y}+\frac{1}{c}\frac{\partial E_x}{\partial t}=0,\quad \frac{\partial E_z}{\partial y}+\frac{1}{c}\frac{\partial E_z}{\partial t}=0\\
z=0:&\quad \frac{\partial E_x}{\partial z}-\frac{1}{c}\frac{\partial E_x}{\partial t}=0,\quad \frac{\partial E_y}{\partial z}-\frac{1}{c}\frac{\partial E_y}{\partial t}=0 \qquad z=L_z:\quad \frac{\partial E_x}{\partial z}+\frac{1}{c}\frac{\partial E_x}{\partial t}=0,\quad \frac{\partial E_y}{\partial z}+\frac{1}{c}\frac{\partial E_y}{\partial t}=0
\end{aligned}$$

(3.31a-f)

Using central differences, the following is derived for the $z = L_z = N_z\Delta z$ boundary (3.31f) in standard FDTD:

$$\frac{1}{2\Delta z}\left[E_x^{n+1}\left(i+\frac{1}{2},j,N_z\right)+E_x^{n}\left(i+\frac{1}{2},j,N_z\right)-E_x^{n+1}\left(i+\frac{1}{2},j,N_z-1\right)-E_x^{n}\left(i+\frac{1}{2},j,N_z-1\right)\right]$$
$$+\frac{1}{2c\Delta t}\left[E_x^{n+1}\left(i+\frac{1}{2},j,N_z-1\right)+E_x^{n+1}\left(i+\frac{1}{2},j,N_z\right)-E_x^{n}\left(i+\frac{1}{2},j,N_z-1\right)-E_x^{n}\left(i+\frac{1}{2},j,N_z\right)\right]=0$$

(3.32a)

$$\frac{1}{2\Delta z}\left[E_y^{n+1}\left(i,j+\frac{1}{2},N_z\right)+E_y^{n}\left(i,j+\frac{1}{2},N_z\right)-E_y^{n+1}\left(i,j+\frac{1}{2},N_z-1\right)-E_y^{n}\left(i,j+\frac{1}{2},N_z-1\right)\right]$$
$$+\frac{1}{2c\Delta t}\left[E_y^{n+1}\left(i,j+\frac{1}{2},N_z-1\right)+E_y^{n+1}\left(i,j+\frac{1}{2},N_z\right)-E_y^{n}\left(i,j+\frac{1}{2},N_z-1\right)-E_y^{n}\left(i,j+\frac{1}{2},N_z\right)\right]=0$$

(3.32b)

Solving for the fields at the boundary and the future time step yields:

$$E_x^{n+1}\left(i+\frac{1}{2},j,N_z\right)=E_x^{n}\left(i+\frac{1}{2},j,N_z-1\right)+\frac{c\Delta t-\Delta z}{c\Delta t+\Delta z}\left[E_x^{n+1}\left(i+\frac{1}{2},j,N_z-1\right)-E_x^{n}\left(i+\frac{1}{2},j,N_z\right)\right] \qquad (3.33a)$$

$$E_y^{n+1}\left(i,j+\frac{1}{2},N_z\right)=E_y^{n}\left(i,j+\frac{1}{2},N_z-1\right)+\frac{c\Delta t-\Delta z}{c\Delta t+\Delta z}\left[E_y^{n+1}\left(i,j+\frac{1}{2},N_z-1\right)-E_y^{n}\left(i,j+\frac{1}{2},N_z\right)\right] \qquad (3.33b)$$

In the ADI-FDTD formulation these equations will be slightly modified due to the presence of the 2 sub-iterations yielding the following for the 1st sub-iteration if the same methodology is followed:

$$E_x^{n+\frac{1}{2}}\left(i+\frac{1}{2},j,N_z\right)=E_x^n\left(i+\frac{1}{2},j,N_z-1\right)+\frac{c\Delta t-2\Delta z}{c\Delta t+2\Delta z}\left[E_x^{n+\frac{1}{2}}\left(i+\frac{1}{2},j,N_z-1\right)-E_x^n\left(i+\frac{1}{2},j,N_z\right)\right] \quad (3.34a)$$

$$E_y^{n+\frac{1}{2}}\left(i,j+\frac{1}{2},N_z\right)=E_y^n\left(i,j+\frac{1}{2},N_z-1\right)+\frac{c\Delta t-2\Delta z}{c\Delta t+2\Delta z}\left[E_y^{n+\frac{1}{2}}\left(i,j+\frac{1}{2},N_z-1\right)-E_y^n\left(i,j+\frac{1}{2},N_z\right)\right] \quad (3.34b)$$

And for the 2nd sub-iteration the equations are simply evolved half a time step:

$$E_x^{n+1}\left(i+\frac{1}{2},j,N_z\right)=E_x^{n+\frac{1}{2}}\left(i+\frac{1}{2},j,N_z-1\right)+\frac{c\Delta t-2\Delta z}{c\Delta t+2\Delta z}\left[E_x^{n+1}\left(i+\frac{1}{2},j,N_z-1\right)-E_x^{n+\frac{1}{2}}\left(i+\frac{1}{2},j,N_z\right)\right] \quad (3.34c)$$

$$E_y^{n+1}\left(i,j+\frac{1}{2},N_z\right)=E_y^{n+\frac{1}{2}}\left(i,j+\frac{1}{2},N_z-1\right)+\frac{c\Delta t-2\Delta z}{c\Delta t+2\Delta z}\left[E_y^{n+1}\left(i,j+\frac{1}{2},N_z-1\right)-E_y^{n+\frac{1}{2}}\left(i,j+\frac{1}{2},N_z\right)\right] \quad (3.34d)$$

The 24 ADI-FDTD equations for the Mur1 absorbing boundary conditions are tabulated below:

| | | |
|---|---|---|
| $x=0$ | 1st | $E_y^{n+\frac{1}{2}}\left(0,j+\frac{1}{2},k\right)=E_y^n\left(1,j+\frac{1}{2},k\right)+\frac{c\Delta t-2\Delta x}{c\Delta t+2\Delta x}\left[E_y^{n+\frac{1}{2}}\left(1,j+\frac{1}{2},k\right)-E_y^n\left(0,j+\frac{1}{2},k\right)\right]$<br>$E_z^{n+\frac{1}{2}}\left(0,j,k+\frac{1}{2}\right)=E_z^n\left(1,j,k+\frac{1}{2}\right)+\frac{c\Delta t-2\Delta x}{c\Delta t+2\Delta x}\left[E_z^{n+\frac{1}{2}}\left(1,j,k+\frac{1}{2}\right)-E_z^n\left(0,j,k+\frac{1}{2}\right)\right]$ |
| | 2nd | $E_y^{n+1}\left(0,j+\frac{1}{2},k\right)=E_y^{n+\frac{1}{2}}\left(1,j+\frac{1}{2},k\right)+\frac{c\Delta t-2\Delta x}{c\Delta t+2\Delta x}\left[E_y^{n+1}\left(1,j+\frac{1}{2},k\right)-E_y^{n+\frac{1}{2}}\left(0,j+\frac{1}{2},k\right)\right]$<br>$E_z^{n+1}\left(0,j,k+\frac{1}{2}\right)=E_z^{n+\frac{1}{2}}\left(1,j,k+\frac{1}{2}\right)+\frac{c\Delta t-2\Delta x}{c\Delta t+2\Delta x}\left[E_z^{n+1}\left(1,j,k+\frac{1}{2}\right)-E_z^{n+\frac{1}{2}}\left(0,j,k+\frac{1}{2}\right)\right]$ |
| $x=L_x$ | 1st | $E_y^{n+\frac{1}{2}}\left(N_x,j+\frac{1}{2},k\right)=E_y^n\left(N_x-1,j+\frac{1}{2},k\right)+\frac{c\Delta t-2\Delta x}{c\Delta t+2\Delta x}\left[E_y^{n+\frac{1}{2}}\left(N_x-1,j+\frac{1}{2},k\right)-E_y^n\left(N_x,j+\frac{1}{2},k\right)\right]$<br>$E_z^{n+\frac{1}{2}}\left(N_x,j,k+\frac{1}{2}\right)=E_z^n\left(N_x-1,j,k+\frac{1}{2}\right)+\frac{c\Delta t-2\Delta x}{c\Delta t+2\Delta x}\left[E_z^{n+\frac{1}{2}}\left(N_x-1,j,k+\frac{1}{2}\right)-E_z^n\left(N_x,j,k+\frac{1}{2}\right)\right]$ |
| | 2nd | $E_y^{n+1}\left(N_x,j+\frac{1}{2},k\right)=E_y^{n+\frac{1}{2}}\left(N_x-1,j+\frac{1}{2},k\right)+\frac{c\Delta t-2\Delta x}{c\Delta t+2\Delta x}\left[E_y^{n+1}\left(N_x-1,j+\frac{1}{2},k\right)-E_y^{n+\frac{1}{2}}\left(N_x,j+\frac{1}{2},k\right)\right]$<br>$E_z^{n+1}\left(N_x,j,k+\frac{1}{2}\right)=E_z^{n+\frac{1}{2}}\left(N_x-1,j,k+\frac{1}{2}\right)+\frac{c\Delta t-2\Delta x}{c\Delta t+2\Delta x}\left[E_z^{n+1}\left(N_x-1,j,k+\frac{1}{2}\right)-E_z^{n+\frac{1}{2}}\left(N_x,j,k+\frac{1}{2}\right)\right]$ |
| $y=0$ | 1st | $E_x^{n+\frac{1}{2}}\left(i+\frac{1}{2},0,k\right)=E_x^n\left(i+\frac{1}{2},1,k\right)+\frac{c\Delta t-2\Delta y}{c\Delta t+2\Delta y}\left[E_x^{n+\frac{1}{2}}\left(i+\frac{1}{2},1,k\right)-E_x^n\left(i+\frac{1}{2},0,k\right)\right]$<br>$E_z^{n+\frac{1}{2}}\left(i,0,k+\frac{1}{2}\right)=E_z^n\left(i,1,k+\frac{1}{2}\right)+\frac{c\Delta t-2\Delta y}{c\Delta t+2\Delta y}\left[E_z^{n+\frac{1}{2}}\left(i,1,k+\frac{1}{2}\right)-E_z^n\left(i,0,k+\frac{1}{2}\right)\right]$ |
| | 2nd | $E_x^{n+1}\left(i+\frac{1}{2},0,k\right)=E_x^{n+\frac{1}{2}}\left(i+\frac{1}{2},1,k\right)+\frac{c\Delta t-2\Delta y}{c\Delta t+2\Delta y}\left[E_x^{n+1}\left(i+\frac{1}{2},1,k\right)-E_x^{n+\frac{1}{2}}\left(i+\frac{1}{2},0,k\right)\right]$<br>$E_z^{n+1}\left(i,0,k+\frac{1}{2}\right)=E_z^{n+\frac{1}{2}}\left(i,1,k+\frac{1}{2}\right)+\frac{c\Delta t-2\Delta y}{c\Delta t+2\Delta y}\left[E_z^{n+1}\left(i,1,k+\frac{1}{2}\right)-E_z^{n+\frac{1}{2}}\left(i,0,k+\frac{1}{2}\right)\right]$ |
| $y=L_y$ | 1st | $E_x^{n+\frac{1}{2}}\left(i+\frac{1}{2},N_y,k\right)=E_x^n\left(i+\frac{1}{2},N_y-1,k\right)+\frac{c\Delta t-2\Delta y}{c\Delta t+2\Delta y}\left[E_x^{n+\frac{1}{2}}\left(i+\frac{1}{2},N_y-1,k\right)-E_x^n\left(i+\frac{1}{2},N_y,k\right)\right]$<br>$E_z^{n+\frac{1}{2}}\left(i,N_y,k+\frac{1}{2}\right)=E_z^n\left(i,N_y-1,k+\frac{1}{2}\right)+\frac{c\Delta t-2\Delta y}{c\Delta t+2\Delta y}\left[E_z^{n+\frac{1}{2}}\left(i,N_y-1,k+\frac{1}{2}\right)-E_z^n\left(i,N_y,k+\frac{1}{2}\right)\right]$ |

| | | |
|---|---|---|
| | 2nd | $E_x^{n+1}\left(i+\frac{1}{2},N_y,k\right)=E_x^{n+\frac{1}{2}}\left(i+\frac{1}{2},N_y-1,k\right)+\frac{c\Delta t-2\Delta y}{c\Delta t+2\Delta y}\left[E_x^{n+1}\left(i+\frac{1}{2},N_y-1,k\right)-E_x^{n+\frac{1}{2}}\left(i+\frac{1}{2},N_y,k\right)\right]$<br>$E_z^{n+1}\left(i,N_y,k+\frac{1}{2}\right)=E_z^{n+\frac{1}{2}}\left(i,N_y-1,k+\frac{1}{2}\right)+\frac{c\Delta t-2\Delta y}{c\Delta t+2\Delta y}\left[E_z^{n+1}\left(i,N_y-1,k+\frac{1}{2}\right)-E_z^{n+\frac{1}{2}}\left(i,N_y,k+\frac{1}{2}\right)\right]$ |
| $z=0$ | 1st | $E_x^{n+\frac{1}{2}}\left(i+\frac{1}{2},j,0\right)=E_x^{n}\left(i+\frac{1}{2},j,1\right)+\frac{c\Delta t-2\Delta z}{c\Delta t+2\Delta z}\left[E_x^{n+\frac{1}{2}}\left(i+\frac{1}{2},j,1\right)-E_x^{n}\left(i+\frac{1}{2},j,0\right)\right]$<br>$E_y^{n+\frac{1}{2}}\left(i,j+\frac{1}{2},0\right)=E_y^{n}\left(i,j+\frac{1}{2},1\right)+\frac{c\Delta t-2\Delta z}{c\Delta t+2\Delta z}\left[E_y^{n+\frac{1}{2}}\left(i,j+\frac{1}{2},1\right)-E_y^{n}\left(i,j+\frac{1}{2},0\right)\right]$ |
| | 2nd | $E_x^{n+1}\left(i+\frac{1}{2},j,0\right)=E_x^{n+\frac{1}{2}}\left(i+\frac{1}{2},j,1\right)+\frac{c\Delta t-2\Delta z}{c\Delta t+2\Delta z}\left[E_x^{n+1}\left(i+\frac{1}{2},j,1\right)-E_x^{n+\frac{1}{2}}\left(i+\frac{1}{2},j,0\right)\right]$<br>$E_y^{n+1}\left(i,j+\frac{1}{2},0\right)=E_y^{n+\frac{1}{2}}\left(i,j+\frac{1}{2},1\right)+\frac{c\Delta t-2\Delta z}{c\Delta t+2\Delta z}\left[E_y^{n+1}\left(i,j+\frac{1}{2},1\right)-E_y^{n+\frac{1}{2}}\left(i,j+\frac{1}{2},0\right)\right]$ |
| $z=L_z$ | 1st | $E_x^{n+\frac{1}{2}}\left(i+\frac{1}{2},j,N_z\right)=E_x^{n}\left(i+\frac{1}{2},j,N_z-1\right)+\frac{c\Delta t-2\Delta z}{c\Delta t+2\Delta z}\left[E_x^{n+\frac{1}{2}}\left(i+\frac{1}{2},j,N_z-1\right)-E_x^{n}\left(i+\frac{1}{2},j,N_z\right)\right]$<br>$E_y^{n+\frac{1}{2}}\left(i,j+\frac{1}{2},N_z\right)=E_y^{n}\left(i,j+\frac{1}{2},N_z-1\right)+\frac{c\Delta t-2\Delta z}{c\Delta t+2\Delta z}\left[E_y^{n+\frac{1}{2}}\left(i,j+\frac{1}{2},N_z-1\right)-E_y^{n}\left(i,j+\frac{1}{2},N_z\right)\right]$ |
| | 2nd | $E_x^{n+1}\left(i+\frac{1}{2},j,N_z\right)=E_x^{n+\frac{1}{2}}\left(i+\frac{1}{2},j,N_z-1\right)+\frac{c\Delta t-2\Delta z}{c\Delta t+2\Delta z}\left[E_x^{n+1}\left(i+\frac{1}{2},j,N_z-1\right)-E_x^{n+\frac{1}{2}}\left(i+\frac{1}{2},j,N_z\right)\right]$<br>$E_y^{n+1}\left(i,j+\frac{1}{2},N_z\right)=E_y^{n+\frac{1}{2}}\left(i,j+\frac{1}{2},N_z-1\right)+\frac{c\Delta t-2\Delta z}{c\Delta t+2\Delta z}\left[E_y^{n+1}\left(i,j+\frac{1}{2},N_z-1\right)-E_y^{n+\frac{1}{2}}\left(i,j+\frac{1}{2},N_z\right)\right]$ |

Table 3-1: Mur1 absorbing boundary conditions for ADI-FDTD.

Since the fields at the absorbing boundary rely on the future time step fields just next to the boundary, the ABC fields should be evaluated just after the for loops solving for the interior fields.

#### 3.4.1.4 Perfectly Matched Layers (PMLs)

As described in section 3.4.1.3, absorbing boundary conditions based on one-way wave equations can introduce significant error when incoming waves deviate from normal incidence. One method of bypassing this issue is to introduce lossy layers adjacent to the boundary which absorb the incoming waves over a distance. Strategies along this line of thinking were first introduced in 1983 by Holland and Berenger [202][203], though these early attempts still suffered from requiring normal incidence. The true explosive growth of the method commenced when Berenger introduced the perfectly matched layer in 1994 [204]. Within this methodology, the lossy layers are matched to the adjacent simulation space such that incident waves do not

change direction as they transmit into the lossy PML region which is backed by a PEC boundary condition as shown in Figure 3-15:

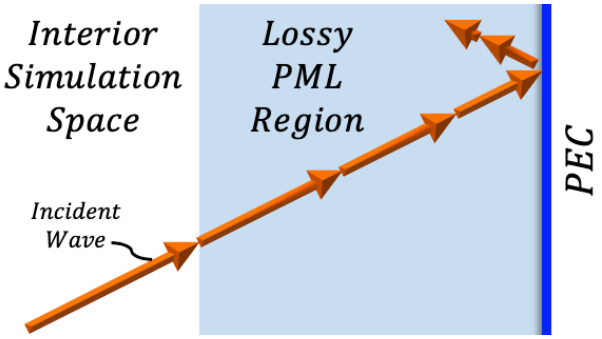


Figure 3-15: Concept of PEC-backed PML regions.

The idea is for all incident waves entering the PML region to die out before bouncing off the PEC and re-entering the simulation space. The loss within the PML region is introduced into the numerical algorithm through the complex frequency shifted (CFS) [178-182] stretched coordinates [205-207] which modify Maxwell's equations, as discussed in section 2.1.3, allowing for the same generalized update scheme to be applied both in the interior and PML regions. The approach highlighted in section 2.1.3 is known as the convolutional PML (CPML) method and, although other strategies exist [208-210], this method, coupled with CFS stretched coordinates, has proven superior for dampening out evanescent (non-propagating) modes [180], although the complementary operator method is another non-PML solution for the evanescent absorption problem [211]. As such, the PML layers may be brought much closer to the radiating elements, which is a must for multiferroic antenna simulations due to the 5 orders of magnitude difference in EM and mechanical wavelengths. To better understand why using CFS stretched coordinates is effective in the near field, recall equation (2.23) for the stretched coordinates below:

$$s_i = \kappa_i + \frac{\sigma_i}{\alpha_i + j\omega\epsilon_0} \tag{2.23}$$

The real components of $s_i$ constitute a stretch of the finite difference cell, and the imaginary parts constitute a wave dampening effect. Rewrite equation (2.23) as follows:

$$s_i = \kappa_i + \frac{\sigma_i / 2\pi\epsilon_0}{\frac{\alpha_i}{2\pi\epsilon_0} + jf} \tag{3.35}$$

Note that at low frequencies ($f \ll \alpha_i / 2\pi\epsilon_0$) the stretched coordinate is essentially real, producing a stretch of $\kappa_i + \sigma_i / \alpha_i$. At high frequencies, equation (3.35) yields both a real stretch and complex dampening effect. These low and high frequency regions are split by the threshold frequency defined below:

$$f_{threshold} = \frac{\alpha_i}{2\pi\epsilon_0} \tag{3.36}$$

In radiation problems, the outgoing waves are generally an amalgamation of multiple frequencies propagating together with low frequency components being evanescent modes, and high frequency components radiating into the far-field, where “low” and “high” are relative to the device cutoff frequency. Therefore, $\alpha_i$ is defined such that the threshold and cutoff frequencies are equivalent so that low frequency evanescent modes experience a real stretch and exponentially decay naturally [180][208], while high frequency radiating modes experience the loss introduced by the PML layers. The CPML methodology was applied to ADI-FDTD in 2001 by Gedney [212], yielding what is termed herein as CPML-ADI-FDTD.

### 3.4.2 Mechanical Boundary Conditions

Recall that the Yee spatial grid is set up such that both of Gauss’s laws are satisfied automatically meaning that the condition that the normal component of the magnetic flux and electric displacement must be continuous at a boundary is automatically satisfied everywhere within the simulation space. For mechanical fields however the spatial grid is not setup to automatically satisfy traction continuity which may be seen by the fact that the normal stresses are evaluated at the center of the cell where no EM fields are evaluated. To show that this is the case, a traction free surface is considered in the next section.

### 3.4.2.1 Traction Free Surfaces

A traction free surface bounds the outer area of a solid structure without external forces applied, and motion is permitted. Within the finite difference grid, this boundary is aligned with the unit cell like the electrical interfaces. Various methods exist to numerically implement these boundary conditions within the FDTD method [192-194]. Due to the small-time step utilized herein (relative to the mechanical stability requirement), a relatively simple method was chosen to avoid undue inaccuracies and was adopted as explained below.

Consider a traction free surface with outward normal in the positive z-direction (top boundary). Evaluation of the non-zero velocity at the surface will involve the adjacent boundary shear stresses which are zero (traction free).

$$T_{yz}^{n+\frac{1}{2}}\left(i+\frac{1}{2},j,k_{top}\right)=0, \qquad T_{xz}^{n+\frac{1}{2}}\left(i,j+\frac{1}{2},k_{top}\right)=0 \tag{3.37}$$

Also involved will be the normal stress just below and above the z-directed velocity term which has the following update equation:

$$v_z^{n+\frac{3}{4}}\left(i+\frac{1}{2},j+\frac{1}{2},k_{top}\right)=v_z^{n+\frac{1}{4}}\left(i+\frac{1}{2},j+\frac{1}{2},k_{top}\right)+\frac{\Delta t\left[T_{zz}^{n+\frac{1}{2}}\left(i+\frac{1}{2},j+\frac{1}{2},k_{top}+\frac{1}{2}\right)-T_{zz}^{n+\frac{1}{2}}\left(i+\frac{1}{2},j+\frac{1}{2},k_{top}-\frac{1}{2}\right)\right]}{\left(\rho_{(1)}^{i+\frac{1}{2},j+\frac{1}{2},k_{top}-\frac{1}{2}}+\rho_{(2)}^{i+\frac{1}{2},j+\frac{1}{2},k_{top}+\frac{1}{2}}\right)\Delta z} \tag{3.38}$$

The densities and stresses located at $(k_{top}+1/2)\Delta z$ are outside the structure and require attention prior to implementation of (3.38). Since the stress is zero at the boundary, the following anti-symmetry equation may be applied to deal with the out-of-bounds stress terms:

$$T_{zz}^{n+\frac{1}{2}}\left(i+\frac{1}{2},j+\frac{1}{2},k_{top}+\frac{1}{2}\right)=-T_{zz}^{n+\frac{1}{2}}\left(i+\frac{1}{2},j+\frac{1}{2},k_{top}-\frac{1}{2}\right) \tag{3.39}$$

Note that (3.26) produces a zero normal stress at the boundary located at $z=k_{top}\Delta z$ when spatial averaging is applied (see section 3.2.3). In (3.39), the stress just outside the boundary is fictious rather than an actual physical stress and therefore this stress should not be applied to

the exterior nodes directly, as the EM portion of the code would then erroneously utilize these stresses. Instead, (3.39) should be handled using if-statements within the code.

The density just outside the material may be defined to be zero in what was referred to as a "vacuum formalism" by Zahradnik et al. in 1993 [213] but was previously proposed by Boore in 1972 [214]. It is tempting to utilize this method due to being easier to implement on more generic structures, but in 1996 Graves [194] warned of numerical issues that this formalism presents so the practice of utilizing the density (and stiffness) of the nearest neighbor node is utilized herein, consistent with authors such as Ugural [215], therefore:

$$\rho_{(2)}^{i+\frac{1}{2},j+\frac{1}{2},k_{top}+\frac{1}{2}} = \rho_{(1)}^{i+\frac{1}{2},j+\frac{1}{2},k_{top}-\frac{1}{2}} \tag{3.40}$$

The velocity update equation at the boundary is now as follows:

$$v_z^{n+\frac{3}{4}}\left(i+\frac{1}{2},j+\frac{1}{2},k_{top}\right) = v_z^{n+\frac{1}{4}}\left(i+\frac{1}{2},j+\frac{1}{2},k_{top}\right) - \frac{\Delta t T_{zz}^{n+\frac{1}{2}}\left(i+\frac{1}{2},j+\frac{1}{2},k_{top}-\frac{1}{2}\right)}{\Delta z \rho_{(1)}^{i+\frac{1}{2},j+\frac{1}{2},k_{top}-\frac{1}{2}}} \tag{3.41a}$$

Thus far, at the boundary, the traction free conditions have been applied either directly (3.37) or through anti-symmetry (3.39) and an expression for the velocity defined at the boundary has been derived (3.41). Continuity of all velocity terms is required, however, so the tangential $v_x$ and $v_y$ seem to also require a boundary condition but note that these are not defined at the boundary. Regardless the traction free surface effects the tangential velocities half a cell to the interior as follows:

$$
\begin{aligned}
&v_x^{n+\frac{3}{4}}\left(i,j+\frac{1}{2},k_{top}-\frac{1}{2}\right)\\
&\quad= v_x^{n+\frac{1}{4}}\left(i,j+\frac{1}{2},k_{top}-\frac{1}{2}\right)\\
&\quad+\frac{\Delta t}{2\rho\left(i,j+\frac{1}{2},k_{top}-\frac{1}{2}\right)\Delta x}\left[T_{xx}^{n+\frac{1}{2}}\left(i+\frac{1}{2},j+\frac{1}{2},k_{top}-\frac{1}{2}\right)-T_{xx}^{n+\frac{1}{2}}\left(i-\frac{1}{2},j+\frac{1}{2},k_{top}-\frac{1}{2}\right)\right]\\
&\quad+\frac{\Delta t}{2\rho\left(i,j+\frac{1}{2},k_{top}-\frac{1}{2}\right)\Delta y}\left[T_{xy}^{n+\frac{1}{2}}\left(i,j+1,k_{top}-\frac{1}{2}\right)-T_{xy}^{n+\frac{1}{2}}\left(i,j,k_{top}-\frac{1}{2}\right)\right]\\
&\quad-\frac{\Delta t}{2\rho\left(i,j+\frac{1}{2},k_{top}-\frac{1}{2}\right)\Delta z}T_{xz}^{n+\frac{1}{2}}\left(i,j+\frac{1}{2},k_{top}-1\right)
\end{aligned}
\tag{3.41b}
$$

$$
\begin{aligned}
&v_y^{n+\frac{3}{4}}\left(i+\frac{1}{2},j,k_{top}-\frac{1}{2}\right)\\
&\quad= v_y^{n+\frac{1}{4}}\left(i+\frac{1}{2},j,k_{top}-\frac{1}{2}\right)\\
&\quad+\frac{\Delta t}{2\rho\left(i+\frac{1}{2},j,k+\frac{1}{2}\right)\Delta x}\left[T_{xy}^{n+\frac{1}{2}}\left(i+1,j,k_{top}-\frac{1}{2}\right)-T_{xy}^{n+\frac{1}{2}}\left(i,j,k_{top}-\frac{1}{2}\right)\right]\\
&\quad+\frac{\Delta t}{2\rho\left(i+\frac{1}{2},j,k+\frac{1}{2}\right)\Delta y}\left[T_{yy}^{n+\frac{1}{2}}\left(i+\frac{1}{2},j+\frac{1}{2},k_{top}-\frac{1}{2}\right)-T_{yy}^{n+\frac{1}{2}}\left(i+\frac{1}{2},j-\frac{1}{2},k_{top}-\frac{1}{2}\right)\right]\\
&\quad-\frac{\Delta t}{2\rho\left(i+\frac{1}{2},j,k+\frac{1}{2}\right)\Delta z}T_{yz}^{n+\frac{1}{2}}\left(i+\frac{1}{2},j,k_{top}-1\right)
\end{aligned}
\tag{3.41c}
$$

Therefore, the tangential velocities adjacent to the boundary will be affected by the boundary from the zeroing out of shear stresses. These conditions may be handled without the use of any if-statements since the shear stresses at the surface are always zero from proper definition of for-loops. The boundary conditions shown here for a horizontal plane may be modified for planes normal to the in-plane direction following the same methodology. For the case where two planes meet (at a corner) the only field shared by both planes is a shear stress which for both planes is zero, so no special if-statements are necessary outside of the ones already used for the velocity components normal to the boundary.

#### 3.4.2.2 Fixed Boundary

For a fixed boundary, all velocity terms are zero while tractions at the boundary are unrestricted. Say a fixed boundary is normal to the z-direction on the bottom of the device (at $z = k_{bot}\Delta z = 0$, then there are two non-zero shear stresses at the boundary which require

velocity components just below the simulation space in order to resolve. The update equations are as follows:

$$
\begin{aligned}
T_{yz}^{n+\frac{1}{2}}\left(i+\frac{1}{2},j,k_{bot}\right) &= T_{yz}^{n}\left(i+\frac{1}{2},j,k_{bot}\right) \\
&+\frac{\Delta t}{2}\frac{1}{4}\Bigg(c_{yzyz}^{i+\frac{1}{2},j+\frac{1}{2},k_{bot}+\frac{1}{2}}+c_{yzyz}^{i-\frac{1}{2},j+\frac{1}{2},k_{bot}+\frac{1}{2}}+c_{yzyz}^{i+\frac{1}{2},j+\frac{1}{2},k_{bot}-\frac{1}{2}} \\
&+c_{yzyz}^{i-\frac{1}{2},j+\frac{1}{2},k_{bot}-\frac{1}{2}}\Bigg)\frac{1}{2}\Bigg[\frac{1}{\Delta z}\Bigg(v_y^{n+\frac{1}{4}}\left(i+\frac{1}{2},j,k_{bot}+\frac{1}{2}\right)-v_y^{n+\frac{1}{4}}\left(i+\frac{1}{2},j,k_{bot}-\frac{1}{2}\right)\Bigg) \\
&+\frac{1}{\Delta y}\Bigg(v_z^{n+\frac{1}{4}}\left(i+\frac{1}{2},j+\frac{1}{2},k_{bot}\right)-v_z^{n+\frac{1}{4}}\left(i+\frac{1}{2},j-\frac{1}{2},k_{bot}\right)\Bigg)\Bigg]
\end{aligned}
\tag{3.42a}
$$

$$
\begin{aligned}
T_{xz}^{n+\frac{1}{2}}\left(i,j+\frac{1}{2},k\right) &= T_{xz}^{n}\left(i,j+\frac{1}{2},k\right) \\
&+\frac{\Delta t}{2}\frac{1}{4}\Bigg(c_{xzxz}^{i+\frac{1}{2},j+\frac{1}{2},k+\frac{1}{2}}+c_{xzxz}^{i-\frac{1}{2},j+\frac{1}{2},k+\frac{1}{2}}+c_{xzxz}^{i+\frac{1}{2},j+\frac{1}{2},k-\frac{1}{2}} \\
&+c_{xzxz}^{i-\frac{1}{2},j+\frac{1}{2},k-\frac{1}{2}}\Bigg)\frac{1}{2}\Bigg[\frac{1}{\Delta z}\Bigg(v_x^{n+\frac{1}{4}}\left(i,j+\frac{1}{2},k_{bot}+\frac{1}{2}\right)-v_x^{n+\frac{1}{4}}\left(i,j+\frac{1}{2},k_{bot}-\frac{1}{2}\right)\Bigg) \\
&+\frac{1}{\Delta x}\Bigg(v_z^{n+\frac{1}{4}}\left(i+\frac{1}{2},j+\frac{1}{2},k_{bot}\right)-v_z^{n+\frac{1}{4}}\left(i-\frac{1}{2},j+\frac{1}{2},k_{bot}\right)\Bigg)\Bigg]
\end{aligned}
\tag{3.42b}
$$

The velocities directly adjacent to the fixed boundary adhere to the following anti-symmetry conditions:

$$
v_x^{n+\frac{1}{4}}\left(i,j+\frac{1}{2},k+\frac{1}{2}\right)=-v_x^{n+\frac{1}{4}}\left(i,j+\frac{1}{2},k-\frac{1}{2}\right),\qquad v_y^{n+\frac{1}{4}}\left(i+\frac{1}{2},j,k+\frac{1}{2}\right)=-v_y^{n+\frac{1}{4}}\left(i+\frac{1}{2},j,k-\frac{1}{2}\right) \tag{3.43a/b}
$$

Where the terms just below the boundary are just outside the simulation space and are therefore imaged, rather than physical, fields. The averages of the velocities in equations (3.43a/b) are located at the fixed boundary and are equal to zero as expected.

At fixed boundaries it is appropriate to take the stiffness from the adjacent material and apply it to a phantom node just outside the simulation space [215], therefore:

$$
c_{ijij}^{i+\frac{1}{2},j+\frac{1}{2},k_{bot}+\frac{1}{2}}=c_{ijij}^{i+\frac{1}{2},j+\frac{1}{2},k_{bot}-\frac{1}{2}} \tag{3.44}
$$

Substituting (3.44) and (3.43a/b) into equations (3.42/b) yields:

$$T_{yz}^{n+\frac{1}{2}}\left(i+\frac{1}{2},j,k_{bot}\right)=T_{yz}^{n}\left(i+\frac{1}{2},j,k_{bot}\right)$$
$$+\frac{\Delta t}{2}\frac{1}{2}\left(c_{yzyz}^{i+\frac{1}{2},j+\frac{1}{2},k_{bot}+\frac{1}{2}}+c_{yzyz}^{i-\frac{1}{2},j+\frac{1}{2},k_{bot}+\frac{1}{2}}\right)\frac{1}{2}\left[\frac{2}{\Delta z}v_{y}^{n+\frac{1}{4}}\left(i+\frac{1}{2},j,k_{bot}+\frac{1}{2}\right)\right. \quad (3.45a)$$
$$\left.+\frac{1}{\Delta y}\left(v_{z}^{n+\frac{1}{4}}\left(i+\frac{1}{2},j+\frac{1}{2},k_{bot}\right)-v_{z}^{n+\frac{1}{4}}\left(i+\frac{1}{2},j-\frac{1}{2},k_{bot}\right)\right)\right]$$

$$T_{xz}^{n+\frac{1}{2}}\left(i,j+\frac{1}{2},k_{bot}\right)=T_{xz}^{n}\left(i,j+\frac{1}{2},k_{bot}\right)$$
$$+\frac{\Delta t}{2}\frac{1}{2}\left(c_{xzxz}^{i+\frac{1}{2},j+\frac{1}{2},k_{bot}+\frac{1}{2}}+c_{xzxz}^{i-\frac{1}{2},j+\frac{1}{2},k_{bot}+\frac{1}{2}}\right)\frac{1}{2}\left[\frac{2}{\Delta z}v_{x}^{n+\frac{1}{4}}\left(i,j+\frac{1}{2},k_{bot}+\frac{1}{2}\right)\right. \quad (3.45b)$$
$$\left.+\frac{1}{\Delta x}\left(v_{z}^{n+\frac{1}{4}}\left(i+\frac{1}{2},j+\frac{1}{2},k_{bot}\right)-v_{z}^{n+\frac{1}{4}}\left(i-\frac{1}{2},j+\frac{1}{2},k_{bot}\right)\right)\right]$$

#### 3.4.2.3 Normal Velocity Prescribed

When a velocity normal to a boundary is applied, the two co-planar shear stress terms will be affected. Suppose a z-directed velocity is applied at the top boundary of the device:

$$v_{z}^{n+\frac{1}{4}}\left(i+\frac{1}{2},j+\frac{1}{2},k_{top}\right)=v_{z_{Prescribed}}^{n+\frac{1}{4}}\left(i+\frac{1}{2},j+\frac{1}{2},k_{top}\right) \quad (3.46)$$

The shear stresses at the excitation plane are $T_{yz}$ and $T_{xz}$. In the simplest case of a uniform velocity input, the shear terms must necessarily be zero everywhere (since shear stresses would warp the excitation plane, destroying the uniformity), therefore:

$$T_{yz}^{n+\frac{1}{2}}\left(i+\frac{1}{2},j,k_{top}\right)=0,\qquad T_{xz}^{n+\frac{1}{2}}\left(i,j+\frac{1}{2},k_{top}\right)=0 \quad (3.47a/b)$$

#### 3.4.2.4 Normal Traction Prescribed

In this case, rather than anti-symmetry for the normal stress, the following applies at the boundary:

$$\frac{1}{2}\left[T_{zz}^{n+\frac{1}{2}}\left(i+\frac{1}{2},j+\frac{1}{2},k_{top}+\frac{1}{2}\right)+T_{zz}^{n+\frac{1}{2}}\left(i+\frac{1}{2},j+\frac{1}{2},k_{top}-\frac{1}{2}\right)\right]=T_{zz_{Prescribed}}^{n+\frac{1}{2}}\left(i+\frac{1}{2},j+\frac{1}{2},k_{top}\right) \quad (3.48a)$$

This yields the following imaged stress above the surface:

$$T_{zz}^{n+\frac{1}{2}}\left(i+\frac{1}{2},j+\frac{1}{2},k_{top}+\frac{1}{2}\right)=2T_{zz_{Prescribed}}^{n+\frac{1}{2}}\left(i+\frac{1}{2},j+\frac{1}{2},k_{top}\right)-T_{zz}^{n+\frac{1}{2}}\left(i+\frac{1}{2},j+\frac{1}{2},k_{top}-\frac{1}{2}\right) \quad (3.48b)$$

So, the normal traction applied at the boundary may be modelled as the following vertical velocity:

$$
\begin{aligned}
v_z^{n+\frac{3}{4}}&\left(i+\frac{1}{2},j+\frac{1}{2},k_{top}\right) \\
&= v_z^{n+\frac{1}{4}}\left(i+\frac{1}{2},j+\frac{1}{2},k_{top}\right) \\
&+ \frac{\Delta t}{\rho\left(i+\frac{1}{2},j+\frac{1}{2},k_{top}\right)\Delta z}\left[T_{zz_{Prescribed}}^{n+\frac{1}{2}}\left(i+\frac{1}{2},j+\frac{1}{2},k_{top}\right)\right. \\
&\left.- T_{zz}^{n+\frac{1}{2}}\left(i+\frac{1}{2},j+\frac{1}{2},k_{top}-\frac{1}{2}\right)\right]
\end{aligned}
\tag{3.49}
$$

Where the shear stress terms do not appear since the applied traction is normal to the boundary surface, i.e., zero shear stress. The horizontal velocity terms just below the free surface remain unaffected.

## 3.5 Unified Grid

A spatial lattice containing all the information needed to write update equations is shown in Figure 3-16. More specifically, the spatial locations of the EM fields discussed in section 3.2.1, the mechanical fields shown in 3.2.2, the EM material properties of section 3.3.1.1, and the mechanical material properties of section 3.3.2.1, are all presented in the figure.

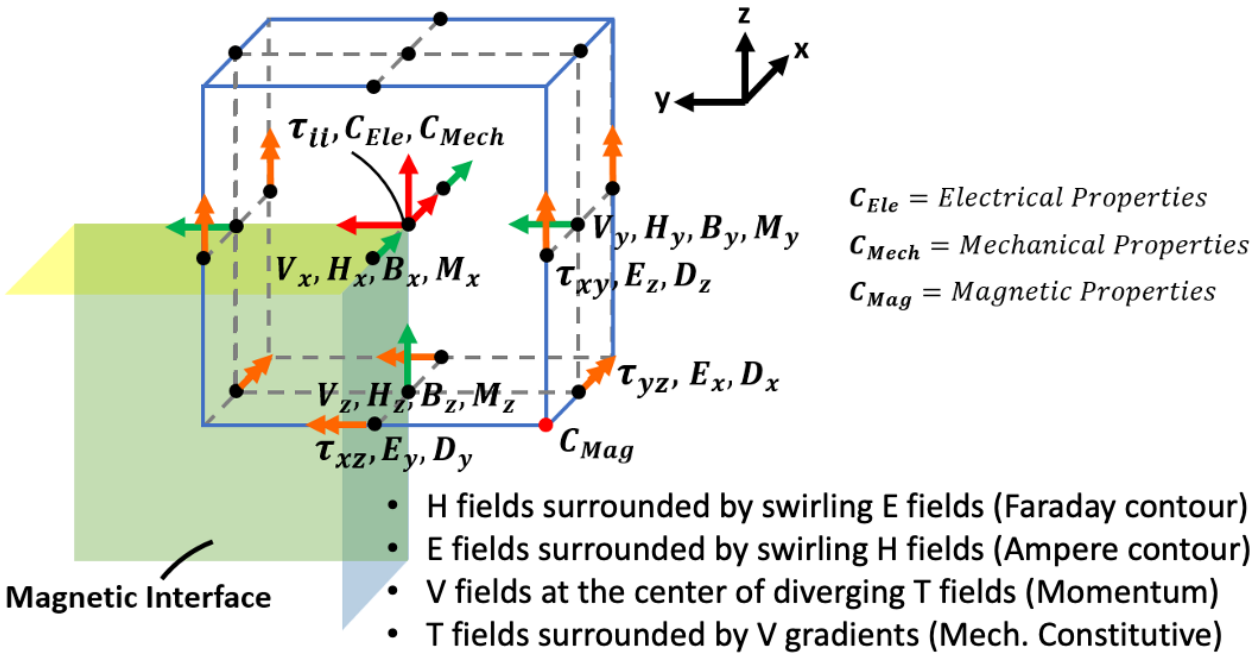


Figure 3-16: Unified spatial grid for mechanical antenna simulations.

Figure 3-16 also reiterates the physical significance of the EM and mechanical field placement (e.g., to create Ampere contours). Recall also that the material properties are defined such that average material properties are utilized at interfaces. Although a full 3D mechanical grid is presented in Figure 3-16 for completeness, only 1D mechanical simulations are performed herein.

### 3.6 ADI-Methodology for Homogenous Free Space with Source Currents

In this section the alternating direction implicit methodology will be derived for free space simulations in the absence of piezomagnetism and piezoelectricity, to simplify the description while providing a basic understanding of the approach. The process flow is shown in Figure 3-17:

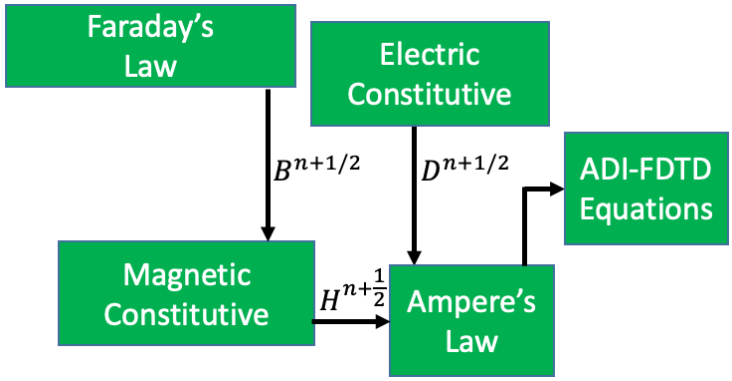


Figure 3-17: Process flow for the free space ADI method.

The accuracy of this method is highlighted in [218][219]. First, the z-component of Faraday's law is written in finite difference form as follows:

$$\begin{aligned}&\frac{2}{\Delta t}\left[B_z^{n+\frac{1}{2}}\left(i+\frac{1}{2},j+\frac{1}{2},k\right)-B_z^{n}\left(i+\frac{1}{2},j+\frac{1}{2},k\right)\right]+\mathcal{M}_z^{n+\frac{1}{2}}\left(i+\frac{1}{2},j+\frac{1}{2},k\right)\\&\quad=\frac{1}{\Delta y}\left[E_x^{n+\frac{1}{2}}\left(i+\frac{1}{2},j+1,k\right)-E_x^{n+\frac{1}{2}}\left(i+\frac{1}{2},j,k\right)\right]\\&\quad-\frac{1}{\Delta x}\left[E_y^{n}\left(i+1,j+\frac{1}{2},k\right)-E_y^{n}\left(i,j+\frac{1}{2},k\right)\right]\end{aligned}\tag{3.50}$$

Note that the magnetic flux current $\dot{B}$ and the curl of the electric field $\nabla\times E$ are evaluated at time $t=(n+1/4)\Delta t$, with the latter term achieving this by having the spatial derivative $E_{x,y}$ evaluated at $t=(n+1/2)\Delta t$, and $E_{y,x}$ at $t=n\Delta t$. This is in stark contrast to the magnetic source current term $\mathcal{M}_z$ which is defined at time $t=(n+1/2)\Delta t$. This time mismatch has been shown to be optimally accurate by Hagness et al. [220][221] and represents a situation where the temporal homogeneity of the finite difference expression need not be rigorously applied. Since the $E_x$ terms are not yet known, (3.50) is implicit (in the y-direction) and further treatment is necessary before Faraday's law may be used as an update equation. Equation (3.50) could have also been made implicit in the x-direction, and this is accomplished in a 2nd sub-iteration.

The magnetic constitutive relation for a vacuum environment is as follows:

$$B_z^{n+\frac{1}{2}} = \mu_0 H_z^{n+\frac{1}{2}} \tag{3.51}$$

Combining (3.50) and (3.51) and solving for $H_z^{n+1/2}$ yields:

$$\begin{aligned} &H_z^{n+\frac{1}{2}}\left(i+\frac{1}{2},j+\frac{1}{2},k\right) \\ &= H_z^n\left(i+\frac{1}{2},j+\frac{1}{2},k\right) + \frac{\Delta t}{2\mu_0 \Delta y}\left[E_x^{n+\frac{1}{2}}\left(i+\frac{1}{2},j+1,k\right) - E_x^{n+\frac{1}{2}}\left(i+\frac{1}{2},j,k\right)\right] \\ &- \frac{\Delta t}{2\mu_0 \Delta x}\left[E_y^n\left(i+1,j+\frac{1}{2},k\right) - E_y^n\left(i,j+\frac{1}{2},k\right)\right] - \frac{\Delta t}{2\mu_0}\mathcal{M}_z^{n+\frac{1}{2}}\left(i+\frac{1}{2},j+\frac{1}{2},k\right) \end{aligned} \tag{3.52}$$

The electric constitutive relation for a vacuum environment is as follows:

$$D_x^{n+\frac{1}{2}} = \epsilon_0 E_x^{n+\frac{1}{2}} \tag{3.53}$$

The x-component of Ampere's law will now be written, which again will involve an implicit direction which is alternated in the 2nd sub-iteration (hence the name alternating direction implicit):

$$\begin{aligned} &\frac{2}{\Delta t}\left[D_x^{n+\frac{1}{2}}\left(i+\frac{1}{2},j,k\right) - D_x^n\left(i+\frac{1}{2},j,k\right)\right] + J_x^{n+\frac{1}{2}}\left(i+\frac{1}{2},j,k\right) \\ &= \frac{1}{\Delta y}\left[H_z^{n+\frac{1}{2}}\left(i+\frac{1}{2},j+\frac{1}{2},k\right) - H_z^{n+\frac{1}{2}}\left(i+\frac{1}{2},j-\frac{1}{2},k\right)\right] \\ &- \frac{1}{\Delta z}\left[H_y^n\left(i+\frac{1}{2},j,k+\frac{1}{2}\right) - H_y^n\left(i+\frac{1}{2},j,k-\frac{1}{2}\right)\right] \end{aligned} \tag{3.54a}$$

Note in (3.54a) that the $H_z$ terms are implicit. Also, the time sampling for the electric current is identical to the magnetic case. Substituting (3.52) and (3.53) into (3.54a) yields:

$$\frac{2\epsilon_0}{\Delta t}\left[E_x^{n+\frac{1}{2}}\left(i+\frac{1}{2},j,k\right)-E_x^n\left(i+\frac{1}{2},j,k\right)\right]$$

$$=\frac{1}{\Delta y}\left[H_z^n\left(i,j+\frac{1}{2},k+\frac{1}{2}\right)+\frac{\Delta t}{2\mu_0\Delta y}\left[E_x^{n+\frac{1}{2}}\left(i+\frac{1}{2},j+1,k\right)-E_x^{n+\frac{1}{2}}\left(i+\frac{1}{2},j,k\right)\right]\right.$$

$$-\frac{\Delta t}{2\mu_0\Delta x}\left[E_y^n\left(i+1,j+\frac{1}{2},k\right)-E_y^n\left(i,j+\frac{1}{2},k\right)\right]-\frac{\Delta t}{2\mu_0}\mathcal{M}_z^{n+\frac{1}{2}}\left(i,j+\frac{1}{2},k+\frac{1}{2}\right)$$

$$-H_z^n\left(i,j-\frac{1}{2},k+\frac{1}{2}\right)+\frac{\Delta t}{2\mu_0\Delta y}\left[E_x^{n+\frac{1}{2}}\left(i+\frac{1}{2},j,k\right)-E_x^{n+\frac{1}{2}}\left(i+\frac{1}{2},j-1,k\right)\right] \tag{3.55}$$

$$-\frac{\Delta t}{2\mu_0\Delta x}\left[E_y^n\left(i+1,j-\frac{1}{2},k\right)-E_y^n\left(i,j-\frac{1}{2},k\right)\right]+\frac{\Delta t}{2\mu_0}\mathcal{M}_z^{n+\frac{1}{2}}\left(i,j-\frac{1}{2},k+\frac{1}{2}\right)\Big]$$

$$-\frac{1}{\Delta z}\left[H_y^n\left(i+\frac{1}{2},j,k+\frac{1}{2}\right)-H_y^n\left(i+\frac{1}{2},j,k-\frac{1}{2}\right)\right]-J_x^{n+\frac{1}{2}}\left(i+\frac{1}{2},j,k\right)$$

Note in (3.55) that now the only fields determined at future time step $n+1/2$ are x-directed electric field terms which occur along a y-directed cut of three nodes, namely $j-1$, $j$, and $j+1$. This so-called "y-cut" equation may be simplified as follows:

$$-\frac{(\Delta t)^2}{4\mu_0\epsilon_0(\Delta y)^2}E_x^{n+\frac{1}{2}}\left(i+\frac{1}{2},j-1,k\right)+\left[1+\frac{(\Delta t)^2}{2\mu_0\epsilon_0(\Delta y)^2}\right]E_x^{n+\frac{1}{2}}\left(i+\frac{1}{2},j,k\right)$$

$$-\frac{(\Delta t)^2}{4\mu_0\epsilon_0(\Delta y)^2}E_x^{n+\frac{1}{2}}\left(i+\frac{1}{2},j+1,k\right)$$

$$=E_x^n\left(i+\frac{1}{2},j,k\right)+\frac{\Delta t}{2\epsilon_0\Delta y}\left[H_z^n\left(i+\frac{1}{2},j+\frac{1}{2},k\right)-H_z^n\left(i+\frac{1}{2},j-\frac{1}{2},k\right)\right]$$

$$-\frac{\Delta t}{2\epsilon_0\Delta z}\left[H_y^n\left(i+\frac{1}{2},j,k+\frac{1}{2}\right)-H_y^n\left(i+\frac{1}{2},j,k-\frac{1}{2}\right)\right]$$

$$-\frac{(\Delta t)^2}{4\mu_0\epsilon_0\Delta x\Delta y}\left[E_y^n\left(i+1,j+\frac{1}{2},k\right)-E_y^n\left(i,j+\frac{1}{2},k\right)\right] \tag{3.56}$$

$$+\frac{(\Delta t)^2}{4\mu_0\epsilon_0\Delta x\Delta y}\left[E_y^n\left(i+1,j-\frac{1}{2},k\right)-E_y^n\left(i,j-\frac{1}{2},k\right)\right]$$

$$-\frac{(\Delta t)^2}{4\mu_0\epsilon_0\Delta y}\left[\mathcal{M}_z^{n+\frac{1}{2}}\left(i+\frac{1}{2},j+\frac{1}{2},k\right)-\mathcal{M}_z^{n+\frac{1}{2}}\left(i+\frac{1}{2},j-\frac{1}{2},k\right)\right]$$

$$-\frac{\Delta t}{2\epsilon_0}J_x^{n+\frac{1}{2}}\left(i+\frac{1}{2},j,k\right)$$

The y-cut equation (3.56) may be written in matrix form as follows:

$$\begin{bmatrix} \ddots & \cdots & 0 & 0 & 0 & 0 \\ \vdots & 1+2c_y & -c_y & 0 & 0 & 0 \\ 0 & -c_y & 1+2c_y & -c_y & 0 & 0 \\ 0 & 0 & -c_y & 1+2c_y & -c_y & 0 \\ 0 & 0 & 0 & -c_y & 1+2c_y & \vdots \\ 0 & 0 & 0 & 0 & \cdots & \ddots \end{bmatrix} \begin{pmatrix} \vdots \\ E_x^{j-2} \\ E_x^{j-1} \\ E_x^{j} \\ E_x^{j+1} \\ \vdots \end{pmatrix} = \begin{pmatrix} \vdots \\ F_1^{j-2} \\ F_1^{j-1} \\ F_1^{j} \\ F_1^{j+1} \\ \vdots \end{pmatrix} \tag{3.57a}$$

$$c_n = \frac{(\Delta t)^2}{4\mu_0 \epsilon_0 (\Delta n)^2}, \qquad n = y \quad (y - cut\ equation)$$

Where the $n$ subscript denotes the cut on $c_n$, the $F_1$ (forcing) terms are composed of everything on the right-hand side of (3.56), and the known matrix on the left-hand side is tri-diagonal in nature, reducing computational load. Equation (3.57a) may be written in more compact form as:

$$[M_y]\left(E_x^{n+1/2}\right) = (F_1) \tag{3.57b}$$

Where the electric field vector contains all the $E_x$ field components along the y direction at a specific $i$ and $k$ node. Say that the simulation space has $N_x \times N_y \times N_z$ nodes in the x, y, and z directions respectively. As such, matrix $M_y$ will be a $N_y \times N_y$ matrix and (3.57b) will need to be solved $N_x \times N_z$ times to completely update the $E_x$ field within the simulation space. This process will also occur for the $E_y$ and $E_z$ fields through the z-cut and x-cut equations respectively, thus advancing the simulation from time $t = n\Delta t$ to $t = (n + 1/2)\Delta t$ and finishing the first sub-iteration. In matrix form this may be written as follows:

$$\begin{bmatrix} M_y[N_y \times N_y] & 0 & 0 \\ 0 & M_z[N_z \times N_z] & 0 \\ 0 & 0 & M_x[N_x \times N_x] \end{bmatrix} \begin{pmatrix} E_x^{n+1/2} \\ E_y^{n+1/2} \\ E_z^{n+1/2} \end{pmatrix} = \begin{pmatrix} F_1 \\ F_2 \\ F_3 \end{pmatrix} \tag{3.58a}$$

In the second sub-iteration, the direction of implicit definition is alternated, yielding for example the following for the x-component of Ampere's law:

$$\frac{2}{\Delta t}\left[D_x^{n+1}\left(i+\frac{1}{2},j,k\right)-D_x^{n+\frac{1}{2}}\left(i+\frac{1}{2},j,k\right)\right]$$

$$=\frac{1}{\Delta y}\left[H_z^{n+\frac{1}{2}}\left(i+\frac{1}{2},j+\frac{1}{2},k\right)-H_z^{n+\frac{1}{2}}\left(i+\frac{1}{2},j-\frac{1}{2},k\right)\right] \tag{3.54b}$$

$$-\frac{1}{\Delta z}\left[H_y^{n+1}\left(i+\frac{1}{2},j,k+\frac{1}{2}\right)-H_y^{n+1}\left(i+\frac{1}{2},j,k-\frac{1}{2}\right)\right]$$

Due to this alternation, the update equation for $E_x$ will now be the z-cut equation. Repeating the process from the first sub-iteration, the following matrix representation describes the second sub-iteration:

$$\begin{bmatrix} M_z[N_z\times N_z] & 0 & 0 \\ 0 & M_x[N_x\times N_x] & 0 \\ 0 & 0 & M_y[N_y\times N_y] \end{bmatrix}\begin{pmatrix} E_x^{n+1} \\ E_y^{n+1} \\ E_z^{n+1} \end{pmatrix}=\begin{pmatrix} F_4 \\ F_5 \\ F_6 \end{pmatrix} \tag{3.58b}$$

Updating electric fields utilizing (3.58a) and (3.58b) yields an unconditionally stable method [216]. Therefore, the Courant-Friedrichs-Lewy (CFL) stability time step $\Delta t^{CFL}$ [177], governing electrodynamics, may be ignored:

$$\Delta t = CFLN * \Delta t^{CFL} = CFLN * \frac{\min(\Delta x, \Delta y, \Delta z)}{\sqrt{3}c} \tag{3.59}$$

Where the CFLN factor expresses what multiple of $\Delta t^{CFL}$ that the simulation time step $\Delta t$ is. Herein, this factor varies in the range from 1 to ~100,000 (matching the mechanical time step).

If the numerical volume is not free space but remains homogenous, then the equations of this section may still be used by substituting $\mu_0 \rightarrow \mu_r\mu_0$ and $\epsilon_0 \rightarrow \epsilon_r\epsilon_0$, where $\mu_r$ and $\epsilon_r$ are the relative permeability and relative permittivity respectively of the homogenous space.

## 3.7 ADI for Heterogeneous Spaces

Previously the simulation space was assumed to be homogeneous and, therefore, no interfaces existed, and the spatial location of the material properties was not considered. More generally, material properties are as defined by Figure 3-16, therefore the magnetic constitutive relation is:

$$B_z^{n+\frac{1}{2}}\left(i+\frac{1}{2},j+\frac{1}{2},k\right)=\mu_{zz}^{i+\frac{1}{2},j+\frac{1}{2},k}H_z^{n+\frac{1}{2}}\left(i+\frac{1}{2},j+\frac{1}{2},k\right) \tag{3.60}$$

Where the permeability is collocated with the magnetic fields via spatial averaging:

$$\mu_{zz}^{i+\frac{1}{2},j+\frac{1}{2},k}=\frac{1}{4}\left(\mu_{zz}^{i,j,k}+\mu_{zz}^{i+1,j,k}+\mu_{zz}^{i,j+1,k}+\mu_{zz}^{i+1,j+1,k}\right) \tag{3.61}$$

Substitution into Faraday's law and rearranging yields:

$$\begin{aligned}
&H_z^{n+\frac{1}{2}}\left(i+\frac{1}{2},j+\frac{1}{2},k\right)\\
&\quad=H_z^n\left(i+\frac{1}{2},j+\frac{1}{2},k\right)\\
&\quad+\frac{\Delta t}{2\mu_{zz}^{i+\frac{1}{2},j+\frac{1}{2},k}\Delta y}\left[E_x^{n+\frac{1}{2}}\left(i+\frac{1}{2},j+1,k\right)-E_x^{n+\frac{1}{2}}\left(i+\frac{1}{2},j,k\right)\right]\\
&\quad-\frac{\Delta t}{2\mu_{zz}^{i+\frac{1}{2},j+\frac{1}{2},k}\Delta x}\left[E_y^n\left(i+1,j+\frac{1}{2},k\right)-E_y^n\left(i,j+\frac{1}{2},k\right)\right]\\
&\quad-\frac{\Delta t}{2\mu_{zz}^{i+\frac{1}{2},j+\frac{1}{2},k}}\mathcal{M}_z^{n+\frac{1}{2}}\left(i+\frac{1}{2},j+\frac{1}{2},k\right)
\end{aligned} \tag{3.62}$$

The electric constitutive relation is as follows:

$$D_x^{n+\frac{1}{2}}\left(i+\frac{1}{2},j,k\right)=\epsilon_{xx}^{i+\frac{1}{2},j,k}E_x^{n+\frac{1}{2}}\left(i+\frac{1}{2},j,k\right) \tag{3.63}$$

Where,

$$\epsilon_{xx}^{i+\frac{1}{2},j,k}=\frac{1}{4}\left(\epsilon_{xx}^{i+\frac{1}{2},j+\frac{1}{2},k+\frac{1}{2}}+\epsilon_{xx}^{i+\frac{1}{2},j-\frac{1}{2},k+\frac{1}{2}}+\epsilon_{xx}^{i+\frac{1}{2},j+\frac{1}{2},k-\frac{1}{2}}+\epsilon_{xx}^{i+\frac{1}{2},j-\frac{1}{2},k-\frac{1}{2}}\right) \tag{3.64}$$

Substituting (3.63) into Ampere's law and utilizing (3.62):

$$\frac{2\epsilon_{xx}^{i+\frac{1}{2},j,k}}{\Delta t}\left[E_x^{n+\frac{1}{2}}\left(i+\frac{1}{2},j,k\right)-E_x^{n}\left(i+\frac{1}{2},j,k\right)\right]$$

$$=\frac{1}{\Delta y}\Bigg[H_z^n\left(i+\frac{1}{2},j+\frac{1}{2},k\right)$$

$$+\frac{\Delta t}{2\mu_{zz}^{i+\frac{1}{2},j+\frac{1}{2},k}\Delta y}\left[E_x^{n+\frac{1}{2}}\left(i+\frac{1}{2},j+1,k\right)-E_x^{n+\frac{1}{2}}\left(i+\frac{1}{2},j,k\right)\right]$$

$$-\frac{\Delta t}{2\mu_0\Delta x}\left[E_y^n\left(i+1,j+\frac{1}{2},k\right)-E_y^n\left(i,j+\frac{1}{2},k\right)\right]$$

$$-\frac{\Delta t}{2\mu_{zz}^{i+\frac{1}{2},j+\frac{1}{2},k}}\mathcal{M}_z^{n+\frac{1}{2}}\left(i+\frac{1}{2},j+\frac{1}{2},k\right)-H_z^n\left(i+\frac{1}{2},j-\frac{1}{2},k\right) \qquad (3.65)$$

$$+\frac{\Delta t}{2\mu_{zz}^{i+\frac{1}{2},j-\frac{1}{2},k}\Delta y}\left[E_x^{n+\frac{1}{2}}\left(i+\frac{1}{2},j,k\right)-E_x^{n+\frac{1}{2}}\left(i+\frac{1}{2},j-1,k\right)\right]$$

$$-\frac{\Delta t}{2\mu_{zz}^{i+\frac{1}{2},j-\frac{1}{2},k}\Delta x}\left[E_y^n\left(i+1,j-\frac{1}{2},k\right)-E_y^n\left(i,j-\frac{1}{2},k\right)\right]$$

$$+\frac{\Delta t}{2\mu_{zz}^{i+\frac{1}{2},j-\frac{1}{2},k}}\mathcal{M}_z^{n+\frac{1}{2}}\left(i+\frac{1}{2},j-\frac{1}{2},k\right)\Bigg]$$

$$-\frac{1}{\Delta z}\left[H_y^n\left(i+\frac{1}{2},j,k+\frac{1}{2}\right)-H_y^n\left(i+\frac{1}{2},j,k-\frac{1}{2}\right)\right]-\frac{\Delta t}{2\epsilon_0}J_x^{n+\frac{1}{2}}\left(i+\frac{1}{2},j,k\right)$$

Which yields the following “y-cut” equation:

$$
\begin{aligned}
&-\frac{(\Delta t)^2}{4\mu_{zz}^{i+\frac{1}{2},j-\frac{1}{2},k}\epsilon_{xx}^{i+\frac{1}{2},j,k}(\Delta y)^2}E_x^{n+\frac{1}{2}}\left(i+\frac{1}{2},j-1,k\right)\\
&+\left[1+\frac{(\Delta t)^2}{4\epsilon_{xx}^{i+\frac{1}{2},j,k}(\Delta y)^2}\left(\frac{1}{\mu_{zz}^{i+\frac{1}{2},j-\frac{1}{2},k}}+\frac{1}{\mu_{zz}^{i+\frac{1}{2},j+\frac{1}{2},k}}\right)\right]E_x^{n+\frac{1}{2}}\left(i+\frac{1}{2},j,k\right)\\
&-\frac{(\Delta t)^2}{4\mu_{zz}^{i+\frac{1}{2},j+\frac{1}{2},k}\epsilon_{xx}^{i+\frac{1}{2},j,k}(\Delta y)^2}E_x^{n+\frac{1}{2}}\left(i+\frac{1}{2},j+1,k\right)\\
&=E_x^n\left(i+\frac{1}{2},j,k\right)\\
&+\frac{\Delta t}{2\epsilon_{xx}^{i+\frac{1}{2},j,k}\Delta y}\left[H_z^n\left(i+\frac{1}{2},j+\frac{1}{2},k\right)-H_z^n\left(i+\frac{1}{2},j-\frac{1}{2},k\right)\right]\\
&-\frac{\Delta t}{2\epsilon_{xx}^{i+\frac{1}{2},j,k}\Delta z}\left[H_y^n\left(i+\frac{1}{2},j,k+\frac{1}{2}\right)-H_y^n\left(i+\frac{1}{2},j,k-\frac{1}{2}\right)\right]\\
&-\frac{(\Delta t)^2}{4\mu_{zz}^{i+\frac{1}{2},j+\frac{1}{2},k}\epsilon_{xx}^{i+\frac{1}{2},j,k}\Delta x\Delta y}\left[E_y^n\left(i+1,j+\frac{1}{2},k\right)-E_y^n\left(i,j+\frac{1}{2},k\right)\right]\\
&+\frac{(\Delta t)^2}{4\mu_{zz}^{i+\frac{1}{2},j-\frac{1}{2},k}\epsilon_{xx}^{i+\frac{1}{2},j,k}\Delta x\Delta y}\left[E_y^n\left(i+1,j-\frac{1}{2},k\right)-E_y^n\left(i,j-\frac{1}{2},k\right)\right]\\
&-\frac{(\Delta t)^2}{4\epsilon_{xx}^{i+\frac{1}{2},j,k}\Delta y}\left[\frac{1}{\mu_{zz}^{i+\frac{1}{2},j+\frac{1}{2},k}}\mathcal{M}_z^{n+\frac{1}{2}}\left(i+\frac{1}{2},j+\frac{1}{2},k\right)\right.\\
&\left.-\frac{1}{\mu_{zz}^{i+\frac{1}{2},j-\frac{1}{2},k}}\mathcal{M}_z^{n+\frac{1}{2}}\left(i+\frac{1}{2},j-\frac{1}{2},k\right)\right]-\frac{\Delta t}{2\epsilon_{xx}^{i+\frac{1}{2},j,k}}J_x^{n+\frac{1}{2}}\left(i+\frac{1}{2},j,k\right)
\end{aligned}
\tag{3.66}
$$

Note that (3.66) simplifies to the homogenous case when the material properties have no spatial dependence. The tridiagonal system of equations for the 1st and 2nd sub-iteration will be:

$$
\begin{bmatrix}
M_{y1}[N_y\times N_y] & 0 & 0\\
0 & M_{z1}[N_z\times N_z] & 0\\
0 & 0 & M_{x1}[N_x\times N_x]
\end{bmatrix}
\begin{pmatrix}
E_x^{n+1/2}\\
E_y^{n+1/2}\\
E_z^{n+1/2}
\end{pmatrix}=
\begin{pmatrix}
F_1\\
F_2\\
F_3
\end{pmatrix}
\tag{3.67a}
$$

$$\begin{bmatrix} M_{z2}[N_z \times N_z] & 0 & 0 \\ 0 & M_{x2}[N_x \times N_x] & 0 \\ 0 & 0 & M_{y2}[N_y \times N_y] \end{bmatrix} \begin{pmatrix} E_x^{n+1} \\ E_y^{n+1} \\ E_z^{n+1} \end{pmatrix} = \begin{pmatrix} F_4 \\ F_5 \\ F_6 \end{pmatrix} \tag{3.67b}$$

Note that an extra subscript is now used for the tri-diagonal matrices to delineate the first and second sub-iteration. Generally, the n-cut matrices only exhibit $M_{n1} = M_{n2} = M_n$ when $\mu_{xx} = \mu_{yy} = \mu_{zz}$. Herein, the simulation space is assumed to be magnetically homogenous (i.e., $\mu_{ij} = \mu_0 \delta_{ij}$ everywhere) and thus the tri-diagonal matrices for like cuts will be the same. Regardless, to maintain some degree of generality, the CPML-ADI-FDTD equations derived subsequently will assume a diagonal permeability with $\mu_{xx} \neq \mu_{yy} \neq \mu_{zz}$. As a final note for readers familiar with material science, the expressions x-cut, y-cut, and z-cut herein refer to the fact that the three unknown electric fields within the ADI-FDTD equations lie along a x, y, and z-directed line respectively. The term “cut” does not refer to a crystalline orientation of a material under investigation.

## 3.8 Convolutional Perfectly Matched Layer (CPML) ADI-FDTD w/ Mesh Grading

The CPML-ADI-FDTD equations will now be derived where the flow is the same as that of the previous two sections except that modified versions on Maxwell’s curl equations are utilized to produce graded meshes as well as perfectly matched layers (PMLs). Since the equations begin to be quite lengthy within this section, spatial definition of the fields is placed as a superscript to shorten the expressions. Also, to sponsor clarity, all six ADI equations are explicitly provided.

### 3.8.1 Faraday’s Law w/ CFS Stretched Coordinates

Faraday’s law is used to write update equations for the magnetic flux ($B_i$) and is substituted into the magnetic constitutive relation to generate the update equations for magnetic fields ($H_i$). Whenever Faraday’s law or Ampere’s law are evoked in an update equation, a different form for the 1st and 2nd sub-iteration will result since the direction of the implicit fields alternate each sub-iteration (Alternating-Direction Implicit scheme). Recall that Faraday’s law, relating the magnetic

currents to the left-handed curl of the electric field, was modified by stretched coordinate metric $s_i$ in section 2.1.3 yielding history variables which included a decaying exponential term. This enables the use of a recursive convolution algorithm which allows the response of the system at time $t$, due to a series of impulses at time $\tau$, to be determined. Algorithms of this type are used extensively herein and involve what are known as history variables. These are so named because they include the progressive effect of the series of impulses on the present response. In other words, these variables track the history of the system excitations and were defined in equation (2.31):

$$\Phi_{Emq} = \int_{0^-}^{t} \zeta_q(t-\tau)\frac{\partial E_m(\tau)}{\partial q}d\tau = -\frac{\sigma_q}{\kappa_q^2\epsilon_0}\int_{0^-}^{t} e^{-\frac{1}{\epsilon_0}\left(\alpha_q+\frac{\sigma_q}{\kappa_q}\right)(t-\tau)}\frac{\partial E_m}{\partial q}d\tau\,, \qquad \begin{matrix} m=x,y,z \\ q=x,y,z \\ m\neq q \end{matrix} \tag{2.31}$$

Note that the history variable is zero in free space (when $\sigma_q = 0$) and say that a $= \frac{1}{\epsilon_0}\left(\alpha_q + \frac{\sigma_q}{\kappa_q}\right)$ is the inverse relaxation time (the time it takes a perturbed system to return to equilibrium). Faraday's law was defined as follows:

$$\dot{B}_i + \mathcal{M}_i^s = \epsilon_{ijk'}E_{j,k'} + \epsilon_{ijk}\Phi_{E_{jk}} \tag{2.34}$$

$$\Phi_{E_{jk}} = \begin{bmatrix} 0 & \Phi_{E_{xy}} & \Phi_{E_{xz}} \\ \Phi_{E_{yx}} & 0 & \Phi_{E_{yz}} \\ \Phi_{E_{zx}} & \Phi_{E_{zy}} & 0 \end{bmatrix} \tag{2.35b}$$

Utilizing the following primed coordinates:

$$dx' = \kappa_x(x)dx, \qquad dy' = \kappa_y(y)dy, \qquad dz' = \kappa_z(z)dz$$

In equation (2.34), the $\mathcal{M}_i$ terms are the fictional magnetic source currents which are included here since some problems allow actual sources to be modeled using these terms. For example, aperture antennas, where the EM fields are known over the aperture, may be modelled using electric and magnetic source currents [25-27]. This is beneficial since the ADI-FDTD algorithm, as proposed herein, does not allow for electric fields to be input explicitly but equivalent magnetic source currents, defined by $\mathcal{M} = E \times \hat{n}$ (see eq. 3.9b), present no issue.

The history variables will be written in finite difference form first, before returning to the full Faraday's law of equation (2.34), with the goal of deriving update equations. For input into a finite difference algorithm say $t^{n+1/2} = t^n + \Delta t^{n+1/2}$, where the superscript indicates the $n^{th}$ time step. For a fixed step solver and two sub-iterations we have time increment $\Delta t^{n+1/2} = \Delta t/2$, for all $n$ but the current notation will be kept until the end of the derivation. The history variables at times $t^n$ and $t^{n+1/2}$ are as follows:

$$\Phi_{Emq}^{n} = -\frac{\sigma_q}{\kappa_q^2 \epsilon_0} \int_{0^-}^{t^n} e^{-\mathrm{a}(t^n - \tau)} \frac{\partial E_m}{\partial q} d\tau \tag{3.68a}$$

$$\begin{aligned} \Phi_{Emq}^{n+\frac{1}{2}} &= -\frac{\sigma_q}{\kappa_q^2 \epsilon_0} \int_{0^-}^{t^{n+\frac{1}{2}}} e^{-\mathrm{a}\left(t^{n+\frac{1}{2}} - \tau\right)} \frac{\partial E_m}{\partial q} d\tau \\ &= -\frac{\sigma_q}{\kappa_q^2 \epsilon_0} \int_{0^-}^{t^n + \Delta t^{n+1/2}} e^{-\mathrm{a}\left(t^n + \Delta t^{n+\frac{1}{2}} - \tau\right)} \frac{\partial E_m}{\partial q} d\tau \end{aligned} \tag{3.68b}$$

Where the $\Phi_{Emq}^{n+1/2}$ integral in (3.68b) may be split into two and the exponential term expanded as follows:

$$\Phi_{Emq}^{n+\frac{1}{2}} = -\frac{\sigma_q}{\kappa_q^2 \epsilon_0} \left\{ \int_{0^-}^{t^n} e^{-\mathrm{a}\left(\Delta t^{n+\frac{1}{2}}\right)} e^{-\mathrm{a}(t^n - \tau)} \frac{\partial E_m}{\partial q} d\tau + \int_{t^n}^{t^{n+1/2}} e^{-\mathrm{a}\left(t^{n+\frac{1}{2}} - \tau\right)} \frac{\partial E_m}{\partial q} d\tau \right\} \tag{3.68c}$$

Substituting equation (3.54a) into (3.54c) yields:

$$\Phi_{Emq}^{n+\frac{1}{2}} = e^{-\mathrm{a}\left(\Delta t^{n+\frac{1}{2}}\right)} \Phi_{Emq}^{n} - \frac{\sigma_q}{\kappa_q^2 \epsilon_0} \int_{t^n}^{t^{n+1/2}} e^{-\mathrm{a}\left(t^{n+\frac{1}{2}} - \tau\right)} \frac{\partial E_m}{\partial q} d\tau \tag{3.68d}$$

Assuming that the time step is small enough, the midpoint rule may be used to approximate the electric field gradient within the integrand, but, as noted by [212], more efficient and accurate results may be obtained if the time designation is as follows:

$$\int_{t^n}^{t^{n+\frac{1}{2}}} e^{-\mathrm{a}\left(t^{n+\frac{1}{2}} - \tau\right)} \frac{\partial E_m}{\partial q} d\tau \cong \int_{t^n}^{t^{n+1/2}} e^{-\mathrm{a}\left(t^{n+\frac{1}{2}} - \tau\right)} d\tau \left[\frac{\partial E_m}{\partial q}\right]_{\tau = t^{n+1/2}}$$

$$= \left[\frac{1}{\mathrm{a}} e^{-\mathrm{a}\left(t^{n+\frac{1}{2}}-\tau\right)}\right]_{t^n}^{t^{n+1/2}} \left(\frac{\Delta E_m^{n+\frac{1}{2}}}{\Delta q}\right) = \frac{1}{\mathrm{a}}\left(1 - e^{-\mathrm{a}\Delta t^{n+\frac{1}{2}}}\right)\left(\frac{\Delta E_m^{n+\frac{1}{2}}}{\Delta q}\right)$$

Therefore, the history variable update equation is as follows:

$$\Phi_{Emq}^{n+\frac{1}{2}} = e^{-\mathrm{a}\Delta t^{n+\frac{1}{2}}}\Phi_{Emq}^{n} + \frac{\sigma_q}{\kappa_q^2 \epsilon_0}\frac{1}{\mathrm{a}}\left(e^{-\mathrm{a}\Delta t^{n+\frac{1}{2}}} - 1\right)\left(\frac{\Delta E_m^{n+\frac{1}{2}}}{\Delta q}\right) \tag{3.68e}$$

Where the first term on the right-hand side of (3.68e) is the time decay of the history variable at time step $t^n$ after time increment $\Delta t^{n+1/2}$, and the second term adds on the additional component of the history variable due to field increment $\Delta E^{n+1/2}$, now substitute in $\Delta t^{n+1/2} = \Delta t/2$, as well as the inverse relaxation time constant, to get:

$$\Phi_{Emq}^{n+\frac{1}{2}} = e^{-\left(\alpha_q+\frac{\sigma_q}{\kappa_q}\right)\frac{\Delta t}{2\epsilon_0}}\Phi_{Emq}^{n} + \frac{\sigma_q}{\kappa_q(\kappa_q\alpha_q + \sigma_q)}\left[e^{-\left(\alpha_q+\frac{\sigma_q}{\kappa_q}\right)\frac{\Delta t}{2\epsilon_0}} - 1\right]\left(\frac{\Delta E_m^{n+\frac{1}{2}}}{\Delta q}\right) \tag{3.69}$$

So far, no spatial indices have been included in order to facilitate a general derivation of the history variable update equations. However, the history variables will, in general, vary in space. For example, the components of the stretched coordinate metric can vary in the direction of stretching, but only in this direction so that the planar boundaries remain plane with a consistent number of cells. The $\Delta E_m$ term will also have unique spatial indices depending on the history variable. For clarity, all the history variables are presented in Table 3-2.

| | |
|---|---|
| $\Phi_{Ezy}^{n+\frac{1}{2}}\left(i, j+\frac{1}{2}, k+\frac{1}{2}\right)$ | $e^{-\left(\alpha_y^j+\frac{\sigma_y^j}{\kappa_y^j}\right)\frac{\Delta t}{2\epsilon_0}}\Phi_{Ezy}^{n} + \frac{\sigma_y^j}{\kappa_y^j\alpha_y^j + \sigma_y^j}\left[e^{-\left(\alpha_y^j+\frac{\sigma_y^j}{\kappa_y^j}\right)\frac{\Delta t}{2\epsilon_0}} - 1\right]\left(\frac{1}{\kappa_y^j \Delta y}\right)\left(E_z^{n+\frac{1}{2}}\left(i, j+1, k+\frac{1}{2}\right) - E_z^{n+\frac{1}{2}}\left(i, j, k+\frac{1}{2}\right)\right)$ |
| $\Phi_{Eyz}^{n+\frac{1}{2}}\left(i, j+\frac{1}{2}, k+\frac{1}{2}\right)$ | $e^{-\left(\alpha_z^k+\frac{\sigma_z^k}{\kappa_z^k}\right)\frac{\Delta t}{2\epsilon_0}}\Phi_{Eyz}^{n} + \frac{\sigma_z^k}{\kappa_z^k\alpha_z^k + \sigma_z^k}\left[e^{-\left(\alpha_z^k+\frac{\sigma_z^k}{\kappa_z^k}\right)\frac{\Delta t}{2\epsilon_0}} - 1\right]\left(\frac{1}{\kappa_z^k \Delta z}\right)\left(E_y^{n+\frac{1}{2}}\left(i, j+\frac{1}{2}, k+1\right) - E_y^{n+\frac{1}{2}}\left(i, j+\frac{1}{2}, k\right)\right)$ |
| $\Phi_{Exz}^{n+\frac{1}{2}}\left(i+\frac{1}{2}, j, k+\frac{1}{2}\right)$ | $e^{-\left(\alpha_z^k+\frac{\sigma_z^k}{\kappa_z^k}\right)\frac{\Delta t}{2\epsilon_0}}\Phi_{Exz}^{n} + \frac{\sigma_z^k}{\kappa_z^k\alpha_z^k + \sigma_z^k}\left[e^{-\left(\alpha_z^k+\frac{\sigma_z^k}{\kappa_z^k}\right)\frac{\Delta t}{2\epsilon_0}} - 1\right]\left(\frac{1}{\kappa_z^k \Delta z}\right)\left(E_x^{n+\frac{1}{2}}\left(i+\frac{1}{2}, j, k+1\right) - E_x^{n+\frac{1}{2}}\left(i+\frac{1}{2}, j, k\right)\right)$ |

| | |
|---|---|
| $\Phi_{Ezx}^{n+\frac{1}{2}}\left(i+\frac{1}{2},j,k+\frac{1}{2}\right)$ | $e^{-\left(\alpha_x^i+\frac{\sigma_x^i}{\kappa_x^i}\right)\frac{\Delta t}{2\epsilon_0}}\Phi_{Ezx}^n+\frac{\sigma_x^i}{\kappa_x^i\alpha_x^i+\sigma_x^i}\left[e^{-\left(\alpha_x^i+\frac{\sigma_x^i}{\kappa_x^i}\right)\frac{\Delta t}{2\epsilon_0}}-1\right]\left(\frac{1}{\kappa_x^i\Delta x}\right)\left(E_z^{n+\frac{1}{2}}\left(i+1,j,k+\frac{1}{2}\right)-E_z^{n+\frac{1}{2}}\left(i,j,k+\frac{1}{2}\right)\right)$ |
| $\Phi_{Eyx}^{n+\frac{1}{2}}\left(i+\frac{1}{2},j+\frac{1}{2},k\right)$ | $e^{-\left(\alpha_x^i+\frac{\sigma_x^i}{\kappa_x^i}\right)\frac{\Delta t}{2\epsilon_0}}\Phi_{Eyx}^n+\frac{\sigma_x^i}{\kappa_x^i\alpha_x^i+\sigma_x^i}\left[e^{-\left(\alpha_x^i+\frac{\sigma_x^i}{\kappa_x^i}\right)\frac{\Delta t}{2\epsilon_0}}-1\right]\left(\frac{1}{\kappa_x^i\Delta x}\right)\left(E_y^{n+\frac{1}{2}}\left(i+1,j+\frac{1}{2},k\right)-E_y^{n+\frac{1}{2}}\left(i,j+\frac{1}{2},k\right)\right)$ |
| $\Phi_{Exy}^{n+\frac{1}{2}}\left(i+\frac{1}{2},j+\frac{1}{2},k\right)$ | $e^{-\left(\alpha_y^j+\frac{\sigma_y^j}{\kappa_y^j}\right)\frac{\Delta t}{2\epsilon_0}}\Phi_{Exy}^n+\frac{\sigma_y^j}{\kappa_y^j\alpha_y^j+\sigma_y^j}\left[e^{-\left(\alpha_y^j+\frac{\sigma_y^j}{\kappa_y^j}\right)\frac{\Delta t}{2\epsilon_0}}-1\right]\left(\frac{1}{\kappa_y^j\Delta y}\right)\left(E_x^{n+\frac{1}{2}}\left(i+\frac{1}{2},j+1,k\right)-E_x^{n+\frac{1}{2}}\left(i+\frac{1}{2},j,k\right)\right)$ |

Table 3-2: History variables for modified Faraday's law.

These expressions will be used in the subsequent two sections to derive the finite difference form of the modified Faraday's law for the first and second sub-iterations respectively. Note that the history variables in Table 3-2 may be adjusted for algorithms without sub-iterations by replacing $n+1/2$ with $n+1$, as well as all $\Delta t/2$ terms with $\Delta t$.

Within the finite difference equations that follow in this chapter, the $\kappa_i$ real stretching factor will include an additional subscript, either E or H, which is introduced due to the staggered finite difference grid. To understand why, note that the space between electric fields and magnetic fields is not the same in Figure 3-18. Within the figure, an xz-planar cut is shown with the solid blue lines representing the cell edges and the dashed grey lines representing the bisections.

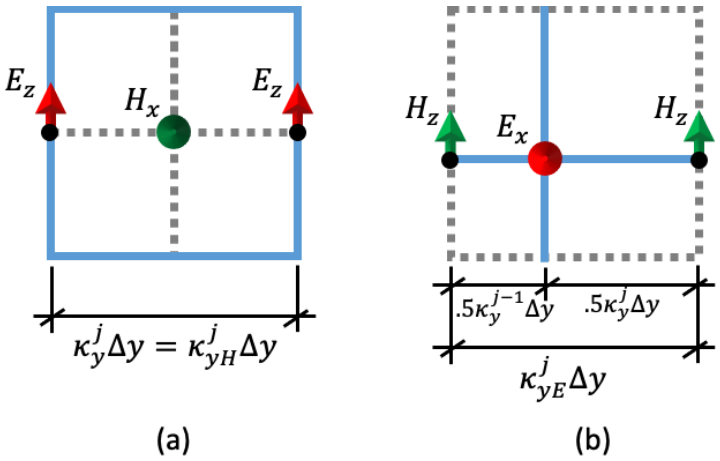


Figure 3-18: Definition of $\boldsymbol{\kappa}$ for update of magnetic fields (a) and electric fields (b).

Note that where mesh grading (stretching) is occurring the relevant spacing, $\kappa_{yH}\Delta y$ vs. $\kappa_{yE}\Delta y$, required to update the magnetic and electric fields respectively will differ (since $\kappa_y^{j-1} \neq \kappa_y^j$ generally), thus requiring a distinction to be made.

#### 3.8.1.1 First Sub-Iteration

Faraday's law may be written in finite difference form for the first sub-iteration as follows:

$$\begin{aligned}
&\frac{2}{\Delta t}\left[B_x^{n+\frac{1}{2}}\left(i,j+\frac{1}{2},k+\frac{1}{2}\right)-B_x^n\left(i,j+\frac{1}{2},k+\frac{1}{2}\right)\right] \\
&\quad=\frac{1}{\kappa_{zH}^k\Delta z}\left[E_y^{n+\frac{1}{2}}\left(i,j+\frac{1}{2},k+1\right)-E_y^{n+\frac{1}{2}}\left(i,j+\frac{1}{2},k\right)\right] \\
&\quad-\frac{1}{\kappa_{yH}^j\Delta y}\left[E_z^n\left(i,j+1,k+\frac{1}{2}\right)-E_y^n\left(i,j,k+\frac{1}{2}\right)\right]-\mathcal{M}_x^{n+\frac{1}{2}}\left(i,j+\frac{1}{2},k+\frac{1}{2}\right) \\
&\quad+\Phi_{Eyz}^n\left(i,j+\frac{1}{2},k+\frac{1}{2}\right)-\Phi_{Ezy}^n\left(i,j+\frac{1}{2},k+\frac{1}{2}\right)
\end{aligned} \tag{3.70a}$$

$$\begin{aligned}
&\frac{2}{\Delta t}\left[B_y^{n+\frac{1}{2}}\left(i,j+\frac{1}{2},k+\frac{1}{2}\right)-B_y^n\left(i,j+\frac{1}{2},k+\frac{1}{2}\right)\right] \\
&\quad=\frac{1}{\kappa_{xH}^i\Delta x}\left[E_z^{n+\frac{1}{2}}\left(i+1,j,k+\frac{1}{2}\right)-E_z^{n+\frac{1}{2}}\left(i,j,k+\frac{1}{2}\right)\right] \\
&\quad-\frac{1}{\kappa_{zH}^k\Delta z}\left[E_x^n\left(i+\frac{1}{2},j,k+1\right)-E_x^n\left(i+\frac{1}{2},j,k\right)\right]-\mathcal{M}_y^{n+\frac{1}{2}}\left(i+\frac{1}{2},j,k+\frac{1}{2}\right) \\
&\quad+\Phi_{Ezx}^n\left(i+\frac{1}{2},j,k+\frac{1}{2}\right)-\Phi_{Exz}^n\left(i+\frac{1}{2},j,k+\frac{1}{2}\right)
\end{aligned} \tag{3.70b}$$

$$\begin{aligned}
&\frac{2}{\Delta t}\left[B_z^{n+\frac{1}{2}}\left(i,j+\frac{1}{2},k+\frac{1}{2}\right)-B_z^n\left(i,j+\frac{1}{2},k+\frac{1}{2}\right)\right] \\
&\quad=\frac{1}{\kappa_{yH}^j\Delta y}\left[E_x^{n+\frac{1}{2}}\left(i+\frac{1}{2},j+1,k\right)-E_x^{n+\frac{1}{2}}\left(i+\frac{1}{2},j,k\right)\right] \\
&\quad-\frac{1}{\kappa_{xH}^i\Delta x}\left[E_y^n\left(i+1,j+\frac{1}{2},k\right)-E_y^n\left(i,j+\frac{1}{2},k\right)\right]-\mathcal{M}_z^{n+\frac{1}{2}}\left(i+\frac{1}{2},j+\frac{1}{2},k\right) \\
&\quad+\Phi_{Exy}^n\left(i+\frac{1}{2},j+\frac{1}{2},k\right)-\Phi_{Eyx}^n\left(i+\frac{1}{2},j+\frac{1}{2},k\right)
\end{aligned} \tag{3.70c}$$

Note that the history variables in equations (3.70a-c) are temporally inhomogeneous, being defined at $t = n\Delta t$, similar to the magnetic source current terms. This method was found to be

computationally optimal and accurate by [212]. From this, update equations for magnetic flux may be acquired as follows:

$$B_x^{n+\frac{1}{2}}\left(i,j+\frac{1}{2},k+\frac{1}{2}\right)=B_x^n\left(i,j+\frac{1}{2},k+\frac{1}{2}\right)+\frac{\Delta t}{2\kappa_{zH}^k\Delta z}\left[E_y^{n+\frac{1}{2}}\left(i,j+\frac{1}{2},k+1\right)-E_y^{n+\frac{1}{2}}\left(i,j+\frac{1}{2},k\right)\right]$$
$$-\frac{\Delta t}{2\kappa_{yH}^j\Delta y}\left[E_z^n\left(i,j+1,k+\frac{1}{2}\right)-E_z^n\left(i,j,k+\frac{1}{2}\right)\right] \quad (3.71a)$$
$$-\frac{\Delta t}{2}\left[\mathcal{M}_x^{n+\frac{1}{2}}\left(i,j+\frac{1}{2},k+\frac{1}{2}\right)-\Phi_{Eyz}^n\left(i,j+\frac{1}{2},k+\frac{1}{2}\right)+\Phi_{Ezy}^n\left(i,j+\frac{1}{2},k+\frac{1}{2}\right)\right]$$

$$B_y^{n+\frac{1}{2}}\left(i+\frac{1}{2},j,k+\frac{1}{2}\right)=B_y^n\left(i+\frac{1}{2},j,k+\frac{1}{2}\right)+\frac{\Delta t}{2\kappa_{xH}^i\Delta x}\left[E_z^{n+\frac{1}{2}}\left(i+1,j,k+\frac{1}{2}\right)-E_z^{n+\frac{1}{2}}\left(i,j,k+\frac{1}{2}\right)\right]$$
$$-\frac{\Delta t}{2\kappa_{zH}^k\Delta z}\left[E_x^n\left(i+\frac{1}{2},j,k+1\right)-E_x^n\left(i+\frac{1}{2},j,k\right)\right] \quad (3.71b)$$
$$-\frac{\Delta t}{2}\left[\mathcal{M}_y^{n+\frac{1}{2}}\left(i+\frac{1}{2},j,k+\frac{1}{2}\right)-\Phi_{Ezx}^n\left(i+\frac{1}{2},j,k+\frac{1}{2}\right)+\Phi_{Exz}^n\left(i+\frac{1}{2},j,k+\frac{1}{2}\right)\right]$$

$$B_z^{n+\frac{1}{2}}\left(i+\frac{1}{2},j+\frac{1}{2},k\right)$$
$$=B_z^n\left(i+\frac{1}{2},j+\frac{1}{2},k\right)+\frac{\Delta t}{2\kappa_{yH}^j\Delta y}\left[E_x^{n+\frac{1}{2}}\left(i+\frac{1}{2},j+1,k\right)-E_x^{n+\frac{1}{2}}\left(i+\frac{1}{2},j,k\right)\right]$$
$$-\frac{\Delta t}{2\kappa_{xH}^i\Delta x}\left[E_y^n\left(i+1,j+\frac{1}{2},k\right)-E_y^n\left(i,j+\frac{1}{2},k\right)\right] \quad (3.71c)$$
$$-\frac{\Delta t}{2}\left[\mathcal{M}_z^{n+\frac{1}{2}}\left(i+\frac{1}{2},j+\frac{1}{2},k\right)-\Phi_{Exy}^n\left(i+\frac{1}{2},j+\frac{1}{2},k\right)+\Phi_{Eyx}^n\left(i+\frac{1}{2},j+\frac{1}{2},k\right)\right]$$

For these equations to be utilized the future electric fields (at time $t=(n+1/2)\Delta t$) must already be known and therefore the magnetic flux is updated after the electric fields.

#### 3.8.1.2 Second Sub-Iteration

The update equations for magnetic flux for the second sub-iterations may be acquired by alternating the direction of the implicit electric fields within the curl expression and forwarding all other time designations by a half time step as follows:

$$B_x^{n+1}\left(i,j+\frac{1}{2},k+\frac{1}{2}\right)=B_x^{n+\frac{1}{2}}\left(i,j+\frac{1}{2},k+\frac{1}{2}\right)+\frac{\Delta t}{2\kappa_{zH}^{k}\Delta z}\left[E_y^{n+\frac{1}{2}}\left(i,j+\frac{1}{2},k+1\right)-E_y^{n+\frac{1}{2}}\left(i,j+\frac{1}{2},k\right)\right]$$
$$-\frac{\Delta t}{2\kappa_{yH}^{j}\Delta y}\left[E_z^{n+1}\left(i,j+1,k+\frac{1}{2}\right)-E_y^{n+1}\left(i,j,k+\frac{1}{2}\right)\right] \quad (3.72a)$$
$$-\frac{\Delta t}{2}\left[\mathcal{M}_x^{n+\frac{1}{2}}\left(i,j+\frac{1}{2},k+\frac{1}{2}\right)-\Phi_{Eyz}^{n+\frac{1}{2}}\left(i,j+\frac{1}{2},k+\frac{1}{2}\right)+\Phi_{Ezy}^{n+\frac{1}{2}}\left(i,j+\frac{1}{2},k+\frac{1}{2}\right)\right]$$

$$B_y^{n+1}\left(i+\frac{1}{2},j,k+\frac{1}{2}\right)=B_y^{n+\frac{1}{2}}\left(i+\frac{1}{2},j,k+\frac{1}{2}\right)+\frac{\Delta t}{2\kappa_{xH}^{i}\Delta x}\left[E_z^{n+\frac{1}{2}}\left(i+1,j,k+\frac{1}{2}\right)-E_z^{n+\frac{1}{2}}\left(i,j,k+\frac{1}{2}\right)\right]$$
$$-\frac{\Delta t}{2\kappa_{zH}^{k}\Delta z}\left[E_x^{n+1}\left(i+\frac{1}{2},j,k+1\right)-E_x^{n+1}\left(i+\frac{1}{2},j,k\right)\right] \quad (3.72b)$$
$$-\frac{\Delta t}{2}\left[\mathcal{M}_y^{n+\frac{1}{2}}\left(i+\frac{1}{2},j,k+\frac{1}{2}\right)-\Phi_{Ezx}^{n+\frac{1}{2}}\left(i+\frac{1}{2},j,k+\frac{1}{2}\right)+\Phi_{Exz}^{n+\frac{1}{2}}\left(i+\frac{1}{2},j,k+\frac{1}{2}\right)\right]$$

$$B_z^{n+1}\left(i+\frac{1}{2},j+\frac{1}{2},k\right)$$
$$=B_z^{n+\frac{1}{2}}\left(i+\frac{1}{2},j+\frac{1}{2},k\right)+\frac{\Delta t}{2\kappa_{yH}^{j}\Delta y}\left[E_x^{n+\frac{1}{2}}\left(i+\frac{1}{2},j+1,k\right)-E_x^{n+\frac{1}{2}}\left(i+\frac{1}{2},j,k\right)\right]$$
$$-\frac{\Delta t}{2\kappa_{xH}^{i}\Delta x}\left[E_y^{n+1}\left(i+1,j+\frac{1}{2},k\right)-E_y^{n+1}\left(i,j+\frac{1}{2},k\right)\right] \quad (3.72c)$$
$$-\frac{\Delta t}{2}\left[\mathcal{M}_z^{n+\frac{1}{2}}\left(i+\frac{1}{2},j+\frac{1}{2},k\right)-\Phi_{Exy}^{n+\frac{1}{2}}\left(i+\frac{1}{2},j+\frac{1}{2},k\right)+\Phi_{Eyx}^{n+\frac{1}{2}}\left(i+\frac{1}{2},j+\frac{1}{2},k\right)\right]$$

Note that the magnetic source current is still rectified at the half time step as championed in [216][217]. Indeed, all source currents are evaluated at the half time step including the electric source currents present in Ampere's law.

### 3.8.2 Magnetic Constitutive Relations

Though a complex magnetic constitutive relation was defined in section 2.3.2, the simulations performed in Chapters 4 and 5 assume a diagonal permeability with no magnetic damping and no piezomagnetism, namely:

$$H_i=\beta_{ij}^{\mu}B_j,\qquad \beta_{ij}^{\mu}\mu_{jk}=\delta_{ik} \quad (2.174)$$

Where $\mu_{jk}$ is the permeability and $\beta_{ij}^{\mu}$ is the inverse permeability. Discretization of the x, y, and z components yields the following updates equations for the magnetic fields for the first sub-iteration:

$$H_x^{n+\frac{1}{2},i,j+\frac{1}{2},k+\frac{1}{2}} = \frac{1}{\mu_{xx}^{i,j+\frac{1}{2},k+\frac{1}{2}}} B_x^{n+\frac{1}{2},i,j+\frac{1}{2},k+\frac{1}{2}} \tag{3.73a}$$

$$H_y^{n+\frac{1}{2},i+\frac{1}{2},j,k+\frac{1}{2}} = \frac{1}{\mu_{yy}^{i+\frac{1}{2},j,k+\frac{1}{2}}} B_y^{n+\frac{1}{2},i+\frac{1}{2},j,k+\frac{1}{2}} \tag{3.73b}$$

$$H_z^{n+\frac{1}{2},i+\frac{1}{2},j+\frac{1}{2},k} = \frac{1}{\mu_{zz}^{i+\frac{1}{2},j+\frac{1}{2},k}} B_z^{n+\frac{1}{2},i+\frac{1}{2},j+\frac{1}{2},k} \tag{3.73c}$$

Where spatial interpolation is utilized for the material properties as usual and it is assumed that the magnetic flux is known at the time of the magnetic field update. Therefore, update the magnetic fields after the fluxes. For the 2nd sub-iteration, simply advance the time designations half a time step as follows:

$$H_x^{n+1,i,j+\frac{1}{2},k+\frac{1}{2}} = \frac{1}{\mu_{xx}^{i,j+\frac{1}{2},k+\frac{1}{2}}} B_x^{n+1,i,j+\frac{1}{2},k+\frac{1}{2}} \tag{3.74a}$$

$$H_y^{n+1,i+\frac{1}{2},j,k+\frac{1}{2}} = \frac{1}{\mu_{yy}^{i+\frac{1}{2},j,k+\frac{1}{2}}} B_y^{n+1,i+\frac{1}{2},j,k+\frac{1}{2}} \tag{3.74b}$$

$$H_z^{n+1,i+\frac{1}{2},j+\frac{1}{2},k} = \frac{1}{\mu_{zz}^{i+\frac{1}{2},j+\frac{1}{2},k}} B_z^{n+1,i+\frac{1}{2},j+\frac{1}{2},k} \tag{3.74c}$$

These constitutive relations are combined with Faraday's law as in Sections 3.6 and 3.7.

#### 3.8.2.1 First Sub-Iteration

Substitution of the magnetic constitutive relation into Faraday's law yields the following for the first sub-iteration:

$$H_x^{n+\frac{1}{2},i,j+\frac{1}{2},k+\frac{1}{2}} = H_x^{n,i,j+\frac{1}{2},k+\frac{1}{2}} + \frac{\Delta t}{2\mu_{xx}^{i,j+\frac{1}{2},k+\frac{1}{2}}\kappa_{zH}^{k}\Delta z}\left[E_y^{n+\frac{1}{2},i,j+\frac{1}{2},k+1} - E_y^{n+\frac{1}{2},i,j+\frac{1}{2},k}\right]$$

$$- \frac{\Delta t}{2\mu_{xx}^{i,j+\frac{1}{2},k+\frac{1}{2}}\kappa_{yH}^{j}\Delta y}\left[E_z^{n,i,j+1,k+\frac{1}{2}} - E_z^{ni,j,k+\frac{1}{2}}\right] \tag{3.75a}$$

$$- \frac{\Delta t}{2\mu_{xx}^{i,j+\frac{1}{2},k+\frac{1}{2}}}\left[\mathcal{M}_x^{n+\frac{1}{2},i,j+\frac{1}{2},k+\frac{1}{2}} - \Phi_{Eyz}^{ni,j+\frac{1}{2},k+\frac{1}{2}} + \Phi_{Ezy}^{n,i,j+\frac{1}{2},k+\frac{1}{2}}\right]$$

$$H_y^{n+\frac{1}{2},i+\frac{1}{2},j,k+\frac{1}{2}} = H_y^{ni+\frac{1}{2},j,k+\frac{1}{2}} + \frac{\Delta t}{2\mu_{yy}^{i+\frac{1}{2},j,k+\frac{1}{2}}\kappa_{xH}^{i}\Delta x}\left[E_z^{n+\frac{1}{2},i+1,j,k+\frac{1}{2}} - E_z^{n+\frac{1}{2},i,j,k+\frac{1}{2}}\right]$$

$$- \frac{\Delta t}{2\mu_{yy}^{i+\frac{1}{2},j,k+\frac{1}{2}}\kappa_{zH}^{k}\Delta z}\left[E_x^{n,i+\frac{1}{2},j,k+1} - E_x^{n,i+\frac{1}{2},j,k}\right] \tag{3.75b}$$

$$- \frac{\Delta t}{2\mu_{yy}^{i+\frac{1}{2},j,k+\frac{1}{2}}}\left[\mathcal{M}_y^{n+\frac{1}{2},i+\frac{1}{2},j,k+\frac{1}{2}} - \Phi_{Ezx}^{n,i+\frac{1}{2},j,k+\frac{1}{2}} + \Phi_{Exz}^{n,i+\frac{1}{2},j,k+\frac{1}{2}}\right]$$

$$H_z^{n+\frac{1}{2},i+\frac{1}{2},j+\frac{1}{2},k} = H_z^{n,i+\frac{1}{2},j+\frac{1}{2},k} + \frac{\Delta t}{2\mu_{zz}^{i+\frac{1}{2},j+\frac{1}{2},k}\kappa_{yH}^{j}\Delta y}\left[E_x^{n+\frac{1}{2},i+\frac{1}{2},j+1,k} - E_x^{n+\frac{1}{2},i+\frac{1}{2},j,k}\right]$$

$$- \frac{\Delta t}{2\mu_{zz}^{i+\frac{1}{2},j+\frac{1}{2},k}\kappa_{xH}^{i}\Delta x}\left[E_y^{n,i+1,j+\frac{1}{2},k} - E_y^{n,i,j+\frac{1}{2},k}\right] \tag{3.75c}$$

$$- \frac{\Delta t}{2\mu_{zz}^{i+\frac{1}{2},j+\frac{1}{2},k}}\left[\mathcal{M}_z^{n+\frac{1}{2},i+\frac{1}{2},j+\frac{1}{2},k} - \Phi_{Exy}^{n,i+\frac{1}{2},j+\frac{1}{2},k} + \Phi_{Eyx}^{n,i+\frac{1}{2},j+\frac{1}{2},k}\right]$$

Where the spatial definition is now included in the superscript of all fields since the equations are beginning to be unruly in length.

#### 3.8.2.2 Second Sub-Iteration

In the second sub-iteration the direction of implicit definition is swapped in Faraday's law yielding the following expressions:

$$H_x^{n+1,i,j+\frac{1}{2},k+\frac{1}{2}} = H_x^{n+\frac{1}{2},i,j+\frac{1}{2},k+\frac{1}{2}} + \frac{\Delta t}{2\mu_{xx}^{i,j+\frac{1}{2},k+\frac{1}{2}}\kappa_{zH}^{k}\Delta z}\left[E_y^{n+\frac{1}{2},i,j+\frac{1}{2},k+1} - E_y^{n+\frac{1}{2},i,j+\frac{1}{2},k}\right]$$

$$- \frac{\Delta t}{2\mu_{xx}^{i,j+\frac{1}{2},k+\frac{1}{2}}\kappa_{yH}^{j}\Delta y}\left[E_z^{n+1,i,j+1,k+\frac{1}{2}} - E_z^{n+1i,j,k+\frac{1}{2}}\right] \tag{3.76a}$$

$$- \frac{\Delta t}{2\mu_{xx}^{i,j+\frac{1}{2},k+\frac{1}{2}}}\left[\mathcal{M}_x^{n+\frac{1}{2},i,j+\frac{1}{2},k+\frac{1}{2}} - \Phi_{Eyz}^{n+\frac{1}{2},i,j+\frac{1}{2},k+\frac{1}{2}} + \Phi_{Ezy}^{n+\frac{1}{2},i,j+\frac{1}{2},k+\frac{1}{2}}\right]$$

$$H_y^{n+1,i+\frac{1}{2},j,k+\frac{1}{2}} = H_y^{n+\frac{1}{2}i+\frac{1}{2},j,k+\frac{1}{2}} + \frac{\Delta t}{2\mu_{yy}^{i+\frac{1}{2},j,k+\frac{1}{2}}\kappa_{xH}^{i}\Delta x}\left[E_z^{n+\frac{1}{2},i+1,j,k+\frac{1}{2}} - E_z^{n+\frac{1}{2},i,j,k+\frac{1}{2}}\right]$$

$$- \frac{\Delta t}{2\mu_{yy}^{i+\frac{1}{2},j,k+\frac{1}{2}}\kappa_{zH}^{k}\Delta z}\left[E_x^{n+1,i+\frac{1}{2},j,k+1} - E_x^{n+1,i+\frac{1}{2},j,k}\right] \tag{3.76b}$$

$$- \frac{\Delta t}{2\mu_{yy}^{i+\frac{1}{2},j,k+\frac{1}{2}}}\left[\mathcal{M}_y^{n+\frac{1}{2},i+\frac{1}{2},j,k+\frac{1}{2}} - \Phi_{Ezx}^{n+\frac{1}{2},i+\frac{1}{2},j,k+\frac{1}{2}} + \Phi_{Exz}^{n+\frac{1}{2},i+\frac{1}{2},j,k+\frac{1}{2}}\right]$$

$$H_z^{n+1,i+\frac{1}{2},j+\frac{1}{2},k} = H_z^{n+\frac{1}{2},i+\frac{1}{2},j+\frac{1}{2},k} + \frac{\Delta t}{2\mu_{zz}^{i+\frac{1}{2},j+\frac{1}{2},k}\kappa_{yH}^{j}\Delta y}\left[E_x^{n+\frac{1}{2},i+\frac{1}{2},j+1,k} - E_x^{n+\frac{1}{2},i+\frac{1}{2},j,k}\right]$$

$$- \frac{\Delta t}{2\mu_{zz}^{i+\frac{1}{2},j+\frac{1}{2},k}\kappa_{xH}^{i}\Delta x}\left[E_y^{n+1,i+1,j+\frac{1}{2},k} - E_y^{n+1,i,j+\frac{1}{2},k}\right] \tag{3.76c}$$

$$- \frac{\Delta t}{2\mu_{zz}^{i+\frac{1}{2},j+\frac{1}{2},k}}\left[\mathcal{M}_z^{n+\frac{1}{2},i+\frac{1}{2},j+\frac{1}{2},k} - \Phi_{Exy}^{n+\frac{1}{2},i+\frac{1}{2},j+\frac{1}{2},k} + \Phi_{Eyx}^{n+\frac{1}{2},i+\frac{1}{2},j+\frac{1}{2},k}\right]$$

These expressions are substituted into Ampere's law which is also modified to allow for graded PML regions. Ampere's law will be presented soon but first the electric constitutive relation shall be discussed.

### 3.8.3 Electric Constitutive Relation

The electric constitutive relation for a non-piezoelectric orthotropic material is, as previously presented in Section 3.7, repeated here for the 1st sub-iteration:

$$D_x^{n+\frac{1}{2},i+\frac{1}{2},j,k} = \epsilon_{xx}^{i+\frac{1}{2},j,k} E_x^{n+\frac{1}{2},i+\frac{1}{2},j,k} \tag{3.77a}$$

$$D_y^{n+\frac{1}{2},i,j+\frac{1}{2},k} = \epsilon_{yy}^{i,j+\frac{1}{2},k} E_y^{n+\frac{1}{2},i,j+\frac{1}{2},k} \tag{3.77b}$$

$$D_z^{n+\frac{1}{2},i,j,k+\frac{1}{2}} = \epsilon_{zz}^{i,j,k+\frac{1}{2}} E_z^{n+\frac{1}{2},i,j,k+\frac{1}{2}} \tag{3.77c}$$

Where all three components are now provided as all ADI expressions are explicitly provided herein. In the 2nd sub-iteration, the expressions are the same, simply advance all time designations by half a time step as follows:

$$D_x^{n+1,i+\frac{1}{2},j,k} = \epsilon_{xx}^{i+\frac{1}{2},j,k} E_x^{n+1,i+\frac{1}{2},j,k} \tag{3.78a}$$

$$D_y^{n+1,i,j+\frac{1}{2},k} = \epsilon_{yy}^{i,j+\frac{1}{2},k} E_y^{n+1,i,j+\frac{1}{2},k} \tag{3.78b}$$

$$D_z^{n+1,i,j,k+\frac{1}{2}} = \epsilon_{zz}^{i,j,k+\frac{1}{2}} E_z^{n+1,i,j,k+\frac{1}{2}} \tag{3.78c}$$

These relations will be substituted into modified Ampere's law which is presented in the following section.

### 3.8.4 Ampere's Law w/ CFS Stretched Coordinates

Now that the electrical constitutive relations have been derived, Ampere's law in finite difference form is written in preparation for deriving the ADI-FDTD equations. Additionally, Ampere's law is used to write update equations for the electric displacement fields ($D_i$), though these may be determined in post processing outside of the main update scheme. Recall that Ampere's law was modified by stretched coordinate metric $s_i$ in section 2.1.3 which, like the magnetic damping case and Faraday's law, included a decaying exponential term which allows for the use of a recursive convolution algorithm with the following history variables:

$$\Phi_{Hmq} = \int_{0^-}^{t} \zeta_q(t-\tau)\frac{\partial H_m(\tau)}{\partial q}d\tau = -\frac{\sigma_q}{\kappa_q^2\epsilon_0}\int_{0^-}^{t} e^{-\frac{1}{\epsilon_0}\left(\alpha_q+\frac{\sigma_q}{\kappa_q}\right)(t-\tau)}\frac{\partial H_m}{\partial q}d\tau, \quad \begin{matrix} m=x,y,z \\ q=x,y,z \\ m\neq q \end{matrix} \tag{2.28}$$

Note that, again, a history variable which is zero in free space (when $\sigma_q = 0$) is attained and say that a $= \frac{1}{\epsilon_0}\left(\alpha_q + \frac{\sigma_q}{\kappa_q}\right)$ is the inverse relaxation time. Therefore, Ampere's law is as follows:

$$\dot{D}_i + \sigma_{ij}E_j + J_i^s = \epsilon_{ij'k}H_{k,j'} - \epsilon_{ijk}\Phi_{H_{jk}} \tag{2.33}$$

$$\Phi_{H_{jk}} = \begin{bmatrix} 0 & \Phi_{H_{xy}} & \Phi_{H_{xz}} \\ \Phi_{H_{yx}} & 0 & \Phi_{H_{yz}} \\ \Phi_{H_{zx}} & \Phi_{H_{zy}} & 0 \end{bmatrix} \tag{2.35a}$$

Which utilize the following primed coordinates:

$$dx' = \kappa_x(x)dx, \qquad dy' = \kappa_y(y)dy, \qquad dz' = s_z(z)dz$$

The history variables will be treated first before returning to the full Ampere's law above. For input into a finite difference algorithm say $t^{n+1/2} = t^n + \Delta t^{n+1/2}$, where the superscript indicates the $n^{th}$ time step. For a fixed step solver and two sub-iterations we have time increment $\Delta t^{n+1/2} = \Delta t/2$, for all $n$ but the current notation will be kept until the end of the derivation. The history variables at times $t^n$ and $t^{n+1/2}$ are as follows:

$$\Phi_{Hmq}^{n} = -\frac{\sigma_q}{\kappa_q^2 \epsilon_0} \int_{0^-}^{t^n} e^{-\mathrm{a}(t^n - \tau)} \frac{\partial H_m}{\partial q} d\tau \tag{3.79a}$$

$$\Phi_{Hmq}^{n+\frac{1}{2}} = -\frac{\sigma_q}{\kappa_q^2 \epsilon_0} \int_{0^-}^{t^{n+\frac{1}{2}}} e^{-\mathrm{a}\left(t^{n+\frac{1}{2}} - \tau\right)} \frac{\partial H_m}{\partial q} d\tau = -\frac{\sigma_q}{\kappa_q^2 \epsilon_0} \int_{0^-}^{t^n + \Delta t^{n+1/2}} e^{-\mathrm{a}\left(t^n + \Delta t^{n+\frac{1}{2}} - \tau\right)} \frac{\partial H_m}{\partial q} d\tau \tag{3.79b}$$

Where the $\Phi_{Hmq}^{n+1/2}$ integral may be split into two and the exponential term expanded as follows:

$$\Phi_{Hmq}^{n+\frac{1}{2}} = -\frac{\sigma_q}{\kappa_q^2 \epsilon_0} \left\{ \int_{0^-}^{t^n} e^{-\mathrm{a}\left(\Delta t^{n+\frac{1}{2}}\right)} e^{-\mathrm{a}(t^n - \tau)} \frac{\partial H_m}{\partial q} d\tau + \int_{t^n}^{t^{n+1/2}} e^{-\mathrm{a}\left(t^{n+\frac{1}{2}} - \tau\right)} \frac{\partial H_m}{\partial q} d\tau \right\} \tag{3.79c}$$

Substituting (3.79a) into (3.79c) yields:

$$\Phi_{Hmq}^{n+\frac{1}{2}} = e^{-\mathrm{a}\left(\Delta t^{n+\frac{1}{2}}\right)} \Phi_{Hmq}^{n} - \frac{\sigma_q}{\kappa_q^2 \epsilon_0} \int_{t^n}^{t^{n+1/2}} e^{-\mathrm{a}\left(t^{n+\frac{1}{2}} - \tau\right)} \frac{\partial H_m}{\partial q} d\tau \tag{3.79d}$$

Assuming that the time step is small enough, the midpoint rule may be used to approximate the magnetic field gradient within the integrand, but, as noted by [211], more efficient and accurate results may be obtained if the time designation is as follows:

$$\int_{t^n}^{t^{n+\frac{1}{2}}} e^{-\mathrm{a}\left(t^{n+\frac{1}{2}} - \tau\right)} \frac{\partial H_m}{\partial q} d\tau \cong \int_{t^n}^{t^{n+1/2}} e^{-\mathrm{a}\left(t^{n+\frac{1}{2}} - \tau\right)} d\tau \left[\frac{\partial H_m}{\partial q}\right]_{\tau = t^{n+1/2}}$$

$$= \left[\frac{1}{\mathrm{a}} e^{-\mathrm{a}\left(t^{n+\frac{1}{2}}-\tau\right)}\right]_{t^n}^{t^{n+1/2}} \left(\frac{\Delta H_m^{n+\frac{1}{2}}}{\Delta q}\right) = \frac{1}{\mathrm{a}}\left(1 - e^{-\mathrm{a}\Delta t^{n+\frac{1}{2}}}\right)\left(\frac{\Delta H_m^{n+\frac{1}{2}}}{\Delta q}\right)$$

Therefore, the history variable update equation is as follows:

$$\Phi_{Hmq}^{n+\frac{1}{2}} = e^{-\mathrm{a}\Delta t^{n+\frac{1}{2}}}\Phi_{Hmq}^{n} + \frac{\sigma_q}{\kappa_q^2 \epsilon_0}\frac{1}{\mathrm{a}}\left(e^{-\mathrm{a}\Delta t^{n+\frac{1}{2}}} - 1\right)\left(\frac{\Delta H_m^{n+\frac{1}{2}}}{\Delta q}\right) \tag{3.79e}$$

Where the first term on the right-hand side is the time decay of the history variable at time step $t^n$ after time increment $\Delta t^{n+1/2}$, and the second term adds on the additional component of the history variable due to field increment $\Delta H^{n+1/2}$, now substitute in $\Delta t^{n+1/2} = \Delta t/2$, as well as the inverse relaxation time constant, to get the history variable update equation:

$$\Phi_{Hmq}^{n+\frac{1}{2}} = e^{-\left(\alpha_q + \frac{\sigma_q}{\kappa_q}\right)\frac{\Delta t}{2\epsilon_0}}\Phi_{Hmq}^{n} + \frac{\sigma_q}{\kappa_q(\kappa_q\alpha_q + \sigma_q)}\left[e^{-\left(\alpha_q + \frac{\sigma_q}{\kappa_q}\right)\frac{\Delta t}{2\epsilon_0}} - 1\right]\left(\frac{\Delta H_m^{n+\frac{1}{2}}}{\Delta q}\right) \tag{3.80}$$

So far, no spatial indices have been included in order to facilitate a general derivation of the history variable update equations. However, the history variables will, in general, vary in space. For example, the components of the stretched coordinate metric can vary in the direction of stretching, but only in this direction so that the planar boundaries remain plane with a consistent number of cells. The $\Delta H_m$ term will also have unique spatial indices depending on the history variable. For clarity, all the history variables are presented in Table 3-3.

| | |
|---|---|
| $\Phi_{Hzy}^{n+\frac{1}{2}}\left(i+\frac{1}{2},j,k\right)$ | $e^{-\left(\alpha_y^j + \frac{\sigma_y^j}{\kappa_y^j}\right)\frac{\Delta t}{2\epsilon_0}}\Phi_{Hzy}^{n} + \frac{\sigma_y^j}{\kappa_y^j\alpha_y^j + \sigma_y^j}\left[e^{-\left(\alpha_y^j + \frac{\sigma_y^j}{\kappa_y^j}\right)\frac{\Delta t}{2\epsilon_0}} - 1\right]\left(\frac{1}{\kappa_y^j \Delta y}\right)\left(H_z^{n+\frac{1}{2}}\left(i+\frac{1}{2},j+\frac{1}{2},k\right) - H_z^{n+\frac{1}{2}}\left(i+\frac{1}{2},j-\frac{1}{2},k\right)\right)$ |
| $\Phi_{Hyz}^{n+\frac{1}{2}}\left(i+\frac{1}{2},j,k\right)$ | $e^{-\left(\alpha_z^k + \frac{\sigma_z^k}{\kappa_z^k}\right)\frac{\Delta t}{2\epsilon_0}}\Phi_{Hyz}^{n} + \frac{\sigma_z^k}{\kappa_z^k\alpha_z^k + \sigma_z^k}\left[e^{-\left(\alpha_z^k + \frac{\sigma_z^k}{\kappa_z^k}\right)\frac{\Delta t}{2\epsilon_0}} - 1\right]\left(\frac{1}{\kappa_z^k \Delta z}\right)\left(H_y^{n+\frac{1}{2}}\left(i+\frac{1}{2},j,k+\frac{1}{2}\right) - H_y^{n+\frac{1}{2}}\left(i+\frac{1}{2},j,k-\frac{1}{2}\right)\right)$ |
| $\Phi_{Hxz}^{n+\frac{1}{2}}\left(i,j+\frac{1}{2},k\right)$ | $e^{-\left(\alpha_z^k + \frac{\sigma_z^k}{\kappa_z^k}\right)\frac{\Delta t}{2\epsilon_0}}\Phi_{Hxz}^{n} + \frac{\sigma_z^k}{\kappa_z^k\alpha_z^k + \sigma_z^k}\left[e^{-\left(\alpha_z^k + \frac{\sigma_z^k}{\kappa_z^k}\right)\frac{\Delta t}{2\epsilon_0}} - 1\right]\left(\frac{1}{\kappa_z^k \Delta z}\right)\left(H_x^{n+\frac{1}{2}}\left(i,j+\frac{1}{2},k+\frac{1}{2}\right) - H_x^{n+\frac{1}{2}}\left(i,j+\frac{1}{2},k-\frac{1}{2}\right)\right)$ |

| | |
|---|---|
| $\Phi_{Hzx}^{n+\frac{1}{2}}\left(i,j+\frac{1}{2},k\right)$ | $e^{-\left(\alpha_x^i+\frac{\sigma_x^i}{\kappa_x^i}\right)\frac{\Delta t}{2\epsilon_0}}\Phi_{Hzx}^n+\frac{\sigma_x^i}{\kappa_x^i\alpha_x^i+\sigma_x^i}\left[e^{-\left(\alpha_x^i+\frac{\sigma_x^i}{\kappa_x^i}\right)\frac{\Delta t}{2\epsilon_0}}-1\right]\left(\frac{1}{\kappa_x^i\Delta x}\right)\left(H_z^{n+\frac{1}{2}}\left(i+\frac{1}{2},j+\frac{1}{2},k\right)-H_z^{n+\frac{1}{2}}\left(i-\frac{1}{2},j+\frac{1}{2},k\right)\right)$ |
| $\Phi_{Hyx}^{n+\frac{1}{2}}\left(i,j,k+\frac{1}{2}\right)$ | $e^{-\left(\alpha_x^i+\frac{\sigma_x^i}{\kappa_x^i}\right)\frac{\Delta t}{2\epsilon_0}}\Phi_{Hyx}^n+\frac{\sigma_x^i}{\kappa_x^i\alpha_x^i+\sigma_x^i}\left[e^{-\left(\alpha_x^i+\frac{\sigma_x^i}{\kappa_x^i}\right)\frac{\Delta t}{2\epsilon_0}}-1\right]\left(\frac{1}{\kappa_x^i\Delta x}\right)\left(H_y^{n+\frac{1}{2}}\left(i+\frac{1}{2},j,k+\frac{1}{2}\right)-H_y^{n+\frac{1}{2}}\left(i-\frac{1}{2},j,k+\frac{1}{2}\right)\right)$ |
| $\Phi_{Hxy}^{n+\frac{1}{2}}\left(i,j,k+\frac{1}{2}\right)$ | $e^{-\left(\alpha_y^j+\frac{\sigma_y^j}{\kappa_y^j}\right)\frac{\Delta t}{2\epsilon_0}}\Phi_{Hxy}^n+\frac{\sigma_y^j}{\kappa_y^j\alpha_y^j+\sigma_y^j}\left[e^{-\left(\alpha_y^j+\frac{\sigma_y^j}{\kappa_y^j}\right)\frac{\Delta t}{2\epsilon_0}}-1\right]\left(\frac{1}{\kappa_y^j\Delta y}\right)\left(H_x^{n+\frac{1}{2}}\left(i,j+\frac{1}{2},k+\frac{1}{2}\right)-H_x^{n+\frac{1}{2}}\left(i,j-\frac{1}{2},k+\frac{1}{2}\right)\right)$ |

Table 3-3: History variables for modified Ampere's law.

These expressions will be used in the subsequent two sections to derive the finite difference form of the modified Ampere's law for the first and second sub-iterations respectively. Recall that an additional subscript, E or H, is required for the constituents of the stretched coordinate metric ($\kappa, \sigma,$ and $\alpha$) as shown in Figure 3-18. As a final note, the history variables in Table 3-3 may be adjusted for algorithms without sub-iterations by replacing $n+1/2$ with $n+1$, as well as all $\Delta t/2$ terms with $\Delta t$.

#### 3.8.4.1 First Sub-iteration

The modified Ampere's law with source currents and conductivity may be discretized into finite difference form as follows:

$$\begin{aligned}\frac{2}{\Delta t}\left[D_x^{n+\frac{1}{2}}\left(i+\frac{1}{2},j,k\right)-D_x^n\left(i+\frac{1}{2},j,k\right)\right]&\\ =\frac{1}{\kappa_{yE}^j\Delta y}\left[H_z^{n+\frac{1}{2}}\left(i+\frac{1}{2},j+\frac{1}{2},k\right)-H_z^{n+\frac{1}{2}}\left(i+\frac{1}{2},j-\frac{1}{2},k\right)\right]&\\ -\frac{1}{\kappa_{zE}^k\Delta z}\left[H_y^n\left(i+\frac{1}{2},j,k+\frac{1}{2}\right)-H_y^n\left(i+\frac{1}{2},j,k-\frac{1}{2}\right)\right]-J_x^c-J_x^S+\Phi_{Hzy}^n&\\ -\Phi_{Hyz}^n&\end{aligned} \tag{3.81a}$$

$$\frac{2}{\Delta t}\left[D_y^{n+\frac{1}{2}}\left(i,j+\frac{1}{2},k\right)-D_y^{n}\left(i,j+\frac{1}{2},k\right)\right]$$
$$=\frac{1}{\kappa_{zE}^{k}\Delta z}\left[H_x^{n+\frac{1}{2}}\left(i,j+\frac{1}{2},k+\frac{1}{2}\right)-H_x^{n+\frac{1}{2}}\left(i,j+\frac{1}{2},k-\frac{1}{2}\right)\right]$$
$$-\frac{1}{\kappa_{xE}^{i}\Delta x}\left[H_z^{n}\left(i+\frac{1}{2},j+\frac{1}{2},k\right)-H_z^{n}\left(i-\frac{1}{2},j+\frac{1}{2},k\right)\right]-J_y^{c}-J_y^{S}+\Phi_{Hxz}^{n} \quad (3.81b)$$
$$-\Phi_{Hzx}^{n}$$

$$\frac{2}{\Delta t}\left[D_z^{n+\frac{1}{2}}\left(i,j,k+\frac{1}{2}\right)-D_z^{n}\left(i,j,k+\frac{1}{2}\right)\right]$$
$$=\frac{1}{\kappa_{xE}^{i}\Delta x}\left[H_y^{n+\frac{1}{2}}\left(i+\frac{1}{2},j,k+\frac{1}{2}\right)-H_y^{n+\frac{1}{2}}\left(i-\frac{1}{2},j,k+\frac{1}{2}\right)\right]$$
$$-\frac{1}{\kappa_{yE}^{j}\Delta y}\left[H_x^{n}\left(i,j+\frac{1}{2},k+\frac{1}{2}\right)-H_x^{n}\left(i,j-\frac{1}{2},k+\frac{1}{2}\right)\right]-J_z^{c}-J_z^{S}+\Phi_{Hyx}^{n} \quad (3.81c)$$
$$-\Phi_{Hxy}^{n}$$

Note that $H_{z,y}$, $H_{x,z}$, and $H_{y,x}$ in (3.81a), (3.81b), and (3.81c) respectively are defined implicitly at the future time step. The history variables $\Phi_{Hmq}^{n}$ are defined at time $n\Delta t$, rather than $(n+1/2)\Delta t$, since numerical experiments performed by previous investigators have shown that this time sampling is more efficient and accurate [211]. As such, the history terms will not affect the tridiagonal matrix. The $J^c$ and $J^S$ terms are the conduction and source currents respectively, with the time sampling left intentionally ambiguous since special considerations must be made. It is intuitive to sample the source current $J^S$ such that temporal homogeneity is maintained, but it has been shown that time sampling should occur at $t=(n+1/2)\Delta t$ for both sub-iterations [216][217], which curiously produces an overall consistent scheme despite the loss of consistency for each half time step. Note that this corresponds to a forward scheme in the 1st sub-iteration and a backward scheme in the 2nd sub-iteration, therefore this may be thought of as a forward-backward scheme. For the conduction current term, a widely utilized method is to take a temporal average of the electric field as follows:

$$J_q^c = \frac{\sigma_{qq}}{2}\left[E_q^{n+\frac{1}{2}}\left(i,j,k+\frac{1}{2}\right) + E_q^n\left(i,j,k+\frac{1}{2}\right)\right] \tag{3.82}$$

Taflove [178] also referred to this as a semi-implicit approximation, which is appealing as temporal homogeneity is maintained. This method does indeed work but produces stability issues for highly conductive media as will been demonstrated shortly. For now, substitution of (3.82) back into Ampere's law (3.81a-c) yields the following:

$$\begin{aligned}
&\frac{2}{\Delta t}\left[D_x^{n+\frac{1}{2}}\left(i+\frac{1}{2},j,k\right) - D_x^n\left(i+\frac{1}{2},j,k\right)\right] \\
&\quad = \frac{1}{\kappa_{yE}^j \Delta y}\left[H_z^{n+\frac{1}{2}}\left(i+\frac{1}{2},j+\frac{1}{2},k\right) - H_z^{n+\frac{1}{2}}\left(i+\frac{1}{2},j-\frac{1}{2},k\right)\right] \\
&\quad - \frac{1}{\kappa_{zE}^k \Delta z}\left[H_y^n\left(i+\frac{1}{2},j,k+\frac{1}{2}\right) - H_y^n\left(i+\frac{1}{2},j,k-\frac{1}{2}\right)\right] \\
&\quad - \frac{\sigma_{xx}}{2}\left[E_x^{n+\frac{1}{2}}\left(i+\frac{1}{2},j,k\right) + E_x^n\left(i+\frac{1}{2},j,k\right)\right] - J_{xS}^{n+\frac{1}{2}}\left(i+\frac{1}{2},j,k\right) + \Phi_{Hzy}^n - \Phi_{Hyz}^n
\end{aligned} \tag{3.83a}$$

$$\begin{aligned}
&\frac{2}{\Delta t}\left[D_y^{n+\frac{1}{2}}\left(i,j+\frac{1}{2},k\right) - D_y^n\left(i,j+\frac{1}{2},k\right)\right] \\
&\quad = \frac{1}{\kappa_{zE}^k \Delta z}\left[H_x^{n+\frac{1}{2}}\left(i,j+\frac{1}{2},k+\frac{1}{2}\right) - H_x^{n+\frac{1}{2}}\left(i,j+\frac{1}{2},k-\frac{1}{2}\right)\right] \\
&\quad - \frac{1}{\kappa_{xE}^i \Delta x}\left[H_z^n\left(i+\frac{1}{2},j+\frac{1}{2},k\right) - H_z^n\left(i-\frac{1}{2},j+\frac{1}{2},k\right)\right] \\
&\quad - \frac{\sigma_{xx}}{2}\left[E_y^{n+\frac{1}{2}}\left(i,j+\frac{1}{2},k\right) + E_y^n\left(i,j+\frac{1}{2},k\right)\right] - J_{yS}^{n+\frac{1}{2}}\left(i,j+\frac{1}{2},k\right) + \Phi_{Hxz}^n - \Phi_{Hzx}^n
\end{aligned} \tag{3.83b}$$

$$\begin{aligned}
&\frac{2}{\Delta t}\left[D_z^{n+\frac{1}{2}}\left(i,j,k+\frac{1}{2}\right) - D_z^n\left(i,j,k+\frac{1}{2}\right)\right] \\
&\quad = \frac{1}{\kappa_{xE}^i \Delta x}\left[H_y^{n+\frac{1}{2}}\left(i+\frac{1}{2},j,k+\frac{1}{2}\right) - H_y^{n+\frac{1}{2}}\left(i-\frac{1}{2},j,k+\frac{1}{2}\right)\right] \\
&\quad - \frac{1}{\kappa_{yE}^j \Delta y}\left[H_x^n\left(i,j+\frac{1}{2},k+\frac{1}{2}\right) - H_x^n\left(i,j-\frac{1}{2},k+\frac{1}{2}\right)\right] \\
&\quad - \frac{\sigma_{zz}}{2}\left[E_z^{n+\frac{1}{2}}\left(i,j,k+\frac{1}{2}\right) + E_z^n\left(i,j,k+\frac{1}{2}\right)\right] - J_{zS}^{n+\frac{1}{2}}\left(i,j,k+\frac{1}{2}\right) + \Phi_{Hyx}^n - \Phi_{Hxy}^n
\end{aligned} \tag{3.83c}$$

Equations (3.83a-c) may be used to write update equations for the electric displacements:

$$
\begin{aligned}
D_x^{n+\frac{1}{2}}\left(i+\frac{1}{2},j,k\right) &= D_x^n\left(i+\frac{1}{2},j,k\right)+\frac{\Delta t}{2\kappa_{yE}^j\Delta y}\left[H_z^{n+\frac{1}{2}}\left(i+\frac{1}{2},j+\frac{1}{2},k\right)-H_z^{n+\frac{1}{2}}\left(i+\frac{1}{2},j-\frac{1}{2},k\right)\right]\\
&-\frac{\Delta t}{2\kappa_{zE}^k\Delta z}\left[H_y^n\left(i+\frac{1}{2},j,k+\frac{1}{2}\right)-H_y^n\left(i+\frac{1}{2},j,k-\frac{1}{2}\right)\right]\\
&-\frac{\sigma_{xx}\Delta t}{4}\left[E_x^{n+\frac{1}{2}}\left(i+\frac{1}{2},j,k\right)+E_x^n\left(i+\frac{1}{2},j,k\right)\right]-\frac{\Delta t}{2}J_{xS}^{n+\frac{1}{2}}\left(i+\frac{1}{2},j,k\right)\\
&+\frac{\Delta t}{2}\left[\Phi_{Hzy}^n\left(i+\frac{1}{2},j,k\right)-\Phi_{Hyz}^n\left(i+\frac{1}{2},j,k\right)\right]
\end{aligned}
\tag{3.84a}
$$

$$
\begin{aligned}
D_y^{n+\frac{1}{2}}\left(i,j+\frac{1}{2},k\right) &= D_y^n\left(i,j+\frac{1}{2},k\right)+\frac{\Delta t}{2\kappa_{zE}^k\Delta z}\left[H_x^{n+\frac{1}{2}}\left(i,j+\frac{1}{2},k+\frac{1}{2}\right)-H_x^{n+\frac{1}{2}}\left(i,j+\frac{1}{2},k-\frac{1}{2}\right)\right]\\
&-\frac{\Delta t}{2\kappa_{xE}^i\Delta x}\left[H_z^n\left(i+\frac{1}{2},j+\frac{1}{2},k\right)-H_z^n\left(i-\frac{1}{2},j+\frac{1}{2},k\right)\right]\\
&-\frac{\sigma_{xx}\Delta t}{4}\left[E_y^{n+\frac{1}{2}}\left(i,j+\frac{1}{2},k\right)+E_y^n\left(i,j+\frac{1}{2},k\right)\right]-\frac{\Delta t}{2}J_{yS}^{n+\frac{1}{2}}\left(i,j+\frac{1}{2},k\right)\\
&+\frac{\Delta t}{2}\left[\Phi_{Hxz}^n\left(i,j+\frac{1}{2},k\right)-\Phi_{Hzx}^n\left(i,j+\frac{1}{2},k\right)\right]
\end{aligned}
\tag{3.84b}
$$

$$
\begin{aligned}
D_z^{n+\frac{1}{2}}\left(i,j,k+\frac{1}{2}\right) &= D_z^n\left(i,j,k+\frac{1}{2}\right)+\frac{\Delta t}{2\kappa_{xE}^i\Delta x}\left[H_y^{n+\frac{1}{2}}\left(i+\frac{1}{2},j,k+\frac{1}{2}\right)-H_y^{n+\frac{1}{2}}\left(i-\frac{1}{2},j,k+\frac{1}{2}\right)\right]\\
&-\frac{\Delta t}{2\kappa_{yE}^j\Delta y}\left[H_x^n\left(i,j+\frac{1}{2},k+\frac{1}{2}\right)-H_x^n\left(i,j-\frac{1}{2},k+\frac{1}{2}\right)\right]\\
&-\frac{\sigma_{zz}\Delta t}{4}\left[E_z^{n+\frac{1}{2}}\left(i,j,k+\frac{1}{2}\right)+E_z^n\left(i,j,k+\frac{1}{2}\right)\right]-\frac{\Delta t}{2}J_{zS}^{n+\frac{1}{2}}\left(i,j,k+\frac{1}{2}\right)\\
&+\frac{\Delta t}{2}\left[\Phi_{Hyx}^n\left(i,j,k+\frac{1}{2}\right)-\Phi_{Hxy}^n\left(i,j,k+\frac{1}{2}\right)\right]
\end{aligned}
\tag{3.84c}
$$

Now the finite difference forms of Ampere's law (3.83a-c) may be treated for use in the ADI-FDTD equations by first substituting in the electric constitutive relations (3.77a-c):

$$
\begin{aligned}
\epsilon_{xx}^{i+\frac{1}{2},j,k}E_x^{n+\frac{1}{2},i+\frac{1}{2},j,k} &= \epsilon_{xx}^{i+\frac{1}{2},j,k}E_x^{n,i+\frac{1}{2},j,k}+\frac{\Delta t}{2\kappa_{yE}^j\Delta y}\left[H_z^{n+\frac{1}{2},i+\frac{1}{2},j+\frac{1}{2},k}-H_z^{n+\frac{1}{2},i+\frac{1}{2},j-\frac{1}{2},k}\right]\\
&-\frac{\Delta t}{2\kappa_{zE}^k\Delta z}\left[H_y^{n,i+\frac{1}{2},j,k+\frac{1}{2}}-H_y^{n,i+\frac{1}{2},j,k-\frac{1}{2}}\right]-\frac{\sigma_{xx}^{i+\frac{1}{2},j,k}\Delta t}{4}\left[E_x^{n+\frac{1}{2},i+\frac{1}{2},j,k}+E_x^{n,i+\frac{1}{2},j,k}\right]\\
&-\frac{\Delta t}{2}J_{xS}^{n+\frac{1}{2},i+\frac{1}{2},j,k}+\frac{\Delta t}{2}\left[\Phi_{Hzy}^{n,i+\frac{1}{2},j,k}-\Phi_{Hyz}^{n,i+\frac{1}{2},j,k}\right]
\end{aligned}
\tag{3.85a}
$$

$$\epsilon_{yy}^{i,j+\frac{1}{2},k} E_y^{n+\frac{1}{2},i,j+\frac{1}{2},k} = \epsilon_{yy}^{i,j+\frac{1}{2},k} E_y^{n,i,j+\frac{1}{2},k} + \frac{\Delta t}{2\kappa_{zE}^{k}\Delta z}\left[H_x^{n+\frac{1}{2},i,j+\frac{1}{2},k+\frac{1}{2}} - H_x^{n+\frac{1}{2},i,j+\frac{1}{2},k-\frac{1}{2}}\right]$$

$$- \frac{\Delta t}{2\kappa_{xE}^{i}\Delta x}\left[H_z^{n,i+\frac{1}{2},j+\frac{1}{2},k} - H_z^{n,i-\frac{1}{2},j+\frac{1}{2},k}\right] - \frac{\sigma_{yy}^{i,j+\frac{1}{2},k}\Delta t}{4}\left[E_y^{n+\frac{1}{2},i,j+\frac{1}{2},k} + E_y^{n,i,j+\frac{1}{2},k}\right] \tag{3.85b}$$

$$- \frac{\Delta t}{2} J_{yS}^{n+\frac{1}{2},i,j+\frac{1}{2},k} + \frac{\Delta t}{2}\left[\Phi_{Hxz}^{n,i,j+\frac{1}{2},k} - \Phi_{Hzx}^{n,i,j+\frac{1}{2},k}\right]$$

$$\epsilon_{zz}^{i,j,k+\frac{1}{2}} E_z^{n+\frac{1}{2},i,j,k+\frac{1}{2}} = \epsilon_{zz}^{i,j,k+\frac{1}{2}} E_z^{n,i,j,k+\frac{1}{2}} + \frac{\Delta t}{2\kappa_{xE}^{i}\Delta x}\left[H_y^{n+\frac{1}{2},i+\frac{1}{2},j,k+\frac{1}{2}} - H_y^{n+\frac{1}{2},i-\frac{1}{2},j,k+\frac{1}{2}}\right]$$

$$- \frac{\Delta t}{2\kappa_{yE}^{j}\Delta y}\left[H_x^{n,i,j+\frac{1}{2},k+\frac{1}{2}} - H_x^{n,i,j-\frac{1}{2},k+\frac{1}{2}}\right] - \frac{\sigma_{zz}^{i,j,k+\frac{1}{2}}\Delta t}{4}\left[E_z^{n+\frac{1}{2},i,j,k+\frac{1}{2}} + E_z^{n,i,j,k+\frac{1}{2}}\right] \tag{3.85c}$$

$$- \frac{\Delta t}{2} J_{zS}^{n+\frac{1}{2},i,j,k+\frac{1}{2}} + \frac{\Delta t}{2}\left[\Phi_{Hyx}^{n,i,j,k+\frac{1}{2}} - \Phi_{Hxy}^{n,i,j,k+\frac{1}{2}}\right]$$

The spatial definitions of the fields in (3.85a-c) are now included in the superscripts as the expressions are becoming lengthy. Rearranging terms yields the following:

$$E_x^{n+\frac{1}{2},i+\frac{1}{2},j,k} = \left[\frac{4\epsilon_{xx}^{i+\frac{1}{2},j,k} - \sigma_{xx}^{i+\frac{1}{2},j,k}\Delta t}{4\epsilon_{xx}^{i+\frac{1}{2},j,k} + \sigma_{xx}^{i+\frac{1}{2},j,k}\Delta t}\right] E_x^{n,i+\frac{1}{2},j,k}$$

$$+ \frac{2\Delta t}{\left(4\epsilon_{xx}^{i+\frac{1}{2},j,k} + \sigma_{xx}^{i+\frac{1}{2},j,k}\Delta t\right)\kappa_{yE}^{j}\Delta y}\left[H_z^{n+\frac{1}{2},i+\frac{1}{2},j+\frac{1}{2},k} - H_z^{n+\frac{1}{2},i+\frac{1}{2},j-\frac{1}{2},k}\right]$$

$$- \frac{2\Delta t}{\left(4\epsilon_{xx}^{i+\frac{1}{2},j,k} + \sigma_{xx}^{i+\frac{1}{2},j,k}\Delta t\right)\kappa_{zE}^{k}\Delta z}\left[H_y^{n,i+\frac{1}{2},j,k+\frac{1}{2}} - H_y^{n,i+\frac{1}{2},j,k-\frac{1}{2}}\right] \tag{3.86a}$$

$$- \frac{2\Delta t}{\left(4\epsilon_{xx}^{i+\frac{1}{2},j,k} + \sigma_{xx}^{i+\frac{1}{2},j,k}\Delta t\right)}\left[J_{xS}^{n+\frac{1}{2},i+\frac{1}{2},j,k} - \Phi_{Hzy}^{n,i+\frac{1}{2},j,k} + \Phi_{Hyz}^{n,i+\frac{1}{2},j,k}\right]$$

$$
\begin{aligned}
E_y^{n+\frac{1}{2},i,j+\frac{1}{2},k} = & \left[\frac{4\epsilon_{yy}^{i,j+\frac{1}{2},k} - \sigma_{yy}^{i,j+\frac{1}{2},k}\Delta t}{4\epsilon_{yy}^{i,j+\frac{1}{2},k} + \sigma_{yy}^{i,j+\frac{1}{2},k}\Delta t}\right] E_y^{n,i,j+\frac{1}{2},k} \\
& + \frac{2\Delta t}{\left(4\epsilon_{yy}^{i,j+\frac{1}{2},k} + \sigma_{yy}^{i,j+\frac{1}{2},k}\Delta t\right)\kappa_{zE}^{k}\Delta z}\left[H_x^{n+\frac{1}{2},i,j+\frac{1}{2},k+\frac{1}{2}} - H_x^{n+\frac{1}{2},i,j+\frac{1}{2},k-\frac{1}{2}}\right] \\
& - \frac{2\Delta t}{\left(4\epsilon_{yy}^{i,j+\frac{1}{2},k} + \sigma_{yy}^{i,j+\frac{1}{2},k}\Delta t\right)\kappa_{xE}^{i}\Delta x}\left[H_z^{n,i+\frac{1}{2},j+\frac{1}{2},k} - H_z^{n,i-\frac{1}{2},j+\frac{1}{2},k}\right] \\
& - \frac{2\Delta t}{\left(4\epsilon_{yy}^{i,j+\frac{1}{2},k} + \sigma_{yy}^{i,j+\frac{1}{2},k}\Delta t\right)}\left[J_{yS}^{n+\frac{1}{2},i,j+\frac{1}{2},k} - \Phi_{Hxz}^{n,i,j+\frac{1}{2},k} + \Phi_{Hzx}^{n,i,j+\frac{1}{2},k}\right]
\end{aligned}
\tag{3.86b}
$$

$$
\begin{aligned}
E_z^{n+\frac{1}{2},i,j,k+\frac{1}{2}} = & \left[\frac{4\epsilon_{zz}^{i,j,k+\frac{1}{2}} - \sigma_{zz}^{i,j,k+\frac{1}{2}}\Delta t}{4\epsilon_{zz}^{i,j,k+\frac{1}{2}} + \sigma_{zz}^{i,j,k+\frac{1}{2}}\Delta t}\right] E_z^{n,i,j,k+\frac{1}{2}} \\
& + \frac{2\Delta t}{\left(4\epsilon_{zz}^{i,j,k+\frac{1}{2}} + \sigma_{zz}^{i,j,k+\frac{1}{2}}\Delta t\right)\kappa_{xE}^{i}\Delta x}\left[H_y^{n+\frac{1}{2},i+\frac{1}{2},j,k+\frac{1}{2}} - H_y^{n+\frac{1}{2},i-\frac{1}{2},j,k+\frac{1}{2}}\right] \\
& - \frac{2\Delta t}{\left(4\epsilon_{zz}^{i,j,k+\frac{1}{2}} + \sigma_{zz}^{i,j,k+\frac{1}{2}}\Delta t\right)\kappa_{yE}^{j}\Delta y}\left[H_x^{n,i,j+\frac{1}{2},k+\frac{1}{2}} - H_x^{n,i,j-\frac{1}{2},k+\frac{1}{2}}\right] \\
& - \frac{2\Delta t}{\left(4\epsilon_{zz}^{i,j,k+\frac{1}{2}} + \sigma_{zz}^{i,j,k+\frac{1}{2}}\Delta t\right)}\left[J_{zS}^{n+\frac{1}{2},i,j,k+\frac{1}{2}} - \Phi_{Hyx}^{n,i,j,k+\frac{1}{2}} + \Phi_{Hxy}^{n,i,j,k+\frac{1}{2}}\right]
\end{aligned}
\tag{3.86c}
$$

Note that the expressions for the unknown electric fields above contain unknown magnetic fields on the right-hand side which are known via equations (3.75a-c). Substituting in these unknown magnetic fields will yield the CPML-ADI-FDTD equations. The electric field update equations above, utilizing $\sigma_{ij}$, may be used in applications where the simulation space does not contain highly lossy media, however, if conductive material is present, stability issues may arise due to the coefficient of the $E_i^n$ term which will change signs:

$$
\left[\frac{4\epsilon_{ii}^{T} - \sigma_{ii}\Delta t}{4\epsilon_{ii}^{T} + \sigma_{ii}\Delta t}\right] \begin{matrix} 1 \\ => 0 \\ < 0 \end{matrix} \quad \begin{matrix} lossless \\ \sigma_{ii} < 4\epsilon_{ii}^{T}/\Delta t \\ \sigma_{ii} > 4\epsilon_{ii}^{T}/\Delta t \end{matrix}
\tag{3.87}
$$

Various authors [222-224] have attempted to deal with the highly conductive case by utilizing time sampling schemes that differ from (3.88), but herein any highly conductive material is either modeled as a PEC or through use of recursive convolution to avoid stability issues, especially at the high CFLN factors heavily leveraged in mechanical antenna simulations. Thus, no more mention of $\sigma_{ij}$ is made and modelers of mechanical antennas should not use this term.

### 3.8.4.2 Second Sub-Iteration

For the second sub-iteration the magnetic fields defined at the half time step $n+1/2$ are again defined temporally as such, and the implicit definition now migrates to the latter magnetic terms in the alternate directions. This yields the following:

$$\begin{aligned}
&\frac{2}{\Delta t}\left[D_x^{n+1}\left(i+\frac{1}{2},j,k\right)-D_x^{n+\frac{1}{2}}\left(i+\frac{1}{2},j,k\right)\right] \\
&\qquad=\frac{1}{\kappa_{yE}^{j}\Delta y}\left[H_z^{n+\frac{1}{2}}\left(i+\frac{1}{2},j+\frac{1}{2},k\right)-H_z^{n+\frac{1}{2}}\left(i+\frac{1}{2},j-\frac{1}{2},k\right)\right] \\
&\qquad-\frac{1}{\kappa_{zE}^{k}\Delta z}\left[H_y^{n+1}\left(i+\frac{1}{2},j,k+\frac{1}{2}\right)-H_y^{n+1}\left(i+\frac{1}{2},j,k-\frac{1}{2}\right)\right]-J_{xS}^{n+\frac{1}{2}}\left(i+\frac{1}{2},j,k\right)+\Phi_{Hzy}^{n+\frac{1}{2}} \\
&\qquad-\Phi_{Hyz}^{n+\frac{1}{2}}
\end{aligned} \tag{3.88a}$$

$$\begin{aligned}
&\frac{2}{\Delta t}\left[D_y^{n+1}\left(i,j+\frac{1}{2},k\right)-D_y^{n+\frac{1}{2}}\left(i,j+\frac{1}{2},k\right)\right] \\
&\qquad=\frac{1}{\kappa_{zE}^{k}\Delta z}\left[H_x^{n+\frac{1}{2}}\left(i,j+\frac{1}{2},k+\frac{1}{2}\right)-H_x^{n+\frac{1}{2}}\left(i,j+\frac{1}{2},k-\frac{1}{2}\right)\right] \\
&\qquad-\frac{1}{\kappa_{xE}^{i}\Delta x}\left[H_z^{n+1}\left(i+\frac{1}{2},j+\frac{1}{2},k\right)-H_z^{n+1}\left(i-\frac{1}{2},j+\frac{1}{2},k\right)\right]-J_{yS}^{n+\frac{1}{2}}\left(i,j+\frac{1}{2},k\right)+\Phi_{Hxz}^{n+\frac{1}{2}} \\
&\qquad-\Phi_{Hzx}^{n+\frac{1}{2}}
\end{aligned} \tag{3.88b}$$

$$\begin{aligned}
&\frac{2}{\Delta t}\left[D_z^{n+1}\left(i,j,k+\frac{1}{2}\right)-D_z^{n+\frac{1}{2}}\left(i,j,k+\frac{1}{2}\right)\right] \\
&\qquad=\frac{1}{\kappa_{xE}^{i}\Delta x}\left[H_y^{n+\frac{1}{2}}\left(i+\frac{1}{2},j,k+\frac{1}{2}\right)-H_y^{n+\frac{1}{2}}\left(i-\frac{1}{2},j,k+\frac{1}{2}\right)\right] \\
&\qquad-\frac{1}{\kappa_{yE}^{j}\Delta y}\left[H_x^{n+1}\left(i,j+\frac{1}{2},k+\frac{1}{2}\right)-H_x^{n+1}\left(i,j-\frac{1}{2},k+\frac{1}{2}\right)\right]-J_{zS}^{n+\frac{1}{2}}\left(i,j,k+\frac{1}{2}\right)+\Phi_{Hyx}^{n+\frac{1}{2}} \\
&\qquad-\Phi_{Hxy}^{n+\frac{1}{2}}
\end{aligned} \tag{3.88c}$$

The update equations for the electric displacement may then be derived as follows:

$$D_x^{n+1}\left(i+\frac{1}{2},j,k\right)=D_x^{n+\frac{1}{2}}\left(i+\frac{1}{2},j,k\right)+\frac{\Delta t}{2\kappa_{yE}^{j}\Delta y}\left[H_z^{n+\frac{1}{2}}\left(i+\frac{1}{2},j+\frac{1}{2},k\right)-H_z^{n+\frac{1}{2}}\left(i+\frac{1}{2},j-\frac{1}{2},k\right)\right]$$
$$-\frac{\Delta t}{2\kappa_{zE}^{k}\Delta z}\left[H_y^{n+1}\left(i+\frac{1}{2},j,k+\frac{1}{2}\right)-H_y^{n+1}\left(i+\frac{1}{2},j,k-\frac{1}{2}\right)\right]-\frac{\Delta t}{2}J_{xS}^{n+\frac{1}{2}}\left(i+\frac{1}{2},j,k\right) \quad (3.89a)$$
$$+\frac{\Delta t}{2}\left[\Phi_{Hzy}^{n+\frac{1}{2}}\left(i+\frac{1}{2},j,k\right)-\Phi_{Hyz}^{n+\frac{1}{2}}\left(i+\frac{1}{2},j,k\right)\right]$$

$$D_y^{n+1}\left(i,j+\frac{1}{2},k\right)=D_y^{n+\frac{1}{2}}\left(i,j+\frac{1}{2},k\right)+\frac{\Delta t}{2\kappa_{zE}^{k}\Delta z}\left[H_x^{n+\frac{1}{2}}\left(i,j+\frac{1}{2},k+\frac{1}{2}\right)-H_x^{n+\frac{1}{2}}\left(i,j+\frac{1}{2},k-\frac{1}{2}\right)\right]$$
$$-\frac{\Delta t}{2\kappa_{xE}^{i}\Delta x}\left[H_z^{n+1}\left(i+\frac{1}{2},j+\frac{1}{2},k\right)-H_z^{n+1}\left(i-\frac{1}{2},j+\frac{1}{2},k\right)\right]-\frac{\Delta t}{2}J_{yS}^{n+\frac{1}{2}}\left(i,j+\frac{1}{2},k\right) \quad (3.89b)$$
$$+\frac{\Delta t}{2}\left[\Phi_{Hxz}^{n+\frac{1}{2}}\left(i,j+\frac{1}{2},k\right)-\Phi_{Hzx}^{n+\frac{1}{2}}\left(i,j+\frac{1}{2},k\right)\right]$$

$$D_z^{n+1}\left(i,j,k+\frac{1}{2}\right)=D_z^{n+\frac{1}{2}}\left(i,j,k+\frac{1}{2}\right)+\frac{\Delta t}{2\kappa_{xE}^{i}\Delta x}\left[H_y^{n+\frac{1}{2}}\left(i+\frac{1}{2},j,k+\frac{1}{2}\right)-H_y^{n+\frac{1}{2}}\left(i-\frac{1}{2},j,k+\frac{1}{2}\right)\right]$$
$$-\frac{\Delta t}{2\kappa_{yE}^{j}\Delta y}\left[H_x^{n+1}\left(i,j+\frac{1}{2},k+\frac{1}{2}\right)-H_x^{n+1}\left(i,j-\frac{1}{2},k+\frac{1}{2}\right)\right]-\frac{\Delta t}{2}J_{zS}^{n+\frac{1}{2}}\left(i,j,k+\frac{1}{2}\right) \quad (3.89c)$$
$$+\frac{\Delta t}{2}\left[\Phi_{Hyx}^{n+\frac{1}{2}}\left(i,j,k+\frac{1}{2}\right)-\Phi_{Hxy}^{n+\frac{1}{2}}\left(i,j,k+\frac{1}{2}\right)\right]$$

In preparation for the derivation of the ADI-FDTD equations, substitute in the electric constitutive relations (3.78a-c) into (3.88a-c) and solve for the unknown electric field as follows:

$$E_x^{n+1,i+\frac{1}{2},j,k}=E_x^{n+\frac{1}{2},i+\frac{1}{2},j,k}+\frac{\Delta t}{2\epsilon_{xx}^{i+\frac{1}{2},j,k}\kappa_{yE}^{j}\Delta y}\left[H_z^{n+\frac{1}{2},i+\frac{1}{2},j+\frac{1}{2},k}-H_z^{n+\frac{1}{2},i+\frac{1}{2},j-\frac{1}{2},k}\right]$$
$$-\frac{\Delta t}{2\epsilon_{xx}^{i+\frac{1}{2},j,k}\kappa_{zE}^{k}\Delta z}\left[H_y^{n+1,i+\frac{1}{2},j,k+\frac{1}{2}}-H_y^{n+1,i+\frac{1}{2},j,k-\frac{1}{2}}\right] \quad (3.90a)$$
$$-\frac{\Delta t}{2\epsilon_{xx}^{i+\frac{1}{2},j,k}}\left[J_{xS}^{n+\frac{1}{2},i+\frac{1}{2},j,k}-\Phi_{Hzy}^{n+\frac{1}{2},i+\frac{1}{2},j,k}+\Phi_{Hyz}^{n+\frac{1}{2},i+\frac{1}{2},j,k}\right]$$

$$E_y^{n+1,i,j+\frac{1}{2},k}=E_y^{n+\frac{1}{2},i,j+\frac{1}{2},k}+\frac{\Delta t}{2\epsilon_{yy}^{i,j+\frac{1}{2},k}\kappa_{zE}^{k}\Delta z}\left[H_x^{n+\frac{1}{2},i,j+\frac{1}{2},k+\frac{1}{2}}-H_x^{n+\frac{1}{2},i,j+\frac{1}{2},k-\frac{1}{2}}\right]$$
$$-\frac{\Delta t}{2\epsilon_{yy}^{i,j+\frac{1}{2},k}\kappa_{xE}^{i}\Delta x}\left[H_z^{n+1,i+\frac{1}{2},j+\frac{1}{2},k}-H_z^{n+1,i-\frac{1}{2},j+\frac{1}{2},k}\right] \quad (3.90b)$$
$$-\frac{\Delta t}{2\epsilon_{yy}^{i,j+\frac{1}{2},k}}\left[J_{yS}^{n+\frac{1}{2},i,j+\frac{1}{2},k}-\Phi_{Hxz}^{n+\frac{1}{2},i,j+\frac{1}{2},k}+\Phi_{Hzx}^{n+\frac{1}{2},i,j+\frac{1}{2},k}\right]$$

$$E_z^{n+1,i,j,k+\frac{1}{2}} = E_z^{n+\frac{1}{2},i,j,k+\frac{1}{2}} + \frac{\Delta t}{2\epsilon_{zz}^{i,j,k+\frac{1}{2}}\kappa_{xE}^{i}\Delta x}\left[H_y^{n+\frac{1}{2},i+\frac{1}{2},j,k+\frac{1}{2}} - H_y^{n+\frac{1}{2},i-\frac{1}{2},j,k+\frac{1}{2}}\right]$$

$$- \frac{\Delta t}{2\epsilon_{zz}^{i,j,k+\frac{1}{2}}\kappa_{yE}^{j}\Delta y}\left[H_x^{n+1,i,j+\frac{1}{2},k+\frac{1}{2}} - H_x^{n+1,i,j-\frac{1}{2},k+\frac{1}{2}}\right] \tag{3.90c}$$

$$- \frac{\Delta t}{2\epsilon_{zz}^{i,j,k+\frac{1}{2}}}\left[J_{zS}^{n+\frac{1}{2},i,j,k+\frac{1}{2}} - \Phi_{Hyx}^{n+\frac{1}{2},i,j,k+\frac{1}{2}} + \Phi_{Hxy}^{n+\frac{1}{2},i,j,k+\frac{1}{2}}\right]$$

These expressions for the unknown electric fields, (3.86a-c) in the 1st sub-iteration and (3.90a-c) in the 2nd sub-iteration, will be used to determine the CPML-ADI-FDTD equations in the following section. This is done by substituting in the expressions for the unknown magnetic fields, (3.75a-c) for the 1st sub-iteration and (3.76a-c) for the 2nd sub-iteration, derived from substituting the magnetic constitutive relations into Faraday's law in Section 3.8.2.

### 3.8.5 CPML-ADI-FDTD Equations

Now that expressions for the future magnetic and electric fields have been attained by utilizing the magnetic/electric constitutive relations and Maxwell's equations, the ADI-FDTD equations may be derived. These will be different for each sub-iteration.

#### 3.8.5.1 First Sub-Iteration

Recall that the expressions for the unknown electric fields (obtained from inputting the electric constitutive relations into Ampere's law) contained unknown magnetic fields on the right-hand side. These unknown magnetic fields were determined via substitution of the magnetic constitutive relations into Faraday's law. Thus, by substitution of the unknown $H_z^{n+1/2}$ terms (3.75c) into the $E_x^{n+1/2}$ expression (3.86a), the following is acquired:

$$E_x^{n+\frac{1}{2},i+\frac{1}{2},j,k} = E_x^{n,i+\frac{1}{2},j,k}$$

$$+\frac{\Delta t}{2\epsilon_{xx}^{i+\frac{1}{2},j,k}\kappa_{yE}^{j}\Delta y}\Bigg[H_z^{n,i+\frac{1}{2},j+\frac{1}{2},k}+\frac{\Delta t}{2\mu_{zz}^{i+\frac{1}{2},j+\frac{1}{2},k}\kappa_{yH}^{j}\Delta y}\left[E_x^{n+\frac{1}{2},i+\frac{1}{2},j+1,k}-E_x^{n+\frac{1}{2},i+\frac{1}{2},j,k}\right]$$

$$-\frac{\Delta t}{2\mu_{zz}^{i+\frac{1}{2},j+\frac{1}{2},k}\kappa_{xH}^{i}\Delta x}\left[E_y^{n,i+1,j+\frac{1}{2},k}-E_y^{n,i,j+\frac{1}{2},k}\right]-\frac{\Delta t}{2\mu_{zz}^{i+\frac{1}{2},j+\frac{1}{2},k}}\left[\mathcal{M}_z^{n+\frac{1}{2},i+\frac{1}{2},j+\frac{1}{2},k}-\Phi_{Exy}^{n,i+\frac{1}{2},j+\frac{1}{2},k}+\Phi_{Eyx}^{n,i+\frac{1}{2},j+\frac{1}{2},k}\right]$$

$$-H_z^{n,i+\frac{1}{2},j-\frac{1}{2},k}+\frac{\Delta t}{2\mu_{zz}^{i+\frac{1}{2},j-\frac{1}{2},k}\kappa_{yH}^{j}\Delta y}\left[E_x^{n+\frac{1}{2},i+\frac{1}{2},j,k}-E_x^{n+\frac{1}{2},i+\frac{1}{2},j-1,k}\right]$$

$$-\frac{\Delta t}{2\mu_{zz}^{i+\frac{1}{2},j-\frac{1}{2},k}\kappa_{xH}^{i}\Delta x}\left[E_y^{n,i+1,j-\frac{1}{2},k}-E_y^{n,i,j-\frac{1}{2},k}\right]-\frac{\Delta t}{2\mu_{zz}^{i+\frac{1}{2},j-\frac{1}{2},k}}\left[\mathcal{M}_z^{n+\frac{1}{2},i+\frac{1}{2},j-\frac{1}{2},k}-\Phi_{Exy}^{n,i+\frac{1}{2},j-\frac{1}{2},k}+\Phi_{Eyx}^{n,i+\frac{1}{2},j-\frac{1}{2},k}\right]\Bigg]$$

$$-\frac{\Delta t}{2\epsilon_{xx}^{i+\frac{1}{2},j,k}\kappa_{zE}^{k}\Delta z}\left[H_y^{n,i+\frac{1}{2},j,k+\frac{1}{2}}-H_y^{n,i+\frac{1}{2},j,k-\frac{1}{2}}\right]-\frac{\Delta t}{2\epsilon_{xx}^{i+\frac{1}{2},j,k}}\left[J_{xS}^{n+\frac{1}{2},i+\frac{1}{2},j,k}-\Phi_{Hzy}^{n,i+\frac{1}{2},j,k}+\Phi_{Hyz}^{n,i+\frac{1}{2},j,k}\right]$$

(3.91)

This may be simplified into the y-cut equation as follows in (3.92a). Recall that the term “y-cut” refers to the three unknown electric fields that appear in the tri-diagonal matrix which lie along a y-directed cut of the simulation space (i.e., at $y = (j-1)\Delta y$, $y = j\Delta y$, and $y = (j-1)\Delta y$). The term y-cut does not refer to a crystalline orientation. Indeed, even when discussing homogeneous free space simulations in Section 3.6, the terms x-cut, y-cut, and z-cut were used.

$$-\frac{\Delta t^2}{4\epsilon_{xx}^{i+\frac{1}{2},j,k}\mu_{zz}^{i+\frac{1}{2},j+\frac{1}{2},k}\kappa_{yE}^{j}\kappa_{yH}^{j}\Delta y^2}E_x^{n+\frac{1}{2},i+\frac{1}{2},j+1,k}+\left[1+\frac{\Delta t^2}{4\epsilon_{xx}^{i+\frac{1}{2},j,k}\kappa_{yE}^{j}\Delta y^2}\left(\frac{1}{\kappa_{yH}^{j}\mu_{zz}^{i+\frac{1}{2},j+\frac{1}{2},k}}+\frac{1}{\kappa_{yH}^{j-1}\mu_{zz}^{i+\frac{1}{2},j-\frac{1}{2},k}}\right)\right]E_x^{n+\frac{1}{2},i+\frac{1}{2},j,k}$$

$$-\frac{\Delta t^2}{4\epsilon_{xx}^{i+\frac{1}{2},j,k}\mu_{zz}^{i+\frac{1}{2},j-\frac{1}{2},k}\kappa_{yE}^{j}\kappa_{yH}^{j-1}\Delta y^2}E_x^{n+\frac{1}{2},i+\frac{1}{2},j-1,k}$$

$$=E_x^{n,i+\frac{1}{2},j,k}+\frac{\Delta t}{2\epsilon_{xx}^{i+\frac{1}{2},j,k}\kappa_{yE}^{j}\Delta y}\left(H_z^{n,i+\frac{1}{2},j+\frac{1}{2},k}-H_z^{n,i+\frac{1}{2},j-\frac{1}{2},k}\right)-\frac{\Delta t}{2\epsilon_{xx}^{i+\frac{1}{2},j,k}\kappa_{zE}^{k}\Delta z}\left(H_y^{n,i+\frac{1}{2},j,k+\frac{1}{2}}-H_y^{n,i+\frac{1}{2},j,k-\frac{1}{2}}\right)$$

$$-\frac{\Delta t^2}{4\epsilon_{xx}^{i+\frac{1}{2},j,k}\kappa_{xH}^{i}\Delta x\kappa_{yE}^{j}\Delta y}\left[\frac{1}{\mu_{zz}^{i+\frac{1}{2},j+\frac{1}{2},k}}\left(E_y^{n,i+1,j+\frac{1}{2},k}-E_y^{n,i,j+\frac{1}{2},k}\right)-\frac{1}{\mu_{zz}^{i+\frac{1}{2},j-\frac{1}{2},k}}\left(E_y^{n,i+1,j-\frac{1}{2},k}-E_y^{n,i,j-\frac{1}{2},k}\right)\right]$$

$$-\frac{\Delta t^2}{4\epsilon_{xx}^{i+\frac{1}{2},j,k}\kappa_{yE}^{j}\Delta y}\left[\frac{1}{\mu_{zz}^{i+\frac{1}{2},j+\frac{1}{2},k}}\left(\mathcal{M}_z^{n+\frac{1}{2},i+\frac{1}{2},j+\frac{1}{2},k}-\Phi_{Exy}^{n,i+\frac{1}{2},j+\frac{1}{2},k}+\Phi_{Eyx}^{n,i+\frac{1}{2},j+\frac{1}{2},k}\right)\right.$$

$$\left.-\frac{1}{\mu_{zz}^{i+\frac{1}{2},j-\frac{1}{2},k}}\left(\mathcal{M}_z^{n+\frac{1}{2},i+\frac{1}{2},j-\frac{1}{2},k}-\Phi_{Exy}^{n,i+\frac{1}{2},j-\frac{1}{2},k}+\Phi_{Eyx}^{n,i+\frac{1}{2},j-\frac{1}{2},k}\right)\right]$$

$$-\frac{\Delta t}{2\epsilon_{xx}^{i+\frac{1}{2},j,k}}\left[J_{xS}^{n+\frac{1}{2},i+\frac{1}{2},j,k}-\Phi_{Hzy}^{n,i+\frac{1}{2},j,k}+\Phi_{Hyz}^{n,i+\frac{1}{2},j,k}\right]$$

(3.92a)

This process is repeated for $E_y^{n+1/2}$ (3.86b) where $H_x^{n+1/2}$ (3.75a) is substituted in yielding the following z-cut equation:

$$-\frac{\Delta t^2}{4\epsilon_{yy}^{i,j+\frac{1}{2},k}\mu_{xx}^{i,j+\frac{1}{2},k+\frac{1}{2}}\kappa_{zE}^{k}\kappa_{zH}^{k}\Delta z^2}E_y^{n+\frac{1}{2},i,j+\frac{1}{2},k+1}+\left[1+\frac{\Delta t^2}{4\epsilon_{yy}^{i,j+\frac{1}{2},k}\kappa_{zE}^{k}\Delta z^2}\left(\frac{1}{\kappa_{zH}^{k}\mu_{xx}^{i,j+\frac{1}{2},k+\frac{1}{2}}}+\frac{1}{\kappa_{zH}^{k-1}\mu_{xx}^{i,j+\frac{1}{2},k-\frac{1}{2}}}\right)\right]E_y^{n+\frac{1}{2},i,j+\frac{1}{2},k}$$

$$-\frac{\Delta t^2}{4\epsilon_{yy}^{i,j+\frac{1}{2},k}\mu_{xx}^{i,j+\frac{1}{2},k-\frac{1}{2}}\kappa_{zE}^{k}\kappa_{zH}^{k-1}\Delta z^2}E_y^{n+\frac{1}{2},i,j+\frac{1}{2},k-1}$$

$$=E_y^{n,i,j+\frac{1}{2},k}+\frac{\Delta t}{2\epsilon_{yy}^{i,j+\frac{1}{2},k}\kappa_{zE}^{k}\Delta z}\left(H_x^{n,i,j+\frac{1}{2},k+\frac{1}{2}}-H_x^{n,i,j+\frac{1}{2},k-\frac{1}{2}}\right)-\frac{\Delta t}{2\epsilon_{yy}^{i,j+\frac{1}{2},k}\kappa_{xE}^{i}\Delta x}\left(H_z^{n,i+\frac{1}{2},j+\frac{1}{2},k}-H_z^{n,i-\frac{1}{2},j+\frac{1}{2},k}\right)$$

$$-\frac{\Delta t^2}{4\epsilon_{yy}^{i,j+\frac{1}{2},k}\kappa_{yH}^{j}\kappa_{zE}^{k}\Delta y\Delta z}\left[\frac{1}{\mu_{xx}^{i,j+\frac{1}{2},k+\frac{1}{2}}}\left(E_z^{n,i,j+1,k+\frac{1}{2}}-E_z^{ni,j,k+\frac{1}{2}}\right)-\frac{1}{\mu_{xx}^{i,j+\frac{1}{2},k-\frac{1}{2}}}\left(E_z^{n,i,j+1,k-\frac{1}{2}}-E_z^{ni,j,k-\frac{1}{2}}\right)\right]$$

$$-\frac{\Delta t^2}{4\epsilon_{yy}^{i,j+\frac{1}{2},k}\kappa_{zE}^{k}\Delta z}\left[\frac{1}{\mu_{xx}^{i,j+\frac{1}{2},k+\frac{1}{2}}}\left(\mathcal{M}_x^{n+\frac{1}{2},i,j+\frac{1}{2},k+\frac{1}{2}}-\Phi_{Eyz}^{ni,j+\frac{1}{2},k+\frac{1}{2}}+\Phi_{Ezy}^{n,i,j+\frac{1}{2},k+\frac{1}{2}}\right)\right.$$

$$\left.-\frac{1}{\mu_{xx}^{i,j+\frac{1}{2},k-\frac{1}{2}}}\left(\mathcal{M}_x^{n+\frac{1}{2},i,j+\frac{1}{2},k-\frac{1}{2}}-\Phi_{Eyz}^{ni,j+\frac{1}{2},k-\frac{1}{2}}+\Phi_{Ezy}^{n,i,j+\frac{1}{2},k-\frac{1}{2}}\right)\right]$$

$$-\frac{\Delta t}{2\epsilon_{yy}^{i,j+\frac{1}{2},k}}\left[J_{yS}^{n+\frac{1}{2},i,j+\frac{1}{2},k}-\Phi_{Hxz}^{n,i,j+\frac{1}{2},k}+\Phi_{Hzx}^{n,i,j+\frac{1}{2},k}\right]$$

(3.92b)

Finally, the process is repeated for $E_z^{n+1/2}$ (3.86c) where $H_y^{n+1/2}$ (3.75b) is substituted in yielding the following x-cut equation:

$$
\begin{aligned}
&-\frac{\Delta t^2}{4\epsilon_{zz}^{i,j,k+\frac{1}{2}}\mu_{yy}^{i+\frac{1}{2},j,k+\frac{1}{2}}\kappa_{xE}^{i}\kappa_{xH}^{i}\Delta x^2}E_z^{n+\frac{1}{2},i+1,j,k+\frac{1}{2}}+\left[1+\frac{\Delta t^2}{4\epsilon_{zz}^{i,j,k+\frac{1}{2}}\kappa_{xE}^{i}\Delta x^2}\left(\frac{1}{\kappa_{xH}^{i}\mu_{yy}^{i+\frac{1}{2},j,k+\frac{1}{2}}}+\frac{1}{\kappa_{xH}^{i-1}\mu_{yy}^{i-\frac{1}{2},j,k+\frac{1}{2}}}\right)\right]E_z^{n+\frac{1}{2},i,j,k+\frac{1}{2}}\\
&\quad-\frac{\Delta t^2}{4\epsilon_{zz}^{i,j,k+\frac{1}{2}}\mu_{yy}^{i-\frac{1}{2},j,k+\frac{1}{2}}\kappa_{xE}^{i}\kappa_{xH}^{i-1}\Delta x^2}E_z^{n+\frac{1}{2},i-1,j,k+\frac{1}{2}}\\
&\quad=E_z^{n,i,j,k+\frac{1}{2}}+\frac{\Delta t}{2\epsilon_{zz}^{i,j,k+\frac{1}{2}}\kappa_{xE}^{i}\Delta x}\left(H_y^{n,i+\frac{1}{2},j,k+\frac{1}{2}}-H_y^{n,i-\frac{1}{2},j,k+\frac{1}{2}}\right)-\frac{\Delta t}{2\epsilon_{zz}^{i,j,k+\frac{1}{2}}\kappa_{yE}^{j}\Delta y}\left(H_x^{n,i,j+\frac{1}{2},k+\frac{1}{2}}-H_x^{n,i,j-\frac{1}{2},k+\frac{1}{2}}\right)\\
&\quad-\frac{\Delta t^2}{4\epsilon_{zz}^{i,j,k+\frac{1}{2}}\kappa_{zH}^{k}\kappa_{xE}^{i}\Delta x\Delta z}\left[\frac{1}{\mu_{yy}^{i+\frac{1}{2},j,k+\frac{1}{2}}}\left(E_x^{n,i+\frac{1}{2},j,k+1}-E_x^{n,i+\frac{1}{2},j,k}\right)-\frac{1}{\mu_{yy}^{i-\frac{1}{2},j,k+\frac{1}{2}}}\left(E_x^{n,i-\frac{1}{2},j,k+1}-E_x^{n,i-\frac{1}{2},j,k}\right)\right]\\
&\quad-\frac{\Delta t^2}{4\epsilon_{zz}^{i,j,k+\frac{1}{2}}\kappa_{xE}^{i}\Delta x}\left[\frac{1}{\mu_{yy}^{i+\frac{1}{2},j,k+\frac{1}{2}}}\left(\mathcal{M}_y^{n+\frac{1}{2},i+\frac{1}{2},j,k+\frac{1}{2}}-\Phi_{Ezx}^{n,i+\frac{1}{2},j,k+\frac{1}{2}}+\Phi_{Exz}^{n,i+\frac{1}{2},j,k+\frac{1}{2}}\right)\right.\\
&\quad\left.-\frac{1}{\mu_{yy}^{i-\frac{1}{2},j,k+\frac{1}{2}}}\left(\mathcal{M}_y^{n+\frac{1}{2},i-\frac{1}{2},j,k+\frac{1}{2}}-\Phi_{Ezx}^{n,i-\frac{1}{2},j,k+\frac{1}{2}}+\Phi_{Exz}^{n,i-\frac{1}{2},j,k+\frac{1}{2}}\right)\right]\\
&\quad-\frac{\Delta t}{2\epsilon_{zz}^{i,j,k+\frac{1}{2}}}\left[J_{zS}^{n+\frac{1}{2},i,j,k+\frac{1}{2}}-\Phi_{Hyx}^{n,i,j,k+\frac{1}{2}}+\Phi_{Hxy}^{n,i,j,k+\frac{1}{2}}\right]
\end{aligned}
\tag{3.92c}
$$

The above y-cut (3.92a), z-cut (3.92b), and x-cut (3.92c) expressions are used to update $E_x^{n+1/2}$, $E_y^{n+1/2}$, and $E_z^{n+1/2}$ respectively. Update expressions in the 2nd sub-iteration may similarly be derived and are presented in the following section.

#### 3.8.5.2 Second Sub-Iteration

In the 2nd sub-iteration, expressions for $E_x^{n+1}$ (3.90a), $E_y^{n+1}$ (3.90b), and $E_z^{n+1}$ (3.90c) are modified via substitution of $H_y^{n+1}$ (3.76b), $H_z^{n+1}$ (3.76c), and $H_x^{n+1}$ (3.76a) yielding the z-cut (3.92d), x-cut (3.92e), and y-cut (3.92f) update equations provided below respectively:

$$
\begin{aligned}
&-\frac{\Delta t^2}{4\epsilon_{xx}^{i+\frac{1}{2},j,k}\mu_{yy}^{i+\frac{1}{2},j,k+\frac{1}{2}}\kappa_{zE}^{k}\kappa_{zH}^{k}\Delta z^2}E_x^{n+1,i+\frac{1}{2},j,k+1}+\left[1+\frac{\Delta t^2}{4\epsilon_{xx}^{i+\frac{1}{2},j,k}\kappa_{zE}^{k}\Delta z^2}\left(\frac{1}{\kappa_{zH}^{k}\mu_{yy}^{i+\frac{1}{2},j,k+\frac{1}{2}}}+\frac{1}{\kappa_{zH}^{k-1}\mu_{yy}^{i+\frac{1}{2},j,k-\frac{1}{2}}}\right)\right]E_x^{n+1,i+\frac{1}{2},j,k}\\
&-\frac{\Delta t^2}{4\epsilon_{xx}^{i+\frac{1}{2},j,k}\mu_{yy}^{i+\frac{1}{2},j,k-\frac{1}{2}}\kappa_{zE}^{k}\kappa_{zH}^{k-1}\Delta z^2}E_x^{n+1,i+\frac{1}{2},j,k-1}\\
&=E_x^{n+\frac{1}{2},i+\frac{1}{2},j,k}+\frac{\Delta t}{2\epsilon_{xx}^{i+\frac{1}{2},j,k}\kappa_{yE}^{j}\Delta y}\left(H_z^{n+\frac{1}{2},i+\frac{1}{2},j+\frac{1}{2},k}-H_z^{n+\frac{1}{2},i+\frac{1}{2},j-\frac{1}{2},k}\right)\\
&-\frac{\Delta t}{2\epsilon_{xx}^{i+\frac{1}{2},j,k}\kappa_{zE}^{k}\Delta z}\left(H_y^{n+\frac{1}{2},i+\frac{1}{2},j,k+\frac{1}{2}}-H_y^{n+\frac{1}{2},i+\frac{1}{2},j,k-\frac{1}{2}}\right)\\
&-\frac{\Delta t^2}{4\epsilon_{xx}^{i+\frac{1}{2},j,k}\kappa_{xH}^{i}\Delta x\kappa_{zE}^{k}\Delta z}\left[\frac{1}{\mu_{yy}^{i+\frac{1}{2},j,k+\frac{1}{2}}}\left(E_z^{n+\frac{1}{2},i+1,j,k+\frac{1}{2}}-E_z^{n+\frac{1}{2},i,j,k+\frac{1}{2}}\right)\right.\\
&\left.-\frac{1}{\mu_{yy}^{i-\frac{1}{2},j,k+\frac{1}{2}}}\left(E_z^{n+\frac{1}{2},i+1,j,k-\frac{1}{2}}-E_z^{n+\frac{1}{2},i,j,k-\frac{1}{2}}\right)\right]\\
&+\frac{\Delta t^2}{4\epsilon_{xx}^{i+\frac{1}{2},j,k}\kappa_{zE}^{k}\Delta z}\left[\frac{1}{\mu_{yy}^{i+\frac{1}{2},j,k+\frac{1}{2}}}\left(\mathcal{M}_y^{n+\frac{1}{2},i+\frac{1}{2},j,k+\frac{1}{2}}-\Phi_{Ezx}^{n+\frac{1}{2},i+\frac{1}{2},j,k+\frac{1}{2}}+\Phi_{Exz}^{n+\frac{1}{2},i+\frac{1}{2},j,k+\frac{1}{2}}\right)\right.\\
&\left.-\frac{1}{\mu_{yy}^{i+\frac{1}{2},j,k-\frac{1}{2}}}\left(\mathcal{M}_y^{n+\frac{1}{2},i+\frac{1}{2},j,k-\frac{1}{2}}-\Phi_{Ezx}^{n+\frac{1}{2},i+\frac{1}{2},j,k-\frac{1}{2}}+\Phi_{Exz}^{n+\frac{1}{2},i+\frac{1}{2},j,k-\frac{1}{2}}\right)\right]\\
&-\frac{\Delta t}{2\epsilon_{xx}^{i+\frac{1}{2},j,k}}\left[J_{xS}^{n+\frac{1}{2},i+\frac{1}{2},j,k}-\Phi_{Hzy}^{n+\frac{1}{2},i+\frac{1}{2},j,k}+\Phi_{Hyz}^{n+\frac{1}{2},i+\frac{1}{2},j,k}\right]
\end{aligned}
\tag{3.92d}
$$

$$
-\frac{\Delta t^2}{4\epsilon_{yy}^{i,j+\frac{1}{2},k}\mu_{zz}^{i+\frac{1}{2},j+\frac{1}{2},k}\kappa_{xE}^{i}\kappa_{xH}^{i}\Delta x^2}E_y^{n+1,i+1,j+\frac{1}{2},k}+\left[1+\frac{\Delta t^2}{4\epsilon_{yy}^{i,j+\frac{1}{2},k}\kappa_{xE}^{i}\Delta x^2}\left(\frac{1}{\kappa_{xH}^{i}\mu_{zz}^{i+\frac{1}{2},j+\frac{1}{2},k}}+\frac{1}{\kappa_{xH}^{i-1}\mu_{zz}^{i-\frac{1}{2},j+\frac{1}{2},k}}\right)\right]E_y^{n+1,i,j+\frac{1}{2},k}
$$

$$
-\frac{\Delta t^2}{4\epsilon_{yy}^{i,j+\frac{1}{2},k}\mu_{zz}^{i-\frac{1}{2},j+\frac{1}{2},k}\kappa_{xE}^{i}\kappa_{xH}^{i-1}\Delta x^2}E_y^{n+1,i-1,j+\frac{1}{2},k}
$$

$$
=E_y^{n+\frac{1}{2},i,j+\frac{1}{2},k}+\frac{\Delta t}{2\epsilon_{yy}^{i,j+\frac{1}{2},k}\kappa_{zE}^{k}\Delta z}\left(H_x^{n+\frac{1}{2},i,j+\frac{1}{2},k+\frac{1}{2}}-H_x^{n+\frac{1}{2},i,j+\frac{1}{2},k-\frac{1}{2}}\right)
$$

$$
-\frac{\Delta t}{2\epsilon_{yy}^{i,j+\frac{1}{2},k}\kappa_{xE}^{i}\Delta x}\left(H_z^{n+\frac{1}{2},i+\frac{1}{2},j+\frac{1}{2},k}-H_z^{n+\frac{1}{2},i-\frac{1}{2},j+\frac{1}{2},k}\right)
$$

$$
-\frac{\Delta t^2}{4\epsilon_{yy}^{i,j+\frac{1}{2},k}\kappa_{xE}^{i}\Delta x\kappa_{yH}^{j}\Delta y}\left[\frac{1}{\mu_{zz}^{i+\frac{1}{2},j+\frac{1}{2},k}}\left(E_x^{n+\frac{1}{2},i+\frac{1}{2},j+1,k}-E_x^{n+\frac{1}{2},i+\frac{1}{2},j,k}\right)\right.
$$

$$
\left.-\frac{1}{\mu_{zz}^{i-\frac{1}{2},j+\frac{1}{2},k}}\left(E_x^{n+\frac{1}{2},i-\frac{1}{2},j+1,k}-E_x^{n+\frac{1}{2},i-\frac{1}{2},j,k}\right)\right]
$$

$$
+\frac{\Delta t^2}{4\epsilon_{yy}^{i,j+\frac{1}{2},k}\kappa_{xE}^{i}\Delta x}\left[\frac{1}{\mu_{zz}^{i+\frac{1}{2},j+\frac{1}{2},k}}\left[\mathcal{M}_z^{n+\frac{1}{2},i+\frac{1}{2},j+\frac{1}{2},k}-\Phi_{Exy}^{n+\frac{1}{2},i+\frac{1}{2},j+\frac{1}{2},k}+\Phi_{Eyx}^{n+\frac{1}{2},i+\frac{1}{2},j+\frac{1}{2},k}\right]\right.
$$

$$
\left.-\frac{1}{\mu_{zz}^{i-\frac{1}{2},j+\frac{1}{2},k}}\left[\mathcal{M}_z^{n+\frac{1}{2},i-\frac{1}{2},j+\frac{1}{2},k}-\Phi_{Exy}^{n+\frac{1}{2},i-\frac{1}{2},j+\frac{1}{2},k}+\Phi_{Eyx}^{n+\frac{1}{2},i-\frac{1}{2},j+\frac{1}{2},k}\right]\right]
$$

$$
-\frac{\Delta t}{2\epsilon_{yy}^{i,j+\frac{1}{2},k}}\left[J_{yS}^{n+\frac{1}{2},i,j+\frac{1}{2},k}-\Phi_{Hxz}^{n+\frac{1}{2},i,j+\frac{1}{2},k}+\Phi_{Hzx}^{n+\frac{1}{2},i,j+\frac{1}{2},k}\right]
$$

(3.92e)

$$
\begin{aligned}
&-\frac{\Delta t^2}{4\epsilon_{zz}^{i,j,k+\frac{1}{2}}\mu_{xx}^{i,j+\frac{1}{2},k+\frac{1}{2}}\kappa_{yE}^{j}\kappa_{yH}^{j}\Delta y^2}E_z^{n+1,i,j+1,k+\frac{1}{2}}+\left[1+\frac{\Delta t^2}{4\epsilon_{zz}^{i,j,k+\frac{1}{2}}\kappa_{yE}^{j}\Delta y^2}\left(\frac{1}{\kappa_{yH}^{j}\mu_{xx}^{i,j+\frac{1}{2},k+\frac{1}{2}}}+\frac{1}{\kappa_{yH}^{j-1}\mu_{xx}^{i,j-\frac{1}{2},k+\frac{1}{2}}}\right)\right]E_z^{n+1,i,j,k+\frac{1}{2}}\\
&\quad-\frac{\Delta t^2}{4\epsilon_{zz}^{i,j,k+\frac{1}{2}}\mu_{xx}^{i,j-\frac{1}{2},k+\frac{1}{2}}\kappa_{yE}^{j}\kappa_{yH}^{j-1}\Delta y^2}E_z^{n+1,i,j-1,k+\frac{1}{2}}\\
&\quad=E_z^{n+\frac{1}{2},i,j,k+\frac{1}{2}}+\frac{\Delta t}{2\epsilon_{zz}^{i,j,k+\frac{1}{2}}\kappa_{xE}^{i}\Delta x}\left(H_y^{n+\frac{1}{2},i+\frac{1}{2},j,k+\frac{1}{2}}-H_y^{n+\frac{1}{2},i-\frac{1}{2},j,k+\frac{1}{2}}\right)\\
&\quad-\frac{\Delta t}{2\epsilon_{zz}^{i,j,k+\frac{1}{2}}\kappa_{yE}^{j}\Delta y}\left(H_x^{n+\frac{1}{2},i,j+\frac{1}{2},k+\frac{1}{2}}-H_x^{n+\frac{1}{2},i,j-\frac{1}{2},k+\frac{1}{2}}\right)\\
&\quad-\frac{\Delta t^2}{4\epsilon_{zz}^{i,j,k+\frac{1}{2}}\kappa_{yE}^{j}\Delta y\kappa_{zH}^{k}\Delta z}\left[\frac{1}{\mu_{xx}^{i,j+\frac{1}{2},k+\frac{1}{2}}}\left(E_y^{n+\frac{1}{2},i,j+\frac{1}{2},k+1}-E_y^{n+\frac{1}{2},i,j+\frac{1}{2},k}\right)\right.\\
&\quad\left.-\frac{1}{\mu_{xx}^{i,j-\frac{1}{2},k+\frac{1}{2}}}\left(E_y^{n+\frac{1}{2},i,j-\frac{1}{2},k+1}-E_y^{n+\frac{1}{2},i,j-\frac{1}{2},k}\right)\right]\\
&\quad+\frac{\Delta t^2}{4\epsilon_{zz}^{i,j,k+\frac{1}{2}}\kappa_{yE}^{j}\Delta y}\left[\frac{1}{\mu_{xx}^{i,j+\frac{1}{2},k+\frac{1}{2}}}\left[\mathcal{M}_x^{n+\frac{1}{2},i,j+\frac{1}{2},k+\frac{1}{2}}-\Phi_{Eyz}^{n+\frac{1}{2},i,j+\frac{1}{2},k+\frac{1}{2}}+\Phi_{Ezy}^{n+\frac{1}{2},i,j+\frac{1}{2},k+\frac{1}{2}}\right]\right.\\
&\quad\left.-\frac{\Delta t}{2\mu_{xx}^{i,j-\frac{1}{2},k+\frac{1}{2}}}\left[\mathcal{M}_x^{n+\frac{1}{2},i,j-\frac{1}{2},k+\frac{1}{2}}-\Phi_{Eyz}^{n+\frac{1}{2},i,j-\frac{1}{2},k+\frac{1}{2}}+\Phi_{Ezy}^{n+\frac{1}{2},i,j-\frac{1}{2},k+\frac{1}{2}}\right]\right]\\
&\quad-\frac{\Delta t}{2\epsilon_{zz}^{i,j,k+\frac{1}{2}}}\left[J_{zS}^{n+\frac{1}{2},i,j,k+\frac{1}{2}}-\Phi_{Hyx}^{n+\frac{1}{2},i,j,k+\frac{1}{2}}+\Phi_{Hxy}^{n+\frac{1}{2},i,j,k+\frac{1}{2}}\right]
\end{aligned}
\tag{3.92f}
$$

For the uniaxial stress piezoelectric antenna problems investigated in Chapter 5, only the update expressions for $E_z$, (3.92c) and (3.92f), need be modified beyond what has been provided in this section. Thus expressions (3.92a), (3.92b), (3.92d), and (3.92e) are already sufficient for the simulations performed herein. In the following sections, EM boundary conditions are further explored.

### 3.8.5.3 Perfect Electric Conductor Boundary Conditions

Now that the tri-diagonal ADI equations have been derived, the EM boundary conditions are revisited. Within this section the following tri-diagonal matrices are synonymous: $M_1 \rightarrow M_{x1}$, $M_2 \rightarrow M_{y1}$, $M_3 \rightarrow M_{z1}$, $M_4 \rightarrow M_{x2}$, $M_5 \rightarrow M_{y2}$, $M_6 \rightarrow M_{z2}$. Firstly, consider the perfect electric conductor (PEC) boundary condition by writing the equation for the ($N_z$-1)$^{th}$ row of the $E_y$ z-cut equation, where $N_z$ is the number of nodes in the z-direction:

$$\begin{aligned} &TRM_2(i,j,N_z-1,N_z-2)E_y^{n+\frac{1}{2}}(i,j,N_z-2) \\ &\quad + TRM_2(i,j,N_z-1,NZ-1)E_y^{n+\frac{1}{2}}(i,j,N_z-1) \\ &\quad + TRM_2(i,j,N_z-1,N_z)E_y^{n+\frac{1}{2}}(i,j,N_z) = q_1(i,j,N_z-1) \end{aligned} \tag{3.93}$$

Where $TRM_2(i,j,m,n)$ is the component of the tri-diagonal matrix $M_2$ associated with the $i^{th}$ and $j^{th}$ node and located in the $m^{th}$ row and the $n^{th}$ column. The forcing vector is $q_1$ and note that a similar equation involving $E_x$ also exists. If there is a PEC boundary condition at z=$N_z\Delta_z$ then:

$$E_y^{n+\frac{1}{2}}(i,j,N_z) = 0 \tag{3.94}$$

Combining (3.93) and (3.94) yields:

$$\begin{aligned} &TRM_2(i,j,N_z-1,N_z-2)E_y^{n+\frac{1}{2}}(i,j,N_z-2) \\ &\quad + TRM_2(i,j,N_z-1,N_z-1)E_y^{n+\frac{1}{2}}(i,j,N_z-1) = q_1(i,j,N_z-1) \end{aligned} \tag{3.95}$$

Since there is no boundary $E_y(i,j,N_z)$ term in (3.95), the top PEC boundary may be modelled by eliminating the final row and column from the tri-diagonal matrix. It is convenient however to maintain the $N_z \times N_z$ size of $M_2$, and this may be accomplished by keeping a diagonal term at the end of the matrix rather than truncation:

$$TRM_2(N_z, N_z) = 1, \qquad TRM_2(N_z - 1, N_z) = TRM_2(N_z, N_z - 1) = 0 \tag{3.96}$$

Therefore the $N_z^{th}$ row of the tri-diagonal matrix yields:

$$E_y^{n+\frac{1}{2}}(i, j, N_z) = q_1(i, j, N_z) \tag{3.97}$$

Zeroing of the tangential electric fields ($E_x$ and $E_y$) is accomplished by setting the forcing vector $q_1$ equal to zero and never updating it, which may be accomplished by omitting the boundary node $N_z$ in any for loops. Recall that at a PEC the normal magnetic fields are also zero and this condition may also be imposed by never updating these fields through the use of for loops. A similar procedure may be followed for all 5 other potential boundaries, and for the second sub-iteration.

#### 3.8.5.4 Perfect Magnetic Conductor Boundary Condition

For a perfect magnetic conductor, the boundary is shifted half a cell into the simulation space. Consider again the ($N_z$-1)$^{th}$ row of the $E_y$ z-cut equation:

$$\begin{aligned} &TRM_2(i, j, N_z - 1, N_z - 2) E_y^{n+\frac{1}{2}}(i, j, N_z - 2) \\ &\quad + TRM_2(i, j, N_z - 1, N_z - 1) E_y^{n+\frac{1}{2}}(i, j, N_z - 1) \\ &\quad + TRM_2(i, j, N_z - 1, N_z) E_y^{n+\frac{1}{2}}(i, j, N_z) = q_1(i, j, N_z - 1) \end{aligned} \tag{3.98}$$

The $E_y$ field at z=$N_z\Delta_z$ is now being determined outside of the simulation space. Fortunately, by image theory, the external electric field is known as shown in Figure 3-19 [225]:

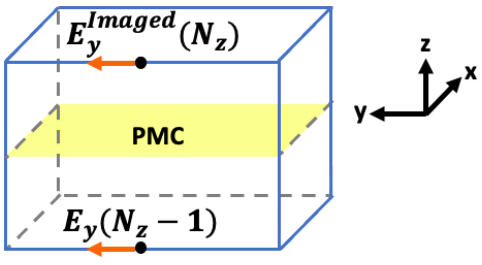


Figure 3-19: Imaged electric field across a PMC boundary.

As such:

$$E_y^{n+\frac{1}{2}}(i,j,N_z) = E_y^{n+\frac{1}{2}}(i,j,N_z-1) \tag{3.99}$$

Therefore,

$$\begin{aligned} &TRM_2(i,j,N_z-1,N_z-2)E_y^{n+\frac{1}{2}}(i,j,N_z-2) \\ &\quad + [TRM_2(i,j,N_z-1,N_z-1) \\ &\quad + TRM_2(i,j,N_z-1,NZ)]E_y^{n+\frac{1}{2}}(i,j,N_z-1) = q_1(i,j,N_z-1) \end{aligned} \tag{3.100}$$

Note that the coefficient in front of the $E_y(i,j,N_z-1)$ term changed and the boundary term $E_y(i,j,N_z)$ is gone in (3.100). Therefore, the top PMC boundary may be modelled by modification of the ($N_z$-1)$^{th}$ row/column term of the tri-diagonal matrix and elimination of the last row/column. A diagonal term may again be added to maintain the $N_z \times N_z$ size of the matrix like the PEC case.

The two tangential magnetic fields at the PMC are zero:

$$H_x^{n+\frac{1}{2}}(i,j,N_z-1) = H_y^{n+\frac{1}{2}}(i,j,N_z-1) = 0 \tag{3.101}$$

This condition may be imposed by never updating these fields through the use of for loops.

#### 3.8.5.5 Absorbing Boundary Conditions

In treating absorbing boundary conditions within the ADI-FDTD some special considerations must be made at the nodes adjacent to the boundary plane. To explain this, recall the Mur1 ABC equation for Ey at z=$N_z\Delta z$ from Section 3.4.1.3.

$$E_y^{n+\frac{1}{2}}(N_z) = E_y^n(N_z-1) + \frac{c\Delta t - 2\Delta z}{c\Delta t + 2\Delta z}\left[E_y^{n+\frac{1}{2}}(N_z-1) - E_y^n(N_z)\right] \tag{3.102}$$

This equation may be used to update the fields on the k=$N_z$ plane. Additionally, in the first sub-iteration, the update equation for the y-directed electric field is the z-cut equation which will

require special treatment for the Ey fields just below the top ABC plane (at k=$N_z$-1). The tri-diagonal matrix for a finite device in the z-direction (one that does not touch the absorbing boundary) yields the following at row NZ-1 for arbitrary node in the xy-plane (omit $i$ and $j$ designations used in the previous two sections):

$$TRM_2(NZ-1,NZ-1)E_y^{n+\frac{1}{2}}(N_z-1)+TRM_2(NZ-1,NZ)E_y^{n+\frac{1}{2}}(N_z) + TRM_2(NZ-1,NZ-2)E_y^{n+\frac{1}{2}}(N_z-2)=q_1(NZ-1) \tag{3.103}$$

Note that these equations are evaluated within free space, therefore the free space values for all coefficients may be used. Substituting (3.102) into (3.103) yields:

$$TRM_2(NZ-1,NZ-1)E_y^{n+\frac{1}{2}}(N_z-1) + TRM_2(NZ-1,NZ)\left\{E_y^n(N_z-1) + \frac{c\Delta t-2\Delta z}{c\Delta t+2\Delta z}\left[E_y^{n+\frac{1}{2}}(N_z-1)-E_y^n(N_z)\right]\right\} + TRM_2(NZ-1,NZ-2)E_y^{n+\frac{1}{2}}(N_z-2)=q_1(NZ-1) \tag{3.104}$$

To reiterate, it has been assumed that piezomagnetic material does not touch the upper boundary of the simulation space which will lead to additional coupling terms since the electric fields in the y and z directions are coupled in the first sub-iteration. Re-writing (3.104) yields:

$$
\begin{aligned}
& TRM_2(NZ-1,NZ-2)E_y^{n+\frac{1}{2}}(N_z-2) \\
& \quad + \Big\{ TRM_2(NZ-1,NZ-1) \\
& \quad + \frac{c\Delta t-2\Delta z}{c\Delta t+2\Delta z} TRM_2(NZ-1,NZ) \Big\} E_y^{n+\frac{1}{2}}(N_z-1) \\
& \quad = \frac{c\Delta t-2\Delta z}{c\Delta t+2\Delta z} TRM_2(NZ-1,NZ)E_y^n(N_z) \\
& \quad - TRM_2(NZ-1,NZ)E_y^n(N_z-1) + q_1(NZ-1)
\end{aligned}
\tag{3.105}
$$

The absorbing boundary conditions introduce additional terms on both the left- and right-hand side of the equation. The former is taken care of within the portion of the code where the ADI coefficients are defined and the latter is included in the portion of the code where the time marching scheme is contained, both through the use of if statements. (3.105) applies to the entire plane one cell adjacent to the boundary. The corresponding ABC condition for electric fields in the x-direction in the first sub-iteration is:

$$
E_x^{n+\frac{1}{2}}(N_z) = E_x^n(N_z-1) + \frac{c\Delta t-2\Delta z}{c\Delta t+2\Delta z}\left[E_x^{n+\frac{1}{2}}(N_z-1) - E_x^n(N_z)\right] \tag{3.106}
$$

This may be applied directly at the k=NZ plane without special treatment being necessary at the k=NZ-1 plane since the update equation for Ex is not the z-cut equation in the first sub-iteration. In the second sub-iteration however, a similar treatment is performed utilizing the following condition:

$$
E_x^{n+1}(N_z) = E_x^{n+\frac{1}{2}}(N_z-1) + \frac{c\Delta t-2\Delta z}{c\Delta t+2\Delta z}\left[E_x^{n+1}(N_z-1) - E_x^{n+\frac{1}{2}}(N_z)\right] \tag{3.107}
$$

Substitute (3.107) into the tri-diagonal matrix at row NZ-1 as follows:

$$
\begin{aligned}
&TRM_4(NZ-1,NZ-1)E_x^{n+1}(N_z-1)\\
&\quad+TRM_4(NZ-1,NZ)\left\{E_x^{n+\frac{1}{2}}(N_z-1)\right.\\
&\quad\left.+\frac{c\Delta t-2\Delta z}{c\Delta t+2\Delta z}\left[E_x^{n+1}(N_z-1)-E_x^{n+\frac{1}{2}}(N_z)\right]\right\}\\
&\quad+TRM_4(NZ-1,NZ-2)E_x^{n+1}(N_z-2)=q_1(NZ-1)
\end{aligned}
\tag{3.108}
$$

Re-writing (3.108) yields:

$$
\begin{aligned}
&TRM_4(NZ-1,NZ-2)E_x^{n+1}(N_z-2)\\
&\quad+\left\{TRM_4(NZ-1,NZ-1)\right.\\
&\quad\left.+\frac{c\Delta t-2\Delta z}{c\Delta t+2\Delta z}TRM_4(NZ-1,NZ)\right\}E_x^{n+1}(N_z-1)\\
&\quad=\frac{c\Delta t-2\Delta z}{c\Delta t+2\Delta z}TRM_4(NZ-1,NZ)E_x^{n+\frac{1}{2}}(N_z)\\
&\quad-TRM_4(NZ-1,NZ)E_x^{n+\frac{1}{2}}(N_z-1)+q_1(NZ-1)
\end{aligned}
\tag{3.109}
$$

The equations for the nodes adjacent to the ABC's are tabulated in Table 3-4:

| | | |
|---|---|---|
| $x=\Delta x$<br>$i=1$ | 1st | $TRM_3(1,2)E_z^{n+\frac{1}{2}}\left(2,j,k+\frac{1}{2}\right)+\left\{TRM_3(1,1)+\frac{c\Delta t-2\Delta x}{c\Delta t+2\Delta x}TRM_3(1,0)\right\}E_z^{n+\frac{1}{2}}\left(1,j,k+\frac{1}{2}\right)$<br>$=\frac{c\Delta t-2\Delta x}{c\Delta t+2\Delta x}TRM_3(1,0)E_z^n\left(0,j,k+\frac{1}{2}\right)-TRM_3(1,0)E_z^n\left(1,j,k+\frac{1}{2}\right)+p_1(1)$ |
| | 2nd | $TRM_5(1,2)E_y^{n+1}\left(2,j+\frac{1}{2},k\right)+\left\{TRM_5(1,1)+\frac{c\Delta t-2\Delta x}{c\Delta t+2\Delta x}TRM_5(1,0)\right\}E_y^{n+1}\left(1,j+\frac{1}{2},k\right)$<br>$=\frac{c\Delta t-2\Delta x}{c\Delta t+2\Delta x}TRM_5(1,0)E_y^{n+\frac{1}{2}}\left(0,j+\frac{1}{2},k\right)-TRM_5(1,0)E_y^{n+\frac{1}{2}}\left(1,j+\frac{1}{2},k\right)+q_2(1)$ |
| $x=L_x$<br>$-\Delta x$ | 1st | $TRM_3(NX-1,NX-2)E_z^{n+\frac{1}{2}}(N_x-2)+\left\{TRM_3(NX-1,NX-1)+\frac{c\Delta t-2\Delta x}{c\Delta t+2\Delta x}TRM_3(NX-1,NX)\right\}E_z^{n+\frac{1}{2}}(N_x-1)$<br>$=\frac{c\Delta t-2\Delta x}{c\Delta t+2\Delta x}TRM_3(NX-1,NX)E_z^n(N_x)-TRM_3(NX-1,NX)E_z^n(N_x-1)+p_1(N_x-1)$ |
| | 2nd | $TRM_5(NX-1,NX-2)E_y^{n+1}(N_x-2)+\left\{TRM_5(NX-1,NX-1)+\frac{c\Delta t-2\Delta x}{c\Delta t+2\Delta x}TRM_5(NX-1,NX)\right\}E_y^{n+1}(N_x-1)$<br>$=\frac{c\Delta t-2\Delta x}{c\Delta t+2\Delta x}TRM_5(NX-1,NX)E_y^{n+\frac{1}{2}}(N_x)-TRM_5(NX-1,NX)E_y^{n+\frac{1}{2}}(N_x-1)+q_2(N_x-1)$ |

| | | |
|---|---|---|
| $y = \Delta y$<br>$j = 1$ | 1st | $TRM_1(1,2)E_x^{n+\frac{1}{2}}\left(i+\frac{1}{2},2,k\right)+\left\{TRM_1(1,1)+\frac{c\Delta t-2\Delta y}{c\Delta t+2\Delta y}TRM_1(1,0)\right\}E_x^{n+\frac{1}{2}}\left(i+\frac{1}{2},1,k\right)$<br>$=\frac{c\Delta t-2\Delta y}{c\Delta t+2\Delta y}TRM_1(1,0)E_x^n\left(i+\frac{1}{2},0,k\right)-TRM_1(1,0)E_x^n\left(i+\frac{1}{2},1,k\right)+r_1(1)$ |
| | 2nd | $TRM_6(1,2)E_z^{n+1}\left(i,2,k+\frac{1}{2}\right)+\left\{TRM_6(1,1)+\frac{c\Delta t-2\Delta y}{c\Delta t+2\Delta y}TRM_6(1,0)\right\}E_z^{n+1}\left(i,1,k+\frac{1}{2}\right)$<br>$=\frac{c\Delta t-2\Delta y}{c\Delta t+2\Delta y}TRM_6(1,0)E_z^{n+\frac{1}{2}}\left(i,0,k+\frac{1}{2}\right)-TRM_6(1,0)E_z^{n+\frac{1}{2}}\left(i,1,k+\frac{1}{2}\right)+p_2(1)$ |
| $y = L_y$<br>$-\Delta y$ | 1st | $TRM_1(NY-1,NY-2)E_x^{n+\frac{1}{2}}(N_y-2)+\left\{TRM_1(NY-1,NY-1)+\frac{c\Delta t-2\Delta y}{c\Delta t+2\Delta y}TRM_1(NY-1,NY)\right\}E_x^{n+\frac{1}{2}}(N_y-1)$<br>$=\frac{c\Delta t-2\Delta y}{c\Delta t+2\Delta y}TRM_1(NY-1,NY)E_x^n(N_y)-TRM_1(NY-1,NY)E_x^n(N_y-1)+r_1(N_y-1)$ |
| | 2nd | $TRM_6(NY-1,NY-2)E_z^{n+1}(N_y-2)+\left\{TRM_6(NY-1,NY-1)+\frac{c\Delta t-2\Delta y}{c\Delta t+2\Delta y}TRM_6(NY-1,NY)\right\}E_z^{n+1}(N_y-1)$<br>$=\frac{c\Delta t-2\Delta y}{c\Delta t+2\Delta y}TRM_6(NY-1,NY)E_z^{n+\frac{1}{2}}(N_y)-TRM_6(NY-1,NY)E_z^{n+\frac{1}{2}}(N_y-1)+p_2(N_y-1)$ |
| $z = \Delta z$<br>$k = 0$ | 1st | $TRM_2(1,2)E_y^{n+\frac{1}{2}}\left(i,j+\frac{1}{2},2\right)+\left\{TRM_2(1,1)+\frac{c\Delta t-2\Delta z}{c\Delta t+2\Delta z}TRM_2(1,0)\right\}E_y^{n+\frac{1}{2}}\left(i,j+\frac{1}{2},1\right)$<br>$=\frac{c\Delta t-2\Delta z}{c\Delta t+2\Delta z}TRM_2(1,0)E_y^n\left(i,j+\frac{1}{2},0\right)-TRM_2(1,0)E_y^n\left(i,j+\frac{1}{2},1\right)+q_1(1)$ |
| | 2nd | $TRM_4(1,2)E_x^{n+1}\left(i+\frac{1}{2},j,2\right)+\left\{TRM_4(1,1)+\frac{c\Delta t-2\Delta z}{c\Delta t+2\Delta z}TRM_4(1,0)\right\}E_x^{n+1}\left(i+\frac{1}{2},j,1\right)$<br>$=\frac{c\Delta t-2\Delta z}{c\Delta t+2\Delta z}TRM_4(1,0)E_x^{n+\frac{1}{2}}\left(i+\frac{1}{2},j,0\right)-TRM_4(1,0)E_x^{n+\frac{1}{2}}\left(i+\frac{1}{2},j,1\right)+r_2(1)$ |
| $z = L_z$<br>$-\Delta z$ | 1st | $TRM_2(NZ-1,NZ-2)E_y^{n+\frac{1}{2}}(N_z-2)+\left\{TRM_2(NZ-1,NZ-1)+\frac{c\Delta t-2\Delta z}{c\Delta t+2\Delta z}TRM_2(NZ-1,NZ)\right\}E_y^{n+\frac{1}{2}}(N_z-1)$<br>$=\frac{c\Delta t-2\Delta z}{c\Delta t+2\Delta z}TRM_2(NZ-1,NZ)E_y^n(N_z)-TRM_2(NZ-1,NZ)E_y^n(N_z-1)+q_1(N_z-1)$ |
| | 2nd | $TRM_4(NZ-1,NZ-2)E_x^{n+1}(N_z-2)+\left\{TRM_4(NZ-1,NZ-1)+\frac{c\Delta t-2\Delta z}{c\Delta t+2\Delta z}TRM_4(NZ-1,NZ)\right\}E_x^{n+1}(N_z-1)$<br>$=\frac{c\Delta t-2\Delta z}{c\Delta t+2\Delta z}TRM_4(NZ-1,NZ)E_x^{n+\frac{1}{2}}(N_z)-TRM_4(NZ-1,NZ)E_x^{n+\frac{1}{2}}(N_z-1)+r_2(N_z-1)$ |

Table 3-4: Free space Mur1 equations for nodes adjacent to ABCs.

Sections 3.6, 3.7, and 3.8 fully define the electrodynamics utilized herein. In the following sections, the mechanical expressions will be introduced and coupled to the CPML-ADI-FDTD equations of this section (3.92a-f) via piezoelectric coupling coefficients.

## 3.9 Uniaxial Stress Update Equations w/ Piezoelectricity

Now that the CPML-ADI-FDTD methodology has been introduced, the 1D mechanical update equations with piezoelectricity will be presented so that the final coupled ADI equations will be clear. The expressions are first presented in continuum form and then discretized. Additionally, guidance for how to temporally define the mechanical stress and velocity is provided.

### 3.9.1 Mechanical Expressions in Continuum Form for Uniaxial Stress

When one dimension of a material is much larger than the other two, as in an axial bar, the normal stresses in the two short dimensions are negligible compared to the normal stress in the axial direction. If additionally, there are no shear stresses then the problem is 1-dimensional and the following relations hold:

$$T_{zz} \neq 0 \tag{3.110a}$$

$$T_{xx} = T_{yy} = T_{yz} = T_{xz} = T_{xy} = S_{yz} = S_{xz} = S_{xy} = 0 \tag{3.110b}$$

$$S_{zz} \neq 0 \tag{3.110c}$$

$$S_{xx} = S_{yy} \neq 0 \tag{3.110d}$$

Where the axial direction is assumed to be the z-direction and the material is assumed to be either isotropic or transversely isotropic about the z-axis. Thus, the stress, strain, and velocity relations are as follows:

$$S_{xx} = S_{yy} = -\frac{c_{xxzz}}{c_{xxxx} + c_{xxyy}} S_{zz} \tag{3.111a}$$

$$T_{zz} = E_{zzzz} S_{zz} \tag{3.111b}$$

$$E_{zzzz} = \frac{1}{s_{zzzz}} = c_{zzzz} - 2\frac{c_{xxzz}^2}{c_{xxxx} + c_{xxyy}} \tag{3.111c}$$

$$\rho \dot{v}_x = 0 \tag{3.111d}$$

$$\rho \dot{v}_y = 0 \tag{3.111e}$$

$$\rho \dot{v}_z = T_{zz,z} \tag{3.111f}$$

Where $E_{zzzz}$ is the Young's modulus and $s_{zzzz}$ is the compliance relating $S_{zz}$ to $T_{zz}$. The "piggybacking" strains ($S_{xx}$ and $S_{yy}$) from Poisson's effect are not necessary to find a solution mechanically. Additionally, piezoelectric descriptions where coupling is via stress (e.g., d-form and g-form [194]) will not need to invoke Poisson's effect (since there are no Poisson's stresses) and piezoelectric descriptions where coupling is via strain (e.g., h-form and e-form) cover Poisson's effect through the $h_{31}$ or $e_{31}$ terms. Thus, Poisson's strains (if properly accounted for) are not needed to find a solution to the piezoelectric problem either. The method of accounting for the Poisson's strains in a piezoelectric problem where coupling is via strain is presented in the following section.

### 3.9.2 Piezoelectric Coupling Under Uniaxial Stress

Emerging technologies are beginning to leverage mechanically 1D axial bar piezoelectric antennas [152]. These devices are the simplest to manufacture and provide significant boosts to dipole moment at electrically small sizes compared to metallic antennas. This 1D axial bar configuration is optimal for piezoelectric devices to minimize depolarization, since the poling and polarization current are in the axial direction and the cross-section is small compared to the length. Therefore, mechanically 1D PEA devices are not only easier to model but also ultimately perform better than 2D/3D devices, especially when metal wiring is added as in [163].

For a purely mechanical system, equations (3.68a-f) are enough to write update equations. Herein, however, piezoelectric coupling [194][198] will be added in. If stress is used for piezoelectric coupling (e.g., when using $D = dT + \epsilon^T E$), then the uniaxial stress state makes writing update equations simple as only one mechanical term appears (namely, the non-zero stress). If, however, the strain is used for piezoelectric coupling (such as when using $D = eS + \epsilon^S E$) within a uniaxial stress problem, then Poisson's strains will appear, complicating the

formulation. These Poisson's strains may be eliminated by solving for the cross-sectional strains and performing substitutions as highlighted next.

Within this section, Voigt's notation is leveraged. Also, numbers are used for subscripts on material properties and letters are used for subscripts on fields. By the mechanical constitutive relation (2.148), and by using $h_{31} = h_{32}$ and $S_{xx} = S_{yy}$, the cross-sectional stresses being zero leads to:

$$T_{xx} = T_{yy} = 0 = (c_{11}^D + c_{12}^D)S_{xx} + c_{13}^D S_{zz} - h_{31} D_z \tag{3.112}$$

Where viscous damping is ignored for brevity and coupling tensors like $h$, $d$, $g$, and $e$ always denote piezoelectric coupling within this chapter (piezomagnetism is ignored). Solving (3.112) for the cross-sectional strain $S_{xx}$ gives:

$$S_{xx} = -\frac{c_{13}^D}{c_{11}^D + c_{12}^D} S_{zz} + \frac{h_{31}}{c_{11}^D + c_{12}^D} D_z \tag{3.113}$$

Substituting (3.113) into the $T_{zz}$ term in (2.148), and simplifying yields:

$$T_{zz} = \left( c_{33}^D - 2\frac{(c_{13}^D)^2}{c_{11}^D + c_{12}^D} \right) S_{zz} - \left( h_{33} - \frac{2c_{13}^D h_{31}}{c_{11}^D + c_{12}^D} \right) D_z \tag{3.114}$$

Where the coefficient in front of strain $S_{zz}$ in (3.114) is the Young's modulus at constant flux ($E_{33}^D$) and the coefficient in front of $D_z$ is the effective piezoelectric coefficient $h_{33,Poi}$. These effective properties take Poisson's effect into account and are denoted by the subscript "*Poi*" herein. Similarly, the z-component of the electric constitutive relation (2.175) will include Poisson's ($e_{31}$) terms for a strain coupled (e-form) uniaxial stress problem:

$$D_z = \epsilon_{33}^S E_z + 2e_{31} S_{xx} + e_{33} S_{zz} \tag{3.115}$$

Where (3.115) utilizes $e_{31} = e_{32}$ and $S_{xx} = S_{yy}$. Since the strain coupled e-form was used in (3.115), an equivalent expression for the cross-sectional strain may been written as follows:

$$S_{xx} = -\frac{c_{13}^E}{c_{11}^E + c_{12}^E} S_{zz} + \frac{e_{31}}{c_{11}^E + c_{12}^E} E_z \tag{3.116}$$

Equation (3.116) is equivalent to (3.113). Thus, there are multiple ways to arrive at an equivalent solution if care is taken with all coefficients. Substitute (3.116) into (3.115):

$$D_z = \left(\epsilon_{33}^S + \frac{2e_{31}^2}{c_{11}^E + c_{12}^E}\right)E_z + \left(e_{33} - \frac{2e_{31}c_{13}^E}{c_{11}^E + c_{12}^E}\right)S_{zz} \tag{3.117}$$

Where the coefficients in front of the $E_z$ and $S_{zz}$ terms are the effective permittivity $\epsilon_{33,Poi}^S$ and piezoelectric coefficient $e_{33,Poi}$. Recall, these terms are not unique, even though their numerical value is, as there are multiple ways to acquire equivalent terms. For example, the effective permittivity for strain coupling under uniaxial stress may also be written as:

$$\epsilon_{33,Poi}^S = \epsilon_{33}^S + \frac{2e_{31}^2}{c_{11}^E + c_{12}^E} = \frac{\epsilon_{33}^S(c_{11}^D + c_{12}^D)}{c_{11}^D + c_{12}^D - 2e_{31}h_{31}} \tag{3.118}$$

Effective properties do not vary much from those that do not take Poisson's effect into account. For example, in X4B PIN-PMN-PT (utilized for simulations herein), the effective permittivity and regular permittivity vary by about 3%.

This section highlights that either stress or strain may be utilized for piezoelectric coupling within a 1D uniaxial stress configuration. Additionally, both methods are equal in complexity if effective properties are derived when using strain for coupling.

### 3.10 Stress Driven Piezoelectric Antenna for Uniaxial Stress

If a uniaxial stress $T_{zz}$ is present, and the piezoelectric tensor has a non-zero $d_{33}$ coefficient somewhere in the simulation space, then additional currents will appear in the forcing vector of the CPML-ADI-FDTD equations. First, consider the electric constitutive relation assuming a diagonal permittivity tensor:

$$D_z^{n+\frac{1}{2}} = \epsilon_{33}^T E_z^{n+\frac{1}{2}} + d_{33}T_{zz}^{n+\frac{1}{2}} \tag{3.119}$$

For both sub-iterations, the piezoelectric term will affect the $E_z$ update matrix expression only as the non-zero $T_{zz}$ effects $E_z$ exclusively. The $E_z$ x-cut and y-cut equations for the 1st and 2nd sub-iterations respectively are derived following the same process as Section 3.8 yielding:

$$-\frac{\Delta t^2}{4\epsilon_{zz}^{i,j,k+\frac{1}{2}}\mu_{yy}^{i+\frac{1}{2},j,k+\frac{1}{2}}\kappa_{xE}^{i}\kappa_{xH}^{i}\Delta x^2}E_z^{n+\frac{1}{2},i+1,j,k+\frac{1}{2}}+\left[1+\frac{\Delta t^2}{4\epsilon_{zz}^{i,j,k+\frac{1}{2}}\kappa_{xE}^{i}\Delta x^2}\left(\frac{1}{\kappa_{xH}^{i}\mu_{yy}^{i+\frac{1}{2},j,k+\frac{1}{2}}}+\frac{1}{\kappa_{xH}^{i-1}\mu_{yy}^{i-\frac{1}{2},j,k+\frac{1}{2}}}\right)\right]E_z^{n+\frac{1}{2},i,j,k+\frac{1}{2}}$$

$$-\frac{\Delta t^2}{4\epsilon_{zz}^{i,j,k+\frac{1}{2}}\mu_{yy}^{i-\frac{1}{2},j,k+\frac{1}{2}}\kappa_{xE}^{i}\kappa_{xH}^{i-1}\Delta x^2}E_z^{n+\frac{1}{2},i-1,j,k+\frac{1}{2}}$$

$$=E_z^{n,i,j,k+\frac{1}{2}}+\frac{\Delta t}{2\epsilon_{zz}^{i,j,k+\frac{1}{2}}\kappa_{xE}^{i}\Delta x}\left(H_y^{n,i+\frac{1}{2},j,k+\frac{1}{2}}-H_y^{n,i-\frac{1}{2},j,k+\frac{1}{2}}\right)-\frac{\Delta t}{2\epsilon_{zz}^{i,j,k+\frac{1}{2}}\kappa_{yE}^{j}\Delta y}\left(H_x^{n,i,j+\frac{1}{2},k+\frac{1}{2}}-H_x^{n,i,j-\frac{1}{2},k+\frac{1}{2}}\right)$$

$$-\frac{\Delta t^2}{4\epsilon_{zz}^{i,j,k+\frac{1}{2}}\kappa_{zH}^{k}\kappa_{xE}^{i}\Delta x\Delta z}\left[\frac{1}{\mu_{yy}^{i+\frac{1}{2},j,k+\frac{1}{2}}}\left(E_x^{n,i+\frac{1}{2},j,k+1}-E_x^{n,i+\frac{1}{2},j,k}\right)-\frac{1}{\mu_{yy}^{i-\frac{1}{2},j,k+\frac{1}{2}}}\left(E_x^{n,i-\frac{1}{2},j,k+1}-E_x^{n,i-\frac{1}{2},j,k}\right)\right]$$

$$-\frac{\Delta t^2}{4\epsilon_{zz}^{i,j,k+\frac{1}{2}}\kappa_{xE}^{i}\Delta x}\left[\frac{1}{\mu_{yy}^{i+\frac{1}{2},j,k+\frac{1}{2}}}\left(\mathcal{M}_y^{n+\frac{1}{2},i+\frac{1}{2},j,k+\frac{1}{2}}-\Phi_{Ezx}^{n,i+\frac{1}{2},j,k+\frac{1}{2}}+\Phi_{Exz}^{n,i+\frac{1}{2},j,k+\frac{1}{2}}\right)\right.$$

$$\left.-\frac{1}{\mu_{yy}^{i-\frac{1}{2},j,k+\frac{1}{2}}}\left(\mathcal{M}_y^{n+\frac{1}{2},i-\frac{1}{2},j,k+\frac{1}{2}}-\Phi_{Ezx}^{n,i-\frac{1}{2},j,k+\frac{1}{2}}+\Phi_{Exz}^{n,i-\frac{1}{2},j,k+\frac{1}{2}}\right)\right]$$

$$-\frac{\Delta t}{2\epsilon_{zz}^{i,j,k+\frac{1}{2}}}\left[J_{zS}^{n+\frac{1}{2},i,j,k+\frac{1}{2}}-\Phi_{Hyx}^{n,i,j,k+\frac{1}{2}}+\Phi_{Hxy}^{n,i,j,k+\frac{1}{2}}\right]-\frac{d_{33}^{i,j,k+\frac{1}{2}}}{\epsilon_{zz}^{i,j,k+\frac{1}{2}}}\left[T_{zz}^{n+\frac{1}{2},i,j,k+\frac{1}{2}}-T_{zz}^{n,i,j,k+\frac{1}{2}}\right]$$

(3.120a)

$$
\begin{aligned}
&-\frac{\Delta t^2}{4\epsilon_{zz}^{i,j,k+\frac{1}{2}}\mu_{xx}^{i,j+\frac{1}{2},k+\frac{1}{2}}\kappa_{yE}^{j}\kappa_{yH}^{j}\Delta y^2}E_z^{n+1,i,j+1,k+\frac{1}{2}}+\left[1+\frac{\Delta t^2}{4\epsilon_{zz}^{i,j,k+\frac{1}{2}}\kappa_{yE}^{j}\Delta y^2}\left(\frac{1}{\kappa_{yH}^{j}\mu_{xx}^{i,j+\frac{1}{2},k+\frac{1}{2}}}+\frac{1}{\kappa_{yH}^{j-1}\mu_{xx}^{i,j-\frac{1}{2},k+\frac{1}{2}}}\right)\right]E_z^{n+1,i,j,k+\frac{1}{2}}\\
&\quad-\frac{\Delta t^2}{4\epsilon_{zz}^{i,j,k+\frac{1}{2}}\mu_{xx}^{i,j-\frac{1}{2},k+\frac{1}{2}}\kappa_{yE}^{j}\kappa_{yH}^{j-1}\Delta y^2}E_z^{n+1,i,j-1,k+\frac{1}{2}}\\
&\quad=E_z^{n+\frac{1}{2},i,j,k+\frac{1}{2}}+\frac{\Delta t}{2\epsilon_{zz}^{i,j,k+\frac{1}{2}}\kappa_{xE}^{i}\Delta x}\left(H_y^{n+\frac{1}{2},i+\frac{1}{2},j,k+\frac{1}{2}}-H_y^{n+\frac{1}{2},i-\frac{1}{2},j,k+\frac{1}{2}}\right)\\
&\quad-\frac{\Delta t}{2\epsilon_{zz}^{i,j,k+\frac{1}{2}}\kappa_{yE}^{j}\Delta y}\left(H_x^{n+\frac{1}{2},i,j+\frac{1}{2},k+\frac{1}{2}}-H_x^{n+\frac{1}{2},i,j-\frac{1}{2},k+\frac{1}{2}}\right)\\
&\quad-\frac{\Delta t^2}{4\epsilon_{zz}^{i,j,k+\frac{1}{2}}\kappa_{yE}^{j}\Delta y\kappa_{zH}^{k}\Delta z}\left[\frac{1}{\mu_{xx}^{i,j+\frac{1}{2},k+\frac{1}{2}}}\left(E_y^{n+\frac{1}{2},i,j+\frac{1}{2},k+1}-E_y^{n+\frac{1}{2},i,j+\frac{1}{2},k}\right)\right.\\
&\quad\left.-\frac{1}{\mu_{xx}^{i,j-\frac{1}{2},k+\frac{1}{2}}}\left(E_y^{n+\frac{1}{2},i,j-\frac{1}{2},k+1}-E_y^{n+\frac{1}{2},i,j-\frac{1}{2},k}\right)\right]\\
&\quad+\frac{\Delta t^2}{4\epsilon_{zz}^{i,j,k+\frac{1}{2}}\kappa_{yE}^{j}\Delta y}\left[\frac{1}{\mu_{xx}^{i,j+\frac{1}{2},k+\frac{1}{2}}}\left[\mathcal{M}_x^{n+\frac{1}{2},i,j+\frac{1}{2},k+\frac{1}{2}}-\Phi_{Eyz}^{n+\frac{1}{2},i,j+\frac{1}{2},k+\frac{1}{2}}+\Phi_{Ezy}^{n+\frac{1}{2},i,j+\frac{1}{2},k+\frac{1}{2}}\right]\right.\\
&\quad\left.-\frac{\Delta t}{2\mu_{xx}^{i,j-\frac{1}{2},k+\frac{1}{2}}}\left[\mathcal{M}_x^{n+\frac{1}{2},i,j-\frac{1}{2},k+\frac{1}{2}}-\Phi_{Eyz}^{n+\frac{1}{2},i,j-\frac{1}{2},k+\frac{1}{2}}+\Phi_{Ezy}^{n+\frac{1}{2},i,j-\frac{1}{2},k+\frac{1}{2}}\right]\right]\\
&\quad-\frac{\Delta t}{2\epsilon_{zz}^{i,j,k+\frac{1}{2}}}\left[J_{zS}^{n+\frac{1}{2},i,j,k+\frac{1}{2}}-\Phi_{Hyx}^{n+\frac{1}{2},i,j,k+\frac{1}{2}}+\Phi_{Hxy}^{n+\frac{1}{2},i,j,k+\frac{1}{2}}\right]-\frac{d_{33}^{i,j,k+\frac{1}{2}}}{\epsilon_{zz}^{i,j,k+\frac{1}{2}}}\left[T_{zz}^{n+1,i,j,k+\frac{1}{2}}-T_{zz}^{n+\frac{1}{2},i,j,k+\frac{1}{2}}\right]
\end{aligned}
\tag{3.120b}
$$

Note that a piezoelectric driven electric field is now present in the forcing vector for both sub-iterations, and that this piezoelectric term includes an unknown stress. For example, in the first sub-iteration the piezoelectric term is written in shorthand as:

$$
E_{z_{d_{33}}}^{n+\frac{1}{4},i,j,k+\frac{1}{2}}=-\frac{d_{33}^{i,j,k+\frac{1}{2}}\Delta t}{2\epsilon_{zz}^{i,j,k+\frac{1}{2}}}\dot{T}_{zz}^{n+\frac{1}{4},i,j,k+\frac{1}{2}} \tag{3.121}
$$

It is not recommended that this unknown stress issue be rectified via substitution of the stress update equation, as this will introduce additional unknown electric fields and the

computationally elegant tri-diagonal matrices will be lost. Attempts to perform simulations for this case also yielded unstable results. If, however, the stresses are hard sourced (i.e., when stresses are known a priori), then there is no longer an issue. In this case, the elastodynamic equation is no longer evoked and a decoupled formulation results. Thus, a full-wave mechanical simulation is bypassed, increasing computational efficiency at the cost of reduced accuracy. Work from Lee in 1989 [104][105] suggests that the stresses and electric fields within a piezoelectric radiator are not significantly changed whether Maxwell's equations are used to update the surrounding EM fields however, therefore the approximation described herein is reasonable. This uncoupled stress driven formulation is utilized in Chapter 5 to simulate an infinite piezoelectric plate.

To solve the fully coupled problem, a simpler approach is to leverage the fact that the velocity terms are a quarter time step staggered with respect to the EM fields and the stresses. Therefore, the strain rate is completely known in terms of velocities and a piezoelectric constitutive relation in terms of strains (e.g., h-form or e-form) is more palatable. A derivation involving strains is presented in the following section.

### 3.11 Strain Driven Piezoelectric Antenna for Uniaxial Stress

If a uniaxial stress $T_{zz}$ is present, and the piezoelectric tensor has non-zero $e_{33}$ and $e_{31}$ coefficients somewhere in the simulation space, then additional currents will appear in the forcing vector of the ADI-FDTD equations. First, consider the electric constitutive relation in rate form:

$$\dot{D}_z^{n+\frac{1}{4}} = \epsilon_{zz}^S \dot{E}_z^{n+\frac{1}{4}} + 2e_{31} v_{x,x}^{n+\frac{1}{4}} + e_{33} v_{z,z}^{n+\frac{1}{4}} \tag{3.122}$$

Where $v_i$ are the internal axial velocities and $e_{31}$ is the Poisson's coupling term. The method of accounting for the Poisson's term was covered in Section 3.9. Note the temporal homogeneity of the expression which is the reason this is the preferred method of coupling Maxwell's to Newton's law via piezoelectricity. For both sub-iterations, the piezoelectric term will

affect the $E_z$ update matrix expression only. The electrical constitutive relation in rate form is substituted into Ampere's law yielding the following x-cut and y-cut expressions for the 1st and 2nd sub-iterations respectively:

$$
\begin{aligned}
&-\frac{\Delta t^2}{4\epsilon_{zz,Poi}^{i,j,k+\frac{1}{2}}\mu_{yy}^{i+\frac{1}{2},j,k+\frac{1}{2}}\kappa_{xE}^{i}\kappa_{xH}^{i}\Delta x^2}E_z^{n+\frac{1}{2},i+1,j,k+\frac{1}{2}}+\left[1+\frac{\Delta t^2}{4\epsilon_{zz,Poi}^{i,j,k+\frac{1}{2}}\kappa_{xE}^{i}\Delta x^2}\left(\frac{1}{\kappa_{xH}^{i}\mu_{yy}^{i+\frac{1}{2},j,k+\frac{1}{2}}}+\frac{1}{\kappa_{xH}^{i-1}\mu_{yy}^{i-\frac{1}{2},j,k+\frac{1}{2}}}\right)\right]E_z^{n+\frac{1}{2},i,j,k+\frac{1}{2}}\\
&\quad-\frac{\Delta t^2}{4\epsilon_{zz,Poi}^{i,j,k+\frac{1}{2}}\mu_{yy}^{i-\frac{1}{2},j,k+\frac{1}{2}}\kappa_{xE}^{i}\kappa_{xH}^{i-1}\Delta x^2}E_z^{n+\frac{1}{2},i-1,j,k+\frac{1}{2}}\\
&\quad=E_z^{n,i,j,k+\frac{1}{2}}+\frac{\Delta t}{2\epsilon_{zz,Poi}^{i,j,k+\frac{1}{2}}\kappa_{xE}^{i}\Delta x}\left(H_y^{n,i+\frac{1}{2},j,k+\frac{1}{2}}-H_y^{n,i-\frac{1}{2},j,k+\frac{1}{2}}\right)-\frac{\Delta t}{2\epsilon_{zz,Poi}^{i,j,k+\frac{1}{2}}\kappa_{yE}^{j}\Delta y}\left(H_x^{n,i,j+\frac{1}{2},k+\frac{1}{2}}-H_x^{n,i,j-\frac{1}{2},k+\frac{1}{2}}\right)\\
&\quad-\frac{\Delta t^2}{4\epsilon_{zz,Poi}^{i,j,k+\frac{1}{2}}\kappa_{zH}^{k}\kappa_{xE}^{i}\Delta x\Delta z}\left[\frac{1}{\mu_{yy}^{i+\frac{1}{2},j,k+\frac{1}{2}}}\left(E_x^{n,i+\frac{1}{2},j,k+1}-E_x^{n,i+\frac{1}{2},j,k}\right)-\frac{1}{\mu_{yy}^{i-\frac{1}{2},j,k+\frac{1}{2}}}\left(E_x^{n,i-\frac{1}{2},j,k+1}-E_x^{n,i-\frac{1}{2},j,k}\right)\right]\\
&\quad-\frac{\Delta t^2}{4\epsilon_{zz,Poi}^{i,j,k+\frac{1}{2}}\kappa_{xE}^{i}\Delta x}\left[\frac{1}{\mu_{yy}^{i+\frac{1}{2},j,k+\frac{1}{2}}}\left(\mathcal{M}_y^{n+\frac{1}{2},i+\frac{1}{2},j,k+\frac{1}{2}}-\Phi_{Ezx}^{n,i+\frac{1}{2},j,k+\frac{1}{2}}+\Phi_{Exz}^{n,i+\frac{1}{2},j,k+\frac{1}{2}}\right)\right.\\
&\quad\left.-\frac{1}{\mu_{yy}^{i-\frac{1}{2},j,k+\frac{1}{2}}}\left(\mathcal{M}_y^{n+\frac{1}{2},i-\frac{1}{2},j,k+\frac{1}{2}}-\Phi_{Ezx}^{n,i-\frac{1}{2},j,k+\frac{1}{2}}+\Phi_{Exz}^{n,i-\frac{1}{2},j,k+\frac{1}{2}}\right)\right]\\
&\quad-\frac{\Delta t}{2\epsilon_{zz,Poi}^{i,j,k+\frac{1}{2}}}\left[J_{zS}^{n+\frac{1}{2},i,j,k+\frac{1}{2}}-\Phi_{Hyx}^{n,i,j,k+\frac{1}{2}}+\Phi_{Hxy}^{n,i,j,k+\frac{1}{2}}\right]-\frac{e_{33,Poi}^{i,j,k+\frac{1}{2}}\Delta t}{2\epsilon_{zz,Poi}^{i,j,k+\frac{1}{2}}\kappa_{zH}^{k}\Delta z}\left(v_z^{n+\frac{1}{4},k+1}-v_z^{n+\frac{1}{4},k}\right)
\end{aligned}
\tag{3.123a}
$$

$$
\begin{aligned}
&-\frac{\Delta t^2}{4\epsilon_{zz,Poi}^{i,j,k+\frac{1}{2}}\mu_{xx}^{i,j+\frac{1}{2},k+\frac{1}{2}}\kappa_{yE}^{j}\kappa_{yH}^{j}\Delta y^2}E_z^{n+1,i,j+1,k+\frac{1}{2}}+\left[1+\frac{\Delta t^2}{4\epsilon_{zz,Poi}^{i,j,k+\frac{1}{2}}\kappa_{yE}^{j}\Delta y^2}\left(\frac{1}{\kappa_{yH}^{j}\mu_{xx}^{i,j+\frac{1}{2},k+\frac{1}{2}}}+\frac{1}{\kappa_{yH}^{j-1}\mu_{xx}^{i,j-\frac{1}{2},k+\frac{1}{2}}}\right)\right]E_z^{n+1,i,j,k+\frac{1}{2}}\\
&\quad-\frac{\Delta t^2}{4\epsilon_{zz,Poi}^{i,j,k+\frac{1}{2}}\mu_{xx}^{i,j-\frac{1}{2},k+\frac{1}{2}}\kappa_{yE}^{j}\kappa_{yH}^{j-1}\Delta y^2}E_z^{n+1,i,j-1,k+\frac{1}{2}}\\
&\quad=E_z^{n+\frac{1}{2},i,j,k+\frac{1}{2}}+\frac{\Delta t}{2\epsilon_{zz,Poi}^{i,j,k+\frac{1}{2}}\kappa_{xE}^{i}\Delta x}\left(H_y^{n+\frac{1}{2},i+\frac{1}{2},j,k+\frac{1}{2}}-H_y^{n+\frac{1}{2},i-\frac{1}{2},j,k+\frac{1}{2}}\right)\\
&\quad-\frac{\Delta t}{2\epsilon_{zz,Poi}^{i,j,k+\frac{1}{2}}\kappa_{yE}^{j}\Delta y}\left(H_x^{n+\frac{1}{2},i,j+\frac{1}{2},k+\frac{1}{2}}-H_x^{n+\frac{1}{2},i,j-\frac{1}{2},k+\frac{1}{2}}\right)\\
&\quad-\frac{\Delta t^2}{4\epsilon_{zz,Poi}^{i,j,k+\frac{1}{2}}\kappa_{yE}^{j}\Delta y\kappa_{zH}^{k}\Delta z}\left[\frac{1}{\mu_{xx}^{i,j+\frac{1}{2},k+\frac{1}{2}}}\left(E_y^{n+\frac{1}{2},i,j+\frac{1}{2},k+1}-E_y^{n+\frac{1}{2},i,j+\frac{1}{2},k}\right)\right.\\
&\quad\left.-\frac{1}{\mu_{xx}^{i,j-\frac{1}{2},k+\frac{1}{2}}}\left(E_y^{n+\frac{1}{2},i,j-\frac{1}{2},k+1}-E_y^{n+\frac{1}{2},i,j-\frac{1}{2},k}\right)\right]\\
&\quad+\frac{\Delta t^2}{4\epsilon_{zz,Poi}^{i,j,k+\frac{1}{2}}\kappa_{yE}^{j}\Delta y}\left[\frac{1}{\mu_{xx}^{i,j+\frac{1}{2},k+\frac{1}{2}}}\left[\mathcal{M}_x^{n+\frac{1}{2},i,j+\frac{1}{2},k+\frac{1}{2}}-\Phi_{Eyz}^{n+\frac{1}{2}i,j+\frac{1}{2},k+\frac{1}{2}}+\Phi_{Ezy}^{n+\frac{1}{2},i,j+\frac{1}{2},k+\frac{1}{2}}\right]\right.\\
&\quad\left.-\frac{\Delta t}{2\mu_{xx}^{i,j-\frac{1}{2},k+\frac{1}{2}}}\left[\mathcal{M}_x^{n+\frac{1}{2},i,j-\frac{1}{2},k+\frac{1}{2}}-\Phi_{Eyz}^{n+\frac{1}{2}i,j-\frac{1}{2},k+\frac{1}{2}}+\Phi_{Ezy}^{n+\frac{1}{2},i,j-\frac{1}{2},k+\frac{1}{2}}\right]\right]\\
&\quad-\frac{\Delta t}{2\epsilon_{zz,Poi}^{i,j,k+\frac{1}{2}}}\left[J_{zS}^{n+\frac{1}{2},i,j,k+\frac{1}{2}}-\Phi_{Hyx}^{n+\frac{1}{2},i,j,k+\frac{1}{2}}+\Phi_{Hxy}^{n+\frac{1}{2},i,j,k+\frac{1}{2}}\right]-\frac{e_{33,Poi}^{i,j,k+\frac{1}{2}}\Delta t}{2\epsilon_{zz,Poi}^{i,j,k+\frac{1}{2}}\kappa_{zH}^{k}\Delta z}\left(v_z^{n+\frac{3}{4},k+1}-v_z^{n+\frac{3}{4},k}\right)
\end{aligned}
\tag{3.123b}
$$

Note that effective properties are utilized to account for Poisson's effect. Since leapfrogging (explicit conditionally stable updating) is utilized on the mechanical side, the velocities are already known. Also, the tri-diagonal matrices remain intact.

Once the electric fields are known the magnetic fluxes and fields are calculated via Faraday's law and the magnetic constitutive relations respectively. Then the electric fluxes may be calculated via Ampere's law. The stress and velocity are then updated using the mechanical

constitutive relation and the elastodynamic equation respectively as discussed in the following sections.

### 3.11.1 Stress Update Equations

The stress is updated via the h-form of the mechanical constitutive relation utilizing effective properties that consider Poisson's effect as follows:

$$T_{zz}^{n+\frac{1}{2},k+\frac{1}{2}} = T_{zz}^{n,k+\frac{1}{2}} + \frac{E_{33}^{D,k+\frac{1}{2}}\Delta t}{2\kappa_{zH}^{k}\Delta z}\left(v_z^{n+\frac{1}{4},k+1} - v_z^{n+\frac{1}{4},k}\right) - h_{33,Poi}^{k+\frac{1}{2}}\left(D_z^{n+\frac{1}{2},i_{int},j_{int},k+\frac{1}{2}} - D_z^{n,i_{int},j_{int},k+\frac{1}{2}}\right) + \frac{\eta_{33}}{\Delta z}\left[v_z^{n+\frac{1}{4},k+1} - v_z^{n+\frac{1}{4},k} - v_z^{n-\frac{1}{4},k+1} + v_z^{n-\frac{1}{4},k}\right] \quad (3.124a)$$

Where (3.124a) assumes that the electric flux has already been updated this time step so the stress must be updated after the flux. The acceleration gradient in (3.124a) used for damping is taken from a slightly earlier time $t = n\Delta t$ and therefore the finite difference expression (3.124a) is not strictly temporally homogenous. This use of a previous time step for the mechanical damping term is consistent with [131] and does not induce significant error due to the mechanically tiny time step used in the simulations. Since the stress $T_{zz}$ is internal to the piezoelectric antenna, and the electric flux $D_z$ is uniform along the cross-section of the bar, the i and j indices are any that would place $D_z$ within the device (i.e., not in free space or at the interface). These indices are denoted as $i_{int}$ and $j_{int}$ in (3.124a). The mechanical constitutive relations used to update the stress are identical in the second sub-iteration since none of Maxwell's equations are present. Simply move all fields forward by a half time step, namely:

$$T_{zz}^{n+1,k+\frac{1}{2}} = T_{zz}^{n+\frac{1}{2},k+\frac{1}{2}} + \frac{E_{33}^{D,k+\frac{1}{2}}\Delta t}{2\kappa_{zH}^{k}\Delta z}\left(v_z^{n+\frac{3}{4},k+1} - v_z^{n+\frac{3}{4},k}\right)$$
$$- h_{33,Poi}^{k+\frac{1}{2}}\left(D_z^{n+1,i_{int},j_{int},k+\frac{1}{2}} - D_z^{n+\frac{1}{2},i_{int},j_{int},k+\frac{1}{2}}\right) \quad (3.124b)$$
$$+ \frac{\eta_{33}}{\Delta z}\left[v_z^{n+\frac{3}{4},k+1} - v_z^{n+\frac{3}{4},k} - v_z^{n+\frac{1}{4},k+1} + v_z^{n+\frac{1}{4},k}\right]$$

The stress update occurs after the EM fields are updated but before the velocity which will now be discussed.

### 3.11.2 Velocity Update Equations

The velocity within the simulation space is updated using the elastodynamic equation which is an expression of the balance of linear momentum and is therefore unaffected by magnetoelastic and piezoelectric coupling. The equation may be written as:

$$\rho\dot{v}_i = T_{ij,j} \quad (2.12b)$$

Recall that the velocities are temporally defined at times $t = ½(\tau\text{-}½)\Delta t,\ \tau = 1,2,3,\ldots$ (i.e., staggered with the stress and EM fields). The velocity at time $t = 1/4\Delta t$ is known since the stresses at time $t = 0$ is known. Thus, the update expressions for the 1st and 2nd sub-iterations yield velocities at times $t = (n + 3/4)\Delta t$ and $t = (n + 5/4)\Delta t$ respectively. Since (2.12b) is relatively simple, the general update expressions will be briefly derived and then simplified for the uniaxial stress case. Equation (2.12b) may be expanded and written in the following finite difference form for the 2nd sub-iteration:

$$\frac{2\rho\left(i,j+\frac{1}{2},k+\frac{1}{2}\right)}{\Delta t}\left[v_x^{n+\frac{3}{4}}\left(i,j+\frac{1}{2},k+\frac{1}{2}\right) - v_x^{n+\frac{1}{4}}\left(i,j+\frac{1}{2},k+\frac{1}{2}\right)\right]$$
$$= \frac{1}{\Delta x}\left[T_{xx}^{n+\frac{1}{2}}\left(i+\frac{1}{2},j+\frac{1}{2},k+\frac{1}{2}\right) - T_{xx}^{n+\frac{1}{2}}\left(i-\frac{1}{2},j+\frac{1}{2},k+\frac{1}{2}\right)\right]$$
$$+ \frac{1}{\Delta y}\left[T_{xy}^{n+\frac{1}{2}}\left(i,j+1,k+\frac{1}{2}\right) - T_{xy}^{n+\frac{1}{2}}\left(i,j,k+\frac{1}{2}\right)\right] \quad (3.125a)$$
$$+ \frac{1}{\Delta z}\left[T_{xz}^{n+\frac{1}{2}}\left(i,j+\frac{1}{2},k+1\right) - T_{xz}^{n+\frac{1}{2}}\left(i,j+\frac{1}{2},k\right)\right]$$

$$\frac{2\rho\left(i+\frac{1}{2},j,k+\frac{1}{2}\right)}{\Delta t}\left[v_y^{n+\frac{3}{4}}\left(i+\frac{1}{2},j,k+\frac{1}{2}\right)-v_y^{n+\frac{1}{4}}\left(i+\frac{1}{2},j,k+\frac{1}{2}\right)\right]$$
$$=\frac{1}{\Delta x}\left[T_{xy}^{n+\frac{1}{2}}\left(i+1,j,k+\frac{1}{2}\right)-T_{xy}^{n+\frac{1}{2}}\left(i,j,k+\frac{1}{2}\right)\right]$$
$$+\frac{1}{\Delta y}\left[T_{yy}^{n+\frac{1}{2}}\left(i+\frac{1}{2},j+\frac{1}{2},k+\frac{1}{2}\right)-T_{yy}^{n+\frac{1}{2}}\left(i+\frac{1}{2},j-\frac{1}{2},k+\frac{1}{2}\right)\right] \quad (3.125b)$$
$$+\frac{1}{\Delta z}\left[T_{yz}^{n+\frac{1}{2}}\left(i+\frac{1}{2},j,k+1\right)-T_{yz}^{n+\frac{1}{2}}\left(i+\frac{1}{2},j,k\right)\right]$$

$$\frac{2\rho\left(i+\frac{1}{2},j+\frac{1}{2},k\right)}{\Delta t}\left[v_z^{n+\frac{3}{4}}\left(i+\frac{1}{2},j+\frac{1}{2},k\right)-v_z^{n+\frac{1}{4}}\left(i+\frac{1}{2},j+\frac{1}{2},k\right)\right]$$
$$=\frac{1}{\Delta x}\left[T_{xz}^{n+\frac{1}{2}}\left(i+1,j+\frac{1}{2},k\right)-T_{xz}^{n+\frac{1}{2}}\left(i,j+\frac{1}{2},k\right)\right]$$
$$+\frac{1}{\Delta y}\left[T_{yz}^{n+\frac{1}{2}}\left(i+\frac{1}{2},j+1,k\right)-T_{yz}^{n+\frac{1}{2}}\left(i+\frac{1}{2},j,k\right)\right] \quad (3.125c)$$
$$+\frac{1}{\Delta z}\left[T_{zz}^{n+\frac{1}{2}}\left(i+\frac{1}{2},j+\frac{1}{2},k+\frac{1}{2}\right)-T_{zz}^{n+\frac{1}{2}}\left(i+\frac{1}{2},j+\frac{1}{2},k-\frac{1}{2}\right)\right]$$

The update equations may easily be acquired from (3.125a-c) and are as follows (where mesh grading kappa terms are also added in):

$$v_x^{n+\frac{3}{4}}\left(i,j+\frac{1}{2},k+\frac{1}{2}\right)=v_x^{n+\frac{1}{4}}\left(i,j+\frac{1}{2},k+\frac{1}{2}\right)$$
$$+\frac{\Delta t}{2\rho^{i,j+\frac{1}{2},k+\frac{1}{2}}\kappa_{xE}^{i}\Delta x}\left[T_{xx}^{n+\frac{1}{2}}\left(i+\frac{1}{2},j+\frac{1}{2},k+\frac{1}{2}\right)-T_{xx}^{n+\frac{1}{2}}\left(i-\frac{1}{2},j+\frac{1}{2},k+\frac{1}{2}\right)\right]$$
$$+\frac{\Delta t}{2\rho^{i,j+\frac{1}{2},k+\frac{1}{2}}\kappa_{yH}^{j}\Delta y}\left[T_{xy}^{n+\frac{1}{2}}\left(i,j+1,k+\frac{1}{2}\right)-T_{xy}^{n+\frac{1}{2}}\left(i,j,k+\frac{1}{2}\right)\right] \quad (3.126a)$$
$$+\frac{\Delta t}{2\rho^{i,j+\frac{1}{2},k+\frac{1}{2}}\kappa_{zH}^{k}\Delta z}\left[T_{xz}^{n+\frac{1}{2}}\left(i,j+\frac{1}{2},k+1\right)-T_{xz}^{n+\frac{1}{2}}\left(i,j+\frac{1}{2},k\right)\right]$$

$$v_y^{n+\frac{3}{4}}\left(i+\frac{1}{2},j,k+\frac{1}{2}\right)=v_y^{n+\frac{1}{4}}\left(i+\frac{1}{2},j,k+\frac{1}{2}\right)+\frac{\Delta t}{2\rho^{i+\frac{1}{2},j,k+\frac{1}{2}}\kappa_{xH}^{i}\Delta x}\left[T_{xy}^{n+\frac{1}{2}}\left(i+1,j,k+\frac{1}{2}\right)-T_{xy}^{n+\frac{1}{2}}\left(i,j,k+\frac{1}{2}\right)\right]$$
$$+\frac{\Delta t}{2\rho^{i+\frac{1}{2},j,k+\frac{1}{2}}\kappa_{yE}^{j}\Delta y}\left[T_{yy}^{n+\frac{1}{2}}\left(i+\frac{1}{2},j+\frac{1}{2},k+\frac{1}{2}\right)-T_{yy}^{n+\frac{1}{2}}\left(i+\frac{1}{2},j-\frac{1}{2},k+\frac{1}{2}\right)\right] \quad (3.126b)$$
$$+\frac{\Delta t}{2\rho^{i+\frac{1}{2},j,k+\frac{1}{2}}\kappa_{zH}^{k}\Delta z}\left[T_{yz}^{n+\frac{1}{2}}\left(i+\frac{1}{2},j,k+1\right)-T_{yz}^{n+\frac{1}{2}}\left(i+\frac{1}{2},j,k\right)\right]$$

$$
\begin{aligned}
&v_z^{n+\frac{3}{4}}\left(i+\frac{1}{2},j+\frac{1}{2},k\right) \\
&\quad = v_z^{n+\frac{1}{4}}\left(i+\frac{1}{2},j+\frac{1}{2},k\right) + \frac{\Delta t}{2\rho^{i+\frac{1}{2},j+\frac{1}{2},k}\kappa_{xH}^{i}\Delta x}\left[T_{xz}^{n+\frac{1}{2}}\left(i+1,j+\frac{1}{2},k\right) - T_{xz}^{n+\frac{1}{2}}\left(i,j+\frac{1}{2},k\right)\right] \\
&\quad + \frac{\Delta t}{2\rho^{i+\frac{1}{2},j+\frac{1}{2},k}\kappa_{yH}^{j}\Delta y}\left[T_{yz}^{n+\frac{1}{2}}\left(i+\frac{1}{2},j+1,k\right) - T_{yz}^{n+\frac{1}{2}}\left(i+\frac{1}{2},j,k\right)\right] \\
&\quad + \frac{\Delta t}{2\rho^{i+\frac{1}{2},j+\frac{1}{2},k}\kappa_{zE}^{k}\Delta z}\left[T_{zz}^{n+\frac{1}{2}}\left(i+\frac{1}{2},j+\frac{1}{2},k+\frac{1}{2}\right) - T_{zz}^{n+\frac{1}{2}}\left(i+\frac{1}{2},j+\frac{1}{2},k-\frac{1}{2}\right)\right]
\end{aligned}
\tag{3.126c}
$$

Since these update equations do not involve Maxwell's equations, the form is the same in both sub-iterations, simply subtract ½ to all time designations (n+½→n+1, n+3/4→n+5/4) in (3.117a-c) to acquire the form for the 1st sub-iteration. For the uniaxial stress case, the velocity update expressions for the 1st and 2nd sub-iterations respectively are as follows:

$$
\begin{aligned}
v_z^{n+\frac{3}{4},i+\frac{1}{2},j+\frac{1}{2},k} &= v_z^{n+\frac{1}{4},i+\frac{1}{2},j+\frac{1}{2},k} \\
&\quad + \frac{\Delta t}{2\rho^{i+\frac{1}{2},j+\frac{1}{2},k}\kappa_{zE}^{k}\Delta z}\left[T_{zz}^{n+\frac{1}{2},i+\frac{1}{2},j+\frac{1}{2},k+\frac{1}{2}} - T_{zz}^{n+\frac{1}{2},i+\frac{1}{2},j+\frac{1}{2},k-\frac{1}{2}}\right]
\end{aligned}
\tag{3.127a}
$$

$$
\begin{aligned}
v_z^{n+\frac{5}{4},i+\frac{1}{2},j+\frac{1}{2},k} &= v_z^{n+\frac{3}{4},i+\frac{1}{2},j+\frac{1}{2},k} \\
&\quad + \frac{\Delta t}{2\rho^{i+\frac{1}{2},j+\frac{1}{2},k}\kappa_{zE}^{k}\Delta z}\left[T_{zz}^{n+1,i+\frac{1}{2},j+\frac{1}{2},k+\frac{1}{2}} - T_{zz}^{n+1,i+\frac{1}{2},j+\frac{1}{2},k-\frac{1}{2}}\right]
\end{aligned}
\tag{3.127b}
$$

Thus, all of the fields within the main simulation space are now accounted for. Recall however that there exists an electrostatic region between the driving electrodes that is modeled separately, but simultaneously, for simplicity (i.e., by not needlessly evoking full Maxwell's equations within an electrostatic region). This so called "Source Space" will contain fields that also need to be updated and will now be discussed.

### 3.12 Source Space Formulation

Excitations discussed thus far such as stress inputs, displacement inputs, electric currents, and magnetic currents are suitable for a myriad of important problems, but herein the input is

voltage across electrodes. The setup will be as is shown in Figure 3-20, where a current source $I_S$ with source resistance $R_S$ feeds current $I_{BAW}$ into an electrode-piezo-electrode driving sandwich producing voltage differential $V_{BAW}$ across the electrodes. The dimensions tangential to the ground plane are $W_x$ and $W_y$ and the out-of-plane length is $L_z$. The electrodes are assumed to be infinitely thin.

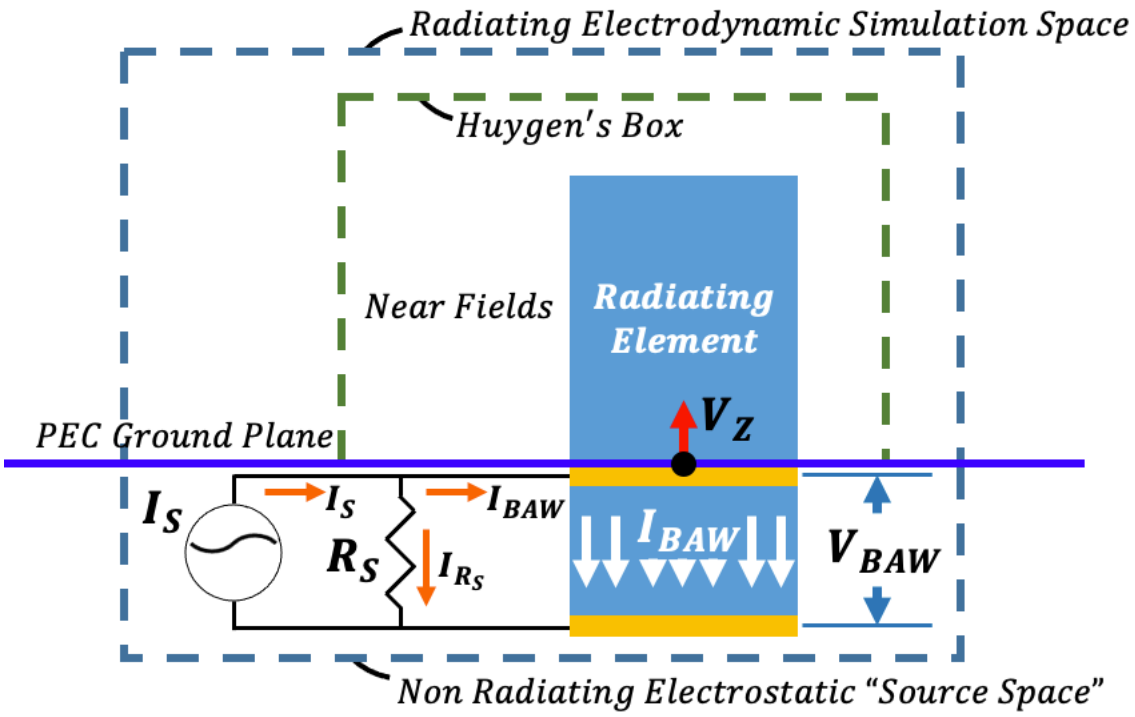


Figure 3-20: Source space formulation where an electrostatic region (source space) is coupled to an electrodynamic region (simulation space) by utilizing interface velocity. Both the source and simulation spaces utilize elastodynamics.

Assuming that all dimensions are on the order of the mechanical wavelength (~$10^{-5}$ $\lambda_{EM}$), the polarization current within the driving sandwich cancels out the electrode current and as such the piezoelectric material within the source space produces no EM radiation. The driving portion therefore acts as a resonating energy storing capacitor (essentially a BAW filter) and thus the

electrostatic assumption is warranted in this region. The source space is coupled to the simulation space through the interface velocity $V_z$ shared by both regions and elastodynamics is applied along the entire solid structure. Therefore, the mechanical resonance can be communicated across both the simulation space and the source space. The bottom mechanical boundary can be made either fixed or traction free.

Now that the source space formulation has been introduced, the relevant expressions shall be derived. Due to the small electrical size, only the out-of-plane electric fields are non-zero within the piezoelectric and these fields vary only in the out-of-plane dimension which is taken as the z-direction. The electrical constitutive relation in rate form, assuming tetragonal 6mm symmetry, is therefore as follows:

$$\frac{2}{\Delta t}\left(E_{z_S}^{n+\frac{1}{2}}\left(k+\frac{1}{2}\right)-E_{z_S}^{n}\left(k+\frac{1}{2}\right)\right)=\frac{1}{\epsilon_{zz}^{S}}\dot{D}_z^{n+\frac{1}{4}}-\frac{h_{33}}{\Delta z_S}\left(v_{z_S}^{n+\frac{1}{4}}(k+1)-v_{z_S}^{n+\frac{1}{4}}(k)\right) \tag{3.128}$$

The subscript "$S$" is used to identify source space for all fields as well as the spatial discretization. The time step is the same in both the source space and simulation space, thus no subscript is used for $\Delta t$. The displacement current is related to the electrode current density ($J_{BAW}$), which is uniform, as follows:

$$\dot{D}_z^{n+\frac{1}{4}}=-J_{BAW}^{n+\frac{1}{4}} \tag{3.129}$$

Note that the displacement current and the electrode current are equal in magnitude and opposite in direction which is why the capacitor does not radiate energy. The following relation holds for the current density:

$$J_{BAW}^{n+\frac{1}{4}}=\frac{1}{W_xW_y}I_{BAW}^{n+\frac{1}{4}}=\frac{1}{W_xW_y}\left[I_S^{n+\frac{1}{4}}-I_{R_S}^{n+\frac{1}{4}}\right]=\frac{1}{W_xW_y}\left[I_S^{n+\frac{1}{4}}-\frac{V_{BAW}^{n+\frac{1}{4}}}{R_S}\right] \tag{3.130}$$

Where all currents are as described in Figure 3-20 and $V_{BAW}$ may be written as follows for $N_{zS}$ nodes within the source space:

$$V_{BAW}^{n+\frac{1}{4}} = -\frac{1}{2}\sum_{k=0}^{k=N_{z_S}-1}\left(E_{z_S}^{n+\frac{1}{2}}\left(k+\frac{1}{2}\right)+E_{z_S}^{n}\left(k+\frac{1}{2}\right)\right)\Delta z_S \tag{3.131}$$

Combining equations (3.128) – (3.131) and solving for the unknown electric fields yields:

$$\begin{aligned} &E_{z_S}^{n+\frac{1}{2}}\left(k+\frac{1}{2}\right)+\frac{\Delta z_S \Delta t}{4\epsilon_{zz}^{S}R_S W_x W_y}\sum_{k=0}^{k=N_{z_S}-1}E_{z_S}^{n+\frac{1}{2}}\left(k+\frac{1}{2}\right) \\ &\quad = E_{z_S}^{n}\left(k+\frac{1}{2}\right)-\frac{\Delta t}{2\epsilon_{zz}^{S}}J_S^{n+\frac{1}{4}}-\frac{\Delta z_S \Delta t}{4\epsilon_{zz}^{S}R_S W_x W_y}\sum_{k=0}^{k=N_{z_S}-1}E_{z_S}^{n}\left(k+\frac{1}{2}\right) \\ &\quad -\frac{h_{33}\Delta t}{2\Delta z_S}\left(v_{z_S}^{n+\frac{1}{4}}(k+1)-v_{z_S}^{n+\frac{1}{4}}(k)\right) \end{aligned} \tag{3.132}$$

Assuming 3 cells (4 nodes) within the source space, equation (3.132) may be written as a matrix expression:

$$\begin{bmatrix} 1+a & a & a \\ a & 1+a & a \\ a & a & 1+a \end{bmatrix}\begin{pmatrix} E_{z_S}^{n+\frac{1}{2}}\left(k+\frac{1}{2}\right) \\ E_{z_S}^{n+\frac{1}{2}}\left(k+\frac{3}{2}\right) \\ E_{z_S}^{n+\frac{1}{2}}\left(k+\frac{5}{2}\right) \end{pmatrix} = \vec{F} \tag{3.133a}$$

$$a = \frac{\Delta z_S \Delta t}{4\epsilon_{zz}^{S}R_S W_x W_y} \tag{3.133b}$$

$$\vec{F} = \begin{pmatrix} E_{z_S}^{n}\left(k+\frac{1}{2}\right)-\frac{\Delta t}{2\epsilon_{zz}^{S}}J_S^{n+\frac{1}{4}}-\frac{\Delta z_S \Delta t}{4\epsilon_{zz}^{S}R_S W_x W_y}\sum_{k=0}^{k=N_{z_S}-1}E_{z_S}^{n}\left(k+\frac{1}{2}\right)-\frac{h_{33}\Delta t}{2\Delta z}\left(v_{z_S}^{n+\frac{1}{4}}(k+1)-v_{z_S}^{n+\frac{1}{4}}(k)\right) \\ E_{z_S}^{n}\left(k+\frac{3}{2}\right)-\frac{\Delta t}{2\epsilon_{zz}^{S}}J_S^{n+\frac{1}{4}}-\frac{\Delta z_S \Delta t}{4\epsilon_{zz}^{S}R_S W_x W_y}\sum_{k=0}^{k=N_{z_S}-1}E_{z_S}^{n}\left(k+\frac{1}{2}\right)-\frac{h_{33}\Delta t}{2\Delta z}\left(v_{z_S}^{n+\frac{1}{4}}(k+2)-v_{z_S}^{n+\frac{1}{4}}(k+1)\right) \\ E_{z_S}^{n}\left(k+\frac{5}{2}\right)-\frac{\Delta t}{2\epsilon_{zz}^{S}}J_S^{n+\frac{1}{4}}-\frac{\Delta z_S \Delta t}{4\epsilon_{zz}^{S}R_S W_x W_y}\sum_{k=0}^{k=N_{z_S}-1}E_{z_S}^{n}\left(k+\frac{1}{2}\right)-\frac{h_{33}\Delta t}{2\Delta z}\left(v_{z_S}^{n+\frac{1}{4}}(k+3)-v_{z_S}^{n+\frac{1}{4}}(k+2)\right) \end{pmatrix} \tag{3.133c}$$

Often the source space does not occupy more than a 20$^{th}$ of a mechanical wavelength and therefore it is not necessary to involve more than three cells such as in equations (3.133a-c). The matrix inversions that are required are thus not computationally heavy. The velocities and stresses within the simulation space may be updated using the elastodynamic and constitutive equations respectively as before, except the stress update utilizes (3.129):

$$T_{zz_S}^{n+\frac{1}{2},k+\frac{1}{2}} = T_{zz_S}^{n,k+\frac{1}{2}} + \frac{E_{33}^{D}\Delta t}{2\kappa_{zH}^{k}\Delta z_S}\left(v_{z_S}^{n+\frac{1}{4},k+1} - v_{z_S}^{n+\frac{1}{4},k}\right) + \frac{h_{33,Poi}^{k+\frac{1}{2}}\Delta t}{2} J_S^{n+\frac{1}{4}} \tag{3.134a}$$

The interface velocity is updated as follows:

$$v_{z_S}^{n+\frac{3}{4}}(N_{z_S}) = v_{z_S}^{n+\frac{1}{4}}(N_{z_S}) + \frac{\Delta t}{2\rho\left(\frac{\Delta z + \Delta z_S}{2}\right)}\left[T_{zz}^{n+\frac{1}{2}}\left(\frac{1}{2}\right) - T_{zz_S}^{n+\frac{1}{2}}\left(N_{z_S} - \frac{1}{2}\right)\right] \tag{3.134b}$$

Where the average spatial discretization is used which produces 2nd order accurate mechanical results [237]. User's may input a modulated Gaussian pulse as source current density $J_S$ to simulate a ringdown and calculate mechanical antenna performance by utilizing a near to far-field (NTFF) transformation to acquire the far-field parameters such as radiated power $P_{rad}$. The input power may then be calculated by taking the FFT of the voltage and current and utilizing:

$$P_{in} = \frac{1}{2} real[\breve{V}_{BAW} \times \breve{I}_{BAW}^{*}] \tag{3.135}$$

The radiation efficiency may then be readily calculated as:

$$e_{rad} = \frac{P_{rad}}{P_{in}} \tag{3.136}$$

Therefore, this input methodology allows for the radiation efficiency to be calculated with high fidelity. The source space formulation herein will be independently validated vs. the analytical solution of a BAW filter device in Chapter 5. Now that the piezoelectric antenna problem has been numerically formulated, it is necessary to focus on post-processing of the data. Herein, the major post-processing that occurs is inputting the near-field data into a near to far-field (NTFF) transformation to acquire far-field performance characteristics. This will be discussed next.

## 3.13 Near to Far-Field (NTFF) Transformations

For the mechanical antenna simulations studied herein, the simulation space representing a physical volume (i.e., excluding PML layers) will always lie in the near field of the radiator. As

such, a method of converting near field numerical results to far-field data is invaluable. To accomplish this, a fictional rectangular volume (Huygen surface), of dimensions $2x_0$, $2y_0$, $2z_0$, may be constructed surrounding the radiator, and, using the surface equivalency theorem [25][26][178], may use tangential fields calculated from the FDTD simulation in order to determine the following equivalent currents on the surface of the volume:

$$J_i^S = \epsilon_{ijk} n_j H_k$$

$$\mathcal{M}_i^S = \epsilon_{ijk} n_k E_j$$

This yields the following electric source currents on the surfaces orthogonal to the global x, y, and z-directions:

$$\hat{n} = \hat{\imath}, \quad J_i^S = -H_z\hat{\jmath} + H_y\hat{k}, \quad \hat{n} = -\hat{\imath}, \quad J_i^S = H_z\hat{\jmath} - H_y\hat{k} \tag{3.137a}$$

$$\hat{n} = \hat{\jmath}, \quad J_i^S = H_z\hat{\imath} - H_x\hat{k}, \quad \hat{n} = -\hat{\jmath}, \quad J_i^S = -H_z\hat{\imath} + H_x\hat{k} \tag{3.137b}$$

$$\hat{n} = \hat{k}, \quad J_i^S = -H_y\hat{\imath} + H_x\hat{\jmath}, \quad \hat{n} = -\hat{k}, \quad J_i^S = H_y\hat{\imath} - H_x\hat{\jmath} \tag{3.137c}$$

And the following magnetic source currents:

$$\hat{n} = \hat{\imath}, \quad \mathcal{M}_i^S = E_z\hat{\jmath} - E_y\hat{k}, \quad \hat{n} = -\hat{\imath}, \quad \mathcal{M}_i^S = -E_z\hat{\jmath} + E_y\hat{k} \tag{3.137d}$$

$$\hat{n} = \hat{\jmath}, \quad \mathcal{M}_i^S = -E_z\hat{\imath} + E_x\hat{k}, \quad \hat{n} = -\hat{\jmath}, \quad \mathcal{M}_i^S = E_z\hat{\imath} - E_x\hat{k} \tag{3.137e}$$

$$\hat{n} = \hat{k}, \quad \mathcal{M}_i^S = E_y\hat{\imath} - E_x\hat{\jmath}, \quad \hat{n} = -\hat{k}, \quad \mathcal{M}_i^S = -E_y\hat{\imath} + E_x\hat{\jmath} \tag{3.137f}$$

Where the EM fields in (3.137a-f) are at the surface of the fictional volume, and therefore will require some spatial averaging for the magnetic fields which are staggered by half a unit cell. Following the approach by [25], these equivalent source currents may be input into the following integrals:

$$\breve{N}_\theta = \iint \left(\breve{J}_x cos\theta cos\emptyset + \breve{J}_y cos\theta sin\emptyset - \breve{J}_z sin\theta\right) e^{jkr' cos\Psi} ds' \tag{3.138a}$$

$$\breve{N}_\emptyset = \iint \left(-\breve{J}_x sin\emptyset + \breve{J}_y cos\emptyset\right) e^{jkr' cos\Psi} ds' \tag{3.138b}$$

$$\breve{L}_{\theta} = \iint \left(\breve{\mathcal{M}}_x cos\theta cos\emptyset + \breve{\mathcal{M}}_y cos\theta sin\emptyset - \breve{\mathcal{M}}_z sin\theta\right) e^{jkr' cos\Psi} ds' \tag{3.138c}$$

$$\breve{L}_{\emptyset} = \iint \left(-\breve{\mathcal{M}}_x sin\emptyset + \breve{\mathcal{M}}_y cos\emptyset\right) e^{jkr' cos\Psi} ds' \tag{3.138d}$$

Primed values above are source coordinates, for example, $ds'$ in (3.138a-d) is a differential area on the Huygen surface within the simulation space. The unprimed $\theta$ and $\emptyset$ are the spherical coordinates pertaining to the far-field observation point, therefore the near-field EM fields within the simulation space are used as sources through (3.137a-f) to determine the integrals (3.138a-d) which apply outside the simulation space. The breve accent marks denote that these are phasor quantities, and the exponential terms may be determined as follows:

$$\hat{n} = \pm\hat{\imath}, \qquad r' cos\Psi = \pm \mathrm{x}_0 sin\theta cos\emptyset + y' sin\theta sin\emptyset + z' cos\theta \tag{3.139a}$$

$$\hat{n} = \pm\hat{\jmath}, \qquad r' cos\Psi = \mathrm{x}' sin\theta cos\emptyset \pm y_0 sin\theta sin\emptyset + z' cos\theta \tag{3.139b}$$

$$\hat{n} = \pm\hat{k}, \qquad r' cos\Psi = \mathrm{x}' sin\theta cos\emptyset + y' sin\theta sin\emptyset \pm z_0 cos\theta \tag{3.139c}$$

Where the primed values ($\mathrm{x}'$, $y'$, and $z'$) denote points on the virtual surface within the near-field/simulation space and $\theta$/$\emptyset$ still describe the far-field observation point. Therefore, for every observation point ($\theta$/$\emptyset$), the collective effect of all EM fields on the virtual surface nodes ($\mathrm{x}'$, $y'$, and $z'$) must be summed up through integrals (3.138a-d). This process is then repeated for different $\theta$/$\emptyset$ values to develop a complete picture of far-field performance, like radiation pattern and radiated power. The EM phasors in spherical coordinates are determined from as follows:

$$\breve{E}_r \cong 0 \tag{3.140a}$$

$$\breve{E}_{\theta} \cong -\frac{jke^{-jkr}}{4\pi r}(\breve{L}_{\emptyset} + \eta_0 \breve{N}_{\theta}) \tag{3.140b}$$

$$\breve{E}_{\emptyset} \cong \frac{jke^{-jkr}}{4\pi r}(\breve{L}_{\theta} - \eta_0 \breve{N}_{\emptyset}) \tag{3.140c}$$

$$\breve{H}_r \cong 0 \tag{3.140d}$$

$$\breve{H}_{\theta} \cong \frac{jke^{-jkr}}{4\pi r}(\breve{N}_{\emptyset} - \breve{L}_{\theta}/\eta_0) \tag{3.140e}$$

$$\breve{H}_{\emptyset} \cong -\frac{jke^{-jkr}}{4\pi r}(\breve{N}_{\theta} + \breve{L}_{\emptyset}/\eta_0) \tag{3.140f}$$

Where $\eta_0 = \sqrt{\mu_0/\epsilon_0} \cong 377$ is the free space impedance and $r$ is the radial distance of the observation point to the source. For the purpose of simulations using the FDTD method, the spatial location of both the $L$ and $N$ terms must lie on the virtual surface, and as such two spatial interpolation terms must be used for the magnetic fields. The radiation intensity and total power may then be calculated respectively as follows:

$$U(\theta, \emptyset) \cong \frac{r^2}{2\eta}\left[\left|\breve{E}_{\theta}(r, \theta, \emptyset)\right|^2 + \left|\breve{E}_{\emptyset}(r, \theta, \emptyset)\right|^2\right] \tag{3.141}$$

$$P_{rad} = \int_0^{2\pi}\int_0^{\pi} U sin\theta d\theta d\emptyset \tag{3.142}$$

These values may now be used to create far-field radiation pattern charts. The procedure is clarified with an example.

### 3.13.1 NTFF Transformation of Planar Array on PEC

In the case of an unphased planar array mounted on a ground plane normal to the z-direction, the radiation moves in the positive z-direction only, and therefore only the surface with $\hat{n} = +\hat{k}$ need be examined for NTFF transformation. On this surface, the source currents are as follows:

$$\breve{J}_i^S = -\breve{H}_y\hat{\imath} + \breve{H}_x\hat{\jmath}, \qquad \breve{\mathcal{M}}_i^S = \breve{E}_y\hat{\imath} - \breve{E}_x\hat{\jmath}$$

Substitution into the $L$ and $N$ terms (3.138a-d) yields:

$$\breve{N}_{\theta} = \int_{-x_0}^{x_0}\int_{-y_0}^{y_0}\left(-\breve{H}_y cos\theta cos\emptyset + \breve{H}_x cos\theta sin\emptyset\right)e^{jk\left(x' sin\theta cos\emptyset + y' sin\theta sin\emptyset + z_0 cos\theta\right)}dx'dy'$$

$$\breve{N}_{\emptyset} = \int_{-x_0}^{x_0}\int_{-y_0}^{y_0}\left(\breve{H}_y sin\emptyset + \breve{H}_x cos\emptyset\right)e^{jk\left(x' sin\theta cos\emptyset + y' sin\theta sin\emptyset + z_0 cos\theta\right)}dx'dy'$$

$$\breve{L}_\theta = \int_{-x_0}^{x_0}\int_{-y_0}^{y_0}\left(\breve{E}_y cos\theta cos\emptyset - \breve{E}_x cos\theta sin\emptyset\right)e^{jk(\mathrm{x}' sin\theta cos\emptyset + y' sin\theta sin\emptyset + z_0 cos\theta)}dx'dy'$$

$$\breve{L}_\emptyset = \int_{-x_0}^{x_0}\int_{-y_0}^{y_0}\left(-\breve{E}_y sin\emptyset - \breve{E}_x cos\emptyset\right)e^{jk(\mathrm{x}' sin\theta cos\emptyset + y' sin\theta sin\emptyset + z_0 cos\theta)}dx'dy'$$

The far-field electric and magnetic phasors may then be determined.

### 3.13.2 General 3D NTFF Transformation

The procedure of Section 3.13.1 must be repeated for each absorbing boundary condition utilized in the simulation, meaning that generally all six surfaces enclosing the radiator will require unique $L$ and $N$ terms. These are summarized in Table 3-5:

| | |
|---|---|
| $\hat{n} = +\hat{\imath}$ | $\breve{N}_\theta^{+\hat{\imath}} = \int_{-z_0}^{z_0}\int_{-y_0}^{y_0}\left(-\breve{H}_z cos\theta sin\emptyset - \breve{H}_y sin\theta\right)e^{jk(\mathrm{x}_0 sin\theta cos\emptyset + y' sin\theta sin\emptyset + z' cos\theta)}dy'dz'$ |
| | $\breve{N}_\emptyset^{+\hat{\imath}} = \int_{-z_0}^{z_0}\int_{-y_0}^{y_0}\left(-\breve{H}_z cos\emptyset\right)e^{jk(\mathrm{x}_0 sin\theta cos\emptyset + y' sin\theta sin\emptyset + z' cos\theta)}dy'dz'$ |
| | $\breve{L}_\theta^{+\hat{\imath}} = \int_{-z_0}^{z_0}\int_{-y_0}^{y_0}\left(\breve{E}_z cos\theta sin\emptyset + \breve{E}_y sin\theta\right)e^{jk(\mathrm{x}_0 sin\theta cos\emptyset + y' sin\theta sin\emptyset + z' cos\theta)}dy'dz'$ |
| | $\breve{L}_\emptyset^{+\hat{\imath}} = \int_{-z_0}^{z_0}\int_{-y_0}^{y_0}\left(\breve{E}_z cos\emptyset\right)e^{jk(\mathrm{x}_0 sin\theta cos\emptyset + y' sin\theta sin\emptyset + z' cos\theta)}dy'dz'$ |
| $\hat{n} = -\hat{\imath}$ | $\breve{N}_\theta^{-\hat{\imath}} = \int_{-z_0}^{z_0}\int_{-y_0}^{y_0}\left(\breve{H}_z cos\theta sin\emptyset + \breve{H}_y sin\theta\right)e^{jk(-\mathrm{x}_0 sin\theta cos\emptyset + y' sin\theta sin\emptyset + z' cos\theta)}dy'dz'$ |
| | $\breve{N}_\emptyset^{-\hat{\imath}} = \int_{-z_0}^{z_0}\int_{-y_0}^{y_0}\left(\breve{H}_z cos\emptyset\right)e^{jk(-\mathrm{x}_0 sin\theta cos\emptyset + y' sin\theta sin\emptyset + z' cos\theta)}dy'dz'$ |
| | $\breve{L}_\theta^{-\hat{\imath}} = \int_{-z_0}^{z_0}\int_{-y_0}^{y_0}\left(-\breve{E}_z cos\theta sin\emptyset - \breve{E}_y sin\theta\right)e^{jk(-\mathrm{x}_0 sin\theta cos\emptyset + y' sin\theta sin\emptyset + z' cos\theta)}dy'dz'$ |
| | $\breve{L}_\emptyset^{-\hat{\imath}} = \int_{-z_0}^{z_0}\int_{-y_0}^{y_0}\left(-\breve{E}_z cos\emptyset\right)e^{jk(-\mathrm{x}_0 sin\theta cos\emptyset + y' sin\theta sin\emptyset + z' cos\theta)}dy'dz'$ |
| $\hat{n} = +\hat{\jmath}$ | $\breve{N}_\theta^{+\hat{\jmath}} = \int_{-z_0}^{z_0}\int_{-x_0}^{x_0}\left(\breve{H}_z cos\theta cos\emptyset + \breve{H}_x sin\theta\right)e^{jk(\mathrm{x}' sin\theta cos\emptyset + y_0 sin\theta sin\emptyset + z' cos\theta)}dx'dz'$ |
| | $\breve{N}_\emptyset^{+\hat{\jmath}} = \int_{-z_0}^{z_0}\int_{-x_0}^{x_0}\left(-\breve{H}_z sin\emptyset\right)e^{jk(\mathrm{x}' sin\theta cos\emptyset + y_0 sin\theta sin\emptyset + z' cos\theta)}dx'dz'$ |

| | |
|---|---|
| | $\breve{L}_{\theta}^{+\hat{\jmath}} = \int_{-z_0}^{z_0}\int_{-x_0}^{x_0}\left(-\breve{E}_z cos\theta cos\emptyset - \breve{E}_x sin\theta\right)e^{jk(x' sin\theta cos\emptyset + y_0 sin\theta sin\emptyset + z' cos\theta)}dx'dz'$ |
| | $\breve{L}_{\emptyset}^{+\hat{\jmath}} = \int_{-z_0}^{z_0}\int_{-x_0}^{x_0}\left(\breve{E}_z sin\emptyset\right)e^{jk(x' sin\theta cos\emptyset + y_0 sin\theta sin\emptyset + z' cos\theta)}dx'dz'$ |
| $\hat{n} = -\hat{\jmath}$ | $\breve{N}_{\theta}^{-\hat{\jmath}} = \int_{-z_0}^{z_0}\int_{-x_0}^{x_0}\left(-\breve{H}_z cos\theta cos\emptyset - \breve{H}_x sin\theta\right)e^{jk(x' sin\theta cos\emptyset - y_0 sin\theta sin\emptyset + z' cos\theta)}dx'dz'$ |
| | $\breve{N}_{\emptyset}^{-\hat{\jmath}} = \int_{-z_0}^{z_0}\int_{-x_0}^{x_0}\left(\breve{H}_z sin\emptyset\right)e^{jk(x' sin\theta cos\emptyset - y_0 sin\theta sin\emptyset + z' cos\theta)}dx'dz'$ |
| | $\breve{L}_{\theta}^{-\hat{\jmath}} = \int_{-z_0}^{z_0}\int_{-x_0}^{x_0}\left(\breve{E}_z cos\theta cos\emptyset + \breve{E}_x sin\theta\right)e^{jk(x' sin\theta cos\emptyset - y_0 sin\theta sin\emptyset + z' cos\theta)}dx'dz'$ |
| | $\breve{L}_{\emptyset}^{-\hat{\jmath}} = \int_{-z_0}^{z_0}\int_{-x_0}^{x_0}\left(-\breve{E}_z sin\emptyset\right)e^{jk(x' sin\theta cos\emptyset - y_0 sin\theta sin\emptyset + z' cos\theta)}dx'dz'$ |
| $\hat{n} = +\hat{k}$ | $\breve{N}_{\theta}^{+\hat{k}} = \int_{-x_0}^{x_0}\int_{-y_0}^{y_0}\left(-\breve{H}_y cos\theta cos\emptyset + \breve{H}_x cos\theta sin\emptyset\right)e^{jk(x' sin\theta cos\emptyset + y' sin\theta sin\emptyset + z_0 cos\theta)}dx'dy'$ |
| | $\breve{N}_{\emptyset}^{+\hat{k}} = \int_{-x_0}^{x_0}\int_{-y_0}^{y_0}\left(\breve{H}_y sin\emptyset + \breve{H}_x cos\emptyset\right)e^{jk(x' sin\theta cos\emptyset + y' sin\theta sin\emptyset + z_0 cos\theta)}dx'dy'$ |
| | $\breve{L}_{\theta}^{+\hat{k}} = \int_{-x_0}^{x_0}\int_{-y_0}^{y_0}\left(\breve{E}_y cos\theta cos\emptyset - \breve{E}_x cos\theta sin\emptyset\right)e^{jk(x' sin\theta cos\emptyset + y' sin\theta sin\emptyset + z_0 cos\theta)}dx'dy'$ |
| | $\breve{L}_{\emptyset}^{+\hat{k}} = \int_{-x_0}^{x_0}\int_{-y_0}^{y_0}\left(-\breve{E}_y sin\emptyset - \breve{E}_x cos\emptyset\right)e^{jk(x' sin\theta cos\emptyset + y' sin\theta sin\emptyset + z_0 cos\theta)}dx'dy'$ |
| $\hat{n} = -\hat{k}$ | $\breve{N}_{\theta}^{-\hat{k}} = \int_{-x_0}^{x_0}\int_{-y_0}^{y_0}\left(\breve{H}_y cos\theta cos\emptyset - \breve{H}_x cos\theta sin\emptyset\right)e^{jk(x' sin\theta cos\emptyset + y' sin\theta sin\emptyset - z_0 cos\theta)}dx'dy'$ |
| | $\breve{N}_{\emptyset}^{-\hat{k}} = \int_{-x_0}^{x_0}\int_{-y_0}^{y_0}\left(-\breve{H}_y sin\emptyset - \breve{H}_x cos\emptyset\right)e^{jk(x' sin\theta cos\emptyset + y' sin\theta sin\emptyset - z_0 cos\theta)}dx'dy'$ |
| | $\breve{L}_{\theta}^{-\hat{k}} = \int_{-x_0}^{x_0}\int_{-y_0}^{y_0}\left(-\breve{E}_y cos\theta cos\emptyset + \breve{E}_x cos\theta sin\emptyset\right)e^{jk(x' sin\theta cos\emptyset + y' sin\theta sin\emptyset - z_0 cos\theta)}dx'dy'$ |
| | $\breve{L}_{\emptyset}^{-\hat{k}} = \int_{-x_0}^{x_0}\int_{-y_0}^{y_0}\left(\breve{E}_y sin\emptyset + \breve{E}_x cos\emptyset\right)e^{jk(x' sin\theta cos\emptyset + y' sin\theta sin\emptyset - z_0 cos\theta)}dx'dy'$ |

Table 3-5: NTFF equations.

Since all multi-physics radiators investigated herein are mounted on a ground plane, the $\hat{n} = -\hat{k}$ terms are unused. For this linear system, the far-field response generated by the six surfaces may be added together to acquire the total response by superposition:

$$\breve{N}_\theta = \breve{N}_\theta^{+\hat{\imath}} + \breve{N}_\theta^{-\hat{\imath}} + \breve{N}_\theta^{+\hat{\jmath}} + \breve{N}_\theta^{-\hat{\jmath}} + \breve{N}_\theta^{+\hat{k}} + \breve{N}_\theta^{-\hat{k}} \tag{3.143a}$$

$$\breve{N}_\emptyset = \breve{N}_\emptyset^{+\hat{\imath}} + \breve{N}_\emptyset^{-\hat{\imath}} + \breve{N}_\emptyset^{+\hat{\jmath}} + \breve{N}_\emptyset^{-\hat{\jmath}} + \breve{N}_\emptyset^{+\hat{k}} + \breve{N}_\emptyset^{-\hat{k}} \tag{3.143b}$$

$$\breve{L}_\theta = \breve{L}_\theta^{+\hat{\imath}} + \breve{L}_\theta^{-\hat{\imath}} + \breve{L}_\theta^{+\hat{\jmath}} + \breve{L}_\theta^{-\hat{\jmath}} + \breve{L}_\theta^{+\hat{k}} + \breve{L}_\theta^{-\hat{k}} \tag{3.143c}$$

$$\breve{L}_\emptyset = \breve{L}_\emptyset^{+\hat{\imath}} + \breve{L}_\emptyset^{-\hat{\imath}} + \breve{L}_\emptyset^{+\hat{\jmath}} + \breve{L}_\emptyset^{-\hat{\jmath}} + \breve{L}_\emptyset^{+\hat{k}} + \breve{L}_\emptyset^{-\hat{k}} \tag{3.143d}$$

The determination of the far-field EM fields may then proceed using equations (3.124a-d) and Table 3-5, then substituting into equations (3.140a-f). Thus, the entire process of determining the performance of a piezoelectric antenna has now been discussed. This process is lengthy, so it is helpful to review the process briefly as presented in the following section.

### 3.14 Numerical Framework Overview

The process of modeling piezoelectric antennas presented thus far is summarized in Figure 3-21. First, the input current $J_S$ is used to update the source space electric fields, stresses, and velocities via (3.133a-c), (3.134a), and (3.127a-b). Then the terminal voltage $V_S$ may be updated via (3.131). The simulation space electric fields are then updated implicitly using the CPML-ADI-FDTD equations; (3.192a) for $E_x^{n+1/2}$, (3.192b) for $E_y^{n+1/2}$, (3.123a) or (3.120a) for $E_z^{n+1/2}$, (3.192d) for $E_x^{n+1}$, (3.192e) for $E_y^{n+1}$, and (3.123b) or (3.120b) for $E_z^{n+1}$. The magnetic flux, magnetic field, electric flux, and history variables may then be readily updated using Faraday's law (3.71a-c) (3.72a-c), the magnetic constitutive relation (3.73a-c) (3.74a-c), Ampere's law (3.84a-c) (3.89a-c), and Table 3-2/Table 3-3 respectively. Stress is then updated using the mechanical constitutive relation (3.124a-b) followed by velocity being updated by the elastodynamic equation (3.127a-b).

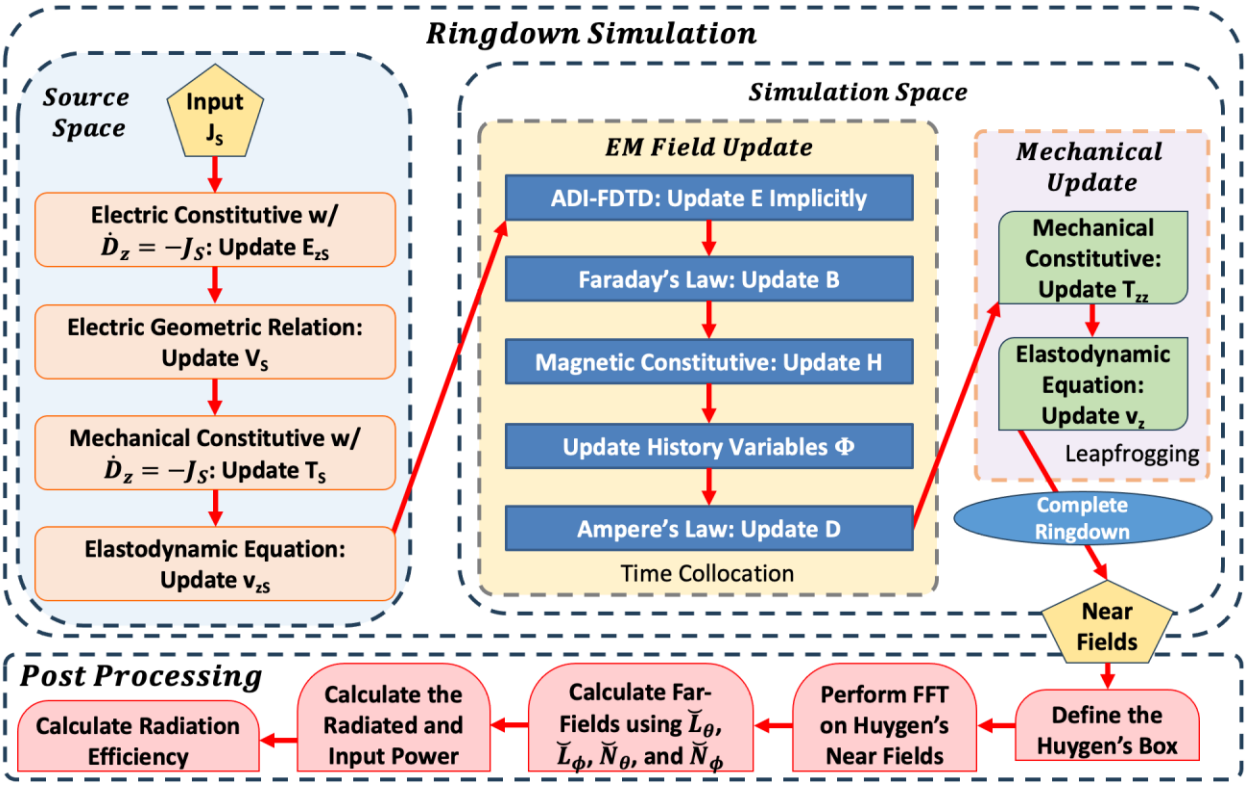


Figure 3-21: Simulation flow chart for piezoelectric antenna simulations via CPML-ADI-FDTD method.

The 2nd sub-iteration then follows the same flow after which the next time step commences. The process should be iterated until the mechanical damping decays the signal enough to allow for FFTs to be performed without introducing significant spectral leakage.

# CHAPTER 4: VERIFICATION TESTING

This chapter focuses on verifying that the three major constituents of the code, i.e., the mechanical, electrodynamic, and magnetic damping portions, are working properly. This is accomplished through comparisons with analytical solutions and/or commercial codes.

## 4.1 Mechanical Test Cases

Mechanically, the elastic waves are assumed to move such that one stress is non-zero known as the uniaxial stress approximation. This assumption is justified if the specimen under load has one dimension at least an order of magnitude larger than either of the other two (i.e., for a slender bar shaped device). A wealth of sources document how such 1D problems behave, [238] being one. This section compares the FDTD simulation to both analytical solutions and commercial software.

### 4.1.1 1D Quasistatic Bar Problem under Force Input

A 2x2x20cm mechanical bar fixed on one end and with a 100Hz harmonic force input (100lbf/445N) on the other (see Figure 4-1 bottom insert) was simulated using the code. The input frequency is significantly below (<10%) the first resonant frequency of the bar and therefore this problem is quasistatic. The bars tip displacement is plotted as a function of time and compared to the analytical solution [238]. There are 40 finite difference cells utilized along the length of the bar (5mm discretization). The maximum amplitude error is 2.84% and no discernable error in phase is present. Therefore, these results provide confidence in the mechanical portion of the ADI-FDTD code.

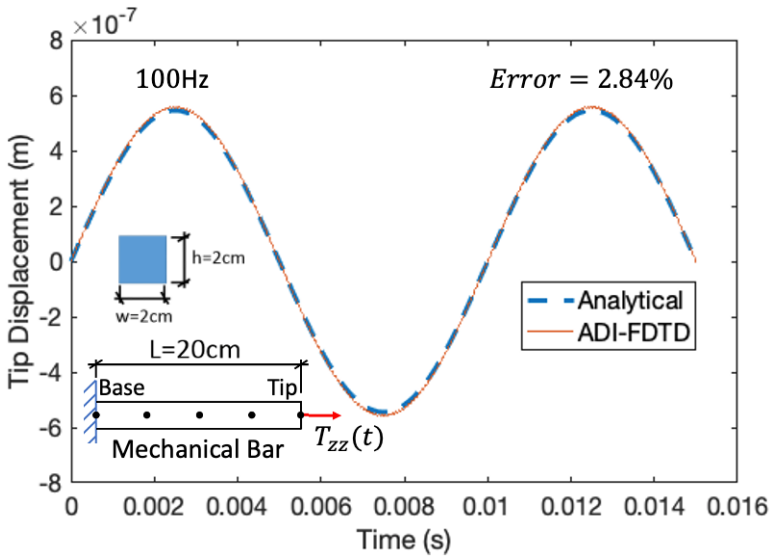


Figure 4-1: 1D mechanical bar operating at a near static frequency (<10% of 1st harmonic).

### 4.1.2 On Resonance 1/4 Wavelength Mechanical Bar under Gaussian Base Excitation

A 100x100x500$\mu$m mechanical bar which is traction free on one end and with an on resonance 5MHz Gaussian pulse base excitation (2.5nm magnitude) applied on the other (see Figure 4-2 bottom insert) was simulated using the code. The axial stress ($T_{zz}$) 50$\mu$m away from the base is plotted as a function of time and compared to the results from a simulation performed using the Comsol multiphysics software [239]. Since the boundary conditions are such that the bar is a quarter wavelength resonator, there are 5 finite difference cells utilized along the length of the bar (100$\mu$m discretization) to achieve a 20 cell per wavelength spatial sampling. The maximum amplitude error is 2.59% and no discernable error in phase is present. Therefore, these results provide confidence in the mechanical portion of the ADI-FDTD code.

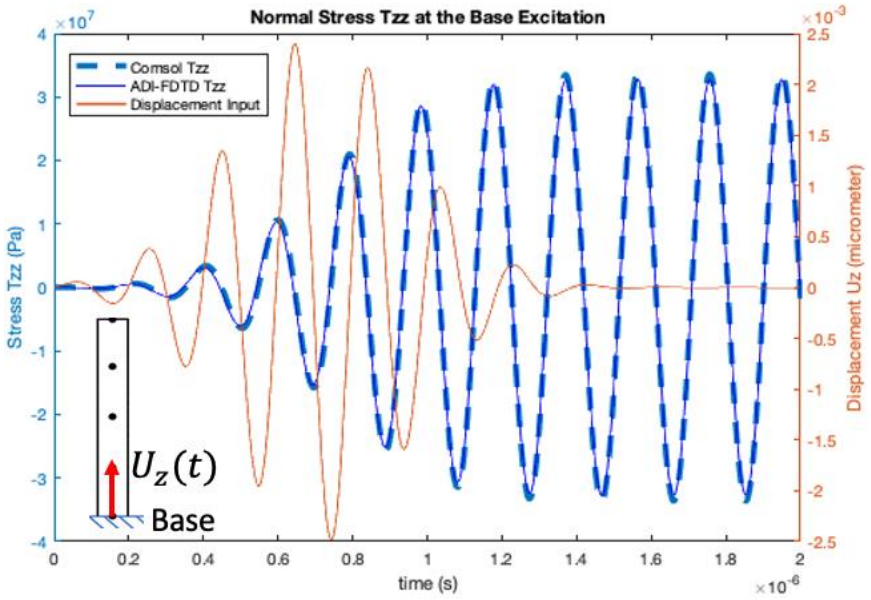


Figure 4-2: On resonance Gaussian base excitation mechanical bar problem.

## 4.2 Electrodynamic Test Cases

This section focuses on the validation of any electrodynamic portions of the code and post-processor and exists to inspire confidence in the results presented in Chapter 5.

### 4.2.1 Aperture Antenna Study

A problem that was solved early on to check that magnetic and electric currents could be input simultaneously and still produce accurate results was the aperture antenna problem. Aperture antennas radiate by forming an area (aperture) of relatively uniform electric and magnetic fields known as the aperture fields ($E_a$ and $H_a$ respectively) which are often generated using a waveguide. A rectangular aperture antenna is shown in Figure 4-3:

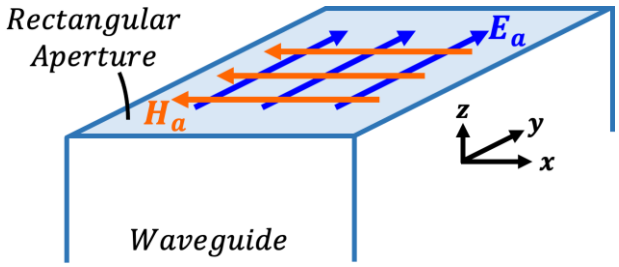


Figure 4-3: Rectangular Aperture Antenna with electric field along the y-direction and magnetic field along the negative x-direction.

Within the literature [25][26], analytical solutions may be found for such a case in the form of far-field approximations which assume that the waveguide has allowed an area (aperture) to contain uniform electric and magnetic fields which oscillate, radiating EM waves into free space. These aperture electric and magnetic fields may then be mapped to equivalent electric and magnetic currents by utilizing the following relations.

$$\overrightarrow{J_s} = \hat{n} \times \overrightarrow{H_a}, \qquad \overrightarrow{M_s} = \overrightarrow{E_a} \times \hat{n} \tag{4.1}$$

An aperture antenna simulation was performed utilizing a 1m cube volume with aperture dimensions of 5x5cm in the xy-plane, and a y-directed aperture electric field. All boundaries are Mur 1st order (Mur1) absorbing boundary conditions (ABCs) [210] and the system was allowed to radiate for 5 cycles at 400MHz with the time step set to 2 times the CFL condition with a spatial discretization of 1cm. The aperture is located at the center of the simulation space. The analytical solution, for the z-directed electric field, applies only for the far field and is as follows:

$$E_z = \frac{|\boldsymbol{E}_a|}{\pi\beta r}\left(\frac{1+cos\theta}{sin\theta cos\emptyset}\right)\sin\left(\frac{\beta a}{2}sin\theta cos\emptyset\right)\sin\left(\frac{\beta b}{2}sin\theta sin\emptyset\right)\sin\left(\omega t - \beta r\right) \tag{4.2}$$

Where a, and b are the in-plane dimensions of the aperture antenna which are both equal to 5cm in this case, and the independent variables are in terms of spherical coordinates about a coordinate system with its origin at the geometrical centroid of the aperture. A plot comparing the z-directed electric field obtained from both the far-field analytical solution [25] and the ADI-

FDTD algorithm is plotted as a function of time in Figure 4-4. The electric field was calculated at the point (x=0, y=0.46m, z=0m) on a coordinate system whose origin is at the center of the aperture. The far-field analytical solutions have a phase error of up to π/8 [25] which is represented using error bars on the analytical solution in the figure. The phase error is caused due to proximity of the MUR1 boundaries. This is also observed for the infinite line source case in section 4.2.2.1, where the phase error is removed by moving the MUR1 boundaries further away.

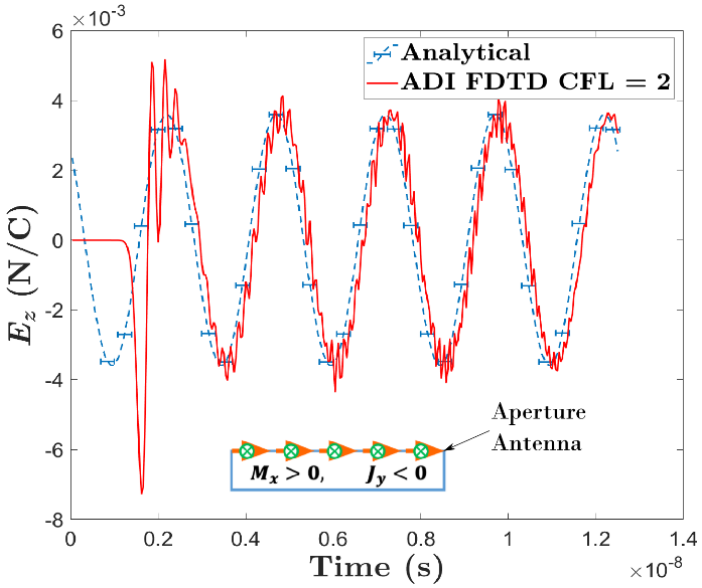


Figure 4-4: Plot comparing $E_z$ from the numerical simulation and the analytical solution.

As can be seen in Figure **4-4**, the ADI solution stays within the error bar of the analytical phase solution. The noise in the ADI-FDTD solution is a result of the excitation not initially being zero which can be rectified by using a modulated Gaussian pulse [240]. Modulated Gaussian pulses are utilized in sections 4.2.2 and 4.2.4. Noise is also produced by numerical reflection and Higher order ABCs reduce this type of noise, but these ABCs are difficult to implement within the implicit ADI methodology without compromising the tri-diagonal matrix [241]. These

results provide confidence in the general response of the code including stability, however, some phase shifts and small oscillation errors emanating from the ABC boundary conditions are present. These errors may be minimized by placing the ABCs further from the source which may be accomplished by cell stretching, as shown in subsequent sections of this chapter.

### 4.2.2 Infinite Line Sources

Sources of this type involve an infinitely long linear currents which may be electric (Figure 4-5a) or magnetic (Figure 4-5b) in nature. For the electromagnetic validation of the code, consider first an infinite z-directed electric line source, excited at 400MHz ($\lambda_0^{EM} = 0.75m$), as shown in Figure 4-5a. The PECs are included to replicate the infinite source currents in the vertical z-direction by image theory (see section 3.4.1.1). Due to the infinite length in the z-direction, there are no spatial variations in that direction, and this is a 2D problem in the rectangular coordinate system.

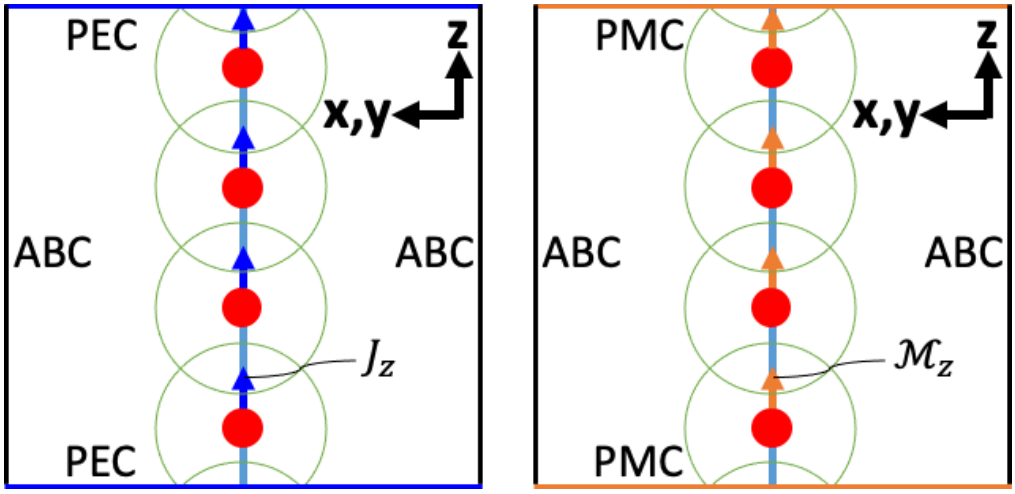


(a) Electric (b) Magnetic

Figure 4-5: Infinite line source cases w/ boundary conditions.

For this case, the analytical solution for the z-directed electric field as a phasor (denoted using a breve accent) is written below [25]:

$$\breve{E}_z(\rho) = -I_0 \frac{\omega\mu_0}{4}[J_0(k\rho) - jY_0(k\rho)] \tag{4.3a}$$

Where $\rho$ is the cylindrical radial coordinate, which originates at the line source, $\omega$ is the circular excitation frequency, $k$ is the wavenumber, $J_0/Y_0$ are Bessel functions of the 1st/2nd kind respectively, and $I_0$ is the magnitude of the line current which is input as 1mA. The steady state instantaneous field is as follows:

$$E_z(\rho, t) = Re\{\breve{E}_z e^{j\omega t}\} = -I_0 \frac{\omega\mu_0}{4}\left[J_0(k\rho)\cos\left(\omega t - \frac{\pi}{2}\right) + Y_0(k\rho)sin\left(\omega t - \frac{\pi}{2}\right)\right] \tag{4.3b}$$

Where the $\pi/2$ phase shifting is included to represent a sinusoidal input. If a modulated Gaussian pulse solution is sought, equation (4.3b) is modified as follows:

$$E_z(\rho, t) = -I_0 \frac{\omega\mu_0}{4}\left[J_0(k\rho)\cos\left(\omega t - \frac{\pi}{2}\right) + Y_0(k\rho)sin\left(\omega t - \frac{\pi}{2}\right)\right] e^{-\frac{(t-t_d-\rho/c)^2}{(t_w)^2}} \tag{4.3c}$$

Where $t_w$ is the pulse half-width, $t_d$ is the time delay at the source, and $\rho/c$ is the additional time delay as the wave propagates to the observation point ($c$ is the speed of light). This latter time delay term may be ignored when the observation point is electrically close to the radiator, i.e., when in the extreme near field which is the case in this section. The Gaussian pulse parameters were chosen as follows:

$$t \to t + \Delta t/2 \tag{4.4a}$$

$$t_d = 3.6/f \tag{4.4b}$$

$$t_w = 1.2\sqrt{2}/f \tag{4.4c}$$

$$e^{-\frac{(t-t_d-\rho/c)^2}{(t_w)^2}} \to e^{-\frac{(t+\Delta t/2-3.6/f-\rho/c)^2}{2(1.2/f)^2}} \tag{4.4d}$$

Where $f$ is the input frequency and $\Delta t$ is the sampling time. Equation (4.3b) generally applies in both the near and far-field and is compared to numerical results in the following sections, along with the modulated Gaussian pulse solution (4.3c).

#### 4.2.2.1 Small/Medium/Large Study

An initial study using three simulated spaces, i.e., a small (0.1m cube), medium (1x1x0.1m), and large (2x2x0.1m), were conducted with the ADI-FDTD code as shown in Figure 4-6. The simulation space was varied to better understand the influence of the MUR1 absorbing boundary conditions on the numerical solution as the boundaries are moved closer to radiating elements.

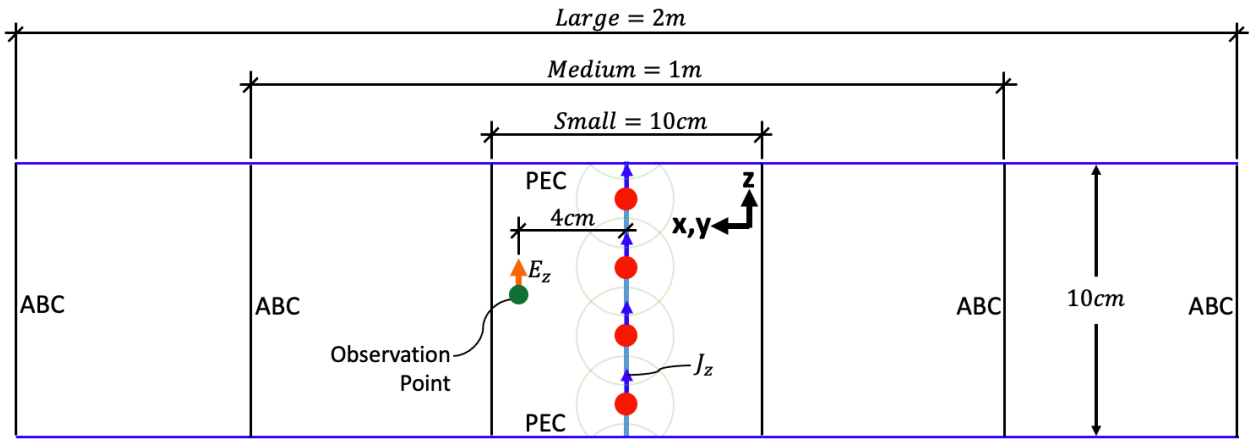


Figure 4-6: Small/Medium/Large Study Geometry

The MUR1 ABCs shown in Figure 4-6 are applied in both the x and y directions. In this study the discretization, time step, and observation point are consistent across all three simulations such that the only variation between runs is the proximity of the absorbing boundaries to the radiator. The discretization for all runs is 1cm ($\Delta x = \Delta y = \Delta z = 1cm$). Figure 4-7 shows the simulation results for the z-directed electric field ($E_z$) compared to the general analytical solution (eq. 4.3b) at an observation point x=0.04m from the source for this axisymmetric problem.

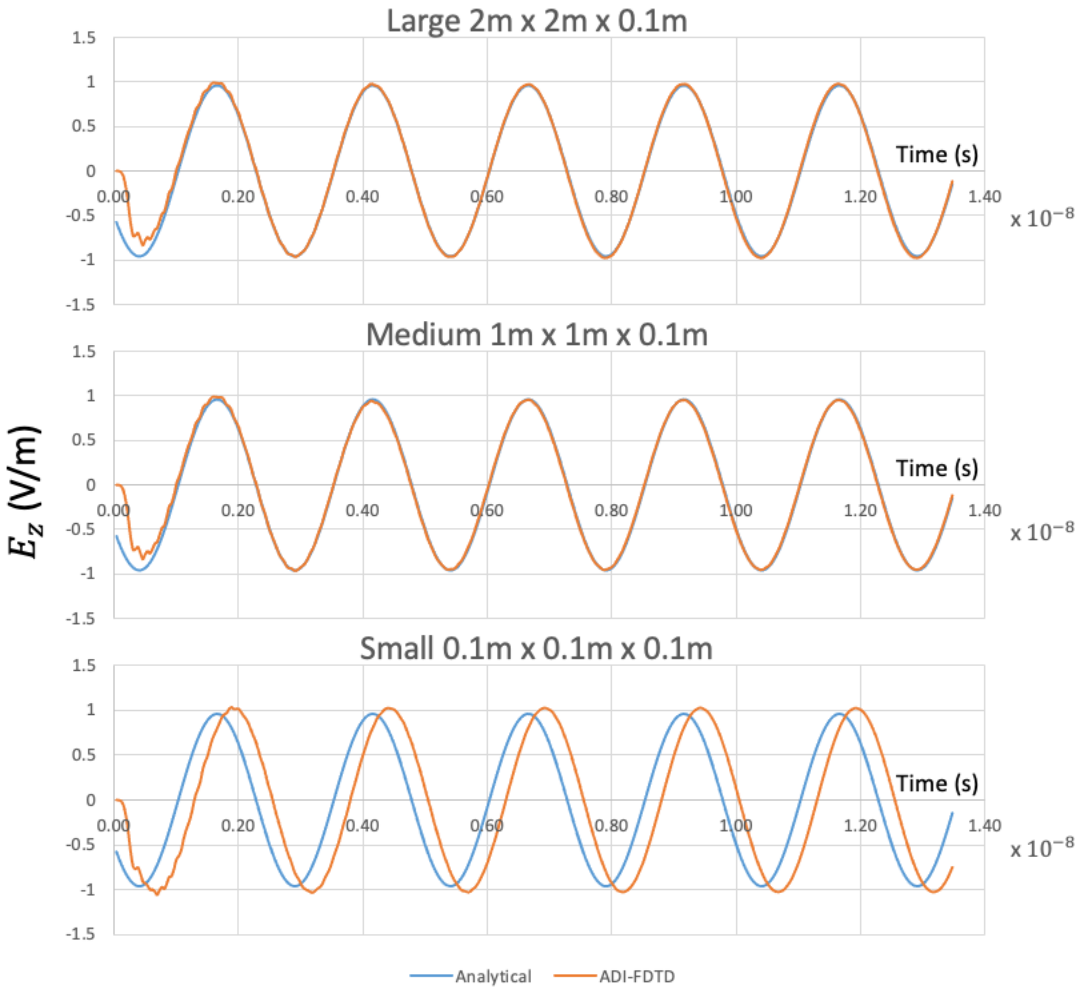


Figure 4-7: $E_z$ Results from the infinite line source study, for all three simulation space sizes, at the observation point which is 4cm away from the line source.

The time step was set to 2 times larger than what is required for stability (CFLN=2). If conventional FDTD were utilized, the results from using this time step would be unstable, but in this ADI-FDTD algorithm the results are not only stable but accurate (with the exception of a phase and amplitude error in the 0.1m small cube) as shown in Figure 4-7. The initial ripples in the ADI results for all three cases are expected transients prior to the system reaching steady state. The phase and amplitude error in the 0.1 m small cube are attributed to the first order Mur absorbing boundary conditions (MUR1 ABCs) [210] utilized in the (xy) directions. It is difficult to

implement higher order ABCs in ADI simulations [241] and thus, to use the ADI approach, ABC boundaries should be placed as far as possible from the source. As can be seen, these errors are absent in the medium and large simulations. Note that, since the spatial discretization, time step, and wavelength are consistent across all simulations, the cause of this phase lag and amplitude error is not numerical dispersion as this is the same in all three cases. Indeed, the cause is that the 1$^{st}$ order Mur absorbing boundaries have been brought too close to the source currents, producing errors. This error may be minimized by stretching the finite difference grid in the xy-plane such that the ABCs are pushed further away from the radiating source currents, or by utilizing PEC-backed lossy perfectly matched layers (PMLs) rather than MUR1 boundaries. Both these methods may be used simultaneously to produce stretched PML regions as will be discussed in the next section.

#### 4.2.2.2 Stretched/Lossy Regions within Progressively Shrinking Simulation Spaces

Often it is necessary to move the simulation boundaries electrically close to the radiating elements due to the computational expense of modeling electrically small radiators as well as in complex coupled problems such as multiferroic antennas requiring both electromagnetic and mechanics modeling. In the case of mechanical resonance-based antennas, the simulation space must shrink to on the order of 1/10,000$^{th}$ of the free space EM wavelength when using a uniform grid of 100x100x100 cells or less to be able to model the structure using conventional computational platforms. However, placing absorbing boundaries based on one-way wave equations, such as the MUR1 ABC [210], introduce significant error to the simulated results, as illustrated in the previous section. Therefore, other approaches need to be considered such as stretching the finite difference mesh so that the simulated boundaries are mathematically pushed further away from the radiator even though the number of elements has not increased. In this graded mesh design, the mesh is geometrically fine near the radiator and progressively coarser near the boundaries. The following subsections explore this avenue of boundary error

reduction on progressively shrinking simulation spaces to gain insight on the multi-physics simulations performed in Chapter 5.

#### 4.2.2.2.1 10cm Cubic Simulation Space

First consider the geometry of Figure 4-8, which is identical to the infinite electric line source problem shown in Figure 4-5a with relevant simulation parameters now defined:

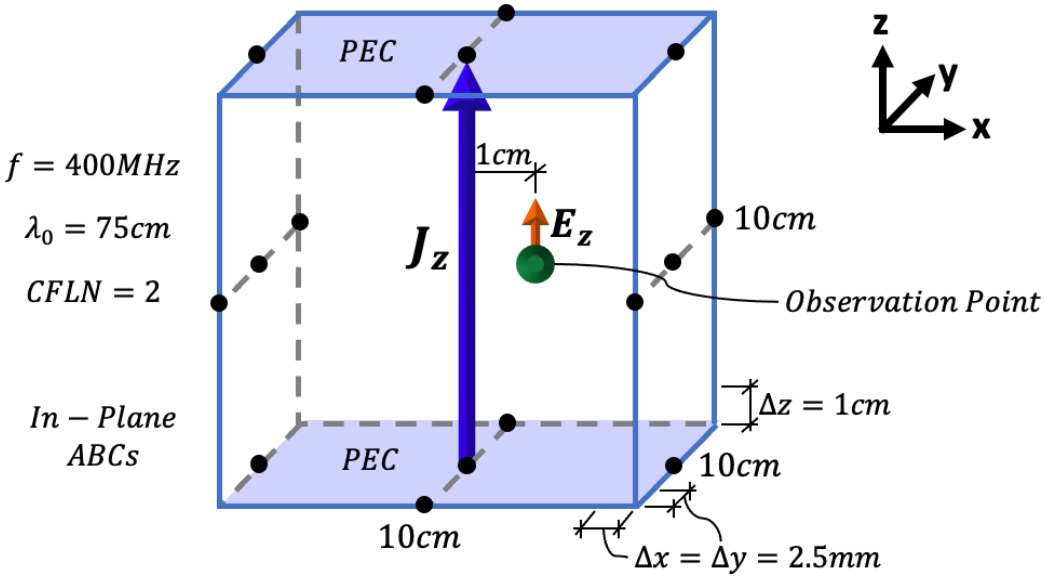


Figure 4-8: 400MHz Infinite line source within a 10cm cubic unstretched simulation space. $\boldsymbol{E_z}$ is measured 1cm away from the source.

The size of the simulation space is identical to the "small" case discussed in the "Small/Medium/Large Study" Section 4.2.2.1 (i.e., a 0.1m cube), but with finer spatial sampling in the x and y directions. The observation point is also now closer to the source (1cm away) with respect to the Small/Medium/Large Study (4cm away). The numerical results for $E_z$ at the observation point shown in Figure 4-8 are compared to the analytical solution in Figure 4-9:

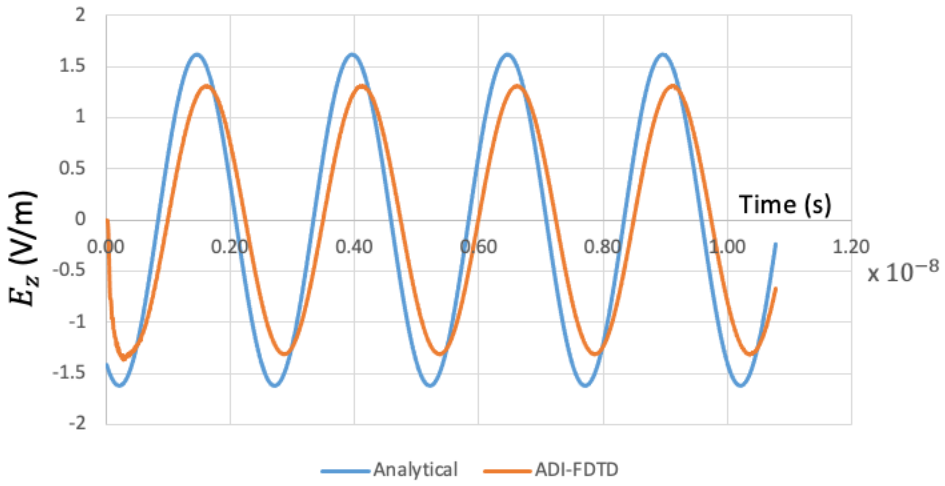


Figure 4-9: $\boldsymbol{E_z}$ at observation point from infinite line source case shown in Figure 4-8.

There is an amplitude and phase error present in these results, like the “small” case previously exhibited (Figure 4-7), caused by the ABCs. To reduce this error, a scheme for stretching the cells is introduced as shown in Figure 4-10. In this figure, the 12 cells adjacent to the boundaries are stretched while the center 16x16 grid remains unstretched (at $\Delta x = \Delta y = 2.5mm$).

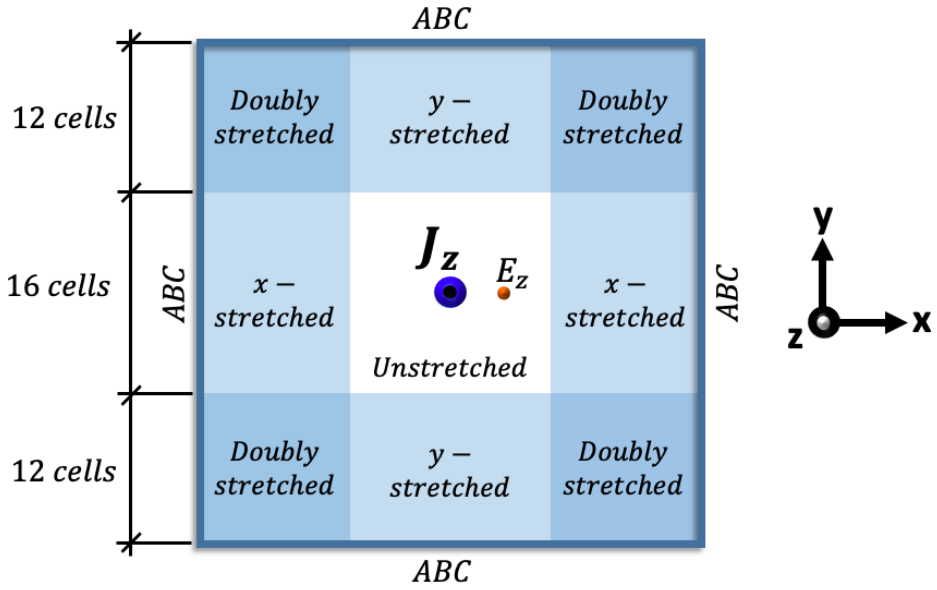


Figure 4-10: 12-cell In-plane stretching scheme for the infinite line source problem.

In the design of this ADI-FDTD code there are three input parameters related to coordinate stretching; the maximum stretching ($\kappa^{max}$), the number of cells across which the stretching occurs, and the polynomial factor describing the fashion in which the stretch increases from 1 to $\kappa^{max}$ (m=1=linear, m=2=quadratic, …). Utilizing a 12-cell stretched region with $\kappa^{max} = 10$, and $m = 1$ yields:

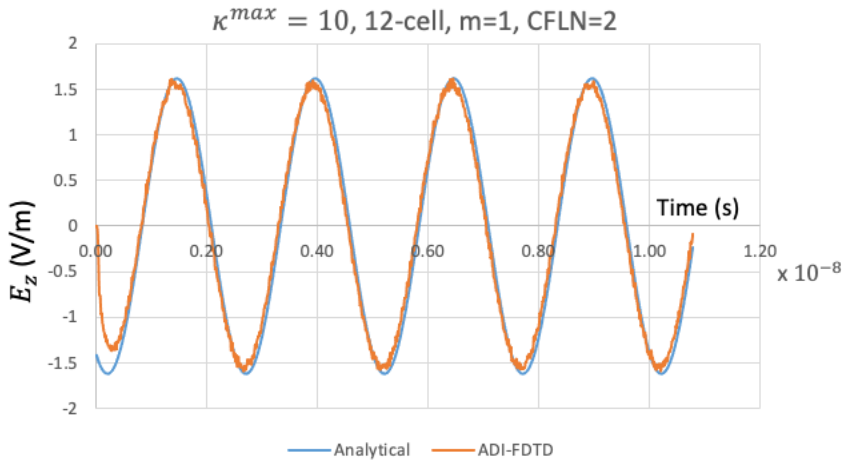


Figure 4-11: Infinite line source results for $\boldsymbol{E_z}$ for an initially 10cm cubic simulation space with $\boldsymbol{\kappa_{max}}$=10, 12-cell, m=1, and CFLN=2.

As can be seen in Figure 4-11, the phase error has been virtually eliminated (compared to Figure 4-9) and the amplitude error significantly reduced as a result of the stretching. Some degree of noise has been introduced into the results; however, this can be mitigated with the use of higher m-factors as well as using a modulated Gaussian pulse input so that the initial input is near zero.

At this time, it is helpful to show one approach to producing more accurate results with a note that there are multiple methods that can be used. For example, Figure 4-12 shows a 14-cell PEC-backed unstretched PML region as contrasted with the 12-cell ABC approach shown in Figure 4-10:

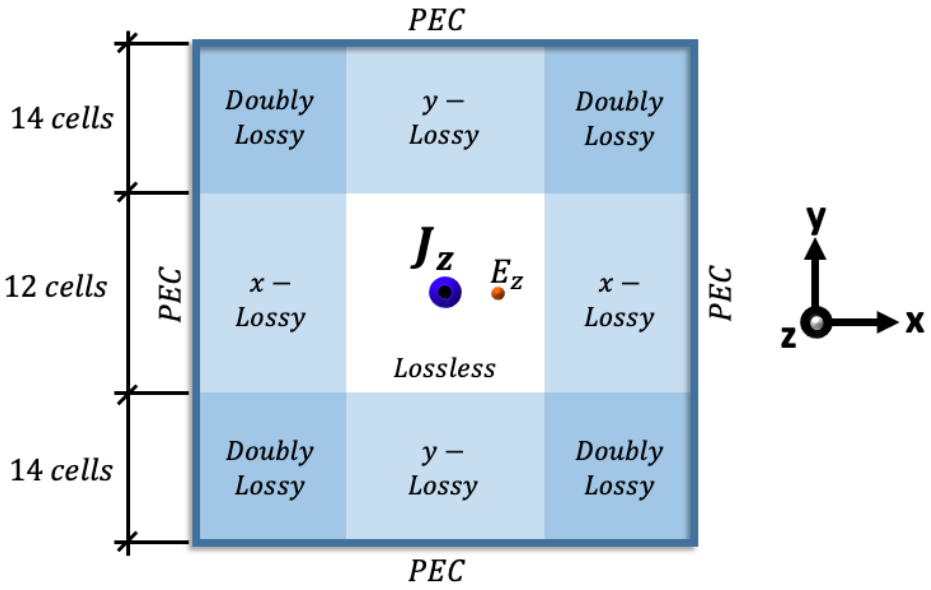


Figure 4-12: 14-cell In-plane PML region for the infinite line source problem.

Figure 4-13 shows the results for a modulated Gaussian pulse rather than a sinusoidal input. In this model the reflection error is set to $e^{-16}$, and a linear interpolation scheme is utilized (m=1). As shown, accurate results are achievable when the stretched region, backed by an ABC, is replaced by a unstretched PML region, backed by a PEC at this size. Therefore, some level of experimentation is open to the modeler with some guardrails in place to ensure accuracy. For example, $\kappa^{max}$ should not cause the spatial discretization to become greater than $\lambda_0^{EM}/20$ within the stretched region.

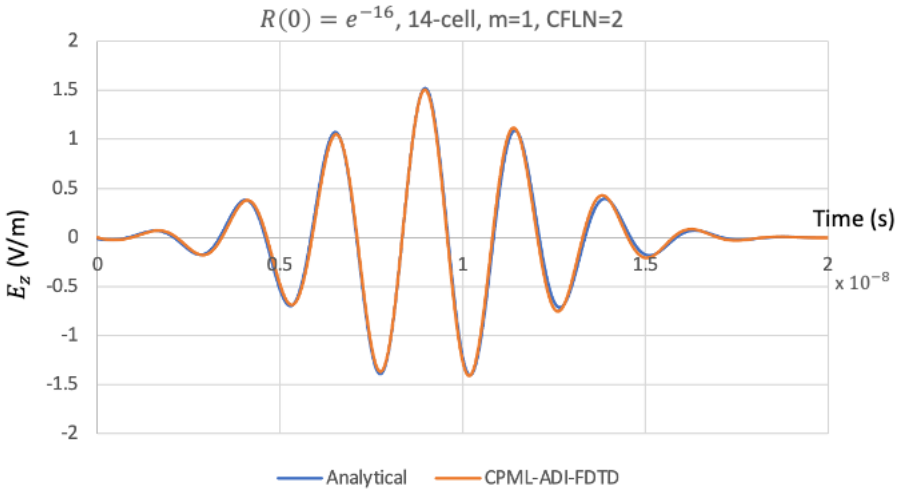


Figure 4-13: Infinite line source results for $\boldsymbol{E_z}$ for an initially 10cm cubic simulation space with reflection error $\boldsymbol{R(0)=e^{-16}}$, 14-cell, m=1, and CFLN=2.

#### 4.2.2.2.2 1cm Cubic Simulation Space

In this section the simulation space and discretization utilized in the previous section are reduced by an order of magnitude while maintaining the same time step by increasing the CFLN factor to 20 from 2. The goal of this study is to retain accuracy as the number of cells is progressively reduced until the unstretched size is on the order of $10^{-4}\lambda_0^{EM}$. This dimension represents the simulation space required for mechanical resonance-based antenna simulations. For clarity, the simulation space is shown in Figure 4-14:

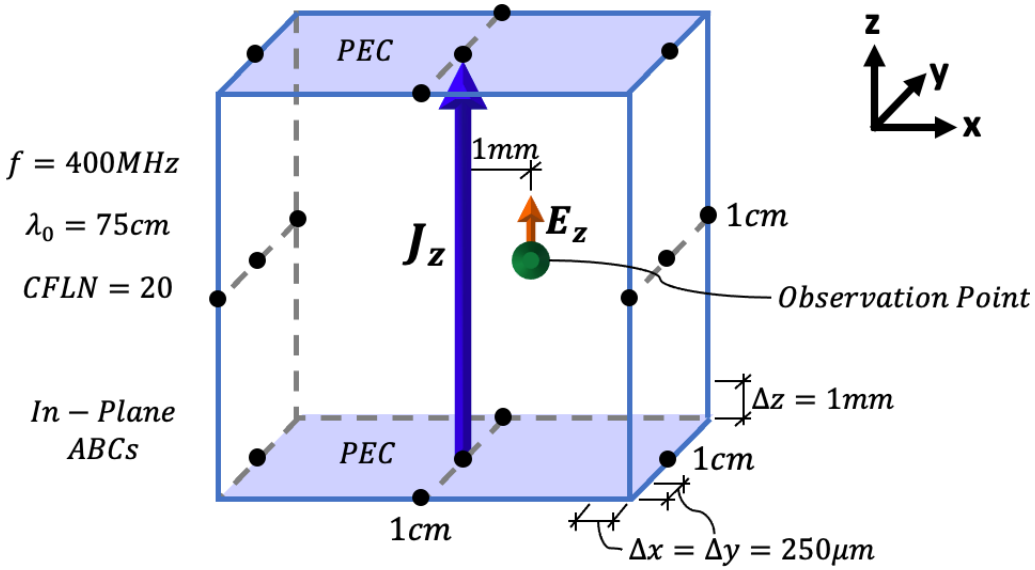


Figure 4-14: 400MHz Infinite line source within a 1cm cubic unstretched simulation space. $\boldsymbol{E_z}$ is measured 1mm away from the source.

The results for $E_z$ at the observation point shown in Figure 4-14 for an unstretched simulation space are shown in Figure 4-15:

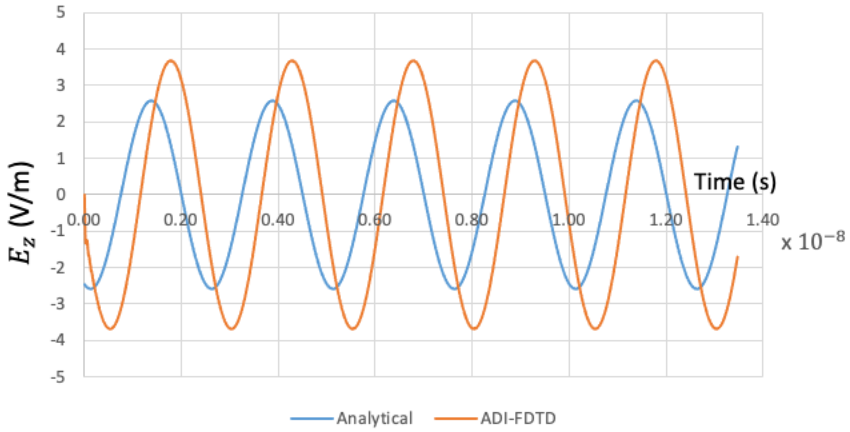


Figure 4-15: $\boldsymbol{E_z}$ at observation point from infinite line source case shown in Figure 4-14.

Note that there is significant amplitude and phase error within the simulation results caused by the absorbing boundaries. In order to mitigate this, the stretching scheme shown in Figure 4-10 is utilized again with $\kappa_{max} = 150$ and $m = 2$ to produce the results in Figure 4-16:

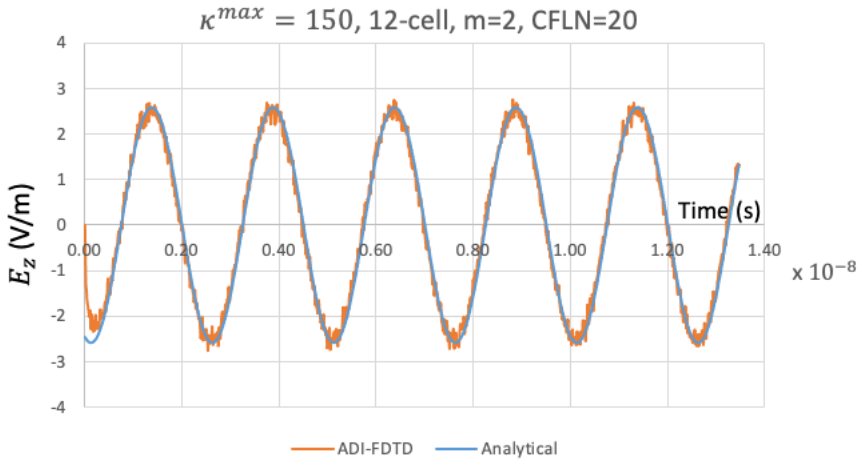


Figure 4-16: Infinite line source results for $\boldsymbol{E_z}$ for an initially 1cm cubic simulation space with $\boldsymbol{\kappa_{max}}$=150, 12-cell, m=1, and CFLN=20.

The phase error has been virtually eliminated in Figure 4-16, and the amplitude error has been significantly reduced, though some noise has been introduced. The noise can be mitigated by utilizing a modulated Gaussian pulse rather than a sinusoidal input along with unstretched PML layers to yield the results in Figure 4-17. As shown in Figure 4-17, the amplitude and phase error are within 10%. Further improvements may be achieved by reducing the time step or beginning to implement both stretching and lossy PML layers simultaneously.

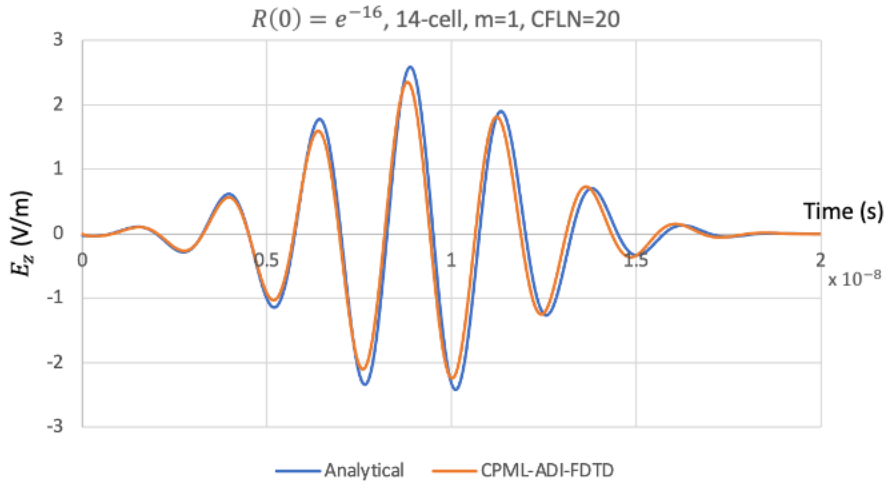


Figure 4-17: Infinite line source results for $\boldsymbol{E_z}$ for an initially 1cm cubic simulation space with $\boldsymbol{R(0)=e^{-16}}$, 14-cell, m=1, and CFLN=20.

#### 4.2.2.2.3 1mm Cubic Simulation Space

In this section the simulation space and discretization utilized in the previous section are reduced by another order of magnitude (i.e., from 1cm to 1mm) while maintaining the same time step by increasing the CFLN factor to 200 from 20, see Figure 4-18. The goal continues to be shrinking the simulation space until the unstretched size is on the order of $10^{-4}\lambda_0^{EM}$ as is the case required for mechanical resonance-based antenna simulations.

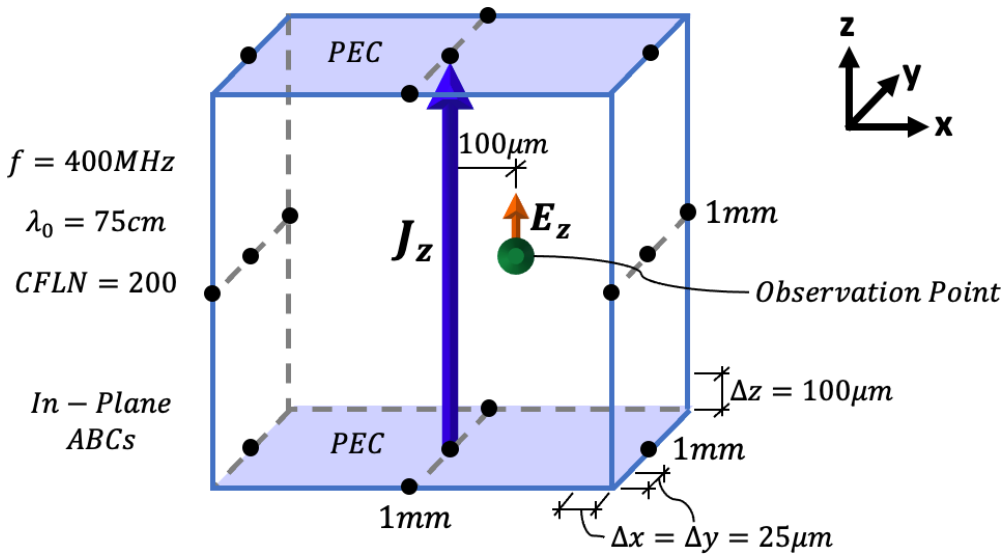


Figure 4-18: 400MHz Infinite line source within a 1mm cubic simulation space. $\boldsymbol{E_z}$ is measured 100$\boldsymbol{\mu}$m away from the source.

The results for $E_z$ at the observation point shown in Figure 4-18 for an unstretched simulation space are shown in Figure 4-19.

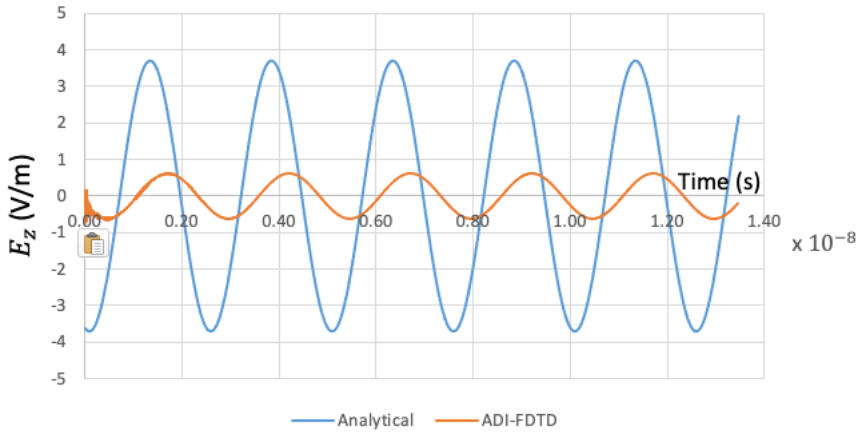


Figure 4-19: $\boldsymbol{E_z}$ at observation point from infinite line source case shown in Figure 4-18.

As can be seen, there is significant amplitude and phase error within the simulation results. To mitigate this, the stretching scheme shown in Figure 4-10 is utilized again with $\kappa_{max} = 1500$ and $m = 2$ to produce the results in Figure 4-20:

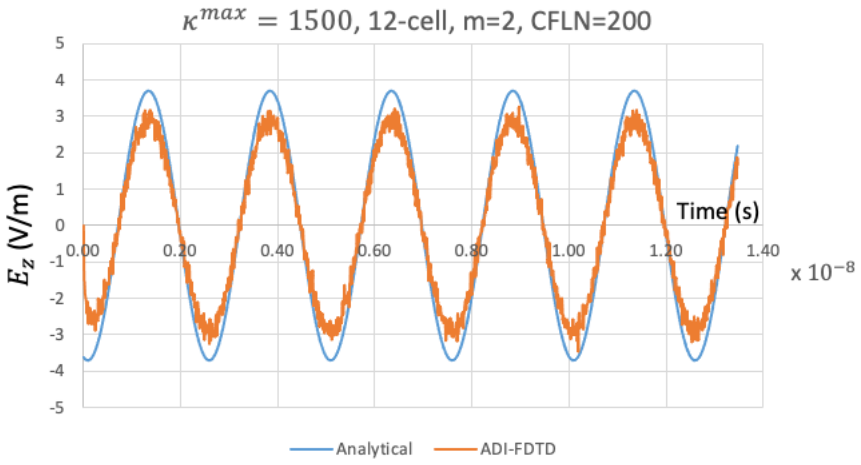


Figure 4-20: Infinite line source results for $\boldsymbol{E_z}$ for 1mm cubic simulation space and $\boldsymbol{\kappa_{max}}$=1500, 12-cell, m=2, and CFLN=200.

Figure 4-20 shows the phase error has been virtually eliminated but the amplitude error persists, and significant noise is present due mainly to the initial excitation being non-zero. Regardless, it is interesting that the results are not unstable even with a cell aspect ratio of 1500. To reduce the amplitude error, the time step may be reduced by a factor of 10 by reducing CFLN to 20, yielding the results of Figure 4-21. Note that the degree of noise has increased. An increase in m-factor will reduce the noise slightly, but the best method of noise reduction is to switch to a modulated Gaussian pulse input such that the initial excitation is near zero as will be shown in the following section.

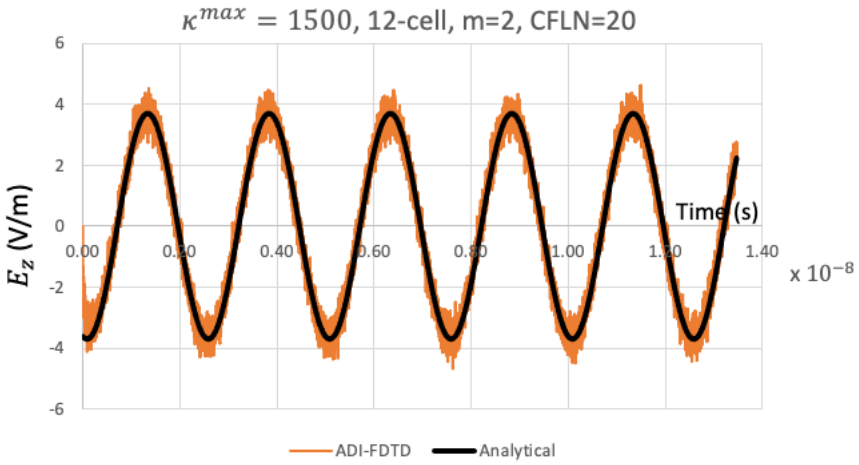


Figure 4-21: Infinite line source results for $\boldsymbol{E_z}$ for 1mm cubic simulation space and $\boldsymbol{\kappa_{max}}$=1500, 12-cell, m=2, and CFLN=20.

#### 4.2.2.2.4 100$\mu$m Cubic Simulation Space

In this section the simulation space and discretization utilized in the previous section are reduced by an order of magnitude (to 100$\mu m$ from 1mm) while maintaining the same time step by increasing the CFLN factor to 2000 from 200, see Figure 4-22 compared to Figure 4-20. The unstretched simulation space is now $\lambda_0/7500$ in size, and therefore has dimensions comparable to mechanical resonance-based antenna simulations.

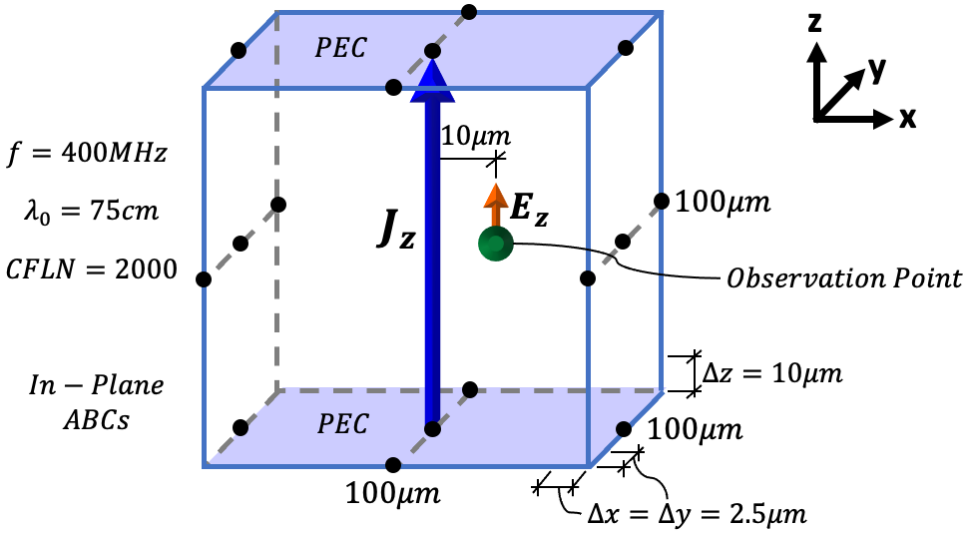


Figure 4-22: 400MHz Infinite line source within a 100$\mu$m cubic unstretched simulation space. $E_z$ is measured 10$\mu$m away from the source.

The results for $E_z$ at the observation point shown Figure 4-22 for an unstretched simulation space are shown in Figure 4-23:

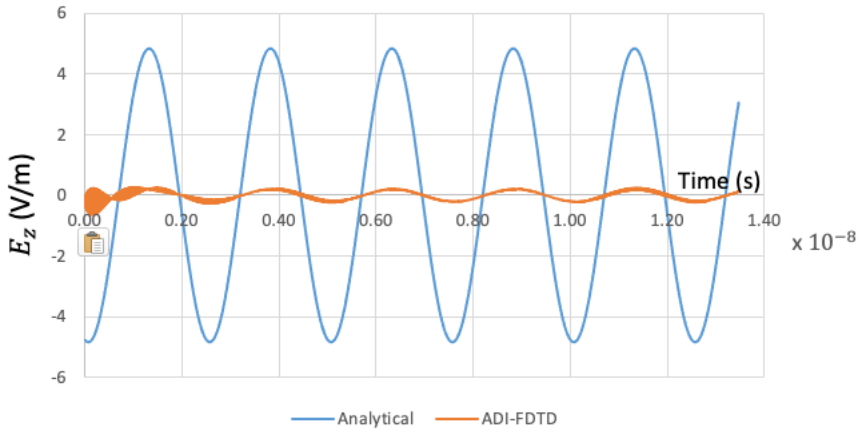


Figure 4-23: $E_z$ at observation point from infinite line source case shown in Figure 4-22.

Note that there is significant amplitude and phase error as well as noise within the simulation results. Given the absence of such high amplitude noise within the unstretched

results of larger simulation spaces (see Figure 4-9 for example), the noise present in Figure 4-23 is caused partly by the close proximity of the MUR1 ABCs utilized. To improve accuracy, the stretching scheme shown in Figure 4-10 is utilized again with $\kappa_{max} = 15000$ and $m = 2$ to produce the results in Figure 4-24:

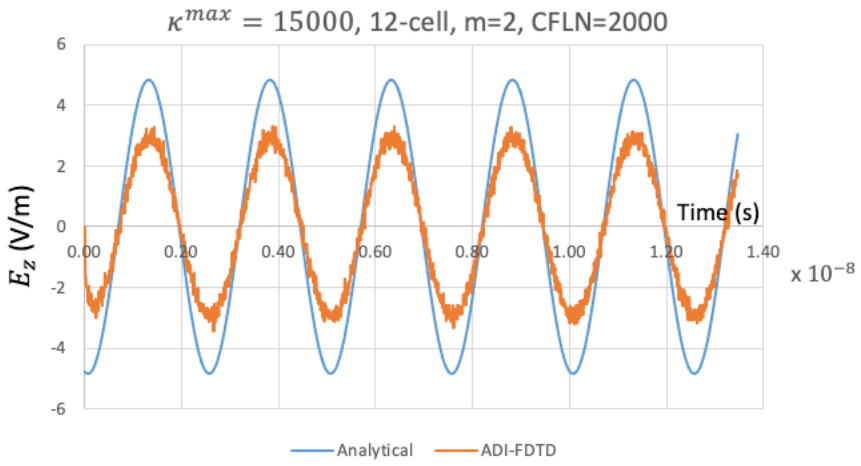


Figure 4-24: Infinite line source results for $\boldsymbol{E_z}$ for 100$\boldsymbol{\mu}$m cubic simulation space and $\boldsymbol{\kappa_{max}}$=15000, 12-cell, m=2, and CFLN=2000.

The phase error has been virtually eliminated but the amplitude error persists. Regardless, it is interesting that the results are not unstable even with a cell aspect ratio of 15,000. To reduce the amplitude error, the time step may be reduced by a factor of 20 to CFLN=100, and the m-factor increased to 4, yielding the results of Figure 4-25:

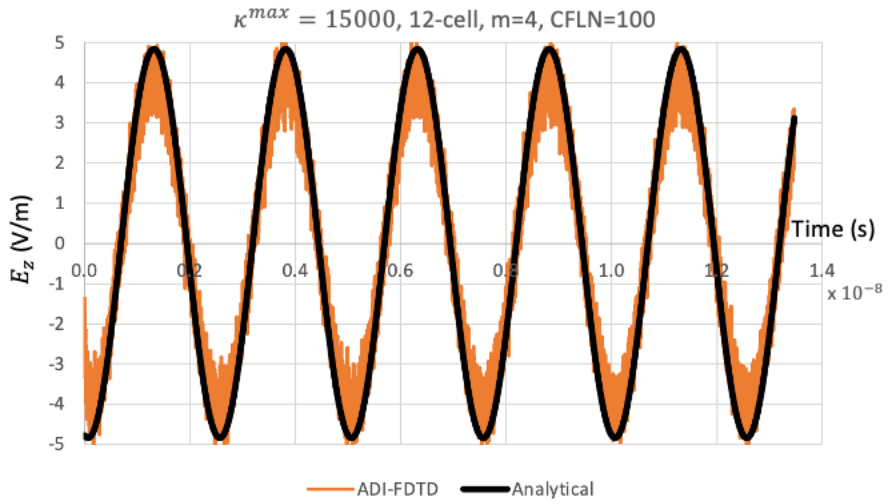


Figure 4-25: Infinite line source results for $\boldsymbol{E_z}$ for 100$\boldsymbol{\mu}$m cubic unstretched simulation space and $\boldsymbol{\kappa_{max}}$=15000, 12-cell, m=4, and CFLN=100.

As well as exhibiting improved amplitude accuracy, the amplitude of the noise has also increased in Figure 4-25. The noise is virtually eliminated by utilizing a modulated Gaussian pulse as shown in Figure 4-26. Note that a 10.1% amplitude error persists. To further improve the results, the time step may be reduced, or the stretched region may be extended, or a PEC-backed PML region may be introduced, or all the above as shown in the following sections.

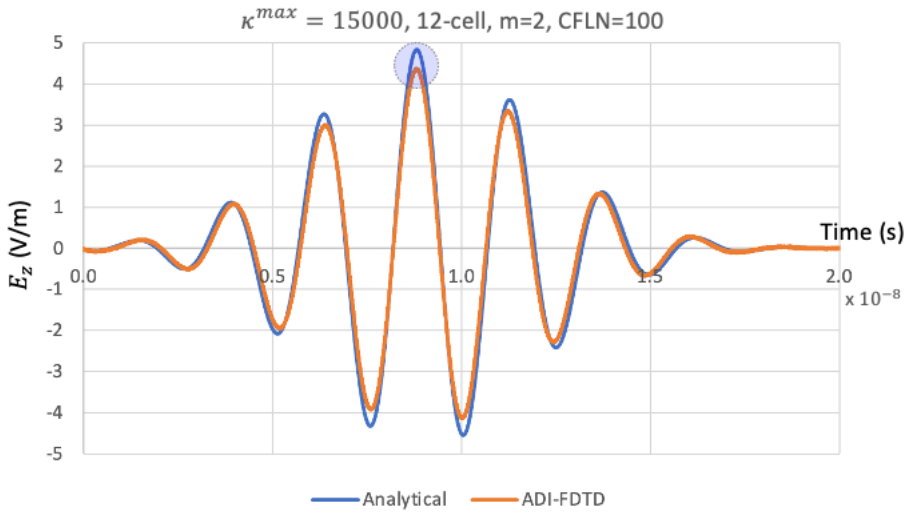


Figure 4-26: Gaussian pulse excitation for the initially 100$\mu$m cubic infinite line source problem.

Note that much of the noise has been eliminated by switching to the modulated Gaussian pulse, but some noise persists. This is the noise introduced by the MUR1 ABCs which can be eliminated by switching to stretched PML layers.

#### 4.2.2.2.5 Variable $\kappa$ Study

Recall that $\kappa_{max} = 15{,}000$ was chosen in Figure 4-26 such that there are 20 cells per free space EM wavelength ($\lambda_0^{EM} = 20\kappa_{max}\Delta$) at the coarsest spatial sampling. This standard is widely used in numerical analysis and a study was performed to prove that this rule is adequate for mechanical antenna analysis as shown in Figure 4-27:

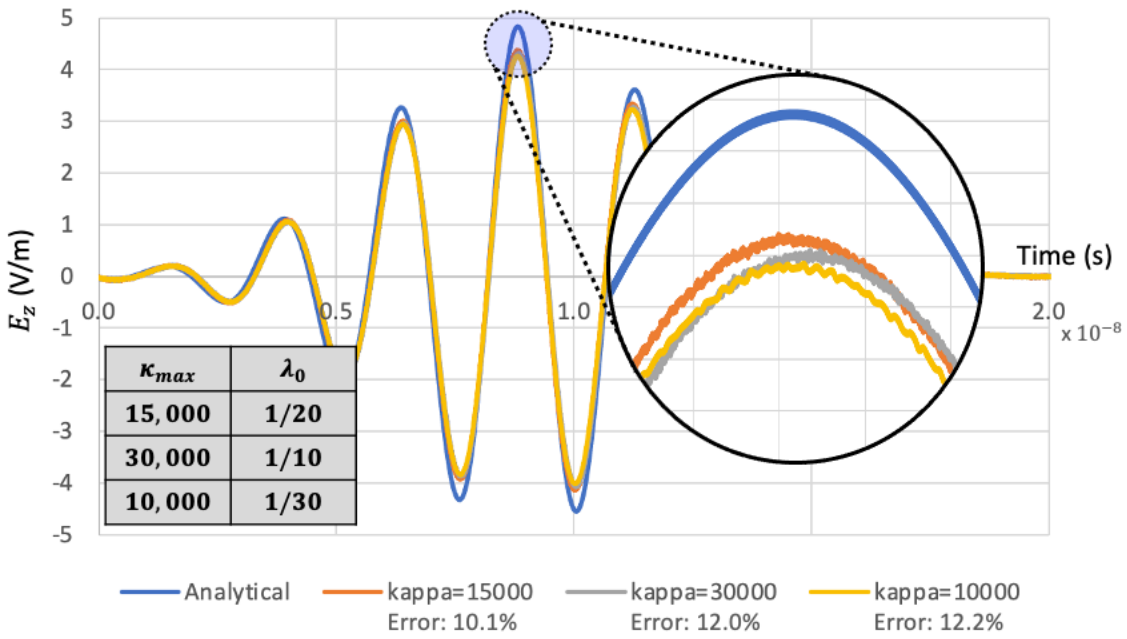


Figure 4-27: Results from study where the value of $\boldsymbol{\kappa_{max}}$ is varied. The steady state analytical solution and numerical results are based on a sinusoidal modulated Gaussian pulse input. The region where the amplitude error is most pronounced is shaded and expanded for clarity. $\boldsymbol{\kappa_{max} = 15000}$ corresponds to 20 cells per free space EM wavelength.

Figure 4-27 shows the results for three $\kappa_{max}$ values (15,000, 30,000, & 10,000) corresponding to the coarsest spatial discretization of 20, 10, and 30 cells per wavelength respectively. The error compared to the analytical model increases as $\kappa_{max}$ moves further from the 20 cells per wavelength standard. When $\kappa_{max} = 30{,}000$ the error increases to 12% since the spatial sampling is considered too coarse as well as some phase error is introduced. When $\kappa_{max} = 10{,}000$ the error increases to 12.2% since the reduced amount of stretching brings the MUR1 ABCs closer to the radiator. Therefore, the $\kappa_{max}$ value should be chosen such that there are 20 cells per wavelength to maximize the separation between the ABCs and the radiating elements, while maintaining adequate spatial sampling.

#### 4.2.2.2.6 Stretched Region Increase

Since increased separation of the boundary from the radiator yields more accurate results, including more cells within the stretched region is beneficial. This is illustrated in Figure 4-28 for the 100$\mu$m infinite line source problem discussed in 4.2.2.2.4, with the time step maintained at CFLN=100:

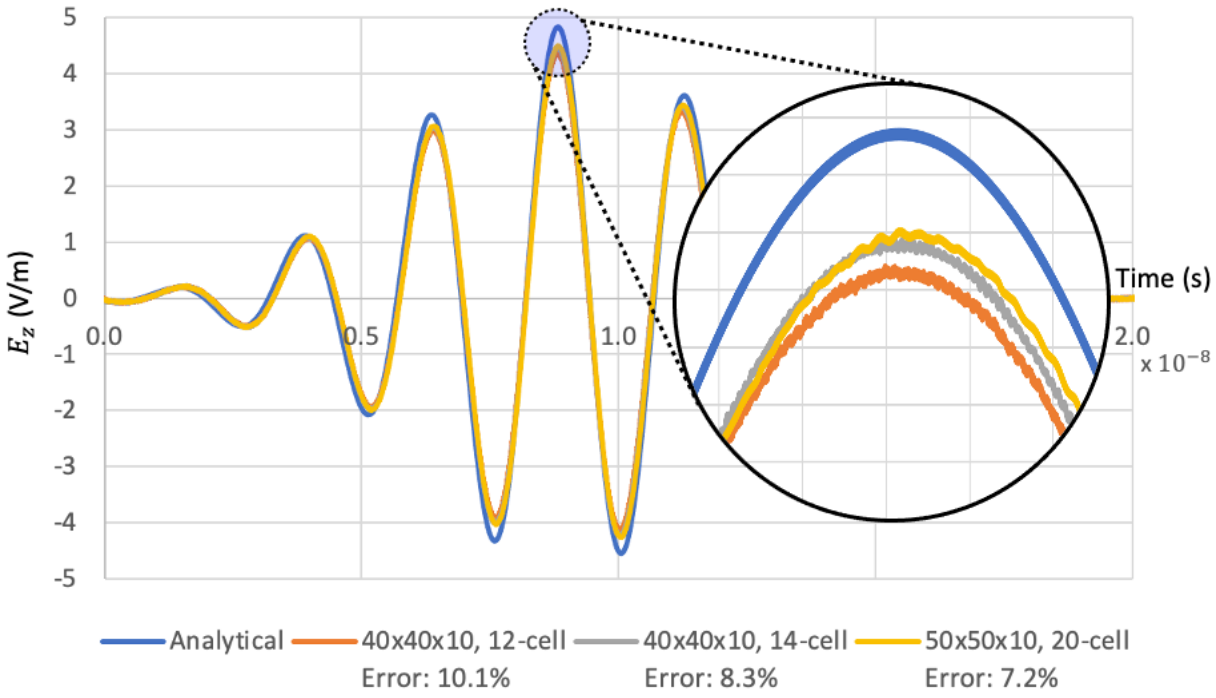


Figure 4-28: Effect of larger stretched regions on accuracy for the infinite line source problem on a 100$\mu$m cubic simulation space.

As seen in the figure, larger stretched regions increase the accuracy but with diminishing returns. For example, going from a 12 to 14 cell stretched region increases the amplitude accuracy from 10.1% to 8.3%, but further increasing the stretched region to 20-cells only increases the accuracy to 7.2%. Also note that, to achieve the 20-cell stretched region, the number of in-plane cells is increased from 40 to 50, adding computational load. The utilization of

a 14-cell stretched region therefore is seen to strike a balance between accuracy and computational efficiency for this case.

#### 4.2.2.2.7 Time Step Reduction Study

Perhaps the most intuitive way to improve results within an electrically small simulation space is to reduce the time step. This is achieved within the ADI-FDTD algorithm by reducing the CFLN factor.

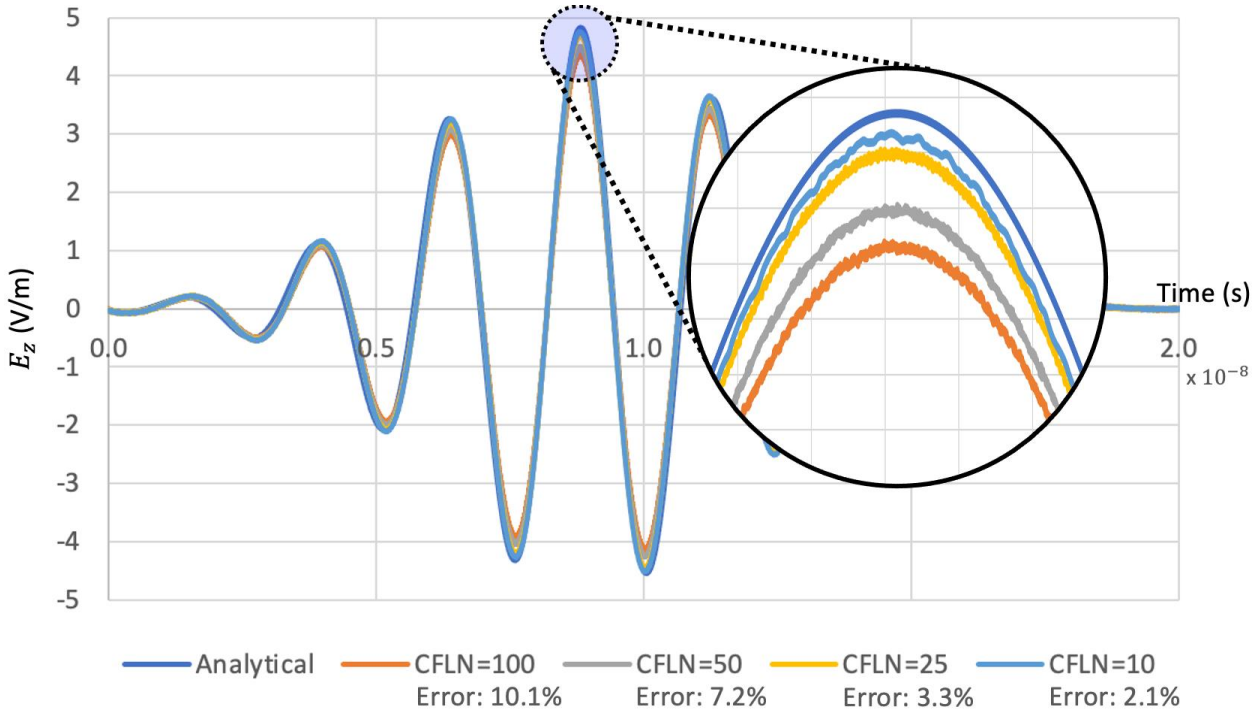


Figure 4-29: Effect of time step reduction on the accuracy of the infinite line source simulations.

Figure 4-29 shows the influence of for different CLFN (i.e. 100, 50, 25 & 10) as compared to the analytical results. As can be seen, for each time step reduction a corresponding improvement in accuracy is achieved with diminishing returns smaller than CFLN=25 for this case.

#### 4.2.2.2.8 PML Stretched Region

Figure 4-30 shows results for a 14-cell stretched PML region (see Figure 4-12 where stretching is now included as well) where the reflection error is set to $e^{-16}$, a cubic interpolation scheme is used (m=3), and $\kappa_{max} = 15{,}000$ stretching is applied.

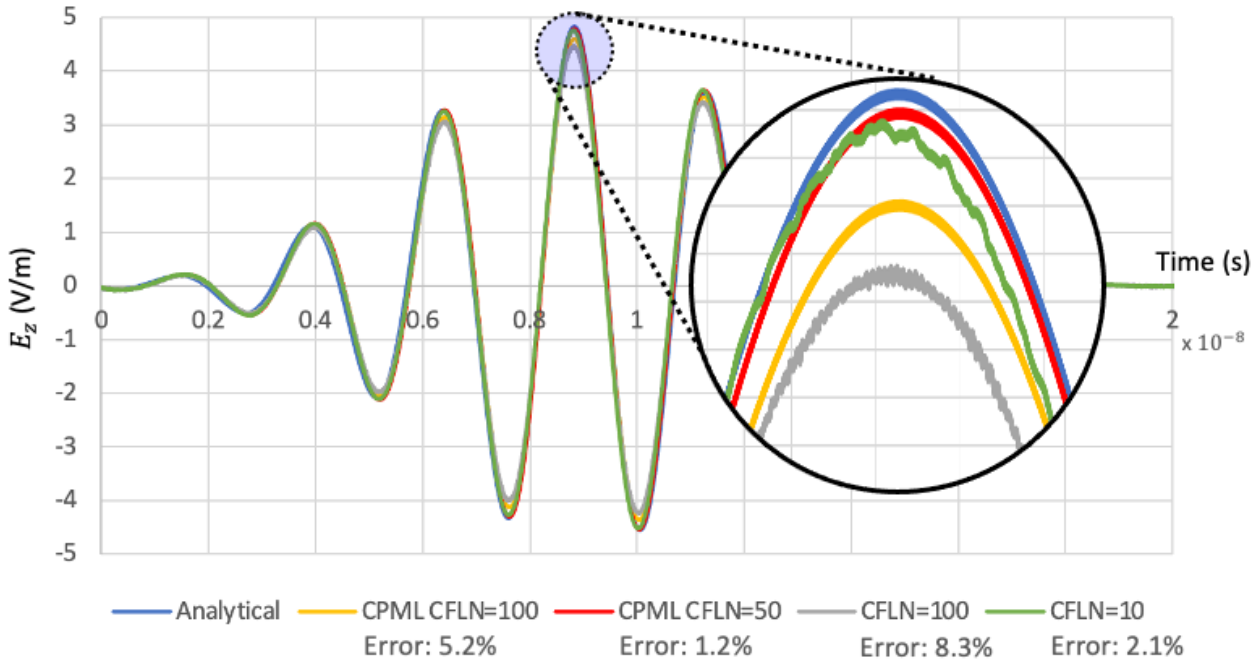


Figure 4-30: Comparison of analytical, stretched, and stretched PML results for $\boldsymbol{E_z}$ for the infinite electric line source problem.

At CFLN=100, the stretched PML solution (CPML) exhibits a 5.2% amplitude error, an improvement over the 8.3% error demonstrated when only stretching is used at this time step. Also, with removal of the MUR1 ABCs the low amplitude noise is eliminated in the CPML solution. The most accurate results exhibited by a scheme that utilizes stretching only (2.1%) was shown in Figure 4-29 when CFLN=10 was used. This particular result is repeated in Figure 4-30 (see green line) in order to compare to the CPML solution with CFLN=50, which displayed

an error of 1.2%. Therefore, including PML layers within a stretching scheme improves the accuracy of results even while utilizing larger time steps.

#### 4.2.2.2.9 CPML w/ Pre-Stretched Regions

Since the PML layers include a fictitious (non-physical) loss the fields within the lossy layers are also fictitious and only the interior nodes contain true near field data which may be used to analyze antenna performance. It can be beneficial then to include a real stretch within the interior nodes, prior to introducing fictitious PML loss, to increase the size of the interior space without increasing computational load. Unfortunately, a degradation of accuracy occurs when the real stretch ($\kappa$) factor is not equal to 1 at the onset of the PML layers. Therefore, the interior nodes must be stretched then compressed back to the original size within the interior as shown in Figure 4-31:

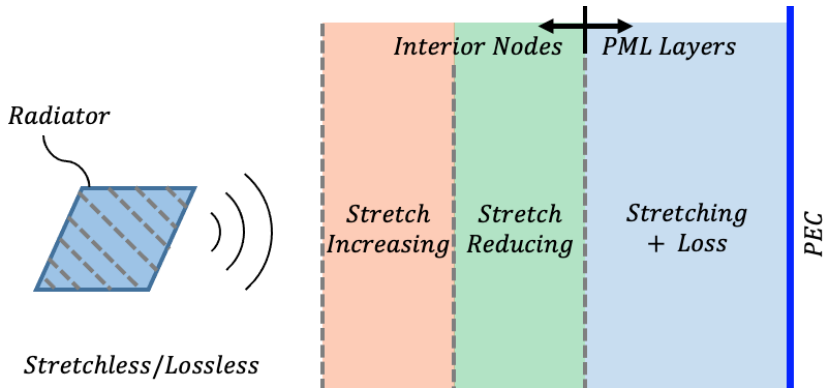


Figure 4-31: Interior stretching scheme adjacent to PML layers.

The pre-stretching scheme shown in Figure 4-32 is utilized for the infinite line source, where the PML scheme is the same as that utilized in the previous section (i.e., 14 cells, $\kappa_{max} = 15{,}000$). Within Figure 4-32 the numbers between the nodes are the kappa (real stretch) factors, the degree of stretching of the cell with respect to the original 2.5$\mu$m. As such, the 2nd node from the line source is now the observation point which is 10$\mu$m away.

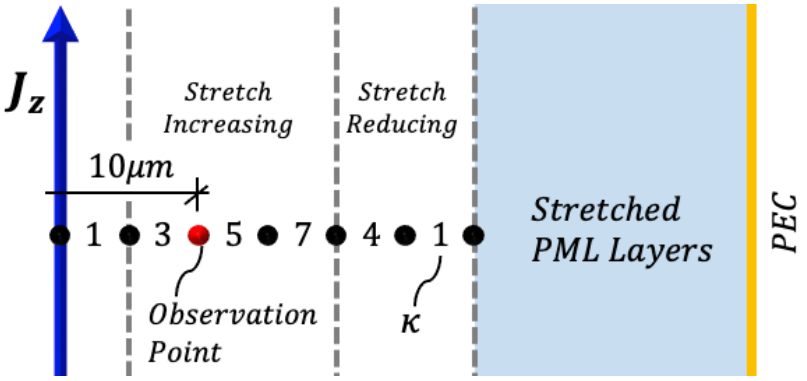


Figure 4-32: Infinite line source pre-stretching scheme.

This scheme will exhibit lower accuracy than the standard stretched PML scheme without interior stretching shown in Figure 4-12, but the accuracy is reasonable as shown in Figure 4-33:

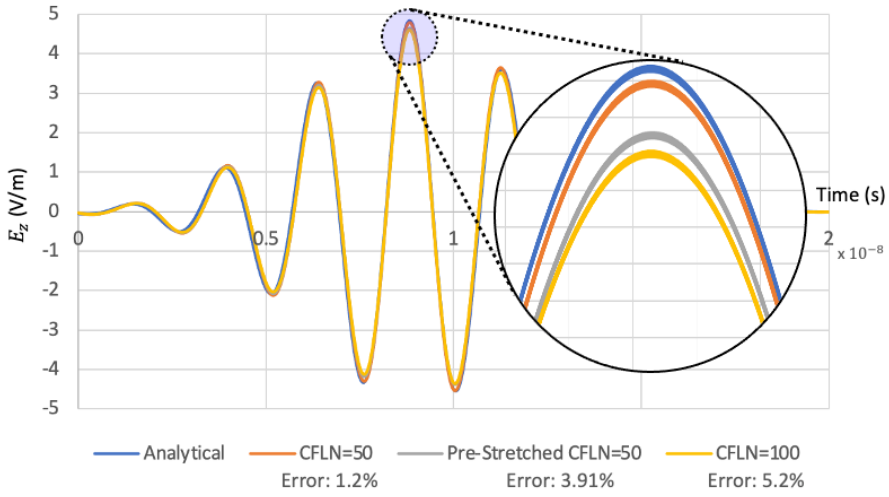


Figure 4-33: Comparison of analytical, stretched PML, and pre-stretched PML results for $\boldsymbol{E_z}$ for the infinite electric line source problem.

As shown, a slight reduction in accuracy at the same time step occurs when pre-stretching to an interior simulation space of over 3x the original size. This will be beneficial if a comparison to experimental near field values is desired, as measurements will typically take place at distances several times that of the geometric size of the radiator which governs the smallest discretization size. Though this pre-stretching method is useful, it was not utilized during any of the device simulations or comparisons performed in Chapter 5.

#### 4.2.2.3 Infinite Mechatronic Line Source

If the infinite electric line currents ($J_z$) of section 4.2.2.2 are replaced by an infinite line of normal stresses $T_{zz}$ which are collocated in space and time (see Figure 4-34), then electric fields will be generated if the piezoelectric coefficient $d_{33}^{PE}$ is not equal to zero.

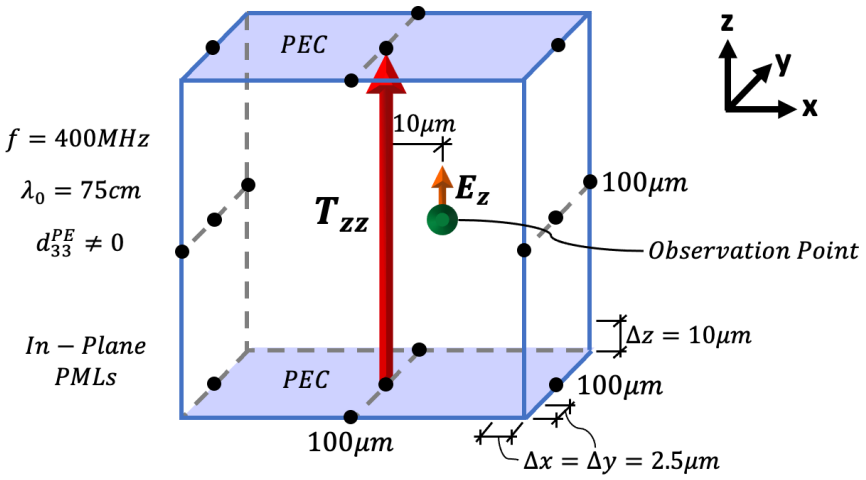


Figure 4-34: Infinite Mechatronic line source.

If the magnitude of the mechanically driven current and the electrically driven current is identical, then the magnitude of the generated electric fields will also be identical:

$$|J_z| = \left|d_{33}^{PE}\dot{T}_{zz}\right| \tag{4.5}$$

This is demonstrated in Figure 4-35, where $E_z$ results from section 4.2.2.2 were also included for comparison.

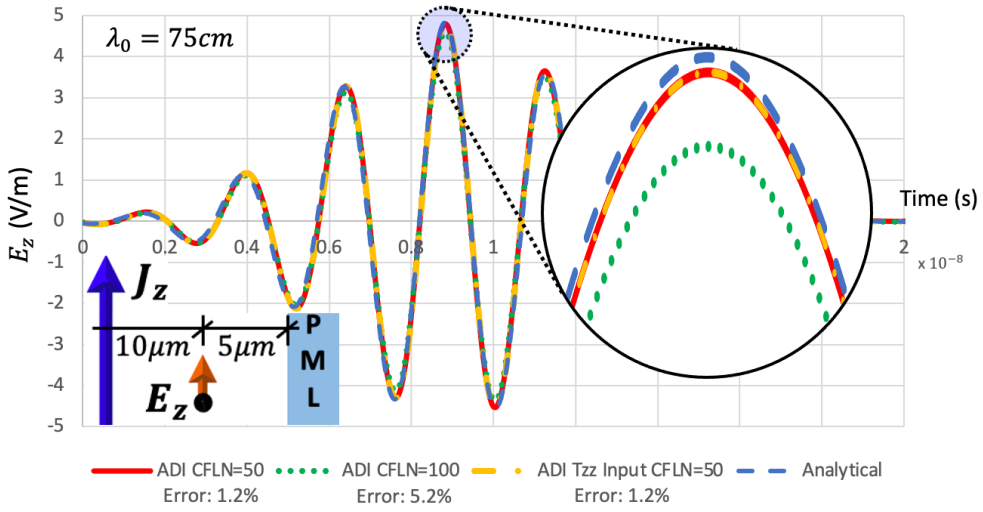


Figure 4-35: Mechatronic and electric infinite line source comparison.

As shown, when utilizing the same time step, identical results for $E_z$ are seen whether driving radiation via electric source current or via the stress induced direct piezoelectric effect.

#### 4.2.2.4 Infinite Magnetic Line Source

As mentioned in section 3.8.5.4, PMC boundaries require some special treatment within the ADI-FDTD framework with implicit electric field update, and boundaries aligned with electrical interfaces. To verify that the PMC boundaries are operating properly an infinite magnetic line source is leveraged, in contrast to the infinite electric line source utilized in previous sections. In this new model the approach illustrated in Figure 4-5b was simulated under the same input frequency, time step, spatial discretization, etc. of the infinite electric line source investigated in the previous section with the magnitude of the input current equal to $I_0 = 377\text{mA}$.

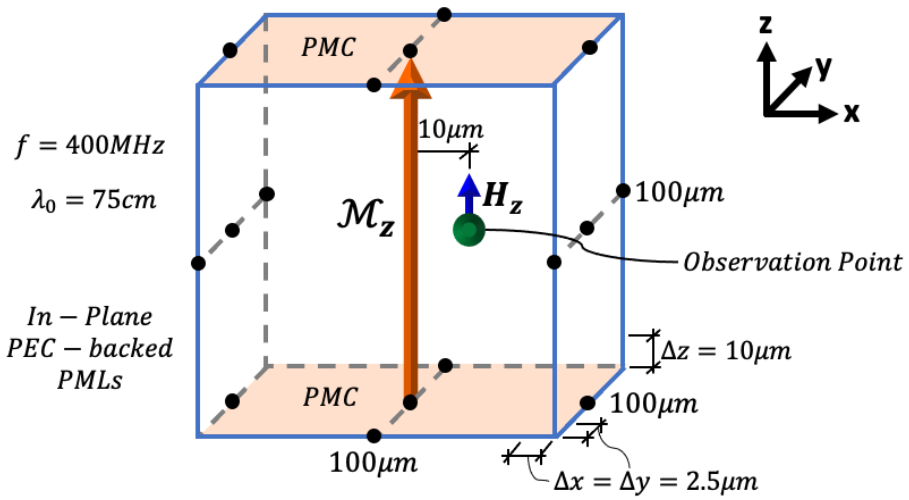


Figure 4-36: 400MHz Infinite magnetic line source within a 100$\boldsymbol{\mu}$m cubic simulation space. $\boldsymbol{H_z}$ is measured 10$\boldsymbol{\mu}$m away from the source.

A 14-cell PEC-backed stretched PML region surrounds the line source in the xy-plane (see Figure 4-10 and Figure 4-12) with a reflection error of $e^{-16}$, maximum stretch of 15,000, and an m-factor of 3. By duality theorem, the steady state time domain solution of the z-directed magnetic field ($H_z$) for a sinusoidal input is as follows:

$$H_z(\rho,t) = Re\{\breve{H}_z e^{j\omega t}\} = -I_0\frac{\omega\epsilon_0}{4}\left[J_0(k\rho)\cos\left(\omega t-\frac{\pi}{2}\right)+Y_0(k\rho)sin\left(\omega t-\frac{\pi}{2}\right)\right] \quad (4.6a)$$

Where $\rho$ is the cylindrical radial coordinate, which originates at the line source, $\omega$ is the circular excitation frequency, $k$ is the wavenumber, $J_0/Y_0$ are Bessel functions of the 1st/2nd kind respectively. This may be multiplied by a Gaussian pulse for comparison with a modulated Gaussian pulse simulation:

$$H_z(\rho,t) = -I_0\frac{\omega\epsilon_0}{4}\left[J_0(k\rho)\cos\left(\omega t-\frac{\pi}{2}\right)+Y_0(k\rho)sin\left(\omega t-\frac{\pi}{2}\right)\right]e^{-\frac{\left(t+\frac{\Delta t}{2}-\frac{3.6}{f}-\frac{\rho}{c}\right)^2}{2\left(\frac{1.2}{f}\right)^2}} \quad (4.6b)$$

Where $f$ is the input frequency and $\Delta t$ is the time sampling. In this section, the observation point is $\lambda_0^{EM}/75{,}000$ away and equation (4.6b) may be used for comparison with modulated

Gaussian pulse excited simulations. The results, comparing the CPML-ADI simulation to the analytical solution for various time steps, are plotted in Figure 4-37:

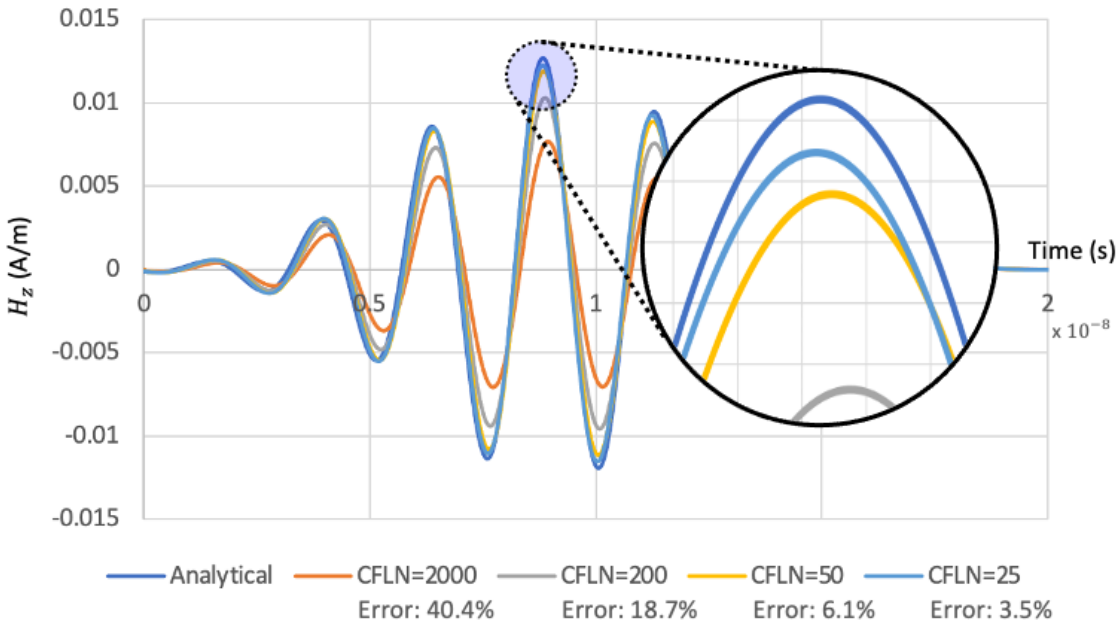


Figure 4-37: Infinite magnetic line source results comparison for 100$\mu$m simulation space with time step reduction.

The amplitude and phase error in the numerical solution is reduced with progressively smaller time steps. The zoomed in image within Figure 4-37 reveals slight error in phase within the CFLN=50 and CFLN=25 simulations but with low amplitude error (6.1% and 3.5% respectively).

#### 4.2.2.5 Conclusions from Line Source Results

To summarize this section 4.2.2, both infinite line source cases shown in Figure 4-5 have been investigated on a simulation space where the smallest spatial discretization is $\lambda_0^{EM}$/3e5. This was done to verify that the CPML method is capable of accurately modeling electrodynamics problems operating on computational volumes originally on the order of $\lambda_0^{EM}$/1e4 in size, as these are the length scales modelers operate on when simulating

mechanical resonance-based antennas. The results demonstrate that errors as low as 1.2% may be achieved when the time step is 50x the stability requirement and the maximal mesh grading is 15e3 (see Figure 4-30) by utilizing the CPML method with stretched PML layers placed $\lambda_0^{EM}$/5e4 away from the source.

### 4.2.3 Near to Far-Field Algorithm Check

The near to far-field transformation is a string of code within the post-processing script that needs verification testing. This is performed by utilizing the analytical solution of the infinitesimal dipole (i.e., no numerical values are utilized). This allows the verification of the NTFF transform to occur separately from the ADI-FDTD algorithm, easing the debugging process. The phasor electric fields for the dipole solution in spherical coordinates, which apply to either the near or far-field, are as follows [25][26]:

$$\breve{E}_r(r,\theta,\emptyset) = \eta_0 \frac{I_0 l cos\theta}{2\pi r^2}\left(1+\frac{1}{j\beta r}\right)e^{-j\beta r} \tag{4.7a}$$

$$\breve{E}_\theta(r,\theta,\emptyset) = j\eta_0 \frac{\beta I_0 l sin\theta}{4\pi r}\left(1+\frac{1}{j\beta r}-\frac{1}{(\beta r)^2}\right)e^{-j\beta r} \tag{4.7b}$$

$$\breve{E}_\emptyset(r,\theta,\emptyset) = 0 \tag{4.7c}$$

Where $\eta_0$ is the free space impedance, $I_0$ is the magnitude of the current, $\beta$ is the wavenumber, and $l$ is the length in which the current acts which should be at least an order of magnitude smaller than the wavelength so that the dipole may be considered infinitesimal. Also, $r$, $\theta$, and $\emptyset$ are the spherical coordinates centered at the dipole point source. In the far-field, the analytical solution is determined by eliminating the $r^{-2}$ and $r^{-3}$ terms from the general solution:

$$\breve{E}_r = 0 \tag{4.8a}$$

$$\breve{E}_\theta = j\eta_0 \frac{\beta I_0 l sin\theta}{4\pi r} e^{-j\beta r} \tag{4.8b}$$

These far-field values produce the following radiation intensity and radiated power:

$$U(\theta,\emptyset) \cong \frac{r^2}{2\eta_0}\left[\left|\breve{E}_\theta(r,\theta,\emptyset)\right|^2 + \left|\breve{E}_\emptyset(r,\theta,\emptyset)\right|^2\right] = \frac{r^2}{2\eta_0}\left[Re\{\breve{E}_\theta\}^2 + Im\{\breve{E}_\theta\}^2\right]$$

$$= \frac{r^2}{2\eta_0}\left[\left(\eta_0\frac{\beta I_0 l sin\theta sin\beta r}{4\pi r}\right)^2 + \left(\eta_0\frac{\beta I_0 l sin\theta cos\beta r}{4\pi r}\right)^2\right] \quad (4.9)$$

$$= \frac{\eta_0}{2}\left(\frac{\beta I_0 l sin\theta}{4\pi}\right)^2$$

$$P_{rad} = \int_0^{2\pi}\int_0^{\pi} U sin\theta d\theta d\emptyset = 2\pi\frac{\eta_0}{2}\left(\frac{\beta I_0 l}{4\pi}\right)^2\int_0^{\pi}\sin^3\theta\, d\theta = \frac{\eta_0(\beta I_0 l)^2}{12\pi} \quad (4.10)$$

Note that the radiation intensity is independent of $\emptyset$ and has $\sin^2\theta$ dependency, which is the famous “donut” omnidirectional pattern characteristic of dipoles. The NTFF algorithm radiation intensity and radiated power results are compared to equations (4.9) and (4.10).

The NTFF algorithm accepts near field time-domain data (non-phasor) in rectangular coordinates, and then transforms into far-field phasor data in spherical coordinates. Therefore, it is necessary to convert into rectangular coordinates and to determine the instantaneous values. To convert equations (4.7) to steady state time domain expressions multiply by $e^{j\omega t}$ and take the real component of the product:

$$E(r,\theta,\emptyset,t) = Re\{\breve{E}(r,\theta,\emptyset)e^{j\omega t}\}$$

$$E_r(r,\theta,\emptyset,t) = Re\left\{\eta_0\frac{I_0 l cos\theta}{2\pi r^2}\left(1-\frac{j}{\beta r}\right)e^{j(\omega t-\beta r)}\right\}$$

$$E_r(r,\theta,\emptyset,t) = \eta_0\frac{I_0 l cos\theta}{2\pi r^2}\left(cos(\omega t-\beta r) + \frac{1}{\beta r}sin(\omega t-\beta r)\right) \quad (4.11a)$$

$$E_\theta(r,\theta,\emptyset,t) = Re\left\{\eta_0\frac{\beta I_0 l sin\theta}{4\pi r}\left(\frac{1}{\beta r} + j\left(1-\frac{1}{(\beta r)^2}\right)\right)e^{j(\omega t-\beta r)}\right\}$$

$$E_\theta(r,\theta,\emptyset,t) = \eta_0\frac{\beta I_0 l sin\theta}{4\pi r}\left(\frac{1}{\beta r}cos(\omega t-\beta r) + \left(\frac{1}{(\beta r)^2}-1\right)sin(\omega t-\beta r)\right) \quad (4.11b)$$

Which may be re-written in rectangular coordinates via the following transformation:

$$\begin{pmatrix} E_x \\ E_y \\ E_z \end{pmatrix} = \begin{bmatrix} sin\theta cos\emptyset & cos\theta cos\emptyset & -sin\emptyset \\ sin\theta sin\emptyset & cos\theta sin\emptyset & cos\emptyset \\ cos\theta & -sin\theta & 0 \end{bmatrix} \begin{pmatrix} E_r \\ E_\theta \\ 0 \end{pmatrix}$$

$$E_x = \eta_0 \frac{I_0 l}{2\pi} \left\{ \frac{sin\theta cos\emptyset cos\theta}{r^2} \left( cos(\omega t - \beta r) + \frac{1}{\beta r} sin(\omega t - \beta r) \right) + \beta \frac{cos\theta cos\emptyset sin\theta}{2r} \left( \frac{1}{\beta r} cos(\omega t - \beta r) + \left( \frac{1}{(\beta r)^2} - 1 \right) sin(\omega t - \beta r) \right) \right\} \quad (4.12a)$$

$$E_y = \eta_0 \frac{I_0 l}{2\pi} \left\{ \frac{sin\theta sin\emptyset cos\theta}{r^2} \left( cos(\omega t - \beta r) + \frac{1}{\beta r} sin(\omega t - \beta r) \right) + \beta \frac{cos\theta sin\emptyset sin\theta}{2r} \left( \frac{1}{\beta r} cos(\omega t - \beta r) + \left( \frac{1}{(\beta r)^2} - 1 \right) sin(\omega t - \beta r) \right) \right\} \quad (4.12b)$$

$$E_z = \eta_0 \frac{I_0 l}{2\pi} \left\{ \frac{\cos^2\theta}{r^2} \left( cos(\omega t - \beta r) + \frac{1}{\beta r} sin(\omega t - \beta r) \right) - \beta \frac{\sin^2\theta}{2r} \left( \frac{1}{\beta r} cos(\omega t - \beta r) + \left( \frac{1}{(\beta r)^2} - 1 \right) sin(\omega t - \beta r) \right) \right\} \quad (4.12c)$$

Where the spherical coordinates may be written in terms of rectangular coordinates as follows:

$$r = \sqrt{x^2 + y^2 + z^2}, \qquad \theta = acos\left(\frac{z}{r}\right), \qquad \emptyset = \begin{matrix} acos\left(\frac{x}{\sqrt{x^2 + y^2}}\right), & y \geq 0 \\ -acos\left(\frac{x}{\sqrt{x^2 + y^2}}\right), & y < 0 \end{matrix} \quad (4.12d)$$

Equations (4.12) describe the electric field from an infinitesimal dipole in the near or far-field. Similarly, the magnetic fields induced by an electric infinitesimal dipole are as follows:

$$\breve{H}_r(r, \theta, \emptyset) = \breve{H}_\theta(r, \theta, \emptyset) = 0 \quad (4.13a/b)$$

$$\breve{H}_\emptyset(r, \theta, \emptyset) = j \frac{\beta I_0 l sin\theta}{4\pi r} \left(1 + \frac{1}{j\beta r}\right) e^{-j\beta r} \quad (4.13c)$$

The time domain equivalent is:

$$H(r, \theta, \emptyset, t) = Re\left\{\breve{H}(r, \theta, \emptyset) e^{j\omega t}\right\}$$

$$H_{\emptyset}(r,\theta,\emptyset,t) = Re\left\{j\frac{\beta I_0 l sin\theta}{4\pi r}\left(1+\frac{1}{j\beta r}\right)e^{j(\omega t-\beta r)}\right\}$$

$$H_{\emptyset}(r,\theta,\emptyset,t) = \frac{\beta I_0 l sin\theta}{4\pi r}\left[\frac{1}{\beta r}cos(\omega t-\beta r) - sin(\omega t-\beta r)\right] \quad (4.14)$$

Which may be re-written in rectangular coordinates:

$$\begin{pmatrix} H_x \\ H_y \\ H_z \end{pmatrix} = \begin{bmatrix} sin\theta cos\emptyset & cos\theta cos\emptyset & -sin\emptyset \\ sin\theta sin\emptyset & cos\theta sin\emptyset & cos\emptyset \\ cos\theta & -sin\theta & 0 \end{bmatrix}\begin{pmatrix} 0 \\ 0 \\ H_{\emptyset} \end{pmatrix}$$

$$H_x = -\frac{\beta I_0 l sin\emptyset sin\theta}{4\pi r}\left[\frac{1}{\beta r}cos(\omega t-\beta r) - sin(\omega t-\beta r)\right] \quad (4.15a)$$

$$H_y = \frac{\beta I_0 l cos\emptyset sin\theta}{4\pi r}\left[\frac{1}{\beta r}cos(\omega t-\beta r) - sin(\omega t-\beta r)\right] \quad (4.15b)$$

$$H_z = 0 \quad (4.15c)$$

The time dependent EM fields (4.12 and 4.15) are then converted to phasors via a Fast Fourier Transform (FFT) which is embedded in the NTFF transformation algorithm. Of course, the FFT could have been bypassed by utilizing the original phasor analytical solutions (4.7 and 4.13), but this is a luxury that is not afforded to the time domain data that comes from the ADI-FDTD simulation. Therefore, validation of the NTFF code requires that the FFT be performed on rectilinear data.

Three dipole cases are run for this validation effort. In the first, the dipole is applied at the center of the simulation space. In the second, the dipole is bisected by an xy-planar PEC, requiring imaged EM fields to be used to perform the NTFF transform. In the third case, the dipole is placed in a corner with the adjacent boundaries tangential to the dipole being set to PMCs and the adjacent boundary normal to the dipole set to a PEC. These cases are shown in Figure 4-38:

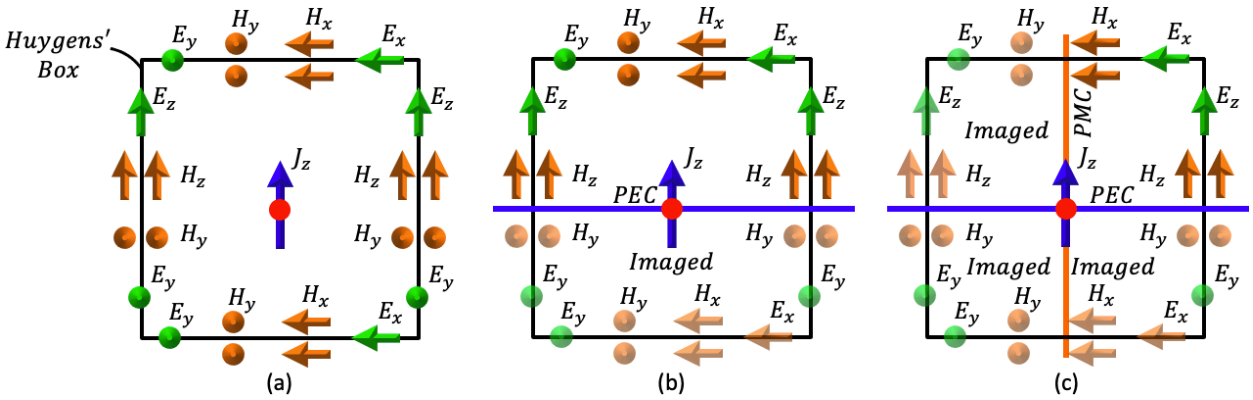


Figure 4-38: NTFF validation cases, (a) dipole applied at the center, (b) dipole bisected via orthogonal PEC such that half the fields used for the transformation are imaged, (c) Dipole cut into eight components using orthogonal PEC and two tangential PMCs such that 7/8ths of the fields used for the transformation are imaged. Case (c) is referred to as the “corner dipole”.

Due to field staggering within the divergence free Yee grid, the actual location of the excitation can vary by half a cell with respect to what is shown in Figure 4-38.

#### 4.2.3.1 Centered Dipole

First, a 400MHz 1mA harmonic source is input along length $l = \Delta x = \Delta y = \Delta z = \Delta = 1.25\mu m = \lambda_0^{EM}/600{,}000$ at the center of the simulation space. The electrically tiny discretization is roughly equal to the spatial sampling required of a mechanical wave at the same frequency ($\approx \lambda^{Mech}/20$). Since the EM fields are taken from the analytical solution (no simulation performed) the time step is immaterial as long as enough samples are taken per period to acquire clean frequency data (20 samples per period herein). A Huygen box with sides of length $2a$ is placed around the dipole and various values for $a$ are investigated as shown in Figure 4-39:

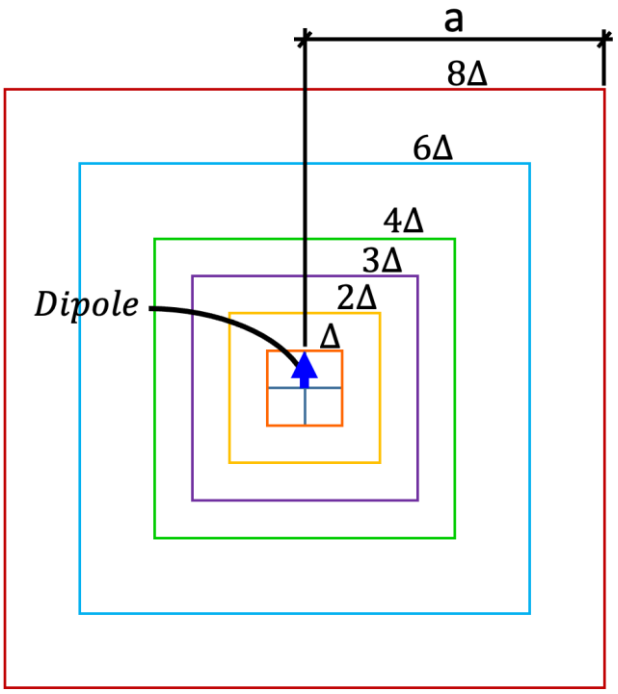


Figure 4-39: Huygen boxes around a dipole at the center of the simulation space.

The radiation intensity calculated via NTFF transformation using EM fields at each Huygen box were compared to the analytical solution (4.9) at the excitation frequency as shown in Figure 4-40. The radiation pattern is omnidirectional about the xy-plane (no $\Phi$ dependence), therefore only one planar cut is reported herein.

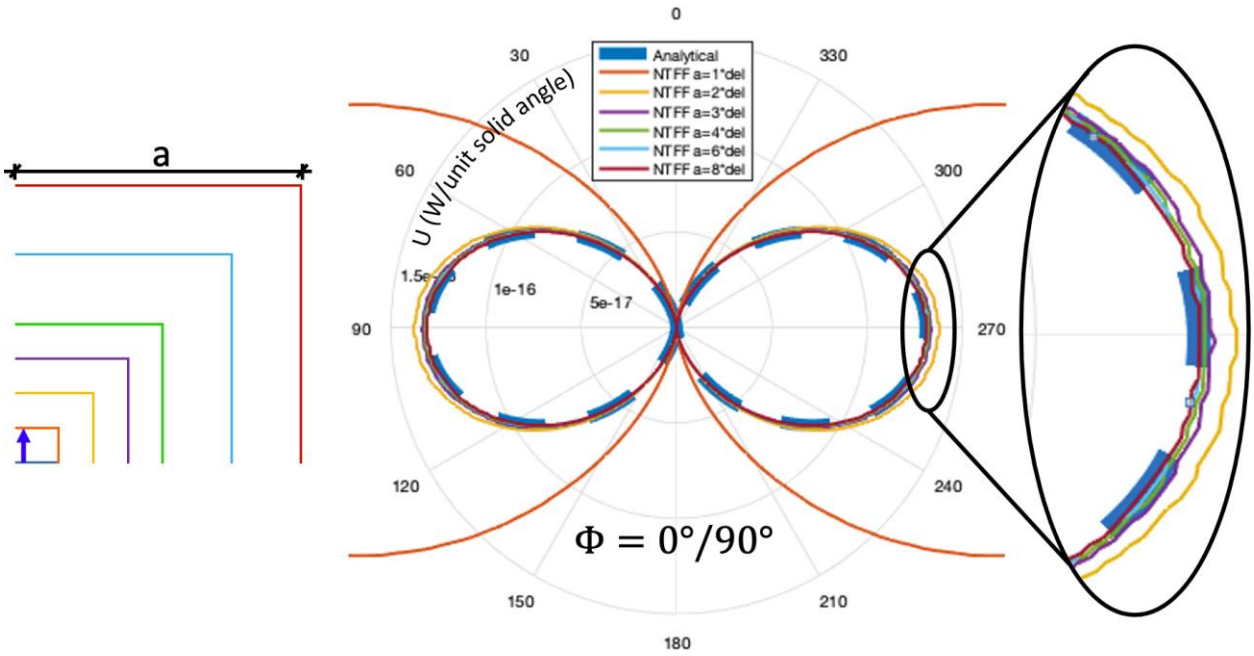


Figure 4-40: Radiation Intensity comparison to the analytical solution for multiple Huygens's boxes with the dipole at the center of the simulation space.

The closest Huygen's box is the only one that exhibits an undue error which is seemingly caused by the fact that the dipole excitation contacts only this Huygen's box. This will be further hinted at in the bisected and corner dipole cases where the Huygen's boxes used never touch the radiator and undue error (>10%) is not seen. Examining Figure 4-40 NTFF results from all the other Huygen's boxes yield acceptable results. Observing the zoomed in image in Figure 4-40, the $a$ = 3Δ, 4Δ, 6Δ, and 8Δ cases are all virtually identical (<5% variance) and in excellent agreement with the analytical solution (<5% error). Therefore, when performing the NTFF transform, the modeler need only verify that two different Huygen's boxes produce virtually identical results to verify convergence and accuracy. The radiated power at the excitation frequency from the NTFF transform is 1.098e-15 Watts, which corresponds to a 0.16% error with respect to the analytical solution.

#### 4.2.3.2 Dipole Bisected by Orthogonal PEC

Utilizing again the 400MHz 1mA harmonic source input along length $l = \Delta x = \Delta y = \Delta z = \Delta = 1.25\mu m = \lambda_0^{EM}/600{,}000$ from the previous section, the excitation is now applied at the bottom of the simulation space ($z = \Delta z/2 \approx 0$) and bisected by an orthogonal PEC as shown in Figure 4-45. As mentioned in the figure, the bisecting PEC may be a symmetry boundary condition, or it may represent a physical ground plane. Regardless, the NTFF algorithm maps the fields within the simulation space to imaged fields below the PEC when performing the transformation. The results need not be modified if the PEC represents a symmetry boundary condition. In the case of a physical ground plane, the radiation intensity of the bottom hemisphere must be zeroed out, and the radiated power will be half.

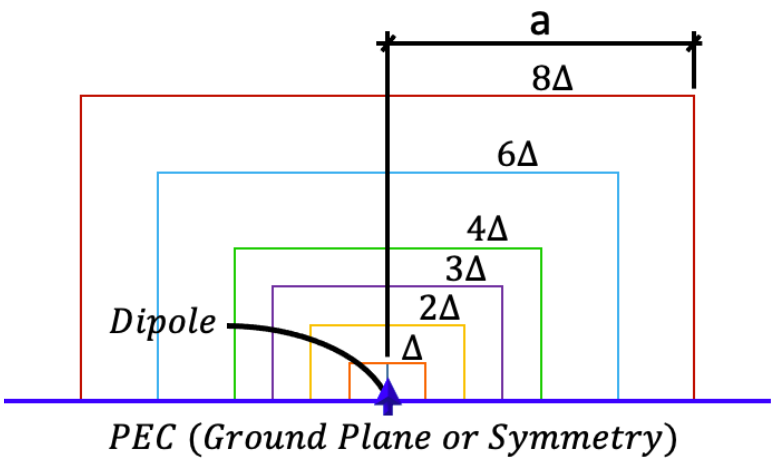


Figure 4-41: Huygen boxes around a dipole bisected by an orthogonal PEC.

The radiation intensity, calculated via NTFF transformation using EM fields and imaged EM fields at each Huygen box, was compared to the analytical solution (4.9) at the excitation frequency as shown in Figure 4-42. The radiation pattern is omnidirectional about the xy-plane (no $\Phi$ dependence), therefore only one planar cut is reported herein.

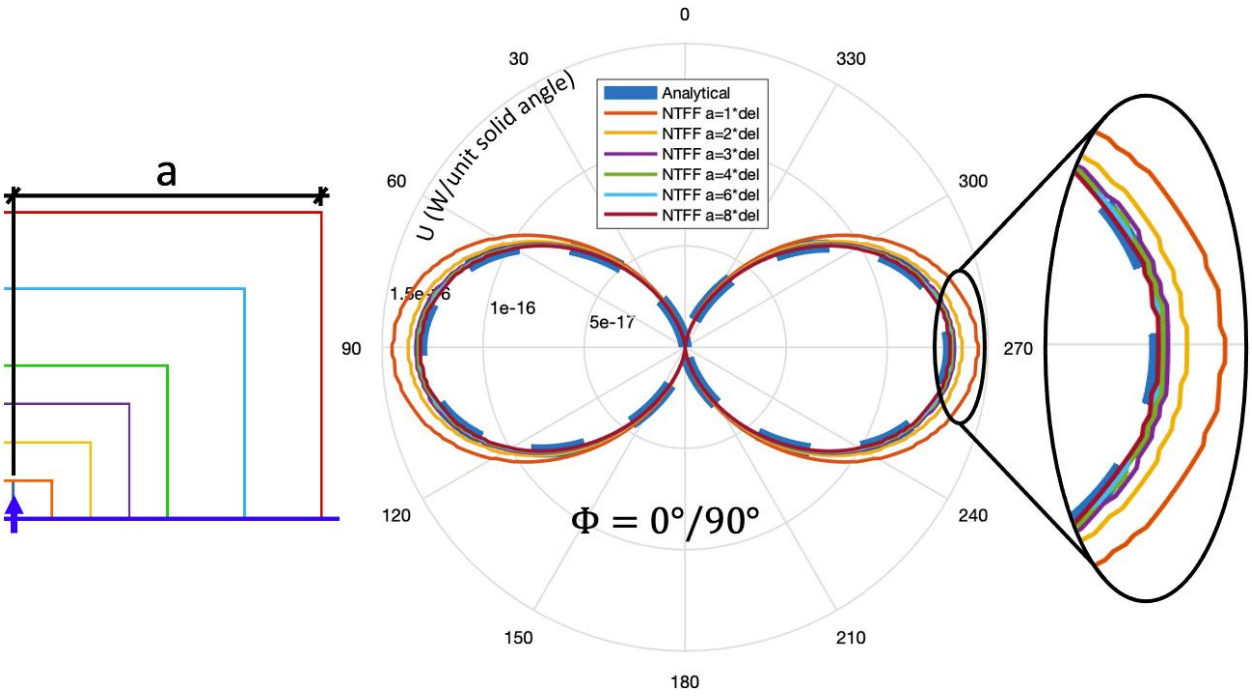


Figure 4-42: Radiation Intensity comparison to the analytical solution for multiple Huygen's boxes with the dipole bisected by an orthogonal PEC.

In this case, none of the Huygen's boxes contact the excitation and therefore all cases have error within tighter margins (<30%). Observing the zoomed in image in Figure 4-46, the $a$ = 3Δ, 4Δ, 6Δ, and 8Δ cases are all virtually identical (<5% variance) and in excellent agreement with the analytical solution (<5% error). Therefore, when performing the NTFF transform, the modeler need only verify that two different Huygen's boxes produce virtually identical results to verify convergence and accuracy. The radiated power at the excitation frequency from the NTFF transform is 1.098e-15 Watts, which corresponds to a 0.15% error with respect to the analytical solution.

#### 4.2.3.3 Corner Dipole

Utilizing again the 400MHz 1mA harmonic source input along length $l = \Delta x = \Delta y = \Delta z = \Delta =$ $1.25\mu m = \lambda_0^{EM}/600{,}000$ from the previous section, the excitation is now applied at the corner of the simulation space ($x = \Delta x/2 \approx 0$, $y = \Delta y/2 \approx 0$, and $z = 0$) as shown in Figure 4-43:

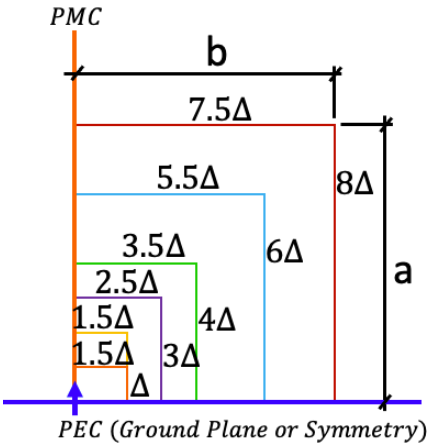


Figure 4-43: Huygen boxes around a dipole at the corner of the simulation space.

The radiation intensity calculated via NTFF transformation using EM fields and imaged EM fields at each Huygen box were compared to the analytical solution (4.9) at the excitation frequency as shown in Figure 4-44. The radiation pattern is omnidirectional about the xy-plane (no $\Phi$ dependence), therefore only one cut is reported herein.

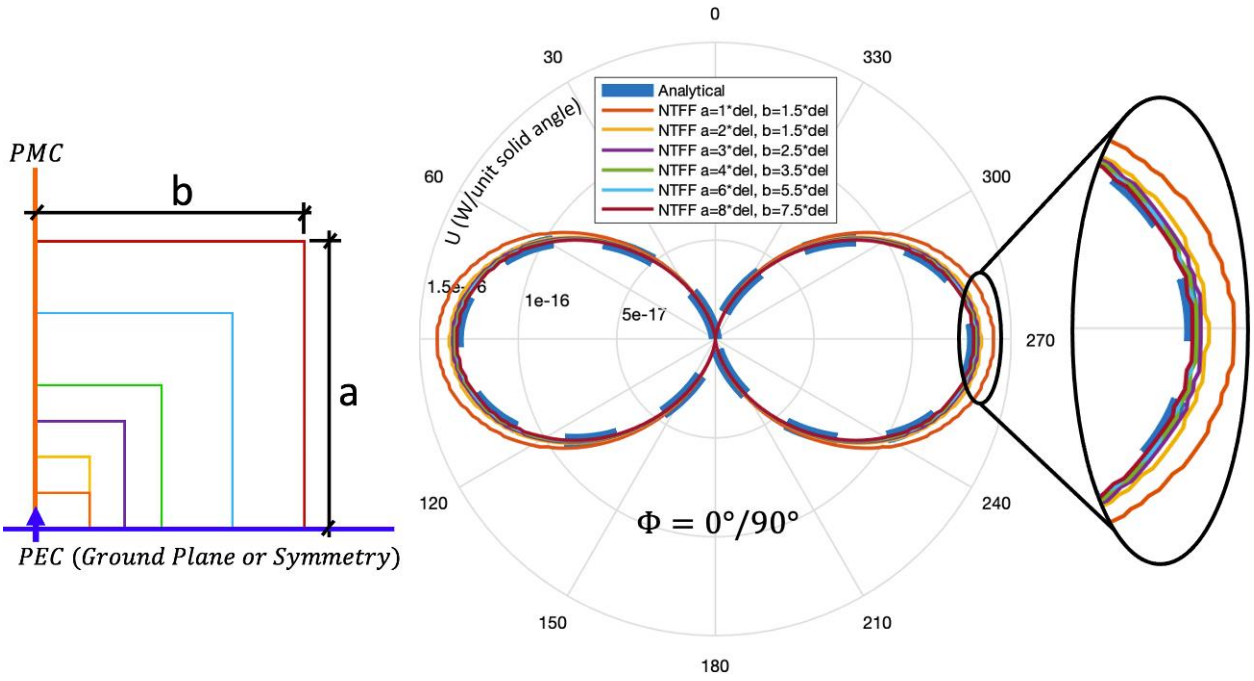


Figure 4-44: Corner Dipole Radiation Intensity comparison to the analytical solution for multiple Huygen's boxes.

In this case, none of the Huygen's boxes contact the excitation and therefore all cases have error within tighter margins (<15%). Observing the zoomed in image in Figure 4-44, the results from all but the smallest box are virtually identical (<5% variance) and in excellent agreement with the analytical solution (<5% error). Therefore, when performing the NTFF transform, the modeler need only verify that two different Huygen's boxes produce virtually identical results to verify convergence and accuracy. The radiated power at the excitation frequency from the NTFF transform is 1.097e-15 Watts, which corresponds to a 0.05% error with respect to the analytical solution.

### 4.2.4 Infinitesimal Dipoles

A pivotal electrodynamic problem is the infinitesimal dipole case which herein is simulated to verify agreement with the ADI-FDTD code.

#### 4.2.4.1 Far-Field Electric Dipole

Consider a simulation space that is cubic, with edge lengths equal to 3x the free space EM wavelength as shown in Figure 4-45. The z-directed electric field will be compared to the analytical dipole solution at the observation point which is located a distance $a$ from the dipole in both the x and y directions:

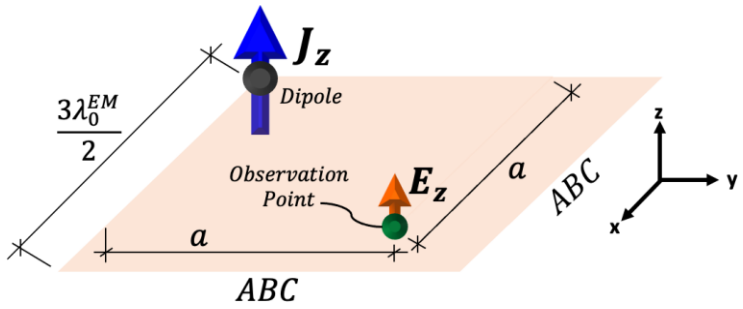


Figure 4-45: Geometry for infinitesimal dipole problem. A single quadrant of an xy-planar cut that bisects the simulation space is shown. The dipole and the observation point both lie on this plane. 1st order MUR1 absorbing boundary conditions are used on all six boundary planes.

The general analytical solution for the infinitesimal dipole, which applies both in the near and far-field, was written in the NTFF validation section and is repeated here in rectangular coordinates:

$$E_x = \eta_0 \frac{I_0 l}{2\pi}\left\{\frac{sin\theta cos\emptyset cos\theta}{r^2}\left(cos(\omega t-\beta r)+\frac{1}{\beta r}sin(\omega t-\beta r)\right)\right. \\ \left. +\beta\frac{cos\theta cos\emptyset sin\theta}{2r}\left(\frac{1}{\beta r}cos(\omega t-\beta r)+\left(\frac{1}{(\beta r)^2}-1\right)sin(\omega t-\beta r)\right)\right\} \tag{4.12a}$$

$$E_y = \eta_0 \frac{I_0 l}{2\pi}\left\{\frac{sin\theta sin\emptyset cos\theta}{r^2}\left(cos(\omega t-\beta r)+\frac{1}{\beta r}sin(\omega t-\beta r)\right)\right. \\ \left. +\beta\frac{cos\theta sin\emptyset sin\theta}{2r}\left(\frac{1}{\beta r}cos(\omega t-\beta r)+\left(\frac{1}{(\beta r)^2}-1\right)sin(\omega t-\beta r)\right)\right\} \tag{4.12b}$$

$$E_z = \eta_0 \frac{I_0 l}{2\pi}\left\{\frac{\cos^2\theta}{r^2}\left(cos(\omega t-\beta r)+\frac{1}{\beta r}sin(\omega t-\beta r)\right)\right.$$
$$\left. -\beta\frac{\sin^2\theta}{2r}\left(\frac{1}{\beta r}cos(\omega t-\beta r)+\left(\frac{1}{(\beta r)^2}-1\right)sin(\omega t-\beta r)\right)\right\} \quad (4.12c)$$

$$r=\sqrt{x^2+y^2+z^2}, \qquad \theta = acos\left(\frac{z}{r}\right), \qquad \emptyset = \begin{cases} acos\left(\frac{x}{\sqrt{x^2+y^2}}\right), & y \geq 0 \\ -acos\left(\frac{x}{\sqrt{x^2+y^2}}\right), & y<0 \end{cases} \quad (4.12d)$$

These equations describe the electric field from an infinitesimal dipole in the near or far-field. Similarly, the magnetic fields induced by an electric infinitesimal dipole are as follows:

$$H_x = -\frac{\beta I_0 l sin\emptyset sin\theta}{4\pi r}\left[\frac{1}{\beta r}cos(\omega t-\beta r)-sin(\omega t-\beta r)\right] \quad (4.15a)$$

$$H_y = \frac{\beta I_0 l cos\emptyset sin\theta}{4\pi r}\left[\frac{1}{\beta r}cos(\omega t-\beta r)-sin(\omega t-\beta r)\right] \quad (4.15b)$$

$$H_z = 0 \quad (4.15c)$$

A comparison between the analytical and numerical solutions at $a=\lambda/4$ (see Figure 4-45) is presented in Figure 4-46. The input frequency is 400MHz and the magnitude of the input current is 1mA.

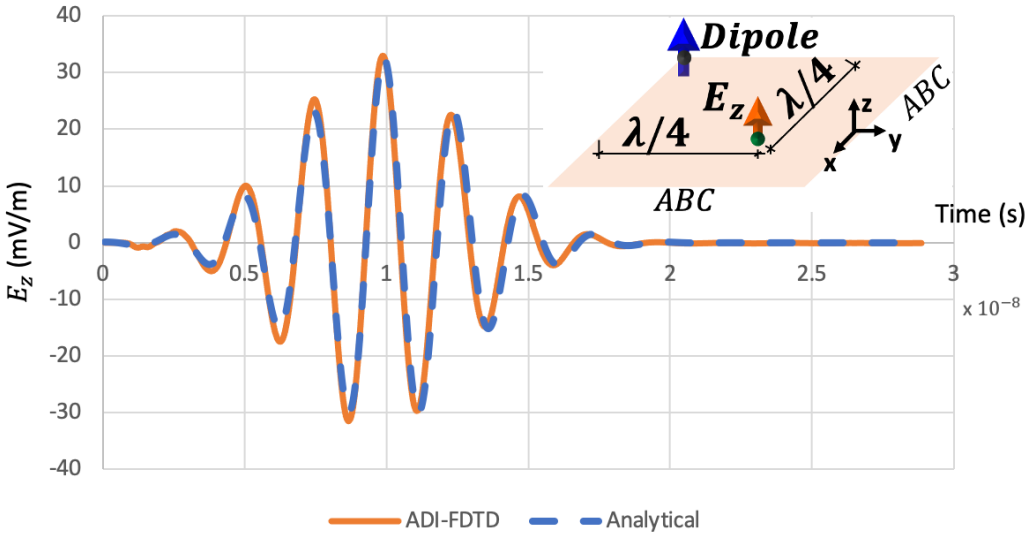


Figure 4-46: Infinitesimal dipole results comparison for $\boldsymbol{E_z}$ at $\boldsymbol{x = y = a = \lambda/4}$.

Figure 4-46 shows good agreement between the ADI-FDTD numerical solution and the analytical solution. As the observation point is moved closer to the MUR1 boundary conditions ($a = 3\lambda/4$) a degradation of results manifests as spurious ripples after the pulse dies out as shown in Figure 4-56:

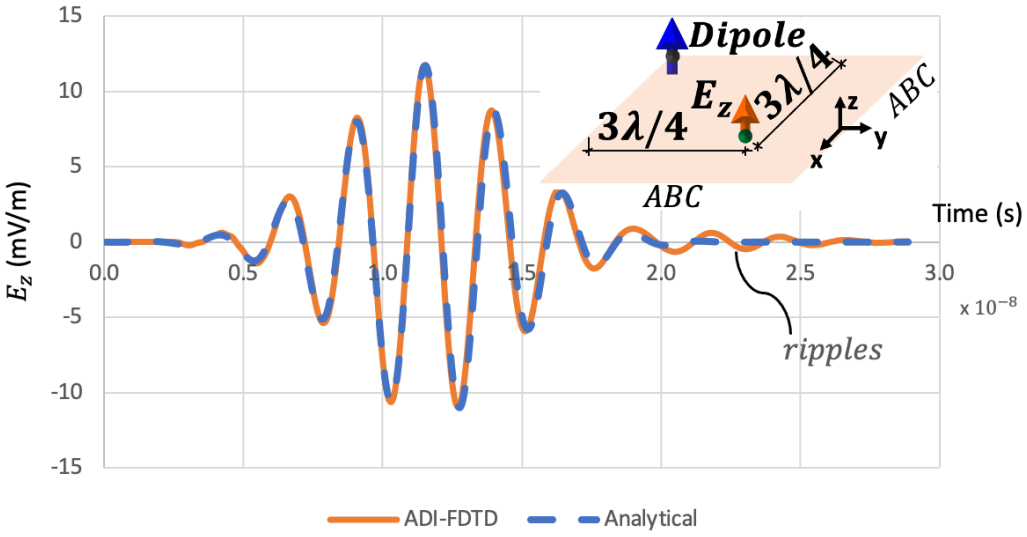


Figure 4-47: Infinitesimal dipole results comparison for $\boldsymbol{E_z}$ at $\boldsymbol{x = y = a = 3\lambda/4}$ (halfway between the radiator and the MUR1 ABCs). Spurious ripples after the modulated Gaussian pulse dies out are observed due to the close proximity of the MUR1 ABCs.

To eliminate the ripples, 14-cell wide perfectly matched layer regions may be added directly adjacent to the boundaries which are switched from MUR1 ABCs to PECs. In this model the reflection error is set to $e^{-64}$ within the lossy PML layers and the loss is increased in cubic fashion (m=3) yielding the results of Figure 4-48:

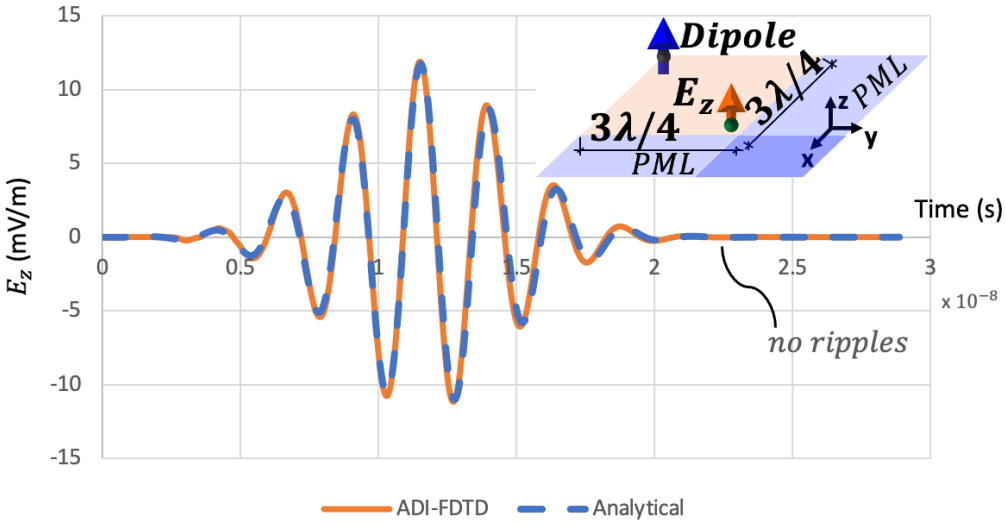


Figure 4-48: Infinitesimal dipole results comparison for $\boldsymbol{E_z}$ at $\boldsymbol{x = y = a = 3\lambda/4}$. This is halfway between the radiator and the PECs and directly adjacent to the onset of the PML layers. Spurious ripples after the modulated Gaussian pulse, seen previously in Figure 4-56, are no longer present.

Figure 4-48 reveals that spurious numerical artifacts may be eliminated by using PEC-backed PML layers. All EM fields within these PML layers are non-physical however, so PML layers should not be used when physical near-fields are to be investigated at distances an order of magnitude of the dimensions of the radiator away or more (i.e., when validation with experimental near-field data is performed). In these cases, ABC backed stretched regions are preferable.

#### 4.2.4.2 Far-Field Mechatronic Dipole

If the point current source ($J_z$) of the previous section 4.2.4.1 is substituted by a point stress source ($T_{zz}$), identical electric fields will be created if the following relation holds:

$$|J_z| = \left|d_{33}^{PE}\dot{T}_{zz}\right| \tag{4.5}$$

Where $d_{33}^{PE}$ is the piezoelectric coefficient coupling normal stresses in the z-direction to the parallel electric fields (assuming the material is poled in the z-direction). This is demonstrated in

Figure 4-49, where the stress input is compared to both the source current input case and the analytical solution with excellent agreement observed.

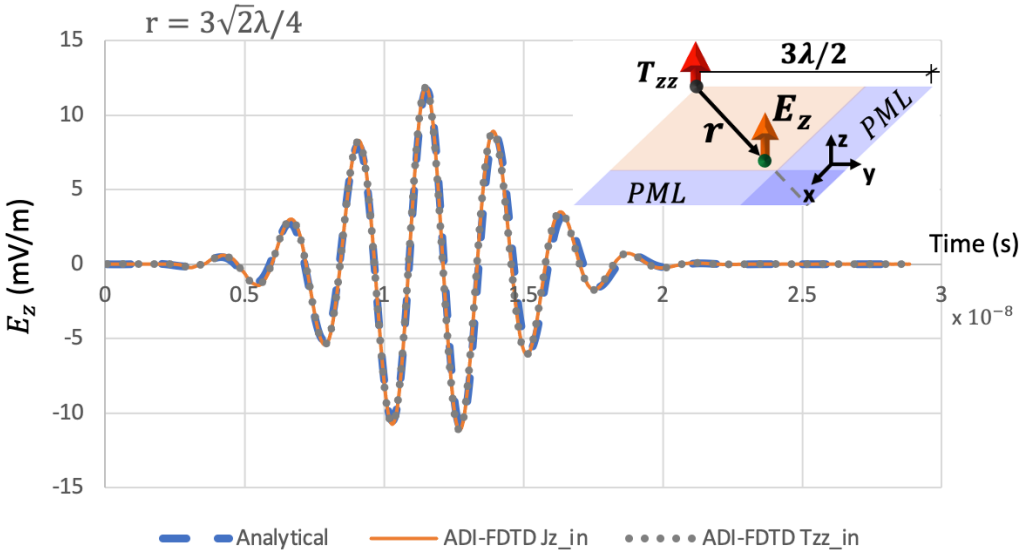


Figure 4-49: Mechatronic Dipole $\boldsymbol{E_z}$ time history comparison for $\boldsymbol{r = 3\sqrt{2}\lambda/2}$. The analytical, source current, and stress input cases all have the same 1mA effective current.

A logarithmic plot of the electric field magnitude versus distance $r$ is below in Figure 4-50:

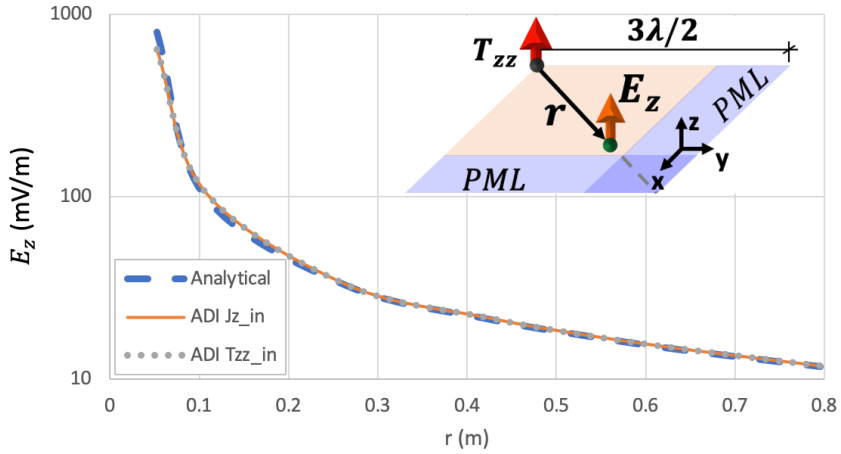


Figure 4-50: Mechatronic Dipole $\boldsymbol{E_z^{max}}$ vs. $\boldsymbol{r}$ comparison. The analytical, source current, and stress input cases all have the same 1mA effective current.

Errors begin to increase closer to the radiator due to geometric issues as the length $\Delta z$ over which the electric current acts becomes roughly equal to the distance $r$ of the measurement.

#### 4.2.4.3 Far-Field Magnetic and Mechnetic Dipole

If the point current source ($J_z$) of the previous section 4.2.4.1 is substituted by a point magnetic current source ($\mathcal{M}_z$) then a magnetic dipole is achieved. The magnetic current will be present in Faraday's law by definition and the ADI forcing vector by substitution. The analytical solution is acquired via duality theorem.

$$H_z = \frac{I_m l}{\eta_0 2\pi}\left\{\frac{\cos^2\theta}{r^2}\left(cos(\omega t-\beta r)+\frac{1}{\beta r}sin(\omega t-\beta r)\right)\right.$$
$$\left. -\beta\frac{\sin^2\theta}{2r}\left(\frac{1}{\beta r}cos(\omega t-\beta r)+\left(\frac{1}{(\beta r)^2}-1\right)sin(\omega t-\beta r)\right)\right\} \quad (4.16)$$

Where $I_m$ is the magnitude of the fictional magnetic current ($I_m = \mathcal{M}_z \Delta x \Delta y$), $\eta_0$ is the free space impedance, and $\beta$ is the wavenumber. Note that the magnitude of $H_z$ will equal $E_z$ from the 1mA electric dipole case of section 4.2.4.1 if:

$$I_m = \eta_0^2 I_0 = \frac{\mu_0}{\epsilon_0}(1mA) = 142\ V \tag{4.17}$$

Additionally, a point stress source ($T_{zz}$), will create identical magnetic fields if the following relation holds:

$$|\mathcal{M}_z| = \left|d_{33}^{PM}\dot{T}_{zz}\right| \tag{4.18}$$

Where $d_{33}^{PM}$ is the piezomagnetic coefficient coupling normal stresses in the z-direction to the parallel magnetic fields (assuming the material is poled in the z-direction). The stress rate may be input into the code through the magnetic constitutive relation:

$$H_z^{n+\frac{1}{2}} = H_z^n + \frac{1}{\mu_0}\left(B_z^{n+\frac{1}{2}} - B_z^n\right) - \frac{\Delta t d_{33}^{PM}}{2\mu_0}\dot{T}_{zz}^{n+\frac{1}{2}} \tag{4.19a}$$

$$H_z^{n+1} = H_z^{n+\frac{1}{2}} + \frac{1}{\mu_0}\left(B_z^{n+1} - B_z^{n+\frac{1}{2}}\right) - \frac{\Delta t d_{33}^{PM}}{2\mu_0}\dot{T}_{zz}^{n+\frac{1}{2}} \tag{4.19b}$$

Since the stress is assumed to be uniform, the stress gradient terms appearing in the ADI forcing vector will be zero. Thus, the mechnetic dipole excites magnetic fields through a piezomagnetic current term that appears in the constitutive relation rather than a magnetic current term in Faraday's law. Fantastic agreement is demonstrated in Figure 4-51, where the stress input is compared to both the magnetic source current input case and the analytical solution at observation distance $r = 3\sqrt{2}\lambda/4$.

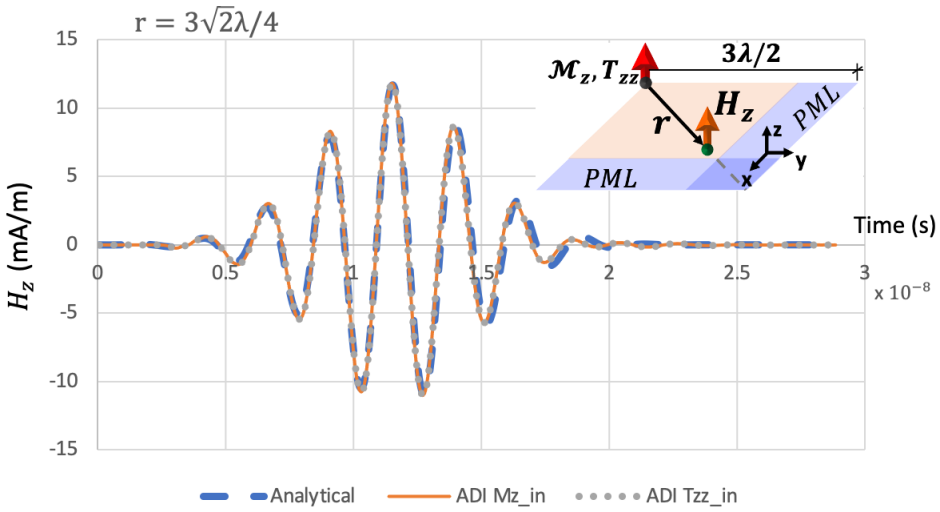


Figure 4-51: Mechnetic Dipole $\boldsymbol{H_z}$ time history comparison for $\boldsymbol{r = 3\sqrt{2}\lambda/2}$. The analytical, magnetic source, and stress input cases all have the same 142V effective voltage.

A logarithmic plot of the magnetic field magnitude versus distance $r$ is below in Figure 4-52:

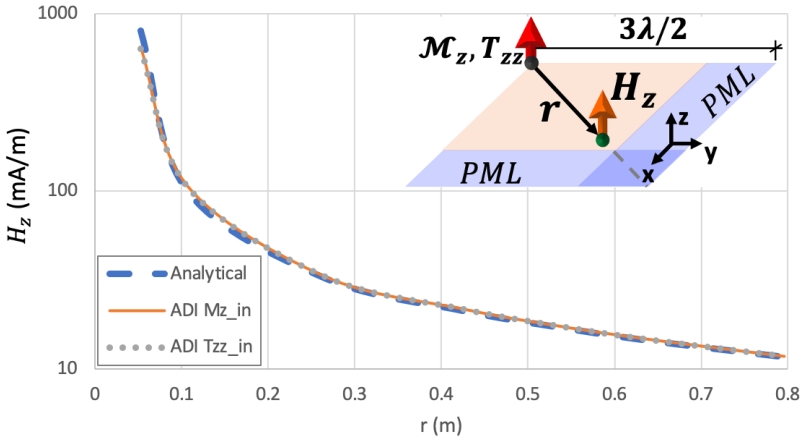


Figure 4-52: Mechnetic Dipole $\boldsymbol{H_z^{max}}$ vs. $\boldsymbol{r}$ comparison. The analytical, magnetic source, and stress input cases all have the same 142V effective voltage.

#### 4.2.4.4 Corner Dipole Case

Mechanical antennas are electrically small enough that many behave as infinitesimal dipoles, especially those with dipole-like geometries (e.g., the SLAC piezoelectric antenna

[152]). As such, symmetry conditions may be leveraged to analyze the performance of such antennas with a computational load reduced by a factor of 8 as shown in Figure 4-53 for a z-directed excitation. The dipole (point source) is applied at the corner of the simulation space with the two adjacent tangential boundaries set to PMCs generating 3 parallel virtual sources as shown in Figure 4-53(b). The adjacent normal boundary is set to a PEC, generating another 4 virtual currents. These 8 sources (1 real, 7 virtual) allow for the dipole to be modelled using an eighth of the computational space.

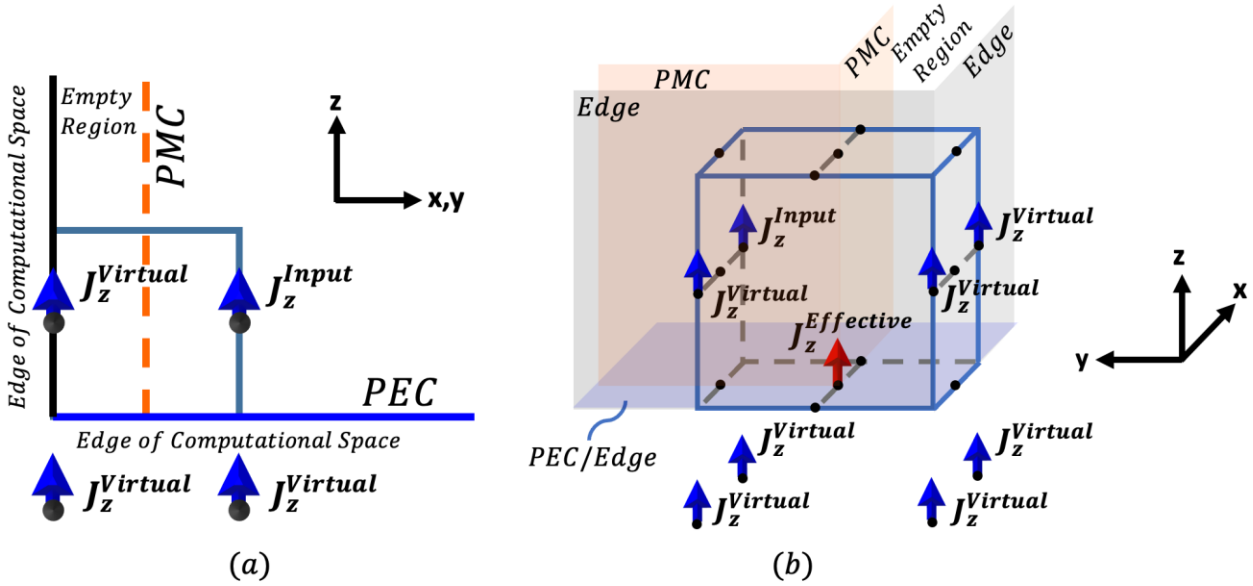


Figure 4-53: Corner dipole case where only the corner cell is represented. Since PMC boundaries truncate half a cell inward, an “empty region” will be present where all fields are not updated. This region does not affect the simulation results. (a) 2D representation showing the current input into the simulation ($J_z^{Input}$) and virtual currents ($J_z^{Virtual}$), (b) 3D representation showing the spatial location of the effective excitation ($J_z^{Effective}$).

The dipole will now effectively act half a cell staggered in the xy-plane and aligned with the cell interface in the z-direction (i.e., collocated with the $H_z$ field) as shown in Figure 4-53(b).

Since this effective point excitation is the amalgamation of the other 8 sources, the input must be set to an eighth of the intended value (e.g., if a 1mA is to be studied, then input 1/8mA at the corner). The corner dipole continues to act over the length $\Delta z$ and the area $\Delta x \Delta y$.

#### 4.2.4.4.1 Far-Field Corner Dipole Case

A comparison between the analytical solution and the corner dipole simulation is made for $x = y = a = 14.5\lambda/20$ in Figure 4-54 where good agreement is demonstrated. The excitation is 1mA and 400MHz with the discretization set to $\Delta = \lambda/20$ and PML layers added as in the previous case (see 4.2.4.1) except now only a 30x30x30 cell simulation space is necessary (due to symmetry conditions of Figure 4-53).

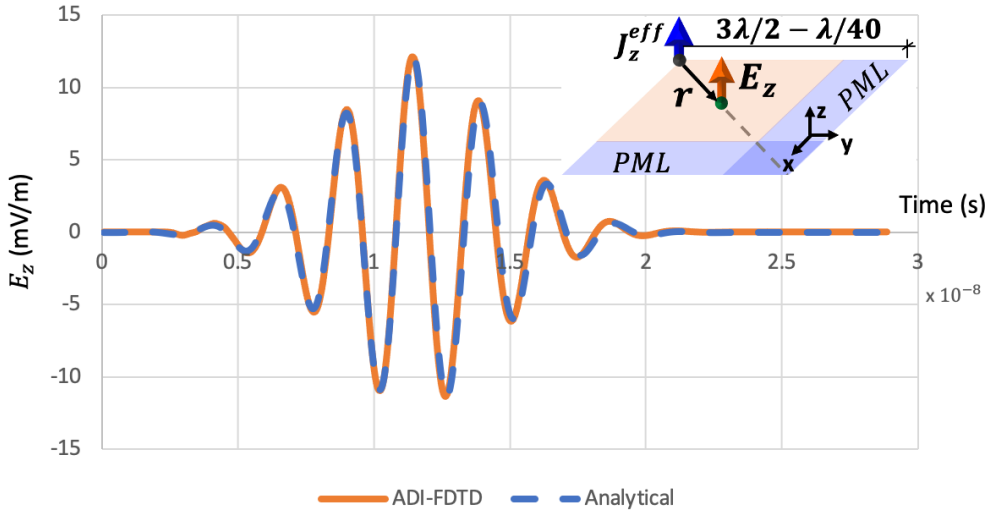


Figure 4-54: Corner infinitesimal dipole case results comparison at $\boldsymbol{x = y = a = 14.5\lambda/20}$ with $\boldsymbol{r = \sqrt{x^2 + y^2}}$.

A comparison of the electric field magnitude versus distance $r$ is below in Figure 4-55:

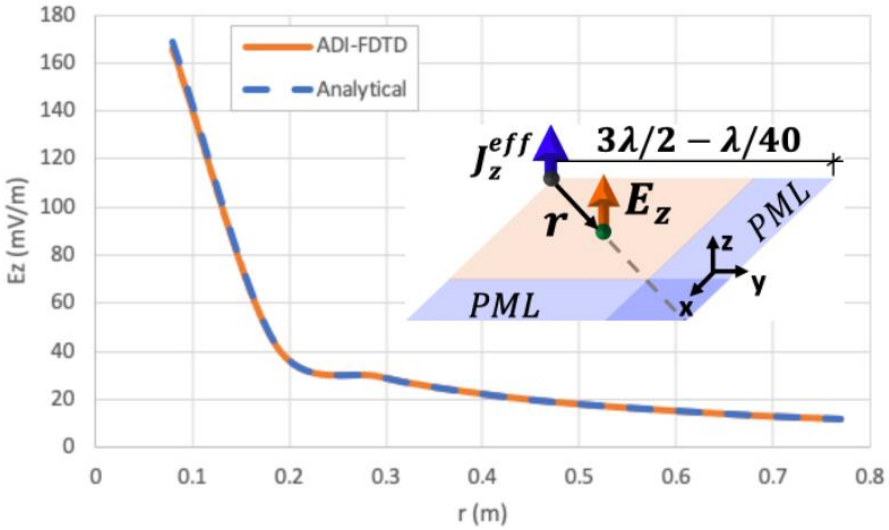


Figure 4-55: Corner dipole case comparison of $E_z$ vs. $r$ between the analytical solution and the ADI-FDTD simulation.

Errors begin to increase closer to the radiator due to geometric issues as the length $\Delta z$ over which the electric current acts becomes roughly equal to the distance $r$ of the measurement. Regardless, both near-field and far-field points are observed to agree with the analytical solution.

#### 4.2.4.4.2 Progressive Shrink Study for Corner Dipole

The corner dipole case will now be validated on progressively shrinking simulation spaces such that the finest discretization is on the order of 1/20 of the mechanical wavelength at the excitation frequency. The source is a 400MHz 1mA infinitesimal dipole. Consider the geometry of Figure 4-56 where the symmetry boundaries are as presented in section 4.2.4.4. the other three boundaries are MUR1 ABCs. Adjacent to these ABCs are 16-cell stretched regions with $\kappa^{max} = 30$ and $m = 3$, such that most of the computational space is stretched.

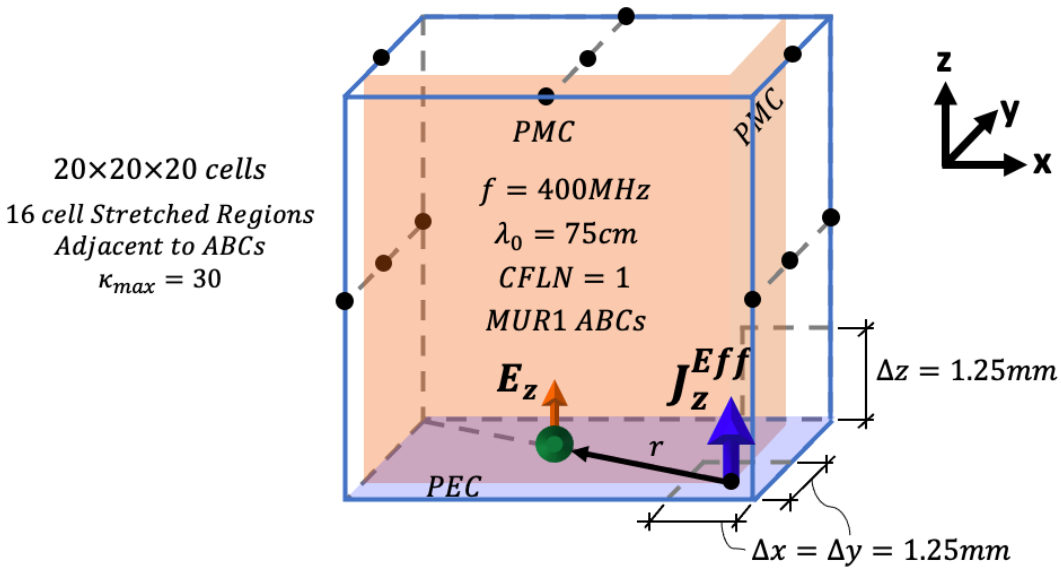


Figure 4-56: 400MHz 1mA corner dipole case within a $\mathbf{20} \times \mathbf{20} \times \mathbf{20}$ cell cubic simulation space. $\boldsymbol{E_z}$ is measured at a distance $\boldsymbol{r}$ away from the effective source.

The goal is to measure EM fields at distances several times larger than the finest discretization ($\Delta_{min}$) which in multiferroic antenna simulations will be related to the mechanical wavelength as $\Delta_{min} \leq \lambda_{mech}/20$. This is crucial when comparisons are to be made with experimental data which is often taken at distances orders of magnitude larger than the physical dimensions of the mechanical antenna (see [152]). As such, most of the observation points are within the stretched region and therefore MUR1 ABCs were used instead PEC-backed PMLs. Inclusion of non-physical PML losses within this stretched region would thus produce erroneous results at such observation points. The modeler may choose instead to retain both the boundary adjacent PMLs and the ability to make comparisons with experimental results by including a purely stretched region interior to the outer PML region and this methodology will be discussed later in this section.

The numerical results with CFLN=1 for $E_z$ vs. $r$ are compared to the analytical solution in Figure 4-57, where $r$ values both inside and outside of the stretched regions are utilized.

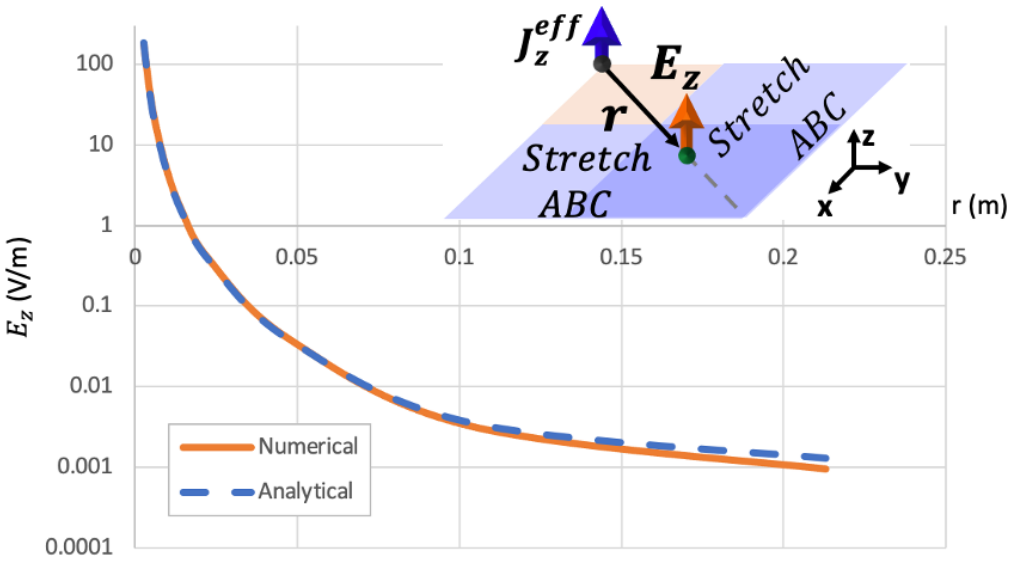


Figure 4-57: Comparison between analytical and numerical solution of $\boldsymbol{E_z}$ vs. $\boldsymbol{r}$ from infinitesimal corner dipole case shown in Figure 4-56 with CFLN=1. Points both inside and outside of the stretched regions were used in the comparison. Onset of error at large $\boldsymbol{r}$ values is caused by reflections off the MUR1 ABCs.

For observation points 8 cells or more away from the ABCs, the amplitude error is negligible (<6%) with errors rising to as high as 27.5% directly adjacent to the boundary. The loss of fidelity at higher $r$ values is caused by the MUR1 absorbing boundaries. To illuminate this, Figure 4-58 shows the time history plots of four observation points where an onset of worsening amplitude and phase degradation is observed at the ABC adjacent node (Figure 4-58(d)). Regardless, due to the cell stretching, this error is confined to the outer periphery of the simulation space and an interior kernel of good agreement is maintained as shown in Figure 4-58(a)-(c) where the observation points are within $\lambda/50$ away from the radiator (i.e., all within the near-field).

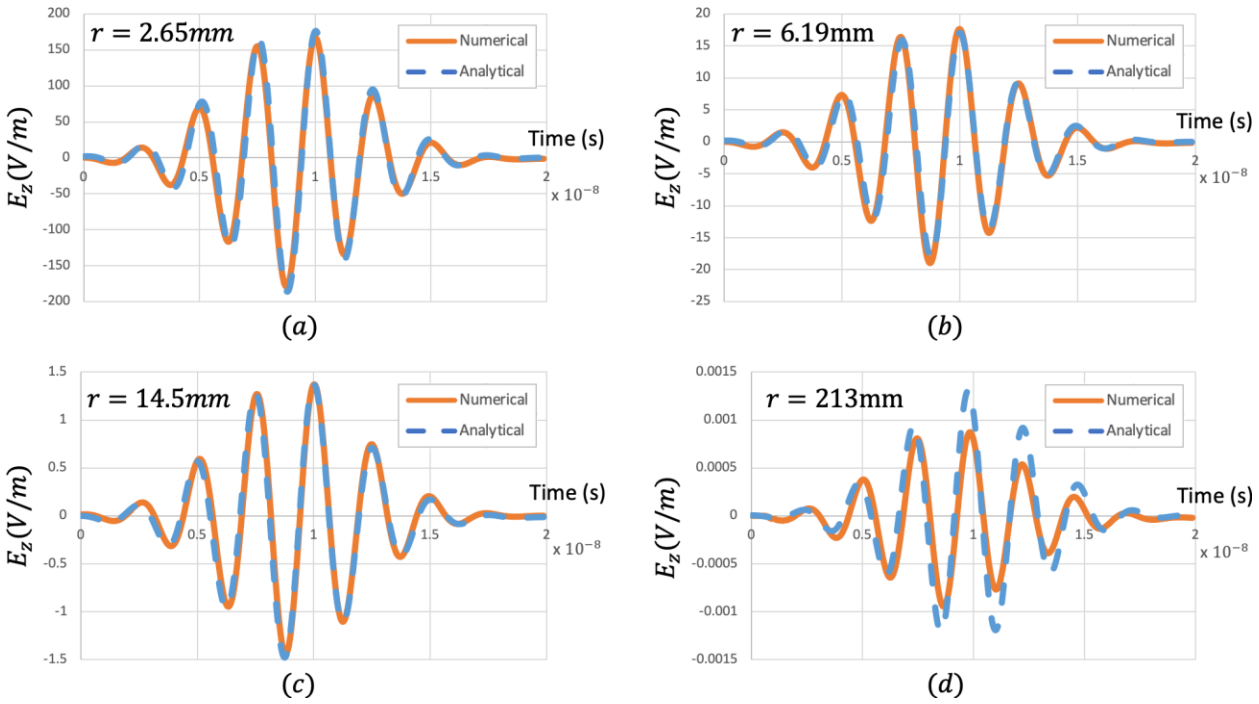


Figure 4-58: Time histories of $\boldsymbol{E_z}$ for various points along $\boldsymbol{r}$. (a) $\boldsymbol{r = 2.65mm}$, (b) $\boldsymbol{r = 6.19mm}$, (c) $\boldsymbol{r = 14.5mm}$, (d) $\boldsymbol{r = 213mm}$. Good agreement is seen save for the point directly adjacent to the MUR1 ABC (i.e., at $\boldsymbol{r = 213mm}$).

The smallest discretization is now reduced by an order of magnitude to $\Delta_{min} = 125\mu m$, while maintaining $\Delta_x^{max} = \Delta_y^{max} = \Delta_z^{max} = \lambda_{EM}/20$ as the largest discretization by increasing the maximum stretch by an order of magnitude ($\kappa^{max} = 300$) as shown in Figure 4-59. The size of the stretched regions is maintained at 16-cells with $m = 3$, the CFLN factor is maintained at 1 such that the $\Delta t$ is reduced by an order of magnitude, and the input current is maintained at 1mA.

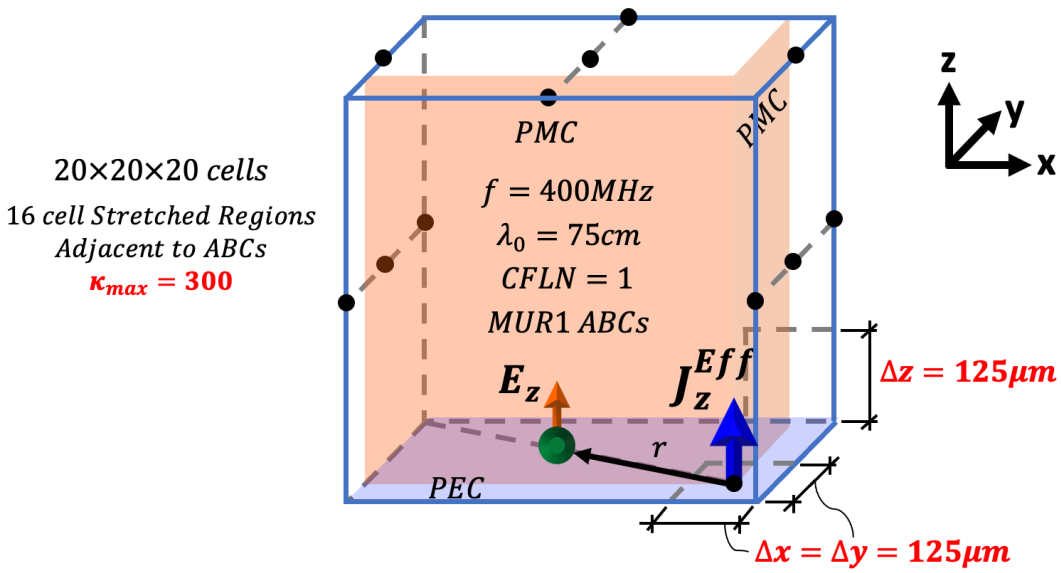


Figure 4-59: 400MHz 1mA corner dipole case within a $\mathbf{20} \times \mathbf{20} \times \mathbf{20}$ cell cubic simulation space. $\boldsymbol{E_z}$ is measured at a distance $\boldsymbol{r}$ away from the effective source.

The numerical results for $E_z$ vs. $r$ are compared to the analytical solution in Figure 4-60, where $r$ values both inside and outside of the stretched regions are utilized.

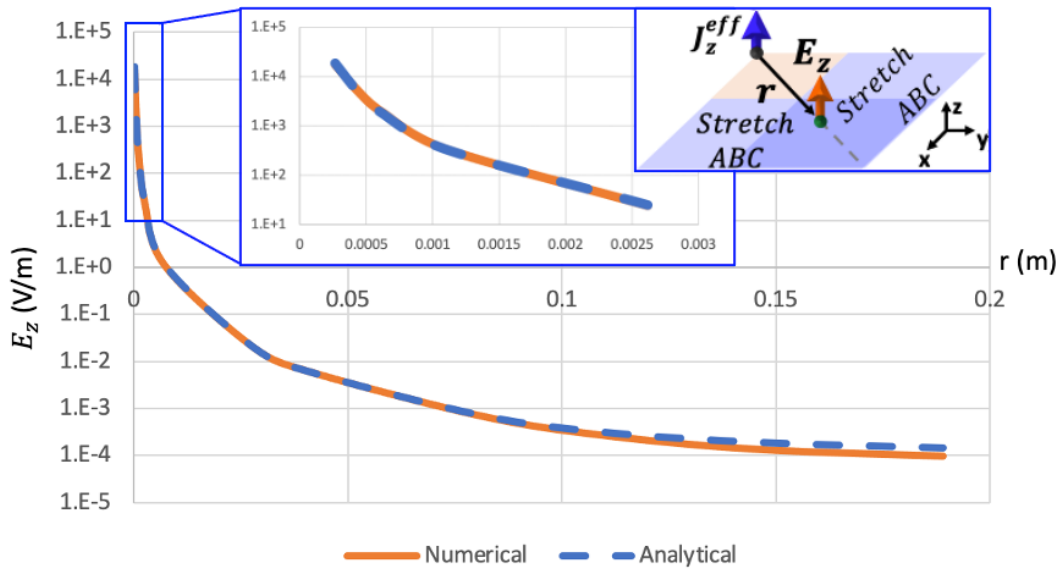


Figure 4-60: Comparison between analytical and numerical solution of $\boldsymbol{E_z}$ vs. $\boldsymbol{r}$ from infinitesimal corner dipole case shown in Figure 4-59 with CFLN=1. Points both inside and outside of the stretched regions were used in the comparison. Onset of error at large $\boldsymbol{r}$ values is caused by reflections off the MUR1 ABCs. Due to large degree of stretching ($\boldsymbol{\kappa^{max} = 300}$) a zoomed in image is included to better highlight to fields at nodes directly adjacent to the radiator.

For observation points 4 cells or more away from the ABCs the amplitude error is negligible (<6%) with errors rising to as high as 33.9% directly adjacent to the boundary. Thus, the low fidelity region, due to ABC spurious reflection, occupies fewer cells in this case (where $\Delta_{min} = 125\mu m$) than that of the previous case (where $\Delta_{min} = 1.25mm$).

There are multiple methods of achieving accurate results. Another approach is to include PML layers directly adjacent to PEC boundaries, with a purely stretched region intermediate between the PMLs and the interior unstretched lossless region as shown in the Figure 4-61 inset. A simulation was performed utilizing 10 PML layers with reflection error set to $R(0)=e^{-16}$ and m=3. A 6-cell wide pre-stretching region internal to the PML layers is utilized where the

cells are stretched to $\kappa = 100$. The degree of stretching is not reduced back to 1 prior the onset of the PML region. Within the PML layers the cells are stretched from $\kappa = 100$ to $\kappa = 300$ at m=3.

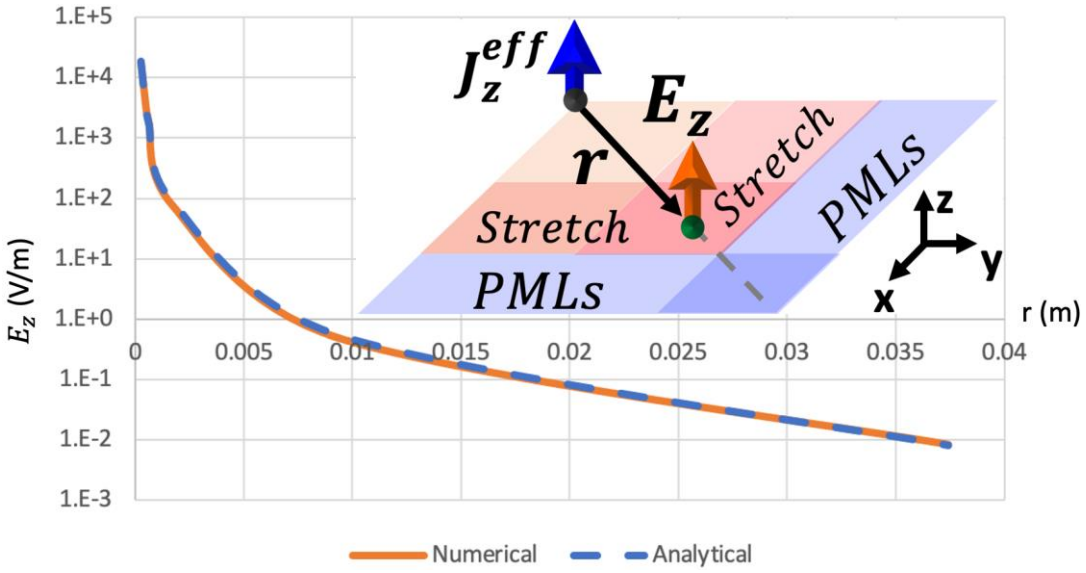


Figure 4-61: Comparison between analytical and numerical solution of $\boldsymbol{E_z}$ vs. $\boldsymbol{r}$ from infinitesimal corner dipole case shown in Figure 4-59 but with a pre-stretched region (highlighted red in the figure). Points both inside and outside of the stretched regions were used in the comparison and CFLN=1.

Note that in Figure 4-61, accurate results are seen up to $r = 0.0375m$. Greater distances are not plotted since these locations are within the PML region and are therefore non-physical. Since in Figure 4-60 accuracy is also seen at $r = 0.0375m$, either approach is acceptable.

### 4.3 Micromagnetic Testing

This section focuses on a validation case for the magnetic damping via convolutional integral approach presented in Chapter 2. Due to a shift in focus on piezoelectric rather than piezomagnetic antenna elements, magnetic damping is not included in the device simulations

and comparisons Chapter 5. This section is only included for completeness. First, the analytical solution for the convolution integral is derived. Then the ADI-FDTD code is compared to commercial software.

### 4.3.1 Analytical Solution of the Convolution Integral

From Section  the convolution integral for the x-directed magnetic field is as follows:

$$H_x(t) = \int_{0^-}^{t} \left[\beta_{xx}^{\mu} + \left(\frac{1}{\mu_0} - \beta_{xx}^{\mu}\right) e^{-\mathrm{a}(t-\tau)}\right] \frac{\partial B_x}{\partial \tau} d\tau + \int_{0^-}^{t} \beta_{xy}^{\mu} \left(1 - e^{-\mathrm{a}(t-\tau)}\right) \frac{\partial B_y}{\partial \tau} d\tau \tag{2.171a}$$

Focusing on an x-directed harmonic excitation of the form $B_x(\tau) = |B|\sin(\omega\tau)$ yields the following:

$$H_x(t) = |B|\omega \int_{0^-}^{t} \left[\beta_{xx}^{T} + \left(\frac{1}{\mu_0} - \beta_{xx}^{T}\right) e^{-\mathrm{a}(t-\tau)}\right] \cos(\omega\tau) d\tau \tag{4.20}$$

Split the integral into two parts as follows:

$$\begin{aligned} H_x(t) &= |B|\beta_{xx}^{T}\omega \int_{0^-}^{t} \cos(\omega\tau)\, d\tau + |B| \left(\frac{1}{\mu_0} - \beta_{xx}^{T}\right) \omega \int_{0^-}^{t} e^{-\mathrm{a}(t-\tau)} \cos(\omega\tau)\, d\tau \\ &= |B|\beta_{xx}^{T}\omega I_1 + |B| \left(\frac{1}{\mu_0} - \beta_{xx}^{T}\right) \omega I_2 \end{aligned} \tag{4.21}$$

The first integral is determined as follows:

$$|B|\beta_{xx}^{T}\omega I_1 = |B|\beta_{xx}^{T}\omega \int_{0^-}^{t} \cos(\omega\tau)\, d\tau = |B|\beta_{xx}^{T}[\sin(\omega\tau)]\Big|_0^t = |B|\beta_{xx}^{T}\sin(\omega t) \tag{4.22}$$

Now focus on the second integral:

$$I_2 = \int_{0^-}^{t} e^{-\mathrm{a}(t-\tau)} \cos(\omega\tau)\, d\tau = \frac{1}{a} cos(\omega\tau) e^{-\mathrm{a}(t-\tau)}\Big|_0^t + \frac{\omega}{a} \int_{0^-}^{t} \sin(\omega\tau) e^{-\mathrm{a}(t-\tau)} d\tau \tag{4.23a}$$

$$I_2 = \frac{1}{a}\left\{cos(\omega t) - e^{-at} + \omega\left[\frac{1}{a} sin(\omega\tau) e^{-\mathrm{a}(t-\tau)}\Big|_0^t - \frac{\omega}{a} \int_{0^-}^{t} e^{-\mathrm{a}(t-\tau)} \cos(\omega\tau)\, d\tau\right]\right\} \tag{4.23b}$$

$$I_2 = \frac{1}{a}\left\{cos(\omega t) - e^{-at} + \frac{\omega}{a}[sin(\omega t) - \omega I_2]\right\} \tag{4.23c}$$

Solving (4.23c) for $I_2$ yields:

$$I_2 = \frac{1}{a\left(1+\left(\frac{\omega}{a}\right)^2\right)}\left\{cos(\omega t) - e^{-at} + \frac{\omega}{a}sin(\omega t)\right\} \tag{4.23d}$$

Therefore, the magnetic field response is as follows:

$$H_x(t) = |B|\beta_{xx}^T \sin(\omega t) + |B|\left(\frac{1}{\mu_0} - \beta_{xx}^T\right)\frac{\omega\tau}{(1+(\omega\tau)^2)}\left\{cos(\omega t) - e^{-\frac{t}{\tau}} + \omega\tau sin(\omega t)\right\} \tag{4.24}$$

Where the Greek letter Tau is now being used to represent the relaxation time rather than the integration dummy variable. Equation (4.24) could be used for validation of the FDTD code, but focus shifted towards comparison with commercial software instead.

#### 4.3.1.1 FDTD Simulation and Comparison

A simulation was performed in which a thin-film strip of y-biased magnetic material, with dimensions 6.224$\mu$m×1mm×492nm, was excited in the x-direction by a 400MHz harmonic magnetic field of amplitude 4.85 kA/m. The saturation magnetization of the material ($M_s$) was set to 4.85e5 A/m and the Gilbert damping constant ($\alpha$) was set to 0.045. For comparison purposes the same magnetic problem is modeled in a commercially available LLG code (MuMax3 [242]). The resulting $M_x$ vs. $H_x$ hysteresis loop for both the FDTD and LLG code are shown in Figure 4-62. The inset of Figure 4-62 provides a zoomed in image near the point $M_x = H_x = 0$ to better compare and contrast the two codes. As one can see there is good agreement between the two codes. Also, if one calculates the energy lost per cycle between the LLG simulation and the FDTD code they are 2.7656 J/$m^3$ and 1.4634 J/$m^3$ respectively. While this is a very reasonable error for damping, this error can be further reduced by modifying the Gilbert damping factor with an effective Gilbert damping term as determined from the LLG simulation, i.e. effective damping for that geometry and material. Using this modified phenomenological approach (FDTD Adjusted curve) almost exact agreement is obtained to the extent that the two lines are indistinguishable.

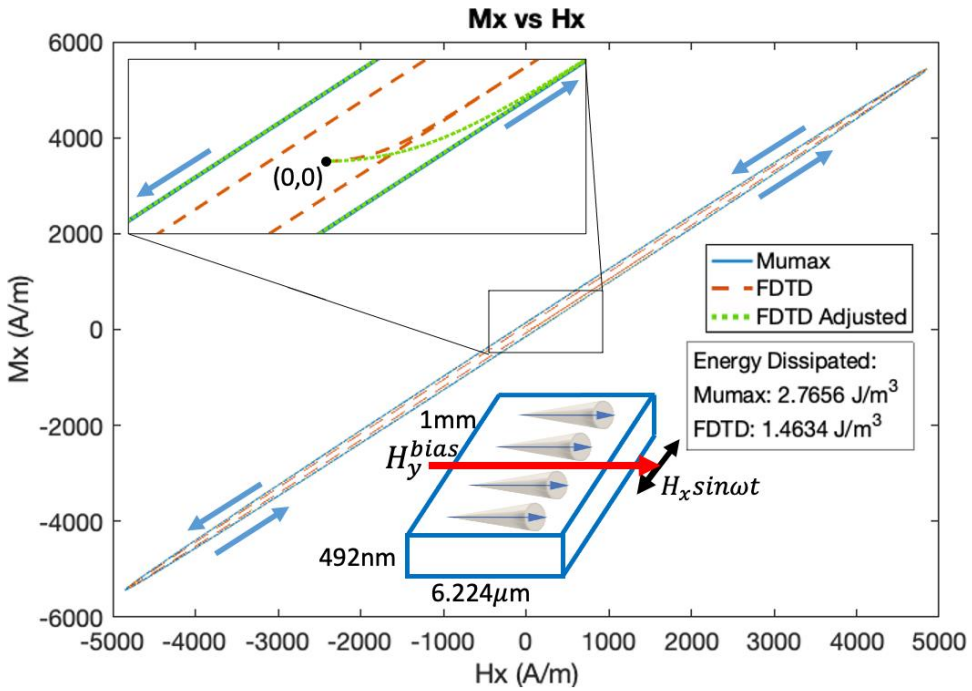


**Figure 4-62: Mx vs. Hx for small x-directed excitation of y-biased thin film magnetic strip.**

# CHAPTER 5: DEVICE SIMULATIONS

In this chapter, simulations on devices are presented. The code of Chapter 3, which was tested in Chapter 4, is compared to experimental data in Section 5.1 for a homogenous free space and electrodynamics only. Subsequently, in Section 5.2, piezoelectric material is introduced to compare to one last analytical solution for the fields within the piezoelectric. The input is a stress that is known a priori, as such the simulation is not yet fully coupled (elastodynamics is not utilized). Then the excitation methodology of Section 3.12 is tested in Section 5.3. At this point it will be clear that the fields both inside and outside the piezoelectric are accurate, and that the excitation methodology is valid. Therefore, fully coupled simulations are ready to be performed with high confidence. In Section 5.4, fully coupled simulations on an infinite planar array of piezoelectric antennas are performed at variable array spacing to characterize the mutual depolarization effect and provide design guidance for future array platforms. Finally, in Section 5.5, a multimode alternate poling piezoelectric antenna capable of expanding the operational bandwidth is discussed.

## 5.1 SLAC Experimental Comparison (Electrodynamics and Homogenous Free Space)

Kemp et al [152] built and tested a very low frequency (VLF) piezoelectric antenna at 35.5kHz, referred to herein as the SLAC antenna due to its development at the SLAC National Accelerator Laboratory. Figure 5-1 shows the SLAC antenna has an axial length of 9.4cm and a 1.6cm diameter with experimental $E_z$ measurements performed in the near field as a function of radial distance $r$ from the antenna with z=0. The measured intrinsic dipole moment rate ($\dot{p}$) was reported to be 7.5mA-m and this value was used as input into the ADI-FDTD solver (i.e. point source current $J_z^S = \dot{p}/\Delta x \Delta y \Delta z$ directly into Ampere's law) to assess the accuracy of the proposed computational model. In this initial model verification, elastodynamics was excluded and the primary focus was on validating the Maxwell portion of the code. In the computational model, we used corner symmetry boundary conditions (PMCs in-plane and a PEC ground as in

Figure 5-1) to reduce the size of the modeled space. Additionally, as shown in Figure 5-1 there are Mur1 ABCs with adjacent stretched regions that are 16-cells wide to reduce error.

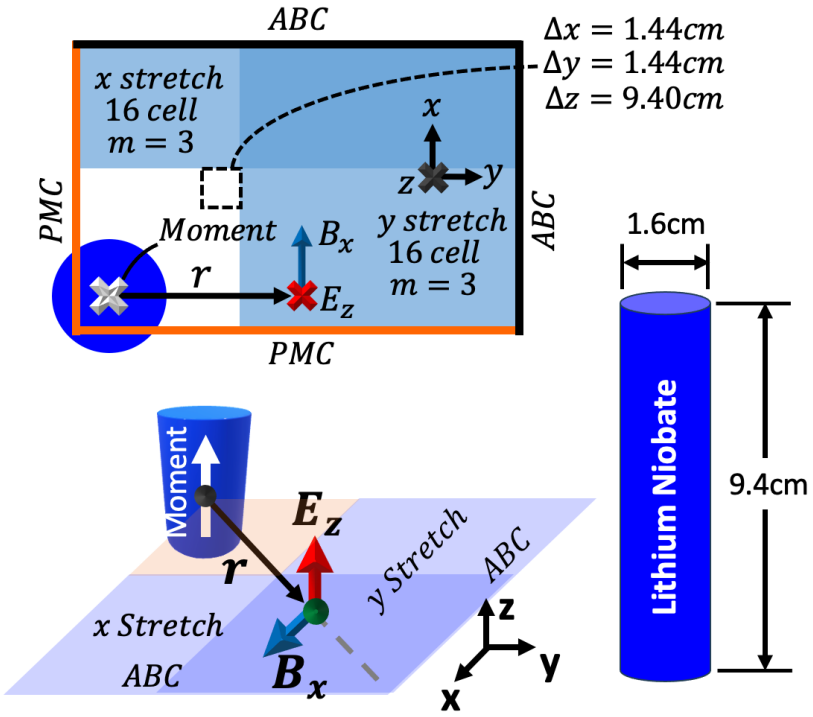


Figure 5-1: Simulation setup for the SLAC antenna experimental validation study.

The smallest cell sizes [$\Delta x = \Delta y = 1.44cm$ and $\Delta z = 9.40cm$] are within the uniform interior non-stretched region. The discretization was selected such that the source current acts along one cell in the z-direction across an area equivalent to the SLAC bar cross-section (1.44cm$^2$). Stretching is cubically ($m = 3$) increased with maximum stretching factors ($\kappa_x$, $\kappa_y$, and $\kappa_z$) chosen such that the largest discretization is $\lambda^{EM}/20$ ($\kappa_x^{max} = \kappa_y^{max} \cong 29340$, and $\kappa_z^{max} \cong 4495$). Figure 5-2 shows the simulated FDTD results ($E_z$ and $B_x$) are compared to the SLAC measured values (e.g. only Ez measured by SLAC) versus the radial distance from the antenna. In addition to these data points a $1/r^3$ electric field decay along with a $1/r^2$ magnetic flux decay are provided. As can be seen when comparing the FDTD with the SLAC electric field decay

there is extremely good agreement between the two as well as agreement with the expected decay from a dipole analytical solution. Furthermore, the FDTD code shows an excellent agreement with the magnetic flux decay pattern from a dipole model.

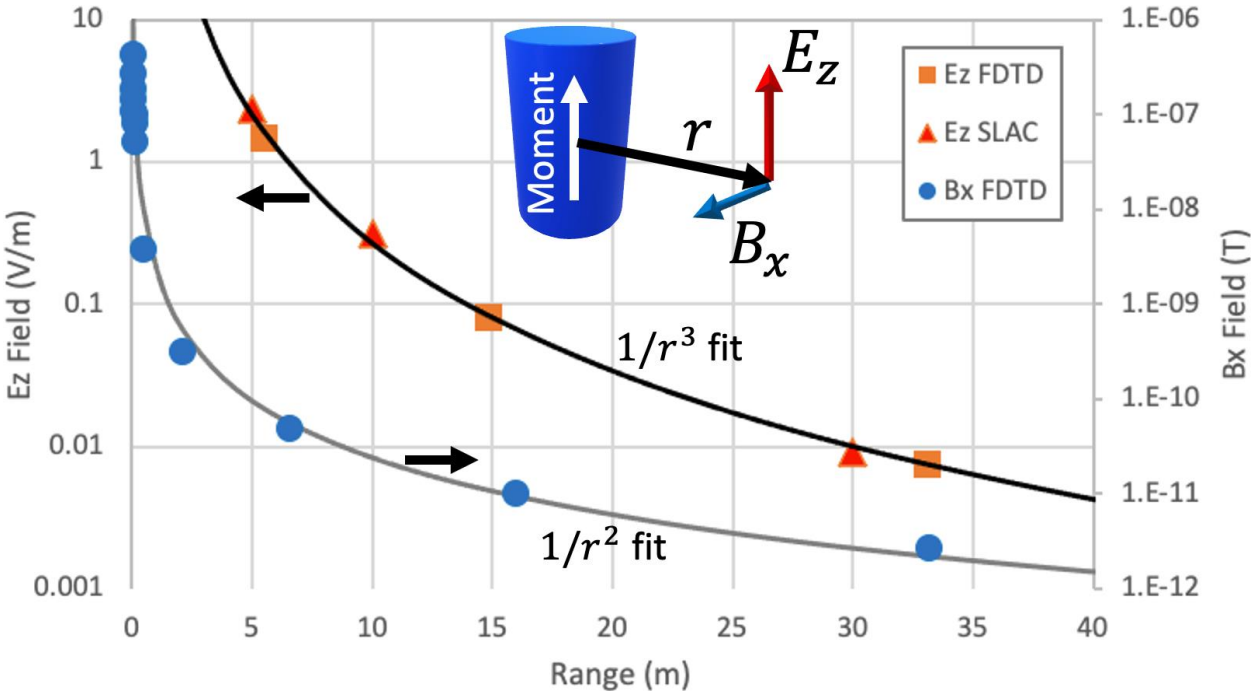


Figure 5-2: Plot of $E_z$ and $B_x$ values from FDTD simulation vs. the range $r$. Measured values for $E_z$ provided by [152] (SLAC) are also shown. The solid lines are fits to the data. The "Moment" from which r originates is a single applied source current $J_z^S$ within the FDTD simulation. This source current represents the SLAC piezoelectric antenna.

These results provide validation of the electromagnetic portion of the code to accurately reflect experimental data as well as being able to represent the electromagnetic field around an extremely electrically small antenna in the near field.

## 5.2 Infinite Piezoelectric Plate Analytical Comparison

In this section, an infinite plate of piezoelectric material is simulated to compare to an analytical solution. First, the analytical solution is derived in Section 5.2.1. Then, the comparison is made in Section 5.2.2 along with a discussion of the results.

### 5.2.1 Analytical Solution for Internal EM Fields within an Infinite Piezoelectric Plate

The filling density $\psi$ describes how much of a plane is made up of piezoelectric material. Thus $\psi = 1$ corresponds to an infinite plate of piezoelectric material and $\psi \to 0$ for a single long slender bar. Consider the infinite square regular array of piezoelectric material of Figure 5-3. The piezoelectric material is transversely isotropic about the out-of-plane $z$ axis.

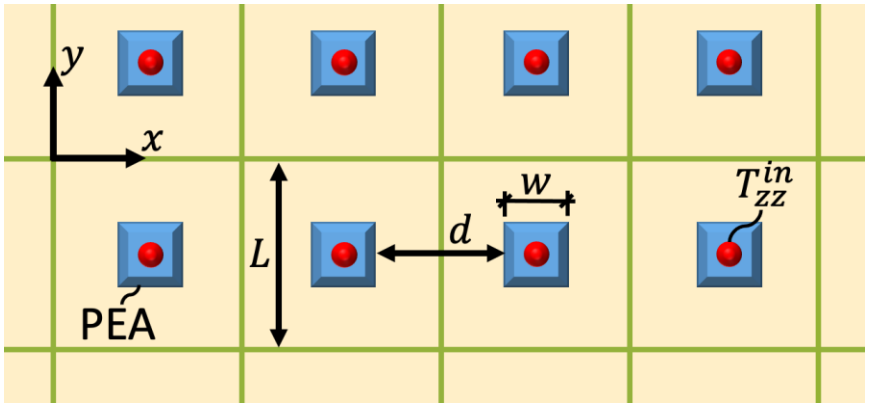


Figure 5-3: Infinite square planar array of piezoelectric material, each excited by stress $T_{zz}^{in}$ which is uniform in-plane. The minimum spacing between elements is defined as $d$. The cross-section of each antenna is square with dimension $w$. The length between lines of symmetry is $L$.

The minimum spacing between the elements is $d$ and the square cross-sectional dimension is $w$. Note in Figure 5-3 that as the spacing $d$ approaches zero, the entire xy-plane fills with piezoelectric material ($\psi = 1$) and an infinite plate is achieved. The filling density for this array may be written as in equation (5.1).

$$\psi = \left(\frac{w}{w+d}\right)^2 = \left(\frac{w}{L}\right)^2 \tag{5.15}$$

Each piezoelectric element is excited by stress $T_{zz}^{in}$ which does not vary in-plane. Thus, as $d \rightarrow 0$ and an infinite plate is achieved, no spatial variation in-plane exists. From Ampere's law within the material, this yields:

$$\dot{D}_z^{int} = H_{y,x} - H_{x,y} = 0 \tag{5.2}$$

Therefore, internal flux $D_z^{int}$ is constant and can be assumed to be zero [102][104][105]. Also, since the piezoelectric material is transversely isotropic about the $z$ axis, and the uniaxial stress state holds ($T_{zz}$ is the only non-zero stress), $D_x^{int}$ and $D_y^{int}$ are also zero. Since electric flux is the source of EM radiation [27], this means that the infinite plate ($\psi = 1$) for out-of-plane uniaxial stress cannot radiate. As internal $D_z^{int}$ is zero, the internal electric field $E_z^{int}$ may be readily determined using the electric constitutive relation as follows:

$$E_z^{int} = -g_{33}T_{zz} = -\frac{d_{33}}{\epsilon_{33}^T}T_{zz} \tag{5.3}$$

Since the flux is constant in the $\psi = 1$ infinite plate, the stiffness that is operative is the $c^D$ value with corresponding resonance frequency of $f_r^{cD}$. Thus, the opposite state of a single long slender element, like [152] which is known to radiate, will exist under a constant field state. The stiffness that is operative is the $c^E$ value with corresponding resonance frequency of $f_r^{cE}$. In this case, the radiation from the piezoelectric antenna is optimal. The characteristics described in this section and the internal fields from (5.2) and (5.3) will be seen to obtain for the $\psi = 1$ infinite plate in the following Section 5.2.2.

### 5.2.2 Simulation Results Comparison to Analytical Solution

Consider a 1.26μm thick infinite piezoelectric plate resting on a ground plane and poled out-of-plane (z-direction) as shown in Figure 5-4(a). If a uniform stress excitation ($T_{zz}^{in}$) is applied, all fields within the plate are spatially invariant in-plane and analytical expressions for the internal

electric field ($E_z^{int}$) and electric flux ($D_z^{int}$) may be determined. In this preliminary study, this uniform stress case is used to verify agreement between the simulated and analytical $E_z^{int}$ and $D_z^{int}$ for the infinite piezoelectric plate of Figure 5-4. The goal is to further assess the accuracy of the proposed computational model. For this study, the uniform stress is known a priori. Thus, piezoelectricity is now utilized but elastodynamics is still omitted to solely focus on validating the EM fields internal to the piezoelectric.

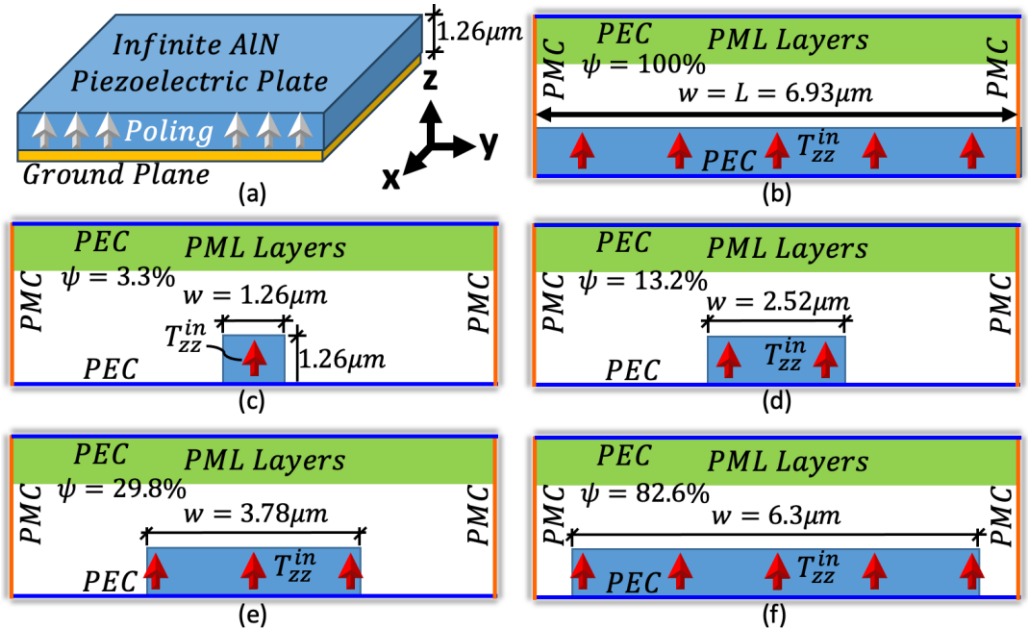


Figure 5-4: Infinite plate of piezoelectric material resting on a ground plane. (a) In-plane directions for the 1.26$\mu$m thick plate are the x/y axes, and the material is Aluminum Nitride AlN poled in the z-direction. (b) Numerical formulation of the infinite plate problem. The ground plane is modeled as a PEC with out-of-plane radiation absorbed by PEC-backed 14-cell thick PML region. Infinite periodicity in the xy-plane is accomplished with PMC boundaries. Since the piezoelectric material is in contact with the PMC boundaries ($w = L$), the filling density $\psi$ is 100%. Stresses are input within the plate, inducing an electric response via the piezoelectric effect. (c) First of four simulations performed at a filling density of 3.3% ($w$ = 1.26μm). (d)

Second simulation performed at filling density $\psi$ of 13.2% ($w$ = 2.52μm). (e) Third simulation performed at $\psi$ of 29.8% ($w$ = 3.78μm). (f) Fourth simulation performed at $\psi$ of 82.6% ($w$ = 6.3μm).

Numerically, an infinite plate may be modeled by using in-plane periodic boundaries (PMCs in this case) and allowing the piezoelectric material to contact these boundaries as shown in Figure 5-4(b). If the piezo material does not contact the PMCs, then an infinite rectangular regular array will be generated with filling density $\psi$. Each array element has a width of $w_x = w_y = w$ and the simulation space width (from PMC to PMC) is $L_x = L_y = L$ = 6.93$\mu$m. Therefore, $\psi = (w/L)^2$ = 100% for an infinite plate. The relevant simulation parameters are tabulated in Table I where the piezoelectric material is Aluminum Nitride (AlN):

| Symbol | Description | Value |
|---|---|---|
| $\boldsymbol{d_{33}}$ | Piezoelectric Constant | 4.9597e-12 C/N |
| $\boldsymbol{\epsilon_{11}^T}$ | Permittivity | $9.2081\epsilon_0$ |
| $\boldsymbol{\epsilon_{33}^T}$ | Permittivity | $10.1192\epsilon_0$ |
| $\boldsymbol{\kappa_z^{max}}$ | Max Mesh Grade | 29,800 |
| $\boldsymbol{\Delta x}$=$\boldsymbol{\Delta y}$ | Spatial Sampling | 0.63μm |
| $\boldsymbol{\Delta z}$ | Spatial Sampling | 1.26μm |
| $\mathbf{f_{in}}$ | Input Frequency | 400MHz |
| $\mathbf{\lvert T_{zz}^{in}\rvert}$ | Stress Magnitude | 10MPa |

Table 5-1: Input parameters for infinite piezoelectric plate analytical validation.

As highlighted in Figure 5-4(c-f), four simulations are performed at increasing filling densities. For a 10MPa 400MHz Gaussian pulse stress excitation, a comparison of the centroidal $E_z$ field between the analytical solution for an infinite plate ($\psi$ = 100%) and numerical results at filling densities of 3.3%, 13.2%, 29.8%, and 82.6% is shown in Figure 5-5(a):

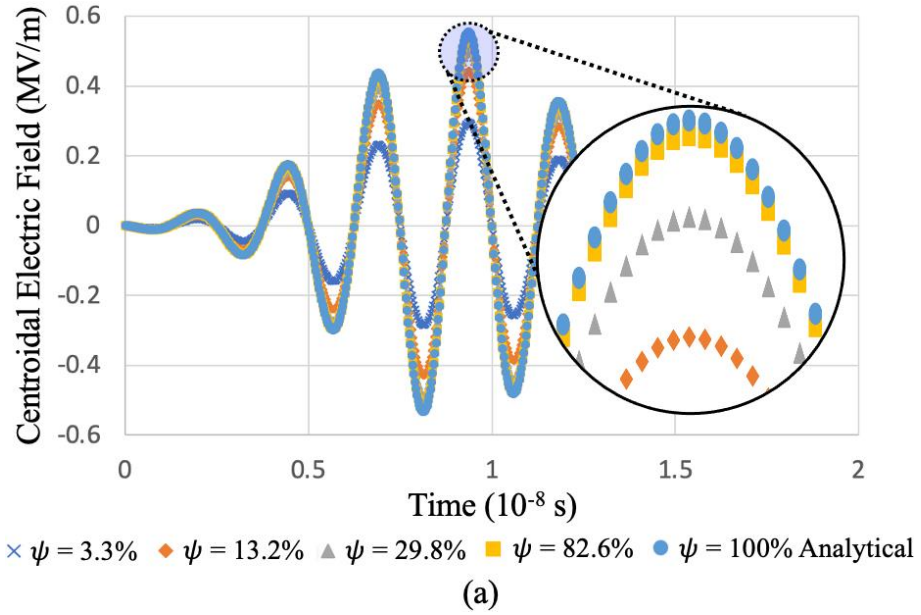


(a)

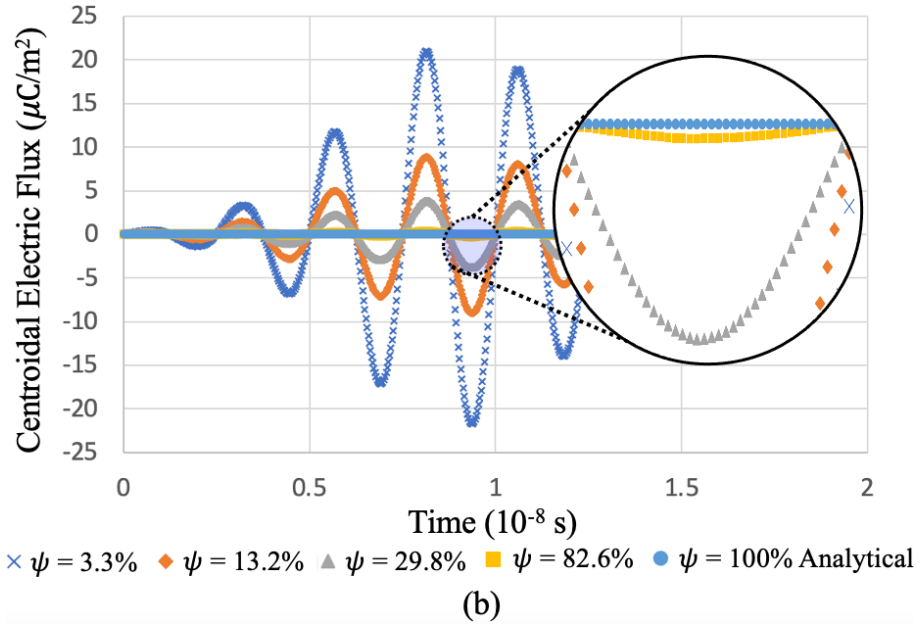


(b)

Figure 5-5: Results comparison between simulated fields within the centroid of the piezoelectric plate at various filling densities $\psi$ and analytical values for $\psi$ = 100%. As the simulated filling densities near 100%, the numerical results converge to that of the analytical solution as expected. (a) Electric field $E_z$ vs. time comparison. (b) Electric flux $D_z$ vs. time comparison.

In Figure 5-5(a), as the piezoelectric filling density is increased closer to 100%, the simulated electric field at the plate centroid converges to the infinite plate analytical solution of equation (5.3). In Figure 5-5(b), the internal electric flux $D_z$ is compared at the same centroidal location and the simulation results again converge to the analytical solution of equation (5.2), namely to zero, as the simulated filling densities approach 100%. Thus, good agreement is reached between the code and the analytical expressions. A discussion on the expected radiation from such a piezoelectric plate follows.

The enlargement of the piezoelectric surface area normal to the polarization currents, as $\psi$ increases, induces worsening self-depolarization within the plate (shape anisotropy). Since the spacing between elements is simultaneously decreasing, mutual depolarization is also exacerbated (the concept of self and mutual depolarization is further elaborated on in Section 5.4). This depolarization degrades the radiation from the plate. When $\psi$ = 100%, no radiation will be seen as predicted by (5.2). Thus, the infinite piezoelectric plate can only radiate if in-plane polarization currents are present, e.g., for a thickness shear mechanical mode as in [102][104][105].

Thus, the fields within the piezoelectric are accurate per this infinite plate analytical comparison and the fields surrounding a radiator in the extreme near field are accurate per the SLAC experimental comparison of Section 5.1. The algorithm is therefore performing well and may be used to provide design guidance to engineers working with piezoelectric antennas. First, however, the input strategy of Section 3.12 is checked in the following Section 5.3.

### 5.3 BAW Resonator Validation

The mechanical antennas investigated herein are more accurately modeled when driven by an electrode-piezoelectric-electrode stack up as introduced in Section 3.12. When no radiating elements are added, this is a BAW filter device with traction free boundaries on the top and

bottom producing a half-sine wave mechanical mode as shown in Figure 5-6. Due to the half-sine wave mode, there needs to be at least 10-cells within the source space.

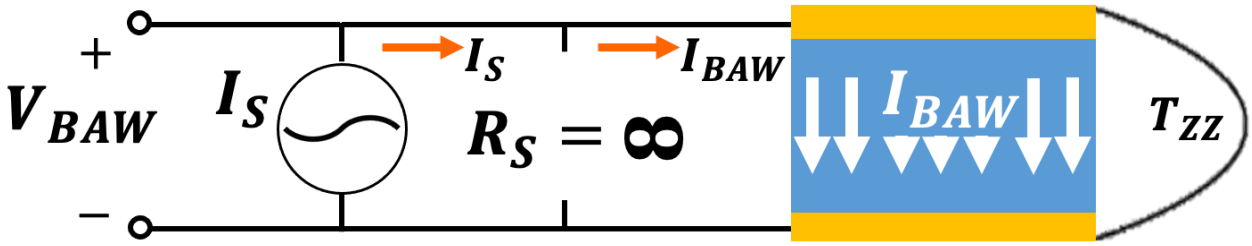


Figure 5-6: BAW Filter where the electrodes are assumed infinitely thin and the piezoelectric is thin enough that the uniaxial strain approximation is warranted. The source resistance is open circuited to adhere to the analytical solution.

Herein a modulated Gaussian pulse of source current $I_S$ is the initial excitation which is directly applied at the terminals since the source resistance $R_S$ is open-circuited ($I_S = I_{BAW}$). This induces terminal voltage $V_{BAW}$ which then induces stress $T_{zz}$ within the piezoelectric material. Due to inclusion of viscous damping, this induced stress rings down (decays) over time. Once the stress is <5% of the original value, the simulation is terminated and FFTs are performed on the voltage, current, and stress to determine frequency results. The damping is therefore essential, as, if no damping occurs, then significant spectral leakage occurs in the FFT results (i.e., FFT assumes original signal is periodic so, if it starts at zero, it should end at zero). The input impedance vs. frequency may then be determined as the ratio of the voltage to the current. The analytical solution for the input impedance to this device is [243]:

$$Z = \left(\frac{1}{j\omega C}\right)\left(1 - K_t^2 \frac{tan(kd)}{kd}\right) \tag{5.4}$$

$$C = \frac{\epsilon_{zz}^S W_x W_y}{W_z}, \qquad W_z = 2d, \qquad k = \frac{2\pi}{\lambda}, \qquad K_t^2 = \frac{e_{33}^2}{c_{zzzz}^D \epsilon_{zz}^S} = \frac{K_l^2}{K_l^2 + 1}, \qquad K_l^2 = \frac{e_{33}^2}{c_{zzzz}^E \epsilon_{zz}^S}$$

Where $W_z$ is the thickness of the filter, $d$ is the half-thickness, $W_x/W_y$ are the in=plane dimensions, and $K_t^2/K_l^2$ are piezoelectric coupling figures of merit (FoMs). These FoMs represent the amount of mechanical energy that is converted to electrical energy and vice versa [114], where $K_t^2$ applies for a transversely clamped material (uniaxial strain) [243] and $K_l^2$ applies for a uniaxially stressed rod [198]. Since $c^D$ is stiffer than $c^E$, energy conversion per volume will be larger in axially excited rods than in thickness excited plates for strong piezoelectrics like PMN-PT and PZT. Herein, aluminum nitride (AlN) is utilized and Table 5-2 documents relevant input parameters (parameters not listed may be derived):

| Parameter | Value | Units | Description |
|---|---|---|---|
| $c_{zzzz}^D$ | 419.1 | GPa | Mechanical Stiffness |
| $\eta_{zzzz}^D$ | 0.025 | Pa-s | Viscoelastic Damping |
| $\rho$ | 3300 | Kg/m$^3$ | Density |
| $\epsilon_{zz}^S$ | 9*8.854 | nF/m | Permittivity |
| $d$ | 7.043 | $\mu$m | Device Half-Thickness |
| $f$ | 400 | MHz | Input Frequency |
| $e_{33}$ | 1.55 | C/m$^2$ | Piezoelectric Coupling Coefficient |
| $C$ | 1.1225e-13 | F | Device Capacitance |
| $K_t^2$ | 0.0719 | Decimal | AlN Thickness Mode FoM |
| $\Delta z_S$ | 1.409 | $\mu$m | Spatial Discretization |
| $\Delta t$ | 6.25 | ns | Temporal Sampling |

Table 5-2: Inputs into BAW Filter validation study.

A comparison between the simulated and analytical impedance is presented in Figure 5-7:

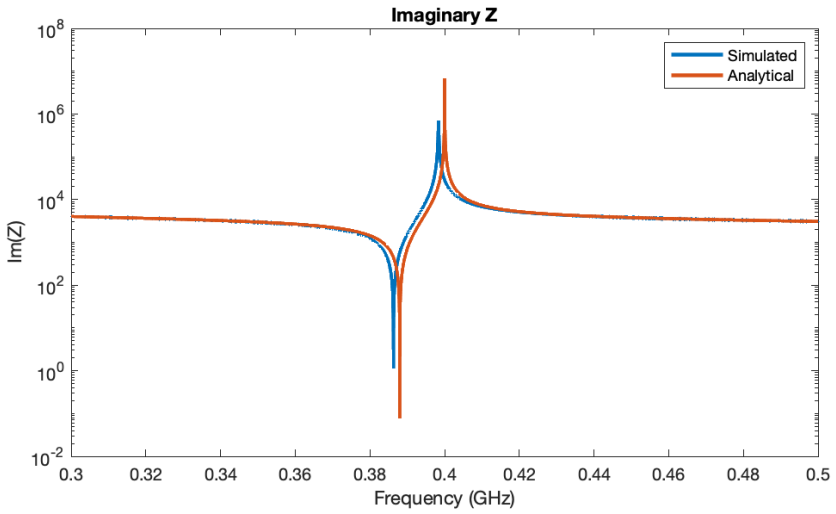


Figure 5-7: Comparison of the simulated and analytical impedance Z.

Note that good agreement is seen with the largest disparity occurring near and at resonance which is caused by the inclusion of mechanical viscous damping within the simulated results. For example, the simulated results predict a left-shifted resonance frequency and underpredict the output at resonance, both of which are characteristic of a damped system versus an undamped system. The damping had to be included in the simulation since the induced stresses needed to ring down prior to performing a fast Fourier transform (FFT) on the time domain data. This is to avoid spectral leakage in the frequency domain results. The results presented in Figure 5-7 are therefore satisfactory. The analytical solution for the stress within the BAW filter is as follows:

$$T_{zz}(z) = \frac{e_{33} D_z}{\epsilon_{zz}^S} \left[ \frac{\cos(kz)}{\cos(kd)} - 1 \right] \tag{5.5}$$

The datum is defined such that the top electrode is at z=d, the bottom electrode at z=-d, and the center along the thickness is z=0. A comparison between the simulated and analytical stress is presented in Figure 5-8:

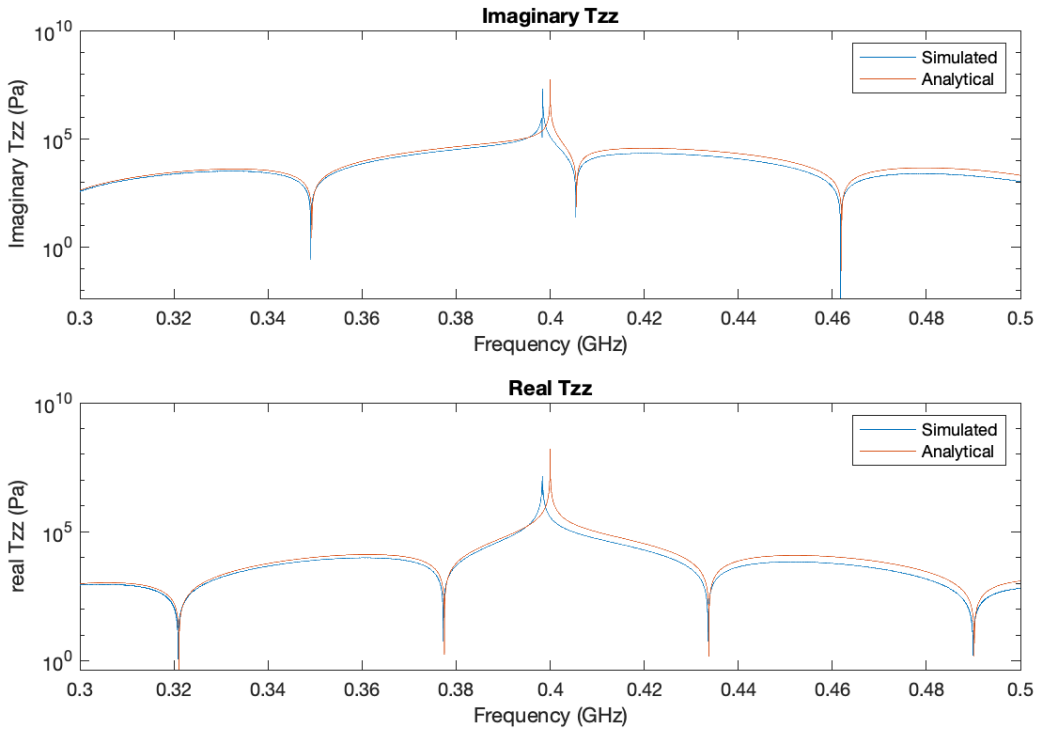


Figure 5-8: Comparison of the simulated and analytical stress measured at the center of the device where the stress is maximal.

Good agreement is again observed for the stress. Therefore, the source space portion of the code is seen to accurately model the BAW filter device which gives confidence in using this input strategy to model mechanical resonance-based antennas. This input strategy is leveraged in the next Section 5.4, where the bottom mechanical boundary will be fixed rather than traction free to model symmetry. Also, the top mechanical boundary will act as an interface between the electrostatic source space and the electrodynamic simulation space (see Section 3.12).

## 5.4 Infinite Planar Array of Piezoelectric Antennas

Fully coupled simulations where both Newton's laws and Maxwell's equations are utilized to update fields within the simulation space simultaneously will now be used to characterize the performance of an infinite planar array of piezoelectric antennas. These arrays are the future as emerging technologies require larger dipole moments from ever shrinking electrically small

antennas. These arrays will induce detrimental mutual depolarization effects amongst elements, however. Thus, an understanding of this mutual depolarization effect is desperately needed. This section first defines depolarization and provides an expression predicting its effects within an array. Next, the radiation performance of a single element within an array is characterized vs. the spacing. Lastly, the array radiation efficiency is presented which reveals a performance peak.

### 5.4.1 Predicted Depolarization

Depolarization is any effect where a piezoelectric material generates a current that is contra to polarization current within either itself or another piezoelectric. The former effect we refer to as self-depolarization which is analogous to demagnetization within magnetostrictive materials and is generally what is referred to when the term depolarization is used. The latter effect occurs when multiple piezoelectric antennas are brought close together, on the order of the physical dimensions of the device, which we refer to as mutual depolarization. This effect is not as widely discussed and will become increasingly problematic as larger dipole moment requirements are pressed on emerging technologies. In this section the coupling Figure of Merit will be discussed as this is an important factor in depolarization. Then, a prediction of the mutual depolarization effect will be derived.

The coupling Figure of Merit (FoM or $K_E^2$) is a measure of efficiency in electrical to mechanical energy transfer, or vice versa, within a piezoelectric material [198] and is provided in (5.6) for coupling in the poling direction via extensional (non-shearing) mechanical modes.

$$K_E^2 = \frac{d_{33}^2}{s_{33}^E \epsilon_{33}^T} \tag{5.6}$$

In (5.6) $s^E$ is the mechanical compliance (inverse of stiffness) at constant electric field. Also, although multiple Figures of Merit exist, no subscripts are added to $K_E^2$ for brevity since only the coupling between the electric field and extensional mechanical stress in the poling direction is operative herein. A $K_E^2$ value of 1 represents a scenario where all electrical energy is converted

to mechanical energy and a $K_E^2$ value of 0 ($d_{33}$=0) represents a material where no electromechanical coupling takes place.

An expression predicting the effects of depolarization, both self and mutual, will now be derived. Within the piezoelectric, the dominant electric field and mechanical normal stress will be in the poling direction yielding the following constitutive relations.

$$\begin{pmatrix} S_{zz} \\ D_z \end{pmatrix} = \begin{bmatrix} s_{33}^E & d_{33} \\ d_{33} & \epsilon_{33}^T \end{bmatrix} \begin{pmatrix} T_{zz} \\ E_z \end{pmatrix} \tag{5.7}$$

Due to polarization within the piezoelectric the $E_z$ term in (5.7) will differ from the incident (external) electric field $E_z^i$ and the relation between the two fields may be written as:

$$E_z = E_z^i - \frac{\psi}{\epsilon_0} P_z \tag{5.8}$$

Where $P_z$ is the polarization density (dipole moment $p$ per volume), $\epsilon_0$ is the free space permittivity, and $\psi$ is a depolarization coefficient that is related to the geometrical features of the piezoelectric antenna. For long slender rods, $\psi$ approaches zero and equals one for an infinite plate. From (5.8), the internal flux may be written as:

$$D_z = \epsilon_0 E_z + P_z = \epsilon_0 E_z^i + (1 - \psi) P_z \tag{5.9}$$

Using the electric constitutive relation in (5.7) along with (5.8) and (5.9), the polarization density may then be written as:

$$P_z = \epsilon_0 \chi_{33}^T E_z + d_{33} T_{zz} = \frac{\epsilon_0 \chi_{33}^T}{1 + \psi \chi_{33}^T} E_z^i + \frac{d_{33}}{1 + \psi \chi_{33}^T} T_{zz} \tag{5.10}$$

Where $\chi_{ij}^T$ is the electric susceptibility at constant stress. The coefficients in front of the incident field $E_z^i$ and the stress $T_{zz}$ are the effective permittivity and piezoelectric coupling coefficient of the system respectively, namely:

$$\epsilon_{33}^{T,eff} = \frac{\epsilon_0 \chi_{33}^T}{1 + \psi \chi_{33}^T} \tag{5.11}$$

$$d_{33}^{eff} = \frac{d_{33}}{1 + \psi\chi_{33}^{T}} \tag{5.12}$$

Both (5.11) and (5.12) degenerate back to the original value for a long slender isolated element (i.e., for $\psi \approx 0$). After manipulation, the mechanical constitutive relation in (5.7) may also be written in terms of the incident electric field as follows:

$$S_{zz} = \left( s_{33}^{E} - \frac{\psi \mathrm{d}_{33}^{2}}{\epsilon_0 (1 + \psi\chi_{33}^{T})} \right) T_{zz} + \frac{d_{33}}{1 + \psi\chi_{33}^{T}} E_z^i \tag{5.13}$$

For large susceptibility $\chi_{33}{}^{T} \gg 1$ ($\epsilon_{33}{}^{T} \approx \epsilon_0 \chi_{33}{}^{T}$), the FoM of (20) becomes:

$$K_E^2 = \frac{d_{33}^2}{\epsilon_0 \chi_{33}^{T} s_{33}^{E}} \tag{5.14}$$

Substituting (5.14) into (5.13) yields the following constitutive relation and effective compliance, respectively:

$$S_{zz} = s_{33}^{E,eff} T_{zz} + d_{33}^{eff} E_z^i \tag{5.15}$$

$$s_{33}^{E,eff} = s_{33}^{E} \left( 1 - K_E^2 \frac{\psi\chi_{33}^{T}}{1 + \psi\chi_{33}^{T}} \right) \tag{5.16}$$

Therefore, the effective coupling coefficient that takes depolarization into account ($K_D{}^2$) is as follows:

$$K_D^2 = \frac{\left(d_{33}^{eff}\right)^2}{\epsilon_{33}^{T,eff} s_{33}^{E,eff}} = \frac{K_E^2}{(1 - K_E^2)(1 + \psi\chi_{33}^{T}) + K_E^2} \tag{5.17}$$

In (5.17), the expected result for a long slender bar with $\psi$ approaching zero ($K_D{}^2 \approx K_E{}^2$) is achieved. Equation (5.17) is also applicable to infinite planar arrays. In this case, $\psi$ is the filling density which for a regular square array is equal to the ratio of the piezoelectric cross-sectional area ($w^2$ for a square cross-section) to the square of the element center-to-center spacing ($L^2$), namely $\psi = (w/L)^2$. Call the power radiated from an isolated antenna element $P_{rad}{}^{Iso}$ and the power radiated from antenna element experiencing mutual depolarization within an array $P_{rad}{}^{D}$. Since the radiated power is proportional to the dipole moment squared, and the dipole moment

is proportional to the FoM, the normalized radiated power is synonymous with the ratio of the depolarized FoM ($K_D^2$) to the FoM ($K_E^2$) squared. Therefore, from (5.17):

$$\frac{P_{rad}^{D}}{P_{rad}^{Iso}} = \left(\frac{K_D^2}{K_E^2}\right)^2 = \left(\frac{1}{(1-K_E^2)(1+\psi\chi_{33}^{T})+K_E^2}\right)^2 \tag{5.18}$$

Equation (5.18) is leveraged in Section 5.4.3 to compare simulated depolarization to the depolarization predicted in this section.

### 5.4.2 Simulation Setup

A piezoelectric antenna is placed on a PEC ground plane with in-plane periodic boundaries (PMCs) generating a regular square infinite planar array as shown in Figure 5-9. The Axial length of the bar is $L_A$ = 4.28μm and the width for the square cross-section is $w = L_A/10$. The spacing $d$ is defined as the minimum distance between array elements and the normalized spacing is defined as $d/w$. The bar is excited to mechanical resonance inducing EM radiation via the piezoelectric effect. For this study, the power radiated by an individual element $P_{rad}^{D}$ is simulated at various array spacings $d$. The goal is to characterize how the radiation is diminished as $d \rightarrow 0$ due to the mutual depolarization effect. Since the mechanical resonance frequency changes from the constant flux value ($f_r^{cD}$) at $d$ = 0 to the constant field value ($f_r^{cE}$) as $d \rightarrow \infty$ (see Section 5.2.1), the resonance frequency is also characterized versus spacing $d$. Fully coupled full-wave simulations are utilized (i.e., electrodynamics and elastodynamics solved simultaneously). Additional details on the model are in the following paragraph.

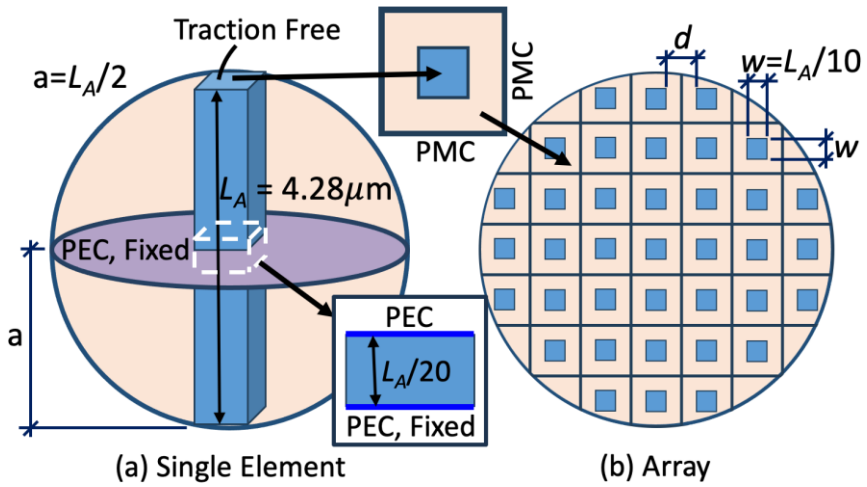


Figure 5-9: Piezoelectric antenna setup for mutual depolarization study. Cross-sectional dimensions are maintained so that self-depolarization is constant. (a) Single element of length $L_A$ = 4.28μm and square cross-sectional width of $w = L_A/10$ which justifies the uniaxial stress assumption. The antenna is bisected by a ground plane PEC and is fully enclosed within a sphere of radius a = $L_A$/2 as utilized by Chu [33][34][35]. (b) By use of PMC periodic boundaries, an infinite regular square antenna array may be investigated. The minimum distance between elements is defined as *d*. On the top boundary, PEC-backed PML layers truncate the simulation space.

Due to the bisecting PEC only the top half of the system is modeled. Input via electrode current is applied at the bar center across electrodes spanning 10% of the axial length, hence the simulated region for electrode current input (source space) is $L_A$/20 long as shown in the Figure 5-9 inset. The electrode current input is a modulated Gaussian pulse generating a 20MPa stress ringdown at the resonance frequency. The bottom and top electrical boundaries within the source space region are PECs, modeling infinitely thin electrodes. The mechanical boundaries are fixed ($v_z = 0$) at the bottom (for symmetry) and traction free ($T_{zz} = 0$) at the top. The simulated near-fields are used to calculate the $P_{rad}^D$ via a NTFF transformation [25][187], where the Huygen's box in-plane surfaces are aligned with the PMC boundaries consistent with

[131] and the top surface is two cells above the top of the radiator. NTFF transformations performed in this fashion yield the performance of a single element with cross coupling (both beneficial and detrimental) included. If the in-plane periodic boundaries (PMCs) are moved sufficiently far away, the coupling becomes negligible, and the isolated element performance is achieved. Since the detrimental mutual depolarization effect is dominant herein, it will be seen that the single element radiated power increases as the periodic boundaries are moved further until a plateau is reached.

The piezoelectric utilized for these simulations is X4B PIN-PMN-PT from TRS Technologies [244]. The mechanical damping is assumed to be the same as AlN as both are class 4mm tetragonal crystals. Relevant simulation parameters are shown in Table 5-3.

| Symbol | Description | Value |
|---|---|---|
| $\boldsymbol{d_{33}}$ | Piezoelectric Constant | 1.320E-9 C/N |
| $\boldsymbol{d_{31}}$ | Piezoelectric Constant | -6.340E-10 C/N |
| $\boldsymbol{\epsilon_{11}^{T}}$ | Permittivity | $1335\epsilon_0$ |
| $\boldsymbol{\epsilon_{33}^{T}}$ | Permittivity | $4200\epsilon_0$ |
| $\boldsymbol{\eta_{33}}$ | Mechanical Damping | 0.02 Pa-s |
| $\boldsymbol{K_{33}^{E}}$ | Figure of Merit FoM | 81.6% |
| $\boldsymbol{\rho}$ | Density | 8141 kg/m^3 |
| $\boldsymbol{E_{33}^{D}}$ | Young's Modulus | 1.74E10 Pa |
| $\Delta\boldsymbol{x}=\Delta\boldsymbol{y}$ | Spatial Sampling | 2.14E-7 m |
| $\Delta\boldsymbol{z}$ | Spatial Sampling | 3.85E-7 m |
| $\Delta\boldsymbol{z_S}$ | Spatial Sampling | 4.28E-8 m |
| $\Delta\boldsymbol{t}$ | Time Sampling | 1.259E-11 s |

Table 5-3: Simulation input parameters for fully coupled simulations of the infinite planar array of piezoelectric antennas.

The next Section 5.4.3 concerns the performance of a single element. Next, the method of deriving the array performance is provided in Section 5.4.4. Lastly, the array efficiency will be discussed in Section 5.4.5 where a performance peak is uncovered.

### 5.4.3 Single Element Performance

Within this section, the spacing *d* is varied by moving the PMC boundaries by adding cells, grading the mesh, or both. Seven simulations were performed to calculate the single element radiated power $P_{rad}{}^{D}$ at variable $d$. At large spacing, $P_{rad}{}^{D}$ reached a plateau value equaling that of an isolated element ($P_{rad}{}^{Iso}$) since mutual depolarization was no longer a factor. All radiated power $P_{rad}{}^{D}$ values are normalized to $P_{rad}{}^{Iso}$ and plotted vs. normalized spacing in Figure 5-10 where the resonant frequency, normalized to the $f_r{}^{cD}$ value, is also presented.

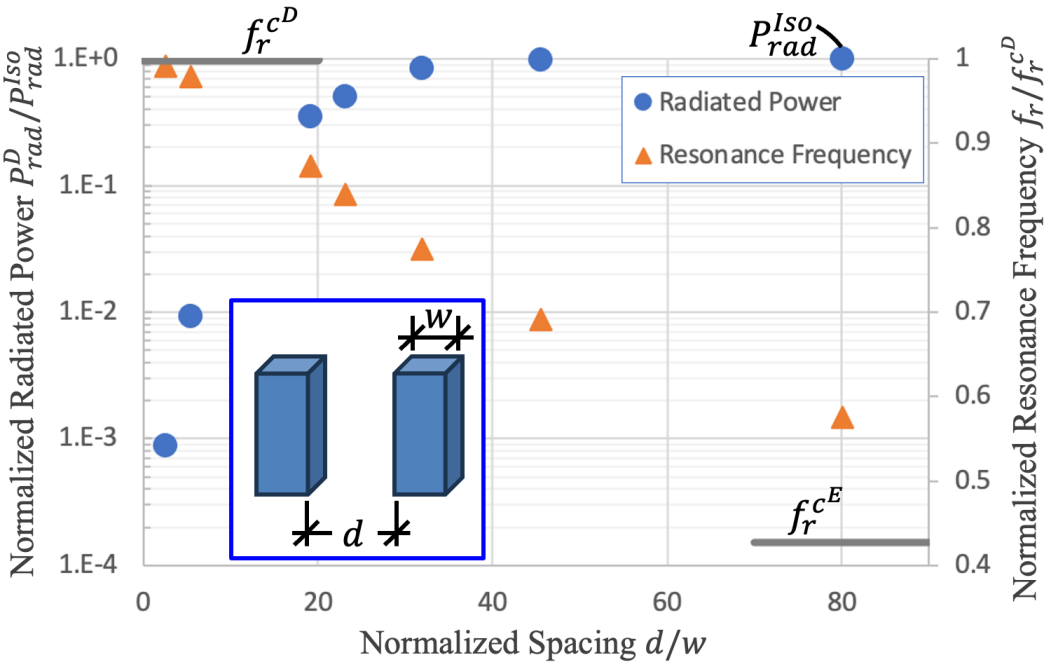


Figure 5-10: Single element normalized radiated power and normalized resonance frequency vs. normalized spacing for the infinite regular square array of Figure 5-9. Normalized power is per the left vertical axis and is logarithmic (hence the grid lines). Normalized frequency

is per the right vertical axis and is not logarithmic and thus the grid lines should not be used when analyzing this data.

In Figure 5-10, $P_{rad}^{D}$ decays by more than two orders of magnitude if the normalized spacing is less than 5. Between 5 and 40 the radiated power quickly increases, and mutual depolarization is negligible at normalized spacing greater than 40 after which $P_{rad}^{D}$ plateaus. As expected, these large changes in radiation are coupled with changes in the mechanical resonance frequency $f_r$. When the spacing is small, the resonance frequency is roughly equal to the constant flux stiffness ($f_r^{cD}$) and as the spacing is increased the resonance frequency trends towards the constant electric field stiffness value ($f_r^{cE}$). Interestingly, this shift in resonance frequency is still quite pronounced after the radiated power steadies at normalized spacings >40. For example, between $d/w$ = 45.5 and $d/w$ = 80.1, the radiated power increases by 1.4% while the resonance frequency reduces by 18.4%. This provides an interesting opportunity to tune resonance frequency within piezoelectric antenna arrays simply by altering the spacing between adjacent elements. This can potentially aid with the bandwidth issues typical of high Q systems.

In Section 5.4.1, a prediction was made in equation (5.18) for how radiated power is affected by mutual depolarization vs. the filling density $\psi$. Define $L$ as the PMC to PMC spacing (see Figure 5-11) and the filling density as $\psi = (w/L)^2$. A comparison of the results from Figure 5-10 to the predicted depolarization (5.18) is presented in Figure 5-11.

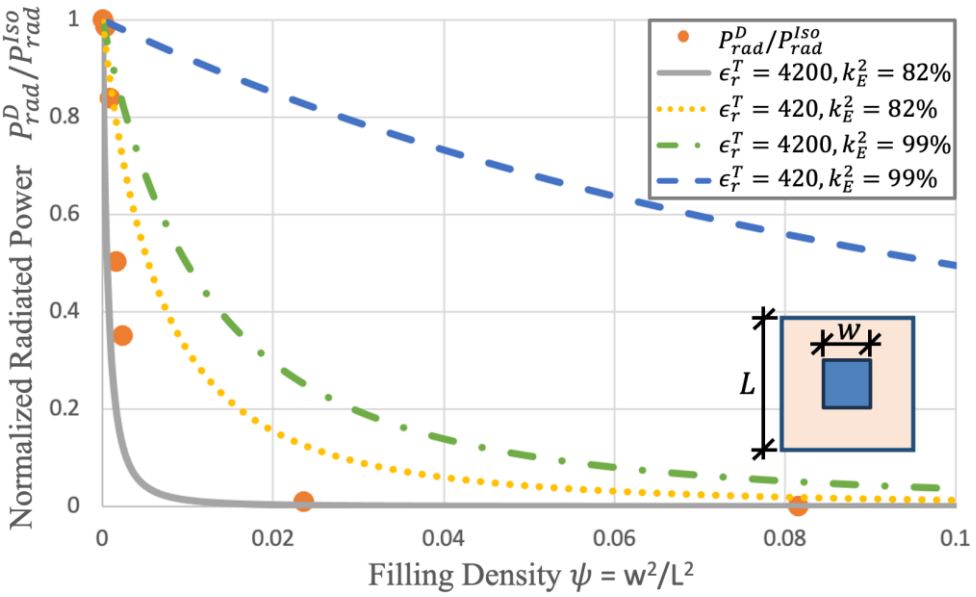


Figure 5-11: Comparison between the simulated (discrete points) and predicted (solid line) normalized radiated power vs. filling density $\psi$ showing good agreement. The prediction is per equation (5.18) as described in Section 5.4.1. Dotted, dashed-dotted, and dashed lines additionally represent theoretical materials that are less susceptible to mutual depolarization.

The discrete points in Figure 5-11 are the normalized radiated power from Figure 5-10, but now plotted versus the filling density $\psi$. The solid line is the predicted depolarization from equation (5.18) for TRS X4B PIN-PMN-PT utilized in the simulation. Good agreement is seen between the model and the prediction though equation (5.18) is shown to be somewhat conservative. Equation (5.18) may thus be utilized by engineers to design piezoelectric antenna array platforms with confidence that the mutual depolarization effect is accounted for. In Figure 5-11, the dotted, dashed-dotted, and dashed lines represent theoretical materials as defined within the figure legend. The dashed line is TRS X4B PIN-PMN-PT if the FoM is maintained but at an order of magnitude smaller permittivity. The dashed-dotted line is for TRS X4B PIN-PMN-PT if the FoM is increased to 99% and with the permittivity remaining constant. The dashed line is for TRS X4B PIN-PMN-PT if the FoM is increased to 99% and at an order of magnitude

smaller permittivity. Clearly much larger filling densities may theoretically be achieved with reduced mutual depolarization if these materials are realizable.

As shown in Figure 5-9, the PEAs under investigation fit within an enclosing sphere of radius a = $L_A/2$ which is normalized by multiplication with the wavenumber (ka). The input power and radiation efficiency were calculated per equations (3.135) and (3.136) respectively for each simulation. The PEA radiation efficiency vs. ka for each spacing is compared to the theoretical upper limit for metallic electrically small antennas (ESAs) per [164] (labelled as Helix) in Figure 5-12. Seven triangles represent the variable spacing simulations with *d/w* values labelled for each numerically and a solid line represents the metallic Helix configuration. In the figure, the SLAC antenna [152] is also included using crosses for comparison and is labelled as Kemp.

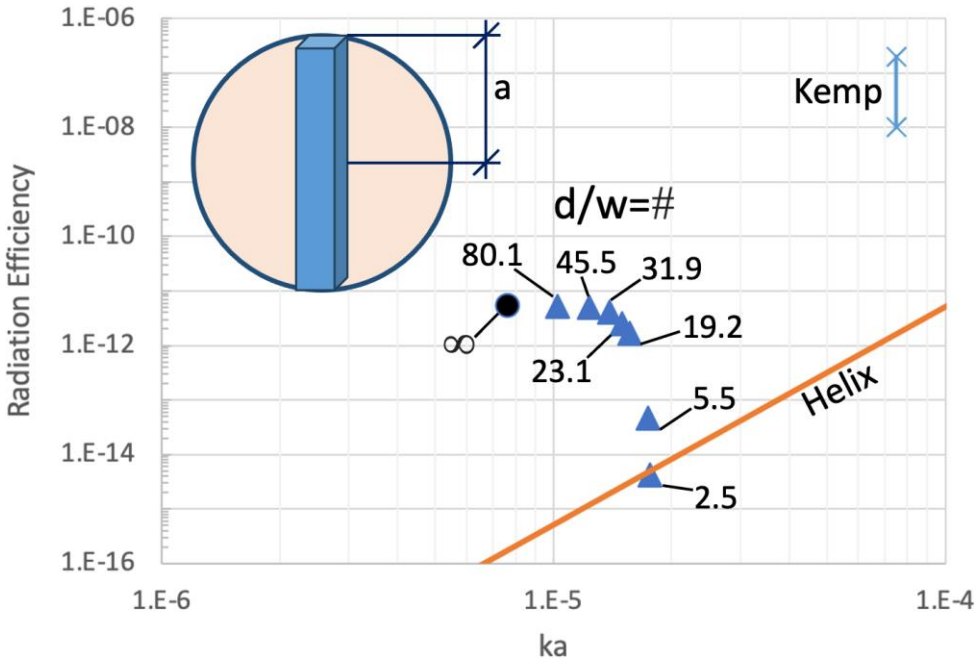


Figure 5-12: Radiation efficiency vs. ka plot for the seven simulations performed marked as discrete triangles. The normalized spacing *d/w* for each run is labelled numerically. The solid line labelled as “Helix” is the theoretical upper limit of metallic electrically small antennas (ESAs) as reported in [164]. Also included is the predicted isolated element performance which is

marked as a discrete circle with *d/w* labelled as ∞. Finally, the SLAC antenna [152] predicted efficiency is marked using crosses. The SLAC authors did not directly measure efficiency but rather performed calculations to estimate efficiency based on device Q. As such, a range is provided for the SLAC efficiency in [152].

Only the single element most burdened by mutual depolarization (at *d/w* = 2.5) does not outperform the metallic ESA prediction and even this element is on par with that upper limit. This is particularly impressive as the axial bar design for the PEAs investigated herein is a 1D element and does not fill much of a 3D sphere, whereas the Helix configuration in [164] is an optimized spherical design. Additional improvements to PEA efficiency at static ka values are therefore realizable. The major reason the metallic ESAs struggle is the small radiation resistance exhibited which drops per square of frequency for electrically small dipoles and fourth order of frequency for electrically small loops [245]. The high Q resonance from the piezoelectric material provides low loss impedance matching and thus mechanical antennas do not suffer from this same affliction.

At larger spacing, the piezoelectric elements exhibit large boosts in efficiency which plateau at *d/w* > 40. The shift in ka value is caused by the shift in mechanical resonance frequency due to the shift in effective stiffness. Thus, piezoelectric array elements not only radiate more efficiently when spacing is increased but do so at smaller ka values where higher efficiency is harder to achieve. The circle in Figure 5-12 is the predicted isolated element performance which has the same efficiency as the *d/w* = 80.1 simulation but with a ka value corresponding to resonance at $f_r^{cE}$ as this is the predicted resonance frequency for infinite spacing (isolated element). This isolated element exhibits 30,000 times higher efficiency than the optimized Helix metallic antenna at the same ka value. Before discussing the array performance in Section

5.4.5, the method of deriving the array efficiency from the single element efficiency will be presented in the following Section 5.4.4.

### 5.4.4 Planar Array Radiation Characteristics

For electrically tiny mechanical resonance-based antennas, it can be beneficial to construct an array of the elements, especially when device dimensions or on the micrometer scale. When determining array vs. single element far-field radiation characteristics, superposition of radiated fields needs to take place utilizing the Array Factor ($AF$) as follows:

$$E_{\theta,\phi}^{Array}(\theta,\phi) = AF(\theta,\phi)E_{\theta,\phi}^{Single}(\theta,\phi) \tag{5.19}$$

Where the array factor varies for array type, spacing between elements, and phase lag between elements. The radiation intensity and radiated power may be calculated as follows:

$$U_{Array}(\theta,\phi) = \frac{R^2}{2\eta_0}\left[\left|AF(\theta,\phi)E_{\theta}^{Single}(\theta,\phi)\right|^2 + \left|AF(\theta,\phi)E_{\phi}^{Single}(\theta,\phi)\right|^2\right] \tag{5.20}$$

$$P_{rad}^{Array} = \int_0^{2\pi}\int_0^{\pi} U_{Array} sin\theta d\theta d\emptyset \tag{5.21}$$

In the case of a rectangular xy-planar array with linear phase progression the array factor is:

$$AF(\theta,\phi) = \frac{sin\left(\frac{M}{2}\left[\beta d_x sin\theta cos\phi + \alpha_x\right]\right)}{sin\left(\frac{1}{2}\left[\beta d_x sin\theta cos\phi + \alpha_x\right]\right)}\frac{sin\left(\frac{N}{2}\left[\beta d_y sin\theta sin\phi + \alpha_y\right]\right)}{sin\left(\frac{1}{2}\left[\beta d_y sin\theta sin\phi + \alpha_y\right]\right)} \tag{5.22}$$

Where $M$ and $N$ are the number of elements in the x and y directions respectively, $\theta$ and $\phi$ are spherical coordinates with an origin at a corner of the array, $d_x$ and $d_y$ are the spacing between elements in the x and y directions respectively, $\alpha_x$ and $\alpha_y$ are the linear phase progression in the x and y directions respectively, and $\beta$ is the wavenumber ($\beta = 2\pi/\lambda_{EM}$). For mechanical antenna arrays, the element spacing $d_x$ and $d_y$ are both substantially smaller than the EM wavelength. For the square array examined in this section ($d_x = d_y = d$), this yields $\beta d \cong 0$. Also, using PMCs as the in-plane periodic boundary, inherently yields an unphased array ($\alpha_x = \alpha_y = 0$). Thus, the array factor for the simulations performed in this section is:

$$AF(\theta,\phi) \cong \frac{sin(0)}{sin(0)}\frac{sin(0)}{sin(0)} \tag{5.23}$$

Thus, L'Hôpital's rule must be used on (5.22), using $d_x = d_y = d$ and $\alpha_x = \alpha_y = 0$, to rectify the indeterminate form of (5.23) yielding:

$$\begin{aligned}\lim_{(\beta d sin\theta cos\phi+\alpha)\to 0} AF(\theta,\phi) \\ = \lim_{(\beta d sin\theta cos\phi+\alpha)\to 0}(M)(N)\frac{cos\left(\frac{M}{2}[\beta d sin\theta cos\phi+\alpha]\right)}{cos\left(\frac{1}{2}[\beta d sin\theta cos\phi+\alpha]\right)}\frac{cos\left(\frac{N}{2}[\beta d sin\theta sin\phi+\alpha]\right)}{cos\left(\frac{1}{2}[\beta d sin\theta sin\phi+\alpha]\right)} \\ = (M)(N)\end{aligned} \tag{5.24}$$

Thus, the maximum array factor ($M * N$) is achieved isotropically (i.e., in all directions with no $\theta$ and $\phi$ spatial dependence). From equations (5.20) and (5.21), the array radiated power is as follows:

$$P_{rad}^{Array} = M^2N^2\int_0^{2\pi}\int_0^{\pi} Usin\theta d\theta d\emptyset = M^2N^2P_{rad} \tag{5.25}$$

The single element input power will be multiplied by the number of elements; thus, the array efficiency is as follows:

$$e_{rad}^{Array} = \frac{P_{rad}^{Array}}{P_{in}^{Array}} = \frac{M^2N^2P_{rad}}{(M)(N)P_{in}} = (M)(N)e_{rad} \tag{5.26}$$

Thus, for unphased mechanical antenna arrays, the array efficiency may be readily determined, once the single element efficiency $e_{rad}$ is known, simply by multiplying by the number of elements. This principle will now be used to determine the array efficiency for the piezoelectric antenna array discussed in Section 5.4.3.

### 5.4.5 Array Efficiency

The array performance will now be considered for elements spaced in square fashion enclosed within a circle of diameter *D* (see Figure 5-13 inset). Two approaches are considered

for defining *D*. One approach is to allow *D* to have a fixed physical size (1mm in this case). Since the resonance frequency shifts with spacing, another approach is to allow *D* to have a fixed electrical size ($\lambda_{EM}$/1000 in this case) such that each data point will be enclosed in a circle of a different physical size. The array efficiency is calculated by multiplying the simulated near-fields and input power by the number of array elements. Due to the tiny electrical spacing, the array factor is nearly isotropic (spherical) as discussed in the previous Section 5.4.4, and this approximation is accurate. The array efficiency versus normalized spacing plot is shown in Figure 5-13.

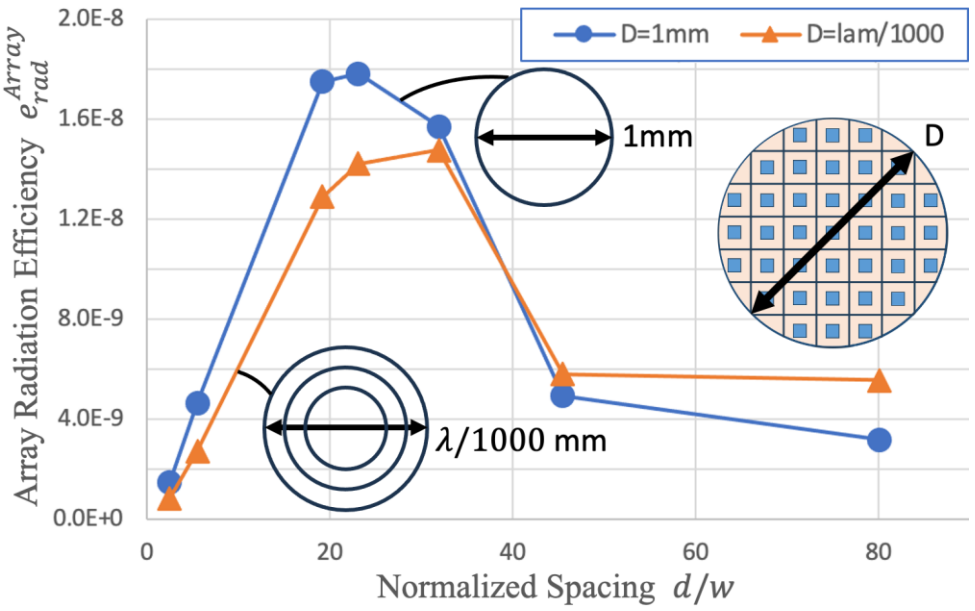


Figure 5-13: Array efficiency versus normalized spacing plot where the solid lines between data points are to guide the eye only. Curve with circles is for array enclosed within circle of fixed physical size of 1mm. Curve with triangles is for array enclosed within circle of fixed electrical size $\lambda_{EM}$/1000. The physical size varies from 0.76mm at d/w = 2.5 to 1.3mm for d/w = 80.1 for the fixed electrical size curve. Thus, the physical dimensions are comparable.

In Figure 5-13 an array efficiency performance peak is revealed for piezoelectric antenna array platforms. If the spacing is too large to mitigate mutual depolarization, then there will not be enough elements and the efficiency will suffer. If too many elements are crammed into the array to boost the radiation, then the mutual depolarization will destroy the efficiency. A performance peak is found as a balance between these two extremes at normalized spacing roughly between 18 and 35.

### 5.4.6 Conclusion

Full wave simulations capturing electrodynamic and elastodynamic wave physics simultaneously within the same simulation space were used to characterize mutual depolarization within piezoelectric antenna array platforms. It was found that spacing within these arrays should not be made too small to induce undue mutual depolarization and not be made too large as to limit the number of array elements. It was also observed that significant changes in resonance frequency could be achieved by changing the spacing between elements. The simulations performed provide guidance for future designs.

## 5.5 Multimode Alternate Poling Piezoelectric Antenna Array

The piezoelectric antenna platform proposed herein leverages multi-resonant elements to improve operational bandwidth. By modulating the 1$^{st}$ and 2$^{nd}$ axial modes (see Figure 5-14) multiple operational frequencies can be achieved.

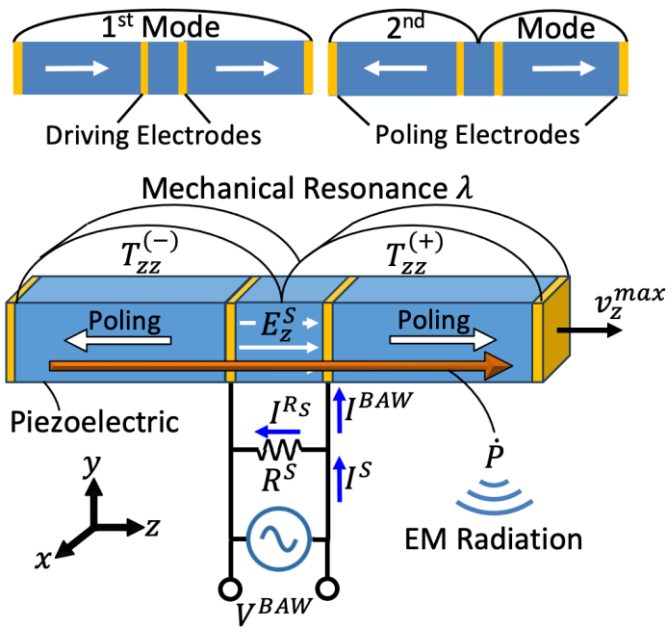


Figure 5-14: Proposed multimode axial resonance mechanical antenna. The 1st mode is a half-sine wave, and the 2nd mode is a full-sine wave. Due to the positive and negative instantaneous stress in the 2nd mode, the poling (white arrows) is alternated such that a coherent polarization current (orange arrow) is generated. A finite source resistance $\boldsymbol{R_S}$ is now included in contrast to the antenna simulations considered in Section 5.4.

Higher harmonics produce a non-coherent stress profile along the axial length (tensile and compression coexisting) by the positive stress producing a polarization current canceling the current generated by the negative stress. The proposed multimode piezoelectric antenna platform mitigates this effect by changing the poling direction along the bar as shown by the white arrows. A negative stress can produce an AC polarization current in the same direction as a tensile stress if the poling direction is opposite. Thus “poling electrodes” are added to the top and bottom of the bar as shown such that complimentary polarization currents may be generated by the 1st and 2nd axial modes. The driving electrodes double as poling electrodes for this purpose. This multi-resonant system with alternating poling directions significantly increases the possible operational bandwidth.

A soft piezoelectric material like PIN-PMN-PT can also be readily repolarized at room temperature by applying an electric field opposite to the original polarization direction. This procedure is commonly practiced in both research and industrial laboratories, such as at UCLA, across various applications and programs. During the poling process, the material's polarization is flipped by 180 degrees. While repeated re-poling cycles may potentially induce minor damage to the crystal structure, extensive research has demonstrated that applying compressive stress effectively mitigates this issue [246]. Moreover, in terms of mechanical performance, it has been shown to surpass conventional fatigue runout tests [247].

Lastly in Figure 5-14, the source resistance $R_S$, ignored in Section 5.4, is now considered. To reiterate, this section expands on Section 5.4 in the following ways:

- Introduces multimode resonance.
- Introduces source resistance $R_S$.
- Introduces concept of mechanically tuned half-power bandwidth (see Section 5.5.6)

In this section, an infinite planar array of piezoelectric antennas is simulated at the 1st and 2nd mode with variable array spacing to characterize far-field performance characteristics and provide design guidance for future array platforms. In Section 5.5.1, an often-leveraged circuit model will be discussed to explain open and short circuit resonance. In Section 5.5.2, the simulation setup is presented. In Section 5.5.3, the source resistance is varied to discern how the stress vs. time and radiated power vs. frequency are affected. In Section 5.5.4, the matched source resistance is utilized and the element spacing is varied to compare the 1st and 2nd mode single element performance. In Section 5.5.5, the array performance is investigated and the concept of the mechanically tuned half-power bandwidth is introduced in Section 5.5.6.

### 5.5.1 Open and Short Circuit Performance

As shown in Figure 5-15 the model for the piezo structure is the classical Butterworth-Van Dyke (BVD) model for piezoelectric resonators. This circuit model is only introduced for its

explanatory power and is not utilized within the simulations herein. The series RLC circuit represents the mechanical resonance, where $R_m$, $L_m$, and $C_m$ represent the motion resistance (mechanical damping), motion inductance (kinetic energy stored particle velocity) and motion capacitance (mechanical stiffness stored energy) respectively. The RLC circuit is shunt with a capacitor $C_0$, which is an electric property of the material (i.e., the capacitance related to the strain free permittivity). The relationship between the mechanical capacitance ($C_m$) and the shunt capacitance is $C_m = C_0 K_E^2$. Tapping the resonator input splits the electric capacitance model into two parts, e.g., $C_0 = C_{01} \,||\, C_{02}$. The maximum polarization current $\dot{P}$ in the motion arm (RLC circuit) is generated at the resonance formed by the loop of $C_0$, $L_m$, and $C_m$, which forms a peak voltage across the two ends of the piezoelectric resonator that electrically radiates from the dipole.

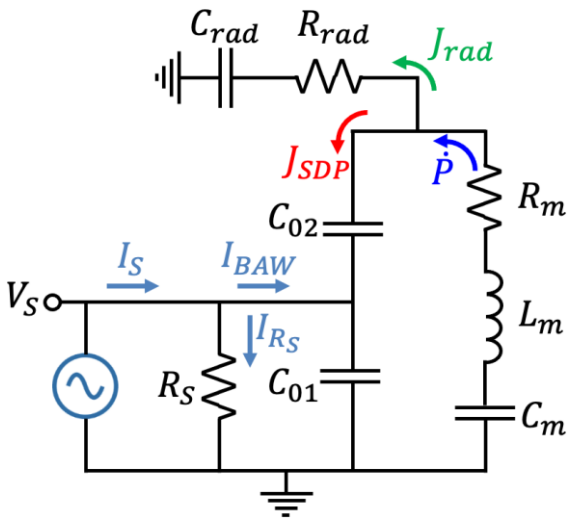


Figure 5-15: Equivalent circuit BVD model for a piezoelectric antenna with emphasis on the self-depolarization current $J_{SDP}$. The input current excitation $I_S$ and source resistance $R_S$ are also depicted.

The radiation into free space is represented by $R_{rad}$ and $C_{rad}$ which are the radiation resistance representing the radiated power and the dipole capacitance that represents the dipolar electric energy stored in free space, respectively. Their relation to Chu's equivalent circuit for electrically small dipole is described in [245]. The radiation resistance increases per square of the dipole length and the capacitance increases per the first order of the length. Once the excitation pulse current $I_S$ dies down, two extreme resonance modes exist: an open circuit case ($R_S = \infty$) and a short circuit case ($R_S = 0$). Both cases resonate at the high Q of the $R_m$, $L_m$, and $C_m$ motional branch, albeit at differing frequencies.

The polarization current ($\dot{P}$) generated by the piezoelectric coupling is split into two paths. One path flows back through the electric capacitance of the material which represents the self-depolarization effect ($J_{SDP}$). The other path is the equivalent radiation flow ($J_{rad}$). Due to large aspect ratio of 10:1 (necessary to justify the uniaxial stress assumption) of the piezoelectric antennas investigated herein, the self-depolarization current is negligible. Thus, the current flowing through capacitance $C_{01}$ is equal to $I_{BAW}$. The depolarization effect is exacerbated by proximity of additional radiators in an array. To minimize the depolarization effect and to enhance the radiation, one must use materials with the smallest electric capacitance comparing to the motion capacitance $C_m$, which translates to the requirement of electromechanical coupling Figure of Merit (FoM or $K_E^2$).

### 5.5.2 Simulation Setup

A piezoelectric antenna is placed on a PEC ground plane with in-plane periodic boundaries (PMCs) generating a regular square infinite planar array as shown in Figure 5-16. The Axial length of the bar is $L_A = 4.28\mu m$ and the width for the square cross-section is $w = L_A/10$. The spacing $d$ is defined as the minimum distance between array elements and the normalized spacing is defined as $d/w$. The bar is excited to the 1st (half sine wave) and 2nd (full sine wave) mechanical resonance modes inducing EM radiation via the piezoelectric effect. For this study,

precursory simulations with source resistance open-circuited ($R_S = \infty$) are performed to determine the matching resistance ($R_S^{Matched}$). The power radiated by an individual element $P_{rad}^{D}$ is then simulated utilizing $R_S^{Matched}$ at various array spacings $d$. The goal is to characterize how the radiation is diminished as $d \to 0$ due to the mutual depolarization effect as well as comparing the 1st and 2nd mode performance. Since the mechanical resonance frequency changes from the constant flux value ($f_r^{cD}$) at $d = 0$ to the constant field value ($f_r^{cE}$) as $d \to \infty$ (see Section 5.2.1), the resonance frequency is also characterized versus spacing $d$ for both modes. Fully coupled full-wave simulations are utilized (i.e., electrodynamics and elastodynamics solved simultaneously). Additional details on the model are in the following paragraphs.

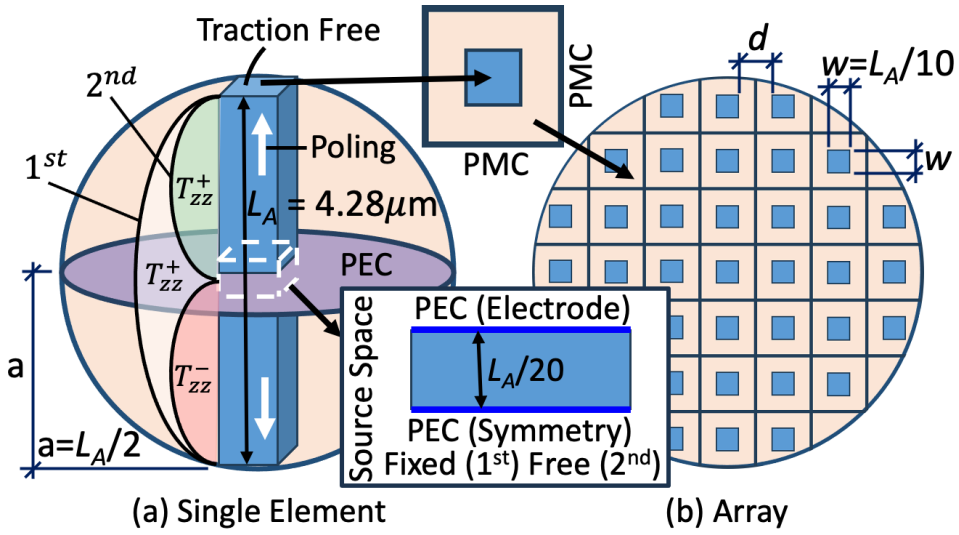


Figure 5-16: Piezoelectric antenna setup for multimode alternate poling study. Cross-sectional dimensions are maintained so that self-depolarization is constant while mutual depolarization varies with spacing. (a) Single element of length $L_A = 4.28\mu m$ and square cross-sectional width of $w = L_A/10$. This large aspect ratio both justifies the uniaxial stress assumption and minimizes self-depolarization. The antenna is bisected by a ground plane PEC and is fully enclosed within a sphere of radius $a = L_A/2$ as utilized by Chu [33][34][35]. The 1st and 2nd mechanical modes are depicted and labelled accordingly. The poling (white arrow) is shown to

be alternating (poled up in the top half and down in the bottom half) which applies for the 2nd mode only. For the 1st mode, the element is uniformly poled. (b) By use of PMC periodic boundaries, an infinite regular square antenna array may be investigated. The minimum distance between elements is defined as *d*. The boundary opposite the bisecting PEC is composed of PML layers adjacent to a PEC.

Due to the bisecting PEC only the top half of the system is modeled. Input via electrode current is applied at the bar center across electrodes spanning 10% of the axial length, hence the simulated region for electrode current input (source space) is $L_A/20$ long as shown in the Fig. 10 inset. The source space has a PEC top and bottom boundary representing an infinitely thin driving electrode and symmetry respectively. Since in the 1st mode the instantaneous stress does not change signs along the axial direction, it is intrinsically symmetrical about the bisecting PEC. The symmetry condition for the 2nd mode is justified by the alternating poling which yields an instantaneous polarization current with consistent sense in the axial direction. The bottom mechanical boundary is fixed ($v_z = 0$) for the 1st mode and traction free ($T_{zz} = 0$) for the 2nd mode to produce the requisite mechanical symmetry and anti-symmetry respectively. The top mechanical boundary is traction free for both modes.

The electrode current input is a modulated Gaussian pulse generating a 20MPa stress ringdown at the resonance frequency with $R_S = \infty$. The impedance $Z$ is then calculated from the terminal voltage and current. The peak value, at resonance, of $Re(Z)$ is the matched resistance ($R_S^{Matched}$) which is then input and a new stress ringdown simulation is performed. The simulated near-fields are used to calculate $P_{rad}^{D}$ via a NTFF transformation [25][187], where the Huygen's box in-plane surfaces are aligned with the PMC boundaries consistent with [131] and the top surface is two cells above the top of the radiator. The piezoelectric utilized for these simulations

is X4B PIN-PMN-PT from TRS Technologies [244]. The mechanical damping is assumed to be similar to AlN. Relevant simulation parameters are shown in Table 5-4.

| Symbol | Description | Value |
|---|---|---|
| $\boldsymbol{d_{33}}$ | Piezoelectric Constant | 1.320E-9 C/N |
| $\boldsymbol{d_{31}}$ | Piezoelectric Constant | -6.340E-10 C/N |
| $\boldsymbol{\epsilon_{11}^{T}}$ | Permittivity | $1335\epsilon_0$ |
| $\boldsymbol{\epsilon_{33}^{T}}$ | Permittivity | $4200\epsilon_0$ |
| $\boldsymbol{\eta_{33}}$ | Mechanical Damping | 0.02 Pa-s |
| $\boldsymbol{K_{33}^{E}}$ | Figure of Merit FoM | 81.6% |
| $\boldsymbol{\rho}$ | Density | 8141 kg/m^3 |
| $\boldsymbol{E_{33}^{D}}$ | Young's Modulus | 1.74E10 Pa |
| $\boldsymbol{\Delta x=\Delta y}$ | Spatial Sampling | 2.14E-7 m |
| $\boldsymbol{\Delta z}$ | Spatial Sampling | 3.85E-7 m |
| $\boldsymbol{\Delta z_S}$ | Spatial Sampling | 4.28E-8 m |

Table 5-4: Input parameters for the fully coupled simulation of the multimode alternate poling piezoelectric antenna array.

In the following section, the source resistance is varied to observe the effect on the stress and radiated power.

### 5.5.3 Variable Source Resistance Simulations

Figure 5-17(a) and Figure 5-17(b) show results for three source resistance $R_S$ values, i.e. 1) infinity, 2) matched value ($R_S^{Matched}$), and 3) 50Ω to evaluate stress ringdown and radiated power as a function of time and frequency respectively. The spacing for these simulations was set to *d/w* = 45.5 as at that spacing mutual depolarization is negligible (demonstrated shortly in Section 5.5.4) and all studies are conducted for the second mode. For all simulations, the

source current magnitude is the same and was set such that the maximum stress at modulated Gaussian pulse end (near time = 0) is 20MPa for the $R_S = \infty$ case.

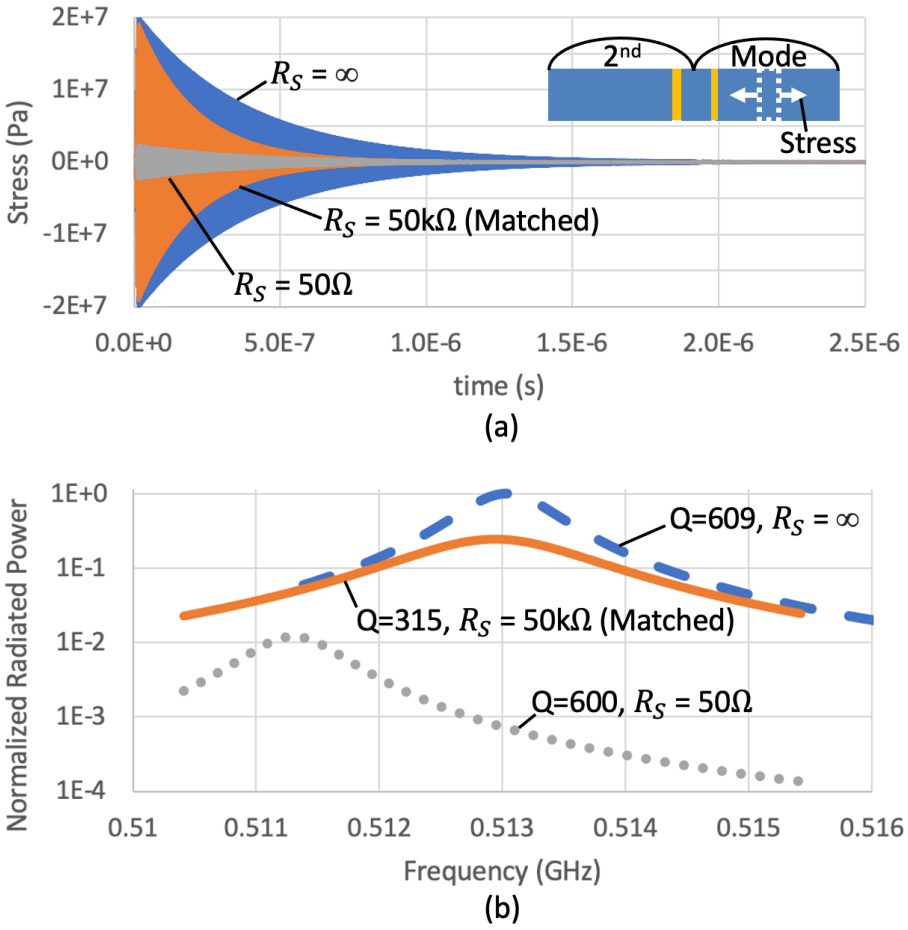


Figure 5-17: Piezoelectric antenna simulations at variable source resistance: $R_S = \infty$ (open-circuit) case, $R_S = R_S^{Matched}$ (matched) case, and $R_S = 50\Omega$ (short-circuit approximation) case. All three simulations are performed at the 2nd mechanical mode as shown in the figure inset. (a) Stress ringdown vs. time. The max stress is 20MPa for $R_S = \infty$, ~19MPa for $R_S = R_S^{Matched}$, and ~2.3 MPa for $R_S = 50\Omega$. The drop in stress is due to reduced acceptance of electrical power away from the idealized $R_S = \infty$ case where all power is accepted. The stress for $R_S = R_S^{Matched}$ rings down quicker than the other cases. (b) Normalized radiated power ($P_{rad}^{D}/P_{rad}^{Rs=\infty}$) vs. frequency plot. Dashed line is for the open circuit case. Solid line is for the matched case.

Lastly, the dotted line is for the short-circuit approximation (50Ω) case. The Q for the matched case is roughly half that of the $R_S = \infty$ and $R_S = 50\Omega$ cases since the former is the open circuit case discussed in Section 5.5.1 and the latter closely approximates the short circuit case.

Figure 5-17(a) shows the matched case reaches a stress of ~19 MPa demonstrating good acceptance of the electrical energy from the source. The 50Ω case only achieves a stress of ~2.3 MPa as the source current readily flows through $R_S$ during the initial excitation, bypassing the PEA. Since $50\Omega \ll R_S^{Matched}$ (50kΩ), the $R_S = 50\Omega$ case closely approximates the short circuit case discussed in Section 5.5.1. There are three dissipation mechanisms that cause the stress to decay: source resistance $R_S$, mechanical viscous damping $\eta_{33}$, and radiation resistance $R_{rad}$. Since the piezoelectric material and geometry are identical for each simulation, the viscous damping and radiation resistance dissipation mechanisms are not altered in this study. Since no energy can transfer to $R_S$ in the open-circuit case (infinite resistance to flow yields no flow), and no energy is lost to $R_S$ in the short-circuit case (no resistance yields no energy loss), only the matched case utilizes all dissipation mechanisms. As such, the matched case is seen to ringdown quickest. In the matched case the energy within the piezoelectric readily crosses the terminals into $R_S$, dissipating the energy. In the open/short-circuited cases, the energy remains within the piezoelectric such that $\eta_{33}$ and $R_{rad}$ are the only loss mechanisms.

Figure 5-17(b) shows the maximum power radiated arises from $R_S = \infty$ case which is because the source current perfectly transfers to the piezoelectric. Additionally, both the $R_S = 50\Omega$ and $R_S = \infty$ cases have similar high Q ~600, although at different frequencies, as expected from Section III. In contrast the matched case yields a lower Q ~315 by approximately half. This is advantageous, as the bandwidth is almost doubled (see broadening of matched case peak vs. open/short-circuited cases). The Q for the 1st mode, while not shown, is roughly twice that of the 2nd (i.e., ~1200 for the open/short-circuited cases and ~600 for the matched case). Larger

source resistances are also required for matching. This point will be further elaborated in Table 5-5 of Section 5.5.4.

While the radiated power for the matched case in Figure 5-17(b) is approximately ~25% of the open-circuited ($R_S = \infty$) case, this is due to the latter being a non-physical idealization where all the source energy is perfectly transmitted to the piezoelectric and then perfectly constrained within the device. For the remainder of this section, all results presented are for antennas where $R_S = R_S^{Matched}$. In the following Section 5.5.4, the single element performance will be determined at variable spacing *d*.

### 5.5.4 Single Element Performance

In this Section, the spacing *d* is varied by moving the in-plane boundaries via adding cells, grading the mesh, or both. For all simulations, the input current pulse is determined by demanding the maximum stress achieved in the piezoelectric is 20MPa for all cases. Figure 5-18 shows results for seven simulations per mode (14 total) to determine the normalized single element radiated power $P_{rad}^{D}/P_{rad,1st}^{Iso}$ on the left ordinate as a function of normalized spacing *d/w*. Also in the figure, the resonant frequency for the 1st and 2nd modes, normalized to constant flux resonance of the first mode $f_{r,1st}^{cD}$, are presented in the right ordinate axis.

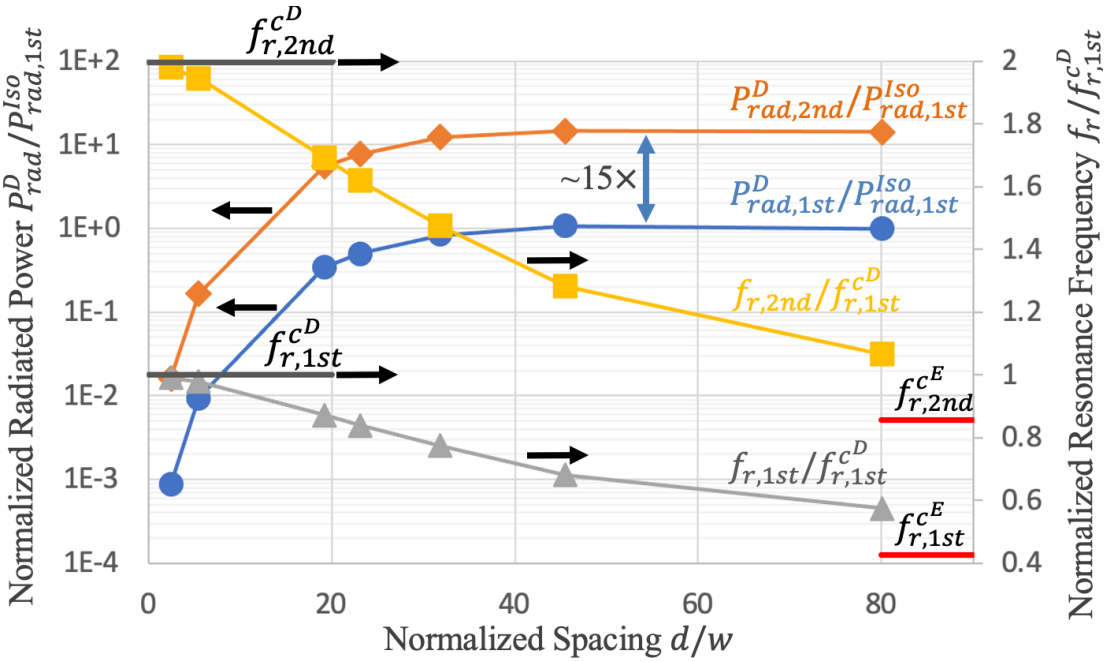


Figure 5-18: Single element normalized radiated power and normalized resonance frequency vs. normalized spacing for both modes of the infinite regular square array of Figure 5-16. Normalized power is per the left vertical axis and is logarithmic (hence the grid lines). Normalized frequency is per the right vertical axis and is not logarithmic and thus the grid lines should not be used when analyzing this data. Arrows next to each curve indicate which vertical axis should be used. The discrete points are simulated data and the solid lines between the points are to guide the eye only. Circles are for the normalized power of the 1st mode. Diamonds are for the normalized power of the 2nd mode. Triangles are for the normalized resonance frequency of the 1st mode. Squares are for the normalized resonance frequency of the 2nd mode. Solid horizontal lines on the left-hand side of the figure provide the mechanical resonance frequency at constant flux for the 1st and 2nd mode ($f_{r,1st}^{cD}$ and $f_{r,2nd}^{cD}$ respectively). Lastly, solid horizontal lines on the right-hand side of the figure provide the constant field resonance frequency ($f_{r,1st}^{cE}$ and $f_{r,2nd}^{cE}$ respectively).

As can be seen in Figure 5-18, at large spacing for both modes, the radiated power reaches a plateau value equaling that of an isolated element ($P_{rad,1st}^{Iso}$ and $P_{rad,2nd}^{Iso}$ for the 1st and 2nd modes respectively) since mutual depolarization is no longer a factor. For both modes, $P_{rad}^{D}$ decays by more than two orders of magnitude with respect to the isolated element performance if the normalized spacing is less than 5. Between 5 and 40 the radiated power quickly increases, and mutual depolarization is negligible at normalized spacing greater than 40 after which $P_{rad}^{D}$ plateaus. Hence the results previously discussed in Figure 5-17, where $d/w$ = 45.5, contain negligible mutual de-polarization. As shown in Figure 5-18, the 2nd mode isolated element radiated power $P_{rad,2nd}^{Iso}$ is ~15 times larger than $P_{rad,1st}^{Iso}$. This occurs since the electrical size of the antenna is larger in the 2nd mode (i.e. frequency 2x larger at fixed physical size) compared to the 1st. As expected from Section 5.2.1, the large changes in radiation are coupled with changes in the mechanical resonance frequency $f_r$ for both modes. When the spacing is small, the resonance frequency is roughly equal to the constant flux stiffness value ($f_r^{cD}$) and as the spacing is increased the resonance frequency trends towards the constant electric field stiffness value ($f_r^{cE}$). Interestingly, the resonance frequency shift is still quite pronounced at d/w > 40 even though the radiated power is fairly constant for each case. For example, in the 2nd mode between $d/w$ = 45.5 and $d/w$ = 80.1, a change in the radiated power of 2.2% corresponds to a change of the resonance frequency by 18.4%. This provides an interesting opportunity to tune resonance frequency within piezoelectric antenna arrays simply by altering the spacing between adjacent elements. This can potentially address concerns with the small bandwidth issues typical of high Q systems. This concept will be further explored in Section 5.5.5.

Figure 5-19 shows PEA radiation efficiency vs ka for both modes compared to the theoretical upper limit for metallic electrically small antennas (ESAs) per [164] (labelled as Helix). Also, the SLAC antenna [152] is included for comparison and labelled as Kemp. Note that the PEA under investigation fits within an enclosing sphere of radius a = $L_A/2$ normalized by

the wavenumber (ka) and the input power and radiation efficiency were calculated per (3.135) and (3.136) respectively for each simulation.

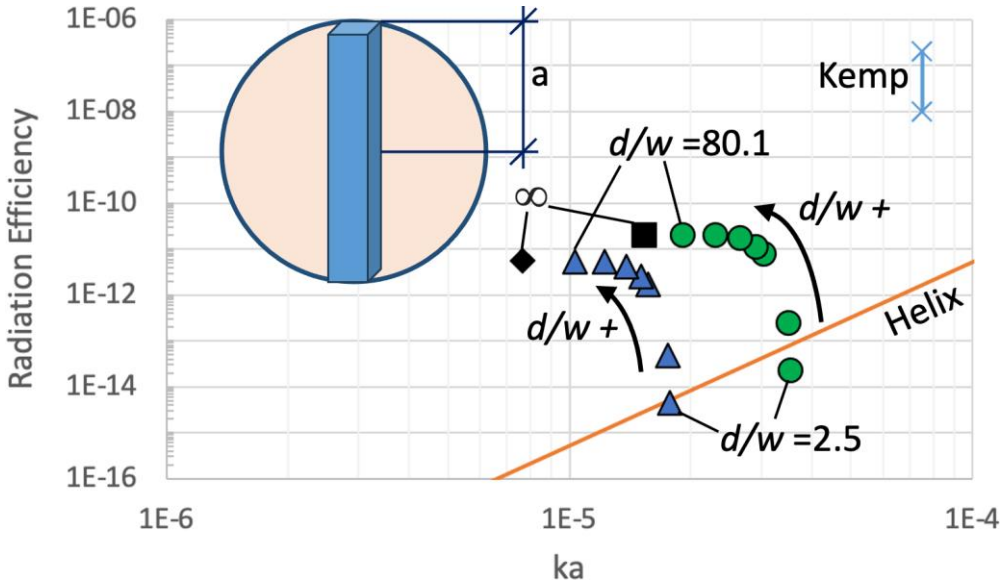


Figure 5-19: Radiation efficiency vs. ka plot for the seven simulations performed for both modes (14 total) marked as discrete points. Triangles are for the 1st mode and circles are for the 2nd mode. The smallest and largest normalized spacing (*d/w* = 2.5 and *d/w* = 80.1) are labelled numerically and arrows indicate the direction of increased spacing for both modes. The solid line labelled as "Helix" is the theoretical upper limit of metallic electrically small antennas (ESAs) as reported in [164]. Also included is the predicted isolated element performance which is marked as a discrete diamond for the 1st mode and square for the 2nd mode with *d/w* labelled as ∞. Finally, the SLAC antenna [152] predicted efficiency is marked using crosses. The SLAC authors did not directly measure efficiency but rather performed calculations to estimate efficiency based on device Q. As such, a range is provided for the SLAC efficiency in [152].

Figure 5-19 shows for both modes, all PEA antennas exceed the performance of the upper bound on metallic ESA predictions except for the single element PEA most burdened by mutual

depolarization (at *d/w* = 2.5). Furthermore, it is remarkable that even for this single element PEA and both modes it is on par with that upper ESA limit (though the 1st mode slightly outperforms the 2nd). This is particularly impressive as the axial bar design for the PEAs investigated herein is a 1D element and does not fill much of a 3D sphere (see Figure 5-16) as compared to the ESA Helix configuration in [164] representing an optimized spherical design. Therefore, while the PEA efficiencies represent significant improvements to optimized ESA, the PEA could be further optimized to increase radiation efficiency. The major reason the metallic ESAs struggle is the small radiation resistance exhibited which drops per square of frequency for electrically small dipoles and fourth order of frequency for electrically small loops [245]. The high Q resonance from the piezoelectric material provides low loss impedance matching and thus mechanical antennas do not suffer from this same problem which is fundamental to metallic ESA.

Figure 5-19 also shows the 2nd mode of the PEA has much larger ka values compared to the 1st mode. Even within the same mode, the ka value in Figure 5-19 skews to the left as *d/w* increases due to the shift in mechanical resonance frequency caused by the change in effective stiffness (see also Figure 5-18). Thus, piezoelectric array elements not only radiate more efficiently when spacing is increased but do so at smaller ka values where higher efficiency is more challenging to achieve.

Figure 5-19 also shows the predicted isolated element performance for the 1st and 2nd mode illustrated with a diamond and square respectively. The isolated elements are assumed to have the same efficiency as the respective *d/w* = 80.1 simulations (due to the plateau) but with a ka value corresponding to resonance at constant field ($f_{r,1st}^{cE}$ and $f_{r,2nd}^{cE}$ for the 1st and 2nd modes). Recall from Section 5.2.1 that the constant field state is predicted at infinite spacing (isolated element). This isolated element exhibits 30,000 times higher efficiency than the optimized Helix metallic antenna at the same ka value in the 1st mode, and 7,000 times higher efficiency in the

2nd mode. Thus, when compared to the Helix configuration, the 1st mode outperforms the 2nd mode. This is due to the larger Q exhibited in the 1st mode as shown in Table 5-5.

| Mode | *d/w* | $R_S^{Matched}$ (Ω) | Matched Q |
|---|---|---|---|
| **1** | 2.5 | 20.3e6 | 883 |
| | 5.5 | 19.7e6 | 925 |
| | 19.2 | 15.2e6 | 817 |
| | 23.1 | 13.9e6 | 779 |
| | 31.9 | 11.5e6 | 708 |
| | 45.5 | 8.84e6 | 616 |
| | 80.1 | 5.67e6 | 487 |
| **2** | 2.5 | 124e3 | 471 |
| | 5.5 | 120e3 | 446 |
| | 19.2 | 90.8e3 | 405 |
| | 23.1 | 82.4e3 | 388 |
| | 31.9 | 67.9e3 | 358 |
| | 45.5 | 50.6e3 | 315 |
| | 80.1 | 34.7e3 | 276 |

Table 5-5: Matched Q and matched resistance values.

Table 5-5 provides the general trend that the 1st mode exhibits roughly double the Q as the 2nd mode for like spacings. However, this comes with the cost of substantially larger matched resistance values, and thus larger voltages. The larger voltages thus make the 1st mode operation more unruly from a systems electronics perspective. Larger spacing does mitigate this issue however as smaller source resistances are required for matching. Regardless, Figure 5-19 demonstrates that properly implemented piezoelectric antennas outperform state-of-the-art metallic antennas for small ka values for both modes. The array performance is explored in the following Section 5.5.5.

### 5.5.5 Array Efficiency for Multimode Alternate Poling Piezoelectric Antenna Array

Figure 5-20 shows array efficiency vs. spacing of PEA elements spread out in square fashion enclosed within a circle of diameter D = 1mm (see Figure 5-20 inset). The array efficiency is calculated by multiplying the simulated near-fields and input power by the number of array elements. Due to the relatively small electrical spacing, the array factor is nearly isotropic (spherical), as discussed in Section 5.4.4, indicating the approximation is accurate.

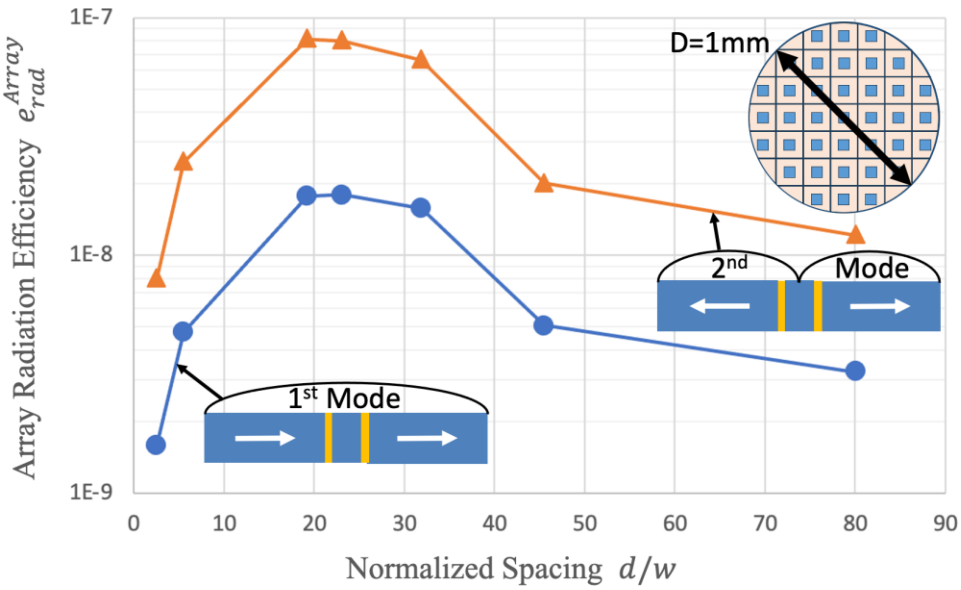


Figure 5-20: Array efficiency versus normalized spacing plot where the solid lines between data points are to guide the eye only. Array is enclosed within circle of fixed physical size of 1mm. Curve with circles is for the 1st mode and curve with triangles is for the 2nd mode. Both modes experience a performance peak at approximately *d/w* = 20.

Figure 5-20 shows an interesting array efficiency performance peak for specific PEA spacings. If the spacing is too large, then there will not be sufficient element density to produce strong radiation efficiencies. If the spacing is too small, then the presence of mutual depolarization between elements dramatically reduces the radiation efficiency. In between these

two extremes, a performance peak is found as a balance between insufficient densities and large depolarization influences. Attempting to approximate an operational range introduces an interesting novel concept as discussed in Section 5.5.6.

### 5.5.6 Mechanically Tuned Half-Power Bandwidth HPBW

To find an approximate optimal spacing range, first note that the input power is relatively unchanged with spacing (<10% variation). Thus, the array efficiency points in Figure 5-20 are synonymous with array radiation, simply multiply each point by the static input power. A common method of defining a performance band is by using the half-power. For example, the half-power bandwidth HPBW is the frequency range where at least half the peak power is achieved. Following this logic, the peak array efficiency value (synonymous with array power) is divided by two and the range of spacings that achieve at least the half efficiency (power) are determined. For the 1$^{st}$ mode, the *d*/*w* range is approximately between 10 and 40.5. For the 2$^{nd}$ mode, the range is approximately between 9.5 and 39.5. Interestingly, per Figure 5-18, changes in spacing correspond to changes in resonance frequency. Thus, the half-power spacing band may be mapped to a half-power frequency band which is referred to as the “mechanically tuned half-power bandwidth” herein. This bandwidth is approximately 286MHz – 378MHz (92MHz) for the 1$^{st}$ mode and 546MHz – 748MHz (202MHz) for the 2$^{nd}$ mode as shown in Figure 5-21 where each band is represented as a bar. The y-axis distinguishes the 1$^{st}$ mode from the 2$^{nd}$.

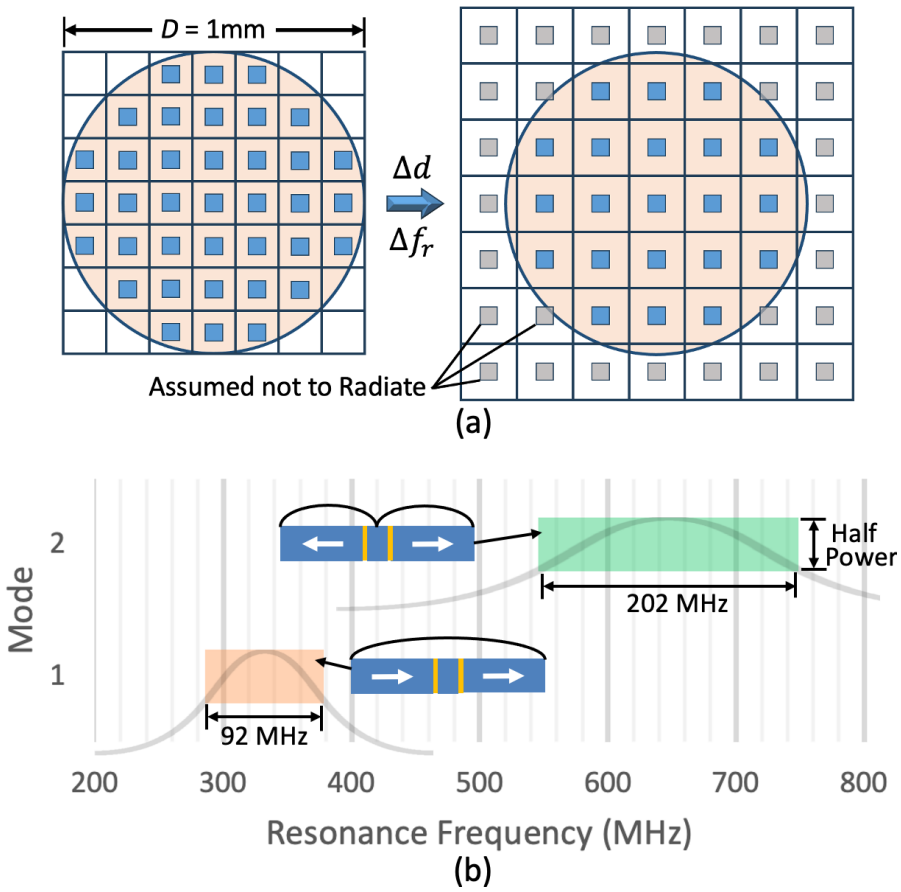


Figure 5-21: Mechanically tuned half-power bandwidth HPBW for the D = 1mm piezoelectric antenna array of Figure 5-20. (a) As the spacing is increased, only the piezoelectric antennas still within the 1mm diameter are assumed to radiate (i.e., the gray semi-transparent elements are assumed not to radiate). The mechanically tuned HPBW determined herein is thus conservative. (b) The HPBW for the 1st and 2nd mode vs. the frequency in Hertz on the horizontal axis. The bottom bar is for the 1st mode and the top bar is for the 2nd mode.

To re-iterate, the mechanically tuned HPBW is 92MHz for the 1st mode and 202MHz for the 2nd mode. This corresponds to ~25% of the maximal $f_r^{cD}$ value for each mode (400MHz and 800MHz respectively). Thus, a broad range of frequencies can be achieved by altering the spacing amongst elements within a piezoelectric antenna array. Coupling this with other methods, such as direct antenna modulation (DAM) [248][249], thus can potentially solve the

bandwidth issue for electrically small high Q piezoelectric antenna arrays. Of course, the source resistance will also need to be changed as the spacing is changed for optimal performance. Still, since the elements lying outside of the 1mm diameter are assumed not to radiate per Figure 5-21a, the mechanically tuned HPBW of Figure 5-21b is a conservative estimate.

### 5.5.7 Conclusion

Full wave simulations capturing electrodynamic and elastodynamic wave physics simultaneously within the same simulation space are used to characterize the performance of multimode piezoelectric antenna array platforms. It was found that spacing within these arrays should not be made too small to induce undue mutual depolarization and not be made too large as to limit the number of array elements. Also, it was found that significant changes in resonance frequency, while still maintaining at least half the peak radiation, can be induced within these arrays by changing the array spacing. This so-called mechanically tuned half-power bandwidth is ~25% the highest resonance frequency. The simulations performed provide guidance for future designs.

# REFERENCES


[1] Newton, Isaac. Philosophiæ Naturalis Principia Mathematica. Vol. 2. typis A. et JM Duncan, 1833.

[2] Newton, Isaac. The mathematical principles of natural philosophy. Beyond Books Hub, 1964.

[3] Geggel, Laura. “Isaac Newton’s Book Auctioned for Record-Setting $3.7 Million” livescience.com, December 15, 2016.

[4] B.A. Auld, Acoustic Fields and Waves in Solids, No. I. Wiley, New York, 1973.

[5] Hibbeler, Russell Charles. Mechanics of materials. Pearson Educación, 2005.

[6] Yang, Bingen. Stress, strain, and structural dynamics: an interactive handbook of formulas, solutions, and MATLAB toolboxes. Academic Press, 2005.

[7] Eisberg, Robert, and Robert Resnick. Quantum physics of atoms, molecules, solids, nuclei, and particles. 1985.

[8] O’Handley, R. C. "Modern Magnetic Materials." Principles and Applications (Johns Wiley & Sons, Inc., 2000) (1999).

[9] Cullity, Bernard Dennis, and Chad D. Graham. Introduction to magnetic materials. John Wiley & Sons, 2011.

[10] Merzbacher, Eugen (1998). Quantum Mechanics (3rd ed.). pp. 372–373.

[11] Griffiths, David (2005). Introduction to Quantum Mechanics (2nd ed.). pp. 183–184.

[12] H. C. Oersted, “Experiments on the effect of a current of electricity on the magnetic needles,” in Proc. Ann. Philos., London, vol. 16. 1820, pp. 273–277.

[13] Oersted, Hans Christian. "On electro-magnetism." Annals of Philosophy 2 (1821): 321-337.

[14] A. G. Gurevich and G. A. Melkov, Magnetization oscillations and waves. CRC press, 1996.

[15] Landau, L. D., and E. M. Lifshitz. 1935. “On the Theory of the Dispersion of Magnetic Permeability in Ferromagnetic Bodies.” Physikalische Zeitschrift Der Sowjetunion 8: 153–169.

[16] Gilbert, Thomas L. "A Lagrangian formulation of the gyromagnetic equation of the magnetization field." Phys. Rev. 100 (1955): 1243.

[17] Maxwell, James Clerk. "Xxv. on physical lines of force: Part i.–the theory of molecular vortices applied to magnetic phenomena." The London, Edinburgh, and Dublin Philosophical Magazine and Journal of Science 21.139 (1861): 161-175.

[18] Maxwell, James Clerk. "LI. On physical lines of force." The London, Edinburgh, and Dublin Philosophical Magazine and Journal of Science 21.141 (1861): 338-348.

[19] Maxwell, James Clerk. "III. On physical lines of force." The London, Edinburgh, and Dublin Philosophical Magazine and Journal of Science 23.151 (1862): 12-24.

[20] Maxwell, James Clerk. "XIV. On physical lines of force." The London, Edinburgh, and Dublin Philosophical Magazine and Journal of Science 23.152 (1862): 85-95.

[21] J. C. Maxwell, A Treatise on Electricity und Magnetism. London, U.K.: Oxford Univ. Press, 1873, 1904.

[22] Heaviside, O. (1893). Electromagnetic Theory. Boston: "The Electrician" printing and publishing company, limited.

[23] J. W. Arthur, "The Evolution of Maxwell's Equations from 1862 to the Present Day," in IEEE Antennas and Propagation Magazine, vol. 55, no. 3, pp. 61-81, June 2013, doi: 10.1109/MAP.2013.6586627.

[24] Guilmette, Lindsay. "The History of Maxwell's Equations." (2012).

[25] C. A. Balanis, Advanced Engineering Electromagnetics, 2nd ed. New York, NY, USA: Wiley, 2012.

[26] C. A. Balanis, Antenna Theory: Analysis and Design (John Wiley & Sons, 2012).

[27] C. A. Balanis, “Antenna theory: A review,” Proc. IEEE 80, 7–23 (1992).

[28] J. D. Kraus, “Antennas since Hertz and Marconi,” IEEE Trans. Antennas Propagut., vol. AP-33, pp. 131-137, Feb. 1985.

[29] D. M. Pozar, Microwave Engineering, 3rd ed. Hoboken, NJ, USA:Wiley, 2005.

[30] D. M. Pozar, “Microstrip Antennas,” Proc. IEEE, vol. 80, no. 1, pp. 79– 81, Jan. 1992.

[31] G. A. Deschamps, “Microstrip microwave antennas,” presented at the Third USAF Symp. on Antennas, 1953.

[32] H. Gutton and G. Baissinot, “Flat aerial for ultra high frequencies,” French Patent no. 703 113, 1955.

[33] L. J. Chu, “Physical limitations of omni-directional antennas,” J. Appl. Phys., vol. 19, no. 12, pp. 1163–1175, Dec. 1948.

[34] R. C. Hansen, “Fundamental limitations in antennas,” Proc. IEEE 69, 170–182 (1981).

[35] J. S. McLean, “A re-examination of the fundamental limits on the radiation Q of electrically small antennas,” IEEE Trans. Antennas Propag. 44, 672 (1996).

[36] H. Wheeler, “Small antennas,” IEEE Trans. Antennas Propag. 23, 462–469 (1975).

[37] Mosallaei, H. & Sarabandi, K. Antenna miniaturization and bandwidth enhancement using a reactive impedance substrate. IEEE Trans. Antennas Propag 52, 2403–2414 (2004).

[38] J. C. -. Sten, A. Hujanen and P. K. Koivisto, "Quality factor of an electrically small antenna radiating close to a conducting plane," in IEEE Transactions on Antennas and Propagation, vol. 49, no. 5, pp. 829-837, May 2001, doi: 10.1109/8.929637.

[39] I. F. Akyildiz, P. Wang, and Z. Sun, “Realizing underwater communication through magnetic induction,” IEEE Commun. Mag. 53, 42 (2015).

[40] Z. Sun and I. F. Akyildiz, “Underground wireless communication using magnetic induction,” in 2009 IEEE International Conference on Communications (IEEE, 2009).

[41] P. Soontornpipit, C. M. Furse, and Y. C. Chung, “Design of implantable microstrip antenna for communication with medical implants,” IEEE Trans. Microw. Theory Tech. 52, 1944 (2004).

[42] Z. -Q. Liu, Y. -S. Zhang, Z. Qian, Z. P. Han and W. Ni, "A Novel Broad Beamwidth Conformal Antenna on Unmanned Aerial Vehicle," in IEEE Antennas and Wireless Propagation Letters, vol. 11, pp. 196-199, 2012, doi: 10.1109/LAWP.2012.2187321.

[43] C. Loecker, P. Knott, R. Sekora and S. Algermissen, "Antenna design for a conformal antenna array demonstrator," 2012 6th European Conference on Antennas and Propagation (EUCAP), 2012, pp. 151-153, doi: 10.1109/EuCAP.2012.6206004.

[44] Tuss, J., et. al., "Conformal Load-bearing Antenna Structure (CLAS)," 37th AIAA SDM Conference, Salt Lake City, UT, April 1996.

[45] Hopkins, Mark, et al. "Smart skin conformal load-bearing antenna and other smart structures developments." 38th Structures, Structural Dynamics, and Materials Conference. 1997.

[46] D. F. Rivera and R. Bansal, “Towed antennas for US submarine communications: A historical perspective,” IEEE Antennas Propag. Mag. 46, 23 (2004).

[47] Tjong FV, Brouwer TF, Smeding L, Kooiman KM, de Groot JR, Ligon D, Sanghera R, Schalij MJ, Wilde AA, Knops RE. Combined leadless pacemaker and subcutaneous implantable defibrillator therapy: feasibility, safety, and performance.Europace. 2016; 18:1740–1747. doi: 10.1093/europace/euv457.

[48] L. Bereuter et al., “Leadless dual-chamber pacing—A novel communication method for wireless pacemaker synchronization,” JACC Basic Transl. Sci., vol. 3, no. 6, pp. 813–822, Dec. 2018.

[49] L. Bereuter et al., "Fundamental Characterization of Conductive Intracardiac Communication for Leadless Multisite Pacemaker Systems," in IEEE Transactions on Biomedical Circuits and Systems, vol. 13, no. 1, pp. 237-247, Feb. 2019, doi: 10.1109/TBCAS.2018.2886042.

[50] S. M. Asif, A. Iftikhar, B. D. Braaten, D. L. Ewert and K. Maile, "A Wide-Band Tissue Numerical Model for Deeply Implantable Antennas for RF-Powered Leadless Pacemakers," in IEEE Access, vol. 7, pp. 31031-31042, 2019, doi: 10.1109/ACCESS.2019.2902981.

[51] G. S. Ohm (1827). Die galvanische Kette, mathematisch bearbeitet (PDF). Berlin: T. H. Riemann. Archived from the original (PDF) on 2009-03-26.

[52] Svoboda, James A., and Richard C. Dorf. Introduction to electric circuits. John Wiley & Sons, 2013.

[53] G. Li and J. Cheng, "Exploring the Effects of Traffic Density on Merging Behavior," in IEEE Access, vol. 7, pp. 51608-51619, 2019, doi: 10.1109/ACCESS.2019.2911302.

[54] Gerhart, Andrew L., John I. Hochstein, and Philip M. Gerhart. Munson, Young and Okiishi's Fundamentals of Fluid Mechanics. John Wiley & Sons, 2020.

[55] Vopson M M 2015 Fundamentals of multiferroic materials and their possible applications Crit. Rev. Solid State Mater. Sci. 40 223–50.

[56] R. J. Miller, W. P. Geren, and S. P. Hubbell, “Multiferroic antenna/sensor,” U.S. Patent 20 110 062 955, Mar. 17, 2011.

[57] M. Manteghi and A. A. Y. Ibraheem, “On the study of the near-fields of electric and magnetic small antennas in lossy media,” IEEE Trans. Antennas Propag. 62, 6491 (2014).

[58] Kittel, Charles. "Introduction to solid state physics Eighth edition." (2021).

[59] Salje, Ekhard KH. "Ferroelastic materials." Annual Review of Materials Research 42 (2012): 265-283.

[60] L.H. Brixner, P.E. Bierstedt, W.F. Jaep, J.R. Barkley, α-Pb3(PO4)2 — A pure ferroelastic, Materials Research Bulletin, Volume 8, Issue 5, 1973, Pages 497-503, ISSN 0025-5408.

[61] Salje, E., and G. Hoppmann. "Direct observation of ferroelasticity in Pb3 (PO4) 2 Pb3 (VO4) 2." Materials Research Bulletin 11.12 (1976): 1545-1549.

[62] Salje, E. K. H., et al. "Lattice parameters, spontaneous strain and phase transitions in Pb3 (PO4) 2." Acta Crystallographica Section B: Structural Science 49.3 (1993): 387-392.

[63] Chopra, Inderjit, and Jayant Sirohi. Smart structures theory. Vol. 35. Cambridge University Press, 2013.

[64] Moulson, Anthony J., and John M. Herbert. Electroceramics: materials, properties, applications. John Wiley & Sons, 2003.

[65] Chaplya, P. M. and Carman, G. P., Dielectric and piezoelectric re- sponse of lead zirconate-lead titanate at high electric and mechanical loads in terms of non-180◦ domain wall motion. J. Appl. Phys. 2001, 90(10), 5278–5286.

[66] Pabst, Willi, and E. V. A. Gregorová. "Elastic properties of silica polymorphs–a review." Ceramics-Silikaty 57.3 (2013): 167-184.

[67] C.S. Lynch, The effect of uniaxial stress on the electro-mechanical response of 8/65/35 PLZT, Acta Materialia, Volume 44, Issue 10, 1996, Pages 4137-4148, ISSN 1359-6454.

[68] Zhou, Dayu, Marc Kamlah, and Dietrich Munz. "Effects of uniaxial prestress on the ferroelectric hysteretic response of soft PZT." Journal of the European Ceramic Society 25.4 (2005): 425-432.

[69] N. A. Hill, “Why are there so few magnetic ferroelectrics?” J. Phys. Chem. B, vol. 104, no. 29, p. 6694, Jun. 2000.

[70] Joule, J. P., (1842) "On a new class of magnetic forces," (Sturgeons) Annals of Electricity, Magnetism, and Chemistry, 8, 219-224.

[71] Joule, J. P., (1847) "On the Effects of Magnetism upon the Dimensions of Iron and Steel Bars," Philisophical Magazine, 30, 76-87.

[72] Villari, E., (1864) "Intorno alle modificazioni del momento magnetico di una verga di ferro e di acciacom, prodotte par la trazione della medisma e pel passagio di una corrente attraverso la stessa," In Nouvo Cimento, 20, 317-362.

[73] Tremolet de Lacheisserie, E., (1993) Magnetostriction : theory and applications of magnetoelasticity, CRC Press.

[74] Schneider, Joseph Devin. *Next Generation Acoustic and Magnetic Devices for Radio Frequency Communication*. University of California, Los Angeles, 2020.

[75] N. A. Spaldin and R. Ramesh, “Advances in magnetoelectric multiferroics,” Nat. Mater., vol. 18, no. 3, pp. 203–212, Mar. 2019, doi: 10.1038/s41563-018-0275-2.

[76] Liu, Ming, and Nian X. Sun. "Voltage control of magnetism in multiferroic heterostructures." Philosophical Transactions of the Royal Society A: Mathematical, Physical and Engineering Sciences 372.2009 (2014): 20120439.

[77] G. P. Carman and N. Sun, “Strain-mediated magnetoelectrics: Turning science fiction into reality,” MRS Bull., vol. 43, no. 11, pp. 822–828, Nov. 2018, doi: 10.1557/mrs.2018.236.

[78] M. Fiebig, T. Lottermoser, D. Meier, and M. Trassin, “The evolution of multiferroics,” Nat. Rev. Mater., vol. 1, no. 8, pp. 1–14, Jul. 2016, doi: 10.1038/natrevmats.2016.46.

[79] A. K. Zvezdin and A. P. Pyatakov, “Phase transitions and the giant magnetoelectric effect in multiferroics,” Physics-Uspekhi, vol. 47, no. 4, pp. 416–421, Apr. 2004, doi: 10.1070/pu2004v047n04abeh001752.

[80] L. Mitoseriu and V. Buscaglia, “Intrinsic/extrinsic interplay contributions to the functional properties of ferroelectric-magnetic composites,” Phase Transitions, vol. 79, no. 12, pp. 1095–1121, Dec. 2006.

[81] S. Gong, R. Lu, Y. Yang, L. Gao and A. E. Hassanien, "Microwave Acoustic Devices: Recent Advances and Outlook," in IEEE Journal of Microwaves, vol. 1, no. 2, pp. 601-609, April 2021, doi: 10.1109/JMW.2021.3064825.

[82] Robert E. Newnham, Properties of materials: anisotropy, symmetry, structure. Oxford University Press on Demand, 2005.

[83] Liang, Xianfeng, et al. "A review of thin-film magnetoelastic materials for magnetoelectric applications." Sensors 20.5 (2020): 1532.

[84] G. Lawes and G. Srinivasan, “Introduction to magnetoelectric coupling and multiferroic films,” J. Phys. D. Appl. Phys., vol. 44, p. 243001, 2011, doi: 10.1088/0022-3727/44/24/243001.

[85] Spaldin, Nicola A., and Manfred Fiebig. "The renaissance of magnetoelectric multiferroics." Science 309.5733 (2005): 391-392.

[86] Buschow, KH Jürgen. Handbook of magnetic materials. Elsevier, 2003.

[87] Hossain, Shadeeb, Ruyan Guo, and Amar Bhalla. "Analysis using physics model to understand magnetoelectric nanorobotic structures for targeted cell manipulation." Ferroelectrics 585.1 (2021): 70-87.

[88] Nye, John Frederick. Physical properties of crystals: their representation by tensors and matrices. Oxford university press, 1985.

[89] P. Curie, “Sur la symétrie dans les phénomènes physiques, symétrie d‘un champ électrique et d’un champ magnétique,” Journal de Physique Théorique et Appliquée, vol. 3, no. 1, pp. 393–415, 1894.

[90] P. Debye, “New experiments on a magneto-electric directive effect,” Z. Phy., vol. 36, no. 4, pp. 300–301, 1926.

[91] H. Schmid, “Multiferroic magnetoelectrics,” Ferroelectrics, 162, 317-338, 1994.

[92] L. Landau and E. Lifshitz, Electrodynamics of continuous medium. Gostechizdat: Moscow, 1957.

[93] Ryu, Jungho, et al. "Magnetoelectric effect in composites of magnetostrictive and piezoelectric materials." *Journal of electroceramics* 8.2 (2002): 107-119.

[94] Van Suchtelen, J. "Product properties: a new application of composite materials." *Phillips Research Reports* 27 (1972): 28-37.

[95] Dong, Shuxiang et al. “Magnetoelectric effect in Terfenol-D/ Pb(ZrTiO)3/u-metallaminate composites.” Applied Physics Letters, 2006, vol. 89, pp. 122903-1-122903-3.

[96] Ma J, Hu J, Li Z and Nan C W 2011 Recent progress in multiferroic magnetoelectric composites: from bulk to thin films Adv. Mater. 23 1062–87.

[97] L. W. Martin, S. P. Crane, Y-H Chu, M. B. Holcomb, M. Gajek, M. Huijben, C-H Yang, N. Balke and R. Ramesh, “Multiferroics and magnetoelectrics: thin films and nanostructures,” J. Phys.: Condens. Matter 20, 2008.

[98] Nan, C.W.; Bichurin, M.I.; Dong, S.; Viehland, D.; Srinivasan, G. Multiferroic magnetoelectric composites: Historical perspective, status, and future directions. J. Appl. Phys. 2008, 103, 031101.

[99] la. P. Terletskii, "Production of very strong magnetic fields by rapid compression of a conducting shell," J. Exptl. Theoret. Phys. Trans!. (U.S.S.R.) 32, 301 (1957) (from a 1952 article).

[100] Fowler, C. M., W. B. Garn, and R. S. Caird. "Production of very high magnetic fields by implosion." Journal of Applied Physics 31.3 (1960): 588-594.

[101] J. H. Rowen, F. G. Eggers, and W. Strauss, “Generation of microwave electromagnetic radiation in magnetic materials,” J. Appl. Phys. 32, S313–S315 (1961).

[102] R. D. Mindlin, “Electromagnetic radiation from a vibrating quartz plate,” Int. J. Solids Structures, vol. 9, pp. 697–702, 1973.

[103] H. F. Tiersten, the radiation and confinement of electromagnetic energy accompanying the oscillation of piezoelectric crystal plates, Recent Advances in Engineering Science, Vol. 5, pp. 63-90. Gordon and Breach (1970).

[104] P. C. Y. Lee, “Electromagnetic radiation from an AT-cut quartz plate under lateral-field excitation,” J. Appl. Phys., vol. 65, no. 4, pp. 1395–1399, Feb. 1989.

[105] P. C. Y. Lee, “Electromagnetic radiation from doubly rotated piezoelectric crystal plates vibrating at thickness frequencies,” J. Appl. Phys., vol. 67, no. 11, pp. 6633–6642, Jun. 1990.

[106] R. V. Petrov et al., “Miniature antenna based on magnetoelectric composites,” Electron. Lett. vol. 44, no. 8, pp. 506–508, Apr. 2008.

[107] G.-M. Yang et al., “Electronically tunable miniaturized antennas on magnetoelectric substrates with enhanced performance,” IEEE Trans. Magn., vol. 44, no. 11, pp. 3091–3094, Nov. 2008.

[108] S. M. Keller, “Wave propagation in multiferroic materials,” Ph.D. thesis, University of California, Los Angeles, 2013.

[109] Yao, Zhi. Dynamic Analysis of Thin Film Multiferroic Radiation via FDTD Methods. University of California, Los Angeles, 2014.

[110] Z. Yao and Y. Ethan Wang, "Dynamic analysis of acoustic wave mediated multiferroic radiation via FDTD methods," 2014 IEEE Antennas and Propagation Society International Symposium (APSURSI), 2014, pp. 731-732, doi: 10.1109/APS.2014.6904695.

[111] T. Nan, H. Lin, Y. Gao, A. Matyushov, G. Yu, H. Chen, N. Sun, S. Wei, Z. Wang, M. Li, X. Wang, A. Belkessam, R. Guo, B. Chen, J. Zhou, Z. Qian, Y. Hui, M. Rinaldi, M. E. McConney, B. M. Howe, Z. Hu, J. G. Jones, G. J. Brown, and N. X. Sun, “Acoustically actuated ultra-compact NEMS magnetoelectric antennas,” Nat. Commun. 8, 1 (2017).

[112] H. J. Kim, S. Wang, C. Xu, D. Laughlin, J. Zhu and G. Piazza, "Piezoelectric/magnetostrictive MEMS resonant sensor array for in-plane multi-axis magnetic field detection," 2017 IEEE 30th International Conference on Micro Electro Mechanical Systems (MEMS), 2017, pp. 109-112, doi: 10.1109/MEMSYS.2017.7863352.

[113] Q. Li, Y. Yao, J. Yu and X. Chen, "Miniaturized Magnetoelectric Antenna Based on FBAR Structured Acoustic Excitation," 2020 Cross Strait Radio Science & Wireless Technology Conference (CSRSWTC), 2020, pp. 1-3, doi: 10.1109/CSRSWTC50769.2020.9372696.

[114] Z. Yao, Y. E. Wang, S. Keller and G. P. Carman, "Bulk Acoustic Wave-Mediated Multiferroic Antennas: Architecture and Performance Bound," in IEEE Transactions on Antennas and Propagation, vol. 63, no. 8, pp. 3335-3344, Aug. 2015, doi: 10.1109/TAP.2015.2431723.

[115] Keller, Scott Macklin, et al. "Multiferroic surface acoustic wave antenna." U.S. Patent No. 9,660,349. 23 May 2017.

[116] A MEchanically Based Antenna (AMEBA) Proposers Day. Available online: https://www.darpa.mil/news-events/ameba-proposers-day (accessed on February 15, 2022).

[117] Underwater Radio, Anyone?. Available online: https://www.darpa.mil/news-events/2016-12-16 (accessed on February 15, 2022).

[118] The Biggest Little Antenna in the World. Available online: http://arlassociates.net/Newman%20AP%20Presentation.pdf (accessed on February 15, 2022).

[119] P. Hansen and D. Rodriguez, “High power VLF/LF transmitting antennas- Wheeler’s circuit approximations applied to power limitations,” in Proc. IEEE Int. Symp. Antennas Propag., 2012, pp. 1–2.

[120] P. Hansen, J. Chavez, VLF Cutler: Four-Panel tests; RADHAZARD Field Strength Measurement, Tech Report 1761, Jan 1998.

[121] J. Xu, C. M. Leung, X. Zhuang, J. Li, S. Bhardwaj, J. Volakis, and D. Viehland, “A low frequency mechanical transmitter based on magnetoelectric heterostructures operated at their resonance frequency,” Sensors 19, E853 (2019).

[122] J. P. Domann and G. P. Carman, “Strain powered antennas,” J. Appl. Phys., vol. 121, no. 4, 2017, Art. no. 044905.

[123] Zaeimbashi, Mohsen, et al. "NanoNeuroRFID: A Wireless Implantable Device Based on Magnetoelectric Antennas." IEEE Journal of Electromagnetics, RF and Microwaves in Medicine and Biology (2019).

[124] Z. Yao and Y. E. Wang, “3D unconditionally stable FDTD modeling of micromagnetics and electrodynamics,” in Proc. IEEE Int. Microw. Symp., Honolulu, HI, USA, Jun. 2017, pp. 12–15.

[125] Z. Yao, R. U. Tok, T. Itoh, and Y. E. Yang, “A Multiscale Unconditionally Stable Time-Domain (MUST) Solver Unifying Electrodynamics and Micromagnetics,” IEEE Trans. Microw. Theory Tech., vol 66, no. 6, pp. 2683-2696, 2018.

[126] R. L. Kubena, X. Pang, K. G. Lee, Y. K. Yong, and W. S. Wall, “Wide-band multiferroic quartz MEMS antennae,” J. Phys. Conf. Ser. 1407, 012026 (2019).

[127] J. D. Schneider et al., “Experimental demonstration and operating principles of a multiferroic antenna,” Journal of Applied Physics 126, 224104 (2019).

[128] Z. Yao, H. Cui and Y. E. Wang, "3D Finite-Difference Time-Domain (FDTD) Modeling of Nonlinear RF Thin Film Magnetic Devices," 2019 IEEE MTT-S International Microwave Symposium (IMS), 2019, pp. 110-113, doi: 10.1109/MWSYM.2019.8700968.

[129] H. Suhl, “The nonlinear behavior of ferrites at high microwave signal levels,” Proceedings of the IRE, vol. 44, no. 10, pp. 1270-1284, Oct. 1956.

[130] C. Dong et al., "A Portable Very Low Frequency (VLF) Communication System Based on Acoustically Actuated Magnetoelectric Antennas," in IEEE Antennas and Wireless Propagation Letters, vol. 19, no. 3, pp. 398-402, March 2020, doi: 10.1109/LAWP.2020.2968604.

[131] Z. Yao et al., "Modeling of Multiple Dynamics in the Radiation of Bulk Acoustic Wave Antennas," in IEEE Journal on Multiscale and Multiphysics Computational Techniques, vol. 5, pp. 5-18, 2020, doi: 10.1109/JMMCT.2019.2959596.

[132] F. Rangriz, A. Khaleghi and I. Balasingham, "Wireless Link for Micro-scale Biomedical Implants using Magnetoelectric Antennas," 2020 14th European Conference on Antennas and Propagation (EuCAP), 2020, pp. 1-4, doi: 10.23919/EuCAP48036.2020.9136028.

[133] Zheng, Xiaojing. "A nonlinear constitutive model for magnetostrictive materials." Acta Mechanica Sinica 21.3 (2005): 278-285.

[134] Luong, Kevin QT, and Yuanxun Ethan Wang. "Analysis of Dynamic Magnetoelastic Coupling in Mechanically Driven Magnetoelectric Antennas." Sensors 22.2 (2022): 455.

[135] Guokai Xu, Shaoqiu Xiao, Yan Li, Bing-Zhong Wang, Modeling of electromagnetic radiation-induced from a magnetostrictive/piezoelectric laminated composite, Physics Letters A, Volume 385, 2021, 126959, ISSN 0375-9601.

[136] Yun, Xiaofan, et al. "Bandwidth-enhanced magnetoelectric antenna based on composite bulk acoustic resonators." *Applied Physics Letters* 121.3 (2022).

[137] F. R. Rostami, A. Khaleghi and I. Balasingham, "Computer Simulation of Magnetoelectric Antenna and Performance Comparison With Micro-Loop," in IEEE Access, vol. 10, pp. 64473-64482, 2022, doi: 10.1109/ACCESS.2022.3183107.

[138] Will-Cole, A. R., et al. "Tutorial: Piezoelectric and magnetoelectric N/MEMS—Materials, devices, and applications." *Journal of Applied Physics* 131.24 (2022).

[139] Zheng, Ruoda, et al. "A Lamb wave magnetoelectric antenna design for implantable devices." *Applied Physics Letters* 122.20 (2023).

[140] M. I. Bichurin et al., “Theory of magnetoelectric effects at microwave frequencies in a piezoelectric magnetostrictive multilayer composite,” Phys. Rev. B, vol. 64, no. 9, p. 094409, Aug. 2001.

[141] R. Ramesh and N. A. Spaldin, “Multiferroics: Progress and prospects in thin films,” Nat. Mater., vol. 6, no. 1, pp. 21–29, Jan. 2007.

[142] C. W. Nan, M. I. Bichurin, S. Dong, D. Viehland, and G. Srinivasan, “Multiferroic magnetoelectric composites: Historical perspective, status, and future directions,” J. Appl. Phys., vol. 103, no. 3, pp. 031101-1– 031101-34, 2008, art. no. 031101.

[143] C. A. F. Vaz, J. Hoffman, C. H. Ahn, and R. Ramesh, “Magnetoelectric coupling effects in multiferroic complex oxide composite structures,” Adv. Mater., vol. 22, nos. 26–27, pp. 2900–2905, 2010.

[144] Nan, C. W., Bichurin, M. I., Dong, S., Viehland, D. & Srinivasan, G. Multiferroic magnetoelectric composites: historical perspective, status, and future directions. J. Appl. Phys. 103, 031101 (2008).

[145] Hu, J.-M., Nan, T., Sun, N. X. & Chen, L.-Q. Multiferroic magnetoelectric nanostructures for novel device applications. MRS. Bull 40, 728–735 (2015).

[146] Chu, Zhaoqiang, MohammadJavad PourhosseiniAsl, and Shuxiang Dong. "Review of multi-layered magnetoelectric composite materials and devices applications." Journal of Physics D: Applied Physics 51.24 (2018): 243001.

[147]Weiler, M. et al. Elastically driven ferromagnetic resonance in nickel thin films. Phys. Rev. Lett. 106, 117601 (2011).

[148]Gowtham, P. G., Moriyama, T., Ralph, D. C. & Buhrman, R. A. Traveling surface spin-wave resonance spectroscopy using surface acoustic waves. J. Appl. Phys. 118, 233910 (2015).

[149]Labanowski, D., Jung, A. & Salahuddin, S. Power absorption in acoustically driven ferromagnetic resonance. Appl. Phys. Lett. 108, 22905 (2016).

[150]Labanowski, D., A. Jung, and S. Salahuddin. "Effect of magnetoelastic film thickness on power absorption in acoustically driven ferromagnetic resonance." *Applied Physics Letters* 111.10 (2017): 102904.

[151]Jung, Adi, et al. "Double-peaked resonance in harmonic-free acoustically driven ferromagnetic resonance." *Applied Physics Letters* 119.14 (2021): 142403.

[152]M. A. Kemp et al., “A high Q piezoelectric resonator as a portable VLF transmitter,” Nature Commun., vol. 10, no. 1, pp. 1715–1721, 2019.

[153]A. E. Hassanien, M. Breen, M.-H. Li, and S. Gong, “Acoustically driven and modulation inducible radiating elements,” 2019, arXiv:1906.07797. [Online]. Available: http://arxiv.org/abs/1906.07797

[154]A. E. Hassanien, M. Breen, M.-H. Li, and S. Gong, “A theoretical study of acoustically driven antennas,” J. Appl. Phys., vol. 127, no. 1, Jan. 2020, Art. no. 014903.

[155]Hassanien, A.E., Breen, M., Li, MH. *et al.* Acoustically driven electromagnetic radiating elements. *Sci Rep* **10,** 17006 (2020). https://doi.org/10.1038/s41598-020-73973-6

[156]J. Weldon, K. Jensen and A. Zettl, “Nanomechanical radio transmitter”, Phys. Stat. Sol. (b) 245, No. 10, 2323-2325 (2008).

[157]H. Dong, J. Li, X. Gan, H. Guo, Y. Gao and W. Ren, "Fdtd Modeling Of Stress Source In Piezoelectric Materials," 2020 15th Symposium on Piezoelectrcity, Acoustic Waves and Device Applications (SPAWDA), 2021, pp. 546-550, doi: 10.1109/SPAWDA51471.2021.9445434.

[158]S. Gong, R. Lu, Y. Yang, L. Gao and A. E. Hassanien, "Microwave Acoustic Devices: Recent Advances and Outlook," in IEEE Journal of Microwaves, vol. 1, no. 2, pp. 601-609, April 2021, doi: 10.1109/JMW.2021.3064825.

[159]Y. Li et al., "Mechanical Principle of Piezoelectric-Promoted Mechanical Antenna," 2021 IEEE 4th International Conference on Electronic Information and Communication Technology (ICEICT), 2021, pp. 955-956, doi: 10.1109/ICEICT53123.2021.9531190.

[160]Cui, Yong, et al. "A survey of mechanical antennas applied for low-frequency transmitting." *Iscience* (2022).

[161] Xu, Jianchun, et al. "Ultra-Wideband Electrostrictive Mechanical Antenna." *Advanced Functional Materials* 33.8 (2023): 2210868.

[162] Cao, Jinqing, et al. "Dual-band piezoelectric artificial structure for very low frequency mechanical antenna." *Advanced Composites and Hybrid Materials* 5.1 (2022): 410-418.

[163] Z. Gao, M. Su, Y. Liu, C. Yan and X. Chen, "Metal-Loaded Acoustically Actuated Piezoelectric Antenna and Its Radiation Efficiency Limit," in IEEE Transactions on Antennas and Propagation, vol. 71, no. 5, pp. 3938-3949, May 2023, doi: 10.1109/TAP.2023.3249115.

[164] C. Pfeiffer, "Fundamental Efficiency Limits for Small Metallic Antennas," in IEEE Transactions on Antennas and Propagation, vol. 65, no. 4, pp. 1642-1650, April 2017, doi: 10.1109/TAP.2017.2670532.

[165] E. Teller, “Electromagnetism and gravitation”, Proc. Natl. Acad. Sci. USA, Vol. 74, No. 7, pp. 2664=2666, July 1977.

[166] J. A. Bickford, R. S. McNabb, P. A. Ward, D. K. Freeman, and M. S. Weinberg, “Low frequency mechanical antennas: Electrically short transmitters from mechanically-actuated dielectrics,” in Proc. IEEE Int. Symp. Antennas Propag. USNC/URSI Nat. Radio Sci. Meeting, 2017, pp. 1475–1476.

[167] N. Barani and K. Sarabandi, "Mechanical Antennas: Emerging Solution for Very-Low Frequency (VLF) Communication," 2018 IEEE International Symposium on Antennas and Propagation & USNC/URSI National Radio Science Meeting, 2018, pp. 95-96, doi: 10.1109/APUSNCURSINRSM.2018.8608412.

[168] J. A. Bickford, A. E. Duwel, M. S. Weinberg, R. C. McNabb, D. K. Freeman, and P. A.Ward, “Performance of electrically small conventional and mechanical antennas1,” IEEE Trans. Antennas Propag., vol. 67, no. 4, pp. 2209–2223, Apr. 2019.

[169] Alfven, H. 1953, Cosmical Electrodynamics (London: Oxford University Press).

[170] Backus, George. "The External Electric Field of a Rotating Magnet." The Astrophysical Journal 123 (1956): 508.

[171] Kaburaki, Osamu. "Determination of the electromagnetic field produced by a magnetic obliquerotator." Astrophysics and Space Science 58.2 (1978): 427-440.

[172] Garraud, A., et al. "Electrodynamic wireless power transmission to rotating magnet receivers." Journal of Physics: Conference Series. Vol. 557. No. 1. IOP Publishing, 2014.

[173] A. Garraud, D. J. Munzer, M. Althar, N. Garraud, D. P. Arnold, “Wattlevel wireless power transmission to multiple compact receivers,” Journal of Physics: Conference Series, Volume 660 (1), 012039 (2015).

[174] S. Selvin, M. N. Srinivas Prasad, Y. Huang, and E. Wang, “Spinning magnet antenna for VLF transmitting,” in 2017 IEEE International Symposium on Antennas and Propagation & USNC/URSI National Radio Science Meeting (IEEE, 2017), pp. 1477–1478.

[175] M. N. S. Prasad, Y. Huang and Y. E. Wang, "Going beyond Chu harrington limit: ULF radiation with a spinning magnet array," 2017 XXXIInd General Assembly and Scientific Symposium of the International Union of Radio Science (URSI GASS), Montreal, QC, 2017, pp. 1-3.

[176] M. N. S. Prasad, R. U. Tok and Y. E. Wang, "Magnetic Pendulum Arrays for ULF Transmission," 2018 IEEE International Symposium on Antennas and Propagation & USNC/URSI National Radio Science Meeting, 2018, pp. 71-72, doi: 10.1109/APUSNCURSINRSM.2018.8609255.

[177] M. N. Srinivas Prasad, R. U. Tok, F. Fereidoony, Y. E. Wang, R. Zhu, A. Propst, and S. Bland, "Magnetic pendulum arrays for efficient ULF transmission," Sci. Rep. 9, 13220 (2019).

[178] H. C. Burch, A. Garraud, M. F. Mitchell, R. C. Moore, and D. P. Arnold, "Experimental generation of ELF radio signals using a rotating magnet," IEEE Trans. Antennas Propag., vol. 66, no. 11, pp. 6265–6272, Nov. 2018.

[179] N. Barani and K. Sarabandi, "A Frequency Multiplier and Phase Modulation Approach for Mechanical Antennas Operating at Super Low Frequency (SLF) Band," 2019 IEEE International Symposium on Antennas and Propagation and USNC-URSI Radio Science Meeting, 2019, pp. 2169-2170, doi: 10.1109/APUSNCURSINRSM.2019.8888459.

[180] J. S. Glickstein, J. Liang, S. Choi, A. Madanayake and S. Mandal, "Power-Efficient ELF Wireless Communications Using Electro-Mechanical Transmitters," in IEEE Access, vol. 8, pp. 2455-2471, 2020, doi: 10.1109/ACCESS.2019.2961708.

[181] A. Hosseini-Fahraji, M. Manteghi and K. D. T. Ngo, "New Way of Generating Electromagnetic Waves," in IEEE Transactions on Antennas and Propagation, vol. 69, no. 10, pp. 6383-6390, Oct. 2021, doi: 10.1109/TAP.2021.3070635.

[182] Mao, Yu, Y. Liu, and Hai Lin. "Angular momenta in fields from a rotational mechanical antenna." Journal of Physics Communications 5.12 (2021): 125012.

[183] Kundu, Auni Aunnoyee. *Multiferroics for Future Cell Sorting Devices*. University of California, Los Angeles, 2019.

[184] C.M. Landis. A continuum thermodynamics formulation for micromagnetomechanics with applications to ferromagnetic shape memory alloys. Journal of the Mechanics and Physics of Solids, 56, 3059–3076, 2008.

[185] A. K. Mal, S. J. Singh *Deformation of Elastic Solids*. Pearson, 1991.

[186] K.S. Yee, Numerical solution of initial boundary value problems involving Maxwell's equations in isotropic media, IEEE Trans Antennas Propagat 14 (1966), 302–307.

[187] A. Taflove, Computational Electrodynamics. Norwood, MA: Artech House, 1995.

[188] Sadiki, M.N.O., Computational Electromagnetics with MATLAB, 4th Edition, CRC Press, 2018.

[189] Bérenger, Jean-Pierre. "Perfectly matched layer (PML) for computational electromagnetics." Synthesis Lectures on Computational Electromagnetics 2.1 (2007): 1-117.

[190] M. Kuzuoglu and R. Mittra, “Frequency dependence of the constitutive parameters of causal perfectly matched absorbers,” IEEE Microw. Guid. Wave Lett., vol. 6, pp. 447–449, 1996. doi:10.1109/75.544545.

[191] J. A. Roden and S. D. Gedney, "Convolutional PML (CPML): An efficient FDTD implementation of the CFS-PML for arbitrary media", *Microwave Opt. Technol. Lett.*, vol. 27, pp. 334-339, Dec. 2000.

[192] Schröder, Jörg, and Doru C. Lupascu. *Ferroic Functional Materials*. Springer International Publishing, 2018.

[193] D. V. Schroeder *An Introduction to Thermal Physics*. Oxford university press, 1999.

[194] Ikeda, Takurō. Fundamentals of piezoelectricity. Oxford university press, 1996.

[195] J.C. Simo, T.J.R. Hughes, *Computational Inelasticity*. Springer-Verlag, New York, 1998.

[196] J. Rivera et al., "Verification Testing of Multi-Dynamical Solver for Multiferroic Antennas," 2021 International Applied Computational Electromagnetics Society Symposium (ACES), 2021, pp. 1-4, doi: 10.1109/ACES53325.2021.00172.

[197] Skomski, Ralph. *Simple models of magnetism*. Oxford University Press on Demand, 2008.

[198] "IEEE Standard on Piezoelectricity," in ANSI/IEEE Std 176-1987 , vol., no., pp.0_1-, 1988, doi: 10.1109/IEEESTD.1988.79638.

[199] "IEEE Standard on Magnetostrictive Materials: Piezomagnetic Nomenclature," in *IEEE Transactions on Sonics and Ultrasonics*, vol. 20, no. 1, pp. 67-77, Jan. 1973, doi: 10.1109/T-SU.1973.29725.

[200] Gerdeen, James C., and Ronald AL Rorrer. *Engineering design with polymers and composites*. Vol. 30. CRC Press, 2011.

[201] K. Uchino and S. Hirose, "Loss mechanisms in piezoelectrics: how to measure different losses separately," in IEEE Transactions on Ultrasonics, Ferroelectrics, and Frequency Control, vol. 48, no. 1, pp. 307-321, Jan. 2001, doi: 10.1109/58.896144.

[202] A. V. Mezheritsky, "Elastic, dielectric, and piezoelectric losses in piezoceramics: how it works all together," in IEEE Transactions on Ultrasonics, Ferroelectrics, and Frequency Control, vol. 51, no. 6, pp. 695-707, June 2004, doi: 10.1109/TUFFC.2004.1304268.

[203] Moczo, P., J. O. A. Robertsson, and L. Eisner (2006), The finite difference time domain method for modeling of seismic wave propagation, in Advances in Wave Propagation in Hetergenous Earth, Adv.

Geophys., vol. 48, edited by R.-S Wu and V. Maupin, edited by R. Dmowska, Elsevier, New York, in press.

[204] Moczo P., Kristek J., Galis M., Pazak P., Balazovjech M., 2007. The finite-difference and finite-element modeling of seismic wave propagation and earthquake motion, Acta Physica Slovaca, 52(2), 177-406.

[205] Graves, R., 1996, Simulating seismic wave propagation in 3D elastic media using staggered-grid finite differences: Bulletin of the Seismological Society of America, 86, 1091–1106.

[206] J. Virieux, “SH wave propagation in heterogeneous media: velocity stress finite-difference method”, Geophysics 49, 1933-1957, 1984.

[207] A. Taflove and M. E. Brodwin, “Numerical solution of steady-state electromagnetic scattering problems using the time-dependant Maxwell’s equations,” IEEE Trans. Microw. Theory Tech., vol. 23, pp. 623–630, 1975. doi:10.1109/TMTT.1975.1128640

[208] R. Holland, “THREDE: A free-field EMP coupling and scattering code,” IEEE Trans. Nucl. Sci., vol. 24, pp. 2416–2421, 1977.

[209] B. Engquist and A. Majda, “Absorbing boundary conditions for numerical simulation of waves,” Proc. Natl. Acad. Sci. USA, vol. 74, no. 5, pp. 1765– 1766, 1977.

[210] G. Mur, "Absorbing Boundary Conditions for the Finite-Difference Approximation of the Time-Domain Electromagnetic-Field Equations," in IEEE Transactions on Electromagnetic Compatibility, vol. EMC-23, no. 4, pp. 377-382, Nov. 1981, doi: 10.1109/TEMC.1981.303970

[211] L. N. Trefethen and L. Halpern, “Well-posedness of one-way wave equations and absorbing boundary conditions,” Math. Comput., vol. 47, pp. 421–435, 1986. doi:10.2307/2008165

[212] Y. Yang, R. S. Chen, W. C. Tang, K. Sha, and E. K. N. Yung, “Analysis of planar circuits using unconditionally stable three-dimensional ADI-FDTD method,” Microw. Opt. Technol. Lett., vol. 46, no. 2, pp. 175–179, Jul. 20, 2005.

[213] R. Holland and J. Williams, “Total-field versus scattered-field finite-difference: A comparative assessment,” IEEE Trans. Nucl. Sci., vol. 30, pp. 4583–4588, 1983.

[214] J.-P. Berenger, “Calcul de la diffraction ´ a l’aide d’une m ` ethode aux diff ´ erences finies,” ´ CEM-83 Proc., Tregastel, France ´ , June 1983.

[215] J.-P. Berenger, “A perfectly matched layer for the absorption of electromagnetic waves,” J. Comput. Phys., vol. 114, no. 2, pp. 185–200, 1994.

[216] W. C. Chew and W. H. Weedon, "A 3-D perfectly matched medium from modified Maxwell's equations with stretched coordinates", Microwave Opt. Tech. Lett., vol. 7, pp. 599-604, Sept. 1994.

[217] C. M. Rappaport, “Perfectly matched absorbing conditions based on anisotropic lossy mapping of space,” IEEE Microw. Guid. Wave Lett., vol. 5–3, pp. 90–92, 1995. doi:10.1109/75.366463

[218] R. Mittra and U. Pekel, “A new look at the perfectly matched layer (PML) concept for the reflectionless absorption of electromagnetic waves,” IEEE Microw. Guid. Wave Lett., vol. 5–3, pp. 84–86, 1995. doi:10.1109/75.366461

[219] J. Fang and Z. Wu, “Generalized perfectly matched layer—An extension of Berenger’s perfectly matched layer boundary condition,” IEEE Microw. Guid. Wave Lett., vol. 5–12, pp. 451–453, 1995. doi:10.1109/75.481858

[220] J.-P. Berenger, “Perfectly matched layer for the FDTD solution of wave-structure interaction problems,” IEEE Trans. Antennas Propagat., vol. 44, pp. 110–117, 1996. doi:10.1109/8.477535

[221] J.-P. Berenger, “Numerical reflection from FDTD-PML’s: A comparison o ´ f the split PML with the unsplit and CFS PML’s,” IEEE Trans. Antennas Propagat., vol. 50, pp. 258–265, 2002. doi:10.1109/8.999615

[222] O. M. Ramahi, “Complementary operators: A method to annihilate artificial reflections arising from the truncation of the computational domain in the solution of partial differential equations,” IEEE Trans. Antennas Propagat., vol. 43, pp. 697–704, 1995. doi:10.1109/8.391141

[223] S. D. Gedney, Gang Liu, J. A. Roden and Aiming Zhu, "Perfectly matched layer media with CFS for an unconditionally stable ADI-FDTD method," in IEEE Transactions on Antennas and Propagation, vol. 49, no. 11, pp. 1554-1559, Nov. 2001, doi: 10.1109/8.964091.

[224] Zahradnik, J., P. Moczo, and F. Hron (1993). Testing four elastic finite difference schemes for behavior at discontinuities, Bull. Seism. Soc. Am. 83, 107-129.

[225] Boore, David M. "A note on the effect of simple topography on seismic SH waves." Bulletin of the seismological Society of America 62.1 (1972): 275-284.

[226] Ugural, Ansel C., and Saul K. Fenster. Advanced mechanics of materials and applied elasticity. Pearson Education, 2011.

[227] F. Zhen, Z. Chen, and J. Zhang, “Toward the development of a three-dimensional unconditionally stable finite-difference time-domain method,” IEEE Trans. Microw. Theory Techn., vol. 48, no. 9, pp. 1550–1558, Sep. 2000.

[228] Zheng, F., “Novel unconditionally stable finite-difference time-domain method for electromagnetic and microwave modeling,” PhD dissertation, Dalhousie University, 2001.

[229] F. Zheng and Z. Chen, "Numerical dispersion analysis of the unconditionally stable 3-D ADI-FDTD method," in IEEE Transactions on Microwave Theory and Techniques, vol. 49, no. 5, pp. 1006-1009, May 2001, doi: 10.1109/22.920165.

[230] S. G. Garcia, Tae-Woo Lee and S. C. Hagness, "On the accuracy of the ADI-FDTD method," in IEEE Antennas and Wireless Propagation Letters, vol. 1, pp. 31-34, 2002, doi: 10.1109/LAWP.2002.802583.

[231] Tae-Woo Lee and S. C. Hagness, "Wave source conditions for the unconditionally stable ADI-FDTD method," IEEE Antennas and Propagation Society International Symposium. 2001 Digest. Held in conjunction with: USNC/URSI National Radio Science Meeting (Cat. No.01CH37229), Boston, MA, USA, 2001, pp. 142-145 vol.4, doi: 10.1109/APS.2001.959419.

[232] Garcia, Bretones, Martin and Hagness, "Accurate implementation of current sources in the ADI-FDTD scheme," in IEEE Antennas and Wireless Propagation Letters, vol. 3, pp. 141-144, 2004, doi: 10.1109/LAWP.2004.831078.

[233] Chenghao Yuan and Zhizhang Chen, "Towards accurate time-domain simulation of highly conductive materials," 2002 IEEE MTT-S International Microwave Symposium Digest (Cat. No.02CH37278), 2002, pp. 1135-1138 vol.2, doi: 10.1109/MWSYM.2002.1011848.

[234] D. Y. Heh and E. L. Tan, "Efficient implementation of 3-D ADI-FDTD method for lossy media," 2009 IEEE MTT-S International Microwave Symposium Digest, 2009, pp. 313-316, doi: 10.1109/MWSYM.2009.5165696.

[235] D. Y. Heh and E. L. Tan, “Unified efficient fundamental ADI-FDTD schemes for lossy media,” Progr. Electromagn. Res. B, vol. 32, pp. 217–242, 2011.

[236] W. C. Tay & E. L. Tan (2010) Implementations of PMC and PEC Boundary Conditions for Efficient Fundamental ADI- and LOD-FDTD, Journal of Electromagnetic Waves and Applications, 24:4, 565-573, DOI: 10.1163/156939310790966187.

[237] Pitarka, Arben. "3D elastic finite-difference modeling of seismic motion using staggered grids with nonuniform spacing." *Bulletin of the Seismological Society of America* 89.1 (1999): 54-68.

[238] W. J. Bottega, Engineering Vibrations. CRC/Taylor & Francis, Boca Raton, 2006.

[239] COMSOL Multiphysics® v. 6.0. www.comsol.com. COMCOL AB, Stockholm, Sweden.

[240] Gedney, Stephen. Introduction to the finite-difference time-domain (FDTD) method for electromagnetics. Springer Nature, 2022.

[241] J. Zhou and J. Zhao, "Efficient High-Order Absorbing Boundary Condition for the ADI-FDTD Method," in IEEE Micro. and Wireless Comp. Letters, vol. 19, no. 1, pp. 6-8, Jan. 2009.

[242] A. Vansteenkiste et al., "The design and verification of mumax3", *AIP Adv.*, vol. 4, no. 10, 2014.

[243] Hashimoto, Ken-ya. RF bulk acoustic wave filters for communications. Artech House, 2009.

[244] TRS Technologies Resources Page. Available online: https://www.trstechnologies.com/Resources (accessed on January 22, 2024).

[245] Y. E. Wang, "Theory of Broadband Noise Matching for HF/VHF Receivers With Electrically Small Antennas," in IEEE Access, vol. 11, pp. 56574-56592, 2023, doi: 10.1109/ACCESS.2023.3282178.

[246] Wang, D., Fotinich, E., and Carman, G.P., “Influence of temperature on the Electro-mechanical and Fatigue Behavior of Piezoelectric Ceramics,” Journal of Applied Physics, May 1998, V 83, (no.10) pp. 5342-5350.

[247] Chaplya, P.M., Mitrovic, M., Carman, G.P., Straub, F.K., "Durability properties of piezoelectric stack actuators under combined electromechanical loading" Journal of Applied Physics, 100(12):124111 – 124124

[248] U. Azad and Y. E. Wang, “Direct antenna modulation (DAM) for enhanced capacity performance of near-field communication (NFC) link,” IEEE Trans. Circuits Syst. I Regul. Pap., vol. 61, no. 3, pp. 902–910, 2014.

[249] J. P. Dytioco Santos, F. Fereidoony, M. Hedayati and Y. E. Wang, "High Efficiency Bandwidth VHF Electrically Small Antennas Through Direct Antenna Modulation," IEEE Transactions on Microwave Theory and Techniques, vol. 68, no. 12, pp. 5029-5041, Dec. 2020.